The whole world is reading pirated papers *pp. 497 & 508*

Neurochemistry of sleeping and waking *pp. 517 & 550*

Halogenated olefins via the *E* train *p. 569*

Science

$15
29 APRIL 2016
sciencemag.org
AAAS

SPECIAL ISSUE

MICROBIOTA AT WORK

CONTENTS

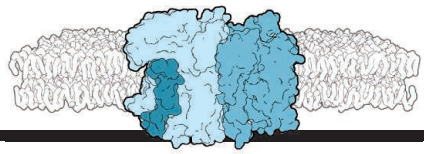

518 & 583
Structure of a membrane oxidase

29 APRIL 2016 • VOLUME 352 • ISSUE 6285

NEWS

IN BRIEF

498 News at a glance

IN DEPTH

501 **HOW EUROPE EXPORTED THE BLACK DEATH**
DNA suggests that the Asia-born pathogen lingered in Europe, then spread eastward *By A. Lawler*

502 **CRITICS COMPLAIN AS U.S. SHOPS IN IRAN'S NUCLEAR BAZAAR**
Heavy water purchase will benefit science, industry
By R. Stone

503 **SAYING NO TO HARASSMENT**
Roiled by high-profile cases in the field and at conferences, anthropology works to change its culture *By A. Gibbons and E. Culotta*

504 **KEPLER ENLISTS RELATIVITY TO FIND PLANETS**
Exotic search technique promises a small but rich harvest of extrasolar worlds *By D. Clery*

506 **SCANDAL CLOUDS CHINA'S GLOBAL VACCINE AMBITIONS**
Porous regulation of private preparations threatens to undermine vaccinemakers' bid to boost exports
By K. McLaughlin

507 **MEXICO STRUGGLES TO WOO EXPAT GENOME JOCKS**
Young guns flocking back to their homeland face a daunting bureaucracy
By L. Wade

FEATURES

508 **WHO'S DOWNLOADING PIRATED PAPERS? EVERYONE**
Data from the controversial website Sci-Hub reveal that the whole world turns to it for journal articles
By J. Bohannon

511 **The frustrated science student behind Sci-Hub** *By J. Bohannon*

▸ EDITORIAL P. 497

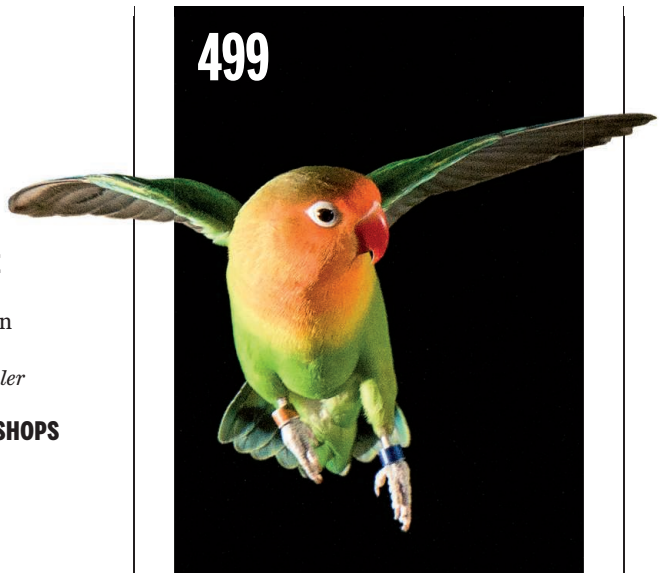

INSIGHTS

PERSPECTIVES

514 **A FRESH EYE ON NONEQUILIBRIUM SYSTEMS**
A noninvasive probe reveals nonequilibrium behavior in systems at steady state *By J.-F. Rupprecht and J. Prost*

▸ REPORT P. 604

516 **LIQUIDITY IN IMMUNE CELL SIGNALING**
Phase separation of proteins into liquid-like microclusters promotes T cell receptor signaling
By M. L. Dustin and J. Muller

▸ REPORT P. 595

517 **IONIC CONTROL OF SLEEP AND WAKEFULNESS**
The ionic composition of brain fluid is linked to neuronal activity and sleep
By H.-P. Landolt and S. C. Holst

▸ RESEARCH ARTICLE P. 550

518 **A BACTERIAL OXIDASE LIKE NO OTHER?**
The structure of an oxidase found in many pathogens will help in drug development *By G. M. Cook and R. K. Poole*

▸ REPORT P. 583

520 **LIGHT FLIPS A MEMBRANE-EMBEDDED HELIX**
A folded helical chain can switch its handedness even in a viscous membrane environment
By C. M. Thiele and A. S. Ulrich

▸ REPORT P. 575

521 **THE GROWING PROBLEM OF PATENT TROLLING**
Cash-hungry patent trolls are squelching innovation—and should be screened out *By L. Cohen* et al.

▸ POCAST

BOOKS *ET AL.*

524 **PANDEMIC**
By S. Shah, reviewed by C. Kemp

525 **ARE WE SMART ENOUGH TO KNOW HOW SMART ANIMALS ARE?**
By F. de Waal, reviewed by N. Clayton

525 **IT'S ALL IN YOUR HEAD**
By S. O'Sullivan

LETTERS

526 ***WOLBACHIA* MOSQUITO CONTROL: TESTED**
By S. L. O'Neill

526 ***WOLBACHIA* MOSQUITO CONTROL: REGULATED**
By S. L. Dobson et al.

527 **TECHNICAL COMMENT ABSTRACTS**

527 **ONLINE BUZZ: BUREAUCRACY OR ACCOUNTABILITY?**

DEPARTMENTS

497 **EDITORIAL**
My love-hate of Sci-Hub
By Marcia McNutt

▸ NEWS STORY P. 508

622 **WORKING LIFE**
The hidden perks of grad school
By Nathan Johnson

Science Staff 496
AAAS News & Notes 529
New Products 617
Science Careers 618

Downloaded from http://science.sciencemag.org/ on April 28, 2016

Published by AAAS

CONTENTS

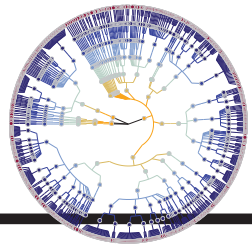

560 & 565
Gut microbiome diversity

29 APRIL 2016 • VOLUME 352 • ISSUE 6285

RESEARCH

IN BRIEF

546 From *Science* and other journals

RESEARCH ARTICLES

549 **STRUCTURAL BIOLOGY**
Structure and organization of heteromeric AMPA-type glutamate receptors *B. Herguedas* et al.
RESEARCH ARTICLE SUMMARY; FOR FULL TEXT: dx.doi.org/10.1126/science.aad3873

550 **SLEEP RESEARCH**
Changes in the composition of brain interstitial ions control the sleep-wake cycle
F. Ding et al.
▸ PERSPECTIVE P. 517

555 **REPRODUCTIVE BIOLOGY**
Unconventional endocannabinoid signaling governs sperm activation via the sex hormone progesterone
M. R. Miller et al.

560 **MICROBIOME**
Population-level analysis of gut microbiome variation *G. Falony* et al.
▸ MICROBIOME SECTION P. 530; REPORT P. 565

REPORTS

565 **MICROBIOME**
Population-based metagenomics analysis reveals markers for gut microbiome composition and diversity *A. Zhernakova* et al.
▸ MICROBIOME SECTION P. 530; RESEARCH ARTICLE P. 560

569 **ORGANIC CHEMISTRY**
Kinetically controlled *E*-selective catalytic olefin metathesis
T. T. Nguyen et al.

575 **CHEMISTRY**
Conformational photoswitching of a synthetic peptide foldamer bound within a phospholipid bilayer
M. De Poli et al.
▸ PERSPECTIVE P. 520

580 **GEOCHEMISTRY**
Pressure-dependent isotopic composition of iron alloys *A. Shahar* et al.

583 **STRUCTURAL BIOLOGY**
Structure of a bd oxidase indicates similar mechanisms for membrane-integrated oxygen reductases
S. Safarian et al.
▸ PERSPECTIVE P. 518

586 **MICROBIOME**
Durable coexistence of donor and recipient strains after fecal microbiota transplantation *S. S. Li* et al.
▸ MICROBIOME SECTION P. 530

590 **REPTILE SLEEP**
Slow waves, sharp waves, ripples, and REM in sleeping dragons
M. Shein-Idelson et al.

595 **SIGNAL TRANSDUCTION**
Phase separation of signaling molecules promotes T cell receptor signal transduction *X. Su* et al.
▸ PERSPECTIVE P. 516

600 **HUMAN GENETICS**
RNA splicing is a primary link between genetic variation and disease
Y. I. Li et al.

604 **BIOPHYSICS**
Broken detailed balance at mesoscopic scales in active biological systems
C. Battle et al.
▸ PERSPECTIVE P. 514

608 **MICROBIOTA**
Helminth infection promotes colonization resistance via type 2 immunity *D. Ramanan* et al.
▸ MICROBIOME SECTION P. 530

SPECIAL SECTION

Microbiome

INTRODUCTION

530 Manipulating the microbiota

REVIEWS

532 Cross-species comparisons of host genetic associations with the microbiome *J. K. Goodrich* et al.

535 Resurrecting the intestinal microbiota to combat antibiotic-resistant pathogens *E. G. Pamer*

539 How colonization by microbiota in early life shapes the immune system *T. Gensollen* et al.

PERSPECTIVE

544 Antibiotic use and its consequences for the normal microbiome *M. J. Blaser*

SEE ALSO

▸ RESEARCH ARTICLE P. 560
▸ REPORT P. 565
▸ REPORT P. 586
▸ REPORT P. 608

ON THE COVER

Artist's interpretation of a person's gut microbiota. Many factors contribute to the overall health of the microbiota: the bacteria themselves (depicted as either "good" or "bad" in blue and red, respectively), parasitic worms, viruses, food, medications, and our genetics, among other factors. Recent research on the microbiota and how it may be manipulated for better health is highlighted in a special section beginning on page 530. *Illustration: Nigel Sussman*

Downloaded from http://science.sciencemag.org/ on April 28, 2016

SCIENCE (ISSN 0036-8075) is published weekly on Friday, except the last week in December, by the American Association for the Advancement of Science, 1200 New York Avenue, NW, Washington, DC 20005. Periodicals mail postage (publication No. 484460) paid at Washington, DC, and additional mailing offices. Copyright © 2016 by the American Association for the Advancement of Science. The title SCIENCE is a registered trademark of the AAAS. Domestic individual membership and subscription (51 issues): $165 ($74 allocated to subscription). Domestic institutional subscription (51 issues): $1522; Foreign postage extra: Mexico, Caribbean (surface mail) $55; other countries (air assist delivery) $89. First class, airmail, student, and emeritus rates on request. Canadian rates with GST available upon request, GST #1254 88122. Publications Mail Agreement Number 1069624. **Printed in the U.S.A.**
Change of address: Allow 4 weeks, giving old and new addresses and 8-digit account number. **Postmaster:** Send change of address to AAAS, P.O. Box 96178, Washington, DC 20090–6178. **Single-copy sales:** $15.00 current issue, $20.00 back issue prepaid includes surface postage; bulk rates on request. **Authorization to photocopy** material for internal or personal use under circumstances not falling within the fair use provisions of the Copyright Act is granted by AAAS to libraries and other users registered with the Copyright Clearance Center (CCC) Transactional Reporting Service, provided that $35.00 per article is paid directly to CCC, 222 Rosewood Drive, Danvers, MA 01923. The identification code for *Science* is 0036-8075. *Science* is indexed in the *Reader's Guide to Periodical Literature* and in several specialized indexes.

Published by AAAS

Science
AAAS
1200 New York Avenue, NW, Washington, DC 20005
Bateman House, 82-88 Hills Road, Cambridge, UK CB2 1LQ

Editor-in-Chief Marcia McNutt
Executive Editor Monica M. Bradford **News Editor** Tim Appenzeller
Managing Editor, Research Journals Katrina L. Kelner
Deputy Editors Lisa D. Chong, Andrew M. Sugden(UK), Valda J. Vinson, Jake S. Yeston

Research and Insights

DEPUTY EDITOR, EMERITUS Barbara R. Jasny **SR. EDITORS** Caroline Ash(UK), Gilbert J. Chin, Julia Fahrenkamp-Uppenbrink(UK), Pamela J. Hines, Stella M. Hurtley(UK), Paula A. Kiberstis, Marc S. Lavine(Canada), Kristen L. Mueller, Ian S. Osborne(UK), Beverly A. Purnell, L. Bryan Ray, Guy Riddihough, H. Jesse Smith, Jelena Stajic, Peter Stern(UK), Phillip D. Szuromi, Sacha Vignieri, Brad Wible, Nicholas S. Wigginton, Laura M. Zahn **ASSOCIATE EDITORS** Brent Grocholski, Keith T. Smith **ASSOCIATE BOOK REVIEW EDITOR** Valerie B. Thompson **LETTERS EDITOR** Jennifer Sills **CHIEF CONTENT PRODUCTION EDITOR** Cara Tate **SR. CONTENT PRODUCTION EDITORS** Harry Jach, Lauren Kmec **CONTENT PRODUCTION EDITORS** Jeffrey E. Cook, Chris Filiatreau, Cynthia Howe, Barbara P. Ordway, Catherine Wolner **SR. EDITORIAL COORDINATORS** Carolyn Kyle, Beverly Shields **EDITORIAL COORDINATORS** Aneera Dobbins, Joi S. Granger, Lisa Johnson, Anita Wynn **PUBLICATIONS ASSISTANTS** Jeffrey Hearn, Dona Mathieu, Le-Toya Mayne Flood, Shannon McMahon, Scott Miller, Caitlyn Phillips, Jerry Richardson, Alice Whaley(UK), Brian White **EXECUTIVE ASSISTANT** Anna Bashkirova **ADMINISTRATIVE SUPPORT** Janet Clements(UK), Lizanne Newton(UK), Maryrose Madrid

News

NEWS MANAGING EDITOR John Travis **INTERNATIONAL EDITOR** Richard Stone **DEPUTY NEWS EDITORS** Robert Coontz, Elizabeth Culotta, David Grimm, David Malakoff, Leslie Roberts **CONTRIBUING EDITOR** Martin Enserink(Europe) **SR. CORRESPONDENTS** Daniel Clery(UK), Jeffrey Mervis, Elizabeth Pennisi **NEWS WRITERS** Adrian Cho, Jon Cohen, Jennifer Couzin-Frankel, Carolyn Gramling, Eric Hand, Jocelyn Kaiser, Catherine Matacic, Kelly Servick, Robert F. Service, Erik Stokstad(Cambridge, UK), Emily Underwood **INTERNS** Patrick Monahan **CONTRIBUTING CORRESPONDENTS** John Bohannon, Warren Cornwall, Ann Gibbons, Mara Hvistendahl, Sam Kean, Eli Kintisch, Kai Kupferschmidt(Berlin), Andrew Lawler, Christina Larson(Beijing), Mitch Leslie, Charles C. Mann, Eliot Marshall, Virginia Morell, Dennis Normile(Shanghai), Heather Pringle, Tania Rabesandratana(London), Gretchen Vogel(Berlin), Lizzie Wade(Mexico City) **CAREERS** Donisha Adams, Rachel Bernstein(Editor) **COPY EDITORS** Julia Cole, Dorie Chevlen, Jennifer Levin (Chief) **ADMINISTRATIVE SUPPORT** Jessica Adams

Executive Publisher Rush D. Holt
Interim Publisher Bill Moran **Chief Digital Media Officer** Rob Covey

BUSINESS OPERATIONS AND PORTFOLIO MANAGEMENT DIRECTOR Sarah Whalen **PRODUCT DEVELOPMENT DIRECTOR** Will Schweitzer **PRODUCT DEVELOPMENT ASSOCIATE** Hal Moore **BUSINESS SYSTEMS AND FINANCIAL ANALYSIS DIRECTOR** Randy Yi **MANAGER OF FULFILLMENT SYSTEMS** Neal Hawkins **SYSTEMS ANALYST** Nicole Mehmedovich **ASSISTANT DIRECTOR, BUSINESS OPERATIONS** Eric Knott **MANAGER, BUSINESS OPERATIONS** Jessica Tierney **SENIOR BUSINESS ANALYST** Cory Lipman **BUSINESS ANALYSTS** Sandy Kim, Meron Kebede **FINANCIAL ANALYST** Robert Clark **DIRECTOR, COPYRIGHTS LICENSING SPECIAL PROJECTS** Emilie David **PERMISSIONS ASSOCIATE** Elizabeth Sandler **RIGHTS, CONTRACTS, AND LICENSING ASSOCIATE** Lili Kiser

MARKETING DIRECTOR Elise Swinehart **ASSOCIATE MARKETING DIRECTOR** Christina Schlecht **MARKETING MANAGER** Elizabeth Sattler **MARKETING ASSOCIATE** Steven Goodman **CREATIVE DIRECTOR** Scott Rodgerson **SENIOR ART ASSOCIATES** Seil Lee, Paula Fry **ART ASSOCIATE** Kim Huynh **PROGRAM DIRECTOR, AAAS MEMBER CENTRAL** Peggy Mihelich **FULFILLMENT SYSTEMS AND OPERATIONS** membership@aaas.org **MANAGER, MEMBER SERVICES** Pat Butler **SPECIALISTS** Terrance Morrison, Latasha Russell **MANAGER, DATA ENTRY** Mickie Napoleoni **DATA ENTRY SPECIALISTS** Brenden Aquilino, Fiona Giblin

PUBLISHER RELATIONS MANAGER Catherine Holland **PUBLISHER RELATIONS, EASTERN REGION** Keith Layson **PUBLISHER RELATIONS, WESTERN REGION** Ryan Rexroth **SALES RESEARCH COORDINATOR** Aiesha Marshall **MANAGER, SITE LICENSE OPERATIONS** Iquo Edim **SENIOR OPERATIONS ANALYST** Lana Guz **FULFILLMENT ANALYST** Judy Lillibridge **ASSOCIATE DIRECTOR, MARKETING** Christina Schlecht **MARKETING ASSOCIATE** Isa Sesay-Bah

WEB TECHNOLOGIES SR. DEVELOPER Chris Coleman **DEVELOPERS** Dan Berger, Jimmy Marks, Ryan Jensen **SR. PROJECT MANAGER** Trista Smith **PROJECT MANAGER** Nick Fletcher

DIGITAL MEDIA DIRECTOR OF ANALYTICS Enrique Gonzales **DIGITAL REPORTING ANALYST** Eric Hossinger **SR. WEB PRODUCER** Sarah Crespi **WEB PRODUCER** Alison Crawford **VIDEO PRODUCER** Nguyen Nguyen **SOCIAL MEDIA PRODUCER** Brice Russ

DIRECTOR OF OPERATIONS PRINT AND ONLINE Lizabeth Harman **DIGITAL/PRINT STRATEGY MANAGER** Jason Hillman **QUALITY TECHNICAL MANAGER** Marcus Spiegler **PROJECT ACCOUNT MANAGER** Tara Kelly **DIGITAL PRODUCTION MANAGER** Lisa Stanford **ASSISTANT MANAGER DIGITAL/PRINT** Rebecca Doshi **SENIOR CONTENT SPECIALISTS** Steve Forrester, Antoinette Hodal, Lori Murphy, Anthony Rosen **CONTENT SPECIALISTS** Jacob Hedrick, Kimberley Oster

DESIGN DIRECTOR Beth Rakouskas **DESIGN EDITOR** Marcy Atarod **SENIOR DESIGNERS** Garvin Grullón, Chrystal Smith **GRAPHICS MANAGING EDITOR** Alberto Cuadra **SENIOR SCIENTIFIC ILLUSTRATORS** Chris Bickel, Katharine Sutliff **SCIENTIFIC ILLUSTRATOR** Valerie Altounian **INTERACTIVE GRAPHICS EDITOR** Jia You **SENIOR ART ASSOCIATES** Holly Bishop, Nathalie Cary, Preston Huey **PHOTOGRAPHY MANAGING EDITOR** William Douthitt **PHOTO EDITORS** Leslie Blizard, Christy Steele

DIRECTOR, GLOBAL COLLABORATION, CUSTOM PUBLICATIONS, ADVERTISING Bill Moran **EDITOR, CUSTOM PUBLISHING** Sean Sanders: 202-326-6430 **ADVERTISING MARKETING MANAGER** Justin Sawyers: 202-326-7061 science_advertising@aaas.org **ADVERTISING SUPPORT MANAGER** Karen Foote: 202-326-6740 **ADVERTISING PRODUCTION OPERATIONS MANAGER** Deborah Tompkins **SR. PRODUCTION SPECIALIST/GRAPHIC DESIGNER** Amy Hardcastle **SR. TRAFFIC ASSOCIATE** Christine Hall **SALES COORDINATOR** Shirley Young **ASSOCIATE DIRECTOR, COLLABORATION, CUSTOM PUBLICATIONS/CHINA/TAIWAN/KOREA/SINGAPORE** Ruolei Wu: +86-186 0082 9345, rwu@aaas.org **COLLABORATION/CUSTOM PUBLICATIONS/JAPAN** Adarsh Sandhu + 81532-81-5142 asandhu@aaas.org **EAST COAST/E. CANADA** Laurie Faraday: 508-747-9395, FAX 617-507-8189 **WEST COAST/W. CANADA** Lynne Stickrod: 415-931-9782, FAX 415-520-6940 **MIDWEST** Jeffrey Dembksi: 847-498-4520 x3005, Steven Loerch: 847-498-4520 x3006 **UK EUROPE/ASIA** Roger Goncalves: TEL/FAX +41 43 243 1358 **JAPAN** Katsuyoshi Fukamizu(Tokyo): +81-3-3219-5777 kfukamizu@aaas.org **CHINA/TAIWAN** Ruolei Wu: +86-186 0082 9345, rwu@aaas.org

WORLDWIDE ASSOCIATE DIRECTOR OF SCIENCE CAREERS Tracy Holmes: +44 (0) 1223 326525, FAX +44 (0) 1223 326532 tholmes@science-int.co.uk **CLASSIFIED** advertise@sciencecareers.org **U.S. SALES** Tina Burks: 202-326-6577, Nancy Toema: 202-326-6578 **EUROPE/ROW SALES** Sarah Lelarge **SALES ASSISTANT** Kelly Grace **JAPAN** Hiroyuki Mashiki(Kyoto): +81-75-823-1109 hmashiki@aaas.org **CHINA/TAIWAN** Ruolei Wu: +86-186 0082 9345 rwu@aaas.org **MARKETING MANAGER** Allison Pritchard **MARKETING ASSOCIATE** Aimee Aponte

AAAS BOARD OF DIRECTORS, CHAIR Geraldine L. Richmond **PRESIDENT** Barbara A. Schaal **PRESIDENT-ELECT** Susan Hockfield **TREASURER** David Evans Shaw **CHIEF EXECUTIVE OFFICER** Rush D. Holt **BOARD** Cynthia M. Beall, May R. Berenbaum, Carlos J. Bustamante, Stephen P.A. Fodor, Claire M. Fraser, Michael S. Gazzaniga, Laura H. Greene, Elizabeth Loftus, Mercedes Pascual

SUBSCRIPTION SERVICES For change of address, missing issues, new orders and renewals, and payment questions: 866-434-AAAS (2227) or 202-326-6417, FAX 202-842-1065. Mailing addresses: AAAS, P.O. Box 96178, Washington, DC 20090-6178 or AAAS Member Services, 1200 New York Avenue, NW, Washington, DC 20005

INSTITUTIONAL SITE LICENSES 202-326-6730 **REPRINTS:** Author Inquiries 800-635-7181 **COMMERCIAL INQUIRIES** 803-359-4578 **PERMISSIONS** 202-326-6765, permissions@aaas.org **AAAS Member Services** 202-326-6417 or http://membercentral.aaas.org/discounts

Science serves as a forum for discussion of important issues related to the advancement of science by publishing material on which a consensus has been reached as well as including the presentation of minority of conflicting points of view. Accordingly, all articles published in *Science*—including editorials, news and comment, and book reviews—are signed and reflect the individual views of the authors and not official points of view adopted by AAAS or the institutions with which the authors are affiliated.

INFORMATION FOR AUTHORS See pages 624 and 625 of the 5 February 2016 issue or access www.sciencemag.org/authors/science-information-authors

SENIOR EDITORIAL BOARD
Gary King, *Harvard University,* **Susan M. Rosenberg,** *Baylor College of Medicine,*
Ali Shilatifard, *Northwestern University Feinberg School of Medicine*

BOARD OF REVIEWING EDITORS (Statistics board members indicated with **(S)**)

Adriano Aguzzi, *U. Hospital Zürich*
Takuzo Aida, *U. of Tokyo*
Leslie Aiello, *Wenner-Gren Foundation*
Judith Allen, *U. of Edinburgh*
Sonia Altizer, *U. of Georgia*
Sebastian Amigorena, *Institut Curie*
Kathryn Anderson, *Memorial Sloan-Kettering Cancer Center*
Meinrat O. Andreae, *Max-Planck Inst. Mainz*
Paola Arlotta, *Harvard U.*
Johan Auwerx, *EPFL*
David Awschalom, *U. of Chicago*
Clare Baker, *University of Cambridge*
Nenad Ban, *ETH Zurich*
Jordi Bascompte, *University of Zurich*
Ray H. Baughman, *U. of Texas, Dallas*
David Baum, *U. of Wisconsin*
Carlo Beenakker, *Leiden U.*
Kamran Behnia, *ESPCI-ParisTech*
Yasmine Belkaid, *NIAID, NIH*
Philip Benfey, *Duke U.*
May Berenbaum, *U. of Illinois*
Gabriele Bergers, *U. of California, San Francisco*
Bradley Bernstein, *Massachusettes General Hospital*
Peer Bork, *EMBL*
Bernard Bourdon, *Ecole Normale Supérieure de Lyon*
Chris Bowler, *École Normale Supérieure*
Ian Boyd, *U. of St. Andrews*
Emily Brodsky, *U. of California, Santa Cruz*
Ron Brookmeyer, *U. of California Los Angeles* **(S)**
Christian Büchel, *U. Hamburg-Eppendorf*
Joseph A. Burns, *Cornell U.*
Carter Tribley Butts, *U. of California, Irvine*
Gyorgy Buzsaki, *New York U. School of Medicine*
Blanche Capel, *Duke U.*
Mats Carlsson, *U. of Oslo*
Ib Chorkendorff, *U. of Denmark*
David Clapham, *Children's Hospital Boston*
Joel Cohen, *Rockefeller U., Columbia U.*
James J. Collins, *MIT*
Robert Cook-Deegan, *Duke U.*
Lisa Coussens, *Oregon Health & Science U.*
Alan Cowman, *Walter & Eliza Hall Inst.*
Robert H. Crabtree, *Yale U.*
Roberta Croce, *Vrije Universiteit*
Janet Currie, *Princeton U.*
Jeff L. Dangl, *U. of North Carolina*
Tom Daniel, *U. of Washington*
Frans de Waal, *Emory U.*
Stanislas Dehaene, *Collège de France*
Robert Desimone, *MIT*
Claude Desplan, *New York U.*
Dennis Discher, *U. of Pennsylvania*
Gerald W. Dorn II, *Washington U. School of Medicine*
Jennifer A. Doudna, *U. of California, Berkeley*
Bruce Dunn, *U. of California, Los Angeles*
William Dunphy, *Caltech*
Christopher Dye, *WHO*
Todd Ehlers, *U. of Tuebingen*
David Ehrhardt, *Carnegie Inst. of Washington*
Tim Elston, *U. of North Carolina at Chapel Hill*
Gerhard Ertl, *Fritz-Haber-Institut, Berlin*
Barry Everitt, *U. of Cambridge*
Ernst Fehr, *U. of Zurich*
Anne C. Ferguson-Smith, *U. of Cambridge*
Michael Feuer, *The George Washington U.*
Toren Finkel, *NHLBI, NIH*
Kate Fitzgerald, *U. of Massachusetts*
Peter Fratzl, *Max-Planck Inst.*
Elaine Fuchs, *Rockefeller U.*
Daniel Geschwind, *UCLA*
Karl-Heinz Glassmeier, *TU Braunschweig*
Ramon Gonzalez, *Rice U.*
Julia R. Greer, *Caltech*
Elizabeth Grove, *U. of Chicago*
Nicolas Gruber, *ETH Zurich*
Kip Guy, *St. Jude's Children's Research Hospital*
Taekjip Ha, *U. of Illinois at Urbana-Champaign*
Wolf-Dietrich Hardt, *ETH Zurich*
Christian Haass, *Ludwig Maximilians U.*
Sharon Hammes-Schiffer, *U. of Illinois at Urbana–Champaign*
Michael Hasselmo, *Boston U.*
Martin Heimann, *Max-Planck Inst. Jena*
Yka Helariutta, *U. of Cambridge*
James A. Hendler, *Rensselaer Polytechnic Inst.*
Janet G. Hering, *Swiss Fed. Inst. of Aquatic Science & Technology*
Kai-Uwe Hinrichs, *U. of Bremen*
David Hodell, *U. of Cambridge*
Lora Hooper, *UT Southwestern Medical Ctr. at Dallas*
Tamas Horvath, *Yale University*
Raymond Huey, *U. of Washington*
Fred Hughson, *Princeton U.*
Auke Ijspeert, *EPFL Lausanne*
Stephen Jackson, *USGS and U. of Arizona*
Steven Jacobsen, *U. of California, Los Angeles*
Kai Johnsson, *EPFL Lausanne*
Peter Jonas, *Inst. of Science & Technology (IST) Austria*
Matt Kaeberlein, *U. of Washington*
William Kaelin Jr., *Dana-Farber Cancer Inst.*
Daniel Kahne, *Harvard U.*
Daniel Kammen, *U. of California, Berkeley*
Abby Kavner, *U. of California, Los Angeles*
Masashi Kawasaki, *U. of Tokyo*
V. Narry Kim, *Seoul National U.*
Joel Kingsolver, *U. of North Carolina at Chapel Hill*
Robert Kingston, *Harvard Medical School*
Etienne Koechlin, *Ecole Normale Suprieure*
Alexander Kolodkin, *Johns Hopkins U.*
Thomas Langer, *U. of Cologne*
Mitchell A. Lazar, *U. of Pennsylvania*
David Lazer, *Harvard U.*
Thomas Lecuit, *IBDM*
Virginia Lee, *U. of Pennsylvania*
Stanley Lemon, *U. of North Carolina at Chapel Hill*
Ottoline Leyser, *Cambridge U.*
Wendell Lim, *U.C. San Francisco*
Marcia C. Linn, *U. of California, Berkeley*
Jianguo Liu, *Michigan State U.*
Luis Liz-Marzan, *CIC biomaGUNE*
Jonathan Losos, *Harvard U.*
Ke Lu, *Chinese Acad. of Sciences*
Christian Lüscher, *U. of Geneva*
Laura Machesky, *CRUK Beatson Inst. for Cancer Research*
Anne Magurran, *U. of St. Andrews*
Oscar Marin, *CSIC & U. Miguel Hernández*
Charles Marshall, *U. of California, Berkeley*
C. Robertson McClung, *Dartmouth College*
Graham Medley, *U. of Warwick*
Tom Misteli, *NCI*
Yasushi Miyashita, *U. of Tokyo*
Mary Ann Moran, *U. of Georgia*
Richard Morris, *U. of Edinburgh*
Alison Motsinger-Reif, *NC State U.* **(S)**
Thomas Murray, *The Hastings Center*
Daniel Neumark, *U. of California, Berkeley*
Kitty Nijmeijer, *U. of Twente*
Pär Nordlund, *Karolinska Inst.*
Helga Nowotny, *European Research Advisory Board*
Ben Olken, *MIT*
Joe Orenstein, *U. of California Berkeley & Lawrence Berkeley National Lab*
Harry Orr, *U. of Minnesota*
Pilar Ossorio, *U. of Wisconsin*
Andrew Oswald, *U. of Warwick*
Steve Palumbi, *Stanford U.*
Jane Parker, *Max-Planck Inst. of Plant Breeding Research*
Giovanni Parmigiani, *Dana-Farber Cancer Inst.* **(S)**
John H. J. Petrini, *Memorial Sloan-Kettering Cancer Center*
Samuel Pfaff, *Salk Institute for Biological Studies*
Joshua Plotkin, *U. of Pennsylvania*
Albert Polman, *FOM Institute AMOLF*
Philippe Poulin, *CNRS*
Jonathan Pritchard, *Stanford U.*
David Randall, *Colorado State U.*
Felix Rey, *Institut Pasteur*
Trevor Robbins, *U. of Cambridge*
Jim Roberts, *Fred Hutchinson Cancer Research Ctr.*
Barbara A. Romanowicz, *U. of California,Berkeley*
Amy Rosenzweig, *Northwestern University*
Mike Ryan, *U. of Texas, Austin*
Mitinori Saitou, *Kyoto U.*
Shimon Sakaguchi, *Kyoto U.*
Miquel Salmeron, *Lawrence Berkeley National Lab*
Jürgen Sandkühler, *Medical U. of Vienna*
Alexander Schier, *Harvard U.*
Vladimir Shalaev, *Purdue U.*
Robert Siliciano, *Johns Hopkins School of Medicine*
Denis Simon, *Arizona State U.*
Uri Simonsohn, *U. of Pennsylvania*
Alison Smith, *John Innes Centre*
Richard Smith, *U. of North Carolina* **(S)**
John Speakman, *U. of Aberdeen*
Allan C. Spradling, *Carnegie Institution of Washington*
Jonathan Sprent, *Garvan Inst. of Medical Research*
Eric Steig, *U. of Washington*
Paula Stephan, *Georgia State U. and National Bureau of Economic Research*
Molly Stevens, *Imperial College London*
V. S. Subrahmanian, *U. of Maryland*
Ira Tabas, *Columbia U.*
Sarah Teichmann, *Cambridge U.*
John Thomas, *North Carolina State U.*
Shubha Tole, *Tata Institute of Fundamental Research*
Christopher Tyler-Smith, *The Wellcome Trust Sanger Inst.*
Herbert Virgin, *Washington U.*
Bert Vogelstein, *Johns Hopkins U.*
Cynthia Volkert, *U. of Göttingen*
David Wallach, *Weizmann Inst. of Science*
Ian Walmsley, *U. of Oxford*
Jane-Ling Wang, *U. of California, Davis* **(S)**
David A. Wardle, *Swedish U. of Agric. Sciences*
David Waxman, *Fudan U.*
Jonathan Weissman, *U. of California, San Francisco*
Chris Wikle, *U. of Missouri* **(S)**
Ian A. Wilson, *The Scripps Res. Inst.* **(S)**
Timothy D. Wilson, *U. of Virginia*
Rosemary Wyse, *Johns Hopkins U.*
Jan Zaanen, *Leiden U.*
Kenneth Zaret, *U. of Pennsylvania School of Medicine*
Jonathan Zehr, *U. of California, Santa Cruz*
Len Zon, *Children's Hospital Boston*
Maria Zuber, *MIT*

BOOK REVIEW BOARD
David Bloom, *Harvard U.,* **Samuel Bowring,** *MIT,* **Angela Creager,** *Princeton U.,*
Richard Shweder, *U. of Chicago,* **Ed Wasserman,** *DuPont*

Published by AAAS

EDITORIAL

My love-hate of Sci-Hub

Marcia McNutt
Editor-in-Chief
Science *Journals*

Like many scientist-editors of journals published by nonprofit scientific societies, I have a love-hate relationship with Sci-Hub, the website operated out of Russia that provides access to 50 million pirated scientific articles to researchers worldwide (see the News story on p. 508). I recognize the underlying motivation of bringing global research content to the developing world. However, I also recognize that much traffic to Sci-Hub is from researchers who already have access to the articles they seek through mechanisms such as site licenses, open access, or other means. Authors who publish in *Science* journals, for example, can make their papers available immediately upon publication through free referrer links at the authors' websites. Research published after 1996 in a *Science* journal is made free with registration 1 year after its publication date. So what does the scientific community risk by gathering papers illegally?

The collateral damage may not seem obvious. When researchers access papers through Sci-Hub, article usage information is lost. Authors do not benefit from download statistics, for example, which are increasingly being used to assess the impact of their work. Libraries cannot properly track usage for the journals they provide and could wind up discontinuing titles that are useful to their institution. As institutions cancel subscriptions, the ability of nonprofit scientific societies to provide journals and support their research communities is diminished. Journals published by scientific societies such as the American Association for the Advancement of Science (the publisher of *Science* journals) are not the sole contribution to the research community; such nonprofit societies also support a range of efforts that have a history of benefiting the greater scientific enterprise, such as fellowships for young scientists, advocacy for science, science diplomacy, science education, and fostering science's many interfaces with culture and society. Like nonprofit scientific societies, university presses, largely subsidized by their parent institutions, are also at risk. These publishers already face many challenges, which now include Sci-Hub's unauthorized collection of their monographs.

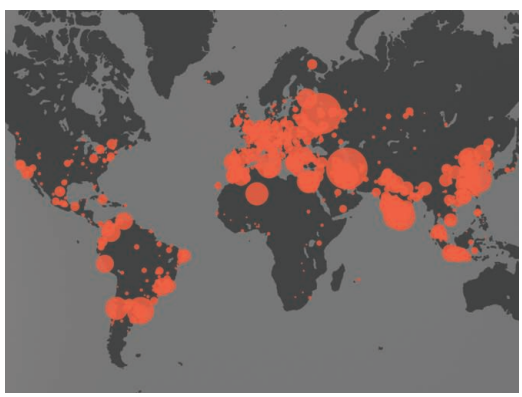

One hour of Sci-Hub activity in February 2016

"...what does the scientific community risk by gathering papers illegally?"

Journals have real costs, even though they don't pay authors or reviewers, as they help ensure accuracy, consistency, and clarity in scientific communication. For most of the *Science* journals, editors are paid professionals who carefully curate the journal content to bring readers an important and exciting array of discoveries. They make sure that papers are complete and conform to standards of quality, transparency, openness, and integrity. There are layers of effort by copyeditors and proofreaders to check for adherence to standards in scientific usage of terms to prevent confusion. Illustrators create original illustrations, diagrams, and charts to help convey complex messages. Scientific communicators spread the word to top media outlets so that authors get excellent coverage and readers do not miss important discoveries. Our news reporters are constantly searching the globe for issues and events of interest to the research and nonscience communities. Our agile Internet technology department continually evolves the website, so that authors can submit their manuscripts and readers can access the journals more conveniently.

The costs of scientific publishing are increasing worldwide, driven by the expansion of content, which includes more contributions from the developing world, as well as open-access papers, which are supported through a different business model. Today, digital publishing is just as expensive as print for a state-of-the-art Web design that incorporates multimedia, is responsive to desktops, tablets, and smartphones, and maintains access to back content.

Scientific nonprofit societies do indeed understand the need to continue addressing research accessibility by those in challenged regions, but through legitimate means. For those who have such avenues but choose to pirate a paper instead, ask yourself whether it is worth risking the viability of a system that supports the quality and integrity of science. And please let us know your view of Sci-Hub: love or hate? (http://bit.ly/Sci-Hub)

– **Marcia McNutt**

10.1126/science.aaf9419

PHOTO: STACEY PENTLAND PHOTOGRAPHY; MAP: J. YOU/*SCIENCE*

Downloaded from http://science.sciencemag.org/ on April 28, 2016

Published by AAAS

> “It’s set up in a way that will breed success.”
>
> Harvard pediatric epidemiologist **Matthew Gillman**, who will head the National Institutes of Health’s Environmental influences on Child Health Outcomes program. The 7-year study will replace the $1.3 billion National Children’s Study, canceled in late 2014. **http://bit.ly/GillmanNIH**

IN BRIEF

Mount Pinatubo’s 1991 eruption was preceded by a magnitude-7.7 earthquake.

Earthquakes can trigger faraway volcanoes

Scientists have long wondered why big earthquakes are sometimes followed by volcanic eruptions far from the quake’s epicenter. For example, the massive 1991 eruption of Mount Pinatubo in the Philippines was suggestively preceded a year earlier by a magnitude-7.7 earthquake 100 kilometers away. In many cases, it may be coincidence: Earthquakes and volcanic eruptions tend to be clumped in space and time, because both often occur along the grinding boundaries of tectonic plates in Earth’s crust. But a new study suggests that the idea that big earthquakes can cause a distant volcanic eruption—called “far-field triggering”—is not so far-fetched as once thought. A team led by volcanologist Atsuko Namiki of Hiroshima University in Japan simulated earthquake shockwaves rocking laboratory chambers of glucose syrup “magma,” testing the quakes’ effect on various viscosities, volumes, crystal contents, and bubble fractions. The experiments revealed that by sloshing around bubbly magma in distant volcanic chambers, big earthquakes may help release gases that can increase magma pressure and lead to an eruption, the researchers report this month in the *Journal of Volcanology and Geothermal Research*. **http://bit.ly/EQvolcanoes**

AROUND THE WORLD

Europe bets big on quantum tech

BRUSSELS | Two years after the European Commission announced its first two Flagship projects, the organization has picked a third research area where it hopes to have a major impact by spending a massive amount of cash. Research groups across the continent will receive up to €1 billion over the next 10 years to develop quantum technologies, which might be used to develop anything from faster computers and very secure communication systems to ultrasensitive sensors and more precise atomic clocks. The project “should place Europe at the forefront of the second quantum revolution, bringing transformative advances to science, industry, and society within the decade to come,” a spokesperson for the European Commission says. Two other Flagship projects have been underway in the European Union since 2014: One focuses on the study of graphene, the other on a computer model of the entire human brain. They were selected after an exhaustive

PHOTO: © ALBERTO GARCIA/CORBIS

Downloaded from http://science.sciencemag.org/ on April 28, 2016

Published by AAAS

high-profile contest and announced with a series of media events. This time, there was no formal competition, and the project's announcement was hidden in a short sentence in a long document this week describing plans to "digitize European industry." http://bit.ly/ECquantumtech

'German Ivy League' gets boost

BERLIN | Germany's Excellence Initiative, a €4.6 billion program launched in 2006, was meant to boost research at German universities to world-class status. On 22 April, the German government announced that the program, which gives extra support to a few top universities, will be extended indefinitely. The new plan will divide an annual sum of €533 million in several ways: Groups of researchers may apply to become an "excellence cluster," and between 45 and 50 such clusters will receive up to €10 million per year; their university hosts will receive an extra €1 million. Universities that host at least two clusters can also apply to be designated an "excellence university." Between eight and 11 excellence universities will receive up to €15 million per year in extra funding starting in 2019. The government will evaluate the winning universities after 7 years to determine whether they should keep their status. Chancellor Angela Merkel and the leaders of the German states are expected to sign off on the plan in June. http://bit.ly/Germanivies

Government hampered probe

MEXICO CITY | The Mexican government obstructed the investigation into the disappearance of 43 students in 2014, says the group of international experts sent by the Inter-American Court of Human Rights to investigate the case. The group's second and final report, issued on 24 April, emphasizes that the Attorney General's office became uncooperative after the release of the group's first report, which criticized the government's story.

Activists call for the investigation of 43 students who went missing in 2014 from a teachers' college.

PHOTOS: (LEFT TO RIGHT) REUTERS/EDGARD GARRIDO; STANFORD NEWS SERVICE

High-speed color video cameras in a new wind tunnel capture the details of bird and drone flight.

What it looks like when birds fly

Drone engineers wish their machines were as agile as birds, which maneuver handily around obstacles and stay airborne and on course even amid gusty winds. Now, a sophisticated new wind tunnel might help reveal some of those secrets of flight. David Lentink, a mechanical engineer at Stanford University in Palo Alto, California, has built a 2-meter-long chamber with a Volkswagen Beetle–sized fan at one end that can blast gusts at speeds of up to 50 meters per second. Previous laboratory wind tunnels have aimed to recreate calm conditions, enabling researchers to study the effects of drag, lift, and other forces involved in flight. But Stanford's new tunnel can also simulate complex turbulence patterns using computer-controlled wind vanes and can create up to 50% turbulence—challenging conditions even for a bird. The new tunnel "is going to be a huge step forward," says physiological ecologist Chris Guglielmo of Western University in London, Canada. Researchers will capture the details of bird and drone flight with high-speed color video, and future plans include the addition of fluoroscopes—medical imaging instruments that use x-rays—in order to visualize how the birds' muscles and skeletons move.

The experts also say they were subjected to a smear campaign in the press. The group stands by the conclusions of an investigation by fire scientist José Torero of the University of Queensland, St. Lucia, in Brisbane, Australia, which concluded that it was impossible that the bodies of the students had been burned in a local dump, as the state originally claimed (*Science*, 11 March, p. 1141).

Pushback at postdocs' lawsuits

MADRID | In the past few years, hundreds of postdocs, technicians, and administrative staff at the Spanish National Research Council (CSIC) have obtained a permanent position in an unusual way: by suing their employer. CSIC has been moving from lifetime civil servant employment to introducing more short-term contracts funded by research grants and industry contracts. But many short-term employees have sued, citing a 2006 law that says that Spanish workers who have served more than 24 months in short-term contracts during the previous 30 months are entitled to an open-ended contract. Now, CSIC is pushing back: An internal memo recently leaked to national newspaper *El País* outlines a series of measures that many say punish the institutes and research groups where such cases have occurred. The memo states that institutes with the highest "litigiousness levels" can only hire new short-term employees if they can demonstrate that their current staff can't do the job, and that institutes with fewer court cases will be given priority in the allocation of 275 new competitive permanent positions that CSIC just announced for 2016. The measures have drawn criticism from the scientific community and angered trade unions. http://bit.ly/CSIClawsuits

NIH to improve hospital safety

BETHESDA, MARYLAND | The U.S. National Institutes of Health (NIH) has pledged to beef up safety at the agency's Clinical Center after a working group found a slew of problems. The review, triggered by the discovery of fungal contamination in two vials of drugs from a pharmacy sterile production unit last year (http://bit.ly/NIHfungalscare), found "substantial operations issues" involving

Downloaded from http://science.sciencemag.org/ on April 28, 2016

Published by AAAS

patient safety, regulatory compliance, and leadership at the 240-bed research hospital. NIH Director Francis Collins announced a series of reforms last week, including a new compliance office and hospital board composed of mostly outside experts. The agency also revealed last week that problems at two other NIH manufacturing facilities had led to the suspension of a brain imaging study and several trials using engineered immune cells to treat cancer.

A giant human genome pool

LONDON | Pharmaceutical giant AstraZeneca is joining forces with several heavy hitters in genetic sequencing to mine up to 2 million people's genomes for new drug targets. The London-based company last week launched an in-house genomics center that will swap data and samples with Human Longevity, Inc.—geneticist J. Craig Venter's ambitious genomics startup—and will embed a research team in the U.K. Wellcome Trust's Sanger Institute. The company expects that whole genomes, combined with individual health data, will reveal rare genetic variants that influence disease and suggest new drug targets. Many in the field hope such an enterprise will jump-start a field that has promised for more than a decade to find drugs based on disease-causing mutations. "This is about finally getting some horsepower to get us to the big data, whole genome level," says geneticist Eric Topol of the Scripps Research Institute in San Diego, California, who is not involved in the partnership. **http://bit.ly/AstraZenpartner**

CSIRO outlines staff cuts

CANBERRA | After months of uncertainty, scientists at Australia's Commonwealth Scientific and Technological Organization (CSIRO) learned their fate this week. More than 275 jobs will be cut as part of a restructuring announced in February by CSIRO Chief Executive Larry Marshall (*Science*, 12 February, p. 649). Climate science will take the biggest hit, with up to 75 jobs lopped from the Oceans and Atmosphere division. In an email to staff sent 26 April, Marshall said that 40 climate research positions would be retained "for the next decade" at a new Climate Science Center in Hobart, Australia; those researchers will "focus on climate modeling." He also guaranteed support for CSIRO's observational infrastructure. "While the retention of some of CSIRO's climate science capabilities is welcome, the level announced is analogous to trying to put a sticking plaster over a gaping wound," says climate scientist Dave Griggs, the former director of the Monash Sustainability Institute at Monash University in Melbourne, Australia. **http://bit.ly/_CSIROcuts**

Divergent paths for U.S. energy research

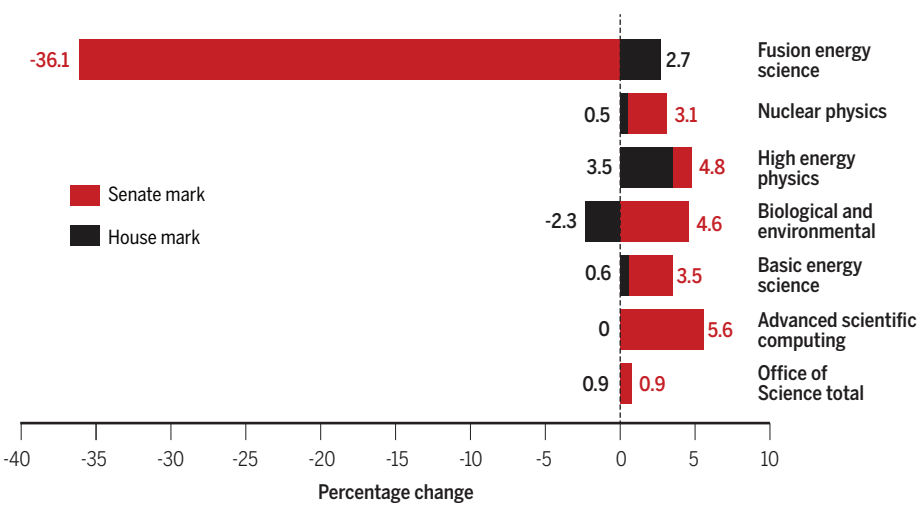

Given the complexity of the U.S. budget process, it's tempting to monitor the health of research by simply looking at the bottom line. But although legislators in both houses of Congress agree that science at the Department of Energy (DOE) should get a $50 million bump in 2017, to $5.4 billion, they are worlds apart on how to reach that number. This week the Senate was expected to complete work on a spending bill that would eliminate support for the international fusion project ITER and would trim domestic fusion research while boosting DOE's five other research programs. But a companion bill in the House of Representatives would continue funding ITER and fusion at the expense of biological and environmental research, while holding most other DOE science programs to tiny increases. Only high-energy physics wins the blessing of both houses. Meanwhile, a Senate spending panel last week approved a nearly flat budget for the National Science Foundation (NSF)—but gave a big boost to the nation's academic research fleet, allocating money to start building a third regional research vessel in addition to the two that NSF requested. NASA's science programs would be shrunk under the bill, which so far has no House counterpart.

NEWSMAKERS

Three Qs

A trio of Nobel laureates heads to North Korea next week on a mission of science diplomacy. On behalf of the private International Peace Foundation, the laureates are tasked with helping "establish common research programs and other sustainable forms of cooperation, therefore enhancing science and education as a basis for peace and development." *Science* caught up with Nobel laureate **Richard Roberts** of New England Biolabs in Ipswich, Massachusetts, on the eve of his departure. Roberts, who will give a speech at Kim Il-sung University in Pyongyang, shared the Nobel Prize for Medicine in 1993 for the discovery of split genes.

Q: Your speech alludes to Biolabs's "philosophy towards business and life." How does that translate to a country devoid of private enterprise in science?
A: I see this as an opportunity to explain how companies work outside North Korea. They need to know what goes on in the rest of the world.

Q: How do you discuss challenging dogma in a society in which people can be sent to labor camps for not towing the line?
A: It's a point I've made in talks in many countries, and I try to do it with humor, and through anecdotes. Later on, they will think about it.

Q: What's one seditious anecdote you'll share?
A: How all of a sudden, your life can change. I stopped going to school because it was so boring, and became extremely proficient at billiards and snooker. I thought about turning professional. But at some point I started reading *The Thread of Life* [: *An Introduction to Molecular Biology*] by John Kendrew. By the time I finished, I wanted to become a molecular biologist.

GRAPHIC: A. CUADRA/*SCIENCE*

Downloaded from http://science.sciencemag.org/ on April 28, 2016

Published by AAAS

The plague strain that killed millions in medieval Europe may have evolved into today's disease.

IMAGE: *BLACK DEATH AT TOURNAI*, 1349 (SEE ALSO 33793), LE MUSIT, GILLES (1272–1352)/BIBLIOTHÈQUE ROYALE DE BELGIQUE, BRUSSELS/BRIDGEMAN IMAGES

ANCIENT DNA

How Europe exported the Black Death

DNA suggests that the Asia-born pathogen lingered in Europe, then spread eastward

By **Andrew Lawler**, *in Orlando, Florida*

The medieval Silk Road brought a wealth of goods, spices, and new ideas from China and Central Asia to Europe. In 1346, the trade also likely carried the deadly bubonic plague that killed as many as half of all Europeans within 7 years, in what is known as the Black Death. Later outbreaks in Europe were thought to have arrived from the east via a similar route. Now, scientists have evidence that a virulent strain of the Black Death bacterium lurked for centuries in Europe while also working its way back to Asia, with terrifying consequences.

At the recent Society for American Archaeology meetings here, researchers reported analyzing the remains of medieval victims in London; Barcelona, Spain; and Bolgar, a city along the Volga River in Russia. They determined that the victims all died of a highly similar strain of *Yersinia pestis*, the plague bacterium, which mutated in Europe and then traveled eastward in the decade following the Black Death. The findings "are like pearls on a chain" that begins in western Europe, said Johannes Krause at the Max Planck Institute for the Science of Human History in Jena, Germany, an author of a soon-to-be-published study. (The lead author is Maria Spyrou, also at Jena.)

> ***"If the plague in China was actually European in origin, it's a cruel irony of history."***
> **Eric Klingelhofer,** Mercer University

That chain may have stretched far beyond Russia. Krause argues that a descendant of the 14th century plague bacterium was the source of most of the world's major outbreaks, including those that raged across East Asia in the 19th and 20th centuries and one afflicting Madagascar today. Eric Klingelhofer, an emeritus archaeologist at Mercer University, Macon, in Georgia, called Krause's presentation "a good piece of research." But molecular microbiologist Holger Scholz at Munich, Germany's Bundeswehr Institute of Microbiology is skeptical. "I just think it's not very likely that a strain from China came to Europe, survived there for a couple of hundred years, and moved back to China," she said. "That sounds pretty adventurous."

Advances in sequencing the DNA of pathogens found in ancient human skeletons are driving new research—and debate—on the spread of plague. Thanks to a series of recent findings, the notion that plague remained in Europe for centuries after the Black Death, rather than arriving in repeated waves from Asia as historians long assumed, is gaining ground.

A team led by Lisa Seifert at Munich, Germany's Ludwig Maximilian University reported in January that the Black Death strain persisted in Europe for at least 3 centuries, based on DNA sequences from

Downloaded from http://science.sciencemag.org/ on April 28, 2016

Published by AAAS

eight skeletons at two burial sites in Germany that spanned the 14th to the 17th centuries. The sequences were "highly similar" to those from earlier European victims, according to the study, which included Scholz. While not precluding continued waves of plague coming from Asia, the team concluded that there was "a long-time persistence of the pathogen in a not-yet-identified reservoir"—perhaps rats.

Also in January, a team led by Kirsten Bos at Jena's Max Planck Institute reported further evidence that a descendant of the Black Death strain hung on in Europe, implicating it in the last major European plague outbreak, in Marseille, France. Using DNA from the teeth of five individuals who died in 1722, the group found that the *Y. pestis* strain in Marseille likely evolved from the Black Death. "Our results suggest that the disease was hiding somewhere in Europe for several hundred years," said Bos, whose team included Krause.

Now, Krause has traced the Black Death's eastward spread. His team studied skeletons from a cemetery near the Tower of London firmly dated to 1348–1350, in the wake of the Black Death, as well as from a Barcelona cemetery radiocarbon-dated to the mid-14th century. The Russian evidence comes from a site that included coins from 1360; the burial is estimated to have taken place between the early 1360s and 1400. DNA sequencing from all three places revealed the same strain of *Y. pestis*. This strain appears to be the ancestor of the one that killed millions in 19th century China, based on phylogenetic clues.

"If the plague in China was actually European in origin, it's a cruel irony of history," says Klingelhofer, who notes that this was the era when Western powers dominated China. Krause adds that the plague affecting Madagascar as recently as last year also seems genetically related to the variety that spread east from Europe in the 14th century.

Researchers are eager to create a plague family tree in order to understand the movements and impact of different varieties of *Y. pestis* across time and space. Krause argues that three of the four branches of plague seem to have evolved in Asia. But he says the branch related to the strain that developed in Europe immediately after the Black Death has proven the most mobile and devastating.

Krause admits that between 14th century London and 21st century Madagascar, there are "a lot of steps missing" to identify the precise movements of the deadly bacterium. But he says that understanding plague's long journey could help researchers limit its future spread. ■

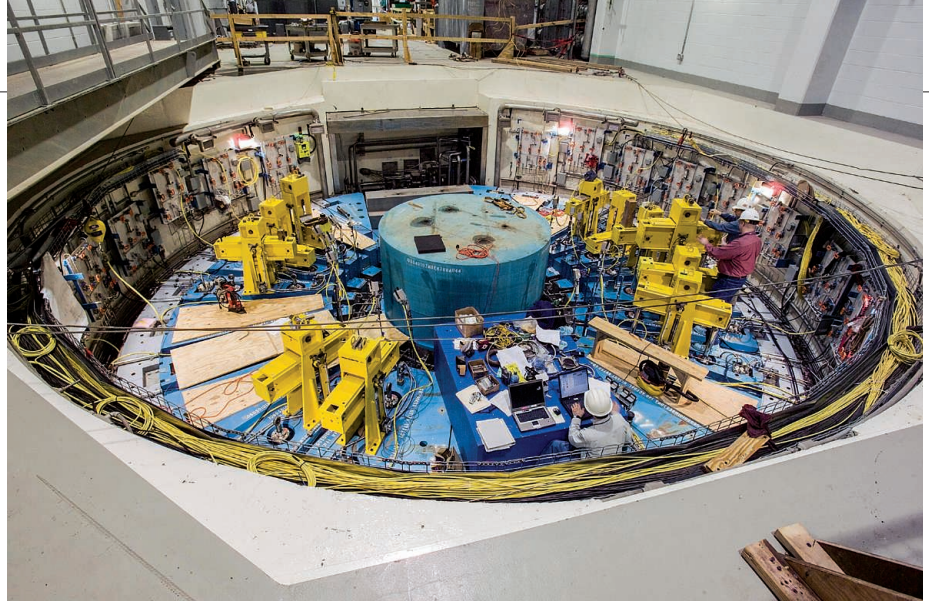

PHOTO: ENERGY.GOV/FLICKR

ARMS CONTROL

Critics complain as U.S. shops in Iran's nuclear bazaar

Heavy water purchase will benefit science, industry

By **Richard Stone**

Mere months ago, Iran's nuclear program was an international pariah. Now, it's supplying the U.S. Department of Energy (DOE) with a strategic substance that the United States itself can't produce. Last week, defying criticism from congressional Republicans and others, DOE consummated a deal to purchase 32 tons of heavy water—water containing the hydrogen isotope deuterium—from the Atomic Energy Organization of Iran.

The $8.6 million sale helps Iran meet a commitment under last July's nuclear deal to shed heavy water—and it will have a swords-to-ploughshares payoff. "We're securing material that will allow us to do great science," says Thom Mason, director of Oak Ridge National Laboratory in Tennessee. DOE will resell a portion to industry for uses such as nuclear MRI and protecting optical fibers and semiconductors against deterioration by blasting them with deuterium gas. DOE will also send 6 tons to Oak Ridge for an upgrade of the Spallation Neutron Source (SNS), an accelerator that generates powerful beams of neutrons for research.

Deuterium—hydrogen with an added neutron—accounts for just one in every 6420 hydrogen atoms. A handful of countries use heavy water (D_2O) as a moderator in nuclear reactors. The extra neutrons make it more efficient than regular water at slowing other neutrons, which gives them a greater chance of initiating fission. But heavy water reactors have a dark side: They can transmute uranium into plutonium, for use in weapons.

In 2002, an Iranian opposition group revealed that Iran was building a secret facility at Arak, later identified as a heavy water production plant, along with a reactor that could breed enough plutonium for one or two bombs a year. That and other revelations led to years of crippling sanctions and finally the agreement with world powers that sharply constrains Iran's nuclear program (*Science*, 24 July 2015, p. 356).

Iran is now working with the United States and China to reconfigure the Arak heavy water reactor to largely eliminate plutonium production. And it has reduced its heavy water stockpile to less than 130 tons, as the deal mandates, by shipping excess stock out of the country for storage. Iran wanted to sell the extra heavy water, "but they were not able to find a market," says Ali Vaez, a senior Iran analyst based in Istanbul, Turkey, for the International Crisis Group.

After the contentious nuclear deal was concluded last July, DOE realized that buying some of the heavy water makes sense, says U.S. Energy Secretary Ernest Moniz. The United States relinquished its own production capacity in 1981, when DOE shuttered a heavy water plant at Savannah River National Laboratory in Georgia to save money. These days, Canada and India satisfy most of the global demand for nonnuclear uses, about 100 tons a year, by distilling heavy water from regular eau, like brandy from wine. A single

Downloaded from http://science.sciencemag.org/ on April 28, 2016

Published by AAAS

Heavy water will boost neutrons from the Spallation Neutron Source's target, seen during construction.

kilogram of reactor-grade heavy water, which is 99.75% D_2O, requires a staggering 340,000 kilograms of purified feed water. U.S. buyers snap up about 75% of global production of heavy water, and appetite is increasing. "Heavy water has been on our radar screen for some time," says a DOE official, who adds that the department is investing in R&D to restart U.S. heavy water production.

Critics blast the decision to buy the material from Iran. "The Obama administration is no longer just carrying water for Iran's nuclear program, it's now paying for it," says Mark Dubowitz, executive director of the Foundation for Defense of Democracies, a think tank in Washington, D.C., that has panned the nuclear agreement. The "U.S. subsidies," as Dubowitz terms the payment, "will simply help Tehran perfect its heavy water production capabilities so it will be fully prepared to develop its plutonium bomb-making capabilities when restrictions on the program sunset."

The shipment, to arrive in a few weeks, will have an immediate payoff for the SNS. "Heavy water is by far the most cost-effective way to increase neutron intensity that I can imagine," says Mason, a condensed matter physicist. Next spring, Oak Ridge will replace an inner reflector plug filled with regular water with one containing Iranian heavy water. Positioned around the target, which produces neutrons when bombarded with protons, the reflector directs the neutrons toward moderators that slow them to energies required for experiments. Heavy water cools the reflector and makes it more efficient, increasing neutron flux by up to 22%.

With more neutrons, "we can measure smaller effects," Mason says. Experiments can be completed faster, freeing up beam time at a facility that now receives four to five times more proposals than it can accommodate. Hundreds of research teams stand to benefit, he says.

Although the heavy water purchase may be a "one-off deal," as Vaez puts it, it could open the floodgates to other nuclear collaborations between the United States and Iran. Under the nuclear agreement, Iran's Fordow uranium enrichment facility is slated to become an international science and technology center. There, Russia is reconfiguring uranium-enrichment centrifuges to produce iridium-191; adding a neutron at the reconfigured Arak reactor would yield iridium-192, which is used in gamma cameras to check for structural flaws in metal. With the D_2O deal done and dusted, Moniz says he has asked DOE rank-and-file "to begin thinking about other areas of collaboration." ■

PHOTO: AMERICAN ASSOCIATION OF PHYSICAL ANTHROPOLOGISTS

SCIENTIFIC COMMUNITY

Saying no to harassment

Roiled by high-profile cases in the field and at conferences, anthropology works to change its culture

By **Ann Gibbons** *and* **Elizabeth Culotta**, *in Atlanta*

An emotionally charged session on sexual harassment in anthropology began with audible gasps last week when a young, untenured professor* described to a standing room–only crowd how she had been humiliated recently when she participated in an otherwise all-male scientific workshop. "I am an expert on this [research] topic," she explained. After she was invited, the organizer told her that there "might" be room for her because another important researcher couldn't come. The organizer instructed her not to talk—just to listen—because ordinarily, "there wouldn't be room for someone like you."

"What should I do?" the professor asked at a Presidential Panel of the American Association of Physical Anthropologists (AAPA) here. Complaining publicly, she said, "might kill my career."

The intense session was one of a half-dozen events at the meeting—mentoring lunches, happy hours, and workshops—on combating discrimination and sexual harassment. "Biological anthropology has a problem," said panelist Robin Nelson of Skidmore College in Saratoga Springs, New York. "But we're not alone."

Yet few fields are confronting the problems as vigorously, perhaps because in this discipline women have reached critical mass. Eight of AAPA's 10 board members are women, as are 56% of AAPA members and the majority of students in most anthropology departments. "Anthropology is 'woke,'" said biological anthropologist Nelson, choosing an expression often used to describe waking up to discrimination. "We're not asleep anymore."

The field has been convulsed by several cases, including that of paleoanthropologist Brian Richmond of the American Museum of Natural History in New York City, who allegedly sexually assaulted a research assistant who worked for him and harassed trainees at a field school (*Science*, 12 February, p. 652). Richmond is working offsite while the museum investigates his actions. His case came to light not long after an influential survey called the SAFE study revealed that sexual harassment is common during fieldwork (*Science*, 19 April 2013, p. 265). The study made it clear that trainees urgently need protection, especially in the field, where people live and work in close quarters. It is time to abandon the old adage that "what happens in the field stays in the field," said biological anthropologist Michelle Bezanson of Santa Clara University in California.

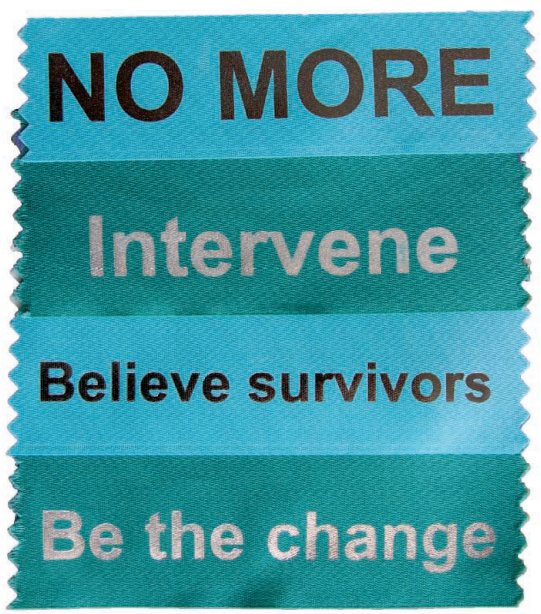

Anthropologists wore these ribbons at a meeting to show support for a more inclusive culture.

Trainees of both sexes also benefit when senior researchers do not tolerate discrimination. "A lot of behavior is learned; we're making sure we are training the kind of professional that we want to be working with down the line," says AAPA President Susan Antón of New York University in New York City, who convened the presidential panel.

Meeting organizers offered a menu of actions to battle harassment, from symbolic to concrete. Meeting registrants were required to agree to AAPA's code of ethics, which forbids sexual harassment and discrimination,

*Participants spoke at sessions under the condition that their names not be used.

Downloaded from http://science.sciencemag.org/ on April 28, 2016

Published by AAAS

and many attendees sported ribbons with antidiscrimination slogans. At the Presidential Panel, the young professor told to be silent at a workshop was bombarded with advice. "Who funded the workshop?" asked paleoanthropologist Leslie Aiello, president of the Wenner-Gren Foundation for Anthropological Research, Inc. in New York City. She suggested that the young professor tell funders the tale. Another panelist added that the professor could contact Title IX coordinators, because this federal law prohibits discrimination on the basis of sex.

Many speakers and attendees said that culture change required action by men as well as women, and noted that male allies can play a crucial role. Those all-male panels, or "manels?" Men should insist on more diversity or spurn the event, said biological anthropologist Susan Sheridan of the University of Notre Dame in Indiana. "If you see a manel, say no," she said.

Biological anthropologist Rebecca Ackermann of the University of Cape Town in South Africa took that one step further. At the end of an invited scientific symposium that she organized (at which seven men and seven women spoke), she urged that all scientific gatherings be representative of the gender and racial diversity in the field. "This is good for science," she said. "Diversity of perspectives leads to better science."

> ***When it comes to harassment, "stop doing it, and we'll stop complaining about it."***
>
> **Susan Sheridan**, The University of Notre Dame

As more women enter the field, blatant discrimination is less common, and harassment often takes the form of "microaggressions," says biological anthropologist Kathryn Clancy of the University of Illinois, Urbana-Champaign, lead author of the SAFE study. For example, one young faculty member* who is gay stood up at a women's mentoring lunch and described how another professor had inquired about her personal life in an offensive and intrusive way. What should she do?

"You need to point out to them that this is inappropriate," said Fred Smith, a paleoanthropologist at Illinois State University in Normal. But not everyone is quick enough on their feet or feels secure enough to speak up, Ackermann retorted. "It never comes up in a context where you have a prepared answer," she says. "I don't think we should be asking students and junior faculty to do that. We need to be training [senior] people like me to [intervene]."

Students and faculty alike should familiarize themselves with the chain of command at their universities so they know whom to contact if problems arise, Aiello says. Another tactic is to actively build a network of allies, both female and male, to talk to. "Active engagement is the only way to change culture," says anthropologist Katie Hinde of Arizona State University, Tempe, a co-author of the SAFE study with Clancy and Nelson.

But confidential discussion of harassment isn't always easy—or even legal. At a panel on Title IX, a lawyer warned about "the confidentiality trap." Under Title IX, universities must designate "responsible employees" who are required by law to report any incident of harassment or discrimination to university officials—even if victims ask that it be kept confidential. For those employees, "even if you have a close, strong, personal relationship [with a student], you don't have confidentiality," said speaker Kristopher Stevens, associate director of the Equal Opportunity Office at the University of Georgia, Athens. If most faculty are designated "responsible," it "could have a chilling effect" on students' willingness to share their stories, said biological anthropologist Catherine Willermet of Central Michigan University in Mount Pleasant.

Clancy and Ackermann, among others, spoke forcefully for a form of social control. They argued that researchers should stop all collaboration, including joint publication, with colleagues who are under investigation for sexual harassment or discrimination. Others worried that such a policy could harm trainees who need to publish. "We need to make sure we don't take actions that negatively affect junior people," says paleoanthropologist David Strait of Washington University in St. Louis in Missouri, who has published with Richmond. "No one wants to damage trainees," countered Hinde, arguing that collaboration by senior scholars sends a terrible signal. "But the role of tenured co-authors is different."

The field is by no means unanimous about what change is needed. "A diminishing number of our colleagues have been less receptive to changing the culture," Hinde says, noting that the SAFE study authors had been disparaged by a few researchers "in conversation, print, and grant review." But she predicted that "those remnants engaged in problematic biases and bad behavior will find themselves increasingly out of step with our community." For any who might complain about "harassment fatigue," panelist Sheridan had an answer: "Stop doing it," she said, "and we'll stop complaining about it." ■

ASTRONOMY

Kepler enlists relativity to find planets

Exotic search technique promises a small but rich harvest of extrasolar worlds

By **Daniel Clery**

When NASA announced last week that it had regained control of Kepler, its exoplanet-hunting spacecraft, after a heartstopping near-shutdown, one handful of astronomers breathed a particularly deep sigh of relief. They were the exoplanet hunters who use a little-known technique called gravitational microlensing. Kepler had gone into "emergency mode" just hours before it was to begin an 80-day microlensing campaign in search of exoplanets and other dim objects. Now, the campaign is back on track, and microlensers hope it will put their work on the map. "People scratch their heads about microlensing. This will show the power of the technique, get people excited and involved," says astronomer Calen Henderson of NASA's Jet Propulsion Laboratory in Pasadena, California, a member of the team that devised the campaign.

Microlensing is unlikely to surpass other techniques in sheer number of discoveries. But whereas the leading planet-finding methods are most sensitive to planets orbiting close to their suns, microlensing can detect planets in distant orbits. That means it offers astronomers a rare opportunity to take a census of all the types of exoplanets. "We don't understand the demography," says Martin Dominik of the University of St. Andrews in the United Kingdom. "Microlensing finds planets no one else can find."

Microlensing springs from Einstein's general theory of relativity. Because gravity bends light, Einstein declared, a massive object can act as a lens, focusing the light of a more distant object as viewed from Earth. Astronomers have found many examples of very massive "lenses," such as whole galaxies or clusters of galaxies, which produce duplicate images of more distant quasars or even stretch the image out into an "Einstein ring."

Downloaded from http://science.sciencemag.org/ on April 28, 2016

Published by AAAS

Microlensing works with much smaller lenses: individual stars or even planets that pass in front of more distant stars. As the lens focuses its light, the background star appears to grow briefly brighter over a couple of weeks, then dims again. In the 1980s, astronomers started using microlensing to detect dim objects such as faint stars and brown dwarfs, gleaning valuable data about them by mapping the rising and falling "light curves" of the distant stars. In the early 1990s, they started looking for exoplanets as well.

The two survey telescopes that have been pursuing microlensing since the 1990s typically identify a couple thousand microlensing events each year, and follow-up networks of other observatories and well-equipped amateurs continue watching each event when daylight blinds the telescope that made the initial detection. "One has to observe millions of stars for months to detect a single microlensing phenomenon," says Andrzej Udalski of the University of Warsaw, who heads the Optical Gravitational Lensing Experiment, based at Las Campanas Observatory in Vallenar, Chile. Most of the microlenses are stars, but in a small fraction—less than 1%—the light curve, instead of having a simple peak, has a more complicated shape or two peaks, indicating a pair of lenses: a planet and its star.

Astronomers using microlensing have so far discovered fewer than 60 exoplanets, but with Kepler, they hope to find more—and also to learn more about the planets' properties. Kepler was designed to stare at nearby stars and detect short-lived dimming when orbiting exoplanets pass in front of them, so it is well-suited to staring at more distant stars and detecting a brief brightening. The spacecraft was hobbled in 2013 by the loss of two reaction wheels, devices that help it keep its aim; it has continued working but can point at targets only in a narrow band of the sky. At this time of year, from early April to early July, its field of view includes the galactic bulge, which is densely packed with stars and an ideal hunting ground for microlensing events.

The upcoming campaign will combine Kepler's observations with those from the ground-based telescopes. Because Kepler watches stars from a vantage point about 120 million kilometers from Earth, it will see each event at a position that is slightly shifted across the background of more distant stars compared with the view from the ground. From that shift, known as parallax, astronomers can use simple trigonometry to work out how far away the lensing object is. A more complex parallax calculation, which involves comparing light curves from the different vantage points, also gives the mass of the lens. "Only by combining space and ground observations can we figure out where most of the lenses are and what their masses are," says Andy Gould of Ohio State University, Columbus, a long-time microlens hunter.

To make such measurements, NASA has "marshaled as many ground-based resources as possible—30 different telescopes across six continents," Henderson says. With the combined Kepler and ground-based data, astronomers hope to start mapping the outer parts of exoplanetary systems. "What sorts of planets exist in outer solar systems? We'll get a better statistical measure of what outer solar systems are like," says Kepler Project Scientist Steve Howell of the NASA Ames Research Center at Moffett Federal Airfield in California.

> ***"People scratch their heads about microlensing. This will show the power of the technique."***
>
> **Calen Henderson**, NASA JPL

Kepler is also keeping a lookout for free-floating planets: mysterious worlds that don't orbit stars. Only a handful of such cosmic vagabonds are known, but recent studies suggest they may outnumber stars by as much as two to one. Detecting and characterizing some of these objects would mark "a major breakthrough" for Kepler's microlensing campaign, Gould says.

Howell says the Kepler campaign will likely net about 100 events, as many as half of them due to free-floating planets. Of the remainder, most will be caused by stars, only a fraction of which will have detectable exoplanets. Even so, Howell says, "we'll take whatever we get." Better hauls should arrive in the next decade, when NASA plans to launch the Wide-Field Infrared Survey Telescope (WFIRST)—a much more powerful space telescope with microlensing high on its agenda. "WFIRST will certainly revolutionize the microlensing field," Udalski says.

In the meantime, microlensers hope that the excitement generated by the Kepler campaign might help push them into the mainstream. "Ultimately, it's a question of the size of telescope you throw at it and the costs," Dominik says. A 4-meter telescope with a mosaic of the latest charge-coupled device detectors would keep them busy until WFIRST arrives. "It's not a large amount of money if you want to learn the demography of all the planets," he says. ■

Finding planets in warped starlight

The NASA Kepler spacecraft has discovered more than a thousand exoplanets by looking for the slight dimming of stars as a planet transits in front. Now, it will try a different approach: detecting the brief brightening of a distant star as another star and its planet move in front of it, acting as a gravitational microlens.

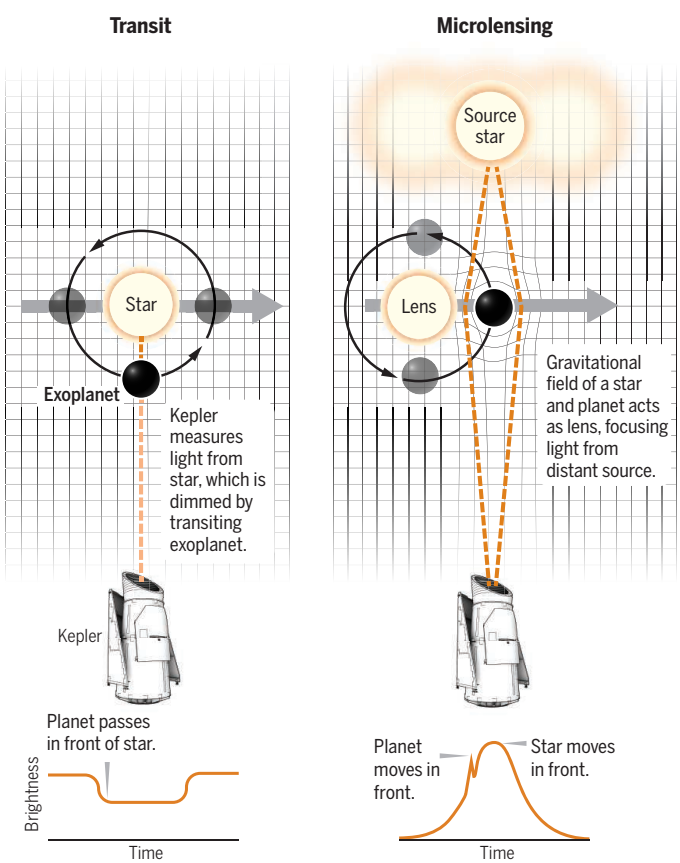

DIAGRAM: V. ALTOUNIAN AND D. CLERY/*SCIENCE*

Downloaded from http://science.sciencemag.org/ on April 28, 2016

Published by AAAS

Hoping to quell public concern, safety officials inspect vaccine doses in Southwest China.

PHOTO: ASSOCIATED PRESS

INFECTIOUS DISEASE

Scandal clouds China's global vaccine ambitions

Porous regulation of private preparations threatens to undermine vaccinemakers' bid to boost exports

By **Kathleen McLaughlin**, *in Beijing*

Last month, a 3-year-old toddler in the southwestern Chinese city of Kunming was the first person in the world inoculated against hand, foot, and mouth disease (HFMD). Health experts hailed the vaccine—one of two new Chinese-made preparations against enterovirus 71—as a milestone against a malady that has run rampant in China. But that triumph was overshadowed by a safety crisis involving other homegrown vaccines.

In recent weeks, police have arrested more than 200 people in connection with the nationwide distribution of 2 million doses of mishandled Chinese-made vaccines against scourges such as hepatitis B and rabies. Even as government officials pledged to shore up oversight, censors worked to quell news of the scandal. No adverse reactions have been confirmed. But the crisis laid bare weak regulation of China's private vaccine market, which handles billions of doses of vaccines that the government does not distribute under its national free inoculation program.

China's vaccine developers hope the safety debacle won't derail efforts to make inroads into the global $33 billion vaccine market. "A major challenge for China's vaccine industry is to overcome concerns about product safety," says Melvin Sanicas, a program officer in Seattle, Washington, with the Bill & Melinda Gates Foundation. The manufacturing system here is not at fault, says Lance Rodewald, China team lead based here for the World Health Organization's (WHO's) Expanded Program on Immunization. "All vaccines made and used in China start their life as safe, pure, and effective," he says. But the less-regulated private vaccine market is plagued with supply-chain problems, from woeful management to improper storage, according to watchdogs. Critics say the system is too vast to watch every step. And if the Chinese public stops trusting homegrown vaccines, the country's bid to become a global producer could be in jeopardy.

China's first big splash in global vaccines came in 2013, when WHO approved a vaccine against Japanese encephalitis. Developed in Chengdu, the vaccine targets a regional threat ignored by Western drug companies. The mosquito-borne virus is endemic in Southeast Asia and the Western Pacific, with an estimated 70,000 annual cases and up to 15,000 deaths. WHO endorsement qualifies a vaccine for inclusion in United Nations aid programs, and with the help of partnerships to fund vaccines in poor countries, China's encephalitis vaccine is expected to reach 290 million people by 2017.

Another ripe target for Chinese vaccinemakers was HFMD, which can trigger dangerous complications like encephalitis. Enterovirus 71 has hammered the country: From 2008 to 2015, China reported 14 million cases and 3391 deaths, primarily in children under 5. Teams here at Sinovac Biotech and the Institute of Medical Biology raced to develop vaccines. China's drug regulator recently approved products from both. Officials are looking to export them to countries struggling with enterovirus 71 outbreaks.

China also made a bold foray into a crowded field with a vaccine against the Ebola virus. In *The Lancet* in March 2015, researchers led by Zhu Fengcai of the Jiangsu Provincial Center for Disease Control and Prevention in Nanjing reported promising early clinical trial results for a vaccine based on the 2014 Ebola strain that sparked the epidemic in West Africa. But China's export prospects dimmed when Gavi, The Vaccine Alliance, struck a deal with Merck in January to stockpile 300,000 doses of its effective Ebola vaccine, also based on the 2014 strain. Gambling on future demand for a Chinese alternative, the vaccine's developers have started work on a facility in Tianjin to mass-produce Ebola vaccine by 2017–18.

At home, however, vaccines face growing wariness. The police sting targeting a syndicate based in Shandong province has eroded shaky confidence in China's ability to safeguard public health. "Of course we know children must be vaccinated, but how can we know the vaccines are safe or even real?" says Pan Zhiyang, a mother of an 18-month-old girl. Such sentiments worry Rodewald, who fears that parents may opt out of China's national vaccine program, which covers 14 diseases, including smallpox, polio, and tetanus. When confidence wanes, he says, "some parents will withhold vaccines from their children in the mistaken belief that it is safer not to vaccinate." Hong Kong, which has limited vaccine stocks, is bracing for an influx of worried mainlanders.

Without a major overhaul, China's vaccine system might not recover quickly. "Unless they have seamless regulation of all vaccines that are available, I think we're probably going to see more of these cases" like the Shandong affair, says Yanzhong Huang, global health fellow at the Council on Foreign Relations in New York City. "As long as vaccines are sold for a profit, there will be room for bad practices." ■

Kathleen McLaughlin is a writer in Beijing.

Downloaded from http://science.sciencemag.org/ on April 28, 2016

Published by AAAS

BRAIN DRAIN

Mexico struggles to woo expat genome jocks

Young guns flocking back to their homeland face a daunting bureaucracy

By **Lizzie Wade**, *in Juriquilla, Mexico*

María Ávila seemed to be living a scientist's dream last October when, fresh from a postdoc in the United States, she walked into the new International Laboratory for Human Genome Research (LIIGH). The institute, in this booming town 300 kilometers northwest of Mexico City, offered the 29-year-old a well-equipped lab and free rein to pursue her interest in Mexico's population genetics. But just 6 months later, Ávila is battling frustration over hidebound bureaucracy and scarce funding. In low moments, she says, "I'm not sure if I will last long."

LIIGH, which marked its first anniversary this month, was built with the express purpose of luring home rising stars in genomics like Ávila who had gone abroad for graduate degrees. It is testimony to Mexico's eagerness to build homegrown expertise in the subject—and to the challenges it faces to fully realizing its potential. "Coming back to Mexico is like a roller coaster," says geneticist Andrés Moreno-Estrada, who did a postdoc at Stanford University in Palo Alto, California, where he worked with Ávila, then returned to Mexico in December 2014 to open a human population genetics lab at the National Laboratory of Genomics for Biodiversity (LANGEBIO) in Irapuato.

The Mexican government has invested heavily in training young scientists in genomics and equipping sequencing labs. "The cost-benefit of genomics equipment is much higher than for other technologies" because it can contribute to research in many fields, says Luis Herrera-Estrella, who in 2005 helped found LANGEBIO in part to provide sequencing services to Mexican colleagues. "That inspired Mexico, as well as other countries, to use genomics as a way to boost the quality of science." The country's funding agency, the National Council on Science and Technology (CONACyT), supports many Mexican students pursuing graduate degrees in the subject abroad.

Rafael Palacios, a prominent biologist with 5 decades of experience at the National Autonomous University of Mexico (UNAM), is a prime mover behind the genomics push. He established an undergraduate program in the discipline at UNAM's Cuernavaca campus in 2003. Its eclectic curriculum—heavy on math and computer sciences—aims to prepare students for a fast-moving field in which a simple biology degree wouldn't cut it. "It was a genius idea," says Tom Gilbert, an ancient DNA researcher at the University of Copenhagen and Ávila's Ph.D. adviser. "Even today I rarely ever encounter people who as undergraduates were getting that wide range of stuff."

Palacios counts Ávila as one of the UNAM program's success stories. After graduating in 2009, she enrolled at Copenhagen and studied how the transatlantic slave trade influenced genetic diversity in the Americas. During her postdoc at Stanford, she developed an idea to probe the understudied African contribution to Mexican genomes with data from ancient DNA and modern genetic surveys. As Ávila sought a permanent position, she thought, "I would like to go back to Mexico, but I don't think it's going to happen." Academic appointments at Mexican universities are few and far between, exacerbated by policies that discourage older scientists from retiring, Herrera-Estrella says. "That's what you hear all the time—someone has to die" for a position to open, Ávila says.

The genome lab in Juriquilla, Mexico, is a magnet for talent.

PHOTO: JUAN VILLAGRAN, HEAD OF CULTURAL ACTIVITIES OF CAMPUS JURIQUILLA, QUERETARO, OF THE NATIONAL AUTONOMOUS UNIVERSITY OF MEXICO

That bottleneck inspired Palacios to hatch the idea for LIIGH. He knew he couldn't guarantee recruits CONACyT funding. But he could promise freedom. In Mexico, as in many countries, young professors usually toil in senior scientists' labs. Palacios didn't think that apprentice model made sense for highly skilled genomics graduates, who had more experience in their emerging field than any senior scientist in Mexico. "They have to be free to pursue their own ideas from the beginning," he says.

UNAM put up approximately $4 million to build LIIGH and provides the lab with a basic yearly budget, but its young hires are expected to seek grants to support research. Besides Ávila, Palacios has hired three other young scientists—all graduates of the UNAM genomics program—on the way toward a goal of 20. He and two other senior scientists are also on staff, but only to offer guidance.

"It is absolutely remarkable that a single person would have this vision and this influence, and really make it work," says David Spector, director of research at Cold Spring Harbor Laboratory in New York, who collaborates with Palacios. But some view LIIGH as only a stop-gap solution to brain drain. "How many people can Palacios repatriate for us? 20? OK, and we'll repatriate 25 [at LANGEBIO]. That's all we can do," Herrera-Estrella says. Until CONACyT bankrolls more new research centers and funds their researchers, he says, many promising Mexican scientists will end up spending their careers abroad.

Those who do return can end up longing for the comparative ease of doing research abroad. "Things don't work at the same pace [in Mexico]," says Lucía Morales, another of LIIGH's early hires. She studied the genetics of yeast hybrids at the Pasteur Institute in Paris before moving here. At first, she couldn't help comparing every customs delay or administrative hurdle with her much smoother experience in France. "I realized I had to stop doing that," she says. In Mexico, "it's slow science, like slow food." Still, Morales believes the opportunity to run her own lab so early in her career is worth the trade-offs.

During LIIGH's first year, none of its young hires received CONACyT funding; a decision on one of Ávila's CONACyT applications is 9 months overdue. "It's not easy for anybody. … It takes all of us a while to start," Palacios says. Even if LIIGH's young researchers end up needing a few years to get established, he says, they will still be ahead of scientists who spend their early years working for someone else.

Ávila knew LIIGH was an experiment when she signed on, and she's not surprised to have hit speed bumps. She says she will tough it out. Science in Mexico "has been done one way for many years," she says. "If [LIIGH] is a mistake, at least it's a new and different mistake." ■

Downloaded from http://science.sciencemag.org/ on April 28, 2016

Published by AAAS

Corrected 28 April 2016; see full text.

FEATURES

WHO'S DOWNLOADING PIRATED PAPERS? EVERYONE

Data from the controversial website Sci-Hub reveal that the whole world turns to it for journal articles

By **John Bohannon**

Just as spring arrived last month in Iran, Meysam Rahimi sat down at his university computer and immediately ran into a problem: how to get the scientific papers he needed. He had to write up a research proposal for his engineering Ph.D. at Amirkabir University of Technology in Tehran. His project straddles both operations management and behavioral economics, so Rahimi had a lot of ground to cover.

But every time he found the abstract of a relevant paper, he hit a paywall. Although Amirkabir is one of the top research universities in Iran, international sanctions and economic woes have left it with poor access to journals. To read a 2011 paper in *Applied Mathematics and Computation*, Rahimi would have to pay the publisher, Elsevier, $28. A 2015 paper in *Operations Research*, published by the U.S.-based company INFORMS, would cost $30.

He looked at his list of abstracts and did the math. Purchasing the papers was going to cost $1000 this week alone—about as much as his monthly living expenses—and he would probably need to read research papers at this rate for years to come. Rahimi was peeved. "Publishers give nothing to the authors, so why should they receive anything more than a small amount for managing the journal?"

Many academic publishers offer programs to help researchers in poor countries access papers, but only one, called Share Link, seemed relevant to the papers that Rahimi sought. It would require him to contact authors individually to get links to their work, and such links go dead 50 days after a paper's publication. The choice seemed clear: Either quit the Ph.D. or illegally obtain copies of the papers. So like millions of other researchers, he turned to Sci-Hub, the world's largest pirate website for scholarly literature. Rahimi felt no guilt. As he sees it, high-priced journals "may be slowing down the growth of science severely."

> ***"The numbers are just staggering. It suggests an almost complete failure to provide a path of access for these researchers."***
>
> **Anonymous science publishing executive**

The journal publishers take a very different view. "I'm all for universal access, but not theft!" tweeted Elsevier's director of universal access, Alicia Wise, on 14 March during a heated public debate over Sci-Hub. "There are lots of legal ways to get access." Wise's tweet included a link to a list of 20 of the company's access initiatives, including Share Link.

But in increasing numbers, researchers around the world are turning to Sci-Hub, which hosts 50 million papers and counting. Over the 6 months leading up to March, Sci-Hub served up 28 million documents. More than 2.6 million download requests came from Iran, 3.4 million from India, and 4.4 million from China. The papers cover every scientific topic, from obscure physics experiments published decades ago to the latest breakthroughs in biotechnology. The publisher with the most requested Sci-Hub articles? It is Elsevier by a long shot—Sci-Hub provided half-a-million downloads of Elsevier papers in one recent week.

These statistics are based on extensive server log data supplied by Alexandra Elbakyan, the neuroscientist who created Sci-Hub in 2011 as a 22-year-old graduate student in Kazakhstan (see bio, p. 511). I asked her for the data because, in spite of the flurry of polarized opinion pieces, blog posts, and tweets about Sci-Hub and what effect it has on research and academic publishing, some of the most basic questions remain unanswered: Who are Sci-Hub's users, where are they, and what are they reading?

For someone denounced as a criminal by powerful corporations and scholarly societies, Elbakyan was surprisingly forthcoming and transparent. After establishing contact through an encrypted chat system, she worked with me over the course of several weeks to create a data set for public release: every download event over the 6-month period starting 1 September 2015, including the

Downloaded from http://science.sciencemag.org/ on April 28, 2016

Published by AAAS

Corrected 28 April 2016; see full text.

IT'S A SCI-HUB WORLD

Server log data for the website Sci-Hub from September 2015 through February paint a revealing portrait of its users and their diverse interests. Sci-Hub had 28 million download requests, from all regions of the world and covering most scientific disciplines. An interactive version of this map is available at bit.ly/Sci-Hub.

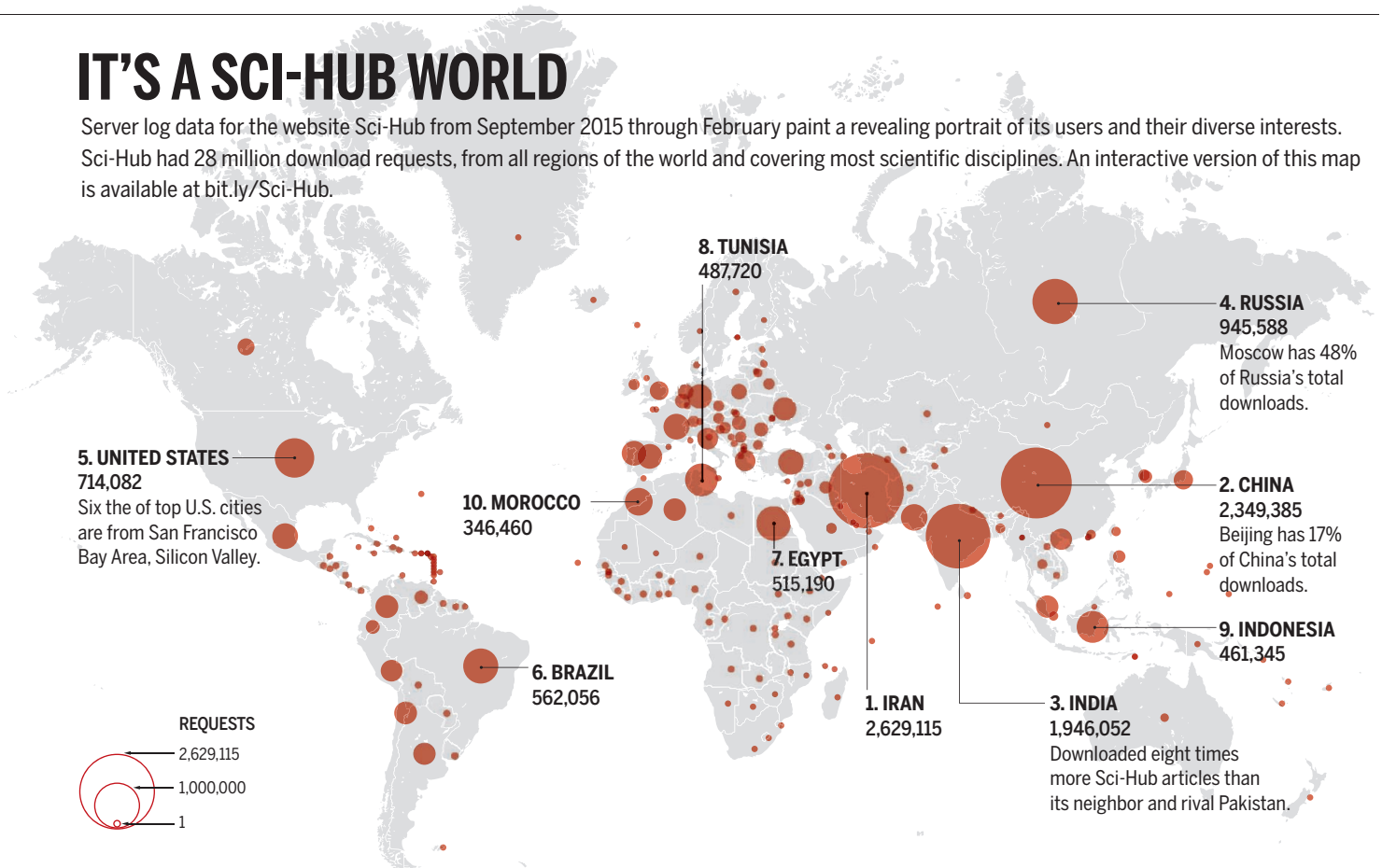

15 most downloaded publishers

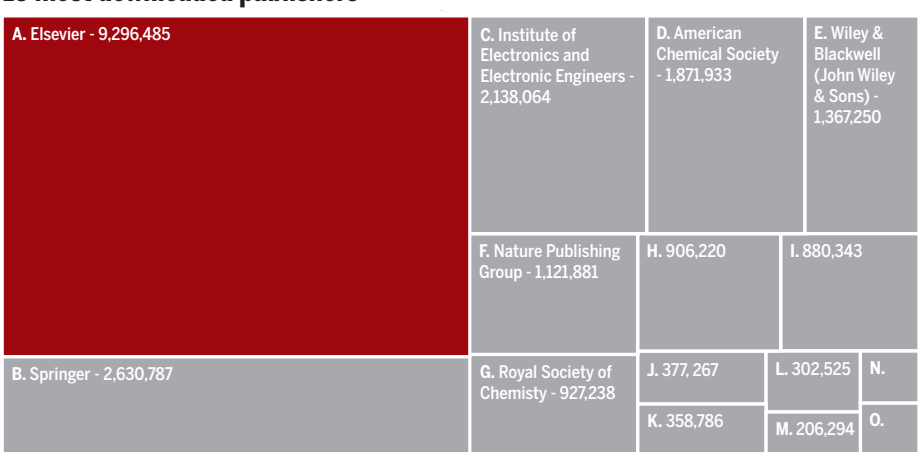

H. Informa UK (T&F) **I.** Wiley Blackwell (Blackwell Publishing) **J.** SAGE Publications **K.** JSTOR **L.** Oxford University Press **M.** AAAS **N.** Informa UK (IH) 165,735 **O.** IOP Publishing 160,073

Five most downloaded papers

1. **Full-scale modal wind turbine tests: comparing shaker excitation with wind excitation,** *Structural Dynamics and Renewable Energy,* 2010 — 7988
2. **Comprehensive, Integrative Genomic Analysis of Diffuse Lower-Grade Gliomas,** *The New England Journal of Medicine,* 2015 — 6117
3. **Photosensitive field emission study of SnS_2 nanosheets** *Journal of Vacuum Science & Technology B,* 2015 — 2991
4. **Griffiths effects and quantum critical points in dirty superconductors without spin-rotation invariance: One-dimensional examples,** *Physical Review B,* 2001 — 2890
5. **Iron deficiency: new insights into diagnosis and treatment,** *Hematology 2015,* 2015 — 2528

Sci-Hub activity over 6 months

Sci-Hub's domain switch in November 2015, forced by a lawsuit against it, led to some missing data during the 6-month period, but usage hit record levels in February.

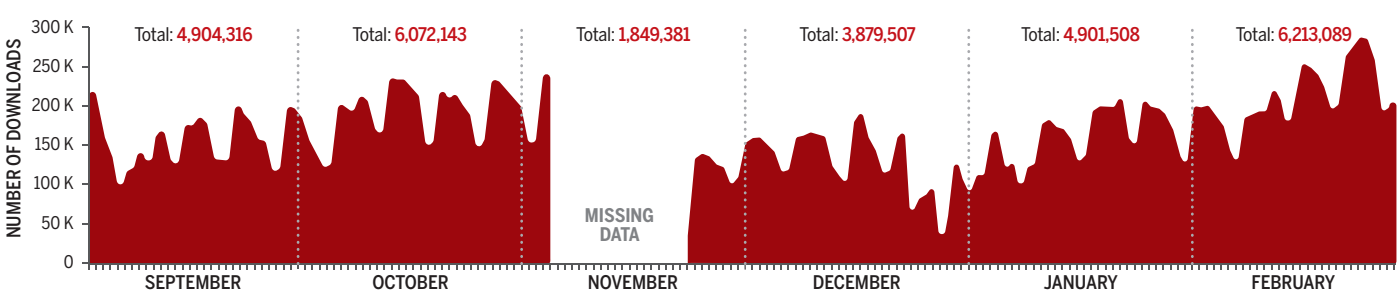

CREDITS: (DATA) SCI-HUB; (MAP) ADAPTED BY G. GRULLÓN/*SCIENCE*

Downloaded from http://science.sciencemag.org/ on April 28, 2016

Published by AAAS

Corrected 28 April 2016; see full text.

digital object identifier (DOI) for every paper. To protect the privacy of Sci-Hub users, we agreed that she would first aggregate users' geographic locations to the nearest city using data from Google Maps; no identifying internet protocol (IP) addresses were given to me. (The data set and details on how it was analyzed are freely accessible at http://dx.doi.org/10.5061/dryad.q447c.)

Elbakyan also answered nearly every question I had about her operation of the website, interaction with users, and even her personal life. Among the few things she would not disclose is her current location, because she is at risk of financial ruin, extradition, and imprisonment because of a lawsuit launched by Elsevier last year.

The Sci-Hub data provide the first detailed view of what is becoming the world's de facto open-access research library. Among the revelations that may surprise both fans and foes alike: Sci-Hub users are not limited to the developing world. Some critics of Sci-Hub have complained that many users can access the same papers through their libraries but turn to Sci-Hub instead—for convenience rather than necessity. The data provide some support for that claim. The United States is the fifth largest downloader after Russia, and a quarter of the Sci-Hub requests for papers came from the 34 members of the Organization for Economic Co-operation and Development, the wealthiest nations with, supposedly, the best journal access. In fact, some of the most intense use of Sci-Hub appears to be happening on the campuses of U.S. and European universities.

In October last year, a New York judge ruled in favor of Elsevier, decreeing that Sci-Hub infringes on the publisher's legal rights as the copyright holder of its journal content, and ordered that the website desist. The injunction has had little effect, as the server data reveal. Although the sci-hub.org web domain was seized in November 2015, the servers that power Sci-Hub are based in Russia, beyond the influence of the U.S. legal system. Barely skipping a beat, the site popped back up on a different domain.

ONLINE SURVEY

Tell us what you think about Sci-Hub at http://bit.ly/Sci-Hub.

It's hard to discern how threatened by Sci-Hub Elsevier and other major publishers truly feel, in part because legal download totals aren't typically made public. An Elsevier report in 2010, however, estimated more than 1 billion downloads for all publishers for the year, suggesting Sci-Hub may be siphoning off under 5% of normal traffic. Still, many are concerned that Sci-Hub will prove as disruptive to the academic publishing business as the pirate site Napster was for the music industry (see editorial, p. 497). "I don't endorse illegal tactics," says Peter Suber, director of the Office for Scholarly Communications at Harvard University and one of the leading experts on open-access publishing. However, "a lawsuit isn't going to stop it, nor is there any obvious technical means. Everyone should be thinking about the fact that this is here to stay."

Need or convenience?

Sci-Hub users in the United States seem to congregate near universities and likely have institutional access to the articles they request. This map excludes 27,000 download requests from anonymous U.S. IP addresses.

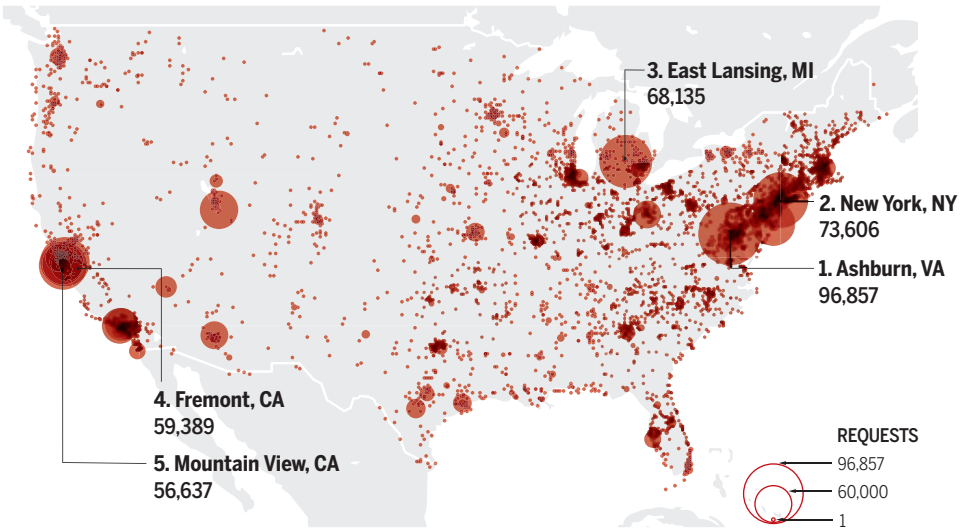

CREDITS: (DATA) SCI-HUB; (MAP) ADAPTED BY G. GRULLÓN/*SCIENCE*

IT IS EASY TO UNDERSTAND why journal publishers might see Sci-Hub as a threat. It is as simple to use as Google's search engine, and as long as you know the DOI or title of a paper, it is more reliable for finding the full text. Chances are, you'll find what you're looking for. Along with book chapters, monographs, and conference proceedings, Sci-Hub has amassed copies of the majority of scholarly articles ever published. It continues to grow: When someone requests a paper not already on Sci-Hub, it pirates a copy and adds it to the repository.

Elbakyan declined to say exactly how she obtains the papers, but she did confirm that it involves online credentials: the user IDs and passwords of people or institutions with legitimate access to journal content. She says that many academics have donated them voluntarily. Publishers have alleged that Sci-Hub relies on phishing emails to trick researchers, for example by having them log in at fake journal websites. "I cannot confirm the exact source of the credentials," Elbakyan told me, "but can confirm that I did not send any phishing emails myself."

So by design, Sci-Hub's content is driven by what scholars seek. The January paper in *The Astronomical Journal* describing a possible new planet on the outskirts of our solar system? The 2015 *Nature* paper describing oxygen on comet 67P/Churyumov-Gerasimenko? The paper in which a team genetically engineered HIV resistance into human embryos with the CRISPR method, published a month ago in the *Journal of Assisted Reproduction and Genetics*? Sci-Hub has them all.

It has news articles from scientific journals—including many of mine in *Science*—as well as copies of open-access papers, perhaps because of confusion on the part of users or because they are simply using Sci-Hub as their all-in-one portal for papers. More than 4000 different papers from PLOS's various open-access journals, for example, can be downloaded from Sci-Hub.

The flow of Sci-Hub activity over time reflects the working lives of researchers, growing over the course of each day and then ebbing—but never stopping—as night falls. (There is an 18-day gap in the data starting 4 November 2015 when the domain sci-hub.org went down and the server logs were improperly configured.) By the end of February, the flow of Sci-Hub papers had risen to its highest level yet: more than 200,000 download requests per day.

How many Sci-Hub users are there? The download requests came from 3 million unique IP addresses, which provides a lower bound. But the true number is much higher because thousands of people on a university campus can share the same IP address. Sci-Hub downloaders live on every continent except Antarctica. Of the 24,000 city locations to which they cluster, the busiest is Tehran, with 1.27 million requests. Much of that is from Iranians using programs to automatically download huge swaths of Sci-

Downloaded from http://science.sciencemag.org/ on April 28, 2016

Published by AAAS

Corrected 28 April 2016; see full text.

Hub's papers to make a local mirror of the site, Elbakyan says. Rahimi, the engineering student in Tehran, confirms this. "There are several Persian sites similar to Sci-Hub," he says. "So you should consider Iranian illegal [paper] downloads to be five to six times higher" than what Sci-Hub alone reveals.

The geography of Sci-Hub usage generally looks like a map of scientific productivity, but with some of the richer and poorer science-focused nations flipped. The smaller countries have stories of their own. Someone in Nuuk, Greenland, is reading a paper about how best to provide cancer treatment to indigenous populations. Research goes on in Libya, even as a civil war rages there. Someone in Benghazi is investigating a method for transmitting data between computers across an air gap. Far to the south in the oil-rich desert, someone near the town of Sabhā is delving into fluid dynamics. (Go to bit.ly/Sci-Hub for an interactive map of the website's data and see what people are reading in cities worldwide.) Mapping IP addresses to real-world locations can paint a false picture if people hide behind web proxies or anonymous routing services. But according to Elbakyan, fewer than 3% of Sci-Hub users are using those.

In the United States and Europe, Sci-Hub users concentrate where academic researchers are working. Over the 6-month period, 74,000 download requests came from IP addresses in New York City, home to multiple universities and scientific institutions. There were 19,000 download requests from Columbus, a city with less than a tenth of New York's population, and 68,000 from East Lansing, Michigan, which has less than a hundredth. These are the homes of Ohio State University and Michigan State University (MSU), respectively.

The numbers for Ashburn, Virginia, the top U.S. city with nearly 100,000 Sci-Hub requests, are harder to interpret. The George Washington University (GWU) in Washington, D.C., has its science and technology campus there, but Ashburn is also home to Janelia Research Campus, the elite Howard Hughes Medical Institute outpost, as well as the servers of the Wikimedia Foundation, the headquarters of the online encyclopedia Wikipedia. Spokespeople for the latter two say their employees are unlikely to account for the traffic. The GWU press office responded defensively, sending me to an online statement that the university recently issued about the impact of journal subscription rate hikes on its library budget. "Scholarly resources are not luxury goods," it says. "But they are priced as though they were."

Several GWU students confessed to being Sci-Hub fans. When she moved from Argentina to the United States in 2014 to start her physics Ph.D., Natalia Clementi says her access to some key journals within the field actually worsened because GWU didn't have subscriptions to them. Researchers in Argentina may have trouble obtain-

The frustrated science student behind Sci-Hub

By **John Bohannon**

Beyond being the founder of Sci-Hub, the world's largest pirate site for academic papers, and risking arrest as a result, Alexandra Elbakyan is a typical science graduate student: idealistic, hard-working, and relatively poor. In 1988, when Elbakyan was born in Kazakhstan, the Soviet Union was just beginning to crumble. Books about dinosaurs and evolution fascinated her early on. "I also remember reading Soviet science books that provided scientific explanations for miraculous events thought previously to be produced by gods or magic." She was hooked.

At university in the Kazakh capital, she discovered a knack for computer hacking. It appealed to her because "unlike higher programming languages that are created by people and are volatile," making and breaking computer security systems requires a deeper knowledge of mathematics and the primitive "assembly language" that computers use to move information.

Like so many of Kazakhstan's brightest, Elbakyan left the country to pursue her dreams. First she worked in Moscow in computer security for a year, and then she used the earnings to launch herself to the University of Freiburg in Germany in 2010, where she joined a brain-computer interface project. She was lured by the possibility that such an interface could one day translate the thought content from one mind and upload it to another. But the work fell short of her dreams. "The lab activity was spiritless," she says. "There was no feeling of pursuing a higher goal."

Elbakyan did find a community of like-minded researchers in transhumanism, a lofty field that encompasses not just neuroscience and computer technology but also philosophy and even speculative fiction about the future of humanity. She discovered a transhumanism conference in the United States and set her heart on attending, but she struggled to get a U.S. visa. She was rejected the first time and only barely made it to the conference. With the remainder of her summer visa, she did a research internship at Georgia Institute of Technology in Atlanta. When she got back to Kazakhstan, frustration with the barriers that scientists face would soon lead her to create Sci-Hub—an awe-inspiring act of altruism or a massive criminal enterprise, depending on whom you ask.

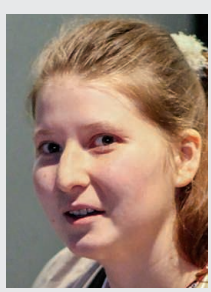

Alexandra Elbakyan, Sci-Hub founder.

Publisher paywalls are the bane of scientists and students in Kazakhstan, she says, and the existing solution was cumbersome: Post a request on Twitter to #IcanhazPDF with your email address. Eventually, a generous researcher at some university with access to the journal will send you the paper.

What was needed, she decided, was a system that allowed that paper to be shared—with absolutely everyone. She had the computer skills—and contacts with other pirate websites—to make that happen, and so Sci-Hub was born (see main story, p. 508). Elbakyan sees the site as a natural extension of her dream of helping humans share good ideas. "Journal paywalls are an example of something that works in the reverse direction," she says, "making communication less open and efficient."

Running a pirate site and being sued for what is likely to be millions of dollars in damages hasn't stopped Elbakyan from pursuing an academic career. Her neuroscience research is on hold, but she has enrolled in a history of science master's program at a "small private university" in an undisclosed location. Appropriately enough, her thesis focuses on scientific communication. "I perceive Sci-Hub as a practical side of my research." ■

PHOTO: APNEET JOLLY/FLICKR

Downloaded from http://science.sciencemag.org/ on April 28, 2016

Published by AAAS

Corrected 28 April 2016; see full text.

ing some specialty journals, she notes, but "most of them have no problem accessing big journals because the government pays the subscription at all the public universities around the country."

Even for journals to which the university has access, Sci-Hub is becoming the go-to resource, says Gil Forsyth, another GWU physics Ph.D. student. "If I do a search on Google Scholar and there's no immediate PDF link, I have to click through to 'Check Access through GWU' and then it's hit or miss," he says. "If I put [the paper's title or DOI] into Sci-Hub, it will just work." He says that Elsevier publishes the journals that he has had the most trouble accessing.

The GWU library system "offers a document delivery system specifically for math, physics, chemistry, and engineering faculty," I was told by Maralee Csellar, the university's director of media relations. "Graduate students who want to access an article from the Elsevier system should work with their department chair, professor of the class, or their faculty thesis adviser for assistance."

The intense Sci-Hub activity in East Lansing reveals yet another motivation for using the site. Most of the downloads seem to be the work of a few or even just one person running a "scraping" program over the December 2015 holidays, downloading papers at superhuman speeds. I asked Elbakyan whether those download requests came from MSU's IP addresses, and she confirmed that they did. The papers are all from chemistry journals, most of them published by the American Chemical Society. So the apparent goal is to build a massive private repository of chemical literature. But why?

Bill Hart-Davidson, MSU's associate dean for graduate education, suggests that the likely answer is "text-mining," the use of computer programs to analyze large collections of documents to generate data. When I called Hart-Davidson, I suggested that the East Lansing Sci-Hub scraper might be someone from his own research team. But he laughed and said that he had no idea who it was. But he understands why the scraper goes to Sci-Hub even though MSU subscribes to the downloaded journals. For his own research on the linguistic structure of scientific discourse, Hart-Davidson obtained more than 100 years of biology papers the hard way—legally with the help of the publishers. "It took an entire year just to get permission," says Thomas Padilla, the MSU librarian who did the negotiating. And once the hard drive full of papers arrived, it came with strict rules of use. At the end of each day of running computer programs on it from an offline computer, Padilla had to walk the resulting data across campus on a thumb drive for analysis with Hart-Davidson.

Yet Sci-Hub has drawbacks for text-mining research, Hart-Davidson says. The pirated papers are in unstructured PDF format, which is hard for programs to parse. But the bigger issue, he says, is that the data source is illegal. "How are you going to publish your work?" Then again, having a massive private repository of papers does allow a researcher to rapidly test hypotheses before bothering with libraries at all. And it's all just a click away.

WHILE ELSEVIER WAGES a legal battle against Elbakyan and Sci-Hub, many in the publishing industry see the fight as futile. "The numbers are just staggering," one senior executive at a major publisher told me upon learning the Sci-Hub statistics. "It suggests an almost complete failure to provide a path of access for these researchers." He works for a company that publishes some of the most heavily downloaded content on Sci-Hub and requested anonymity so he could speak candidly.

> ***"A lawsuit isn't going to stop [Sci-Hub], nor is there any obvious technical means. Everyone should be thinking about the fact that this is here to stay."***
>
> **Peter Suber**, Harvard University

For researchers at institutions that cannot afford access to journals, he says, the publishers "need to make subscription or purchase more reasonable for them." Richard Gedye, the director of outreach programs for STM, the International Association of Scientific, Technical and Medical Publishers, disputes this. Institutions in the developing world that take advantage of the publishing industry's outreach programs "have the kind of breadth of access to peer-reviewed scientific research that is pretty much the equivalent of typical institutions in North America or Europe."

And for all the researchers at Western universities who use Sci-Hub instead, the anonymous publisher lays the blame on librarians for not making their online systems easier to use and educating their researchers. "I don't think the issue is access—it's the perception that access is difficult," he says.

"I don't agree," says Ivy Anderson, the director of collections for the California Digital Library in Oakland, which provides journal access to the 240,000 researchers of the University of California system. The authentication systems that university researchers must use to read subscription journals from off campus, and even sometimes on campus with personal computers, "are there to enforce publisher restrictions," she says.

Will Sci-Hub push the industry toward an open-access model, where reader authentication is unnecessary? That's not clear, Harvard's Suber says. Although Sci-Hub helps a great many researchers, he notes, it may also carry a "strategic cost" for the open-access movement, because publishers may take advantage of "confusion" over the legality of open-access scholarship in general and clamp down. "Lawful open access forces publishers to adapt," he says, whereas "unlawful open access invites them to sue instead."

EVEN IF ARRESTED, Elbakyan says Sci-Hub will not go dark. She has failsafes to keep it up and running, and user donations now cover the cost of Sci-Hub's servers. She also notes that the entire collection of 50 million papers has been copied by others many times already. "[The papers] do not need to be downloaded again from universities."

Indeed, the data suggest that the explosive growth of Sci-Hub is done. Elbakyan says that the proportion of download requests for papers not contained in the database is holding steady at 4.3%. If she runs out of credentials for pirating fresh content, that gap will grow again, however—and publishers and universities are constantly devising new authentication schemes that she and her supporters will need to outsmart. She even asked me to donate my own *Science* login and password—she was only half joking.

For Elbakyan herself, the future is even more uncertain. Elsevier is not only charging her not only with copyright infringement but with illegal hacking under the U.S. Computer Fraud and Abuse Act. "There is the possibility to be suddenly arrested for hacking," Elbakyan admits. Others who ran afoul of this law have been extradited to the United States while traveling. And she is fully aware that another computer prodigy–turned-advocate, Aaron Swartz, was arrested on similar charges in 2011 after mass-downloading academic papers. Facing devastating financial penalties and jail time, Swartz hanged himself.

Like the rest of the scientific community, Elbakyan is watching the future of scholarly communication unfold fast. "I will see how all this turns out." ■

Downloaded from http://science.sciencemag.org/ on April 28, 2016

Published by AAAS

Dynamic liquid phases govern signaling p. 516 ▸

Patent trolling harms innovation p. 521

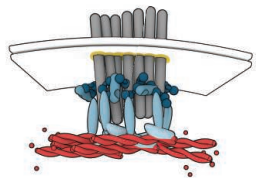

PERSPECTIVES

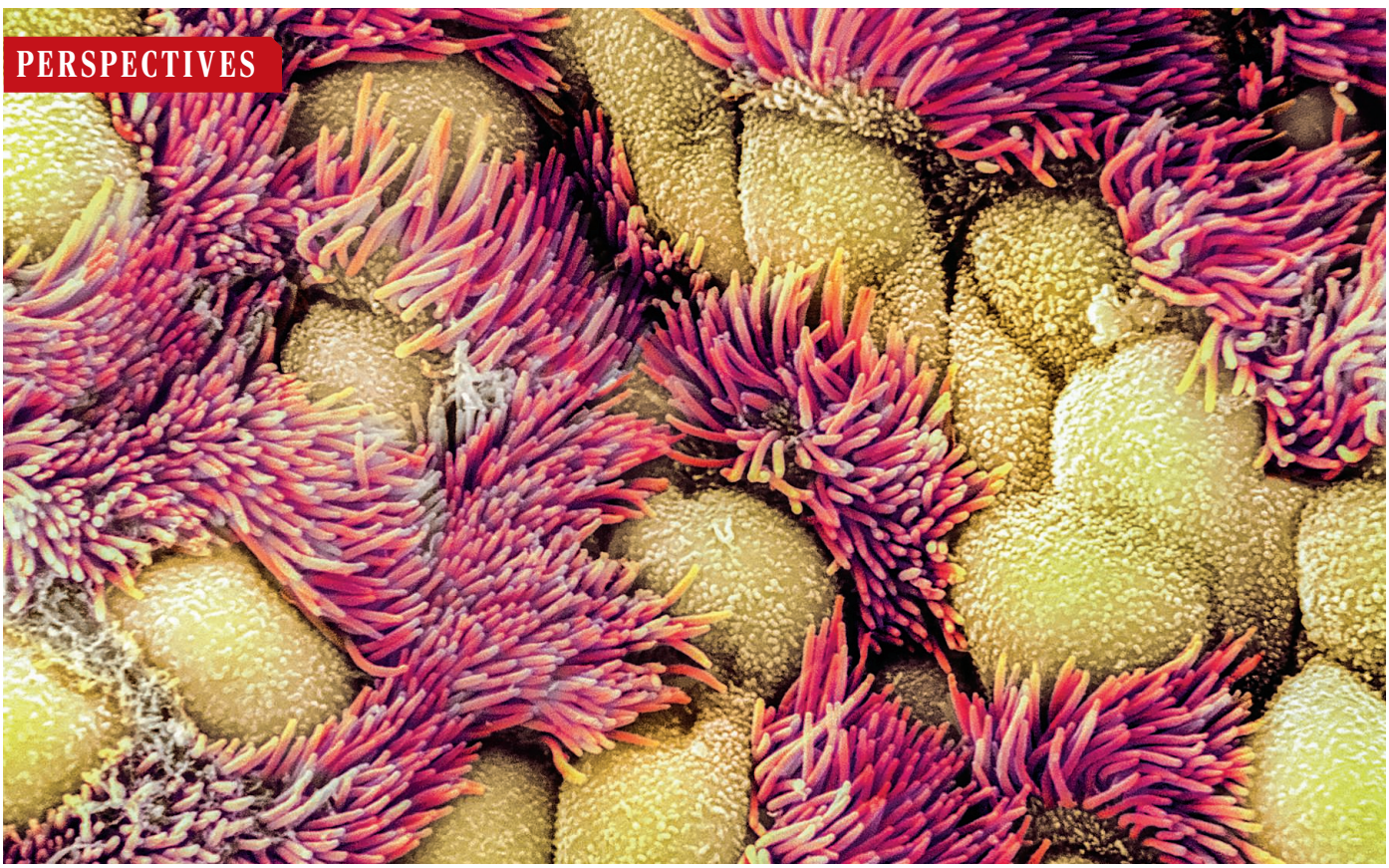

Cilia out of equilibrium. A colorized scanning electron micrograph of the tracheal lining shows hair-like cilia (red). Biological systems such as cilia and flagella often operate in a nonequilibrium steady state. Being able to identify these states is important in the study of how such systems function.

PHYSICAL BIOLOGY

A fresh eye on nonequilibrium systems

A noninvasive probe reveals nonequilibrium behavior in systems at steady state

By **Jean-Francois Rupprecht**[1] *and* **Jacques Prost**[1,2,3]

According to the physicist Richard Feynman, a system is in equilibrium when "all the fast things have happened but the slow things have not" (*1*). This definition really applies to a system at steady state, which can either be in thermodynamic equilibrium or in a nonequilibrium steady state. Most systems in nature are not in equilibrium; they exchange fluxes of matter or energy with their surroundings or undergo chemical reactions. When the fast "things" have happened but the slow ones have not, such systems are in a nonequilibrium steady state. The properties of nonequilibrium steady states are currently under intense theoretical investigation, and their similarities and differences with thermodynamic equilibrium states are starting to emerge (*2*). On page 604 of this issue, Battle *et al.* (*3*) propose a new way of probing the nonequilibrium nature of an apparent steady state and demonstrate how such nonequilibrium dynamics can be identified.

Being able to characterize the nature of nonequilibrium steady states is critical because it is not possible to use standard thermodynamic concepts to study them. However, it can be difficult to determine whether the observed dynamics differ from that expected for a system at thermal equi-

[1]*Mechanobiology Institute, National University of Singapore, 117411 Singapore.* [2]*Laboratoire Physico Chimie Curie, Institut Curie, PSL Research University, CNRS, 75005 Paris, France.* [3]*Sorbonne Universities, UPMC Univ Paris 06, CNRS, Laboratoire Physico Chimie Curie, 75005 Paris, France. Email: jacques.prost@curie.fr*

PHOTO: NIBSC/SCIENCE SOURCE

Downloaded from http://science.sciencemag.org/ on April 28, 2016

Published by AAAS

librium. In cellular processes, for example, it is often unclear whether particular stochastic fluctuations of cellular components (e.g., proteins, membranes, organelles) are driven by thermal or nonthermal processes. This is important because, in contrast to thermal noise, nonthermal noise can generate a spontaneous motion even in the absence of an external driving force (*4*). This possibility is well illustrated by the Feynman-Smoluchowski ratchet, where a paddle and a pawl are connected by an axle on which a ratchet is fixed (*1*). When the whole system is kept at a uniform temperature, no net motion is possible: Perpetual motion at thermal equilibrium does not exist. As soon as the paddle and the pawl are exposed to different temperatures, the ratchet can rectify noise, and the axle can rotate and perform useful work—for instance, lifting a weight. Similar concepts apply to isothermal molecular motors that play a fundamental role in biology. In that case, the energy is derived from chemical reactions (*5*).

Until now, there was essentially only one method for determining whether a steady state is at equilibrium or not. This method relies on the conventional fluctuation dissipation theorem (FDT). In the context of Einstein's seminal paper on the Brownian motion of a small particle in a fluid (*6*), the FDT takes the form of a proportionality relation between the diffusion coefficient of the particle at rest and the dissipative frictional force that an operator would need to balance in order to pull the particle in a particular direction. In a more general context, the FDT states that the time derivative of the two-point correlation function—a measure of the intensity of spontaneous fluctuations—is proportional to the response function, which quantifies the mean reaction exerted by the environment due to an external perturbation. In both contexts, the proportionality factor provides a measure of the temperature of the system. In general, one can define a frequency-dependent effective temperature, $T_{\mathrm{eff}}(w)$. For a system in thermodynamic equilibrium, $T_{\mathrm{eff}}(w)$ is constant and equal to the sample temperature; any deviation indicates that the system is out of equilibrium. The simplest violation concerns systems for which the proportionality relation still holds, but where the extracted temperature differs from that of the surrounding passive material. More pronounced deviations have been observed in living sound-detecting cells (hair cells) (*7*). The effective temperature is found to be negative at low frequency, to diverge at a characteristic frequency, and to become positive at high frequency. In contrast, as one should expect, dead cells, which are at thermal equilibrium, exhibit a constant effective temperature that is equal to the temperature of the sample.

In other cases, the situation is more complex. For instance, it has taken decades to pinpoint the out-of-equilibrium nature of red blood cell membranes. Initial indications of the out-of-equilibrium nature of these fluctuations were obtained by reducing the adenosine triphosphate (ATP) content of the cells. Although suggestive of the violation of the FDT, this method did not provide a definitive demonstration, because ATP could also influence purely passive properties, such as membrane elasticity. More recent work showing an unequivocal violation of the FDT finally provided a solution to this long-standing problem (*8*).

Despite these successes, searching for FDT violations as a method to identify nonequilibrium steady states suffers from several drawbacks. First, this method requires that two separate measures of the correlation function and of the response function be available. Second, the measure of the response function is intrinsically invasive, because it relies on the application of controlled external perturbations. Furthermore, it is not always easy to guarantee that the measurements are made within the linear response regime—that is, involving small perturbations.

"...if loops or vortices are observed, then the system is necessarily out of equilibrium."

Other proposed methods have, until now, failed to be convincing as effective tools for characterizing nonequilibrium steady states. Higher-order time-correlation functions can reveal out-of-equilibrium conditions (*9*) but have not been fully exploited yet because of technical challenges. The existence of non-Gaussian distribution fluctuations has been associated in the literature with a nonequilibrium steady state. However, equilibrium systems can exhibit non-Gaussian fluctuations—e.g., in the presence of anharmonic potentials (*10*)—and nonequilibrium systems can exhibit Gaussian fluctuations (see the analysis presented in the supplemental materials of Battle *et al.*).

Battle *et al.* use the knowledge that fluxes between any microstate defining a system are pairwise balanced at equilibrium, as proposed by Boltzmann. The critical step was to define such a microstate at an intermediate spatiotemporal scale that is sufficiently small to observe a large number of transitions, while sufficiently large to be compatible with the time resolution of the experiment. The averaged flux between microstates is represented as a vector within a phase space plot. Within this phase space, at equilibrium there can be neither a flux loop nor a vortex involving three or more states, as a direct consequence of Boltzmann's condition for equilibrium. Conversely, if loops or vortices are observed, then the system is necessarily out of equilibrium.

A simple theoretical example is considered by the authors, which enables a direct comparison of equilibrium and nonequilibrium situations. The system consists of two elastically coupled Brownian particles in contact with two reservoirs generating Brownian noise at two prescribed temperatures. A prominent vortex appears when the two temperatures differ. More elaborate biological examples such as the beating of the *Chlamydomonas reinhardtii* flagellum or of the primary cilia of epithelial cells are also described by the authors. Battle *et al.*'s new insight also lies in designing an efficient bootstrap allowing for the correct use of experimental data.

In contrast to previous methods, the technique developed by Battle *et al.* requires neither the invasive injection of probes nor external perturbations of the system under study. Instead, it relies only on the observation of spontaneous fluctuations of the system itself using simple time-resolved imaging. The method is not limited to mechanical degrees of freedoms such as flagellar position, but can be extended to chemical or electrical variables, such as electron currents or calcium concentration. Its main limitation stems from the fact that systems in nonequilibrium steady states, and which thus break detailed balance at the microscopic scale, might, in some circumstances, restore detailed balance at a larger scale (*11*). Whether the theoretical system of (*11*) can be experimentally relevant or not is still an open question. The flux method presented by Battle *et al.* has the potential to become a standard tool not only in biological physics, but also more generally in the study of fluctuating systems. ■

Downloaded from http://science.sciencemag.org/ on April 28, 2016

REFERENCES

1. R. P. Feynman, *Statistical Mechanics: A Set of Lectures* (Westview, Boulder, CO, 1972).
2. G. Verley, *Phys. Rev. E* **012111**, 1 (2016).
3. C. Battle *et al.*, *Science* **352**, 604 (2016).
4. M. C. Marchetti *et al.*, *Rev. Mod. Phys.* **85**, 1143 (2013).
5. F. Julicher, A. Ajdari, J. Prost, *Rev. Mod. Phys.* **69**, 1269 (1997).
6. A. Einstein, *Ann. Phys.* **322**, 549 (1905).
7. P. Martin, J. M. Hudspeth, F. Julicher, *Proc. Natl. Acad. Sci. U.S.A.* **98**, 14380 (2001).
8. H. Turlier *et al.*, *Nature Phys.* 10.1038/nphys3621 (2016).
9. I. Z. Steinberg, *Biophys. J.* **50**, 171 (1986).
10. C. Bustamante, J. Liphardt, F. Ritort, *Phys. Today* **58**, 43 (2005).
11. D. A. Egolf, *Science* **287**, 101 (2000).

10.1126/science.aaf4611

Published by AAAS

CELL SIGNALING

Liquidity in immune cell signaling

Phase separation of proteins into liquid-like microclusters promotes T cell receptor signaling

By Michael L. Dustin[1,2] and James Muller[2]

T lymphocytes of the immune system need to integrate myriad signals to decide on life and death matters in defending the host from pathogens and in distinguishing normal from transformed cells, all while minimizing immunopathology. On page 595 in this issue, Su *et al.* (*1*) provide insight into how phase separation of signaling proteins in the two-dimensional (2D) liquid of the plasma membrane enables these critical decisions.

Phase separation in live cells has become a useful concept in explaining the formation of μm-scale spherical, liquid-like compartments that are held together by weak, rapidly reversible interactions and that exchange components with the surrounding bulk phase (*2*). Phase separation is also well studied in 2D systems such as biological membranes, where coexisting liquid disordered and liquid ordered phases are important for signaling by many transmembrane receptor systems (*3*), including the T cell receptor (TCR) signaling process. In response to binding antigen peptides, the TCR triggers a series of biochemical events orchestrated by various enzymes and adaptor proteins. This signaling cascade impinges on the nucleus and the actin cytoskeleton to alter T cell behavior. Su *et al.* examined how soluble and membrane-anchored adapter proteins downstream of the TCR form a 2D phase–separated system that depends fully on protein-protein interactions on top of a liquid disordered bilayer.

Su *et al.* looked at the behavior of a signaling effector of the TCR called linker of activated T cells (LAT), and two of its binding partners—growth factor receptor–bound protein 2 (Grb2), which binds to phosphorylated LAT; and son of sevenless (Sos), which binds to the N- and C- termini of Grb2 (*1*). This protein trio is critical for activating the signaling protein Ras as part of the TCR signaling pathway. The authors found that physiological amounts of bilayer-anchored prephosphorylated LAT (pLAT), plus soluble Grb2 and Sos proteins, formed micrometer-scale pLAT clusters on a supported lipid bilayer in vitro. The pLAT clusters have characteristics of a liquid phase in that they fuse with each other while maintaining a roughly round shape and allow rapid exchange of pLAT between a cluster and surrounding unclustered pLAT. Su *et al.* expanded the system of purified proteins to include kinases and phosphatases that act downstream of the TCR signaling cascade and generate pLAT. The authors also overlaid an actin polymerizing system on the pLAT clusters, which consisted of globular actin (G-actin) and five proteins: Grb2-related adapted downstream of Shc (Gads), SH2 contains leukocyte protein of 76 kDa (SLP-76), noncatalytic region of tyrosine kinase adapted protein 1 (Nck), actin-related protein 2/3 (Arp2/3), and neuronal Wiskott-Aldrich syndrome protein (N-WASP). The 2D pLAT clusters could interact with the actin-nucleating factor N-WASP to trigger formation of an elongated filamentous actin (F-actin) gel (see the figure). The F-actin gel appears to act like a solid container that absorbs liquid-phase pLAT and takes the shape of the F-actin.

The pLAT clusters are likely to be components of TCR "microclusters," where antigenic major histocompatibility complex-peptide ligand (antigen) are engaged and signaling reactions occur on the cytoplasmic face of the T cell plasma membrane. These microclusters are highly dynamic and display fusion events to form larger clusters (*4*). TCR microcluster formation in response to physiological ligands depends on F-actin remodeling. It is possible that the complex interaction between the pLAT-rich liquid phase and F-actin is related to this requirement—that is, initial TCR triggering could induce pLAT phase separation and signal actin remodeling, which would feed forward to promote further TCR interaction with antigen.

Concepts of 2D phase separation can also be applied to reconstituted cell adhesion systems. The adhesion of T cells that express the receptor CD2 to an artificial lipid bilayer bearing its ligand CD58, displays characteristics of a phase-separated system with the precisely apposed membranes contributing the necessary dynamic multipoint attachments (*5*). Furthermore, different size receptor systems that bridge the gap between the T cell and artificial lipid bilayer further subdivide the interface into TCR and adhesion molecule–rich domains of the immunological synapse (the interface between the antigen-presenting cell and the T cell) (*6*), the natural setting for the reactions studied by Su *et al.* It may be that the actinomyosin–based trans-

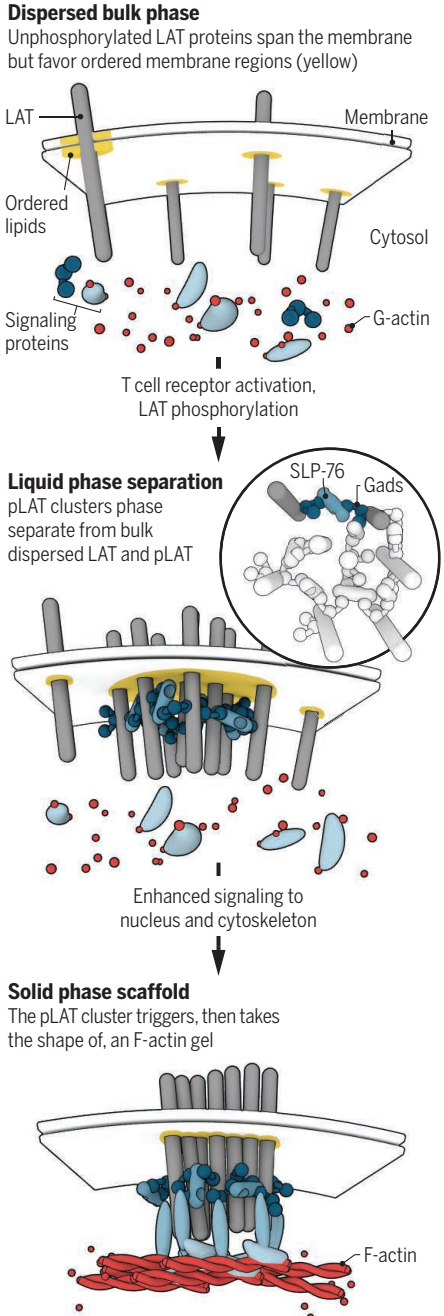

Fluid signals. Signaling molecules (blue) form liquid-like phases, instead of static aggregates, in a reconstituted system using an artificial lipid bilayer. Shown is a model of clustered pLAT and associated signaling molecules that phase separate into a liquid-like droplet in response to TCR activation. The cluster induces actin polymerization, which is a solid phase gel that changes the shape of the liquid-like droplet.

ILLUSTRATION: V. ALTOUNIAN/*SCIENCE*

[1]Kennedy Institute of Rheumatology, The University of Oxford, Oxford, UK. [2]Skirball Institute, New York University School of Medicine, New York, NY, USA.
Email: michael.dustin@kennedy.ox.ac.uk

Downloaded from http://science.sciencemag.org/ on April 28, 2016

Published by AAAS

port system, which drives centripetal transport in the immunological synapse, moves the TCR and pLAT clusters by using the F-actin–based "container" that was observed by the authors in their reconstituted system.

Su *et al.* focused on phenomena largely confined to the 2D supported lipid bilayer surface by tethering key components to the bilayer's surface. It is not clear whether 2D phase separation of pLAT could also nucleate a 3D phase–separated structure that would be released into the cytoplasm. Such a structure appears to be formed during T cell stimulation by immobilized antibodies to TCR, where foci (containing SLP-76) are released as particles from TCR microclusters and trafficked toward the microtubule-organizing center (*7*). These particles seem to dissipate in the center of the immunological synapse, consistent with reversible phase separation.

The findings of Su *et al.* provide insights into characteristics of TCR signaling that are otherwise hard to reconcile. Recent super-resolution microscopy studies suggest that substrate-adherent T cells display basal segregation of TCR and pLAT into distinct "protein islands" on a ~100- to 300-nm length scale (*8*). It is possible that interaction between layered dynamic liquid phases could govern signal integration. Segregation of TCR clusters from pLAT may be mediated by the tendency of the TCR to reside in liquid disordered bilayer phases, whereas LAT, which is palmitoylated, resides in liquid ordered domains. These interactions between phases may also govern important regulators like the transmembrane tyrosine phosphatase CD45. The large extracellular domain of CD45 excludes it from TCR microclusters, which is important for the phosphorylating tyrosine kinase cascades proximal to the TCR (*9*). Su *et al.* found that CD45 is also excluded from pLAT clusters, likely due to charge repulsion between the phosphatase domain and pLAT cluster components. It may be important that CD45 is excluded in this way; segregation of TCR clusters and pLAT clusters suggests that extracellular domain size does not exclude CD45 from the pLAT clusters. The tools generated by Su *et al.* have the potential to further address underlying principles governing the dynamic, layered circuitry of transmembrane signaling. ■

REFERENCES

1. X. Su *et al.*, *Science* **352**, 595 (2016).
2. C. P. Brangwynne, T. J. Mitchison, A. A. Hyman, *Proc. Natl. Acad. Sci. U.S.A.* **108**, 4334 (2011).
3. A. T. Hammond *et al.*, *Proc. Natl. Acad. Sci. U.S.A.* **102**, 6320 (2005).
4. R. Varma *et al.*, *Immunity* **25**, 117 (2006).
5. M. L. Dustin, *J. Biol. Chem.* **272**, 15782 (1997).
6. A. Grakoui *et al.*, *Science* **285**, 221 (1999).
7. S. C. Bunnell *et al.*, *J. Cell Biol.* **158**, 1263 (2002).
8. B. F. Lillemeier *et al.*, *Nat. Immunol.* **11**, 90 (2010).
9. V. T. Chang *et al.*, *Nat. Immunol.* 10.1038/ni.3392 (2016).

10.1126/science.aaf8179

NEUROSCIENCE

Ionic control of sleep and wakefulness

The ionic composition of brain fluid is linked to neuronal activity and sleep

By **Hans-Peter Landolt**[1,2] *and* **Sebastian C. Holst**[1,2]

Brain electrical activity differs markedly between wakefulness and sleep. Concomitant shifts in the ion composition of brain extracellular fluids were thought to be a consequence rather than a cause of the sleep-wake–dependent changes in neuronal activity. On page 550 of this issue, Ding *et al.* (*1*) report the surprising observation that ionic changes in the extracellular fluid are a potent control of sleep-wake–dependent neuronal activity.

Although the biological functions of sleep are still elusive, sleep is essential for optimal brain functioning and general physiology that varies in synchrony with the sleep-wake cycle. In wakefulness, cortical brain activation is driven by wake-promoting neuromodulators (acetylcholine, hypocretin, histamine, serotonin, noradrenaline, and dopamine) produced in the basal forebrain, hypothalamus, and brain stem (*2*). These regions are interconnected in an excitatory network that sends projections to the thalamus and cerebral cortex. Together with neurons that produce glutamate and γ-aminobutyric acid (GABA), this ascending arousal system maintains conscious and alert wakefulness, characterized by low-voltage, fast-frequency activity in an electroencephalogram (EEG).

In deep non–rapid eye movement (NREM) sleep, the EEG of animals and humans is characterized by large, slow waves of electrical activity with frequencies of roughly 1 to 4 Hz. Synchronous oscillations between "up states" and "down states" in the membrane potential of cortical neurons underlie these slow waves (*3, 4*). Sleep deprivation increases the number, amplitude, and slope of EEG slow waves in recovery sleep (*5*), reflecting their robust homeostatic regulation.

Neuronal activity is controlled by ion flow across the plasma membrane. It has been thought that during wakefulness, the breakdown of energy-rich compounds increases the transmembrane conductance of potassium (*6*). This may play a role in restoring brain energy metabolism during sleep, and in the homeostatic regulation of sleep need in response to prolonged wakefulness. Increased transmembrane conductance of potassium underlies membrane hyperpolarization in cortical neurons that produces EEG slow oscillations in NREM sleep (*6*). Furthermore, increases and decreases in the extracellular concentration of potassium ions ($[K^+]_e$) parallel the alternating periods of depolarization and hyperpolarization of neurons and glial cells during the natural slow oscillation and when under anesthesia (*7*).

The idea that positively charged ions affect the sleep-wake cycle was proposed in the 1930s, and calcium contained in breast milk was hypothesized to promote sleep in infants (*8*). Injecting calcium chloride ($CaCl_2$) into the pituitary of cats could induce sleep for up to 3 hours (*9*). Additionally, $CaCl_2$ and magnesium chloride ($MgCl_2$) injected near the hypothalamus of different animal models promoted sleep, whereas potassium chloride (KCl) promoted wakefulness (*8*). Analyses of brain tissue from dogs and rabbits revealed a slight increase in brain calcium during sleep when compared to wakefulness (*10*).

> ***"...that positively charged ions affect the sleep-wake cycle was proposed in the 1930s..."***

Ding *et al.* found that alterations in the ion composition of the brain's extracellular fluid are sufficient to control sleep-wake–dependent changes in neuronal activity. Noting that modifications of ionic concentrations in the bathing solution of cortical slices of adult mice induced stable changes in neuronal excitability, they determined that a "wake-up cocktail"—an artificial cerebrospinal fluid (CSF) containing acetylcholine, hypocretin, histamine, serotonin, noradrenaline, and dopamine—altered $[K^+]_e$ in brain-slice preparations. Micromolar concentration of this cocktail increased $[K^+]_e$, even when neuronal activity was silenced

[1]*Institute of Pharmacology and Toxicology, University of Zürich, Zürich, Switzerland.* [2]*Zürich Center for Interdisciplinary Sleep Research, University of Zürich, Zürich, Switzerland. Email: landolt@pharma.uzh.ch*

Downloaded from http://science.sciencemag.org/ on April 28, 2016

Published by AAAS

pharmacologically with tetrodotoxin. Thus, the shift in $[K^+]_e$ is not the consequence of local changes in synaptic activity.

In mice, wakefulness defined by electrical activity also was linked to increased $[K^+]_e$, whereas natural sleep and anesthesia were associated with decreased $[K^+]_e$. These sleep-wake–associated changes in $[K^+]_e$ were accompanied by inverse shifts in extracellular calcium ($[Ca^{2+}]_e$), magnesium ($[Mg^{2+}]_e$), and hydrogen ($[H^+]_e$) ion concentrations, as well as extracellular space volume (see the figure).

Can simple alterations in the extracellular ion composition wake a sleeping animal and put an awake animal to sleep? Ding *et al.* formulated sleep-inducing and wake-inducing artificial CSFs with ion concentrations that mimicked those during natural sleep or wakefulness, and examined how these solutions affect neuronal activity and extracellular space volume in mice. Cranial windows were implanted in the left and right cortices, allowing the infusion of artificial CSF into one neural hemisphere and direct comparison with the contralateral hemisphere. Remarkably, directed local and brainwide manipulations of extracellular ions can control neuronal activity and extracellular volume, and can even override the overarching behavioral state. Thus, extracellular ions contribute to the state-dependent control of neuronal activity across sleep and wakefulness.

Whether changes in the brain's ionic milieu control enhanced sleep drive after prolonged wakefulness, and/or sleep satiation after extended recovery sleep, is not known. It is also unclear whether regional ionic shifts explain local sleep—that is, neuronal down states in one cortical area but not in another. Pumps and transporters that control ion flow across cell membranes may be promising new targets for treating sleep-wake disorders. Future work may also assess the effects of REM sleep on extracellular ions, a sleep state characterized by neurophysiological features that are common to both sleep and wakefulness (*11*). ■

REFERENCES

1. F. Ding *et al.*, *Science* **352**, 550 (2016).
2. R. E. Brown *et al.*, *Physiol. Rev.* **92**, 1087 (2012).
3. I. Timofeev *et al.*, *Proc. Natl. Acad. Sci. U.S.A.* **98**, 1924 (2001).
4. Y. Nir *et al.*, *Neuron* **70**, 153 (2011).
5. S. C. Holst *et al.*, *J. Neurosci.* **34**, 566 (2014).
6. J. H. Benington, H. C. Heller, *Prog. Neurobiol.* **45**, 347 (1995).
7. J. Seigneur *et al.*, *Cereb. Cortex* **16**, 655 (2006).
8. N. Kleitman, in *Sleep and Wakefulness*, N. Kleitman, Ed. (Univ. of Chicago Press, Chicago, IL, 1963), pp. 195–207.
9. V. Demole, *Naunyn Schmiedebergs Arch. Pharmacol.* **120**, 229 (1927).
10. M. Cloëtta *et al.*, *Naunyn Schmiedebergs Arch. Pharmacol.* **174**, 589 (1934).
11. G. Tinguely *et al.*, *NeuroImage* **32**, 283 (2006).

10.1126/science.aaf8178

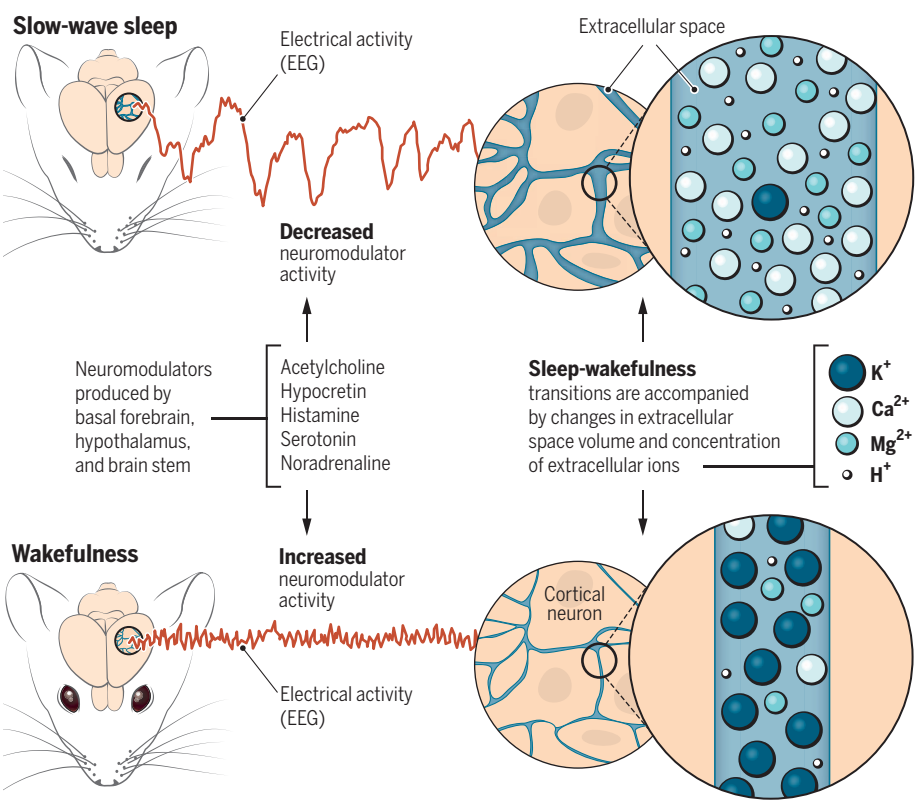

Ionic milieu of sleep. Wakefulness and slow-wave sleep differ markedly in polysomnographic signals (EEG, electroencephalogram), brain neuromodulator activity, extracellular ion concentrations, and interstitial volume.

BIOCHEMISTRY

A bacterial oxidase like no other?

The structure of an oxidase found in many pathogens will help in drug development

By **Gregory M. Cook**[1,2] *and* **Robert K. Poole**[3]

Most biological oxygen consumption is carried out by membrane-integrated oxidases, which fall into three main classes. The heme-copper oxidases (HCOs) of mitochondria and many bacteria (*1*) have a binuclear active site that contains a heme and a copper atom. They achieve rapid, virtually complete reduction of oxygen to water. The alternative oxidases (AOXs) found in certain plants, fungi, and bacteria have a heme-free iron-iron reactive site (*2*) that confers nitric oxide–resistant respiration (*3*). The last class, the bacterial cytochrome bd–type oxidases (*4*), are found in many pathogenic bacteria and have a distinctive heme composition consisting of two hemes b and one heme d. On page 583 of this issue, Safarian *et al.* report the atomic-resolution structure of a cytochrome bd–type oxidase from *Geobacillus thermodenitrificans* (*5*). The structure will facilitate targeted and rational drug development against cytochrome bd–type oxidases.

The unique spectral signatures of heme d have made identification of cytochrome bd–type oxidases in numerous types of bacteria straightforward. Indeed, such an oxidase was first described in the 1930s (*6*). They have extraordinary ligand-binding activities: Respiration via cytochrome bd exhibits nanomolar affinity for oxygen (*7*), even though oxygen can form a uniquely stable oxygenated complex (*8*) that is the first intermediate in the accepted oxygen reduction mechanism (*4*). Cytochrome bd also plays special roles in pathogenic bacteria (*9*). For

[1]*Department of Microbiology and Immunology, Otago School of Medical Sciences, University of Otago, Dunedin 9054, New Zealand.* [2]*Maurice Wilkins Centre for Molecular Biodiscovery, University of Auckland, Auckland 1042, New Zealand.* [3]*Department of Molecular Biology and Biotechnology, University of Sheffield, Sheffield S10 2TN, UK.*
Email: greg.cook@otago.ac.nz

ILLUSTRATION: K. SUTLIFF/*SCIENCE*

Downloaded from http://science.sciencemag.org/ on April 28, 2016

Published by AAAS

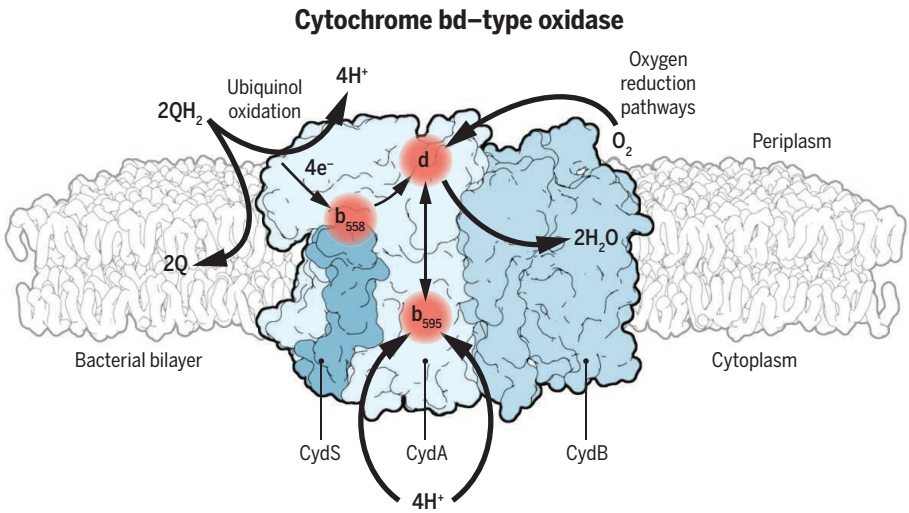

A unique bacterial oxidase with recognizable elements. The high-resolution structure of a cytochrome bd–type oxidase reported by Safarian *et al.* contains the established subunits CydA and CydB as well as a third subunit, CydS, that appears to stabilize heme b_{558}. Ubiquinol (QH_2) is oxidized to ubiquinone (2Q) at the ubiquinol oxidation site on CydA, liberating protons to the periplasm; electrons are then passed to heme d and heme b_{595}. The latter heme pair has previously been considered to represent a binuclear site where oxygen is activated and reduced to water, as in mitochondrial oxidases. However, the new structure reveals a triad (rather than linear) heme arrangement; the distances between the two b–type hemes is greater than that between b_{558} and d, which suggests that electron transfer proceeds from b_{558} to d, followed by equilibration with heme b_{595}. Protons may then move from the bacterial cytoplasm to the oxygen reduction site via two possible pathways identified in CydA and CydB.

example, *Brucella* species, the causative agents of brucellosis in swine and cattle, depend on cytochrome bd for replication and survival in macrophages. One reason for this may be that cytochrome bd is insensitive to nitric oxide and hydrogen peroxide (*9*).

The studies reviewed in (*9*) and other experiments in *Salmonella* and *Mycobacterium tuberculosis* strongly suggest that cytochrome bd may be an attractive therapeutic target. Indeed, mutants of *M. tuberculosis* and *M. smegmatis* lacking cytochrome bd are hypersensitive to bedaquiline, a tuberculosis drug that targets the respiration-driven membrane-bound F_1F_o-ATP synthase (*10*, *11*). Furthermore, cytochrome bd mutants of *M. smegmatis* are hypersusceptible to clofazimine (*12*), a leprosy drug, and many antimicrobials rely on respiration mediated by cytochrome bd for killing *Escherichia coli* (*13*).

Atomic-resolution structures of oxidases from the HCO and AOX classes have been reported, but despite decades of research, no cytochrome bd structure has been forthcoming. Scientists have long argued, on the basis of the primary sequence of the cytochrome bd–type oxidases and of models derived from hydrophobicity profiles and biochemical approaches (*4*), that this class of oxidase has no structural resemblance to the heme-copper superfamily. The most extensively studied cytochrome bd oxidase is that of *Escherichia coli*. In *E. coli*, cytochrome bd consists of two integral membrane subunits CydA and CydB (heterodimer) made up of nine and eight transmembrane-spanning segments, respectively. The enzyme catalyzes the two-electron oxidation of quinol and the four-electron reduction of dioxygen to water to generate a proton motive force.

Safarian *et al.*'s structure shows that the bd oxidase from *G. denitrificans* has 19 helices that span the bacterial cytoplasmic membrane (see the figure). CydA and CydB each have nine helices; the 19th helix is the small peptide called CydS. In contrast to *E. coli*, the CydA and CydB protein subunits in *G. denitrificans* share the same fold, most likely as a result of gene duplication of a single ancestral gene that encoded a homodimeric oxidase. However, the three hemes are associated only with CydA, which also harbors the site of ubiquinol oxidation (see the figure). CydS is a single transmembrane helix of 33 amino acid residues and may stabilize the b_{558} heme next to the quinol oxidation site. Hoeser *et al.* have reported a third subunit, CydX, in the *E. coli* oxidase (*14*), and it may be noteworthy that, despite numerous attempts over many years to crystallize the *E. coli* enzyme, no success was obtained with two-subunit preparations that lack CydX.

A surprising feature of Safarian *et al.*'s structure is the triad arrangement of the hemes (see the figure). Models of electron transfer have suggested a linear arrangement, with stepwise transfer from quinol to heme b_{558} and then to b_{595} and d, where oxygen is reduced to water. Instead, the distance between the two b-type hemes is greater than that between b_{558} and d, suggesting that electron transfer proceeds from b_{558} to d, followed by equilibration with heme b_{595}. Thus, there is no clear analogy to the active site in HCOs, in which the heme and copper centers are only 4 to 5 Å apart (*15*), or to the nonheme di-iron carboxylate found in AOXs (*2*). Whatever the details of the oxygen-reduction mechanism, which is not dealt with in detail by Safarian *et al.*, cytochrome bd must achieve a concerted four-electron reduction of oxygen to avoid deleterious release of partially reduced oxygen intermediates.

Unlike all members of the HCO superfamily, cytochrome bd does not pump protons across the membrane. However, it does result in net proton translocation as a result of proton extrusion from quinol oxidation and the uptake of protons from the cytoplasm for oxygen reduction. In the *Geobacillus* oxidase, there appear to be two probable channels, one in each major subunit, that converge on cytochrome b_{595} within the bilayer (see the figure). An onward route to heme d has not been identified.

Further detailed experimental approaches informed by Safarian *et al.*'s structure, as well as high-resolution structures of other cytochrome bd–type oxidases, will be required to precisely delineate the oxygen reduction mechanism and the two proposed proton channels in CydA and CydB. But for the present, the structural framework provided by Safarian *et al.* will lead the way in our understanding of this fascinating and important enzyme. ■

REFERENCES AND NOTES

1. J. Abramson, M. Svensson-Ek, B. Byrne, S. Iwata, *Biochim. Biophys. Acta* **1544**, 1 (2001).
2. T. Shiba *et al.*, *Proc. Natl. Acad. Sci. U.S.A.* **110**, 4580 (2013).
3. A. K. Dunn *et al.*, *Mol. Microbiol.* **77**, 44 (2010).
4. V. B. Borisov, R. B. Gennis, J. Hemp, M. I. Verkhovsky, *Biochim. Biophys. Acta Bioenerg.* **1807**, 1398 (2011).
5. S. Safarian *et al.*, *Science* **352**, 583 (2016).
6. D. Keilin, *The History of Cell Respiration and Cytochrome* (Cambridge Univ. Press, Cambridge, 1966).
7. R. D'mello, S. Hill, R. K. Poole, *Microbiology* **142**, 755 (1996).
8. R. K. Poole, C. Kumar, I. Salmon, B. Chance, *J. Gen. Microbiol.* **129**, 1335 (1983).
9. G. M. Cook, C. Greening, K. Hards, M. Berney, *Adv. Microb. Physiol.* **65**, 1 (2014).
10. M. Berney, T. E. Hartman, W. R. Jacobs, *mBio* **5**, e01275 (2014).
11. K. Hards *et al.*, *J. Antimicrob. Chemother.* **70**, 2028 (2015).
12. P. Lu *et al.*, *Sci. Rep.* **5**, 10333 (2015).
13. M. A. Lobritz *et al.*, *Proc. Natl. Acad. Sci. U.S.A.* **112**, 8173 (2015).
14. J. Hoeser, S. J. Hong, G. Gehmann, R. B. Gennis, T. Friedrich, *FEBS Lett.* **588**, 1537 (2014).
15. J. Koepke *et al.*, *Biochim. Biophys. Acta Bioenerg.* **1787**, 635 (2009).

ACKNOWLEDGMENTS

R.K.P. thanks J. Rafferty and H. Southam for assistance in preparing this Perspective.

10.1126/science.aaf5514

ILLUSTRATION: C. BICKEL/*SCIENCE*

Downloaded from http://science.sciencemag.org/ on April 28, 2016

Published by AAAS

SYNTHETIC FOLDAMERS

Light flips a membrane-embedded helix

A folded helical chain can switch its handedness even in a viscous membrane environment

By **Christina M. Thiele**[1] *and* **Anne S. Ulrich**[2]

Signaling proteins embedded in cell membranes can transmit information from one side to another, usually by a conformational change within a bundle of transmembrane helices. The challenge of mimicking these proteins with smaller molecules has been picked up by synthetic chemists. On page 575 of this issue, De Poli *et al.* (*1*) show that a conformational change in a helical foldamer not only can be elicited by irradiation with light, it can also be allosterically transmitted within a membrane over a distance of up to 2 nm.

Helical biomolecules exist in two enantiomeric forms, right-handed and left-handed mirror images (see the figure). In natural proteins and polypeptides, the helix sense is dictated by the stereogenic center of the constituent L–amino acids, and these α helices are usually right-handed. A conversion into the left-handed form is possible only in rare cases (*2*).

Synthetic efforts have been devoted to the design of one-handed helical oligomers without a backbone stereogenic center (*3*). They can be distinguished according to their helix inversion barrier. Static oligomers are characterized by a high barrier. More intriguing are those with low barriers, such as polyisocyanates, polyacetylenes, polysilanes (*3*), or polypeptides made of achiral C_α-alkylated amino acids (*4*). These helices rapidly interconvert and exist in a dynamic equilibrium between right- and left-handed forms. A small chiral bias leads to a strong preference for one of the two helix senses (*5*).

Oligomers of the noncanonical achiral amino acid Aib (2-aminoisobutyric acid) represent dynamically interconverting helices. Clayden and co-workers have systematically studied the factors that govern their sense preference (*6*). De Poli *et al.* now show how a photoswitchable moiety can control the helix preference. Such investigations had only been performed in isotropic solution so far (*7*). The hydrophobic milieu of the lipid chains and the amphiphilic head groups of the membrane could have a drastic influence on the dynamical structure of these delicate helices. After all, lipid bilayers are viscous, and they constitute a highly anisotropic matrix. However, De Poli *et al.* show that the conformational change induced in the foldamers by light can still occur. Apparently, neither the viscosity of the hydrophobic core (which is comparable to that of olive oil) nor its low dielectric environment (which stabilizes polar hydrogen bonds) prevents the fast helical interconversion on the nuclear magnetic resonance (NMR) time scale.

An elegant NMR approach was used to monitor the screw sense and to quantify the helical excess of one population over the other. A pair of chemically equivalent atoms A and B (pink and green atoms in panel A of the figure) experience the presence of the chiral helical environment in a distinctive manner; that is, they are diastereotopic. Their chemical shifts are separated by $\Delta\delta_{slow}$ if the interconversion between helices is slow (panel B of the figure). If the rate accelerates—for example, at higher temperatures—the NMR signals of the reporter groups become averaged. The corresponding $\Delta\delta_{fast}$ collapses to zero if and only if the two helical conformations are present in equal amounts (see panel C of the figure, $K = 1$). When there is a certain preference for one screw sense, $\Delta\delta_{fast}$ becomes a direct measure for helical excess as the ratio $\Delta\delta_{fast}/\Delta\delta_{slow}$ (*8*).

Fluorine atoms were used as sensitive NMR reporter groups, both on the azobenzene group—which is photoswitched from its *E* to its *Z* isomer—and for the diastereotopic readout. Helices consisting of four Aib units underwent fast interconversion, so changes in $\Delta\delta_{fast}$ could be interpreted quantitatively in terms of changes in helical excess (see panel D of the figure). Upon doubling the helix length, the rate got slowed down beyond this regime once the foldamer was embedded in a lipid bilayer. A change in helical excess could still be detected, although it could no longer be quantified.

One of the next challenges in the design of structures that can transmit information within membranes will be to construct and use longer polypeptides. Recently, a cyclic decapeptide was reported whose amphiphilic structure and membrane interactions could be modulated by light. Its use as an antibiotic (*9*) and anticancer agent (*10*) points toward practical applications of membrane-embedded photoswitchable agents in photodynamic therapy. ■

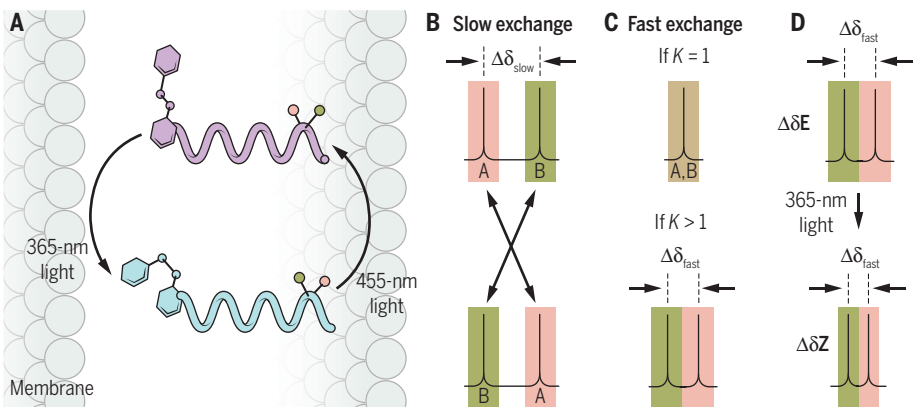

Twisting in the spotlight. (**A**) Fluorine atoms (A and B, colored pink and green) near the C terminus of an Aib helix are used as NMR reporter groups. (**B**) For slow helical exchange, their chemical shifts are separated by $\Delta\delta_{slow}$. (**C**) For fast exchange, the signals collapse for equal amounts of the two helical senses, but they have a new separation ($\Delta\delta_{fast}$) if one helical sense predominates. (**D**) Photoswitching of the N-terminal azobenzene moiety from its *E* to its *Z* isomer leads to a change in the helical preference reflected in a change in $\Delta\delta_{fast}$.

[1]*Clemens Schöpf Institute for Organic Chemistry and Biochemistry, Technische Universität Darmstadt, Darmstadt, Germany.* [2]*Institute of Biological Interfaces (IBG-2), Karlsruhe Institute of Technology, Karlsruhe, Germany. Email: cthiele@thielelab.de*

REFERENCES

1. M. De Poli *et al.*, *Science* **352**, 575 (2016).
2. M. De Zotti *et al.*, *J. Peptide Sci.* **20**, 307 (2014).
3. E. Yashima, K. Maeda, H. Iida, Y. Furusho, K. Nagai, *Chem. Rev.* **109**, 6102 (2009).
4. M. Crisma *et al.*, *J. Peptide Sci.* **21**, 148 (2015).
5. M. M. Green, M. P. Reidy, *J. Am. Chem. Soc.* **111**, 6452 (1989).
6. B. A. F. Le Bailly, J. Clayden, *Chem. Commun.* **52**, 4852 (2016).
7. D. Pijper, B. L. Feringa, *Angew. Chem. Int. Ed.* **46**, 3693 (2007).
8. J. Solá, G. A. Morris, J. Clayden, *J. Am. Chem. Soc.* **133**, 3712 (2011).
9. O. Babii *et al.*, *Angew. Chem. Int. Ed.* **53**, 3392 (2014).
10. O. Babii *et al.*, *Angew. Chem.* 10.1002/ange.201600506 (2016).

10.1126/science.aaf6191

ILLUSTRATION: P. HUEY/*SCIENCE*

Downloaded from http://science.sciencemag.org/ on April 28, 2016

Published by AAAS

The growing problem of patent trolling

Cash-hungry patent trolls are squelching innovation—and should be screened out

By **Lauren Cohen,[1,2]* Umit G. Gurun,[2,3]* Scott Duke Kominers[1,2,4]***

The last decade has seen a sharp rise in patent litigation in the United States; 2015 has one of the highest patent lawsuit counts on record (*1*). In theory, this could reflect growth in commercialization of technology and innovation—lawsuits increase as more firms turn to intellectual property (IP) protection to safeguard their competitive advantages. However, the majority of recent patent litigation is driven by nonpracticing entities (NPEs), firms that generate no products but amass patent portfolios for the sake of "enforcing" IP rights (*2*). We discuss new, large-sample evidence adding to a growing literature (*3*–*7*) that suggests that NPEs—in particular, large patent aggregators—on average, act as "patent trolls," suing cash-rich firms seemingly irrespective of actual patent infringement. This has a negative impact on innovation activity at targeted firms. These results suggest a need to change U.S. IP policy, particularly to screen out trolling early in the litigation process.

POLICY

How does NPE patent litigation affect innovation? One hypothesis suggests that NPEs are efficient intermediaries that enforce small inventors' patents against large, well-funded firms that could otherwise infringe on small inventors' patents without consequence. A conflicting hypothesis suggests that NPEs are patent trolls, extracting rents from productive, innovative firms by exploiting the fact that—because defending against litigation is costly, and the legal system is imperfect—a threat of legal action is sufficient to induce most targeted firms to settle, whether the asserted patent is valid and/or infringed.

We use two large data sets that capture the complete universe of U.S. NPE litigation from 2005 through 2015 to provide evidence on determinants of NPE litigation (*8*). We explore how patent trolling has evolved in recent years, despite legislation intended to reduce trolling (e.g., the America Invents Act of 2011). We focus on publicly traded firms, for which there are rich, publicly available measures of firm characteristics, external activities, income, profitability, and patent holdings.

NPE PATENT LITIGATION. Anecdotal evidence suggests that NPEs target firms opportunistically. Some high-profile NPEs have brought flurries of lawsuits on the basis of low-quality patents. We also see empirical markers of potential NPE opportunism. First, it is estimated that 59% of patents owned by NPEs have at least one claim that is invalid (*9*) [compared with 42% for all asserted patents (*10*)]. Second, there appears to be "forum shopping" by NPEs. Some well-known innovation hubs (e.g., Silicon Valley) have large numbers of NPE suits. However, the preponderance of NPE patent litigation (>43% of all cases) is brought in the Eastern District of Texas, which is not a major innovation center; its courts are favored by NPEs because they are perceived to be plaintiff-friendly [anecdotally and because of specific procedural rules; see (*3*, *11*, *12*)].

NPEs target cash-rich firms

"Cash-rich" describes a firm with 1 SD more cash than the average firm in the sample. The difference for NPEs is highly statistically significant ($P < 0.001$). The difference for PEs is in the opposite direction and statistically insignificant. See SM for data and methods.

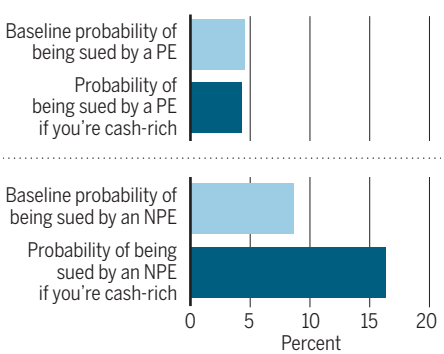

We find strong evidence that cash is the main correlate of NPE litigation (see the first figure). NPEs frequently sue firms with large cash holdings or that have recently accumulated large amounts of cash. We find that NPEs are especially likely to sue firms that are engaged in other (non–IP-related) lawsuits, as well as firms that have especially small legal teams (*13*).

When viewing firms' profits by business segment, we see that cash holdings in segments unrelated to alleged infringement drive NPE litigation just as much as holdings in related business segments do. Even when the allegedly infringing segment is losing money, NPEs still sue in order to claim profits from unrelated segments; this is hardly litigation in response to "profitable infringement."

Wouldn't anyone suing for patent infringement display the behaviors we see for NPEs? This is not what we find. The cash-targeting that we observe is primarily the behavior of large patent aggregators—not small inventors (*8*). There has not been an increase in patent litigation among practicing entities (PEs, e.g., Apple, Microsoft, and GE) commensurate with the rise in NPE litigation (see the second figure). In stark contrast to NPEs' record, PE patent litigation is not driven by cash (see the first figure), and only 7% of suits by PEs are brought in Eastern Texas.

One might also think that litigation behavior more broadly should be related to defendant cash holdings; however, this is not the case. When replicating the analysis underlying the first figure for other types of litigation against publicly traded firms, no other type of litigation (environmental, labor, contract, securities, or tort) involves the same cash focus that we see in NPE-driven patent litigation (*8*). This suggests that the main determinant of non-IP litigation is the infraction itself (e.g., polluting a waterway in the case of an environmental suit). Both within the patent space and across litigation more broadly, NPE patent litigation is unique in the extent to which it is driven by cash.

NPES' IMPACT ON INNOVATION. Patent trolling by NPEs has a sizable negative impact on innovation at targeted firms. We estimate that, after settling with NPEs (or losing to them in court), firms on average reduce research and development (R&D) investment by >25% (*8*). Others have found similarly sized reductions in R&D (*14*, *15*) and other negative impacts of NPE litigation (*16*, *17*).

[1]*Harvard Business School, Boston, MA 02163, USA.* [2]*National Bureau of Economic Research, Cambridge, MA 02138, USA.* [3]*University of Texas at Dallas, Richardson, TX 75080, USA.* [4]*Society of Fellows, Department of Economics, Center of Mathematical Sciences and Applications, Center for Research on Computation and Society, and Program for Evolutionary Dynamics, Harvard University, Cambridge, MA 02138, USA.* *Corresponding authors contributed equally. Email: lcohen@hbs.edu, umit.gurun@utdallas.edu, kominers@fas.harvard.edu*

GRAPHIC: C. SMITH/*SCIENCE*

Downloaded from http://science.sciencemag.org/ on April 28, 2016

Published by AAAS

Recent trends in patent litigation

NPE, PE, and total patent litigation against publicly traded firms, 2005–2015. Data derived from public filings [Public Access to Court Records (PACER)]. See SM for data and methods.

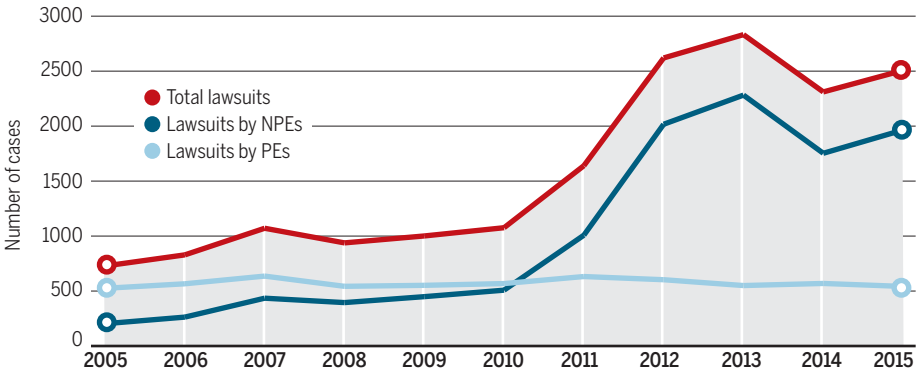

Causes of the R&D reductions at NPE-targeted firms are not directly identifiable, and deserve further study: Do firms reduce innovation because they have lost resources through litigation and/or settlement? Do they shift focus in order to avoid future litigation? Furthermore, it is not evident that this reduction in innovation is made up for by increased invention elsewhere. In theory, NPEs could improve small inventors' incentives to innovate by reducing infringement by other firms and by promoting a financial transfer to inventors when infringement occurs. However, the value of NPEs to small inventors (through direct transfers or in terms of increased bargaining power) is mediated by the fractions of settlements and damage awards that NPEs pass through to small inventors (*8*)—only money that reaches inventors matters for those inventors' incentives. The pass-through of NPE patent litigation proceeds to inventors is estimated to be low (*18–20*), so even large settlements or damage payments from targeted firms to NPEs do not clearly support external innovation. Evidence also indicates that NPE patent litigation has not resulted in increased small-inventor activity (*8, 21*).

POLICY OPTIONS. Our results imply a need to reduce patent trolling by NPEs, through legislation or changes in the IP marketplace. Since 2010, Congress has considered more than a dozen bills that seek to reduce patent trolling (H.R.9, the "Innovation Act" is currently on the docket). But most of the proposed policy changes focus on punishing trollers "after the fact" for bringing lawsuits that are declared to be frivolous (or "extraordinary") after court proceedings. The Innovation Act, for example, would require mandatory fee-shifting for patent lawsuits that the courts determine not to be "reasonably justified."

However, the average costs of patent litigation are large [$1 to $4 million (*22*)], and the process is drawn out. Even with the prospect of posttrial fee-shifting, patent litigation targets may find it cost-effective and less disruptive to simply settle with NPEs—even in unfounded lawsuits. Consequently, punishing trolling after the fact is not enough. Policies should screen out trolling at or before the time of patent assertion.

Part of the solution is to reduce the cost of challenges to low-quality patents. In the United States, patents can be contested on the basis that the claimed inventions are not truly "original" (i.e., prior art exists). But filing a single such inter partes review challenge costs tens or hundreds of thousands of dollars. Thus, even easily identifiable "junk patents" remain in force. Such patents can be used in trolling litigation and rarely see court challenges because most trolling actions end in settlement.

Additionally, mechanisms should be adopted to weed out low-quality patent lawsuits. A system of "advance screening" could require that patent litigation be preceded by a brief court appearance and/or patent review. The review would provide preliminary evaluation of whether the plaintiff's infringement claims are reasonable and of whether the asserted patents are of high quality. The cost of review must be set so as not to crowd out small plaintiffs.

Advance review could cripple trolling. A finding against the plaintiff would bolster the targeted firm's defense against unfounded patent infringement claims. In extreme cases, advance review could trigger reexamination (and potential invalidation) of asserted patents of sufficiently low quality. Nevertheless, advance review should generally benefit patent holders that have legitimate infringement claims; plaintiff-favoring findings might help patent holders by encouraging infringers to settle or by making it easier to secure litigation financing.

Prelitigation review could provide ex ante and ex post aid in separating meritorious infringement claims from opportunistically motivated ones. It could reduce stress on the patent litigation system, freeing up resources for resolution of credible claims. Screening mechanisms should garner widespread support. They stand to save firms and small inventors from frivolous, opportunistic infringement claims and thus to separate legitimate NPE claims from trolling. ■

REFERENCES AND NOTES

1. J. Mullin, *Ars Technica*, 5 January 2016.
2. In line with the definition used by our data sources, by NPEs we mean "firms that derive the majority of their revenues from licensing and enforcement of patents." Traditional "patent assertion entities" make up the majority of NPEs. Individual inventors are sometimes counted as NPEs, but universities are not (unless they have enforcement subsidiaries). In 2012, the America Invents Act changed the rules of patent litigation by "disjoining" lawsuits based on unrelated infringement claims. Thus, figures of patent lawsuits filed before and after 2012 are not quite comparable, especially because many NPEs file suits against multiple parties.
3. J. R. Allison, M. A. Lemley, D. L. Schwartz, "How often do patent assertion entities win patent suits?" (Working paper, Northwestern Univ., Evanston, IL, 2015).
4. C. Cotropia, J. Kesan, D. Schwartz, *Minn. Law Rev.* **99**, 649 (2014).
5. R. Feldman, E. Frondorf, *Stanford Technol. Law Rev.* **19**, 52 (2015).
6. J. O. Lanjouw, M. Schankerman, *J. Law Econ.* **47**, 45 (2004).
7. R. Feldman, T. Ewing, S. Jeruss, *UCLA J. Law Technol.* **18**, 1 (2013).
8. L. Cohen, U. G. Gurun, S. D. Kominers, "Patent trolls: Evidence from targeted firms" (Finance working paper no. 15-002, Harvard Business School, Boston, MA, 2015).
9. S. P. Miller, *Virginia J. Law Technol.* **18**, 1 (2012).
10. J. R. Allison, M. A. Lemley, D. L. Schwartz, *Tex. Law Rev.* **92**, 1769 (2014).
11. J. J. Anderson, *Univ. Pa. Law Rev.* **163**, 631 (2015).
12. Y. Leychkis, *Yale J. Law Technol.* **9**, Art. 6 (2007).
13. Most data we used are from RPX, Inc., which provides systematic data from Public Access to Court Electronic Records (PACER) on every lawsuit filed by more than 4000 NPEs back to 1977. We have replicated our results outside this sample on the publicly available data set of (*4*) hosted on www.npedata.org. For details, see Table A4 in (*8*).
14. R. Smeets, "Does patent litigation reduce corporate R&D? An analysis of US public firms" (Working paper, Rutgers Univ, New Brunswick, NJ, 2014).
15. C. Tucker, *Patent Trolls and Technology Diffusion: The Case of Medical Imaging* (Working paper, Massachusetts Institute of Technology, Cambridge, MA, 2014).
16. C. V. Chien, *Stanford Technol. Law Rev.* **17**, 461 (2014).
17. S. Kiebzak, G. Rafert, C. E. Tucker, *Res. Policy* **45**, 218 (2016).
18. J. E. Bessen, M. J. Meurer, *Cornell Law Rev.* **99**, 387 (2014).
19. J. E. Bessen, J. Ford, M. J. Meurer, *Regulation* **34**, 26 (2011).
20. F. M. Scott Morton, C. Shapiro, *Antitrust Law J.* **79**, 463 (2014).
21. R. Feldman, M. A. Lemley, *Iowa Law Rev.* **101**, 137 (2015).
22. American Intellectual Property Law Association, "AIPLA Report of the Economic Survey 2013" (AIPLA, Arlington, VA, 2013).

ACKNOWLEDGMENTS

The authors thank D. McCurdy, C. Reohr, and S. Tiwari at RPX for data used in (*8*) and this study, and thank S. Dickstein, K. Felter, J. Golden, J. E. Humphries, P. Kominers, J. Lerner, O. Luk, D. Schwartz, and several reviewers for helpful comments. The authors acknowledge funding from the NSF (grants SciSIP-1535813, SES-0847395, SES-1459912, and CCF-1216095). S.D.K. acknowledges the support of the Harvard Milton Fund and the Wu Fund for Big Data Analysis.

SUPPLEMENTARY MATERIALS

www.sciencemag.org/content/352/6285/521/suppl/DC1

10.1126/science.aad2686

GRAPHIC: C. SMITH/*SCIENCE*

Downloaded from http://science.sciencemag.org/ on April 28, 2016

Published by AAAS

BOOKS *et al.*

EPIDEMIOLOGY

After Ebola

Lessons learned from past pandemics offer insight into how to stop the next one

By **Christopher Kemp**

In the 1760s, the British made a fateful decision to inhabit the Sundarbans, a wild coastal region in India, near Bangladesh. There, for the first time, humans came into direct contact with copepods, tiny zooplankton that were infested with a bacterium called *Vibrio cholerae*. Before 1760, it had killed no one. But once in contact with humans, it mutated and became pathogenic and transmissible from one person to another. By 1817, and for the next 100 years, *V. cholerae* was an efficient killer.

The story of cholera, and the death and destruction it has wrought on humankind, provides the backdrop for Sonia Shah's excellent *Pandemic: Tracking Contagions, from Cholera to Ebola and Beyond*. Shah explores the essential factors needed to ignite a pandemic: from its initial jump to humans to its global spread, pathogens are often aided by lack of hygiene, overcrowding, and political corruption.

Shah began thinking about emerging pathogens when multiple-resistant *Staphylococcus aureus* (MRSA) entered her house, infecting and reinfecting her family for 3 years. Using the cholera pandemics of the 19th century for context, she writes about the emergence of modern pandemics. They are legion: West Nile virus, severe acute respiratory syndrome (SARS), MRSA, Lyme disease, Ebola, and others. What factors caused them? How do we contain them? Which terrifying pathogen comes next? Can we stop it?

Pandemic is enlightening—and relentlessly frightening—on every single page. With cholera, the bodies turn blue; the blood thickens. At one point, about halfway through the book, I noticed an itchy red blemish on one of my toes and was convinced I had two or three days left. The monkeypox, I surmised. And you will, too.

The reviewer is at the Department of Translational Science and Molecular Medicine, Michigan State University, Grand Rapids, MI 49503, USA. Email: cjkemp@gmail.com

Vibrio cholerae was inadvertently introduced into a major Haitian water source by United Nations peacekeepers in the aftermath of the 2010 earthquake, leading to the worst cholera epidemic in recent history.

Pandemic
Tracking Contagions, from Cholera to Ebola and Beyond
Sonia Shah
Sarah Crichton Books, 2016. 287 pp.

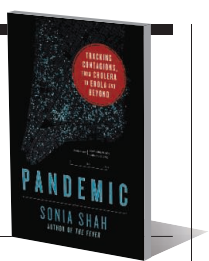

Since the beginning of the Industrial Age, humans have been perturbing the natural world in ways that bring us closer to the pathogens that kill us. Often, we are not their intended host. But we'll do.

In 1832, when cholera made it to Canada via steamship, it killed 3000 people in 11 days in Montreal and Quebec City. With advances in technology, the modes of transport have only become quicker. In 2003, SARS—a coronavirus that causes an acute respiratory sickness—passed from horseshoe bats to palm civets in a market where exotic animals were sold for food in Guangzhou, China. A few dozen people were sickened. SARS became a global concern when an infected doctor checked into the Metropole Hotel in central Hong Kong and transmitted the disease to his fellow tenants. Within 24 hours, it was in Singapore, Vietnam, Canada, Ireland, and the United States. It eventually made it to 32 countries.

SARS is gone, for now. But cholera is back, erupting across Haiti after a 2010 earthquake. MRSA now kills more Americans each year than AIDS. The next great contagion is out there: waiting, hiding, weaponizing.

Sixty percent of newly emerged pathogens originate in animals. Cows gave us measles; pigs brought pertussis; ducks provided influenza. About 70% of new pathogens come from wild animals. The suspected host species for the Ebola virus is a bat. Although primates represent only 0.5% of vertebrates, a fifth of all zoonotic pathogens come from them—including HIV and malaria.

During the winter, writes Shah, in urban areas across the United States, the majority of aerosolized bacteria come from dog feces. My neighbor, who twirls a heavy-looking bag of dog feces in the air twice a day on his walks around the block, is just one culprit among millions.

We know that the pathogens come from the wild and that our encroachments influence their mutability and enable their spread, but epidemiologists still can't predict how or when our perturbations will cause an outbreak. In 2009, Shah writes, dengue fever erupted in Florida for the first time in 70 years. A peak in home foreclosures had left water in abandoned swimming pools across Key West, a haven for dengue-carrying mosquitoes.

Every time humans disrupt fragile ecosystems, we stumble farther into the darkness. Will we eventually encounter a copepod that harbors a bacterium even worse than cholera? Or a primate whose immune system is overrun with a virus we can't control? Will gradual climate change allow fungi the opportunity to evolve the ability to survive within the relative furnace of a human body?

Whatever comes, this time a global army of virologists, epidemiologists, and doctors will be waiting for it.

10.1126/science.aaf6279

PHOTO: ASSOCIATED PRESS

Downloaded from http://science.sciencemag.org/ on April 28, 2016

Published by AAAS

ETHOLOGY

Animal acumen

Biased notions of what constitutes intelligence may lead us to underestimate the cognitive capacity of other creatures

By **Nicola Clayton**

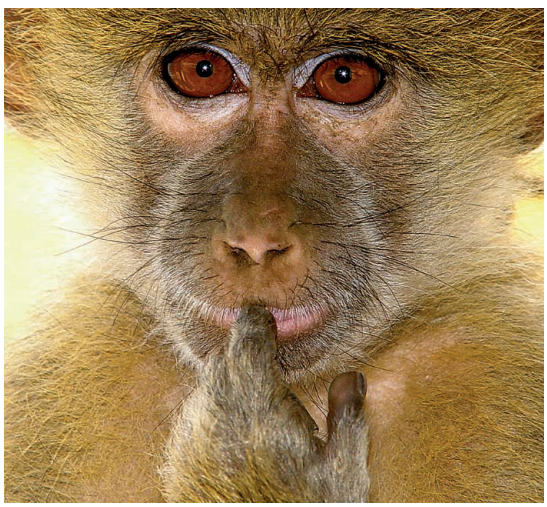

It's time to rethink what we think we know about animal cognition.

Ever since the seminal writings of Charles Darwin, it has been well established that minds, like bodies, have evolved through the processes of natural and sexual selection. As a consequence, Darwin himself once argued that any difference between human and nonhuman animals "is one of degree, not kind."

Yet it is equally well established that no other animal can read and write. Language provides our species with an adaptive specialization that, in addition to enabling communication, facilitates important cultural elements, such as storytelling and imagination, as well as the ability to self-reflect and monitor our thoughts.

Just how do we address the question of what it is like to think without and beyond language? And what might these abilities tell us about the evolution of animal, or even alien, intelligence?

In *Are We Smart Enough to Know How Smart Animals Are?*, Frans de Waal explores whether our mode of investigating animal cognition is inherently biased against manifestations of intelligence that are decidedly nonhumanlike. As the physicist Werner Heisenberg so eloquently observed, "what we observe is not nature in itself, but nature exposed to our method of questioning."

In addition to an eminent career as a primatologist and ethologist, de Waal is also a wonderful writer of popular science and a stunning photographer. Indeed, it's this combination that makes *Are We Smart Enough* so inspiring. I admit, I was disappointed not to see some of his gorgeous photographs in this book; however, the illustrations—drawn by de Waal—are quite nice and complement the text well.

The book covers many of the hot topics in comparative cognition, particularly the relatively new focus on the convergent evolution of cognition. This emphasis on evolution has resulted in a number of studies with a comparative focus. In recent years, animal behavior researchers have begun investigating the intellectual capacities of corvids (crows, jays, and ravens), cephalopods (octopuses and giant squids), elephants, dogs, and cetaceans (dolphins, porpoises, and orcas), to name but a few.

I loved that de Waal was brave enough to tackle the consciousness issue in this book, specifically *The Cambridge Declaration on Consciousness*. In 2012, a group of prominent scientists released this document, which, contrary to popular media reports, did not assert that all nonhuman animals are conscious beings. Instead, it declared that given the biological and behavioral similarities between humans and other large-brained species, we must conclude that "humans are not unique in possessing the neurological substrates that generate consciousness." De Waal ultimately accepts this assertion, writing "I can live with that."

De Waal is not afraid to take strong perspectives. His insights are backed by deep knowledge, not just of the empiricism of the subject but also of its history. The book is interwoven with insightful comments about Konrad Lorenz and Nikolaas Tinbergen, whose seminal work on animal behavior continues to inform the study of comparative cognition to this day.

All in all, this is a beautifully written and delightfully conceived popular science book, written by an eminent researcher who has dedicated his career to making the general public aware of just how smart animals are. *Are We Smart Enough* is on par with de Waal's pioneering book *Chimpanzee Politics*: It is both a lovely read and, given its provocative premise, one that may antagonize the critic.

The reviewer is at the Department of Psychology, University of Cambridge, Cambridge CB2 1TN, UK. Email: nsc22@hermes.cam.ac.uk

10.1126/science.aaf2217

Are We Smart Enough to Know How Smart Animals Are?
Frans de Waal
Norton, 2016. 352 pp.

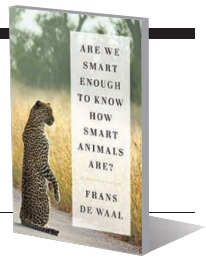

WELLCOME BOOK PRIZE WINNER

On 25 April, the Wellcome Book Prize 2016 was awarded to Suzanne O'Sullivan for her probing portrait of psychosomatic illness, *It's All in Your Head*. Inspired by O'Sullivan's work as a neurology consultant, the book explores the dramatic symptoms—from blindness to paralysis to chronic fatigue—that can arise in the absence of any discernible physical cause. Three other nonfiction titles—Amy Liptrot's memoir on addiction and recovery (*The Outrun*), Steve Silberman's treatise on autism (*NeuroTribes*; reviewed in *Science*, 25 September 2015, p. 1455), and Cathy Rentzenbrink's memoir on the aftermath of a tragic accident (*The Last Act of Love*)—as well as two works of fiction—Alex Pheby's historical novel about a famous case of schizophrenia (*Playthings*) and Sarah Moss's account of a female doctor's pioneering work in the 19th century (*Signs for Lost Children*)—were shortlisted for the 2016 prize. Billed as "books for the incurably curious," the Wellcome Book Prize recognizes outstanding new titles in health and medicine. Past winners include Marion Coutts (*The Iceberg*), Thomas Wright (*Circulation*), and Rebecca Skloot (*The Immortal Life of Henrietta Lacks*).

10.1126/science.aaf6856

It's All in Your Head
Suzanne O'Sullivan
Chatto & Windus, 2015. 336 pp.

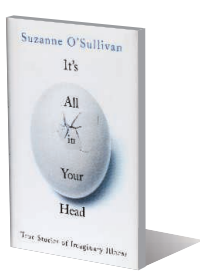

PHOTO: RUISERGIO/ISTOCKPHOTO

Downloaded from http://science.sciencemag.org/ on April 28, 2016

Published by AAAS

LETTERS

Edited by **Jennifer Sills**

Wolbachia *mosquito control: Tested*

E. L. S. LORETO and G. L. Wallau ("Risks of *Wolbachia* mosquito control," Letters, 18 March, p. 1273) suggest that the risks associated with the Eliminate Dengue Program's release of *Wolbachia*-infected mosquitoes have been insufficiently assessed. In particular, they raise the possibility that *w*Mel (the *Wolbachia* strain used by Eliminate Dengue to reduce dengue transmission) could be horizontally transferred to other insect species, with unknown consequences.

Eliminate Dengue's approach has been the subject of multiple independent governmental risk assessments, and regulatory approval for release has been granted in five countries (*1*). Each risk analysis found that the release of mosquitoes infected with *Wolbachia* carried negligible risk—the lowest level possible. They found that there was both a low risk of horizontal transfer of *Wolbachia* to other organisms and a low risk of harm even if such a transfer occurred.

Although horizontal transfer of *Wolbachia* between host species is known to occur, it is the scientific consensus that it is rare (*2*). This is demonstrated by many natural experiments. For example, *Aedes aegypti* shares breeding sites with *A. albopictus*, which is naturally infected with two strains of *Wolbachia*, yet there is no evidence of horizontal transfer of either strain. We have also tested specifically for evidence of horizontal transfer of *w*Mel from *A. aegypti* to other species from their natural environment, and we found no evidence that this has occurred even fleetingly (*3*).

It is estimated that there are 3 to 8 million species of insects on the planet (*4*) and that *Wolbachia* is naturally present in approximately half of them (*5*). Given this natural abundance, the release of *Wolbachia*-infected *A. aegypti* makes no meaningful difference to the likelihood of horizontal transfer of *Wolbachia* to a new host species. Furthermore, Eliminate Dengue's activities are unlikely to introduce this strain into locations where it does not already exist. The natural host of *w*Mel, *Drosophila melanogaster*, has a cosmopolitan geographic distribution that completely encompasses that of *A. aegypti* (*6*). Any risk to other species due to the presence of *w*Mel in their environment already exists.

Aedes aegypti

Loreto and Wallau suggest that the consequences of pesticide usage are well known, whereas those of *Wolbachia* are not. To the contrary: *Wolbachia* has been transferred between insect species, both vertically and horizontally, for millions of years (*7*) with no known adverse consequences. Similarly, no adverse consequences have been observed from more than 5 years of open field release of *A. aegypti* containing *Wolbachia* in different countries. In March, the World Health Organization recommended the deployment of *Wolbachia* to counter the growing problem to human health of *Aedes*-transmitted viruses (*8*). Now is the time to be testing new approaches like *Wolbachia* at deployment scale, given the current health crisis that the routine use of pesticides has not been able to contain.

Scott L. O'Neill

Eliminate Dengue Program, School of Biological Sciences, Monash University, Clayton, Victoria 3800, Australia. Email: scott.oneill@monash.edu

REFERENCES

1. Eliminate Dengue Program (www.eliminatedengue.com/our-research).
2. C. A. Hamm *et al.*, *Mol. Ecol.* **23**, 4871 (2014).
3. J. Popovici *et al.*, *Mem. Inst. Oswaldo Cruz* **105**, 957 (2010).
4. N. E. Stork, J. McBroom, C. Gely, A. J. Hamilton, *Proc. Natl. Acad. Sci. U.S.A.* **112**, 7519 (2015).
5. R. Zug, P. Hammerstein, *PLOS One* **7**, e38544 (2012).
6. J. R. David, P. Capy, *Trends Genet.* **4**, 106 (1988).
7. M. Gerth, M. T. Gansauge, A. Weigert, C. Bleidorn, *Nat. Commun.* **5**, 5117 (2014).
8. WHO, "Mosquito (vector) control emergency response and preparedness for Zika virus" (2016); www.who.int/neglected_diseases/news/mosquito_vector_control_response/en/.

Wolbachia *mosquito control: Regulated*

E. L. S. LORETO and G. L. Wallau ("Risks of *Wolbachia* mosquito control," Letters, 18 March, p. 1273) discuss applied strategies that use *Wolbachia* bacteria to infect natural populations of *Aedes aegypti* mosquitoes in an effort to inhibit the spread of disease. They emphasize the risk of *Wolbachia* horizontal transfer to distantly related arthropods and state that "…no country has regulations specifically pertaining to *Wolbachia*-infected insect release…." This is not the case.

In the United States, the Environmental Protection Agency (EPA) Office of Pesticide Programs, Biopesticides and Pollution Prevention Division, has been regulating *Wolbachia* as a biopesticide since 2011. This includes experimental use permits for *A. polynesiensis* (*1*), *A. albopictus* (*2*), and *A. aegypti* (*3*). After EPA review of the technology with open public comment, releases of adult male mosquitoes have thus far been performed in California, Kentucky, and New York, resulting in substantial suppression of the targeted mosquito populations (*4*). State permits were also obtained, and in New York, additional approval was obtained from the U.S. Department of the Interior, National Park Service.

Wolbachia is the most widespread group of obligate intracellular bacteria, infecting an estimated 40 to 52% of all terrestrial arthropod species (*5*, *6*). Given that there are estimated to be 5 million insect species in the Arthropoda (*7*), the introduction of trans-infected male mosquitoes would not substantially increase the existing rate of *Wolbachia* lateral transfer. *Wolbachia* is maternally inherited (*8*), and thus the introduced, *Wolbachia*-infected males are dead-end hosts. Furthermore, the *Wolbachia* infection type present in the introduced males can occur naturally within the targeted areas. For example, the *w*AlbB *Wolbachia* that infects the EPA-regulated *A. aegypti Wolbachia* biopesticide occurs naturally in *A. albopictus* (*9*), which is often sympatric with *A. aegypti*. The "risks of host shift" from introducing male mosquitoes with *Wolbachia* are therefore semantic, as relatively high infection frequencies, extinction rates, and degrees of horizontal transmission already occur in nature (*8*, *10*, *11*).

Stephen L. Dobson,[1,2]*
Seth R. Bordenstein,[3] Robert I. Rose[4]

[1]University of Kentucky, Lexington, KY 40546, USA. [2]MosquitoMate Inc., Lexington, KY 40503, USA. [3]Vanderbilt University, Nashville, TN, 37235, USA. [4]Biotechnology Regulatory Consulting, Frederick, MD 21704, USA.

*Corresponding author. Email: sdobson@uky.edu

REFERENCES

1. Federal Register, "Issuance of two experimental use permits" **78**, 130 (2013).

PHOTO: TACIO PHILIP/ISTOCKPHOTO

Downloaded from http://science.sciencemag.org/ on April 28, 2016

Published by AAAS

2. Federal Register, "Amendment of an experimental use permit" **78**, 117 (2013).
3. Federal Register, "Pesticide experimental use permit; receipt of application; comment request" **80**, 145 (2015).
4. S. Chakradhar, *Nat. Med.* **21**, 416 (2015).
5. L. A. Weinert, E. V. Araujo-Jnr, M. Z. Ahmed, J. J. Welch, *Proc. R. Soc. London. Ser. B Biol. Sci.* **282**, 20150249 (2015).
6. R. Zug, P. Hammerstein, *PLOS One* **7**, e38544 (2012).
7. A. D. Chapman, *Numbers of Living Species in Australia and the World, 2nd Edition* (Australian Government, Department of the Environment, Water, Heritage and the Arts, 2009).
8. S. L. O'Neill, R. Giordano, A. M. Colbert, T. L. Karr, H. M. Robertson, *Proc. Natl. Acad. Sci. U.S.A.* **89**, 2699 (1992).
9. Z. Xi, C. C. H. Khoo, S. L. Dobson, *Science* **310**, 326 (2005).
10. W. Zhang, L. R. Guo, *Proc. R. Soc. London Ser. B Biol. Sci.* **261**, 55 (1995).
11. A. Koehncke *et al.*, *PLOS One* **4**, 12 (2009).

TECHNICAL COMMENT ABSTRACTS

Comment on "Extended-resolution structured illumination imaging of endocytic and cytoskeletal dynamics"

Steffen J. Sahl, Francisco Balzarotti, Jan Keller-Findeisen, Marcel Leutenegger, Volker Westphal, Alexander Egner, Flavie Lavoie-Cardinal, Andriy Chmyrov, Tim Grotjohann, Stefan Jakobs

Li *et al.* (Research Articles, 28 August 2015, aab3500) purport to present solutions to long-standing challenges in live-cell microscopy, reporting relatively fast acquisition times in conjunction with improved image resolution. We question the methods' reliability to visualize specimen features at sub–100-nanometer scales, because the mandatory mathematical processing of the recorded data leads to artifacts that are either difficult or impossible to disentangle from real features. We are also concerned about the chosen approach of subjectively comparing images from different super-resolution methods, as opposed to using quantitative measures.
Full text at http://dx.doi.org/10.1126/science.aad7983

Response to Comment on "Extended-resolution structured illumination imaging of endocytic and cytoskeletal dynamics"

Dong Li and Eric Betzig

Sahl *et al.* in their Comment raise criticisms of our work that fall into three classes: image artifacts, resolution criteria, and comparative performance on live cells. We explore each of these in turn.
Full text at http://dx.doi.org/10.1126/science.aad8396

ONLINE BUZZ

Bureaucracy or accountability?

In his Working Life "Battling the bureaucracy hydra" (29 January, p. 530), J. Johansson bemoaned the bureaucracy he had to navigate to obtain funding from the European Research Council (ERC). He describes the arduous process of negotiating a contract, adding amendments, and submitting his first financial report. Jennifer Gabrys, also a recipient of an ERC grant, calls Johansson's description "off the mark" in her 2 February eLetter.

Gabrys writes that Johansson's trouble "potentially reveals less an issue with the ERC as such, and more a problem with the differing levels of experience that universities…offer in supporting ERC projects…. In this context, rather than deride the ERC, it seems imperative for researchers and smaller institutions to share best practice and experience so as to ensure the widest possible participation in ERC projects."

Gabrys emphasizes that, as Johansson acknowledged, ERC grants provide benefits including the opportunity to "undertake high-risk research" and "gain valuable experience." She continues that it is reasonable to expect that "with these opportunities…come responsibilities to ensure that institutions and individuals are able to support the research, which the contract ensures. These responsibilities also include accounting for the expenditure of public money in the pursuit of pioneering research through regular reporting."

Gabrys concludes, "In his 27 January 2016 statement to the Budgets Committee, ERC President Jean-Pierre Bourguignon notes just how successful the ERC has been in supporting research that produces radical breakthroughs and top-quality publications, all with incredibly low operating costs. Far from being a bureaucratic hydra, the ERC is an ambitious and original funding scheme that is transformative for both research and researchers."

See the full eLetter, and add your own, at http://science.sciencemag.org/content/351/6272/530.e-letters.

Downloaded from http://science.sciencemag.org/ on April 28, 2016

Published by AAAS

TECHNICAL COMMENT

ADVANCED IMAGING

Comment on "Extended-resolution structured illumination imaging of endocytic and cytoskeletal dynamics"

Steffen J. Sahl,[1]* Francisco Balzarotti,[1]* Jan Keller-Findeisen,[1] Marcel Leutenegger,[1] Volker Westphal,[1] Alexander Egner,[2] Flavie Lavoie-Cardinal,[3] Andriy Chmyrov,[4,5] Tim Grotjohann,[1] Stefan Jakobs[1,6]*

Li *et al*. (Research Articles, 28 August 2015, aab3500) purport to present solutions to long-standing challenges in live-cell microscopy, reporting relatively fast acquisition times in conjunction with improved image resolution. We question the methods' reliability to visualize specimen features at sub–100-nanometer scales, because the mandatory mathematical processing of the recorded data leads to artifacts that are either difficult or impossible to disentangle from real features. We are also concerned about the chosen approach of subjectively comparing images from different super-resolution methods, as opposed to using quantitative measures.

Li *et al.* (*1*) extend structured illumination microscopy (SIM) (*2*, *3*) by exploiting a higher numerical aperture (NA) lens and using standing light waves to switch reversibly switchable fluorescent proteins (RSFPs). The patterned on-switching of RSFPs yields a spatially controlled distribution of fluorophores in the fluorescent "on" state, adding spatial frequencies of higher order to the fluorescence emission. These higher-order frequencies improve SIM resolution, provided that they can be disentangled from the low-frequency signals. According to Li *et al.*, even moderate illumination intensities lead to higher frequencies of enhanced amplitudes, making their method more applicable to living cells than other super-resolution approaches. Employing Skylan-NS, an apparently quite photostable—but undisclosed—RSFP, recordings of a few tens of images were made. The resolution was reportedly improved to nominally 84 nm by SIM with an NA 1.7 lens and improved to nominally 62 nm when performing the RSFP switching with sinusoidal on-switching and readout patterns. By saturating the on-switching of the fluorescent proteins, Li *et al.* extended the resolution to nominally 45 nm.

[1]Max Planck Institute for Biophysical Chemistry, Department of NanoBiophotonics, Am Fassberg 11, 37077 Göttingen, Germany. [2]Laser Laboratory Göttingen, Hans-Adolf-Krebs-Weg 1, 37077 Göttingen, Germany. [3]Institut Universitaire en Santé Mentale de Québec, Cellular and Molecular Neuroscience Research Axis, 2601 Chemin de la Canardière, Québec, G1J 2G3, Canada. [4]Helmholtz Zentrum München, Institute of Biological and Medical Imaging, Ingolstädter Landstrasse 1, 85764 Neuherberg, Germany. [5]Technische Universität München, Chair for Biological Imaging, Ismaningerstrasse 22, 81675 München, Germany. [6]University of Göttingen Medical Faculty, Department of Neurology, Robert-Koch-Str. 40, 37075 Göttingen, Germany.
***Corresponding author. Email: ssahl@mpibpc.mpg.de (S.J.S.); fbalzar@mpibpc.mpg.de (F.B.); sjakobs@mpibpc.mpg.de (S.J.)**

In this latter approach, which Li *et al.* call saturated (S) patterned-activation (PA) nonlinear (NL) SIM, fluorophores are first transferred from an inactive ("off") to an active ("on") state, preparing them in the inactive state at a set of positions defined by the minima of the activation light. This is followed by saturated readout (*4*)—first patterned, then uniform—which returns the active fluorophores to the nonfluorescent "off" state. Both the activation and the readout steps thus spatially confine a defined state by exploiting a reversible state transition as described within the reversible saturable/switchable optical (fluorescence) transitions (RESOLFT) concept (*5*–*11*). In a new twist, the activation and readout light patterns employed by Li *et al.* feature minima at the same positions. For much of their work, Li *et al.* moved to nonsaturated activation and only moderately saturated readout in an acquisition sequence termed PA NL-SIM.

Although not new, the application of standing wave illumination for reversible photo-switching (*5*–*11*) is a promising direction, which had been previously pursued also by Gustafsson (*12*). In these methods (*1*, *12*), making images requires mathematical reconstruction from the raw data in the presence of noise. Such reconstructions introduce artifacts that were not acknowledged by Li *et al.* This is of particular concern when imaging small, intricate structures located at or near extended objects generating a strong low-frequency signal. Compare Fig. 1A and B (data from figures S31 and 3A of Li *et al.*), where filaments of actin in dimmer image regions appear to be periodically fragmented. Structures imaged by Li *et al.* with (S)PA NL-SIM appear continuous in large-scale overviews. Yet the periodic artifacts may manifest as punctate or thin-segment features sticking out of or showing up parallel to a genuine structure. This hampers the interpretation of details. For example, a characterization of genuinely periodic features would be difficult. Zooming in on a further actin image example (Fig. 1C; taken from Fig. 3B of Li *et al.*) uncovers problems at the very spatial scale for which super-resolution methods are intended. The effects are less easily noticeable for brighter features. Even there, however, they frequently create the illusion of periodic patterns (Fig. 1D; data from figure S17 of Li *et al.*).

The raw data generated by (S)PA NL-SIM contains a dominant low-resolution component that superposes the weak contributions of aliased higher-resolution components. Due to noise from all components, we deem it challenging to differentiate and reassemble them reliably, despite the beneficial two-step readout in (S)PA NL-SIM. The recovery of the high-resolution information therefore requires high signal-to-noise ratios (SNRs) in the raw images and a sophisticated analysis.

We inferred by a spatial frequency analysis of the published data that the obvious artifacts are related to the five-phase/five-orientation PA NL-SIM raw data acquisition (compare the PA NL-SIM optical transfer function (OTF) shown in green in Fig. 1E). This acquisition sequence leaves its clear signature: The two-dimensional (2D) spatial frequency ($\boldsymbol{k}$) spectrum (Fig. 1F) taken from an image region (Fig. 1G, reconstructed image provided by Li *et al.*) reveals a 10-fold symmetric amplitude enhancement at a $|\boldsymbol{k}|$ of the first harmonic k_1 of PA NL-SIM. This reflects the presence of periodic patterns at spatial frequency ~k_1, which has no real-space match in the imaged actin filaments. Filtering the image by limiting the frequencies to $|\boldsymbol{k}| < 10\ \mu m^{-1}$ does not fully remove the artifacts (Fig. 1, H and I). Limiting to $|\boldsymbol{k}| < 5\ \mu m^{-1}$ avoids the spurious patterns, yet at the loss of high-resolution information (Fig. 1, J and K). Thus, we could link the patterns' source directly to the spectral region around k_1. We note that the sought-after high-resolution information is encoded in components with $|\boldsymbol{k}| > k_1$. Whether dedicated filtering or weighting in reciprocal space could attenuate the problematic frequency components—and still make use of the higher frequencies (i.e., of higher resolution)—should be a matter of further investigation. In any case, the peaked shape of the (S)PA NL-SIM OTF causes artifacts. Such reconstruction challenges still persist after many years of SIM development [see also the artifacts in (*12*)]. This is because the phase noise in the spatial frequency spectrum critically affects the reconstruction and is difficult to eliminate.

Unfortunately, all resolution values reported by Li *et al.* are asserted on the basis of frequency-space arguments, lacking any demonstration in real space. All resolutions stated are "theoretical" (figure S6 in Li *et al.*), and no evaluations are presented as to what extent the claims are supported by the data. Instead, inadequate comparisons with other investigators' work (e.g., figures S6 and S31 in Li *et al.*) are shown. We are led to speculate that the presence of high-frequency artifacts hampered the experimental verification of the resolution claims. Understandably, small details can be created in the reconstructions of Li *et al.*, but at the risk of misrepresentation.

Downloaded from http://science.sciencemag.org/ on April 28, 2016

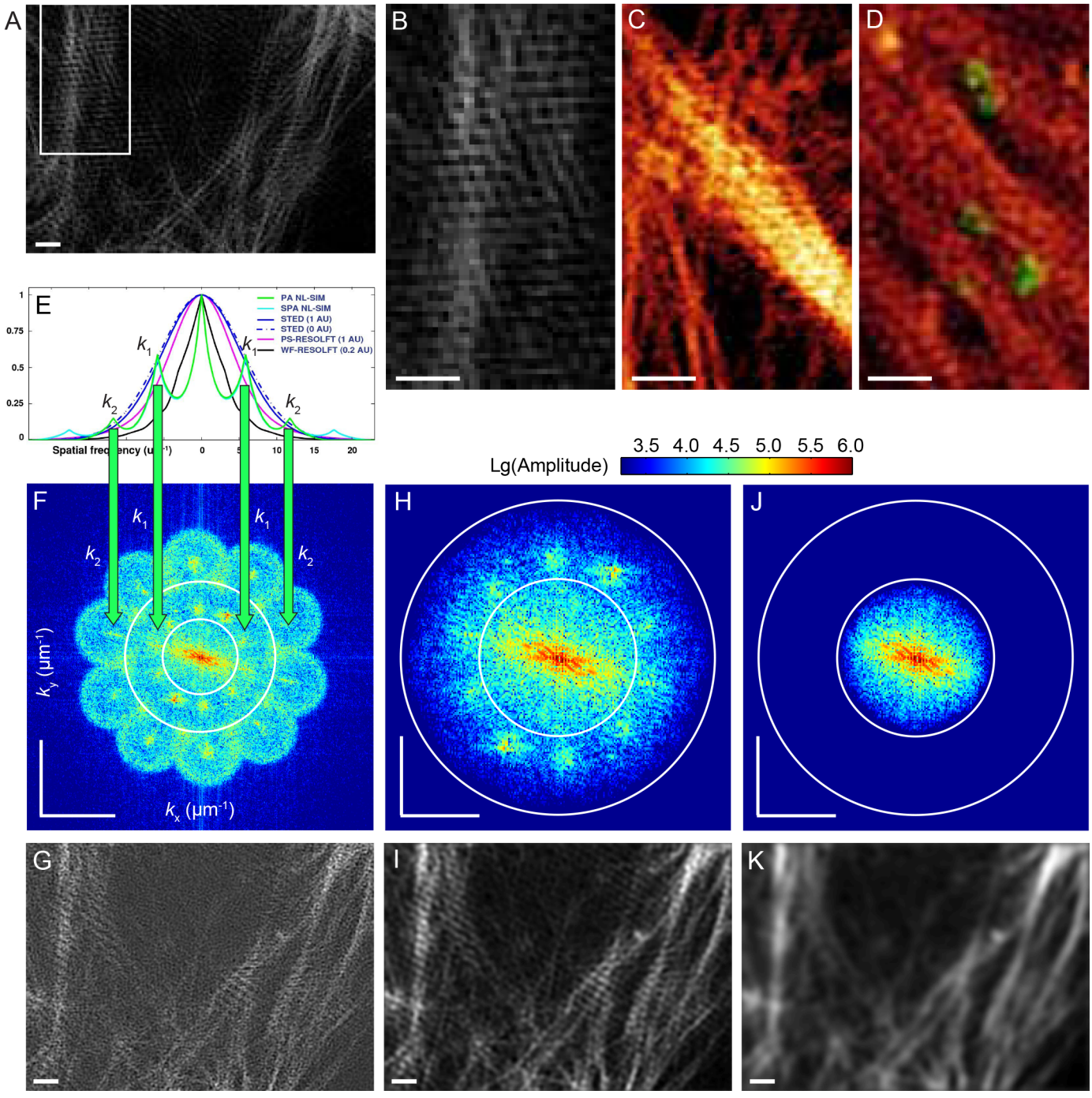

Fig. 1. Artifacts in (S)PA NL-SIM extended-resolution methods. Image details recorded by (S)PA NL-SIM exhibit conspicuous patterns, gaps, and other spurious spatial structures. These patterns do not originate from incomplete fluorescent labeling but are artifactual and inherent to the current implementations of the methods. (**A** to **D**) Magnified image regions from figures published by Li *et al*. (*1*). (A) Figure S31 (same region as in figure 3A). (B) Enlarged view of region in the white rectangle in (A). (C) Figure 3B. (D) Figure S17. (**E**) Optical transfer functions of several imaging methods, taken from figure S24 (Li *et al*.). (**F**) Amplitude of the 2D Fourier transform of the region shown in (A), which reveals enhancements of 10-fold symmetry in $\boldsymbol{k}$ space. This occurs at frequencies that correspond to the secondary and tertiary peaks of the OTF [green arrows from (E)]. (**G**) Original data of the region shown in (A) (unthresholded, linear colormap) used for the calculation of (F) (kindly provided by Li *et al*.). The insufficient attenuation of the problematic frequency components visible in (F) is directly responsible for artifactual spatial image patterns. This is illustrated by low-pass filtering the original image (G): leaving only the components below the second harmonics ($|\boldsymbol{k}| < 10\ \mu m^{-1}$), shown in (**H**), still contains the artifacts (**I**); further filtering to exclude the first harmonics ($|\boldsymbol{k}| < 5\ \mu m^{-1}$), shown in (**J**), removes the spurious patterns (**K**), but also comes with a loss of resolution. A Lanczos window with hard edges at the white circles was applied in the retransforms [(H) to (K)] to avoid the undesired introduction of additional high-frequency structure. Scale bars [(A) to (D) and (G), (I), and (K)]: 500 nm. Scale lines represent 10 μm^{-1} (F) and 5 μm^{-1} [(H) and (J)]. The circles' radii in (F), (H), and (J) correspond to 5 μm^{-1} and 10 μm^{-1}, respectively.

Downloaded from http://science.sciencemag.org/ on April 28, 2016

RESOLFT microscopy had previously also been implemented with the intensity minima leaving emitters confined in the "off" state (*13*, *14*). However, in the works using photoswitchable proteins (*8*–*12*), the strategy was to spatially confine the "on" state rather than the "off" state, because the image is then directly obtained from the raw data in real space. If sufficient "on-off" state contrast is achieved, the signals are read out without much contribution from (off-state) fluorophores located outside the targeted feature. The image consists mainly of high-resolution signal. Therefore, there is no strict minimal signal required to maintain correct spatial assignment, even down to the regime of a few registered photons.

Li *et al.* state that RESOLFT and stimulated emission depletion (STED) nanoscopy are "ill-equipped to study live-cell dynamics noninvasively." However, fast imaging, to date mostly by STED nanoscopy, has been used to record various structures quickly and repeatedly in living cells and has, for example, recently revealed genuinely periodic actin in living neurons (*15*). Moreover, dendritic spines in living brain slices have been followed over hours by RESOLFT nanoscopy (*16*).

Several aspects of Li *et al.*'s analysis of RESOLFT nanoscopy do not reflect the state of the art. For typical RSFPs, the switching behavior between inactive and active states is not well modeled by the $1/(1 + I/I_s)$ scaling used by Li *et al.* (with I the applied intensity and I_s the characteristic switching intensity), but better described by a (multi) exponential dependence (*17*). Li *et al.* model the RESOLFT readout at saturated levels, which also unnecessarily implies high levels of illumination and is typically avoided to better preserve the contrast between "on" and "off" states (*17*). Li *et al.*'s assessment of RESOLFT and STED nanoscopy does not seem to vary the applied intensity with the desired resolution (compare figure S2 of Li *et al.*). Tuning of resolution by varying the intensity is, however, a key benefit of RESOLFT, STED, and similar methods.

Li *et al.* emphasize that they achieve the claimed resolution gains "even at low activation and excitation saturation factors," yet it remains unclear as to what extent this can be relied on in practice. Adjusting resolution gains by applying lower intensities is routinely done in RESOLFT and STED nanoscopy in favor of increasing the number of images taken before bleaching. A lower-end choice of intensity entails less photodamage and readily delivers resolution in the regime claimed to be achieved by Li *et al.*

Although lower light levels are desirable by definition, and Li *et al.* are correct in pointing out this issue, it is worth noting that microscopy illumination is virtually always at unnaturally high light levels. Light-induced effects are wavelength-dependent, and they are often acceptable as long as they do not distort the sought-after information. Furthermore, mere comparisons of absolute photon numbers and deduced "photon efficiency" are questionable without considering sample absorption and creation of phototoxic molecular species.

The potential of using switchable fluorescent proteins for realizing low-light-level super-resolution was already pointed out in 2003 (*5*–*7*) and fervently advocated since then, also for structured illumination (*5*–*7*, *9*). Since then, it has been clear that RSFPs can provide super-resolution at low photon fluxes (*5*–*11*) due to their long-lived active and inactive states. This has now been reconfirmed by Li *et al.* In fact, the identification of fluorophore states and the implementation of selected "on-off" state transitions have always been at least as essential for providing super-resolution as the optical system in use.

Although Li *et al.* have added a valid new twist to the RESOLFT concept, their work again shows that the actual limitations lie in the properties of the fluorophores. As enough factors already complicate the rigorous analysis of biological systems, new super-resolution variants should produce data that can be interpreted with high levels of confidence.

REFERENCES

1. D. Li *et al.*, *Science* **349**, aab3500 (2015).
2. M. G. L. Gustafsson, *J. Microsc.* **198**, 82–87 (2000).
3. J. T. Frohn, H. F. Knapp, A. Stemmer, *Proc. Natl. Acad. Sci. U.S.A.* **97**, 7232–7236 (2000).
4. R. Heintzmann, T. M. Jovin, C. Cremer, *J. Opt. Soc. Am. A Opt. Image Sci. Vis.* **19**, 1599–1609 (2002).
5. S. W. Hell, S. Jakobs, L. Kastrup, *Appl. Phys., A Mater. Sci. Process.* **77**, 859–860 (2003).
6. S. W. Hell, *Nat. Biotechnol.* **21**, 1347–1355 (2003).
7. S. W. Hell, M. Dyba, S. Jakobs, *Curr. Opin. Neurobiol.* **14**, 599–609 (2004).
8. M. Hofmann, C. Eggeling, S. Jakobs, S. W. Hell, *Proc. Natl. Acad. Sci. U.S.A.* **102**, 17565–17569 (2005).
9. M. A. Schwentker *et al.*, *Microsc. Res. Tech.* **70**, 269–280 (2007).
10. T. Brakemann *et al.*, *Nat. Biotechnol.* **29**, 942–947 (2011).
11. T. Grotjohann *et al.*, *Nature* **478**, 204–208 (2011).
12. E. H. Rego *et al.*, *Proc. Natl. Acad. Sci. U.S.A.* **109**, E135–E143 (2012).
13. M. G. L. Gustafsson, *Proc. Natl. Acad. Sci. U.S.A.* **102**, 13081–13086 (2005).
14. E. Rittweger, D. Wildanger, S. W. Hell, *Europhys. Lett.* **86**, 14001 (2009).
15. E. D'Este, D. Kamin, F. Göttfert, A. El-Hady, S. W. Hell, *Cell Reports* **10**, 1246–1251 (2015).
16. I. Testa *et al.*, *Neuron* **75**, 992–1000 (2012).
17. W. Vandenberg, M. Leutenegger, T. Lasser, J. Hofkens, P. Dedecker, *Cell Tissue Res.* **360**, 151–178 (2015).

6 November 2015; accepted 5 April 2016
10.1126/science.aad7983

Downloaded from http://science.sciencemag.org/ on April 28, 2016

TECHNICAL RESPONSE

ADVANCED IMAGING

Response to Comment on "Extended-resolution structured illumination imaging of endocytic and cytoskeletal dynamics"

Dong Li[1,2]* and Eric Betzig[2]*

Sahl *et al*. in their Comment raise criticisms of our work that fall into three classes: image artifacts, resolution criteria, and comparative performance on live cells. We explore each of these in turn.

Sahl *et al*. (*1*) highlight a subregion of figure 3A from Li *et al*. (*2*) (reproduced here in Fig. 1A) that exhibits periodic image reconstruction artifacts (Fig. 1B and Sahl figure 1A, B, G, and I), and argue that these hamper "the interpretation of details." Although one always needs to be vigilant to minimize such artifacts during structured illumination microscopy (SIM) reconstruction and identify them in the final image when they occur, their selected subregion represents only 1.7% of the original image area, the remainder over which such artifacts are not notable (e.g., Fig. 1C). Furthermore, these are not "difficult or impossible to disentangle from real features." Indeed, Sahl *et al*. correctly note that they arise at the discrete spatial frequencies corresponding to the harmonics of the applied activation/excitation pattern. They are incorrect, however, that their appearance is intrinsic in SIM due to "the peaked shape of the (S)PA NL-SIM OTF." Instead, they are due to strong frequency-shifted signals arising from greater out-of-focus background in the affected region than elsewhere (compare insets in Fig. 1, B and C). As such, they can be eliminated by reducing such background. They are also easily suppressed to better reveal the underlying structure (Fig. 1D) by applying notch filters confined to just these frequencies (*3*), rather than by the unnecessarily aggressive approach of removing all information content beyond the diffraction limit (Sahl *et al*. figure 1, H to K). Sahl *et al*. also argue that such artifacts preclude the use of our methods to study periodic structures. However, truly periodic structures are rare in cell biology and can be distinguished from reconstruction artifacts in SIM, in that only the latter will rotate if the excitation pattern is itself rotated. In short, reconstruction artifacts affect only a small fraction of the image area in more than 30 data sets of live cell dynamics in Li *et al*. and its supplementary materials (SM), can be suppressed when necessary, and rarely stand in the way of revealing new biological phenomena.

Concerning resolution, the assertion by Sahl *et al*. that our claims are "lacking any demonstration in real space" is erroneous. For example, Li *et al*. figure 3C shows a clear and quantifiable progression of increased resolution in a field of caveolae successively imaged by diffraction-limited total internal reflection fluorescence (TIRF), linear SIM, patterned-activated non-linear SIM (PA NL-SIM), and saturated PA NL-SIM. Furthermore, Li *et al*.'s SM figure S37 contains linecuts through caveolar rings of various sizes that confirm experimental resolution at the theoretical limit of each method. Nevertheless, we are loath to use linewidths of isolated linear structures, as is common in the super-resolution (SR) literature, as a metric of resolution. Indeed, we argue that this metric is incomplete and often overstates the practical resolution. To illustrate, the predicted point spread function (PSF) of a reversible saturable/switchable optical (fluorescence) transitions (RESOLFT) microscope under reported conditions (Li ref. 10) of live-cell imaging has a full width at half maximum of 54 nm (Fig. 1E), yet in simulations (Fig. 1F) is unable, unlike PA NL-SIM, to resolve 25-nm-wide squares separated 80 nm edge-to-edge from adjacent 125-nm-wide squares. This is because the weak signal generated by the RESOLFT maximum when over a small square is masked by the strong background from adjacent large squares excited by tails of the PSF (red in Fig. 1E) that contain 76% of the total energy.

Moreover, measured linecuts often inaccurately report the true PSF. In parallelized, widefield (WF) RESOLFT (Li *et al*. ref. 11), for example, "background" is reduced by ad hoc subtraction, from each signal maximum, of 80% of the values at the neighboring points of greatest depletion, and enforcing a nonnegative result. Neither the spatial shift of information nor the nonnegativity constraint is a linear operation. Consequently, simulated WF-RESOLFT images show that the apparent width of a 50-nm-wide line flanked by 250-nm-wide lines varies along its length, as well as with the distance to the flanking lines (Fig. 1G) and the magnitude of "background" subtracted (Fig. 1H). Any "resolution" can be claimed by tuning these parameters. In addition, defining resolution by the narrowest observed linewidths, as is common in the SR field, risks self-selecting for artifacts, as well as for features artificially narrowed by noise. As a result, WF-RESOLFT and point scanning (PS) RESOLFT images from the literature of keratin (Li *et al*. ref. 11) and caveolin (Li *et al*. ref. 33), having linewidth-based resolution estimates of 80 nm and <50 nm respectively, appear more similar in resolution across their fields of view to diffraction-limited, deconvolved TIRF images of similar structures (Li *et al*. SM figures S6 and S34) than to PA NL-SIM or even linear SIM images of such features.

Finally, defining the resolution of a microscope by a single number is both incomplete and naïve. Every microscope acts as a filter that increasingly attenuates information associated with increasingly fine features (Li *et al*. SM note 1). Therefore, every raw image is a distorted map of the specimen that emphasizes large structures while blurring small ones. Deconvolution (*4*) corrects for this distortion but requires knowledge of the entire spectrum of attenuation in Fourier space [known as the optical transfer function (OTF)]. A practical resolution limit is reached at the spatial frequency where the OTF falls below the experimental noise floor (e.g., Li *et al*. SM figure S52). Therefore, in live-cell time-lapse SR imaging, where the potential for photobleaching and phototoxicity demands low signal-to-noise ratio (SNR) operation, how rapidly the OTF rolls off toward zero is even more important than where it reaches zero (i.e., the theoretical resolution limit). Experimental measurements of microtubules in macrophages (*5*) (Fig. 1I) show that the frequency spectrum of linear SIM data is larger than for stimulated emission depletion (STED) in the regime between 200 and 100 nm, and our calculated OTFs (Li *et al*. SM note 2 and figure S24) indicate that the same holds true for PA NL-SIM and saturated PA NL-SIM below 100 nm. Thus, the SIM-based methods are capable of achieving higher practical resolution than STED and RESOLFT for a given SNR or require far fewer emitted photons to achieve the same practical resolution (Li *et al*. SM note 5 and figures S51 and S54).

Clearly, the issue of resolution is a complex one. A full description requires the measured OTF, the SNR across each image, and the imaging conditions (as in Li *et al*. SM table S1) giving rise to this SNR. Even then, the noise, and hence the practical resolution, depends on the brightness, background level, and sparsity of the specimen—the latter because the image of a sparse specimen is weighted more strongly to high spatial frequencies that can rise above the noise floor (Li *et al*. SM note 5 and figure S55). This may help explain why many

[1]National Laboratory of Biological Macromolecules, Institute of Biophysics, Chinese Academy of Sciences, Beijing 100101, P.R. China. [2]Janelia Research Campus, Howard Hughes Medical Institute, Ashburn, VA 20147.
*Corresponding author. Email: lidong@ibp.ac.cn (D.L.); betzige@janelia.hhmi.org (E.B.)

Downloaded from http://science.sciencemag.org/ on April 28, 2016

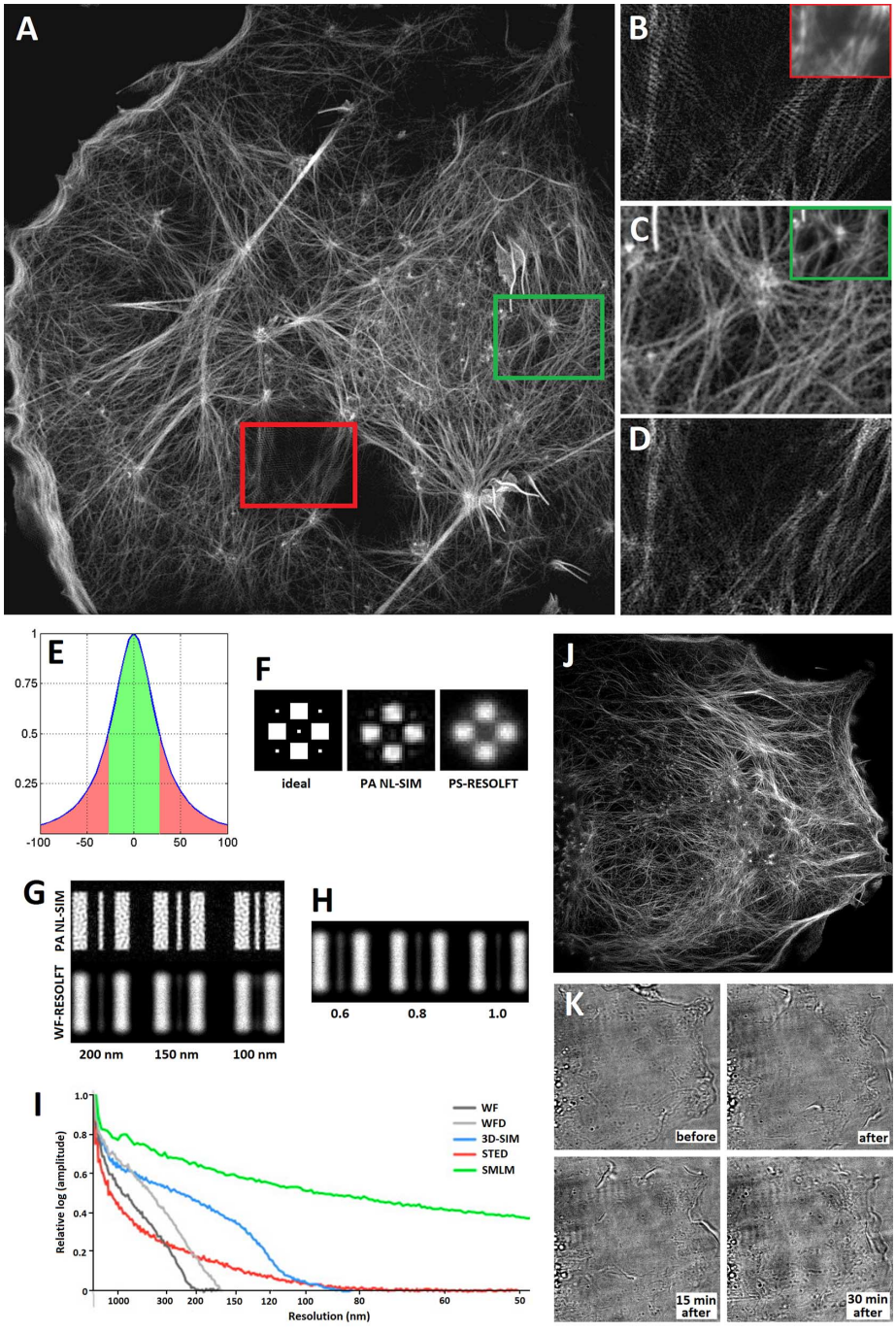

Fig. 1. Issues relevant to live-cell SR microscopy. (**A**) PA NL-SIM image of actin filaments in a COS-7 cell, from a movie of 30 such images. (**B**) Subregion highlighted by a red box in (A) and used by Sahl *et al*. to show periodic reconstruction artifacts. (**C**) Another subregion denoted by a green box in (A), without such artifacts. (**D**) Suppression of artifacts in (B) without loss of resolution by selective notch filtering of spurious spatial frequencies. Widefield insets in (B) and (C) show higher out-of-focus background in (B). (**E**) A 54-nm-wide linecut through the theoretical PSF of a PS-RESOLFT microscope. (**F**) Simulated resolvability of a test pattern of alternating large and small squares, separated 80 nm edge-to-edge, by PA NL-SIM and PS-RESOLFT at SNR = 20. (**G**) Simulated PA NL-SIM and WF-RESOLFT images at SNR = 20 of a 50-nm-wide line flanked by 250-nm-wide lines for three different line gaps. (**H**) Spurious linewidth variability in WF-RESOLFT for different degrees of background subtraction, 200-nm line gap case. (**I**) Frequency spectra from images of microtubules in macrophages obtained by various SR methods. [Reprinted with permission from (*5*).] (**J**) PA NL-SIM image of actin filaments in another cell, from a movie of 30 image frames. (**K**) Oblique illumination images of the same cell at times relative to the PA NL-SIM imaging. Each image represents one frame from a series of 1000 taken at 0.1-s intervals at each inspection time to assess any changes to cell morphology or dynamics.

examples of live-cell STED and RESOLFT are of sparse, exceptionally bright filamentous or punctate objects and may not achieve the same resolution, speed, imaging duration, and noninvasiveness that we demonstrate on dense networks of dim, individual actin filaments (Li *et al*. figures 3 and 4), clathrin or caveoli clusters (Li *et al*. figures 2F and 3F), striated focal contacts (Li *et al*. figure 1, C to F), and membrane ruffles (Li *et al*. figure 4, D to F).

An alternative to such a complete description is simply to compare images of similar features as imaged by different methods. Sahl *et al*. argue that such comparisons are subjective and "inadequate," yet exactly this approach is commonly used to compare STED or RESOLFT to diffraction-limited images (e.g., Sahl *et al*. refs. 8–11 and 16 and Li *et al*. ref. 11). We see no problem in such comparisons, provided that (i) the performance of each method is fairly presented; (ii) OTF, SNR, and imaging condition data are given; (iii) all image manipulations are described fully; and (iv) all previous biological knowledge of the specimen is used to identify possible artifacts. Supreme Court Justice Potter Stewart famously stated in a case on the limits of free speech that he couldn't define hardcore pornography, but "I know it when I see it." We feel similarly about resolution. We invite readers to review our comparisons of high NA SIM and PA NL-SIM to other SR methods (Li *et al*. SM figures. S4, S6, S13, S31, S34, and S44) and draw their own conclusions.

With regard to live-cell imaging, there exist inevitable trade-offs between spatial resolution, imaging speed, and phototoxicity. Yet, in cases where direct experimental comparisons are available, high NA SIM and PA NL-SIM outperform RESOLFT and single-molecule localization microscopy (SMLM) by nearly every metric relevant to live cell imaging simultaneously, often by one or two orders of magnitude (Table 1). These gains are consistent with our theoretical estimates (Li *et al*. SM notes 2–7 and figures S28, S45, S51, and S54)

Downloaded from http://science.sciencemag.org/ on April 28, 2016

Table 1. Comparative live-cell imaging performance of high NA TIRF SIM and PA NL-SIM to other SR imaging modalities. Colored groups represent comparisons for similar subcellular features. Parameters of competing SR methods are normalized to results of Li *et al*. and are shown in green or red if better or worse, respectively. Total dose across all time-lapse image frames (bottom section) is normalized to wavelength-dependent phototoxic levels estimated from (*8*) as follows: 1.0 kJ/cm^2 at 405 nm; 5.0 kJ/cm^2 at 488 nm; and 100 kJ/cm^2 at 561 nm.

Citation	Sahl, ref. 11	Li, ref. 11	Li SM	Li, ref. 33	Li and Li SM	Li, ref. 6	Li, ref. 15	Li and Li SM	Li SM, ref. 68	Li and Li SM
Figure number	Fig. 3B	Fig. 2	Fig. S6, Movie S11	Fig. 2C	Figs. S32, S34, Movie 7	Fig. 5C	Fig. 3C	Fig. S13, Movie 2	Video 2	Fig. S4, Movie 3
SR method	PS-RESOLFT	WF-RESOLFT	PA NL-SIM	PS-RESOLFT	PA NL-SIM	SMLM	PS-RESOLFT	TIRF SIM	SMLM	TIRF SIM
Specimen	Keratin	Keratin	Keratin	Caveolin	Caveolin	Paxillin	Zyxin	Paxillin	Clathrin	Lathrin
Image comparison figure		Fig. S6	Fig. S6	Fig. S34	Fig. S34	Fig. S13		Fig. S13	Fig. S4	Fig. S4
Field of view (µm x µm)	4.0 x 5.0	100 x 120	45 x 45	2.8 x 2.8	45 x 45	33 x 33	19 x 19	45 x 45	12 x 20	16 x 25
Normalized field of view	0.0099	5.9	1	0.0039	1	0.54	0.18	1	0.6	1
Acquisition time (sec)	4420	3.17	1.17	184	0.347	55	401	0.745	2	0.475
Normalized acquisition time	3778	2.7	1	530	1	74	538	1	4.2	1
Imaging duration (frames)	1	1	11	1	20	25	3	71	22	201
Normalized duration	0.091	0.091	1	0.05	1	0.35	0.042	1	0.11	1
Peak activation intensity (W/cm^2)	1000	500	2	1500	2	50	2000	0	0.9	0
Normalized peak activation intensity	500	250	1	750	1	∞	∞		∞	
Activation dose/frame (J/cm^2)	164	72	0.05	80.7	0.05	2750	8.91	0	1.8	0
Normalized activation dose/frame	3280	1440	1	1614	1	∞	∞		∞	
Peak depl.+read intensity (W/cm^2)	1000	1000	100	49000	1000	1000	2600	75	5000	140
Normalized peak depl.+read inten.	10	10	1	490	1	13.3	34.7	1	35.7	1
Depl.+read dose/frame (kJ/cm^2)	36.2	2.3	0.1	253	0.018	55	0.176	0.054	10	0.063
Normalized depl.+read dose/frame	362	23	1	14400	1	1019	3.3	1	159	1
Total activation dose (J/cm^2)	164	72	0.55	80.7	1	68800	26.7	0	39.6	0
Total activation dose / toxic level	0.16	0.072	0.00055	0.081	0.001	68.8	0.027	0	0.04	0
Total depl.+read dose (kJ/cm^2)	36.2	2.3	1.1	253	0.35	1375	0.529	3.83	220	12.7
Total depl.+read dose / toxic level	7.24	0.46	0.22	2.53	0.07	13.8	0.11	0.77	2.2	2.54

and underscore again how a strong OTF (Li *et al*. SM figure S24) in the SR regime is essential for optimal live-cell performance. They are also indicative of the penalties imposed by saturated depletion, which is at the heart of STED and RESOLFT, where fewer and fewer fluorescence state transitions produce a useful signal as higher and higher resolution is demanded. Thus, although Sahl *et al*. argue that "STED nanoscopy…has been used to record various structures quickly and repeatedly in living cells and…neurons," their cited example (Sahl *et al*. ref. 15) (i) does not report acquisition times; (ii) uses a peak intensity (~600 MW/cm^2) 20-fold higher than that shown to induce photodamage in spermatozoa (*6*) and *Escherichia coli* (*7*) in optical trapping experiments at similar wavelengths; (iii) resolves a structure barely below the diffraction limit; and (iv) provides no examples of time-lapse imaging of subcellular dynamics—arguably the main point of live-cell imaging.

Even when multiple frames are shown, as in the example of "dendritic spines…followed over hours by RESOLFT" (Sahl *et al*. ref. 16), the small field of view (7.7 × 16.3 µm), prolonged acquisition time (348 s), long imaging interval (900 s), and limited number of frames (9) preclude study of dynamical processes at speeds and durations common in living cells. In fact, time-lapse images by STED and RESOLFT are often notable for how little motion is observed, given the long acquisition times. This may be a harbinger of phototoxicity or even light-induced fixation that produces "frozen" cells (*8*). It is also notable that independent metrics of cell health, such as differential interference contrast (Li *et al*. ref. 6) or oblique illumination imaging (Fig. 1K) before, during, and after SR imaging (Fig. 1J) to check for changes in cell morphology or dynamics, are largely absent from the STED and RESOLFT literature. This is perhaps not surprising, given that these methods often exceed expected levels of toxic exposure (Table 1 and Li *et al*. SM movie S1).

Viability metrics are essential to have any confidence in the validity in live SR findings. Even so, more sophisticated measures are needed. For example, microtubule growth rates have been shown to decline significantly at a dose of 640-nm irradiation, only 3% of that at which nearly all cells still divide (*8*). Thus, the development of noninvasive, broadly applicable assays to measure the immediate and local effects of light on cellular physiology should be a major thrust of live-cell imaging research, for diffraction-limited as well as SR methods. Until then, every effort should be made to minimize both the light dose and peak intensity and to restrict the illumination in time and space. We view the low-intensity, short-exposure, TIRF-confined methods of high NA SIM and PA NL-SIM that we have developed to be important steps in this regard.

Space restrictions preclude us from addressing all our points of disagreement with Sahl *et al*. However, researchers considering building or purchasing an SR microscope for their own work are well advised to insist on demonstration of the practical resolution, field of view, and imaging speed on their own specimens, and to evaluate the extent to which photobleaching and phototoxicity are debilitating, before making a decision.

In the final analysis, the only metric that matters for a new imaging technology is whether it can address important questions to the satisfaction of the biological community that could not be answered by previous methods. In our case, we studied: the relationship between the sizes and lifetimes of clathrin-coated pits (CCPs), the role of actin in clathrin-mediated endocytosis, the dynamics at clathrin patches and hot spots of CCP formation, the formation of nanoscale actin rings, the diversity of caveolin-rich structures, and the nanoscale recruitment of α-actinin during

Downloaded from http://science.sciencemag.org/ on April 28, 2016

the formation of actin-rich structures. Elsewhere, in the past year or two live-cell SIM has been used to investigate the dynamics of MreB filaments in bacteria (*9*) and cortical microtubules (*10*), microtubule-dependent transport of vimentin filaments (*11*), vesicle formation at the inner nuclear membrane (*12*), centrosome assembly in *Drosophila* (*13*), a dorsal actomyosin network that drives cell motility (*14*), and the assembly of isoforms of nonmuscle myosin II (*15*) and combinations of myosin II and myosin 18 (*16*) into bipolar filaments. We look forward to revisiting our debate with Sahl *et al.* a decade from now to see which SR methods have had the broadest effect in biology.

REFERENCES

1. S. J. Sahl *et al.*, *Science* **352**, 527 (2016).
2. D. Li *et al.*, *Science* **349**, aab3500 (2015).
3. E. Hecht, *Optics* (Addison Wesley, ed. 4, 2002), Fig. 13.34, p. 616.
4. E. Pantin, J.-L. Starck, F. Murtagh, in *Blind Image Deconvolution: Theory and Applications*, K. Egiazarian, P. Campisi, Eds. (CRC Press, 2007), pp 277—317.
5. J. Demmerle, E. Wegel, L. Schermelleh, I. M. Dobbie, *Methods* **88**, 3–10 (2015).
6. K. König, Y. Tadir, P. Patrizio, M. W. Berns, B. J. Tromberg, *Hum. Reprod.* **11**, 2162–2164 (1996).
7. K. C. Neuman, E. H. Chadd, G. F. Liou, K. Bergman, S. M. Block, *Biophys. J.* **77**, 2856–2863 (1999).
8. S. Wäldchen, J. Lehmann, T. Klein, S. van de Linde, M. Sauer, *Sci. Rep.* **5**, 15348 (2015).
9. P. V. Olshausen *et al.*, *Biophys. J.* **105**, 1171–1181 (2013).
10. G. Komis *et al.*, *Plant Physiol.* **165**, 129–148 (2014).
11. C. Hookway *et al.*, *Mol. Biol. Cell* **26**, 1675–1686 (2015).
12. C. Hagen *et al.*, *Cell* **163**, 1692–1701 (2015).
13. P. T. Conduit *et al.*, *eLife* **3**, e03399 (2014).
14. D. T. Burnette *et al.*, *J. Cell Biol.* **205**, 83–96 (2014).
15. J. R. Beach *et al.*, *Curr. Biol.* **24**, 1160–1166 (2014).
16. N. Billington *et al.*, *Curr. Biol.* **25**, 942–948 (2015).
17. M. Ratz, I. Testa, S. W. Hell, S. Jakobs, *Sci. Rep.* **5**, 9592 (2015).

4 January 2016; accepted 5 April 2016
10.1126/science.aad8396

Downloaded from http://science.sciencemag.org/ on April 28, 2016

Marijuana policy patchwork not based on science

Meanwhile, federal laws hobble research into the dangers, and the potential benefits, of the drug

By **Michaela Jarvis**

As a physician and a scientist, J. Michael Bostwick values logic and scientific evidence. But when the Mayo Clinic College of Medicine professor first immersed himself in the topic of marijuana, he says he found very little of either.

"I want to underscore my exasperation. When I set out to try to understand this topic, I couldn't find logic," said Bostwick, who spoke at a 30 March Neuroscience & Society event cosponsored by AAAS and the Dana Foundation. "I couldn't find logic in the law, in the way the federal government was acting, or in the way the states were acting. It was very frustrating."

When marijuana was outlawed in 1970 and classified as a Schedule I drug—signifying that it had a high potential for abuse and no scientifically proven therapeutic value—it had not been significantly studied. Similarly, with 23 states and the District of Columbia currently implementing a hugely wide range of state laws allowing marijuana's use as medicine and even as a recreational drug, scientific studies demonstrating its medicinal properties, as well as its risks, are still lacking, Bostwick said.

"I would contend that cannabis was 'scheduled' in the absence of science," said Bostwick, "just as there's a problem now with the lack of science."

For researchers who would provide scientific evidence of marijuana's potential benefits and dangers, the plant's classification as a Schedule I substance creates huge obstacles.

"The Drug Enforcement Administration has to give you a registration," said Nora Volkow, director of the National Institute on Drug Abuse (NIDA), who is noted for her research on addiction. "I know from researchers that this has been very, very difficult. Whether you are studying cannabidiol for the treatment of seizure disorders or for analgesia, it is a slow process."

"I think everyone on the panel agreed," said event moderator Mark Frankel, director of the AAAS Scientific Responsibility, Human Rights and Law Program, "that we need more research conducted by more scientists, but that federal policy impedes those efforts."

Cannabidiol (CBD) is one of the most closely observed substances derived from the marijuana plant. It has shown promise in medical treatment, particularly for controlling seizures. Unlike the other most well-known compound in marijuana, delta-9-tetrahydrocannabinol (THC), CBD is not euphorigenic, meaning it does not create a "high." To make further research on CBD less cumbersome, Volkow said that she advocates classifying the compound in a less rigid category than its marijuana parent plant.

"I have continuing dialogue with the [Food and Drug Administration], trying to figure out ways in which we can make research easier, such as scheduling cannabidiol," Volkow said. "I'm very much for facilitating research on cannabis and changing some of this scheduling of these substances."

Some Schedule I substances, such as heroin, have related counterparts, such as morphine and oxycontin, that are less regulated.

Volkow said that she does not advocate the legalization of marijuana. She made the point that legal drugs, like tobacco and alcohol, can have hugely detrimental effects on individuals and on society, but their legality grants them a certain societal acceptance that may invite more young people to try them. At the same time, some studies have shown that marijuana use at an early age can affect brain development, impair cognition, and lessen motivation.

"If you are smoking marijuana as a teenager," Volkow said, "trust me, your educational achievement is going to be signficantly worse."

Volkow explained that the brain and the body have their own endocannabinoid system. "Just like we produce endogenous opioids and endorphins that make us high, we also produce endogenous cannabinoids that make us feel good, create a sense of well-being. So what cannabis is doing is just binding to the receptors that are there in our brains." The problem with using marijuana, Volkow said, is that "you saturate your system in ways that are not physiologically relevant, and that triggers neuronal adaptations in the brain and also in the body, which can result in adverse consequences and, in the case of the brain, can lead to addiction."

Still, Volkow acknowledged that more controlled studies are needed to understand marijuana's addiction potential and possible impairment of the brain, especially the developing brain. "In the field, there have been many, many studies, and all of them can be questioned because certain parameters were not controlled," Volkow said. "As a result of that, we are in a situation where we are vulnerable to criticisms of the robustness of the findings."

Jars containing marijuana are displayed at the RiverRock medical marijuana center in Denver.

In response, NIDA, in partnership with other branches of the National Institutes of Health, has launched the Adolescent Brain Cognition and Development research effort, a longitudinal study that will follow 10,000 children from ages 8 to 21 to assess the effects of marijuana, nicotine, and alcohol on their brains. The results of the study, however, will not be available for 10 years, and in the meantime, other research efforts are stymied, said Bostwick.

"We've really begun to understand the endocannabinoid system and how potentially important it could be, like any other neurotransmitter system, for coming up with medications that might be able to be used," Bostwick said. However, he added, "It appears there is no end in sight to this federal-state standoff, and the result is that a protean source of potential pharmaceuticals is moribund." ■

Since 2012, AAAS and the Dana Foundation have collaborated on the Neuroscience & Society lecture series, with 15 events reaching 2700 attendees. The purpose of the series is to provide a public forum for members of the community to hear outstanding speakers address the status of brain research and what it might mean for ordinary individuals, as well as for society.

PHOTO: © TRIBUNE CONTENT AGENCY LLC/ALAMY STOCK PHOTOW

Downloaded from http://science.sciencemag.org/ on April 28, 2016

Published by AAAS

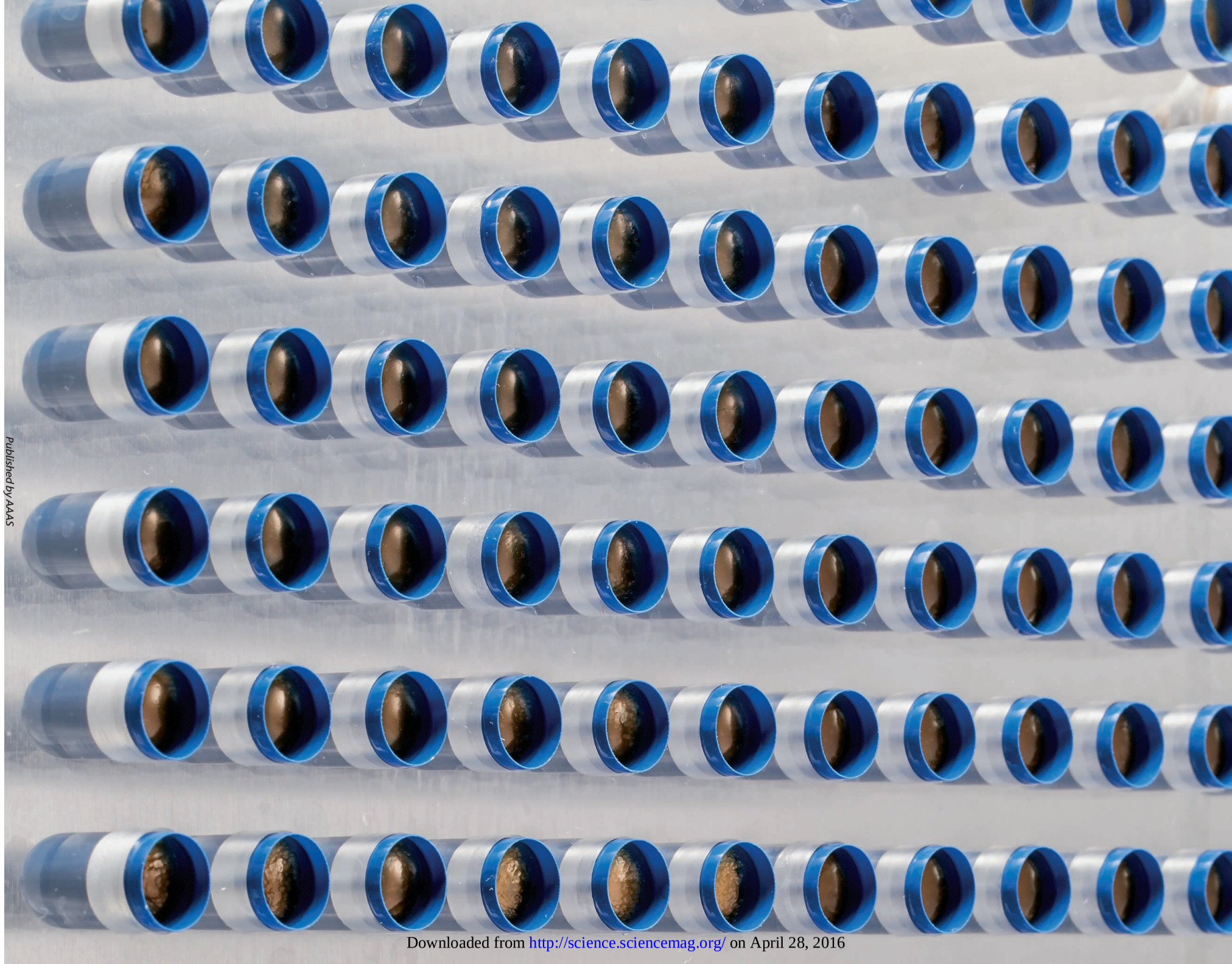

Published by AAAS

Downloaded from http://science.sciencemag.org/ on April 28, 2016

MANIPULATING THE MICROBIOTA

By **Caroline Ash** *and* **Kristen Mueller**

In John Donne's famous words, no man is an island. Rather, all organisms, including humans, exist within a sea of microorganisms. A select few microbes cause great harm, but most are benign, some essential. In fact, many aspects of normal plant and animal development require benign microbial colonization and the establishment of specific relationships that have probably coevolved since the origins of life.

Perhaps not surprisingly, the human genes masterminding the selection of symbiotic microbes are largely those involved in immune regulation and barrier defense. In turn, the microbes that colonize mucosal tissues after birth play a pivotal role in shaping the development of the host immune system. Consequently, the effectiveness of early microbial colonization may have long-term effects on susceptibility to inflammatory diseases, such as allergy and autoimmunity.

Maintaining a healthy microbiota is no easy task. Diet, severe disease, and medications can all wreak havoc on the microbiota. Our current understanding of how this happens and what the long-term consequences might be is very limited. Nevertheless, the list of commensal bacterial species with remarkable protective effects continues to grow, and the exploitation of the microbiota is increasingly big business. However, the probiotic industry currently faces huge challenges. These range from exaggerated health claims to the difficulties of developing rigorous testing protocols within existing regulatory frameworks. All the same, probiotic development shows great promise for rebuilding microbiotas and restoring health, certainly for some individuals.

INSIDE

REVIEWS

Cross-species comparisons of host genetic associations with the microbiome *p. 532*

Resurrecting the intestinal microbiota to combat antibiotic-resistant pathogens *p. 535*

How colonization by microbiota in early life shapes the immune system *p. 539*

PERSPECTIVE

Antibiotic use and its consequences for the normal microbiome *p. 544*

RELATED ITEMS

▸ **RESEARCH ARTICLE p. 560**
▸ **REPORT p. 565**
▸ **REPORT p. 586**
▸ **REPORT p. 608**

PHOTO: KEN RICHARDSON

Capsules being prepared for fecal transplantation therapy, which is used, often successfully, to treat intractable gut disorders such as *Clostridium difficile* infection.

Downloaded from http://science.sciencemag.org/ on April 28, 2016

Published by AAAS

REVIEW

Cross-species comparisons of host genetic associations with the microbiome

Julia K. Goodrich,[1]* Emily R. Davenport,[1]* Jillian L. Waters,[1,3]* Andrew G. Clark,[1] Ruth E. Ley[1,2,3]†

Recent studies in human populations and mouse models reveal notable congruences in gut microbial taxa whose abundances are partly regulated by host genotype. Host genes associating with these taxa are related to diet sensing, metabolism, and immunity. These broad patterns are further validated in similar studies of nonmammalian microbiomes. The next generation of genome-wide association studies will expand the size of the data sets and refine the microbial phenotypes to fully capture these intriguing signatures of host-microbiome coevolution.

Microbes coat the surfaces of the human body in highly adapted microbiomes. The vast majority of human-associated microbial cells are bacterial, with archaeal and eukaryotic cells also present in lower numbers. Together they reach their highest biomass in the distal gut. These microbial communities vary in composition across the body, depending on niches defined physically, chemically, and immunologically. Although a handful of animal species have been reared germfree under highly artificial axenic conditions, germfree animals are physiologically abnormal in several fundamental ways (*1*). Human biology and health assume the presence of a "healthy" microbiome, one whose interactions with its host are generally beneficial.

The gut microbiome is said to encode a second genome, and its functions expand the host's physiological potential. In the gut, microbes extend digestive capabilities, prime the immune system, produce vitamins, degrade xenobiotics, and resist colonization by pathogens. In principle, selection for host genotypes that promote a beneficial microbiome is possible. This might be expected for microbial functions (e.g., production of metabolites) or taxa that encode functions beneficial to fitness. When functions are restricted phylogenetically to specific taxa, such as methanogenesis to Euryarchaeota, associations between host alleles and specific taxonomic abundances could emerge. Conversely, functional gene counts or expression levels may associate with host genotypes when those functions are encoded across disparate taxa. There are examples of specific host genes whose variants are associated with different gut microbiomes, particularly for immune genes implicated in disease or secretor status (*2*, *3*).

Genome-wide scans hold the promise of finding novel associations between host genes and the microbiome. A major concern with this approach in humans is that environmental factors, such as diet, can strongly and rapidly alter gut community composition and function (*4*). Nonetheless, recent studies highlight a select suite of taxa whose abundances are partially genetically influenced, as well as the human genes involved. Cross-study comparisons show some of the same taxa to be influenced by host genetics. Comparisons across species, including plants, reveal a common theme: Host genes associated with microbiome variation are involved in immune regulation and barrier defense. In human populations where the diet is unrestricted, genes related to diet preference and metabolism also emerge.

[1]Department of Molecular Biology and Genetics, Cornell University, Ithaca NY, USA. [2]Department of Microbiology, Cornell University, Ithaca NY, USA. [3]Department of Microbiome Science, Max Planck Institute for Developmental Biology, Tübingen, Germany.
*These authors contributed equally to this work. †Corresponding author. Email: rel222@cornell.edu

Heritability: Estimates of the strength of the host genetic effect on microbiota

Heritability is the proportion of variance in a host trait, such as height or body mass index (BMI), measured across a population, that is explained by genetic rather than environmental effects. Heritability, a term widely used in genetics, is unrelated to the concept of inheritance (vertical transmission from parent to offspring). Height, for example, is highly heritable, meaning that variation in height across a population has strong genetic underpinnings. Components of the microbiome, such as taxa, can be quantified across subjects and treated as quantitative traits in estimates of their heritability, just like height or BMI. Statistical models use the known genetic relatedness of twin pairs, or single-nucleotide polymorphism (SNP) genotype data that allow direct assessment of the genetic relatedness between individuals, to calculate the heritability (ranging from 0 to 1) for each microbial trait. For twins, the vertical transmission of microbes from parents is assumed to be equivalent and is thus controlled for.

For several decades, twins served to address the question of whether host genetic variation is associated with the microbiome. Identical [monozygotic (MZ)] twin pairs share 100% of the genes across their genome, whereas fraternal [dizygotic (DZ)] twins share, on average, 50%. This, combined with the assumption that twins raised together experience similar environments, has formed the basis of twin heritability studies. For quantitative traits derived from the microbiome, such as bacterial relative abundances, greater similarity for MZ twins compared with DZ twins can be ascribed to shared genes, and by definition such bacteria are heritable. With a large enough population sample, the heritabilities of taxon abundances or other quantitative aspects of the microbiome, such as species richness, can be quantified.

Early studies in twins included small numbers of subjects and employed either culture or DNA fingerprinting-based techniques, and results suggested a genetic effect on the gross composition of the gut microbiome (*5*, *6*). Later, studies using sequence-based techniques and larger cohorts reported a similar trend, albeit weaker. Turnbaugh *et al.* (2009) and Yatsunenko *et al.* (2012) sampled equivalent numbers of young-adult twin pairs (~50) from Missouri and characterized their gut microbiomes by sequencing partial 16*S* ribosomal RNA (rRNA) genes amplified from fecal DNA (*7*, *8*). Comparisons of microbiomes using the UniFrac metric in both studies showed the trend that MZ twin microbiomes were more similar than those of DZ twins; however, this result was not statistically significant. Together these studies highlight a global effect of environmental factors on the composition of the microbiome. They also hinted at a host genetic effect on gut microbiome variation.

Accurate assessment of genetic effects requires larger sample sizes. The work of Goodrich and colleagues included an initial sample size of 416 twin pairs (*9*). The patterns from earlier twin studies were successfully replicated: MZ twin microbiomes were overall more similar than those of DZ twins, but with the increased sample size the difference reached statistical significance (*9*). More important, the larger sample size allowed heritability estimates for many individual taxa to be calculated.

The taxon with the highest heritability was Christensenellaceae, a family within the Firmicutes that forms a co-occurrence consortium with other heritable taxa, including the dominant human gut methanogen *Methanobrevibacter smithii*. MZ twins were previously shown to have greater concordance for the carriage of *M. smithii* compared with DZ twins (*10*). Studies across mammalian species (*11*) and within bovine lines (*12*) have also shown that host genetics influence levels of gut methanogens. Previous work in humans has also associated methanogens and species richness with leanness (*13*) and Christensenellaceae with low serum triglyceride levels (*14*). Transplant experiments of feces from an obese human donor lacking this consortium to germfree mice were conducted with and without addition of *Christensenella minuta*. Addition of *C. minuta* resulted in reduced adiposity in the recipient mice (*9*), suggesting that host genes may influence phenotype via control of microbiome components.

Cross-study comparisons

Quantitative measures of the microbiome constitute a novel complex trait in human genome-wide association studies (GWAS). Microbiome data are costly and cumbersome to generate for large numbers of subjects. So far, compared with the accepted norm in the GWAS field, sample sizes for microbiome GWA studies have been small, and as a result findings may be spurious. Until sample sizes increase and meta-analyses are conducted, cross-validation is important to cement confidence in the results. Comparisons can be made for human and mouse studies that have

Downloaded from http://science.sciencemag.org/ on April 28, 2016

(i) estimated taxon heritabilities directly or (ii) identified taxa linked to host genes in genetic association analyses [human GWAS or quantitative trait locus (QTL) analysis in mice and plants]. Cross-kingdom comparisons with similar studies in other genetic models are also possible. The advantage of model systems is that environmental conditions are controlled; however, the extent of the genetic variation examined is less than the variation segregating in outbred populations (*15*) (Fig. 1).

Several of the same taxa have been estimated as heritable or linked to host genes in at least two human GWA or mouse QTL studies. The human-based studies include the UK Twins (*9*), the Human Microbiome Project (HMP) subjects (*16*), and the Hutterites (*17*); the mouse QTL studies include advanced intercrossed lines (*18*, *19*), the Hybrid Mouse Diversity Panel (*20*), collaborative cross/diversity outbred mapping panels (*21*), and recombinant inbred strains (*22*). The majority of these heritable taxa belong to the phylum Firmicutes, whereas Bacteroidetes are generally not heritable. Technical issues preclude direct comparisons for some taxa; for instance, not all taxonomies presently include the Christensenellaceae. Also, heritability estimates tend to be higher on average for mice, most likely because environmental variability is controlled. Nevertheless, some of the same taxa are identified repeatedly across studies.

GWAS in humans

The HMP characterized microbiomes across body sites for 350 individuals, using both 16*S* rRNA genes and metagenomes (*23*). Skin-derived metagenomes contained human DNA "contamination" that Blekhman and colleagues used to obtain genotype data for 93 individuals (*16*). Without accounting for population structure, ethnicity, or geographic stratification, a relationship emerged between host genotype and the overall composition of the fecal microbiome. This is likely due to differences in nongenetic factors (e.g., diet) that correlate with genetic ancestry, and this ancestry effect was again captured from an analysis that used HMP mitochondrial haplotype data (*24*). Gut microbiome differences between populations are often ascribed to differences in diet (*8*), but genetic differences may be more important than previously thought (and, indeed, genetic differences may in part drive differences in dietary preferences).

Underpowered for GWAS, Blekhman *et al.* performed a pathway-based analysis and examined associations with genic SNPs. Significant enrichment in genes related to immunity was driven by nose, oral, and skin associations. One notable association with stool microbiota emerged: Relative abundance of the genus *Bifidobacterium* was related to loci within the *LCT* gene region (discussed below).

Immune genes also came to the fore in a study of gut microbiota in the Hutterites (*17*). The North American Hutterites descended from a small European founder population in the late 1800s and reside in independent farming communities. Notably for microbiome research, they live and eat communally, which reduces the effect of inter-individual differences in diet on microbiome composition. Genetic analysis of the Hutterite fecal microbiota in two seasons revealed ~15 taxa heritable in winter, summer, or both (*17*). Interestingly, some taxa were only heritable in one season, suggesting the diet dependence of gene-microbe associations. Most of the heritable bacteria identified in the Hutterites belong to the Proteobacteria and Firmicutes phyla. Additionally, the top GWAS hits for a member of the heritable family Clostridiaceae were enriched near genes related to immune processes, and top hits for several taxa, including *Bifidobacterium*, were enriched near olfactory receptor genes, leading us to speculate about the possibility of genetic differences in dietary preferences.

We have performed GWA on an expanded data set (1126 twin pairs). GWA studies of the microbiome are a challenge because they entail simultaneous testing for upwards of 1000 phenotypes versus millions of SNPs. Starting with a focus restricted to candidate gene sets and heritable microbiota, the number of tests was greatly reduced, and these yielded many significant results. As in the Blekhman study, *Bifidobacterium* was strongly associated with the *LCT* gene region (Fig. 2). Other associations were with genes implicated in immunity and barrier function. However, when the study was broadened to assess associations genome-wide and microbiome-wide, none attained study-wide significance (this effort entailed 10^9 tests).

QTL studies of gut microbiota in mice

QTL mapping in laboratory mice has the advantage that environmental conditions are tightly controlled (Fig. 1). It should be noted that linkage intervals around identified QTLs can be large and encompass many genes, hampering interpretation and comparisons across studies. Nevertheless, the four murine gut microbiome GWAS conducted to date yielded a number of consistent results. First, four of 18 QTLs identified by Benson *et al.* (*18*) were replicated in a follow-up study using a further generation of the same mouse breeding regime (*19*). In addition, several studies identified genes involved in immune function within linkage intervals. Both Benson *et al.* (*18*) and Org *et al.* (*20*) identified associations between members of the phylum Firmicutes and variants in or the expression of host genes involved in the Toll-like receptor and T cell receptor pathways (*IRAK4* and *IRAK3*, respectively). Additionally, a region encompassing *IRAK4* was associated with Rikenellaceae by McKnite *et al.* (*22*), who further identified an association between Prevotellaceae abundance and *TGFB3*, a cytokine that modulates barrier function of the intestine. Host genes involved in barrier integrity have also been implicated in fly (*25*) and plant (*26*) microbiome GWAS.

GWAS of plant and fly microbiomes

As in mammals, plant-associated microbiomes are environmentally acquired, and a selection process occurs when microbiota assemble on their surfaces (*27*–*29*). Several studies within a plant species have noted genotypic effects on microbiome composition (*26*, *27*, *30*–*32*). Horton and colleagues examined bacteria and fungi that compose the leaf endophyte microbiome in 196 accessions of *Arabidopsis thaliana* and identified QTLs for both species richness and the abundances of individual taxa (*26*). Peiffer *et al.* examined the soil rhizosphere microbiota of 27 maize lines grown in five different fields in two

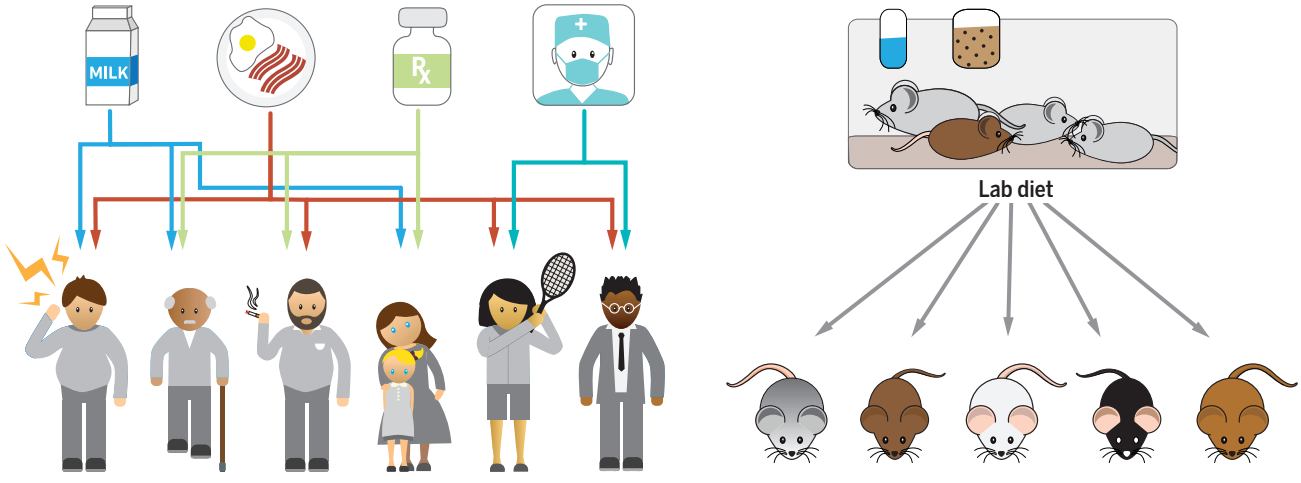

Fig. 1. Environmental factors influence the gut microbiota and are controlled in model systems. (**Left**) Many factors affect the human gut microbiome, adding noise to quantitative measures. (**Right**) Mice are an attractive model for studying host genetic-microbiome interactions because environmental variation is more tightly controlled.

Downloaded from http://science.sciencemag.org/ on April 28, 2016

distinct geographical regions and found that ~19% of the interline variation of species richness could be attributed to host genotype (*31*). Similarly, measures of alpha diversity are heritable in the Hutterites (*17*). The mechanisms by which this occurs are unknown but may include broad immune responses or differences in host physiology, such as variation in pH levels or gut length, surface area, or rate of peristalsis.

A subset of QTLs identified in Horton *et al.* was associated with the abundances of multiple bacterial and fungal taxa (*26*). The top gene ontology (GO) categories associated with fungal and bacterial taxa were involved in host defense, and the top GO enrichment category for species richness was regulation of viral reproduction (*26*). Genes for cell wall components, also part of barrier defense, were also implicated in the GWAS (*26*). Thus, genetic control of species richness, and associations with immune genes, are common themes between mammal and plant studies.

Genes related to barrier defense and immunity were also detected in GWAS of the gut microbiomes of flies (*Drosophila* Genetic Reference Panel) raised germfree and then inoculated with five bacterial species (*25*, *33*). Further analysis showed gene-bacterial interactions to influence the nutritional status of the fly. Overall, these results are broadly similar to those conducted in mice and humans.

Specific taxa related to host genotype across multiple studies

Bifidobacterium

The association between *Bifidobacterium* levels in stool and the *LCT* gene region was a strong signal in both the HMP (*16*) and the TwinsUK data sets. *Bifidobacterium* is moderately heritable in both human studies and one mouse study (*21*). It is an important member of the gut microbiome and can use the primary milk sugar lactose. The host *LCT* gene encodes lactase, the enzyme that cleaves lactose, and its haplotypes are linked to lactase persistence and lactose tolerance in adults. In the twins, the haplotype of *LCT* associated with lactase nonpersistence associates with higher levels of *Bifidobacterium*. A possible explanation for this pattern is presented in Fig. 2. Although the associations of *Bifidobacterium* abundance to the variant conferring lactase persistence did not reach genome-wide significance in the Hutterites, the same trend is apparent as in the twins: Lactase nonpersisters have higher levels of *Bifidobacterium* than persisters ($P = 4 \times 10^{-5}$). Additionally, the top genome-wide associations with *Bifidobacterium* in the Hutterites are enriched near genes encoding olfactory receptors (*17*).

Turicibacter and Peptostreptococcaceae

The taxa *Turicibacter* and *Peptostreptococcaceae* are heritable across humans and mice, co-occur, and inhabit the small intestine. *Turicibacter* directly contacts host cells and is implicated in inflammation and cancer (*34*). Org *et al.* revealed associations between *Turicibacter* and tissue-specific expression QTLs (*20*). Benson *et al.* (*18*) associated *Turicibacter* with a QTL on MMU7 that overlaps with the HCS1 QTL for susceptibility to murine hepatocellular carcinomas (*35*). How host genotype interacts with these taxa remains unclear.

Akkermansia

Akkermansia, a mucin-dwelling and degrading genus, is enriched in lean individuals (*14*) and linked to improved glucose metabolism (*36*). In mice, *Akkermansia* associated with loci on chromosomes 2 and 7 (*20*). The locus on chromosome 7 was also detected as a QTL for triglyceride levels and gonadal fat and lies near genes involved in glucose and insulin regulation. Davenport detected an association in Hutterites between *Akkermansia* and the untranslated region of *PLD1*, previously associated with obesity (*17*). In the TwinsUK data set, *Akkermansia* associated with *SIGLEC15*, a sialic acid binding lectin. The outermost decoration of gut mucin is sialic acid, which *Akkermansia* can cleave. Both *PLD1* and *SIGLEC15* are expressed in villus tips in mice (*37*), suggesting a direct interaction with *Akkermansia*.

Improving GWAS in humans requires large sample sizes

Despite a sample size of ~3000 subjects, the TwinsUK study still fails to deliver study-wide significance in genome-wide and microbiome-wide association tests. Although tests focused on a few candidate host genes or candidate microbes have produced encouraging results, genome-wide tests provide the best opportunity for new discoveries. Although meta-analyses of human GWA studies have included pooled sample sizes exceeding 350,000 (*38*), such aggregation across multiple disparate microbiome studies will present its own set of challenges. However, it appears inescapable that improved power for genome-wide tests requires increasing the sample size, and doing so with a unified sampling, sequencing, and analysis pipeline will require sample processing infrastructures that include roboticized sample handling. Studies of skin and oral microbiota, which are more easily obtained compared to gut microbiota, may be the first to reach that mark.

The microbiome as a complex trait

What is the best microbiome "trait" for GWAS? The microbiome is a complex, high-dimensional trait that can be described in myriad ways. Specific functional interactions likely underlie host gene-microbe associations, and 16*S* rRNA gene data, which are used in GWAS now, are often a poor proxy for function. This problem is similar to modeling BMI; it is easy to obtain measurements in large numbers, but it is not the best measure for adiposity. Metagenomes provide functional gene counts but are costly to generate. When predicted from 16*S* rRNA data, they are unreliable for genes that are variable among the genomes of strains, which may be the best phenotypes to model, along with their gene expression patterns. As sequencing and computational technologies continue to evolve, the goal of obtaining gene-specific and even strain-specific counts may soon be achievable.

To date, gut microbiome GWAS have relied on stool samples. Fecal microbiota are a mix of mucosally associated microbes, mostly from the colon, and lumenal microbes (*39*). At least half of the cells may be dead, and many are enriched in stool compared with farther up the gastrointestinal tract. Small intestinal microbiota are rare in stool, and important stomach microbes such as *Helicobacter pylori* may be undetectable. Thus, small-scale interactions between the microbiome and mucosal surfaces that underlie genetic associations may not be detectable from stool data. Studies using alternative sampling techniques, such as ingested capsules that capture small intestinal biopsies, might reveal associations lost in stool.

Prospectus

Environmental factors are more influential than host genetics in shaping the overall composition of

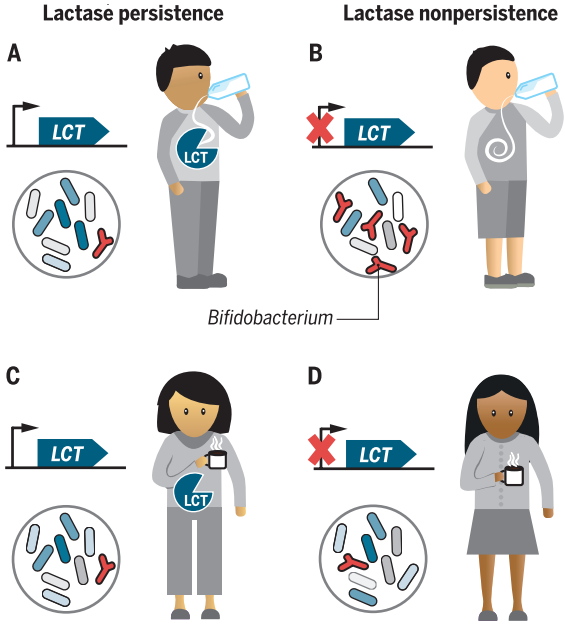

Fig. 2. Lactase persistence and *Bifidobacterium*. *LCT* gene loci are linked to the relative abundances of Bifidobacteria. The direction of the effect indicates that lactase persisters harbor fewer Bifidobacteria compared with lactase nonpersisters, which suggests the following hypothesis: (**A**) Lactase persisters who ingest lactose (shown as milk) digest it directly, reducing lactose availability to *Bifidobacterium* and its relative levels. (**B**) Nonpersisters consuming dairy products allow for lactose use by *Bifidobacterium*, thereby promoting its abundance. (**C** and **D**) When no lactose is consumed (shown as espresso), *Bifidobacterium* is low regardless of lactase persistence status.

Downloaded from http://science.sciencemag.org/ on April 28, 2016

the gut microbiome. However, across host species, a handful of Bacteria and Archaea, with known importance for health, have emerged as heritable and associate with host genes related to immunity and diet. These interactions may be fairly sensitive to diet, making the gut microbiome a tractable therapeutic target. The field of microbiome GWAS is in its infancy. Developments in sample acquisition, data generation, and analysis will continue to reveal informative and biologically relevant associations between taxa and host genetic variants. These associations, which underlie interactions yet to be described, are the signatures of an ongoing coevolution between host and microbiome.

REFERENCES AND NOTES

1. K. Smith, K. D. McCoy, A. J. Macpherson, *Semin. Immunol.* **19**, 59–69 (2007).
2. A. Spor, O. Koren, R. Ley, *Nat. Rev. Microbiol.* **9**, 279–290 (2011).
3. A. D. Kostic, M. R. Howitt, W. S. Garrett, *Genes Dev.* **27**, 701–718 (2013).
4. L. A. David *et al.*, *Nature* **505**, 559–563 (2014).
5. J. P. van de Merwe, J. H. Stegeman, M. P. Hazenberg, *Antonie van Leeuwenhoek* **49**, 119–124 (1983).
6. E. G. Zoetendal, A. D. L. Akkermans, W. M. Akkermans-van Vliet, J. A. G. M. de Visser, W. M. de Vos, *Microb. Ecol. Health Dis.* **13**, 129–134 (2001).
7. P. J. Turnbaugh *et al.*, *Nature* **457**, 480–484 (2009).
8. T. Yatsunenko *et al.*, *Nature* **486**, 222–227 (2012).
9. J. K. Goodrich *et al.*, *Cell* **159**, 789–799 (2014).
10. E. E. Hansen *et al.*, *Proc. Natl. Acad. Sci. U.S.A.* **108** (suppl 1), 4599–4606 (2011).
11. J. H. P. Hackstein, T. A. van Alen, *Evolution* **50**, 559–572 (1996).
12. R. Roehe *et al.*, *PLOS Genet.* **12**, e1005846 (2016).
13. E. Le Chatelier *et al.*, *Nature* **500**, 541–546 (2013).
14. J. Fu *et al.*, *Circ. Res.* **117**, 817–824 (2015).
15. E. R. Davenport, *Gut Microbes* **7**, 10.1080/19490976.2016.1155022 (2016).
16. R. Blekhman *et al.*, *Genome Biol.* **16**, 191 (2015).
17. E. R. Davenport *et al.*, *PLOS One* **10**, e0140301 (2015).
18. A. K. Benson *et al.*, *Proc. Natl. Acad. Sci. U.S.A.* **107**, 18933–18938 (2010).
19. L. J. Leamy *et al.*, *Genome Biol.* **15**, 552 (2014).
20. E. Org *et al.*, *Genome Res.* **25**, 1558–1569 (2015).
21. A. O'Connor, P. M. Quizon, J. E. Albright, F. T. Lin, B. J. Bennett, *Mamm. Genome* **25**, 583–599 (2014).
22. A. M. McKnite *et al.*, *PLOS One* **7**, e39191 (2012).
23. Human Microbiome Project Consortium, *Nature* **486**, 207–214 (2012).
24. J. Ma *et al.*, *BMC Genomics* **15**, 257 (2014).
25. J. M. Chaston, A. J. Dobson, P. D. Newell, A. E. Douglas, *Appl. Environ. Microbiol.* **82**, 671–679 (2016).
26. M. W. Horton *et al.*, *Nat. Commun.* **5**, 5320 (2014).
27. D. S. Lundberg *et al.*, *Nature* **488**, 86–90 (2012).
28. D. Bulgarelli *et al.*, *Nature* **488**, 91–95 (2012).
29. S. Hacquard *et al.*, *Cell Host Microbe* **17**, 603–616 (2015).
30. N. A. Bokulich, J. H. Thorngate, P. M. Richardson, D. A. Mills, *Proc. Natl. Acad. Sci. U.S.A.* **111**, E139–E148 (2014).
31. J. A. Peiffer *et al.*, *Proc. Natl. Acad. Sci. U.S.A.* **110**, 6548–6553 (2013).
32. N. Bodenhausen, M. Bortfeld-Miller, M. Ackermann, J. A. Vorholt, *PLOS Genet.* **10**, e1004283 (2014).
33. A. J. Dobson *et al.*, *Nat. Commun.* **6**, 6312 (2015).
34. J. P. Zackular *et al.*, *MBio* **4**, e00692-e13 (2013).
35. M. Gariboldi *et al.*, *Cancer Res.* **53**, 209–211 (1993).
36. A. Everard *et al.*, *Proc. Natl. Acad. Sci. U.S.A.* **110**, 9066–9071 (2013).
37. F. Sommer, I. Nookaew, N. Sommer, P. Fogelstrand, F. Bäckhed, *Genome Biol.* **16**, 62 (2015).
38. P. K. Joshi *et al.*, *Nature* **523**, 459–462 (2015).
39. P. B. Eckburg *et al.*, *Science* **308**, 1635–1638 (2005).

ACKNOWLEDGMENTS

We thank T. Spector, J. Bell, and C. Ober. This work was funded by NIH RO1 DK093595, a David and Lucile Packard Foundation Fellowship (R.E.L.), The Cornell Center for Comparative Population Genomics (R.E.L. and J.K.G.), and a National Science Foundation Graduate Fellowship (J.K.G.)

10.1126/science.aad9379

REVIEW

Resurrecting the intestinal microbiota to combat antibiotic-resistant pathogens

Eric G. Pamer

The intestinal microbiota, which is composed of diverse populations of commensal bacterial species, provides resistance against colonization and invasion by pathogens. Antibiotic treatment can damage the intestinal microbiota and, paradoxically, increase susceptibility to infections. Reestablishing microbiota-mediated colonization resistance after antibiotic treatment could markedly reduce infections, particularly those caused by antibiotic-resistant bacteria. Ongoing studies are identifying commensal bacterial species that can be developed into next-generation probiotics to reestablish or enhance colonization resistance. These live medicines are at various stages of discovery, testing, and production and are being subjected to existing regulatory gauntlets for eventual introduction into clinical practice. The development of next-generation probiotics to reestablish colonization resistance and eliminate potential pathogens from the gut is warranted and will reduce health care–associated infections caused by highly antibiotic-resistant bacteria.

Antibiotic treatment has saved millions of lives. Penicillins, sulfa drugs, macrolides, aminoglycosides, quinolones, cephalosporins, and carbapenems are used to "target" pathogens that cause potentially lethal infections, resulting in marked reductions in morbidity and mortality. None of these antibiotics, however, are selective for pathogens, and their administration leads to collateral destruction of commensal bacterial populations constituting the microbiota. Furthermore, many pathogens have acquired resistance to antibiotics, reducing treatment options and cure rates in a broadening range of clinical settings. The impact of broad-spectrum antibiotics on commensal inhabitants of our mucosal surfaces, in particular the gastrointestinal tract, has increasingly been the focus of laboratory investigation (*1*–*3*). It is well appreciated that a side effect of antibiotic treatment is increased susceptibility to a range of bacterial infections (*4*). An intact microbiota can exclude invading bacteria by direct and indirect mechanisms that, in aggregate, provide "colonization resistance."

Although not a new idea, administration of live bacteria to compensate for loss of commensal microbes and colonization resistance after antibiotic treatment is becoming increasingly plausible, largely because the bacterial species that promote high-level colonization resistance to infection are being defined (*5*–*9*). The effectiveness of these bacterial species is impressive, and (for the most part) these organisms are not associated with disease states, nor do they express virulence factors associated with pathogenic bacteria. This review summarizes recent studies identifying protective commensal bacterial species and discusses the need for a development path for these potential next-generation probiotics that demonstrates their effectiveness, ensures their safety, and promotes their eventual production, distribution, and affordability.

Infectious Diseases Service, Department of Medicine, Immunology Service, and Lucille Castori Center for Microbes, Inflammation and Cancer, Sloan Kettering Institute, Memorial Sloan Kettering Cancer Center, New York, NY 10065, USA.
Email: pamere@mskcc.org

Colonization resistance mediated by commensal bacteria

Not long after antibiotics were introduced for the treatment of bacterial infections, investigators noted that antibiotic administration to animals markedly reduced colonization resistance against a range of pathogens. Early studies demonstrated that antibiotic administration to mice or hamsters rendered these animals more susceptible, by as much as six orders of magnitude, to infection by common enteric pathogens (*10*–*13*). More than 50 years ago, it was found that loss of obligate anaerobic bacterial populations from the lower gastrointestinal tract strongly correlated with susceptibility to infection, which suggests that these commensal organisms were providing colonization resistance (*13*). Compositional analyses of colonic microbial populations in humans after antibiotic treatment demonstrated that loss of obligate anaerobes frequently results in expansion of γ-proteobacteria and enterococci; these findings suggest that the complex, pre-antibiotic commensal microbiota suppresses the expansion of the oxygen-tolerant bacterial species (*14*, *15*).

Microbiota destruction and antibiotic-resistant infections

Increasing antibiotic resistance, according to the World Health Organization, is one of the most important threats to human health (www.who.int/entity/drugresistance/en). Bacterial resistance to antibiotics has become a formidable problem for the treatment of many infections. A subset of these infections—indeed, some of the most antibiotic-resistant forms—occur in hospitalized patients, where they achieve very high densities that facilitate patient-to-patient spread. Extended-spectrum β-lactamase (ESBL)–producing Enterobacteriaceae,

Downloaded from http://science.sciencemag.org/ on April 28, 2016

carbapenem-resistant Enterobacteriaceae (CRE), vancomycin-resistant enterococci (VRE), and *Clostridium difficile* are listed by the Centers for Disease Control and Prevention (CDC) as urgent and serious threats, and they have become so common within hospitals that donning of gloves and gowns to visit patients is now practically routine.

A seminal clinical study investigating the impact of different antibiotics on the density of colonization by VRE demonstrated that an antibiotic's ability to destroy obligate anaerobes correlates with VRE expansion (*16*). A critical point is that the antibiotic that promotes expansion of an antibiotic-resistant bacterial species may not be the one it is resistant to (such as vancomycin in the case of VRE), but rather an antibiotic that kills bacterial species that provide colonization resistance. The density of colonization by VRE approaches 10^{10} colony-forming units per gram of intestinal content, which leads to high rates of transmission within a hospital setting. Studies focusing on patients undergoing bone marrow transplantation demonstrated that many patients develop intestinal domination with VRE and that bacteremia strongly correlates with preceding intestinal domination (*2*). Administration of an antibiotic with high specificity for obligate anaerobic bacteria was the major risk factor for development of VRE intestinal domination (*17*).

Antibiotic-resistant Enterobacteriaceae were also found to dominate the intestinal tract in bone marrow transplant patients and to correlate with the development of bacteremia (*17*). It remains unclear whether bacterial species that confer colonization resistance to VRE similarly protect against Enterobacteriaceae such as antibiotic-resistant *Klebsiella pneumoniae*. However, at least in mouse models, reestablishment of a normal microbiota in VRE- or *K. pneumoniae*–dominated mice by transplantation of feces from antibiotic-naïve mice leads to the elimination of both bacterial species (*18*). With respect to VRE domination, deep 16*S* rRNA gene sequence analysis demonstrated a strong correlation between the presence of bacteria belonging to the *Barnesiella* genus and colonization resistance to VRE (*8*). Whether *Barnesiella* strains directly mediate VRE clearance or work together with other commensal bacterial species to establish colonization resistance remains to be determined. Although the effectiveness of the microbiota in protecting humans against infection by antibiotic-resistant bacteria is unknown, two recent reports suggest that reestablishment of a diverse microbiota reduces intestinal colonization by VRE and antibiotic-resistant *Escherichia coli* (*19*, *20*).

Clostridium difficile is perhaps the best-known pathogen associated with infections that follow antibiotic-mediated damage to the microbiota. The ability of normal fecal microbiota to provide colonization resistance against *C. difficile* has been suspected for many decades but was finally proven in a randomized study (*21*). Tvede and colleagues demonstrated nearly 30 years ago that administration of a cocktail of 10 commensal bacterial species, including some obligate anaerobic bacteria, could cure *C. difficile* infection in patients (*22*). Subsequent studies from several laboratories have demonstrated that even smaller consortia of commensal bacterial species can provide protection against *C. difficile* infection (*5*–*7*, *9*). A recent study identified *C. scindens*, an obligate anaerobic bacterial species that inhabits the colon and that has the rare ability to convert primary to secondary bile salts, as highly associated with resistance to *C. difficile* colitis in mice and humans (*7*). Administration of *C. scindens* to susceptible mice corrected the deficiency in secondary bile salts and rendered them more resistant to *C. difficile* colitis. Other studies have demonstrated that commensal bacterial strains can introduce sialic acids into the gut lumen, a potential energy source for invading pathogens, and that antibiotic administration transiently increases sialic acid levels, thereby enhancing *C. difficile* growth (*23*).

Microbiota-mediated colonization resistance against pathogens such as VRE, *K. pneumoniae*, and *C. difficile* is often indirect—for example, by inducing antibacterial factors such as RegIIIγ (*24*), a C-type lectin that selectively kills Gram-positive bacteria (*25*), or by modifying host factors such as bile salts to render them toxic to other bacteria (*7*) (Fig. 1). On the other hand, inhibition can be more direct, such as by nutrient depletion (*26*, *27*) or potentially by direct attacks (e.g., by the type 6 secretion systems harbored by some bacterial species that enable them to attack and kill other bacterial species) (*28*). Although the mechanisms underlying colonization resistance are complex and remain incompletely defined, there is little doubt that high levels of colonization resistance can be induced by transfer of specific commensal bacteria to vulnerable individuals, and that the degree of colonization resistance—with reductions in colonization density exceeding six orders of magnitude—resembles the degree of resistance induced by some of the most effective vaccines. Thus, from a clinical standpoint, the development of commensal bacteria as preventive and therapeutic agents is a high priority.

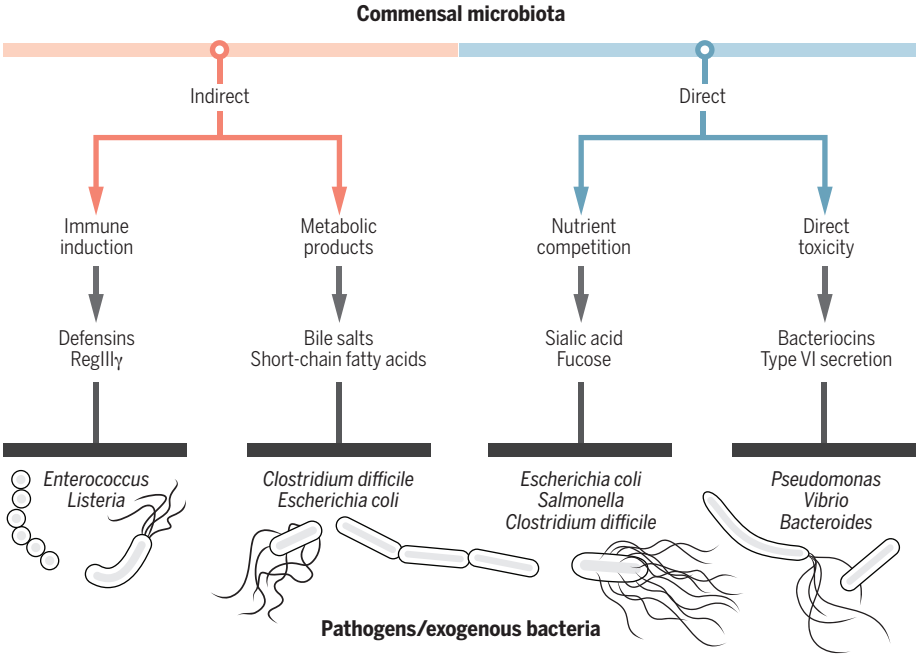

Fig. 1. The intestinal commensal microbiota provides colonization resistance against a wide range of pathogens by indirect and direct mechanisms. Commensal bacteria activate innate immune defenses in the mucosa, produce or modify host-derived metabolites, deplete nutrients, or produce substances that are directly toxic to competing bacteria. These mechanisms in aggregate can induce a high level of resistance against colonization by exogenous bacteria.

Correcting colonization resistance to reduce antibiotic-resistant infections

A document published in 2013 by the CDC outlined the major antibiotic-resistant pathogens that are continuing to emerge as threats to human health (www.cdc.gov/drugresistance/threat-report-2013). Recommendations to combat the progression of antibiotic resistance included barrier and hygiene approaches to reduce transmission, limits on antibiotic use, and development of new and more effective antibiotics. A major concern with these approaches, however, is that antibiotic resistance has grown despite their implementation. Recently, the White House provided a national action plan for combating antibiotic-resistant bacteria, which included specific milestones that introduced the potential role of the microbiome and the microbiota in combating antibiotic resistance (www.whitehouse.gov/sites/default/files/docs/national_action_plan_for_combating_antibiotic-resistant_bacteria.pdf). The plan calls for the "characterization of the gut microbiome of at least one animal species raised for food, to determine

Downloaded from http://science.sciencemag.org/ on April 28, 2016

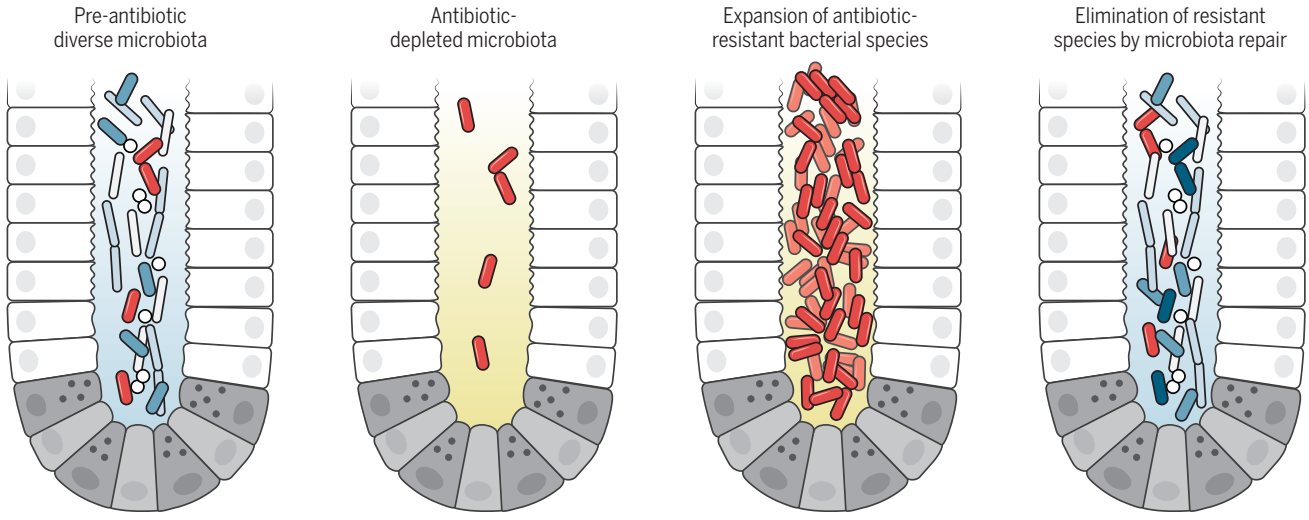

Fig. 2. Antibiotic treatment eliminates many commensal bacterial species from the gut lumen and reduces antimicrobial defenses. Antibiotic-resistant bacterial species can thrive, undergo expansion, and traverse the intestinal epithelial barrier. Antibiotic-induced microbiota defects and the resulting loss of colonization resistance can be corrected by administration of commensal bacterial species.

how antibiotic treatments disrupt normal gut bacteria and how animal growth might be promoted—and bacterial diseases might be treated—without using antibiotics. USDA, in consultation with NIH and CDC, will support research to map the gut microbiome using metagenomic techniques and big data analysis tools" and "developing products that restore or preserve beneficial bacteria in human and animal microbiomes and prevent colonization with harmful bacteria (e.g., probiotics, prebiotics, or synthetic microbiota)."

The mention within the White House document of microbiome-derived probiotics as a potential intervention for dealing with antibiotic resistance is important, and the proposed NIH support for basic and clinical studies to investigate the relationship between the microbiome and antibiotic resistance will undoubtedly move this field forward and lead to new probiotic agents. Although commensal bacterial strains that confer colonization resistance are referred to as probiotics below, they differ substantially from probiotics that are currently marketed. Recent studies confirm the original suggestion that obligate anaerobes are the major contributors to colonization resistance (*5*–*7*).

Probiotics: From Metchnikov to Activia

The idea that administration of live bacteria to humans can lead to health benefits likely originated with Élie Metchnikov, a Nobel laureate in 1908. Toward the end of his career, he became fascinated with the longevity of yogurt-eating people in Bulgaria (*29*). He postulated that lactate-producing bacteria were health-promoting and that other bacteria inhabiting the host were responsible for age-related decompensation and tissue destruction. A century later, this general notion remains popular and has led to the concept that certain bacteria—in particular, lactate-producing genera such as *Lactobacillus*—promote health and thus are referred to as probiotics (*30*). Other probiotic bacteria, such as Bifidobacteria, have similarly been proposed to enhance health and have recently been associated with enhanced responses to cancer immunotherapy (*31*) and resistance to infection by enteropathogenic *Escherichia coli* (*32*) in animal models. Despite the popularity of these probiotics, there is little solid evidence in humans of their effectiveness in enhancing health, promoting longevity, or reducing infections.

Worldwide, probiotics are a big business, with more than $30 billion in sales annually. Because specific health claims are not made, most probiotics are not regulated as drugs by the U.S. Food and Drug Administration. However, at times manufacturers cross the line, as occurred with Activia yogurt in 2010. In that case, ingestion of Activia, which contains *Bifidobacterium*, was advertised to reduce bowel transit time, but the claim had not been substantiated by clinical studies (www.ftc.gov/news-events/press-releases/2010/12/dannon-agrees-drop-exaggerated-health-claims-activia-yogurt) and was challenged by the U.S. Federal Trade Commission. The exaggerated health claims were dropped and the parent company, Danone, was fined roughly $35 million.

The limited regulation of probiotics has occasionally resulted in exaggerated claims that have left at least some health professionals skeptical of the entire field. The recently characterized bacterial species that constitute a small fraction of the commensal microbiota but have been shown in the laboratory to provide colonization resistance will be new members of the probiotic club; presumably, specific claims about their benefits will be substantiated by careful clinical studies to demonstrate safety and effectiveness.

Next-generation probiotics: Clinical studies of safety and effectiveness

Movement of laboratory discoveries to the clinic requires clinical trials, safe manufacturing, distribution, and, ultimately, delivery to the patient. Development and safe delivery of a medicine consisting of live bacteria poses special but not unprecedented challenges. For example, live *Mycobacterium bovis* BCG is currently being used and is FDA-approved for treatment of superficial bladder cancer (www.fda.gov/downloads/BiologicsBloodVaccines/Vaccines/ApprovedProducts/UCM163039.pdf), and live bacterial vaccines such as the typhoid vaccine (www.fda.gov/BiologicsBloodVaccines/Vaccines/ApprovedProducts/ucm201437.htm) have been developed and administered. Because next-generation probiotics will make health claims (i.e., to treat or prevent a disease), the FDA will regulate their progression to the clinic. Probiotic bacteria that treat or prevent *C. difficile* or that reduce intestinal colonization with highly antibiotic-resistant pathogens would be classified as drugs and should therefore be rigorously tested for effectiveness and safety.

That said, there are many different stringencies of FDA regulation, depending on the potential risks associated with the drug and the specificity of the health claims. Food supplements are regulated by the FDA, but mostly at the level of ensuring proper branding and lack of "adulteration" (www.fda.gov/Food/DietarySupplements). Commercially available homeopathic agents make specific health claims but have generally not been regulated by the FDA because of their assumed lack of toxicity. However, even homeopathic agents occasionally result in toxic reactions (*33*). The line distinguishing a health claim that defines a substance as an FDA-regulated drug versus a claim that is more general and not requiring FDA regulation is, to say the least, unclear.

Clinical studies to demonstrate safety and effectiveness leading to eventual FDA approval are expensive and are generally beyond the capacity of an academic research laboratory. Giving companies incentives to perform these studies requires some form of protection, usually defining a drug

Downloaded from http://science.sciencemag.org/ on April 28, 2016

as intellectual property through a patent that prevents, for a defined period of time, competitors from producing and selling the same drug without having shouldered the development costs. Intellectual property can be thought of as a creation or invention that resulted from intellectual creativity that yielded a material, or property, that did not exist prior to its invention. In the field of biomedicine, a typical example of intellectual property is an engineered antibody that can be administered as a clinically beneficial drug.

The patenting of a natural product, by contrast, is more controversial and may have an adverse impact on its clinical development. For example, after the sequencing of the human genome in 2001, it was possible to patent individual genes, which restricted the ability of other investigators to study these genes and held back research groups and potential competitors from developing diagnostic tests (*34*). The U.S. Supreme Court struck down the ability to patent genes in 2013. Bacterial strains that have been genetically manipulated to modify or enhance a specific function have been patented since 1981 (US 4259444 A). Whether unmanipulated bacterial strains isolated from human donors can be patented and protected as intellectual property is unclear. Recently, however, a patent has been issued to protect a consortium of genetically unmanipulated bacterial spores isolated from human feces (US 8906668 B2).

Given the potential difficulties associated with patenting bacterial species, commercial development of colonization resistance–promoting bacterial strains will be challenging. One example of an unpatented drug being brought forward is Taxol, a natural product (paclitaxel) that was purified from the Pacific yew and is an effective treatment for some cancers (*35*). In this case, production and delivery of Taxol by a major pharmaceutical company was promoted by an unusual 5-year guarantee of exclusivity that was extended another 5 years through a series of legal maneuvers.

Producing and delivering probiotic bacteria

Unlike chemical drugs, whose composition and purity can be determined with precision, live bacteria must be cultured, often in complex media, and, even if maintained in pure form, can mutate and either gain or lose functions upon extended culturing. Thus, guaranteeing uniformity, purity, and effectiveness becomes a substantial challenge that can be overcome with a high level of vigilance. Repopulating the human gut with commensal bacterial species has been performed by infusion of fecal material to the upper gastrointestinal tract by nasogastric tube (*21*) and to the lower gastrointestinal tract by colonoscopy or enema (*36*). Recently, capsules containing spores isolated from human feces have been administered orally and have effectively treated recurrent *C. difficile* infection (*37*). These results suggest that administration of probiotic commensal bacteria can occur by different routes; orally administered capsules likely represent the simplest approach.

The most common role of next-generation probiotics will likely be preventive rather than therapeutic. Routine administration of bacterial consortia to hospitalized patients to optimize resistance against infection with antibiotic-resistant pathogens, or to individuals traveling to areas where enteric infections are common, is certainly conceivable (Fig. 2). Replenishment of microbiota after treatment with antibiotics is another intervention that would likely reduce secondary infections. Because these commensal bacterial species have a long history of inhabiting the human intestine and are not associated with diseases or infections, it is unclear whether the FDA might regulate them as loosely as homeopathic agents (*33*). Similarly, it remains unclear whether next-generation probiotics should be made available on store shelves for over-the-counter purchase or whether they will require a physician prescription.

For now, clinical studies need to be performed to establish effectiveness and safety, and such studies require funding. Extensive analyses of the intestinal microbiota have revealed the impact of distinct commensal bacterial populations on the development of obesity (*38*), metabolic syndrome (*39*), intestinal inflammation (*40*), autoimmunity (*41*), and potentially even psychoneurologic states (*42*). The broad impact of commensal bacterial species on a wide range of health issues will require consideration in settings of microbiota reconstitution with designer microbial consortia. Thus, studies of next-generation probiotics will require long-term follow-up to evaluate study participants for development of obesity, metabolic syndrome, or autoimmune diseases and to monitor long-term colonization by probiotic agents.

Conclusion

The discovery that a subset of commensal bacteria can provide colonization resistance against many of the most threatening antibiotic-resistant pathogens causing disease in patients is exciting, and their development as preventive or therapeutic agents is important. For now, we remain in the discovery phase, but commercial interests are already growing, and companies are positioning themselves within the context of the existing rules and regulations for drug development. A rush to protect bacterial strains or consortia as intellectual property is under way and may promote their development as important therapies in the battle against antibiotic-resistant pathogens. On the other hand, as occurred with the patenting of genes, declaring bacterial strains isolated from the microbiota intellectual property may restrict their development. Unlike conventional drugs, commensal bacterial species have coevolved with us and are a normal part of the human superorganism. Indeed, these microbial populations are the product of tens of millions of years of coevolution with humans, and thus their safety might be considered well established. Indeed, it is their absence that is associated with susceptibility to a wide range of infections.

Although protective commensal bacterial strains developed for the resurrection of a healthy microbiota will be considered drugs, the established regulatory hurdles for conventional drug development require recalibration for these normal components of the human superorganism. The clinical development of these strains and their affordability will also be affected by whether they can be declared intellectual property. The potential for these next-generation probiotics in enhancing resistance to infection and reducing antibiotic-resistant infections is real, and their development should be supported by research funding, as proposed by the White House national action plan, and by the delineation of a regulatory path that balances concerns about safety with expediency.

REFERENCES AND NOTES

1. L. Dethlefsen, S. Huse, M. L. Sogin, D. A. Relman, *PLOS Biol.* **6**, e280 (2008).
2. C. Ubeda *et al.*, *J. Clin. Invest.* **120**, 4332–4341 (2010).
3. C. G. Buffie *et al.*, *Infect. Immun.* **80**, 62–73 (2012).
4. C. G. Buffie, E. G. Pamer, *Nat. Rev. Immunol.* **13**, 790–801 (2013).
5. A. E. Reeves, M. J. Koenigsknecht, I. L. Bergin, V. B. Young, *Infect. Immun.* **80**, 3786–3794 (2012).
6. T. D. Lawley *et al.*, *PLOS Pathog.* **8**, e1002995 (2012).
7. C. G. Buffie *et al.*, *Nature* **517**, 205–208 (2015).
8. C. Ubeda *et al.*, *Infect. Immun.* **81**, 965–973 (2013).
9. E. O. Petrof *et al.*, *Microbiome* **1**, 3 (2013).
10. R. Freter, *J. Infect. Dis.* **97**, 57–65 (1955).
11. D. J. Hentges, R. Freter, *J. Infect. Dis.* **110**, 30–37 (1962).
12. M. Bohnhoff, B. L. Drake, C. P. Miller, *Proc. Soc. Exp. Biol. Med.* **86**, 132–137 (1954).
13. M. Bohnhoff, C. P. Miller, *J. Infect. Dis.* **111**, 117–127 (1962).
14. E. J. Vollaard, H. A. Clasener, A. J. van Griethuysen, A. J. Janssen, A. J. Sanders-Reijmers, *J. Antimicrob. Chemother.* **20** (suppl. B), 131–138 (1987).
15. E. J. Vollaard, H. A. Clasener, A. J. Janssen, H. J. Wynne, *J. Antimicrob. Chemother.* **25**, 861–871 (1990).
16. C. J. Donskey *et al.*, *N. Engl. J. Med.* **343**, 1925–1932 (2000).
17. Y. Taur *et al.*, *Clin. Infect. Dis.* **55**, 905–914 (2012).
18. S. Caballero *et al.*, *PLOS Pathog.* **11**, e1005132 (2015).
19. J. Stripling *et al.*, *Open Forum Infect. Dis.* **2**, ofv078 (2015).
20. R. Singh *et al.*, *Clin. Microbiol. Infect.* **20**, O977–O978 (2014).
21. E. van Nood *et al.*, *N. Engl. J. Med.* **368**, 407–415 (2013).
22. M. Tvede, J. Rask-Madsen, *Lancet* **1**, 1156–1160 (1989).
23. K. M. Ng *et al.*, *Nature* **502**, 96–99 (2013).
24. K. Brandl *et al.*, *Nature* **455**, 804–807 (2008).
25. H. L. Cash, C. V. Whitham, C. L. Behrendt, L. V. Hooper, *Science* **313**, 1126–1130 (2006).
26. S. M. Lee *et al.*, *Nature* **501**, 426–429 (2013).
27. E. D. Sonnenburg *et al.*, *Cell* **141**, 1241–1252 (2010).
28. M. J. Coyne, K. G. Roelofs, L. E. Comstock, *BMC Genomics* **17**, 58 (2016).
29. A. C. Brown, A. Valiere, *Nutr. Clin. Care* **7**, 56–68 (2004).
30. S. L. Gorbach, *Am. J. Gastroenterol.* **95** (suppl.), S2–S4 (2000).
31. A. Sivan *et al.*, *Science* **350**, 1084–1089 (2015).
32. S. Fukuda *et al.*, *Nature* **469**, 543–547 (2011).
33. S. H. Podolsky, A. S. Kesselheim, *N. Engl. J. Med.* **374**, 201–203 (2016).
34. J. S. Sherkow, H. T. Greely, *Annu. Rev. Genet.* **49**, 161–182 (2015).
35. K. Garber, *J. Natl. Cancer Inst.* **94**, 324–326 (2002).
36. E. Gough, H. Shaikh, A. R. Manges, *Clin. Infect. Dis.* **53**, 994–1002 (2011).
37. S. Khanna *et al.*, *J. Infect. Dis.* jiv766 (2016).
38. P. J. Turnbaugh, F. Bäckhed, L. Fulton, J. I. Gordon, *Cell Host Microbe* **3**, 213–223 (2008).
39. M. Vijay-Kumar *et al.*, *Science* **328**, 228–231 (2010).
40. I. I. Ivanov *et al.*, *Cell* **139**, 485–498 (2009).
41. J. U. Scher *et al.*, *eLife* **2**, e01202 (2013).
42. E. Y. Hsiao *et al.*, *Cell* **155**, 1451–1463 (2013).

ACKNOWLEDGMENTS

Supported by NIH grants RO1 AI095706, AI042135, UO1 AI124275, and PO1 CA023766 and by the Leonard Tow Foundation. E.G.P. is an inventor on patent application WPO2015179437A1, entitled "Methods and compositions for reducing *Clostridium difficile* infection."

10.1126/science.aad9382

Downloaded from http://science.sciencemag.org/ on April 28, 2016

REVIEW

How colonization by microbiota in early life shapes the immune system

Thomas Gensollen,[1] Shankar S. Iyer,[1] Dennis L. Kasper,[2] Richard S. Blumberg[1]*

Microbial colonization of mucosal tissues during infancy plays an instrumental role in the development and education of the host mammalian immune system. These early-life events can have long-standing consequences: facilitating tolerance to environmental exposures or contributing to the development of disease in later life, including inflammatory bowel disease, allergy, and asthma. Recent studies have begun to define a critical period during early development in which disruption of optimal host-commensal interactions can lead to persistent and in some cases irreversible defects in the development and training of specific immune subsets. Here, we discuss the role of early-life education of the immune system during this "window of opportunity," when microbial colonization has a potentially critical impact on human health and disease.

The commensal microbiota, which widely colonize the body, strongly influence the host immune system. Most of the internal and external surfaces of a mammals' body during adult life—including the gastrointestinal tract, skin, and oral mucosa—are heavily colonized by microbiota, with the largest congregation of organisms contained within the colon. The human body was recently estimated to be composed of 3×10^{13} eukaryotic cells and 4×10^{13} colonizing bacteria (*1*). The exposure of the mammal to microbiota begins in utero and expands rapidly after birth. For example, maternal gut bacteria can be detected in the amniotic fluid of pregnant mice (*2*), and bacteria can be isolated in the meconium from preterm human babies (*3*). After birth, the composition of microbiota is initially derived from opportunistic colonization by the first types of bacteria to which a baby is exposed in his or her environment, which together with other environmental factors, such as diet, may substantially affect the entry of subsequent microbial species into the various mucosal niches. As such, the mode of delivery and subsequent environmental exposures greatly influence the composition of the microbiota in the infant (*4*). The microbiota composition of an adult may therefore in part reflect the history of exposure to microbes and environmental factors in early life. This concept is supported by experiments with mice (*5*, *6*) and familial studies in humans (*7*) that indicate that the environment in early life may account for, at least in part, microbial composition in the adult. These events and their immune consequences are perhaps most important during the first year of life, when the microbial composition is highly variable (*8*), with progressive stabilization to an adult-like community structure after 3 years of age (*9*). The instability of the microbiota during early life makes the community structure of microbiota during this time more sensitive to environmental incursions (*10*). It is now increasingly clear that early-life colonization also coincides with a potentially time-limited period during which the immune system is permissive to microbial instruction. Further, emerging evidence suggests that the immune influences induced by the microbiota during this early period of life may be durable, creating a "window of opportunity" for proper (or improper) immune education to occur and resistance (or susceptibility) to disease in later life. This Review focuses on these issues and the recent evidence in support of this concept.

Evidence that the microbiota influences the immune system: Lessons from germ-free animal studies

The use of germ-free (GF) animals allowed for development of the concept that the microbiota influences the immune system. In 1885, Louis Pasteur first proposed the generation of animals deprived of common microorganisms to understand the relationship between microbes and their host (*11*). Ten years later, Nuttall and Thierfelder used guinea pigs to produce the first GF animals by means of cesarean section (*12*). It took around another 50 years, however, until enough was known about the nutrition of newborn animals to enable production of the first GF rats (*13*) and mice (*14*). The first comparisons of GF rodents with "microbiota-colonized animals" resulted in the observation that there were gross physiological differences between GF and the specific pathogen–free (SPF) state, including an enlarged cecum, principally due to an accumulation of undegraded mucus (*15*), and reduced gastrointestinal motility (*16*), due to the loss of the critical digestive functions of the inhabiting microbiota. In parallel, GF rodents display an aberrant intestinal epithelial cell (IEC) morphology that includes longer villi and shorter crypts in comparison with that observed in conventionalized mice (*17*) and reduced antimicrobial peptides (*18*, *19*). Of most relevance, the absence of commensals has profound effects on the structural and functional development of the immune system, including but not limited to defects in lymphoid tissue development within the spleen, thymus, and lymph node (*20*, *21*). Moreover, these structural abnormalities were most striking near the mucosal interface, suggesting that interactions with specific communities of microbes directly modulate development of these gut-associated lymphoid structures (GALTs). For instance, a type of lymphoid tissue called isolated lymphoid follicles (ILFs) are minimally present in the absence of microbiota in the small intestine but not the colon (*22*–*24*). In addition, GF animals contain smaller Peyer's patches (PPs) and mesenteric lymph nodes (MLNs) (*23*). Collectively, these studies demonstrate that the microbiota participates in the maturation of the immune system and suggests that specific events in association with the process of microbial colonization may be important in the development of a normal immune system in a healthy individual.

Microbial colonization modulates early development of the immune system in mucosal tissues

Colonization of mucosal surfaces is characterized by fluctuating changes in microbial diversity during the first few years of life, until reaching a point of equilibrium that remains relatively stable throughout adulthood in the absence of environmental insults (*25*). In association with this, the early-life ecological succession of mucosal colonization occurs concomitantly with the development, expansion, and education of the mucosal immune system. It therefore follows that immune maturation is likely influenced directly and/or indirectly by the presence of commensal microbes (*26*, *27*). The postnatal period thus represents a potentially critical time in which early-life microbial exposures can have profound influences on the morphological and functional development of the immune system. Neonatal immune cells differ in function from adult immune cells so that they preferentially develop tolerance in response to antigen exposure in a process that still remains to be defined but does not involve an intrinsic property of the T cell but rather the environment in which the T cell develops (*28*–*30*). Neonatal immune cells therefore learn to tolerate the new environment experienced after birth, such as the commensal microbiota. These concepts have been experimentally tested by varying the time of microbiota introduction into GF animals and observing the changes in immune development and/or function.

Although most abnormalities in GF animals are age-independent and can be corrected by introducing commensals at any age (*31*), the ability to restore a few cellular defects that occur in the absence of microbiota is restricted to a short time interval in early life and thus is

[1]Division of Gastroenterology, Hepatology, and Endoscopy, Department of Medicine, Brigham and Women's Hospital, Harvard Medical School, Boston, MA, USA. [2]Division of Immunology, Department of Microbiology and Immunobiology, Harvard Medical School, Boston, MA, USA.
*Corresponding author. Email: rblumberg@partners.org

Downloaded from http://science.sciencemag.org/ on April 28, 2016

age-dependent. Consistent with this, GF mice conventionalized during adult life possess a different transcriptional profile in the jejunum and colon in comparison with conventionally raised SPF mice, suggesting that if colonization does not occur during a critical "window of opportunity," intestinal immune development cannot be fully achieved in the adult (*32*). This supports the notion that early exposure to microbes may have durable consequences for the host that may extend into adult life. As a corollary, in the absence of appropriate microbial exposures in early life, the immune consequences may elicit irreversible and potentially deleterious implications for the host.

Age-independent influences

T cell subsets

GF animals exhibit major defects in the development of primary and secondary lymphoid organs—including the GALT, spleen, and thymus—which is associated with a decreased frequency of $CD4^+$ and $CD8^+$ intestinal T cell subsets as well as reduced numbers of intraepithelial lymphocytes that express the αβ T cell receptor (TCR) (*33*). Normalization of these morphological and cellular defects in αβ T cells can be achieved by reintroducing standard mouse or human microbiota in adult mice (*33*–*36*). Furthermore, characterization of the TCR repertoire in intestinal tissues at the time of initial commensalization suggests an influx of polyclonal TCR-$\alpha\beta^+$ T cells early in life that lose diversity and revert to an oligoclonal state in the adult (*37*). To address this, subsequent studies comparing colonized and monocolonized mice with GF animals have begun to clarify the role of distinct commensal bacterial communities in modulating specific T cell effects. GF mice are typically T helper 2 (T_H2)–skewed. A balancing of systemic T_H1 and T_H2 cells is observed after monocolonization of GF mice with *Bacteroides fragilis* that is due to a single microbial molecule, polysaccharide A (PSA) (*38*). In another example, segmented filamentous bacteria (SFB) play a key role in intestinal T_H cell responses and the induction of secretory immunoglobulin A (IgA) (*39*, *40*). Colonization with rat microbiota or monocolonization with SFB, however, only partially restores $CD4^+$ and $CD8^+$ T cell numbers, suggesting that a diverse microbial population is necessary to restore a fully mature immune system in the adult (*39*). Particular bacterial populations have been linked to the development of specific T effector subsets, such as T_H17 cells, a potent source of interleukin-17 (IL-17) that plays an important role in the maintenance of mucosal barrier integrity and clearance of pathogens in the tissues. T_H17 development is dependent on microbiota and is absent in the small intestine of GF animals. T_H17 cells can be restored in GF adult mice through colonization with standard mouse microbiota or SFB but not others (*41*). Consequently, SFB colonization confers enhanced protection compared with GF animals after infection with the bacterial pathogen *Citrobacter rodentium*, which is a direct result of enrichment of T_H17 cells in the small bowel (*41*).

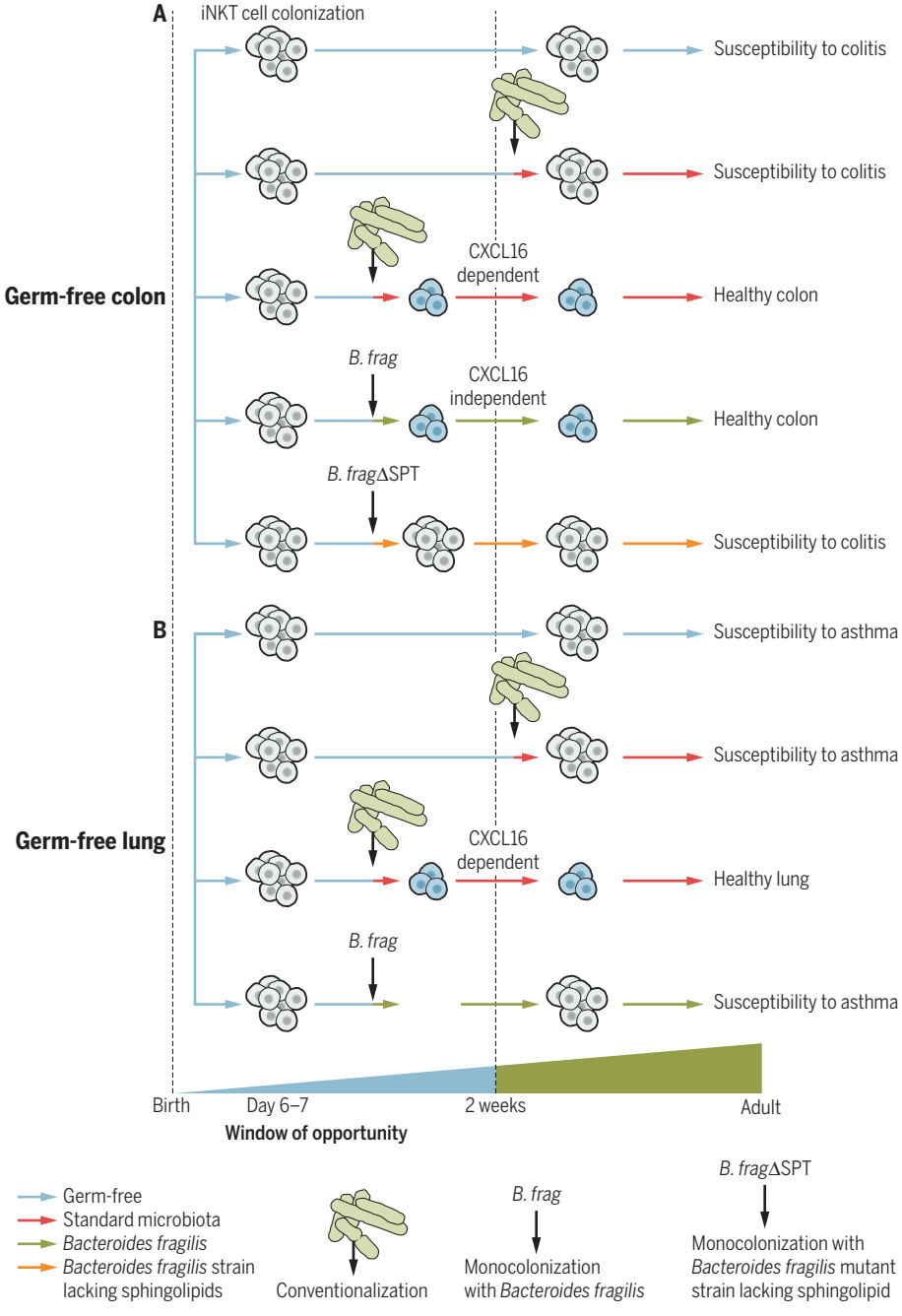

Fig. 1. iNKT cell colonization is regulated by the microbiota during early life and influences susceptibility to colitis and asthma later in life. (**A**) iNKT cells migrate from the thymus to the colon during the first weeks of life. Their abnormal accumulation in the colon of GF mice leads to later-life susceptibility to oxazolone-induced colitis. Conventionalization with a standard microbiota or monocolonization with *B. fragilis* (*B. frag*) but not *B. fragilis* deficient in sphingolipids (*B. frag*ΔSPT) during the window of opportunity restores colonic iNKT cell numbers and abrogates the increased susceptibility to colitis. In contrast to conventionalization with a standard microbiota during the first 2 weeks of life that decrease iNKT cell number in a mechanism dependent on CXCL16, monocolonization with *B. fragilis* regulates colonic iNKT cell number in a CXCL16-independent manner that depends on inhibitory sphingolipids from *B. fragilis* that impede iNKT cell proliferation. (**B**) iNKT cell accumulation in lungs of GF mice lead to later-life susceptibility to asthma. Conventionalization with a standard microbiota but not monocolonization with *B. fragilis* during the window of opportunity restores colonic iNKT cell numbers in a CXCL16-dependent manner and abrogates the increased susceptibility to asthma.

Downloaded from http://science.sciencemag.org/ on April 28, 2016

Regulatory T cells (T_{reg} cells) are a major source of IL-10 and capable of recognizing commensal-derived antigens (*42*), which supports the maintenance of tolerance to intestinal microbes (*43*). GF mouse colon, but not small intestine, contains decreased T_{reg} cells, which can be normalized through standard conventionalization and monocolonization with certain *Clostridium* species or a variety of intestinal microbes, regardless of age (*44*, *45*).

B cells

B cells are essential to the immune system as a source of the five different isotypes of functionally distinct antibodies: IgA, IgE, IgG, IgD, and IgM. GF mice exhibit normal numbers and phenotypic maturation of B cells. However, they exhibit a general defect in the production of IgA and IgG1 antibodies in mucosal and nonmucosal organs that can be normalized after conventionalization by microbiota (*31*). Consistent with this, GF mice possess few IgA-expressing B cells in the small intestine. This decrease in IgA is likely due to ILF deficiency. Conventionalization of adult GF mice thus restores ILF numbers and rescues IgA production by B cells in the small intestine (*31*, *46*). This may be through dendritic cells that do not migrate outside of intestinal tissues and retain live microorganisms for prolonged periods of time, which allows them the ability to induce IgA expression in the adult mouse intestine (*47*).

Innate lymphoid cells

Innate lymphoid cells (ILCs) represent lymphoid cells with innate immune function that lack a B or T cell receptor (*48*). Conflicting results surround our understanding of ILC regulation by microbiota. Natural killer (NK) cells (ILC group 1) exhibit reduced phenotypic evidence of activation in nonmucosal organs of GF mice, a process that is orchestrated by mononuclear phagocytes in a Toll-like receptor (TLR)–dependent manner and can be reversed through the colonization of adult mice with a standard microbiota (*49*). It has also been shown that GF mice display impaired development of Nkp46$^+$ RAR-related orphan receptor–γt (RORγt)–dependent group 3 ILCs (*50*) and decreased expression of IL-22 by these cells, an important cytokine in epithelial responses to microbes in the small intestine (*50*, *51*). However, another study has shown that GF mice exhibit no change in the numbers of Nkp46$^+$ RORγt–dependent ILCs and increased IL-22 expression owing to IL-25 production by IECs (*52*, *53*). In either case, dysregulation of IL-22 expression in GF mice can be normalized by means of standard microbiota conventionalization in adult mice (*50*, *52*). Despite these inconsistencies, it is clear that microbiota regulate ILCs in an age-independent manner.

Epithelial cells

IECs are found at the interface between the lumenal microbiota and immune system in the mucosa and play an increasingly recognized role in a variety of immune functions (*54*). One of the functions of IECs is to produce antimicrobial peptides. RegIIIγ is a secreted C-type lectin that regulates the interaction between microbiota and the host through its antibacterial activity on Gram-positive microbes and is mainly expressed by Paneth cells at the base of the crypts of Lieberkuhn in the small intestine. In GF mice, IECs exhibit decreased expression of RegIIIγ that can be rescued after colonization with standard microbiota (*55*) or monocolonization with *Bacteroides thetaiotaomicron* in small intestine and colon (*56*). RegIIIγ expression is also regulated by IL-22 derived from Nkp46$^+$ RORγt–dependent ILC3 (*57*). Resistin-like molecule β (RELMβ) is a secreted protein highly expressed in the intestinal tract and goblet cells in particular. In GF mice, RELMβ expression by goblet cells is strongly decreased when compared with that in SPF mice but can be rescued after colonization with standard microbiota (*58*). RELMβ can regulate the expression of inflammatory cytokines through intestinal macrophages influencing host responses to artificially induced colitis (*59*). Separately, GF mice exhibit a lower expression of major histocompatibility complex (MHC) class II on IECs that can be rescued through colonization with microbiota, an interferon-γ–dependent event (*60*). In parallel, microbial derived factors such as acetate from *Bifidobacterium longum* can enhance protective functions of IECs in response to infection (*61*). Current studies also suggest that conventionalization of GF adult animals leads to substantial changes in gene expression associated with IECs (*62*). In future studies, it will be interesting to examine the age dependency of these effects and the manner in which they alter epithelial expression of factors well known to play an important role in epithelial cell–immune interactions such as IL-25, transforming growth factor–β (TGF-β), B cell activating factor (BAFF), a proliferator-inducing ligand (APRIL), and thymic stromal lymphopoietin (TSLP).

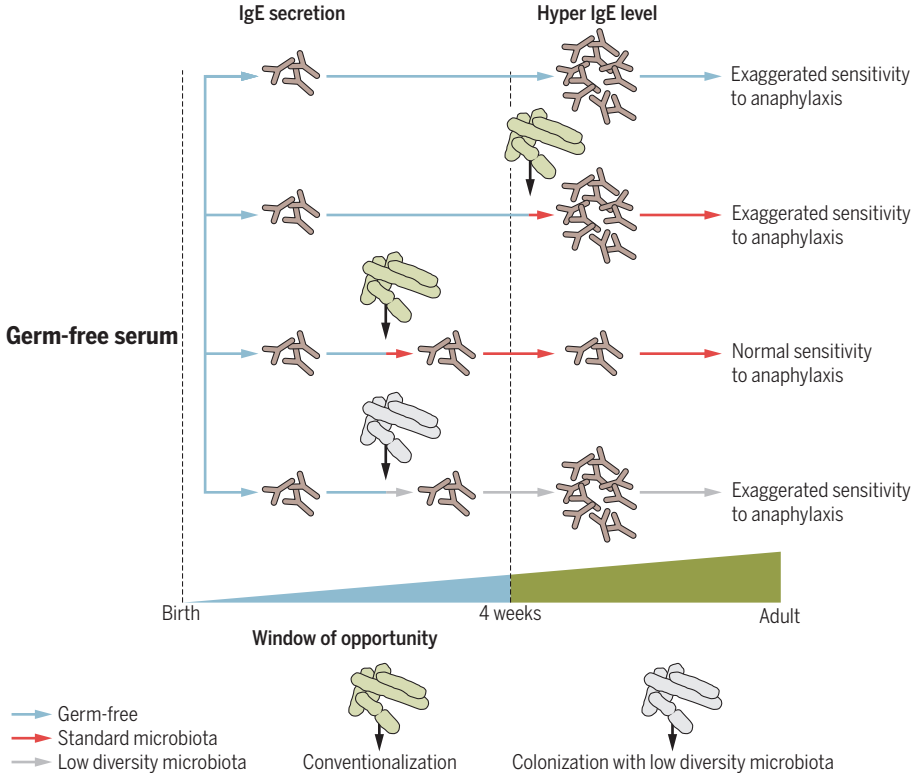

Fig. 2. Exposure to a microbiota during early life regulates IgE levels in serum of adult mice and their sensitivity to orally induced anaphylaxis. IgE accumulates in the serum of GF mice 4 weeks after birth because of an isotype switch to IgE in mucosal B cells. "Hyper-IgE levels" lead to an exaggerated sensitivity to orally induced anaphylaxis that can be resolved through conventionalization with a standard microbiota during early life but not thereafter. Colonization of GF mice with low-diversity microbiota during the window of opportunity fails to normalize hyper-IgE levels in adult life.

Age-dependent influences *iNKT cells in colon and lung*

Invariant natural killer T (iNKT) cells express an invariant TCR-α chain and a diverse array of TCR-β chains and recognize endogenous and exogenous (bacterial) lipid antigens when presented by CD1d, a MHC class I–like molecule (*63*). In GF animals, iNKT cells are decreased in peripheral tissues such as the spleen and liver and are hyporesponsive to lipid antigen stimulation, which is normalized by monocolonization with bacteria expressing iNKT antigens in adult mice (*64*). In distinct contrast, mucosal tissues such as the lung and colon contain substantially increased quantities of iNKT cells when mice are GF in comparison with that observed

Downloaded from http://science.sciencemag.org/ on April 28, 2016

in SPF mice in association with augmented inflammatory responses in experimental models of colitis and airway hyperresponsiveness (AHR) (*65*, *66*). This exaggerated accumulation of iNKT cells and hyperresponsiveness to environmental triggers of iNKT cells that induce colitis can be normalized through colonization of GF mice with standard microbiota, *Bacteroides fragilis* monocolonization, or treatment with *B. fragilis*–derived sphingolipid antigens during the first 2 weeks of life but not thereafter (Fig. 1A) (*65*, *66*). iNKT cell accumulation in the lung and susceptibility to asthma of GF mice can be rescued by colonization with standard microbiota but not by monocolonization with *B. fragilis* during the first 2 weeks of life (Fig. 1B).

These studies have revealed at least two nonmutually exclusive mechanisms by which the microbiota can modulate iNKT frequency in the colon and lung. Accumulation of iNKT cells in the colon in GF animals is associated with elevated levels of the chemokine ligand CXCL16, whose expression is normalized by conventionalization during this critical 2-week time period in a pathway dependent on microbiota-induced epigenetic changes of the *Cxcl16* gene (*65*). In contrast, normalization of iNKT cell frequency by the human commensal *B. fragilis* appears to involve an inhibition of iNKT cell proliferation and expansion in early life through *B. fragilis*–derived sphingolipids that are inhibitory (*66*). It is particularly interesting that the effects of intestinal *B. fragilis* colonization is tissue-specific because it is restricted to the colon, strongly supporting the idea that specific microbes and potentially signals can regulate iNKT recruitment and proliferation in distinct organs.

B cells and IgE

IgE are antibodies produced by B cells that play a pivotal role in response to allergens and immunity to pathogens. Whereas IgA and IgG1 levels are decreased in GF mice, a recent study showed that GF mice have elevated levels of serum IgE after weaning (~30 days) because of enhanced rates of B cell isotype class switching to IgE in PPs and MLNs (*67*). Elevated IgE levels in GF animals was associated with exaggerated responses to orally induced systemic anaphylaxis (*67*). Hyper-IgE levels in GF mice serum are associated with a concomitant increase in IL-4 production in PPs and MLNs and are dependent on $CD4^+$ T cells. Colonization of GF mice with standard microbiota from birth to 4 weeks of age but not thereafter normalizes the IgE levels in adults, which is consistent with a regulation of IgE production by the microbiota that is specific to this time frame (Fig. 2). IgE production in adult mice is dependent on intestinal bacterial diversity in neonates rather than on colonization with specific bacterial species so that a low diversity of microbiota is not sufficient to normalize IgE levels during early life.

T_{reg} cells in lung and skin

Exposure to house dust mite (HDM) antigen—which possesses CD1d-restricted antigens for iNKT cells (*68*), during the first 2 weeks of life, but not thereafter—induces a helios-negative (presumably induced) subset of T_{reg} cells from conventional $CD4^+$ T cells in the lung (*69*). Consequently, initial HDM exposure during adult life results in increased AHR relative to that observed when HDM exposure first occurs in early life. Mechanistically, the allergen-induced development of the helios-negative T_{reg} cells in early life is dependent on microbiota and involves the expression of the immune checkpoint molecule programmed cell death protein 1 (PD1) on the T cell and PD-L1 on dendritic cells so that early-life blockade of PD-L1 abrogates the expansion of the helios-negative T_{reg} cell and increased asthma upon HDM exposure. Thus, a 2-week window of opportunity exists in which allergen exposure can induce a specific group of T_{reg} cells and protection from asthma. Consistent with a prevalent role of microbiota in the regulation of lung allergic disease during early life, antibiotic treatment of mice during early life enhances susceptibility to allergic asthma (*6*).

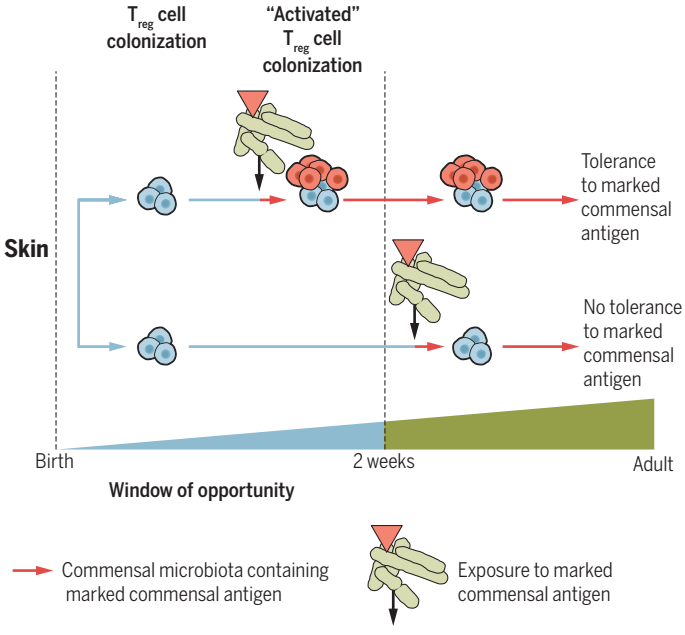

Fig. 3. T_{reg} cells colonize the skin of neonatal mice and induce tolerance to commensal bacteria. Colonization of neonatal skin with a commensal microbiota leads to an accumulation of "activated" T_{reg} cells (red cells) that specifically recognize an artificially marked antigen, with consequent tolerance to this same antigen in later life. Colonization of adult animals with the same microbiota containing the marked commensal microbiota (red triangle) does not lead to T_{reg} cell accumulation in the skin or establish immune tolerance.

A similar age-restricted regulation of T_{reg} cells also exists in skin. Colonization of mice with a commensal skin bacterial strain during the first 2 weeks of life, but not thereafter, induces accumulation of activated T_{reg} cells in the skin that are derived from the thymus and which maintain tolerance to commensal derived antigens in the adult (*70*). When colonization is initiated in adult mice after the time of weaning, such commensal antigen-specific tolerance is not initiated (Fig. 3). Further, the accumulation of activated T_{reg} cells during this early-life period appears to be specific to the skin and is not observed in the intestinal lamina propria. Antibiotic treatment in neonatal mice can induce long-term modification of microbial composition of the skin and susceptibility to psoriasis development in adulthood, which is associated with increased IL-22–producing γδ T cells (*71*). Regulation of thymically derived and induced T_{reg} cells by microbiota during early life therefore appears to be tissue-specific, suggesting that even the same cell type (such as T_{reg}) is under the influence of distinct organ-specific mechanisms.

Epithelial cells

The establishment of tolerance during the neonatal period can be regulated by non-immune cells. As an example, TLR signaling is specifically down-regulated during the first 2 weeks of life in mouse IECs but not thereafter (*72*, *73*). This renders epithelial cells hyporesponsive to TLR stimuli such as lipopolysaccharide derived from Gram-negative bacteria. This neonatal tolerance is dependent on TLR4 and the mode of birth delivery. Indeed, IECs from cesarean-born neonates do not down-regulate TLR signaling and are more prone to develop epithelial damage, suggesting an important role of specific types of microbial exposure in the development of epithelial tolerance. These studies emphasize the important potential role played by epithelial cells in the tolerance pathways that are established during early life.

Erythrocytes in spleen

A small subset of erythrocytes express the transferrin receptor CD71. $CD71^+$ erythrocytes are enriched in spleen from birth to 2 weeks of age and diminished in adult life (*74*). Their development is independent of microbiota; similar numbers are observed in GF and SPF mice. However, they function in suppressing responses of myeloid cells to pathogens (for example, *Listeria monocytogenes*) or commensals. In the latter case, CD71 inhibition leads to increased basal expression levels of the inflammatory cytokine tumor necrosis factor in intestinal myeloid cells in

Downloaded from http://science.sciencemag.org/ on April 28, 2016

neonates maintained under SPF conditions. These studies show that not only do microbial exposures regulate immune development during early life, but also that the host maintains critical and specific mechanistic pathways that regulate host response to microbes during this critical period of life.

Early-life perturbations of microbiota and their relationship to human disease

Because microbe-immune interactions appear to play an important role in early-life development of the immune system and when disrupted may result in potentially persistent immune abnormalities, it is worth considering whether early-life exposure to microbes may affect later-life susceptibility to disease. There is emerging evidence to support this hypothesis.

Children exposed to farm environments have a decreased risk for the development of allergic disease, possibly through mechanisms that involve the ubiquitin-modifying enzyme A20 (*75*, *76*). Moreover, farming exposure during pregnancy modulates immune responses and protects against asthma in a mother's offspring (*77*). This protective effect can be correlated with increased T_{reg} cell activity in the infant. Although it is not firmly proven, one of the plausible explanations for the protective effect of early-life farm exposure is the role of microbiota because individuals exposed to a farm environment possess different microbial diversity compared with other lifestyles (*78*). In an opposite manner, exposure to antibiotics is associated with persistent changes in microbial composition in studies performed in human adults (*79*–*81*) that may potentially apply to early periods of life (*82*). As an example, antibiotic use within the first 6 months of life is associated with an increased susceptibility to allergy and asthma at 6 years of age (*83*). Another study has shown that antibiotic exposure during the first year of life is associated with the development of wheezing and eczema at 8 years of age, even after taking into account early-life respiratory infections (*84*). In parallel, exposure to antibiotics in childhood, and especially during the first year of life, is associated with an increased risk for development of inflammatory bowel disease (IBD) (*85*, *86*). Antibiotic exposure during the first year of life is also associated with increased susceptibility to being overweight and developing central adiposity and may lead to increased development of type 2 diabetes mellitus later in life (*87*, *88*). Moreover, a recent study has shown that microbiota composition shifts occur in the infant before development of type 1 diabetes mellitus (*89*). Consistent with this, early-life exposure of female NOD mice to microbiota from male NOD mice can confer protection against diabetes mellitus in a testosterone-dependent pathway (*90*). Children born by means of cesarean section have an altered microbiota composition and may be more susceptible to obesity, type 1 diabetes mellitus, allergy, and asthma during childhood and adult life (*91*–*93*). The mechanistic basis for this latter example is unclear and may involve numerous factors, including the exposure to antibiotics with this intervention.

Together, these studies support an indirect association between perturbations of microbial composition during early life and development of disease later in life. This potential association is investigated in a recent clinical study of children with eosinophilic esophagitis (EoE), which mouse models suggest is an iNKT cell–mediated disease (*94*). In this example, young children (<6 years of age) with EoE exhibited increased transcriptional levels of TCR Vα24 (the canonical TCR-α chain of iNKT cells), CD1d, and CXCL16 in the esophagi, which was normalized by a dietary intervention to treat the EoE, but not in those who did not respond to the therapy (*95*). Retrospective data suggested that those with increased iNKT cell–associated transcripts were exposed in early life to antibiotics (*95*).

Breast milk contains proteins, maternal bacteria, and nutrients important for the development of the newborn that may also participate in the establishment of the neonatal microenvironment (*96*, *97*). This includes the neonatal immune system given the protective effects of breastfeeding on the development of obesity or IBD in adult life (*98*, *99*). However, the specific maternal factors, including microbes and the mechanisms involved, remain to be identified.

Concluding remarks

The mucosal tissues of the host are a highly dynamic set of structures that reside at the interface between the external world and the internal immune and nonimmune tissues. These surfaces are also a critical site of microbial commensalism that plays a critical role in defining the morphology and function of the host and are, like the host that they serve, under the influence of a variety of environmental factors. It is becoming increasingly clear that the ordered establishment of this interface is critically important to the proper development of the immune system and likely the microbiota themselves. Moreover, there has been a recent recognition that a number of the critical immune mechanisms that determine the maintenance of homeostasis and tolerance to environmental exposures at this interface are determined by a set of poorly defined microbial-host interactions that occur during a narrow time frame contained within the earliest days of life. This specifically has lead to the notion of a "window of opportunity," in which particular microbial exposures during early life determine specific immune events that are durably imprinted, or not. This time frame correlates with the suckling period of rodents, whose relation to human development remains to be defined. A recent study nicely demonstrates that such early-life influences by the microbiota may even be evident during gestation, in that microbial colonization during pregnancy regulates the number of specific innate immune cells and their activity in the offspring (*100*). This process is dependent on microbially induced, maternal antibodies specific for microbial-derived molecules that are present in the milk and transferred to the neonate during the period of suckling. In their totality, these insights have profound implications for human disease by suggesting that disease risk may begin at the earliest days of life, including the antenatal period. Defining the specific details of these events will therefore have great implications for intervention and understanding in the prevention of complex disease mechanisms.

REFERENCES AND NOTES

1. R. Sender, S. Fuchs, R. Milo, *Cell* **164**, 337–340 (2016).
2. E. Jiménez *et al.*, *Curr. Microbiol.* **51**, 270–274 (2005).
3. L. Moles *et al.*, *PLOS ONE* **8**, e66986 (2013).
4. M. G. Dominguez-Bello *et al.*, *Proc. Natl. Acad. Sci. U.S.A.* **107**, 11971–11975 (2010).
5. A. K. Benson *et al.*, *Proc. Natl. Acad. Sci. U.S.A.* **107**, 18933–18938 (2010).
6. S. L. Russell *et al.*, *EMBO Rep.* **13**, 440–447 (2012).
7. P. J. Turnbaugh *et al.*, *Nature* **457**, 480–484 (2009).
8. C. Palmer, E. M. Bik, D. B. DiGiulio, D. A. Relman, P. O. Brown, *PLOS Biol.* **5**, e177 (2007).
9. T. Yatsunenko *et al.*, *Nature* **486**, 222–227 (2012).
10. J. E. Koenig *et al.*, *Proc. Natl. Acad. Sci. U.S.A.* **108** (Suppl 1), 4578–4585 (2011).
11. L. Pasteur, *Compte Rendus Ge Acad. Sci.* **100**, 68 (1885).
12. G. H. F. Nuttall, H. Thierfelder, *Physiological Chem.* **21**, 109–121 (1896).
13. J. A. Reyniers, P. C. Trexler, R. F. Ervin, *Lobund Rep.* **1**, 1–84 (1946).
14. J. R. Pleasants, *Ann. N. Y. Acad. Sci.* **78**, 116–126 (1959).
15. B. E. Gustafsson, T. Midtvedt, K. Strandberg, *Scand. J. Gastroenterol.* **5**, 309–314 (1970).
16. G. D. Abrams, J. E. Bishop, *Proc. Soc. Exp. Biol. Med.* **126**, 301–304 (1967).
17. G. D. Abrams, H. Bauer, H. Sprinz, *Lab. Invest.* **12**, 355–364 (1963).
18. N. H. Salzman, D. Ghosh, K. M. Huttner, Y. Paterson, C. L. Bevins, *Nature* **422**, 522–526 (2003).
19. S. Vaishnava, C. L. Behrendt, A. S. Ismail, L. Eckmann, L. V. Hooper, *Proc. Natl. Acad. Sci. U.S.A.* **105**, 20858–20863 (2008).
20. H. Bauer, R. E. Horowitz, S. M. Levenson, H. Popper, *Am. J. Pathol.* **42**, 471–483 (1963).
21. H. A. Gordon, E. Bruckner-Kardoss, T. E. Staley, M. Wagner, B. S. Wostmann, *Cells Tissues Organs* **64**, 367–389 (1966).
22. I. Mosconi *et al.*, *Mucosal Immunol.* **6**, 1157–1167 (2013).
23. A. J. Macpherson, N. L. Harris, *Nat. Rev. Immunol.* **4**, 478–485 (2004).
24. A. P. Baptista *et al.*, *Mucosal Immunol.* **6**, 511–521 (2013).
25. A. Spor, O. Koren, R. Ley, *Nat. Rev. Microbiol.* **9**, 279–290 (2011).
26. M. B. Geuking *et al.*, *Immunity* **34**, 794–806 (2011).
27. S. Rakoff-Nahoum, R. Medzhitov, *Mucosal Immunol.* **1** (suppl. 1), S10–S14 (2008).
28. J. P. Ridge, E. J. Fuchs, P. Matzinger, *Science* **271**, 1723–1726 (1996).
29. T. Forsthuber, H. C. Yip, P. V. Lehmann, *Science* **271**, 1728–1730 (1996).
30. M. Sarzotti, D. S. Robbins, P. M. Hoffman, *Science* **271**, 1726–1728 (1996).
31. P. A. Crabbé, D. R. Nash, H. Bazin, H. Eyssen, J. F. Heremans, *Lab. Invest.* **22**, 448–457 (1970).
32. S. El Aidy, G. Hooiveld, V. Tremaroli, F. Bäckhed, M. Kleerebezem, *Gut Microbes* **4**, 118–124 (2013).
33. Y. Umesaki, H. Setoyama, S. Matsumoto, Y. Okada, *Immunology* **79**, 32–37 (1993).
34. H. Chung *et al.*, *Cell* **149**, 1578–1593 (2012).
35. H. A. Gordon, E. Bruckner-Kardoss, *Acta Anat. (Basel)* **44**, 210–225 (1961).
36. M. Kawaguchi *et al.*, *Proc. Natl. Acad. Sci. U.S.A.* **90**, 8591–8594 (1993).
37. C. S. J. Probert, L. J. Saubermann, S. Balk, R. S. Blumberg, *Immunol. Rev.* **215**, 215–225 (2007).
38. S. K. Mazmanian, C. H. Liu, A. O. Tzianabos, D. L. Kasper, *Cell* **122**, 107–118 (2005).
39. V. Gaboriau-Routhiau *et al.*, *Immunity* **31**, 677–689 (2009).
40. H. L. Klaasen *et al.*, *Infect. Immun.* **61**, 303–306 (1993).
41. I. I. Ivanov *et al.*, *Cell* **139**, 485–498 (2009).
42. S. K. Lathrop *et al.*, *Nature* **478**, 250–254 (2011).
43. A. Cebula *et al.*, *Nature* **497**, 258–262 (2013).
44. K. Atarashi *et al.*, *Science* **331**, 337–341 (2011).
45. E. Sefik *et al.*, *Science* **349**, 993–997 (2015).
46. S. Hapfelmeier *et al.*, *Science* **328**, 1705–1709 (2010).
47. A. J. Macpherson, T. Uhr, *Science* **303**, 1662–1665 (2004).
48. H. Spits *et al.*, *Nat. Rev. Immunol.* **13**, 145–149 (2013).
49. S. C. Ganal *et al.*, *Immunity* **37**, 171–186 (2012).
50. S. L. Sanos *et al.*, *Nat. Immunol.* **10**, 83–91 (2009).

Downloaded from http://science.sciencemag.org/ on April 28, 2016

51. N. Satoh-Takayama *et al.*, *Immunity* **29**, 958–970 (2008).
52. A. Reynders *et al.*, *EMBO J.* **30**, 2934–2947 (2011).
53. S. Sawa *et al.*, *Nat. Immunol.* **12**, 320–326 (2011).
54. L. W. Peterson, D. Artis, *Nat. Rev. Immunol.* **14**, 141–153 (2014).
55. H. L. Cash, C. V. Whitham, C. L. Behrendt, L. V. Hooper, *Science* **313**, 1126–1130 (2006).
56. J. M. M. Natividad *et al.*, *Appl. Environ. Microbiol.* **79**, 7745–7754 (2013).
57. S. L. Sanos, C. Vonarbourg, A. Mortha, A. Diefenbach, *Immunology* **132**, 453–465 (2011).
58. W. He *et al.*, *Gastroenterology* **125**, 1388–1397 (2003).
59. L. D. McVay *et al.*, *J. Clin. Invest.* **116**, 2914–2923 (2006).
60. S. Matsumoto, H. Setoyama, Y. Umesaki, *Gastroenterology* **103**, 1777–1782 (1992).
61. S. Fukuda *et al.*, *Nature* **469**, 543–547 (2011).
62. F. Sommer, I. Nookaew, N. Sommer, P. Fogelstrand, F. Bäckhed, *Genome Biol.* **16**, 62 (2015).
63. J. M. van Dieren *et al.*, *Inflamm. Bowel Dis.* **13**, 1146–1152 (2007).
64. G. Wingender *et al.*, *Gastroenterology* **143**, 418–428 (2012).
65. T. Olszak *et al.*, *Science* **336**, 489–493 (2012).
66. D. An *et al.*, *Cell* **156**, 123–133 (2014).
67. J. Cahenzli, Y. Köller, M. Wyss, M. B. Geuking, K. D. McCoy, *Cell Host Microbe* **14**, 559–570 (2013).
68. G. Wingender *et al.*, *J. Exp. Med.* **208**, 1151–1162 (2011).
69. E. S. Gollwitzer *et al.*, *Nat. Med.* **20**, 642–647 (2014).
70. T. C. Scharschmidt *et al.*, *Immunity* **43**, 1011–1021 (2015).
71. P. Zanvit *et al.*, *Nat. Commun.* **6**, 8424 (2015).
72. C. Chassin *et al.*, *Cell Host Microbe* **8**, 358–368 (2010).
73. S. Stockinger, M. W. Hornef, C. Chassin, *Cell. Mol. Life Sci.* **68**, 3699–3712 (2011).
74. S. Elahi *et al.*, *Nature* **504**, 158–162 (2013).
75. J. Riedler *et al.*, *Lancet* **358**, 1129–1133 (2001).
76. M. J. Schuijs *et al.*, *Science* **349**, 1106–1110 (2015).
77. B. Schaub *et al.*, *J. Allergy Clin. Immunol.* **123**, 774–82.e5 (2009).
78. J. Dicksved *et al.*, *Appl. Environ. Microbiol.* **73**, 2284–2289 (2007).
79. D. A. Antonopoulos *et al.*, *Infect. Immun.* **77**, 2367–2375 (2009).
80. L. Dethlefsen, S. Huse, M. L. Sogin, D. A. Relman, *PLOS Biol.* **6**, e280 (2008).
81. L. Dethlefsen, D. A. Relman, *Proc. Natl. Acad. Sci. U.S.A.* **108** (Suppl 1), 4554–4561 (2011).
82. S. Zeissig, R. S. Blumberg, *Nat. Immunol.* **15**, 307–310 (2014).
83. K. R. Risnes, K. Belanger, W. Murk, M. B. Bracken, *Am. J. Epidemiol.* **173**, 310–318 (2011).
84. X.-M. Mai, I. Kull, M. Wickman, A. Bergström, *Clin. Exp. Allergy* **40**, 1230–1237 (2010).
85. S. Y. Shaw, J. F. Blanchard, C. N. Bernstein, *Am. J. Gastroenterol.* **105**, 2687–2692 (2010).
86. M. P. Kronman, T. E. Zaoutis, K. Haynes, R. Feng, S. E. Coffin, *Pediatrics* **130**, e794–e803 (2012).
87. M. B. Azad, S. L. Bridgman, A. B. Becker, A. L. Kozyrskyj, *Int. J. Obes. (Lond)* **38**, 1290–1298 (2014).
88. B. Boursi, R. Mamtani, K. Haynes, Y.-X. Yang, *Eur. J. Endocrinol.* **172**, 639–648 (2015).
89. A. D. Kostic *et al.*, *Cell Host Microbe* **17**, 260–273 (2015).
90. J. G. M. Markle *et al.*, *Science* **339**, 1084–1088 (2013).
91. J. Blustein *et al.*, *Int. J. Obes. (Lond)* **37**, 900–906 (2013).
92. J. Neu, J. Rushing, *Clin. Perinatol.* **38**, 321–331 (2011).
93. S. Thavagnanam, J. Fleming, A. Bromley, M. D. Shields, C. R. Cardwell, *Clin. Exp. Allergy* **38**, 629–633 (2008).
94. P. Rajavelu, M. Rayapudi, M. Moffitt, A. Mishra, A. Mishra, *Am. J. Physiol. Gastrointest. Liver Physiol.* **302**, G645–G654 (2012).
95. W. S. Lexmond *et al.*, *Am. J. Gastroenterol.* **109**, 646–657 (2014).
96. N. J. Andreas, B. Kampmann, K. Mehring Le-Doare, *Early Hum. Dev.* **91**, 629–635 (2015).
97. E. W. Rogier *et al.*, *Proc. Natl. Acad. Sci. U.S.A.* **111**, 3074–3079 (2014).
98. C. G. Owen, R. M. Martin, P. H. Whincup, G. D. Smith, D. G. Cook, *Pediatrics* **115**, 1367–1377 (2005).
99. A. R. Barclay *et al.*, *J. Pediatr.* **155**, 421–426 (2009).
100. M. Gomez de Agüero *et al.*, *Science* **351**, 1296–1302 (2016).

ACKNOWLEDGMENTS

D.L.K. is an inventor on patents licensed to Symbiotic Biotherapies by Brigham and Women's Hospital and Harvard Medical School related to PSA of *B. fragilis* and its use as an immunomodulator for treating immune-mediated diseases. D.L.K. and R.S.B. are paid consultants for Symbiotic Biotherapies. R.S.B. is supported by NIH grant DK44319 and the Harvard Digestive Diseases Center (DK0034854). D.L.K is supported by NIH grant R21 AI090102 and the U.S. Department of Defense (W81XWH-15-1-0368).

10.1126/science.aad9378

PERSPECTIVE

Antibiotic use and its consequences for the normal microbiome

Martin J. Blaser[1,2,3]

Anti-infectives, including antibiotics, are essentially different from all other drugs; they not only affect the individual to whom they are given but also the entire community, through selection for resistance to their own action. Thus, their use resides at the intersection of personal and public health. Antibiotics can be likened to a four-edged sword against bacteria. The first two edges of the antibiotic sword were identified immediately after their discovery and deployment in that they not only benefit an individual in treating their infection but also benefit the community in preventing the spread of that infectious agent. The third edge was already recognized by Alexander Fleming in 1945 in his Nobel acceptance speech, which warned about the cost to the community of antibiotic resistance that would inevitably evolve and be selected for during clinical practice. We have seen this cost mount up, as resistance curtails or precludes the activities of some of our most effective drugs for clinically important infections. But the fourth edge of the antibiotic sword remained unappreciated until recently, i.e., the cost that an antibiotic exerts on an individual's own health via the collateral damage of the drug on bacteria that normally live on or in healthy humans: our microbiota. These organisms, their genes, metabolites, and interactions with one another, as well as with their host collectively, represent our microbiome. Our relationship with these symbiotic bacteria is especially important during the early years of life, when the adult microbiome has not yet formed.

For 70 years, antibiotics have been a pillar of medicine and are being used worldwide on an enormous scale. In many countries, antibiotic use exceeds one course per capita per year. In 2010, the top seven antibiotic classes were consumed in an estimated 70 billion individual doses, which equates to about 10 pills, capsules, or teaspoons for every man, woman, and child on earth (*1*), an annual rate that appears to be rising. This magnitude of use is based at least in part on the perception, among both health professionals and the public, that antibiotics are completely safe. We all are aware of mild, self-limited problems, such as rashes and drug reactions, and doctors know about serious but very rare side effects, yet at a functional level, most of us consider these risks so close to zero that they do not usually factor into the equation about use. There also is the cost of antibiotic resistance, but because it predominantly affects the community rather than the treated individual, its avoidance does not usually affect clinical judgments about whether or not treatment should be given. Parents would rather have their ill child treated with a drug they see as safe and effective than worry about the impact of that single course on the future of humankind, and their doctors generally agree.

However, this construct of essentially complete personal safety is illusory. Shortly after antibiotics began to be used to treat ill people and animals, farmers discovered that adding low doses of antibiotics to the food or water of their livestock would promote their growth; the earlier in life the exposure began, the more profound the effect (*2*). This observation alone provides an important clue that antibiotic exposure affects metabolic development. Antibiotic use has been widespread because it leads to growth promotion and, therefore, increased profit for farmers. But does this massive decades-long worldwide "experiment" on the farm teach us anything about human health? Is it possible that the antibiotics that we give our children early in life to treat their infections—whether severe (uncommon) or mild (very common)—are influencing a critical window in the development of their own metabolism?

In recent years, scientists have been exploring this question, with mostly consistent results. Observational, clinical, and epidemiologic studies focused on young children are providing a growing body of evidence that antibiotic exposure is associated with increased risk for a variety of diseases including obesity, types 1 and 2 diabetes, inflammatory bowel diseases, celiac disease, allergies, and asthma [see (*3*, *4*) for examples]. Experimental models are providing increasing evidence that these associations are not just correlative but are causal. Studies in mice have found that antibiotic exposure, by disrupting the development of the early-life microbiome, which often causes loss of species and strain diversity (i.e., biodiversity loss), leads to metabolic perturbations that affect adiposity and bone growth and alter normal immunologic development (*5*, *6*).

A variety of evidence indicates that the risks appear greatest for young children (*7*). Paradoxically,

[1]Division of Translational Medicine, Department of Medicine, New York University Langone Medical Center (NYULMC), New York, NY 10016, USA. [2]Department of Microbiology, NYULMC, New York, NY 10016, USA. [3]Department of Veterans Affairs New York Harbor Medical Center, New York, NY 10010, USA.
Email: martin.blaser@nyumc.org

Downloaded from http://science.sciencemag.org/ on April 28, 2016

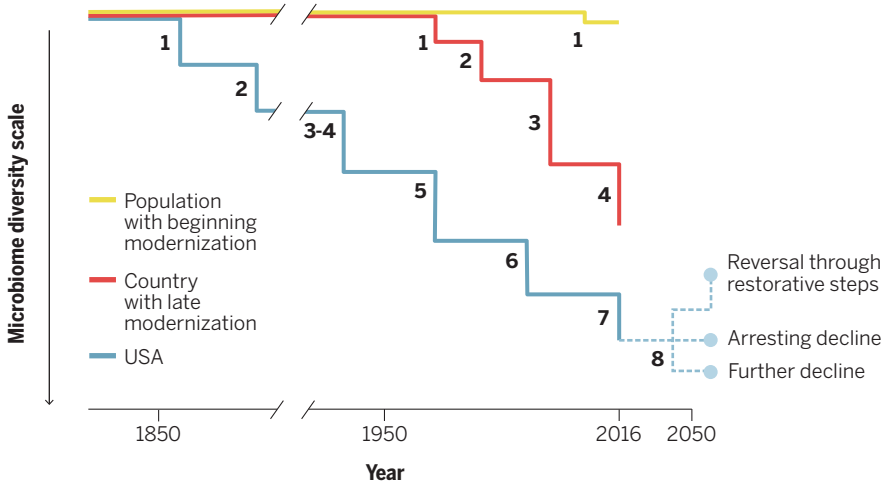

Fig. 1. Models of microbiota change in different societies. The decline in microbiota diversity in the United States happened simultaneously with the early introduction of sanitation, including filtered and chlorinated drinking water, and early antibiotic use. The scale is arbitrary and reflects the aggregate of species and strain losses. The numbers shown represent the generations since the earliest population-wide microbiota species and strain losses and show progressive and cumulative loss of diversity. Each line represents an average; within every generation, there is variation in individual positions, based on their founding populations, exposures, and timing. In a country with late modernization, the diversity loss occurred later, but generation times are shorter, and the steps more irregular and increasing, which reflects the effects of the accelerated pace of modernization in recent years on human microbiota biodiversity loss in developing countries. For the future, three trajectories are shown for the developed country.

the perinatal period through the first 2 years of life is the time when per capita antibiotic usage is most intensive. An emerging concept to consider is that the effects of antibiotics may be cumulative in an individual, with both epidemiologic and experimental data supporting that view (*8*). One hypothesis is that antibiotic courses may lead to species loss, especially for taxa that were low in number at that time, yet which may have important metabolic functions. The problem would be most important for taxa with unique functions, although this may not happen in all patients or with all courses. Because we each inherit much of our microbiome from our mother, a further hypothesis is that environmental impacts on the microbiome (including antibiotic and dietary exposures) are cumulative across generations (*8*, *9*) (Fig. 1). We need to carefully assess these hypotheses, because the implications are substantial.

Yet antibiotics are vital for health care. It is difficult to imagine optimal health without an umbrella of antibiotics to use when needed. Nevertheless, practitioners have not been taking the biologic cost of antibiotic use into account sufficiently in making treatment decisions. Differences in perceptions about how risk-free antibiotic treatment is may in part account for the enormous variation in rates of their use from practitioner to practitioner, between localities and across countries (*10*). The emergence of awareness of the biologic costs of a treatment surely requires modulation of its usage. We must clearly understand the real costs, including the differences between particular antimicrobial agents in their effects on the microbiome (*11*) and, thus, the consequent sequelae on child development (*12*).

Rather than carpet-bombing germs into submission with broad-spectrum antibiotics, we will need more laserlike approaches to develop drugs against specific pathogens, minimize damage to essential symbiotic microbial species, and preserve community structure and function in the healthy (and developing) microbiome. Future research, based on our extensive and growing knowledge of bacterial genes and genomes, should aim to develop truly narrow-spectrum agents, each ideally targeting a single pathogen. This strategy also requires new diagnostic tests that accurately and economically differentiate between bacterial and viral infections, among specific bacteria, and also distinguish between colonization and infection. Host-specific, indeed individual, differences may require more personalized approaches to antibacterial therapies. Shortening treatment courses is another approach that needs more research, as do the complex trade-offs that arise between emergence of resistance and collateral damage.

There always will be instances in which children must be treated with an antibiotic, but the collateral effects could be mitigated. Should we bank every healthy child's fecal specimen, so we can chase each antibiotic course with a dose of their own pretreatment microbiota? Or by studying microbiota before and after antibiotic treatment, can we identify a few key organisms to replace in that child and then prescribe well-characterized pharmaceutical-grade standard strains, the probiotics of the future, to be administered in the appropriate vehicle?

We also are learning that other drugs are affecting the microbiome in ways that were not anticipated. For example, metformin, widely used in the treatment of type 2 diabetes, has important effects on microbial populations. It may be that metformin's antimicrobial actions, which in turn affect short-chain fatty acid metabolism, determine the efficacy of the drug, rather than its direct effects on tissues (*13*). However, no drugs are as important as antibiotics because of their usage in virtually all children worldwide and because their activities, specifically targeted to bacteria, strongly select and shape microbial community structure. Even later in life, antibiotic exposures may have consequences in terms of risks for metabolic (*14*) and neoplastic diseases and for acquisition of resistant organisms.

The third and fourth edges of the antibiotic sword—cost to the community and to a person's future health—are both being driven by antibiotic overuse. First, we must control those excesses, but mitigation will only stabilize the situation not reverse the deterioration that likely has progressively occurred with socioeconomic development (*15*). Ultimately, we may need to recover the biodiversity lost as a result of these generations of antibiotic use (and other insults). The goal should be to restore the status quo ante, using probiotics, perhaps with accompanying prebiotics, to replace vital missing and/or extinct species and strains that modulate crucial developmental pathways. This critically important next scientific frontier in human health will require much research.

REFERENCES AND NOTES

1. T. P. Van Boeckel *et al.*, *Lancet Infect. Dis.* **14**, 742–750 (2014).
2. D. R. Zimmerman, *J. Anim. Sci.* **62** (suppl. 3), 6–16 (1986).
3. M. C. Arrieta *et al.*, *Sci. Transl. Med.* **7**, 307ra152 (2015).
4. M. B. Azad, S. L. Bridgman, A. B. Becker, A. L. Kozyrskyj, *Int. J. Obes. (London)* **38**, 1290–1298 (2014).
5. I. Cho *et al.*, *Nature* **488**, 621–626 (2012).
6. L. M. Cox *et al.*, *Cell* **158**, 705–721 (2014).
7. T. Yatsunenko *et al.*, *Nature* **486**, 222–227 (2012).
8. M. J. Blaser, S. Falkow, *Nat. Rev. Microbiol.* **7**, 887–894 (2009).
9. E. D. Sonnenburg *et al.*, *Nature* **529**, 212–215 (2016).
10. L. A. Hicks, T. H. Taylor Jr., R. J. Hunkler, *N. Engl. J. Med.* **368**, 1461–1462 (2013).
11. Y. R. Nobel *et al.*, *Nat. Commun.* **6**, 7486 (2015).
12. K. Korpela *et al.*, *Nat. Commun.* **7**, 10410 (2016).
13. K. Forslund *et al.*, *Nature* **528**, 262–266 (2015).
14. K. H. Mikkelsen, F. K. Knop, M. Frost, J. Hallas, A. Pottegård, *J. Clin. Endocrinol. Metab.* **100**, 3633–3640 (2015).
15. J. C. Clemente *et al.*, *Sci. Adv.* **1**, e1500183 (2015).

ACKNOWLEDGMENTS

Supported in part by R01DK090989 and U01AI122285 from NIH, the Diane Belfer Program in Human Microbial Ecology, and the Knapp Family Fund.

10.1126/science.aad9358

Downloaded from http://science.sciencemag.org/ on April 28, 2016

RESEARCH ARTICLE SUMMARY

STRUCTURAL BIOLOGY

Structure and organization of heteromeric AMPA-type glutamate receptors

Beatriz Herguedas,* Javier García-Nafría,* Ondrej Cais, Rafael Fernández-Leiro, James Krieger, Hinze Ho, Ingo H. Greger†

INTRODUCTION: Ionotropic glutamate receptors (iGluRs) are cation channels that mediate signal transmission by depolarizing the postsynaptic membrane in response to L-glutamate release from the presynaptic neuron. There are three major iGluR subtypes, and together their activity is pivotal to learning and memory. The first subtype, the AMPA-type receptor (AMPAR), initiates signaling and activates the second subtype, the N-methyl-D-aspartate receptor (NMDAR), thereby admitting Ca^{2+} ions that drive synaptic plasticity and ultimately enabling learning. The rapid submillisecond response of the AMPAR permits accurate transmission of high-frequency presynaptic impulses. In the brain, AMPARs preferentially exist as heterotetramers composed of the GluA1 to GluA4 subunits in various combinations. Their signaling properties are dominated by the GluA2 subunit, which is present in the majority of AMPARs, yet the architecture and subunit arrangement of GluA2-containing AMPAR heteromers has thus far been elusive.

RATIONALE: So far, AMPAR structures have been limited to GluA2 homomers. We used a combination of x-ray crystallography and cryogenic electron microscopy (cryo-EM) to obtain structural information for AMPAR heteromers. We first solved crystal structures of the N-terminal domain (NTD) layer, which constitutes the more sequence-diverse upper half of the receptor. Our structures of the GluA2/3 and GluA2/4 NTDs provide atomic resolution of the interface that initiates subunit assembly and reveal tetrameric arrangements in both of these heteromeric combinations that are distinct from known homomers. Cysteine cross-linking confirmed this architecture in full-length receptors and permitted us to determine cryo-EM structures of an intact GluA2/3 heteromer, which is a prominent variety in neural tissue.

RESULTS: In both GluA2/3 and GluA2/4 NTD crystal structures, the four subunits alternate around a central axis to create a compact O shape that deviates from the loose N shape commonly found in GluA2 homomers. Simulations suggest that the receptor can transition between these two states. Structure-guided cysteine mutants allowed us to trap receptors in the O state and facilitated further analysis by cryo-EM. The GluA2/3 receptor was captured in a ligand-free state and resulted in two models, determined at 8.2 and 10.3 Å. Both deviate from existing GluA2 homomer structures. Associated with the compact conformation of the NTD layer was a substantial vertical compression of the receptor heteromer, forming distinct interlayer interfaces. Contact points between the NTD and the ligand-binding domain (LBD) suggest that the NTD can contribute to signaling. We also observed a rearrangement of the gating machinery at the level of the LBD layer, and our results provide a structural snapshot of a desensitized receptor in the absence of agonist. Our data indicate that subunit placement in AMPAR tetramers is not strict, unlike in NMDARs, a finding that may extend the functional spectrum of heteromeric AMPARs.

ON OUR WEBSITE

Read the full article at http://dx.doi.org/10.1126/science.aad3873

CONCLUSION: The GluA2/3 structure and our simulations emphasize that AMPARs are dynamic complexes. The observed rearrangements of the extracellular region are expected to be of functional consequence in synaptic environments, where the NTD engages various interaction partners. Transitioning between N and O states could break existing contacts and make new ones, thereby affecting AMPAR clustering, a prerequisite for synaptic plasticity. Moreover, the vertical compression observed in GluA2/3 would permit crosstalk between the NTD and LBD, thus incorporating the NTD in allosteric regulation, as has been observed in NMDARs. The sequence-diverse AMPAR NTD, like that of NMDARs, may therefore offer a target for drug development—one that is as yet unexplored. ■

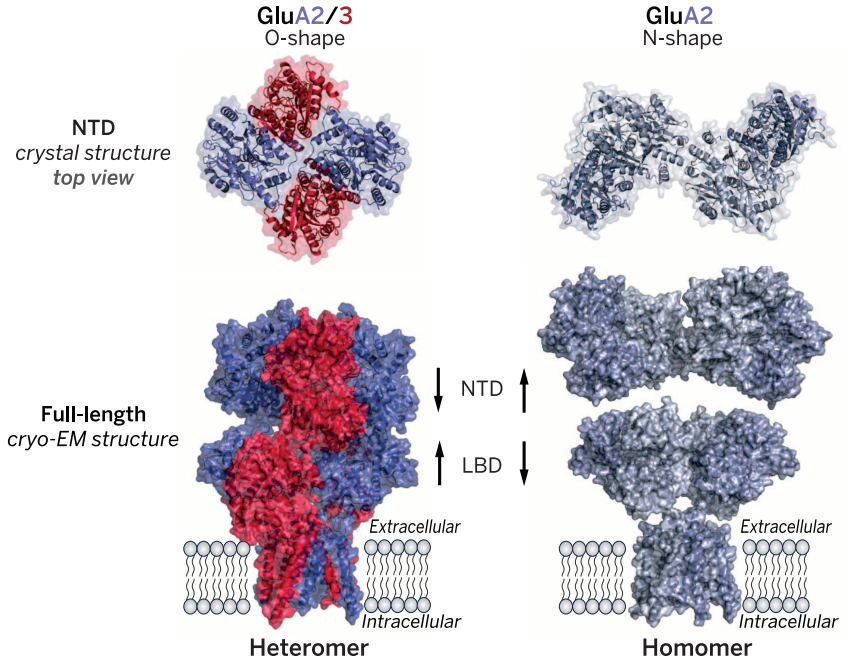

Structure of a GluA2/3 AMPAR heteromer. A GluA2/3 heteromer (left) is shown with a GluA2 homomer (right) for comparison. The top panel shows the NTD layers of the compact O-shaped GluA2/3 and the loose N-shaped GluA2 [Protein Data Bank identifier (PDB ID) 3H5V], viewed from the top. The bottom panel shows full-length cryo-EM structures of GluA2/3 (ligand-free) and a GluA2 homomer (antagonist-bound; PDB ID 4UQJ). The difference in vertical packing between the NTD and LBD is indicated by arrows.

The list of author affiliations is available in the full article online.
*These authors contributed equally to this work.
†Corresponding author. Email: ig@mrc-lmb.cam.ac.uk
Cite this article as B. Herguedas *et al.*, *Science* 352, aad3873 (2016). DOI: 10.1126/science.aad3873

Downloaded from http://science.sciencemag.org/ on April 28, 2016

RESEARCH ARTICLE

STRUCTURAL BIOLOGY

Structure and organization of heteromeric AMPA-type glutamate receptors

Beatriz Herguedas,[1]* Javier García-Nafría,[1]* Ondrej Cais,[1] Rafael Fernández-Leiro,[2] James Krieger,[1] Hinze Ho,[1] Ingo H. Greger[1]†

AMPA-type glutamate receptors (AMPARs), which are central mediators of rapid neurotransmission and synaptic plasticity, predominantly exist as heteromers of the subunits GluA1 to GluA4. Here we report the first AMPAR heteromer structures, which deviate substantially from existing GluA2 homomer structures. Crystal structures of the GluA2/3 and GluA2/4 N-terminal domains reveal a novel compact conformation with an alternating arrangement of the four subunits around a central axis. This organization is confirmed by cysteine cross-linking in full-length receptors, and it permitted us to determine the structure of an intact GluA2/3 receptor by cryogenic electron microscopy. Two models in the ligand-free state, at resolutions of 8.25 and 10.3 angstroms, exhibit substantial vertical compression and close associations between domain layers, reminiscent of N-methyl-D-aspartate receptors. Model 1 resembles a resting state and model 2 a desensitized state, thus providing snapshots of gating transitions in the nominal absence of ligand. Our data reveal organizational features of heteromeric AMPARs and provide a framework to decipher AMPAR architecture and signaling.

Ionotropic glutamate receptors (iGluRs) are tetrameric cation channels that mediate fast excitatory signal transmission upon binding presynaptically released glutamate (*1*). They are essential for brain development and experience-dependent synaptic plasticity, which underlies learning. iGluR dysfunction is implicated in a number of neurological disorders, including dementia, mood disorders, and epilepsy (*2*). Three major subtypes—the α-amino-3-hydroxy-5-methyl-4-isoxazolepropionic acid, N-methyl-D-aspartate, and kainate receptors (AMPARs, NMDARs and KARs)—each contribute a different component to the synaptic signal (*1*). AMPARs mediate the initial depolarization of the postsynaptic membrane, triggering NMDAR activation and the generation of an excitatory postsynaptic potential. The rapid kinetics of AMPARs permit moment-to-moment signaling, and their trafficking to synapses is central to synaptic plasticity (*3*).

Gating kinetics, ion permeation, and trafficking are set by the subunit stoichiometry and ultimately shape the synaptic response. AMPAR tetramers are composed of the subunits GluA1 to GluA4; the vast majority contain GluA2, which renders the channel impermeable to Ca^{2+}, lowers its conductance, and alters its voltage dependence (*1*, *4*).

[1]Neurobiology Division, Medical Research Council (MRC) Laboratory of Molecular Biology, Cambridge, UK. [2]Structural Studies Division, MRC Laboratory of Molecular Biology, Cambridge, UK.
*These authors contributed equally to this work. †Corresponding author. Email: ig@mrc-lmb.cam.ac.uk

Structures of GluA2 homomers have been instrumental in clarifying AMPAR modular architecture (*5*). The receptor is arranged in domain layers (Fig. 1A). A twofold symmetrical extracellular region (ECR), composed of the N-terminal domain (NTD) and ligand-binding domain (LBD), is attached to the transmembrane ion channel domain (TMD), which has approximately fourfold symmetry (Fig. 1A); a cytoplasmic tail mediates trafficking and anchorage at synapses. The four chains (A to D) in the tetramer are conformationally nonequivalent and probably contribute differently to gating: The AC pair is positioned closer to the ion conduction pore axis (at the level of the LBD and TMD; pore-proximal) than the BD pair is (pore-distal). In NMDARs, which are obligatory heteromers, the GluN2 subunits occupy the BD position (*6*, *7*) and exert a greater pulling force on the gate (*8*). The domain architecture of heteromeric AMPARs is currently unknown, and their intersubunit arrangement has only been inferred from modeling studies (*9*).

We used x-ray crystallography and single-particle cryogenic electron microscopy (cryo-EM) in combination with electrophysiology, biochemistry, and coarse-grained simulations to decipher the organization of GluA2-containing AMPAR heteromers.

Crystal structures and organization of the GluA2/3 and GluA2/4 NTD layers

Toward resolving the organization of AMPAR heteromers, we first targeted the NTD layer for structural analysis. This membrane-distal domain encompasses 50% of the receptor mass and reaches midway into the synaptic cleft, where it forms a key platform for protein interactions and mediates AMPAR clustering (Fig. 1A) (*10*, *11*). The bilobate NTD "clamshell" contributes powerful allosteric modulation in NMDARs and thus represents a key drug target (*12*).

This highly sequence-diverse domain also initiates iGluR assembly (*13*–*15*). Although structures for the obligatorily heteromeric NMDAR and KAR NTDs exist (*16*, *17*), AMPAR NTD heteromers have remained elusive, because they are preferentially rather than obligatorily heteromeric (*14*, *18*). AMPAR NTDs form tight homodimers (nanomolar dissociation constant) (*18*), which have been crystallized previously (*14*, *15*). We developed a strategy to crystallize AMPAR NTD heteromers from purified homomers (Materials and Methods) and tested all combinations harboring the critical GluA2 subunit.

We obtained crystals of the GluA2/3 and GluA2/4 NTDs and determined their structures at 2.1 and 2.5 Å resolution, respectively (table S1). The overall structure of both of these heterodimers is similar to most AMPAR NTD homodimers [average root mean square deviation (RMSD), ~1 Å], with the upper lobe (UL) and lower lobe (LL) engaging a dimer interface of ~1400 $Å^2$ (Fig. 1B and fig. S1). However, they deviate substantially from GluA3 NTD homodimers (average RMSD, ~2.5 Å), which are destabilized by like-charge repulsion between Arg^{163} residues in the LLs (fig. S1, B and C) (*19*). In GluA2/3, salt bridges between GluA3 Arg^{163} and GluA2 Asp^{145} and H bonds between GluA3 Arg^{184} and GluA2 Ala^{148} and Glu^{149} zip up the heterodimer, explaining why its affinity is higher than that of GluA3 homodimers (fig. S1, A to C) (*18*). The structures underscore that differences in the LL interface are key determinants of selective heteromerization; UL interactions are mostly conserved between AMPAR paralogs.

Both NTD heterodimers assemble into a novel tetrameric arrangement (Fig. 1C). Whereas GluA2 homomers adopt a loose N shape when viewed from the top (Fig. 1D) (*5*), the heteromers adopt a compact O shape with the four subunits alternating around a central axis (Fig. 1C), an arrangement that is reminiscent of NMDARs (*6*, *7*). In both heteromers, GluA2 lies at specific positions, resulting in a diagonal alignment of the GluA2 loops that cap the dimer interface (Fig. 1C, yellow and black diamond).

The tetrameric interface has three major contact regions, with most of the interactions mediated by the ULs (Fig. 1C and fig. S2). In region 1, the GluA2 back (helices J and K) engages the front face of the GluA3 or GluA4 NTD (helix A, beta strand 2, loop after helix I), predominantly via polar and ionic contacts (Fig. 1C and fig. S2B). These are more extensive for GluA2/4 because of a more compact, near-parallel alignment of the two heterodimers along their vertical axis; in GluA2/3, the two dimers are separated at their LLs, resulting in a tilt angle of ~30° relative to GluA2/4 (fig. S3A). A key interface element is a loop emanating from helix I (loop I) in the non-GluA2 subunits, where an arginine (Arg^{265} in

Downloaded from http://science.sciencemag.org/ on April 28, 2016

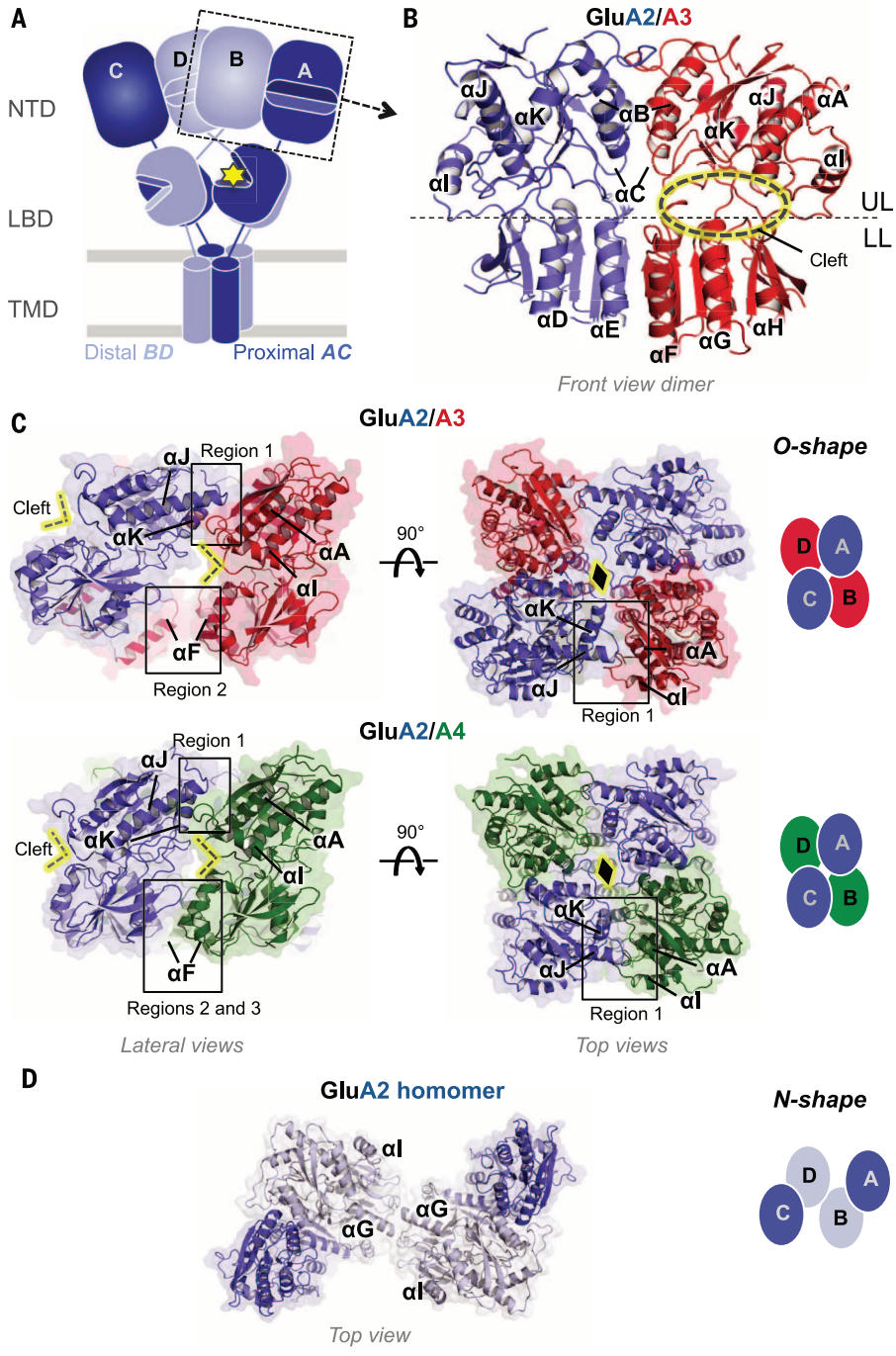

Fig. 1. Structure and organization of the GluA2/3 and GluA2/4 NTD layers. (**A**) Overall organization of an iGluR, showing the typical layered architecture (TMD, LBD, and NTD layers) and quaternary arrangement (the pore-proximal AC and pore-distal BD chains are depicted). The cytoplasmic tails are omitted for simplicity. The yellow star indicates L-glutamate in the LBD cleft. (**B**) The GluA2/3 NTD heterodimer in front view (GluA2, blue; GluA3, red). The UL and LL are separated by a stippled line; helices are labeled αA to αK. The subunits face opposite directions, providing a view of the GluA2 back and the GluA3 cleft (indicated by the yellow ellipse). (**C**) O-shaped tetrameric arrangement of GluA2/3 (upper panels) and GluA2/4 (lower panels). Lateral (left panels) and top views (right panels) are shown. A yellow and black diamond marks the contact point between the two GluA2 protomers in the tetramer. A top-view schematic of the O shape is shown on the far right, with the four chains (A to D) indicated. GluA2, GluA3, and GluA4 are colored blue, red, and green, respectively. Tetrameric assembly regions 1 to 3 are boxed. (**D**) Top view of the classical N-shaped arrangement found in GluA2 homomers (PDB ID 3KG2). Two shades of blue are used to distinguish the different positions, according to (A).

GluA3 and Arg^{264} in GluA4) contacts a highly conserved glutamate (Glu^{288}) on GluA2 helix J (Fig. 1C and fig. S2B). GluA2 helix K and the hinge loop that follows it form additional ionic interactions with helix A and beta strand 2 in GluA3 or GluA4; the latter two have been proposed to interact with N-cadherin in GluA2 (*20*). In region 2, diagonal contacts are mediated between the LLs of the non-GluA2 subunits via their F helices (fig. S2C), similar to the GluN2B interactions in NMDARs (*6*, *7*). In the more compact GluA2/4 heteromer, helix F interacts with GluA2 LL helix E (region 3). This alternative arrangement is expected to affect NTD interaction with synaptic proteins that mediate AMPAR clustering (*10*).

Mapping NTD interface contacts in full-length AMPAR heteromers

To validate this organization in intact AMPARs, we introduced cysteines to cross-link region 1. The mutations Asn^{292}Cys in GluA2myc and Arg^{265}Cys in GluA3FLAG (Arg^{264}Cys in GluA4FLAG) are expected to spontaneously cross-link the O shape (Fig. 2, A and B). Isolation of the heteromers by FLAG immunoprecipitation, followed by Western blotting of the partner subunit on nonreducing SDS–polyacrylamide gel electrophoresis (SDS-PAGE), revealed cross-linked dimers only when both cysteine mutant subunits were present (Fig. 2, C and D; lane 3 versus lane 2). Similarly, diagonal cross-linking of GluA4 F helices in region 2 (Ser^{172}Cys and Gln^{175}Cys) produced spontaneous cross-links of purified GluA2/4 heteromers (fig. S3B). These results support formation of the compact O arrangement in intact AMPAR heteromers.

Whereas GluA2/4 NTDs crystallized solely in the O shape, the GluA2/3 crystal lattice also contained N-shaped tetramers (Fig. 2A). N-shaped GluA2 homotetramers can be cross-linked via the Val^{209}Cys mutation (Fig. 2B) (*5*). Cross-linking of GluA2-Val^{209}Cys in GluA2/3 heteromers [containing GluA3–wild-type (WT) subunits] suggests that the N arrangement can also occur in heteromers (Fig. 2C; lane 4), with GluA2 at the cross-linked NTD central position and GluA3 at the periphery. This also was the case for the GluA2-Val^{209}Cys/GluA4-WT heteromer (Fig. 2D; lane 4). Two possible mechanisms could underlie the O arrangement: (i) lateral interactions between N-shaped receptors or (ii) an alternative NTD tetramer configuration within receptors. To resolve this question, we generated a GluA2 double mutant with cysteines in both the N and O tetrameric interfaces. When combining GluA2-Val^{209}Cys/Asn^{292}Cys with GluA3-Arg^{265}Cys, cross-linked dimers would appear if alternative conformers arose within receptors, whereas clustering of receptors in the O arrangement would give rise to higher molecular weight aggregates. Consistent with the former, we observed cross-linked dimers, but not larger complexes, on SDS-PAGE (Fig. 2, C and D; lane 6) and tetramers on native PAGE (fig. S3C), supporting the existence of alternative arrangements in the AMPAR NTD layer. Rearrangements of the NTD layer have been linked previously to the gating cycle (*21*–*23*).

N–cross-linked dimers migrated faster on SDS-PAGE than O–cross-linked dimers did, permitting

Downloaded from http://science.sciencemag.org/ on April 28, 2016

us to distinguish between the two (Fig. 2, C and D; lanes 3 and 4, purple and green arrowheads, respectively). The heteromer containing both mutations in GluA2 (permitting the N or O cross-links) migrated at the level of the O and not the N dimer in GluA2/3 and GluA2/4 (Fig. 2, C and D; lane 6); this behavior may indicate that the O arrangement forms preferentially.

Characterization of the O-shaped GluA2/3 receptor

Negative-stain single-particle EM

To further validate this new conformation in intact GluA2/3, O–cross-linked GluA2/3 heteromers (GluA2/3$_{xlink}$) were isolated through tandem affinity purifications and subjected to negative-stain single-particle EM (Materials and Methods and fig. S4). Three-dimensional (3D) reconstruction yielded a map at ~20 Å resolution with a compact O-shaped NTD layer; the GluA2/3 tetrameric crystal structure could be fitted into the EM density unambiguously (fig. S4C). A similar NTD organization was observed in 3D reconstructions of GluA2 homomers, although the rest of the receptor differed (*24*).

Agonist-induced desensitization triggers rearrangements in the LBD region (*25*). Recent AMPAR structures reveal the complete rupture of both LBD dimers upon desensitization and suggest that this is coupled to a rearrangement of the NTD layer (*21*–*23*). We likewise observed heterogeneity and rupture of the LBD layer in response to saturating L-glutamate, despite trapping the NTDs in the O shape (fig. S5, A to C). Hence, a compact NTD layer permits LBD dynamics and is compatible with gating transitions. Reducing the cross-links with 10 mM dithiothreitol (DTT) before the glutamate pulse resulted in additional heterogeneity in the NTD layer, as evident in 2D averages (fig. S5D), revealing that the receptor can transition from the O shape.

Coarse-grained simulations

Transitions of the NTD layer between the N and O conformations were also evident in coarse-grained simulations performed with the anisotropic network model (ANM). The ANM calculates accessible conformational changes or global modes of motion, with the first modes describing the energetically most favorable motions (Materials and Methods) (*26*). One low-energy mode of a GluA2 homomer [Protein Data Bank identifier (PDB ID) 3KG2], which was previously shown to vertically compress the AMPAR to an NMDAR-like conformation (mode 4) (*27*), also enables a transition from the N shape to an O-like NTD arrangement (fig. S6, left, and Movie 1). Moreover, ANM analysis of the GluA2/3 NTD crystal structure reveals a pathway for the reverse transition from O to N (fig S6, right, and movie S1), further suggesting that AMPARs can populate both conformations.

Functional characterization

To test the functional impact of the O shape, we expressed GluA2/3 or GluA2/4 heteromers in human embryonic kidney (HEK) 293 T cells and recorded whole-cell current (*I*) responses to rapid glutamate application in oxidizing (copper phenanthroline, CuPhe) or reducing (DTT) conditions. Peak currents were similarly redox-sensitive in O–cross-linked mutants and WT heteromers (Fig. 2, E and F, and fig. S7, A, B,

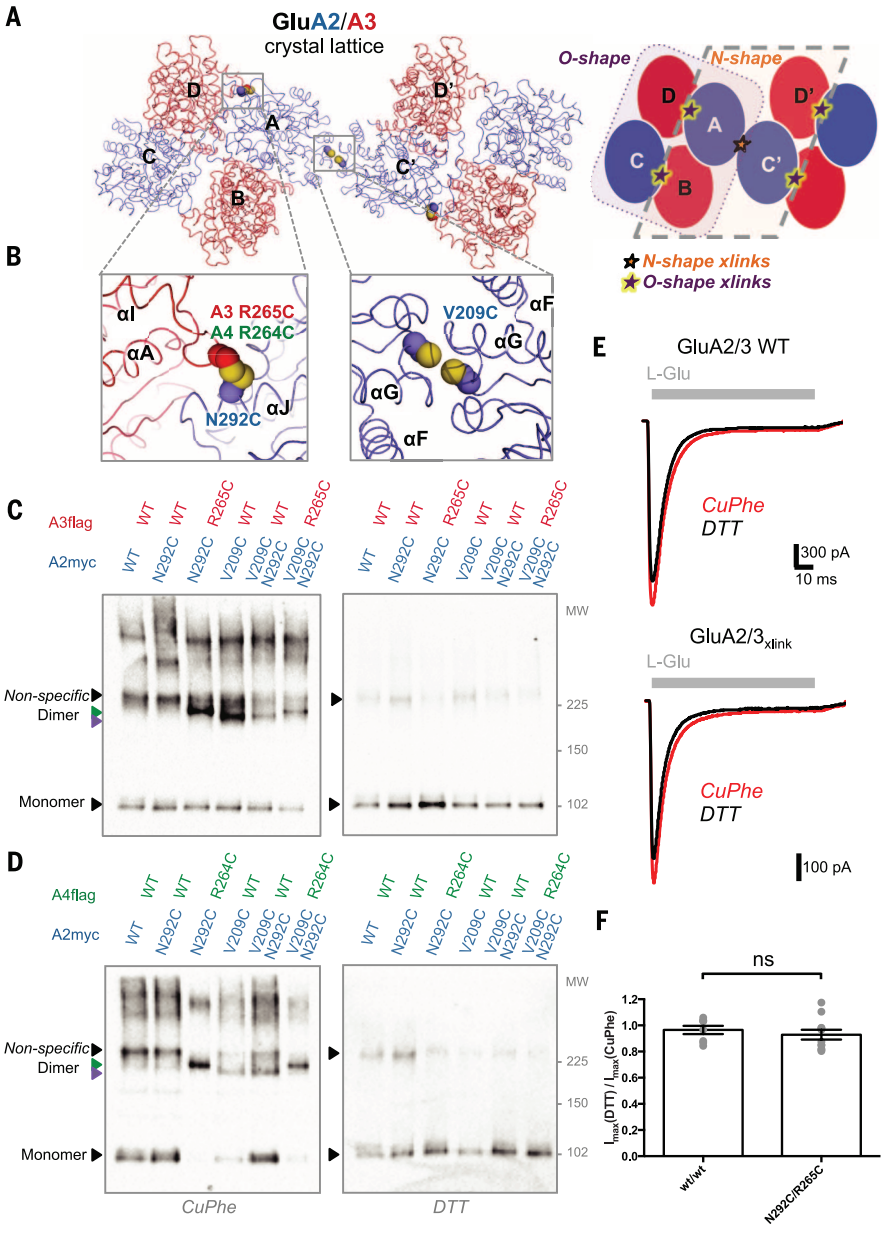

Fig. 2. Probing the O shape in full-length AMPARs with cysteine cross-linking and electrophysiology. (**A**) The O- and N-shaped arrangements coexist in the GluA2/3 crystal lattice (GluA2, blue; GluA3, red). N and O tetramers are highlighted in the schematic on the right; their interfaces are indicated with stars. (**B**) Close-up views of the boxed regions in (A), with the cysteines that were introduced into the two tetrameric interfaces shown as spheres to mark the positions used for cross-linking. (**C** and **D**) Western blots showing cross-linked dimers for GluA2/3 (C) and GluA2/4 (D) on nonreducing SDS-PAGE (left panels; the Glu prefix is omitted from the labeling). Green and purple arrowheads indicate N and O dimers, respectively. These disappear in the presence of DTT; nonspecific dimers remain (right panels). Lanes 1 and 2, negative controls; lane 3, O-shaped cross-links; lane 4, N-shaped cross-links; lane 5, N-shaped cross-link control; lane 6, combined N- and O-shaped cross-links. (**E**) Example traces showing AMPAR currents from HEK293T cells expressing GluA2/3 WT/WT (top) or GluA2/3$_{xlink}$ (N292C/R265C; bottom). Responses to a 100-ms application of 10 mM glutamate were recorded in oxidizing (CuPhe; red) and reducing (DTT; black) conditions. (**F**) The peak current ratio between CuPhe and DTT for GluA2/3 WT/WT and GluA2/3$_{xlink}$ (N292C/R265C). No significant difference (ns) was found (P = 0.4883; unpaired t test). Single-letter abbreviations for the amino acid residues are as follows: A, Ala; C, Cys; D, Asp; E, Glu; F, Phe; G, Gly; H, His; I, Ile; K, Lys; L, Leu; M, Met; N, Asn; P, Pro; Q, Gln; R, Arg; S, Ser; T, Thr; V, Val; W, Trp; and Y, Tyr.

Downloaded from http://science.sciencemag.org/ on April 28, 2016

and E). The near equality in the peak amplitude ratios ($I_{max\text{-}DTT}/I_{max\text{-}CuPhe}$) for mutants (cross-linked at either region 1 or region 2; Fig. 1C and fig. S3B) and WT heteromers suggests that the receptors trapped in this conformation remain functional.

Desensitization kinetics and recovery from desensitization showed no greater effect of the oxidizing and reducing treatments in the two O–cross-linked heteromers than in the respective wild types (Fig. 2E; fig. S7, C, D, F, and G; and fig. S8); together with the negative stain data (fig. S5), this suggests that rupture of the NTD layer (*21*–*23*) is not a prerequisite for desensitization.

Cryo-EM structure of a GluA2/3 AMPAR heteromer

Structure determination

To determine the molecular organization of GluA2/3, we recorded a cryo-EM data set for $GluA2/3_{xlink}$ in the ligand-free (apo) state, using a Titan Krios microscope equipped with a Gatan K2 Summit electron detector (Materials and Methods). The direct electron detector allowed us to collect individual subframes and correct for beam-induced motion; 3D classification using maximum likelihood methods was instrumental for isolating different conformations of the sample (*28*, *29*). 3D classification of 107,939 motion-corrected particles using RELION (*30*) resulted in three classes with O-shaped NTDs (73,885 particles), one class (16,697 particles) resembling the classical Y-shaped receptor observed in GluA2 homomers (N-shaped when viewed from the top), and one class without AMPAR-like features (fig. S9). Although processing of data from the Y-shaped class did not yield a model of sufficient quality, additional steps of 3D classification improved the models for the O-shaped classes, especially at the heterogeneous LBD layer. Two final models, M1 and M2, were obtained. These models differ in both the orientation of the NTD tetramer and the arrangement of the LBDs (Figs. 3 and 4 and figs. S10 and S11). Refinement led to improved maps at 8.25 Å resolution for M1 and 10.3 Å resolution for M2, allowing us to identify individual domains and secondary structure elements, with clear densities for the NTD, LBD, and most TMD helices (Fig. 3 and fig. S10B).

Overall architecture of GluA2/3 (M1)

Unlike GluA2 homomers, the heteromer is contracted along its vertical axis (Figs. 3B and 5). A compact NTD assembly closely nests between widely separated LBD dimers, deviating from the loosely arranged (Y-shaped) GluA2 homomer (*5*) and approaching an NMDAR-like architecture (Fig. 5B) (*6*, *7*). We performed rigid-body fitting of nine independent crystal structures into the M1 density (Materials and Methods), resulting in a model composed of two GluA2 NTD protomers, two GluA3 NTD protomers, four LBD protomers, and the TMD of GluA2 (PDB ID 3KG2) (Fig. 3, C to E, and fig. S10). Although the NTD protomers were fitted independently, the resulting tetramer closely resembles our NTD crystal structure (RMSD, ~3 Å). The distance between the Cβ of GluA2 Asn^{292} and GluA3 Arg^{265} is ~6 Å, thus marking the position of the introduced disulfide bond. We observed clear density for the GluA3-specific N-glycosylation site at Asn^{35} (fig. S10, A and B), signifying that the positioning of the GluA2 and GluA3 subunits is in agreement with the NTD crystal structure (Fig. 1C).

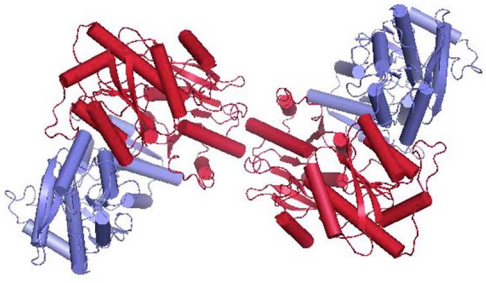

Movie 1. ANM mode 4 of a GluA2 homomer, showing an N-to-O transition. The formation of a compact NTD arrangement resembling the GluA2/3 heteromer is evident in a simulation of a GluA2 homomer (PDB ID 3KG2); this is accompanied by a separation of the LBD dimers and a vertical compression of the receptor toward an NMDAR-like conformation, as previously described (*27*). The ANM creates springs between interacting residues (Cα within 15 Å), and therefore the LL interdimer interface contacts are maintained. Strain within this interface is apparent, and rearrangement of this region probably follows (movie S1).

The diagonal subunit pairs in GluA2 homomers, AC and BD, are conformationally distinct (Figs. 1A and 5A), which is expected to be of functional consequence (*5*). In particular, the linker connecting the LBD to TM3 in the BD pair is predicted to have a greater influence on gating (*5*, *31*). In our structure, GluA2 occupies the AC position and GluA3 occupies the BD position. As a consequence, GluA3 is placed pore-distally at the level of the LBD and TMD, whereas GluA2 is pore-proximal (Fig. 5A). This positioning appears not to be strict in AMPARs, given that GluA2 can also locate to the BD position, according to the GluA2/3 crystal lattice (Fig. 2A) and the cross-linking data (Fig. 2C). Hence, rules underlying subunit placement in preferentially heteromeric iGluRs may be relaxed (*14*), unlike in obligatory heteromers (*6*, *7*, *17*).

NTD-LBD contacts are apparent in the compact heteromer

One of the most distinctive features of the heteromer is the vertical compression relative to existing AMPAR homomer structures (Fig. 5, A and B). To describe this difference in M1, we used the center-of-mass distance between the NTD layer and the gate residue Thr^{625} in TM3 as a metric (*21*). This distance was 21 Å shorter in GluA2/3 M1 (76 Å) than in the antagonist-bound GluA2 cryo-EM structure (97 Å; Fig. 5B) (*22*). The two LBD dimers of the heteromer are splayed apart to accommodate the compact NTD assembly, which partially fills the interlayer cavity that is characteristic of GluA2 homomers.

The compression gives rise to novel interfaces between the NTD and LBD layers (Fig. 5C), a region that is pivotal to allosteric signal transmission in NMDARs triggered by NTD ligands (*6*, *7*, *12*). The interlayer contact points are approximately equidistant in all chains of M1 (Fig. 5, B and C) but are more extensive in the BD chains (GluA3). In GluA2, a loop (Ile^{444}–Gly^{462}) in the LBD projects toward helices D and E at the backside of the NTD. The GluA3 NTDs wedge into the LBD interdimer interface, with NTD helix H contacting LBD helix B. These GluA3 contacts are also apparent in M2, where GluA2 interactions are lost (Fig. 4A and fig. S11). In contrast, complete separation of the ECR layers is evident in GluA2 cryo-EM structures (Fig. 5B) (*22*) and in a crystal structure of a GluA2–snail toxin complex, in which the toxin pushes the NTD away (*31*). Such a separation between the NTD and LBD layers may also occur in the O-shaped receptors, as revealed by ANM mode 6 of GluA2/3 M1 (fig. S12 and movie S2), further highlighting the flexible nature of the AMPAR ECR. These interlayer dynamics may alter AMPAR interactions at synapses and enable allosteric modulation by the NTD, akin to what occurs in NMDARs.

GluA2/3 in a desensitized state (M2)

Glutamate binding to the LBD (Fig. 1A, star) triggers conformational changes that result in activation and desensitization. Individual LBDs can gate the receptor in response to agonist, and occupation of a single subunit triggers desensitization (*32*, *33*). The two loosely associated back-to-back dimers rupture upon desensitization in AMPARs and KARs (*22*, *25*, *34*). This dynamic architecture underlies the speed of AMPAR gating (*25*, *35*).

Heterogeneity in our O-shaped classes largely results from mobility of the LBD layer. Dramatic rearrangements of the LBD layer are apparent in M2; the BC dimer completely ruptures, whereas the AD dimer remains intact, indicating the resting (nondesensitized) state (Fig. 4 and fig. S11). The BC chains mimic agonist-bound desensitized GluA2 (*21*) and provides structural evidence that the receptor can transition into desensitized-like states in the nominal absence of agonist (*32*, *35*, *36*). M1, however, could be fitted best with agonist-free open-cleft LBD conformations (PDB IDs 1FTO and 3UA8; fig. S10C).

Downloaded from http://science.sciencemag.org/ on April 28, 2016

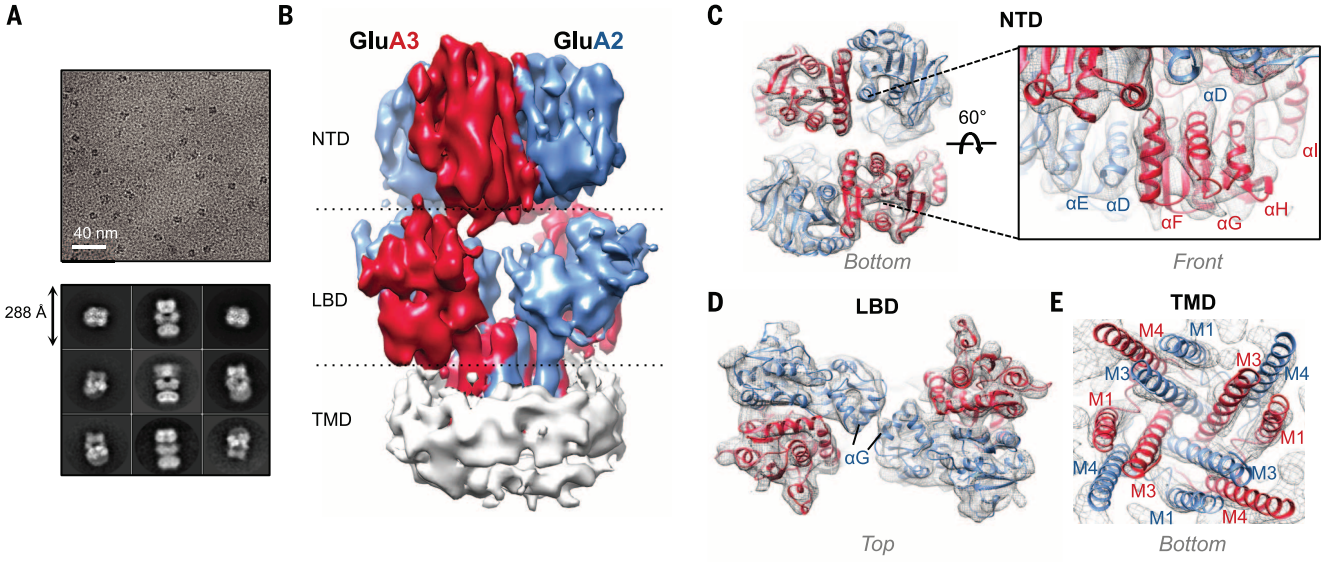

Fig. 3. Cryo-EM structure of GluA2/3$_{xlink}$. (**A**) Sample micrograph at 3.5-μm defocus and a nominal magnification of 28,409×, with representative 2D class averages shown below. (**B**) 8.25 Å–resolution map of GluA2/3 M1 with GluA3 in red, GluA2 in blue, and micelle in white. (**C**) Sample fitting of the NTD bottom (left), showing individual densities for secondary structure elements. The front view (right) shows a close-up of the front face of the GluA3 NTD LL (αF to αH). Individual protomers were fitted (GluA2, PDB ID 3HSY, chain B; GluA3, PDB ID 3O21, chain D). (**D**) Sample fitting of the individual LBD protomers (GluA2, PDB ID 1FTO, chain B; GluA3, PDB ID 3UA8). (**E**) Fitting of the TMD from a GluA2 homomer (PDB ID 3KG2). Good densities were obtained for the gate helices but not for the reentrant pore loops, which were omitted.

Rearrangements of the LBD gating machinery in M1

Rearrangements in the GluA2/3 LBD layer are also evident in M1, which exhibits intact dimers (Fig. 6, A and B, and fig. S11D). The interaction between LBD dimers changes during gating, and their tilting apart has been linked to activation (Fig. 6A) (*21*, *22*). In GluA2/3 M1, the angle between the LBD dimers is relatively open, substantially deviating from that of the GluA2 ligand-free receptor and surpassing that of the activated-state conformation (by 15°) (Fig. 6A). ANM-based simulations suggest that this separation is associated with NTD "sinking" (M1 mode 6) (fig. S12 and movie S2). Together, these data raise the possibility that NTD-LBD interlayer dynamics affect the gating machinery.

When viewing the LBD layer from the top, a new arrangement is apparent. The channel-active state has been suggested to be accompanied by an iris-like opening of the LBD tetramer interface, formed between the G helices of chains A and C (*21*, *22*). These helices, which are arranged head-on in the activated (and resting) states of GluA2 homomers, lie parallel in GluA2/3 M1, essentially closing the LBD gating ring (Fig. 6B and Movie 2). This suggests that the receptor can access a multitude of conformations, with both a separation of the LBD dimers and an open gating ring required for activation.

Conclusion

Here we present the first views of AMPAR heteromers containing the GluA2 subunit, which is the prevailing variety in the brain. We have delineated the most sequence-diverse subunit interface at atomic resolution and have shown that heterodimers associate to form a tetramer with the four subunits alternating around the pore axis. Although GluA2 occupies the pore-proximal (AC) position, subunit placement does not appear to follow strict rules, unlike in obligatorily heteromeric iGluRs (*6*, *7*, *17*). Whether and how these relaxed assembly rules affect signaling in preferentially heteromeric iGluRs (AMPARs and low-affinity KARs) is now an open question.

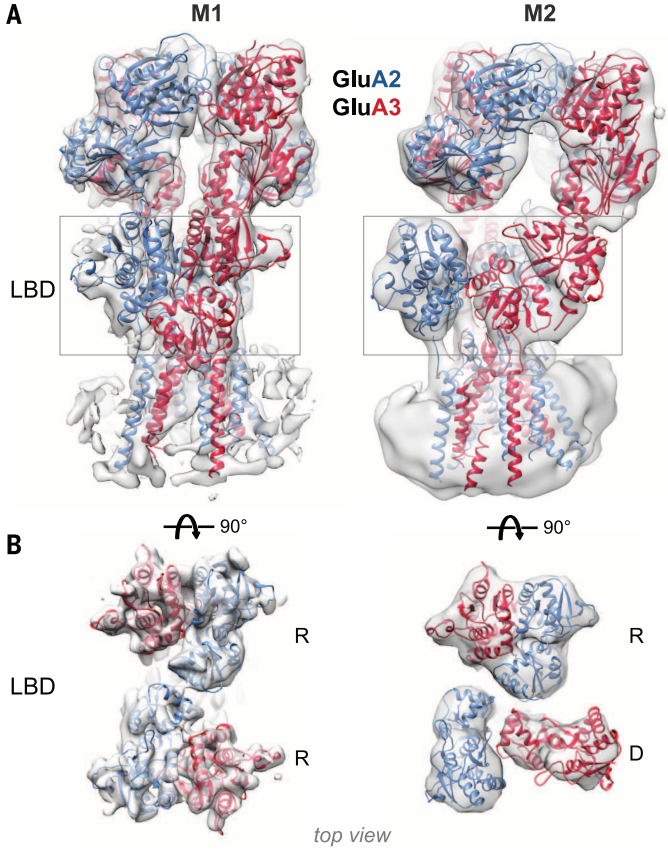

Fig. 4. Ligand-free GluA2/3 in resting and desensitized conformations. (**A**) A view of a LBD dimer and the NTD interdimer interface in M1 of GluA2/3$_{xlink}$ (left panel). The LBD dimer interface is intact and is mediated by the backs of the LBD ULs (boxed). In an equivalent view of M2 (right panel), one LBD dimer has ruptured (chains B and C; boxed), adopting a state observed in desensitized structures (*21*). (**B**) Top views of the LBD layers of M1 (left) and M2 (right). In M1, both LBD dimers are intact (resting, R). In M2, chains A and D form an R dimer and chains B and C are desensitized (D).

Downloaded from http://science.sciencemag.org/ on April 28, 2016

Ligand-free GluA2/3 was captured in resting (M1) and desensitized (M2) conformations, providing structural evidence that the apo receptor can transition between states. Overall, its architecture departs from the classical Y shape and approximates that of NMDARs. We have described a conformational trajectory, supported by ANM simulations, in which the NTDs transition from an N shape into a compact O assembly, which is associated with a vertical compression (Fig. 6C and Movie 1). This receptor conformation could be of functional consequence. First, the interfaces resulting from approximation of the NTD and LBD could permit allosteric coupling within the ECR and provide a novel substrate for AMPAR therapeutics, analogous to that in NMDARs (*12*). Second, because the NTD mediates AMPAR clustering at synapses and dendritic spine dynamics (*11*, *20*), the transition from N to O could alter a strategic docking platform for synaptic interaction partners, including pentraxins (*11*) and AMPAR auxiliary subunits (*37*). The GluA2/3 structure opens avenues to further understanding of AMPAR signal transmission.

Materials and methods

Cloning, expression, and protein purification

The plasmids used for full-length receptors were (i) the rat *Gria2* cDNA (flip splice variant, fully edited at the R/G and Q/R editing sites) containing an N-terminal c-myc tag or an N-terminal FLAG tag in the pIRES2-EGFP (plasmid internal ribosomal entry site 2–enhanced green fluorescent protein) vector; (ii) the rat *Gria3* cDNA (flip, R439G) with an N-terminal FLAG tag in the pRK5 vector (for protein production and biochemical assays) or in the pIRES2-mCherry vector (for electrophysiological studies); and (iii) the rat GluA4 cDNA (flip) with and without an N-terminal FLAG tag in the pRK5 vector. All site-directed mutagenesis was performed on these constructs; mutants included GluA2myc N292C, V209C, and N292C+V209C; GluA3FLAG R265C and GluA4FLAG R264C; and GluA4 S172C and Q175C.

For crystallization, GluA2 NTD (residues 1 to 379 of the mature protein), GluA3 NTD (1 to 380 of the mature protein), and GluA4 NTD (1 to 380 of the mature protein) were produced in stably transfected HEK293S-GnTI$^-$ cells, as previously described (*18*). Briefly, purification consisted of cross-flow concentration and dialysis (in 1 M NaCl and 50 mM tris at pH 8), followed by affinity (His-trap HP column, GE Healthcare) and size exclusion chromatography (S200, GE Healthcare). Oligosaccharides were removed from the protein sample by means of enzymatic EndoH treatment in 100 mM sodium acetate (pH 5.2) and, for further purification, size exclusion chromatography in 50 mM Hepes (pH 7.4) and 150 mM NaCl.

For the purification of the full-length cross-linked receptor, GluA2myc N292C (flip, R/G, Q/R) and GluA3FLAG R265C (flip, R439G) plasmids were transfected into HEK293S-GnTI$^-$ cells (*38*) grown in suspension. Cell culture and transfection followed recently described protocols (*39*, *40*). For 1 liter of cells (3×10^6 cells/ml), a transfection mixture was prepared containing 0.8 mg of GluA2 plasmid, 0.2 mg of GluA3 plasmid, and 3 ml of polyethylenimine "Max" (Polysciences) at 1 mg/ml in 80 ml of hybridoma medium (Life Technologies). Before transfection, cells were centrifuged at 400*g* and supernatant was removed. Cells were resuspended in the transfection mixture and added to 670 ml of freestyle medium supplemented with 1% fetal bovine serum. Cells were grown at 37°C for 60 hours and harvested by centrifugation. Cell pellets were resuspended in ice-cold phosphate-buffered saline (PBS) containing 10 μM CuPhe (mixed from $CuCl_2$ and 1,10- phenanthroline at a 1:3 molar ratio; values in the text represent the $CuCl_2$ concentration) and harvested by centrifugation at 800*g*. Cells were lysed for 90 min at 4°C in 25 mM tris (pH 7.4), 150 mM NaCl, 1% *n*-dodecyl-β-D-maltoside (DDM), 1× protease inhibitor cocktail (Roche), 30 mM *N*-ethylmaleimide (NEM), and 1 mM phenylmethanesulfonyl fluoride (PMSF). After centrifugation, the supernatant was incubated with anti-FLAG M2 beads (Sigma) for 2 hours at 4°C. The sample was eluted with buffer containing 0.15 mg/ml FLAG peptide (Sigma), 0.25% DDM, 25 mM tris (pH 7.4), and 150 mM NaCl. To isolate the heteromeric pool of receptors, a second affinity purification was performed, incubating with anti-myc affinity beads (Pierce). The sample was eluted with 0.5 mg/ml c-myc peptide (Pierce), 0.25% DDM, 25 mM tris (pH 7.4), and 150 mM NaCl. The eluted sample at 0.03 mg/ml showed two bands in nonreducing SDS-PAGE,

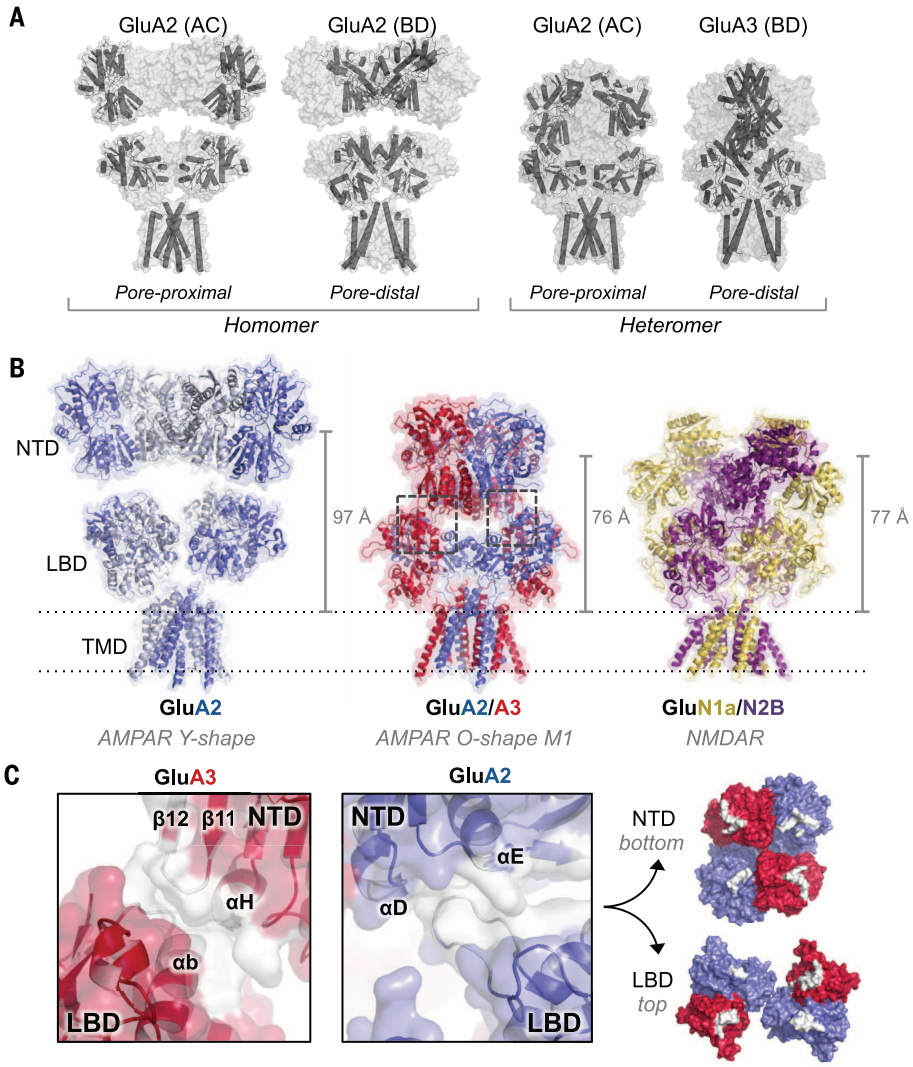

Fig. 5. Architecture of GluA2/3 M1. (**A**) Distinct conformations of the nonequivalent chain pairs (AC and BD) in the Y-shaped GluA2 homomer (PDB ID 4UQJ; left) and the O-shaped GluA2/3 heteromer (right). (**B**) The GluA2/3 heteromer (middle) exhibits a substantial vertical compression relative to GluA2 homomers (PDB ID 4UQJ; left), akin to that of NMDARs (PDB ID 4PE5; right). Compression of the GluA2/3 ECR is indicated by the center-of-mass distance between the NTD and Thr^{625} (vertical bars on the right of each panel). (**C**) NTD-LBD contact regions for GluA2 and GluA3 are shown in white [boxed in (B)]. The protein backbone is depicted in cartoon representation under a transparent surface. A surface view of the interlayer interface is shown on the far right; contacts formed between the NTD and LBD are in white.

Downloaded from http://science.sciencemag.org/ on April 28, 2016

corresponding to monomers and disulfide-linked dimers (fig. S4A).

Crystallization, data collection, and structure determination of NTD heteromers

For GluA2/3 crystallization, GluA3 NTD was diluted to 5 mg/ml, and GluA2 NTD (0.5 mg/ml) was added and concentrated in sequential steps until the GluA2/3 molar ratio reached 1:1, achieving a final concentration of 22 mg/ml. For GluA2/4 heteromers, both GluA2 and GluA4 NTDs were diluted to 0.5 mg/ml, mixed at 1:1 molar ratio, and concentrated to 14 mg/ml. Crystallization screens were set in 96-well MRC plates in 150-plus-150 nl drops, with the protein at 12.5 mg/ml. GluA2/3 crystals appeared in drops containing 14 to 16% PEG-3350 (polyethylene glycol, molecular weight 3350), 0.27 M ammonium sulfate, and 0.1 M bicine (pH 9). GluA2/4 crystals grew in 17% PEG-3350 with 0.1 to 0.35 M ammonium sulfate. Crystals were cryoprotected with 20% glycerol and flash-frozen in liquid nitrogen. Data collection was performed in Diamond Light Source at the I04-1 beamline (0.9163 Å wavelength), and data were collected to 2.12 (GluA2/3) and 2.5 Å resolution (GluA2/4). GluA2/3 data were integrated, scaled, and reduced with Xia2 (*41*). GluA2/4 data were integrated with iMosflm (*42*) and scaled and reduced with AIMLESS (*43*). The GluA2/3 structure was determined by molecular replacement, using monomers from the structures with PDB IDs 3HSY (GluA2) (*18*) and 3O21 (GluA3) (*19*) as search models in MOLREP (*44*). Structures 3HSY (GluA2) and 4GPA (GluA4) (*45*) were used as search models in PHASER (*46*) to phase the GluA2/4 structure by molecular replacement. Both structures were refined using REFMAC5 (*47*) from the CCP4 suite of programs (*48*), and manual modifications were performed with COOT (*49*). The GluA2/3 and GluA2/4 structures were refined to an R_{work}/R_{free} (R factor over free R factor) of 19.2%/23.1% and 17.4%/23.8%, respectively, with both presenting good geometry as defined by the Ramachandran plot. TLS and individual isotropic B factors were refined in both structures. The GluA2/4 structure presented pseudosymmetry (as shown by the Patterson map) and pseudomerohedral twinning with a monoclinic cell with a β angle close to 90°. To overcome this problem, refinement was carried out by computing the twinning fraction in REFMAC5 (twinning fraction of 0.5).

Disulphide cross-linking experiments with full-length heteromers

Mutants were transfected into HEK293T cells by using the Effectene transfection reagent (Qiagen), at a 1:4 ratio of the GluA3-pRK5: GluA2–pIRES2-EGFP plasmids. After expression for ~60 hours, cells were treated with ice-cold PBS containing 10 μM CuPhe (as above) for 45 min before harvesting and lysing in 25 mM Hepes (pH 7.5), 150 mM NaCl, 1 mM EDTA, 1% Triton X-100, and 50 mM NEM, together with PMSF and protease inhibitor cocktail (Roche). The lysate was incubated overnight with anti-FLAG M2 magnetic beads and washed three times with lysis buffer; protein was eluted with 2× SDS-PAGE loading dye. After 10 min incubation at 70°C, samples were loaded into 3 to 8% tris acetate polyacrylamide gels, transferred into nitrocellulose membranes, and probed with the Millipore antibodies to GluA2 (AB1768) and GluA4 (AB1508). The light-chain MAB-201P secondary antibody was used. Signal was achieved using Supersignal WestDura (Thermo Scientific), and images were recorded in a ChemiDoc MP system (BioRad). For native gels, cells were lysed in 1% DDM instead of Triton X-100. Lysate was incubated with anti-FLAG M2 magnetic beads, washed three times, and eluted with 6 volumes of 0.1 mg/ml FLAG peptide in native PAGE sample buffer supplemented with 1% DDM. Samples were loaded into native PAGE Novex 4-to-16% bis-tris gels and run following the manufacturer protocol. Samples were transferred to polyvinylidene difluoride membranes before blocking with 5% milk and probed with GluR2 C-terminal antibody (Sigma). Signal development was carried out as described above. Controls including SDS and SDS+DTT were also included in the gel.

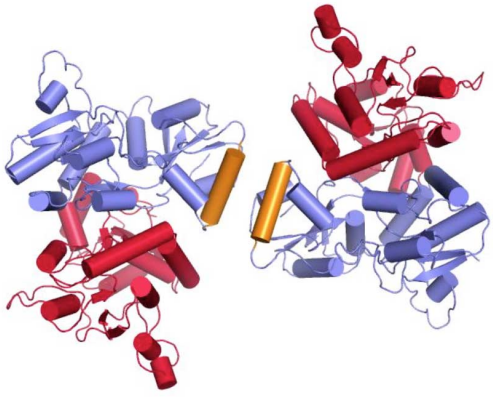

Movie 2. Morph animation showing conformational changes in the LBD layer revealed by GluA2/3 M1. The "morph" command in PyMOL (*61*) was used to generate a series of intermediate conformations between the LBD layer of a GluA2 homomer (PDB ID 4U2P) and that of GluA2/3 M1. A rotation of the two dimers about the interdimer interface is apparent, resulting in an approximation of G helices in chains A and C (orange). This is accompanied by an opening of the roll angle between the LBDs.

EM sample preparation and data acquisition

For negative staining, 4-μl aliquots of sample at ~0.03 mg/ml were stained using 0.75% (w/v) uranyl formate on glow-discharged 400-mesh copper grids (Agar Scientific) covered with a thin layer of carbon. When appropriate, samples were mixed with 100 mM glutamate immediately before grid preparation, or they were incubated with 10 mM DTT for 1 hour at 4°C before adding 100 mM glutamate. Images were recorded using a Tecnai T12 electron microscope (FEI) operated at 120 kV with a nominal magnification of 30,000× (pixel size, 3.286 Å) for the cross-linked apo and glutamate samples and at 26,000× (pixel size, 3.84 Å) for the glutamate+DTT samples. All data were collected at ~1-μm defocus, 1-s exposure, and 20 electrons per square angstrom per second, using a Gatan Ultrascan 1000 2K × 2K with a 14-μm pixel size.

For cryo-EM, R1.2/1.3 Quantifoil 300-mesh copper grids covered with a thin layer of carbon were rendered hydrophilic by means of glow discharge. Vitrified specimens were prepared using a Vitrobot MKIII (FEI) at 100% humidity and 4°C, in which 4-μl samples at 0.03 mg/ml were incubated for 1 min, blotted for 3 s, and plunge-frozen in liquid ethane. Images were recorded on a Titan Krios microscope (FEI) operated at 300 kV and using a K2 Summit detector in single-electron counting mode, resulting in a calibrated magnification of 28,409× (1.76 Å per pixel). The K2 Summit detector was mounted after a Gatan Imaging Filter (GIF Quantum energy filter) and a slit width of 20 eV was used to remove inelastic scattered electrons. A dose rate of 1.6 electrons per square angstrom per second and a total exposure of 40 electrons per square angstrom were used, with a total of 20 movie frames recorded. Defocus values ranged from 1 to 4 μm.

Image processing and model building

In the analysis of images from negatively stained samples, EMAN2 (*50*) was used for initial manual and semiautomated particle picking, and RELION (*30*) was used for all subsequent steps. Initial 2D representative classes were used for automated selection of particles in RELION. Four to six rounds of false-positive elimination by reference-free 2D classification rendered 34,836 particles for the GluA2/3_{xlink}, 27,648 particles for the glutamate-treated sample, and 36,966 particles for the sample treated with glutamate and DTT. For the 3D classification, two different initial models were used. First, an O-shaped model was built by using the TMD and LBD of the GluA2 crystal structure (PDB ID 3KG2) and our tetrameric crystal structure of the GluA2/3 NTD. A second model, with an N-shaped NTD, was generated using the whole GluA2 homomer structure (PBD ID 3KG2). Both models were low pass–filtered to 60 Å. Using these as starting references for 3D classification in the GluA2/3_{xlink} data set, we obtained classes with O-like arrangements at the NTD layer. For the remaining data sets, the O model was used as the starting model for 3D classification. All data sets were divided into five classes, and the cleanest model was chosen for refinement. Both GluA2/3_{xlink} and glutamate-treated GluA2/3_{xlink} samples yielded maps at

Downloaded from http://science.sciencemag.org/ on April 28, 2016

~20 Å resolution, with models containing 9211 particles for the GluA2/3_{xlink} and 6684 particles for the glutamate-treated sample. To further validate the model, an NTD-lacking map, filtered at 60 Å, was generated and used as the initial model for the refinement. The resulting map showed an O-shaped structure that appeared unambiguously after refinement. A population of Y-shaped receptors also appeared in the 3D classification, but the number varied randomly with the sample preparation.

For cryo-EM, movie frames for each micrograph were aligned for whole-image drift using MOTIONCORR (*51*), and contrast transfer function parameters were estimated with Gctf (*52*). EMAN2 was used for initial manual and semi-automated particle picking, and RELION was used for 2D classification, as well as for subsequent classification and refinement, unless otherwise stated. Resulting 2D classes were fed as references for automated picking with RELION. Particles were extracted in a 288 Å box for reference-free 2D classification, which rendered 107,939 particles to be used for subsequent 3D analysis. To produce a starting reference free of bias, an ab initio model was created, starting with representative 2D classes in EMAN2. Beam-induced movement correction and B-factor weighting were performed by applying statistical movie processing in RELION (*30*). 3D classification resulted in three classes featuring O-like NTDs (73,885 particles) and one class resembling the classical Y-shaped receptor (16,697 particles) (fig. S9). The fifth class contained particles forming an uninterpretable model and was therefore discarded. Further 3D classification of the O-like classes by using a soft mask allowed us to eliminate false positives and to obtain two improved classes with two different conformations at the LBD layer (fig. S9). The soft-edge mask was created with the relion_mask_create command, extending the map by five pixels with a five-pixel fall-off. The two classes were further classified into three classes to improve homogeneity; we thereby obtained two maps that, after refinement, produced the final models, M1 and M2, with overall resolutions of 8.25 and 10.3 Å, respectively (figs. S10 and S11). Reported resolutions were calculated using the Fourier shell correlation (FSC) criterion of 0.143 (*53*). Convolution effects on the FSC curves were corrected by means of high-resolution noise substitution (fig. S10) (*54*). Maps were corrected for the modulation transfer function of the detector and sharpened by applying a negative B-factor. Xmipp (*55*) was used to calculate the FSC of the model versus the map. Local resolution analysis was performed with ResMap (*56*). A tilt-pair validation was performed to confirm the correctness of the map (fig. S10F).

Using Chimera (*57*), nine independent crystal structures of the different domains were rigid-body fitted into the M1 model. The NTD layer was fitted by using the GluA2 NTD (PDB ID 3HSY, chain B) (*18*) and GluA3 NTD (PDB ID 3O21, chain D) (*19*). For the TMD layer, coordinates of the antagonist-bound GluA2 homomer (PDB ID 3KG2) (*5*) were used with the reentrant pore loop removed, for which density was absent. For the LBDs, over 100 crystal structures in complex with different ligands are currently available, displaying different levels of clam-shell closure. We used the program NORMA (*58*) to assign the conformation of each LBD protomer in the EM map. The ligand-free GluA2 LBD monomer (PDB ID 1FTO) (*59*), placed in each of the four LBD positions in the EM map, was subjected to coordinate normal mode calculation coupled to a scoring system that assessed the fitness of each conformation to the EM map. For GluA2, the resulting conformation corresponded to the ligand-free state (PDB ID 1FTO, chain B). For GluA3, the resulting conformation was similar to GluA2 in complex with a 6-aminoquinazolinedione sulfonamide antagonist (PDB ID 3UA8) (*60*), with an opening angle higher than in any existing GluA3 LBD structure and similar to that of the structure with PDB ID 1FTO. The same coordinates were used in the fitting of M2; however, the resolution of M2 did not allow for a calculation of the LBD cleft angle. Final PDBs were created by renumbering and merging the fitted PDBs in PyMOL (*61*). Although the GluA2 and GluA3 C termini were

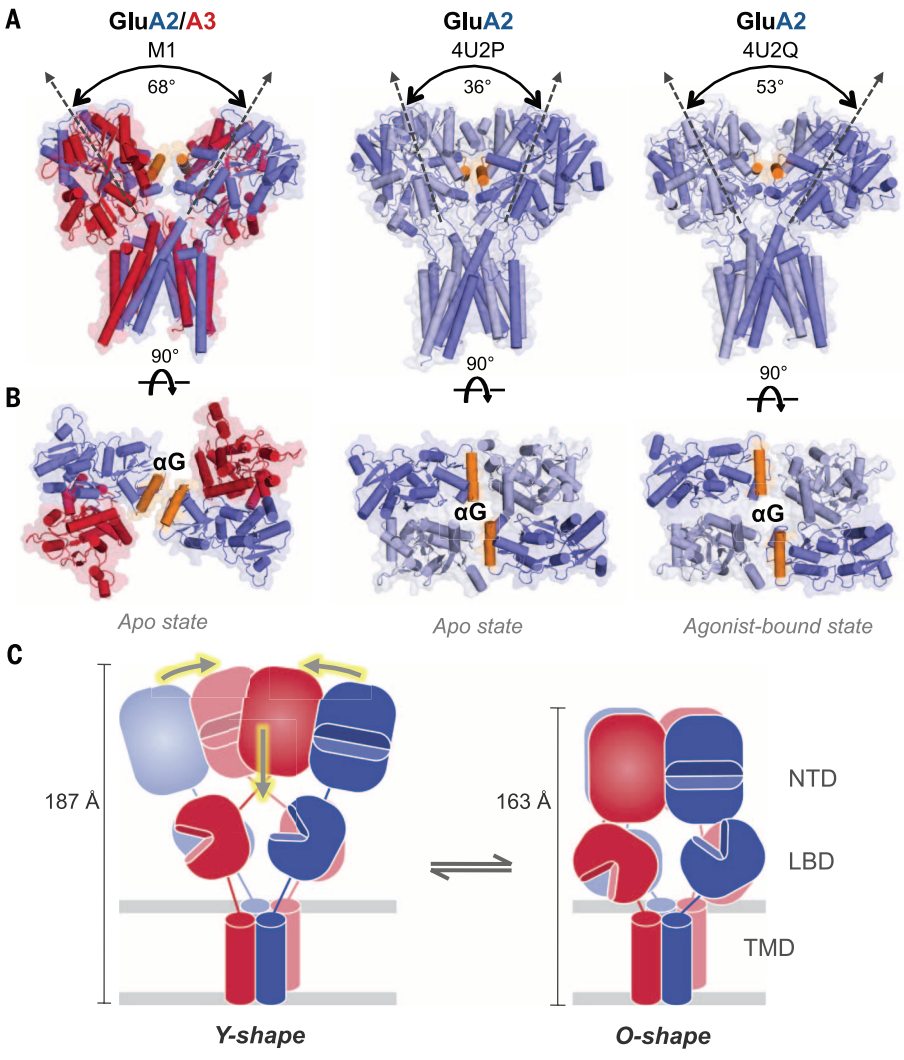

Fig. 6. Novel conformation of the LBD layer in GluA2/3 M1. (**A**) Front view of the GluA2/3 LBD and TMD layers (left); the LBD dimers are more separated and reach down toward the TMD, as compared with the ligand-free and agonist-bound GluA2 crystal structures [PDB ID 4U2P (middle) and 4U2Q (right), respectively]. The roll angle, measured between the twofold pseudosymmetry axes of the two LBD dimers, is indicated. G helices are shown in orange. (**B**) Top view of the two LBD dimers, revealing a novel parallel approximation of G helices in chains A and C of GluA2 (left). In contrast, the ligand-free (apo) homomer (PDB ID 4U2P; middle) exhibits a head-to-head placement of these helices, forming a gating ring, which opens further in the agonist-bound structure (PDB ID 4U2Q; right). This ring is closed in GluA2/3. (**C**) Models of a Y-shaped AMPAR (left), characteristic of GluA2 homomers, and an O-shaped AMPAR (right), as observed for GluA2/3_{xlink}. Double gray arrows indicate the ability of receptors to transition between the Y and O shapes, as suggested by the ANM simulations. Yellow arrows show potential movements permitting this interconversion: Horizontal arrows compact the NTD layer toward an O shape, and vertical arrows indicate vertical compression of the receptor tetramer. Vertical heights of the receptors are indicated on their right sides.

Downloaded from http://science.sciencemag.org/ on April 28, 2016

present, no corresponding densities were observed in any of the cryo-EM maps, suggesting that these 50 amino acid segments are disordered.

Electrophysiology, data acquisition, and analysis

HEK293T cells were cotransfected with GluA2 (flip) and GluA3 (flip, R439G) or GluA4 (flip) plasmids by using the Effectene transfection reagent (Qiagen), at ratios favoring the formation of heteromers (checked for each cell by recording the current-voltage characteristics of the responses in the presence of intracellular spermine).

Current responses of whole lifted cells, voltage-clamped at –60 mV, were elicited by fast application of 10 mM L-glutamate via a θ tube and recorded using an Axopatch-1D, -200B, or -700B amplifier, a Digidata1322/1440A interface, and pClamp 9.2/10.5 software (Molecular Devices). Cells were perfused with external solution containing (in mM) NaCl (145), KCl (3), $CaCl_2$ (2), $MgCl_2$ (1), glucose (10), and Hepes (10), adjusted to pH 7.4 with NaOH and supplemented with either 10 μM CuPhe or 10 mM DTT. Electrodes were fabricated from borosilicate glass (1.5-mm outer diameter, 0.86-mm inner diameter; Science Products GmbH) pulled with a PC-10 vertical puller (Narishige). When filled with the internal solution—containing (in mM) CsF (120), CsCl (10), EGTA (10), ATP-sodium salt (2), Hepes (10), and spermine (0.1), adjusted to pH 7.3 with CsOH—they had a final resistance of 2 to 5 megohms. The oxidizing (reducing) potency of the CuPhe (DTT) solutions was checked routinely by using the GluA2 S729C mutant (*62*).

To assess desensitization kinetics, responses to 100-ms glutamate pulses were recorded, and the current decay during the agonist application was fitted with a one- or two-exponential function to obtain the (weighted) time constant of desensitization. Recovery from desensitization was tested by using a two-pulse protocol with a desensitizing 100-ms pulse, followed by a 10-ms pulse in increasing intervals. The relative responses to the second pulse (an average of three consecutive runs) were plotted against the time elapsed from the end of the first pulse and fitted by the Hodgkin-Huxley equation, as in (*63*).

The effect of forming and breaking the introduced Cys bond was examined by recording each cell under both oxidizing and reducing conditions and comparing the parameters with the corresponding WT receptors by means of repeated-measures two-way analysis of variance. This provided information about the effect of the mutation, the treatment (oxidation versus reduction), and the interaction of the two factors—i.e., whether the effect of the treatment is different for the mutant and the WT.

ANM analysis

Normal mode analysis is a method for determining modes of motion that are accessible to a protein, given a particular starting structure and a model describing forces between atoms.

The ANM is a coarse-grained elastic network model with a single node for each amino acid residue. Interactions are modeled as uniform harmonic springs between residues within a cutoff (15 Å between Cα atoms) (*26*, *64*). The Hessian matrix of force constants (second derivative of the energy potential function) is decomposed to give a unique set of normal modes. Modes are represented by 3*N*-dimensional eigenvectors $\mathbf{u}_k$ (for *N* residues in 3D space) with corresponding eigenvalues λ_k. The first modes (those with low eigenvalues) describe low-energy global motions, and the higher-eigenvalue modes describe less favorable local deformations. Conformations $\mathbf{R}^{(k)}$ along a given mode *k* were generated using the equation $\mathbf{R}^{(k)} = \mathbf{R}^{(0)} \pm (s\lambda^{-1/2}\,\mathbf{u}_k)$, where $\mathbf{R}^{(0)}$ is a 3*N*-dimensional vector representing the initial coordinates, and *s* is a scaling constant that can be adjusted to fit experimental data (*65*). Normal mode analysis with the ANM was carried out using the ANM server (*66*) and Python extension ProDy (*67*), as previously described (*27*). The similarity between conformations in ANM mode 4 and the GluA2/3 NTD crystal structure was assessed using the Normal Mode Wizard (*67*) in VMD (*68*).

Comparing normal modes with transitions between N and O crystal structures

Transitions were calculated as the displacement vector for all corresponding Cα atoms required to interconvert the two aligned structures [the N-shaped NTD layer from the GluA2 homomer (PDB ID 3KG2) and our O-shaped GluA2/3 NTD crystal structure]. The extent of directional overlap between a displacement vector $\mathbf{d}$ and a normal mode vector $\mathbf{u}_k$, generated from one of the aligned structures, could then be calculated as the correlation cosine $\mathbf{d}\cdot\mathbf{u}_k$ (shown as blue bars in fig. S6). To assess whether a combination of modes would better describe the transition than any given single mode, we also calculated cumulative overlaps as the square root of the sum of squared overlaps (red curves in fig. S6); no noticeable improvement was evident. These calculations were also carried out using Python with ProDy (*67*).

LBD transitions

Conformational changes within the LBD layer were calculated as transitions between aligned structures from GluA2/3 M1 and either the apo GluA2 homomer (PDB ID 4U2P) or an antagonist-bound GluA2 homomer (PDB ID 3KG2), as described above for the NTD transition. The correlation cosine between these transitions was 0.95, confirming that they follow a shared pathway. The transition between the antagonist-bound GluA2 homomer and GluA2/3 M1 was also calculated using the "morph" command of PyMOL, which was also used for the creation of Movie 2.

REFERENCES AND NOTES

1. S. F. Traynelis *et al.*, Glutamate receptor ion channels: Structure, regulation, and function. *Pharmacol. Rev.* **62**, 405–496 (2010). doi: 10.1124/pr.109.002451; pmid: 20716669
2. D. Bowie, Ionotropic glutamate receptors & CNS disorders. *CNS Neurol. Disord. Drug Targets* **7**, 129–143 (2008). doi: 10.2174/187152708784083821; pmid: 18537642
3. R. L. Huganir, R. A. Nicoll, AMPARs and synaptic plasticity: The last 25 years. *Neuron* **80**, 704–717 (2013). doi: 10.1016/j.neuron.2013.10.025; pmid: 24183021
4. J. T. Isaac, M. C. Ashby, C. J. McBain, The role of the GluR2 subunit in AMPA receptor function and synaptic plasticity. *Neuron* **54**, 859–871 (2007). doi: 10.1016/j.neuron.2007.06.001; pmid: 17582328
5. A. I. Sobolevsky, M. P. Rosconi, E. Gouaux, X-ray structure, symmetry and mechanism of an AMPA-subtype glutamate receptor. *Nature* **462**, 745–756 (2009). doi: 10.1038/nature08624; pmid: 19946266
6. E. Karakas, H. Furukawa, Crystal structure of a heterotetrameric NMDA receptor ion channel. *Science* **344**, 992–997 (2014). doi: 10.1126/science.1251915; pmid: 24876489
7. C. H. Lee *et al.*, NMDA receptor structures reveal subunit arrangement and pore architecture. *Nature* **511**, 191–197 (2014). doi: 10.1038/nature13548; pmid: 25008524
8. R. Kazi, J. Dai, C. Sweeney, H. X. Zhou, L. P. Wollmuth, Mechanical coupling maintains the fidelity of NMDA receptor-mediated currents. *Nat. Neurosci.* **17**, 914–922 (2014). doi: 10.1038/nn.3724; pmid: 24859202
9. M. Mansour, N. Nagarajan, R. B. Nehring, J. D. Clements, C. Rosenmund, Heteromeric AMPA receptors assemble with a preferred subunit stoichiometry and spatial arrangement. *Neuron* **32**, 841–853 (2001). doi: 10.1016/S0896-6273(01)00520-7; pmid: 11738030
10. J. García-Nafría, B. Herguedas, J. F. Watson, I. H. Greger, The dynamic AMPA receptor extracellular region: A platform for synaptic protein interactions. *J. Physiol.* (2016). doi: 10.1113/JP271844; pmid: 26891027
11. G. M. Sia *et al.*, Interaction of the N-terminal domain of the AMPA receptor GluR4 subunit with the neuronal pentraxin NP1 mediates GluR4 synaptic recruitment. *Neuron* **55**, 87–102 (2007). doi: 10.1016/j.neuron.2007.06.020; pmid: 17610819
12. S. Zhu, P. Paoletti, Allosteric modulators of NMDA receptors: Multiple sites and mechanisms. *Curr. Opin. Pharmacol.* **20**, 14–23 (2015). doi: 10.1016/j.coph.2014.10.009; pmid: 25462287
13. K. B. Hansen, H. Furukawa, S. F. Traynelis, Control of assembly and function of glutamate receptors by the amino-terminal domain. *Mol. Pharmacol.* **78**, 535–549 (2010). doi: 10.1124/mol.110.067157; pmid: 20660085
14. B. Herguedas, J. Krieger, I. H. Greger, Receptor heteromeric assembly—How it works and why it matters: The case of ionotropic glutamate receptors. *Prog. Mol. Biol. Transl. Sci.* **117**, 361–386 (2013). doi: 10.1016/B978-0-12-386931-9.00013-1; pmid: 23663975
15. J. Kumar, M. L. Mayer, Functional insights from glutamate receptor ion channel structures. *Annu. Rev. Physiol.* **75**, 313–337 (2013). doi: 10.1146/annurev-physiol-030212-183711; pmid: 22974439
16. E. Karakas, N. Simorowski, H. Furukawa, Subunit arrangement and phenylethanolamine binding in GluN1/GluN2B NMDA receptors. *Nature* **475**, 249–253 (2011). doi: 10.1038/nature10180; pmid: 21677647
17. J. Kumar, P. Schuck, M. L. Mayer, Structure and assembly mechanism for heteromeric kainate receptors. *Neuron* **71**, 319–331 (2011). doi: 10.1016/j.neuron.2011.05.038; pmid: 21791290
18. M. Rossmann *et al.*, Subunit-selective N-terminal domain associations organize the formation of AMPA receptor heteromers. *EMBO J.* **30**, 959–971 (2011). doi: 10.1038/emboj.2011.16; pmid: 21317873
19. M. Sukumaran *et al.*, Dynamics and allosteric potential of the AMPA receptor N-terminal domain. *EMBO J.* **30**, 972–982 (2011). doi: 10.1038/emboj.2011.17; pmid: 21317871
20. L. Saglietti *et al.*, Extracellular interactions between GluR2 and N-cadherin in spine regulation. *Neuron* **54**, 461–477 (2007). doi: 10.1016/j.neuron.2007.04.012; pmid: 17481398
21. K. L. Dürr *et al.*, Structure and dynamics of AMPA receptor GluA2 in resting, pre-open, and desensitized states. *Cell* **158**, 778–792 (2014). doi: 10.1016/j.cell.2014.07.023; pmid: 25109876
22. J. R. Meyerson *et al.*, Structural mechanism of glutamate receptor activation and desensitization. *Nature* **514**, 328–334 (2014). doi: 10.1038/nature13603; pmid: 25119039
23. T. Nakagawa, Y. Cheng, E. Ramm, M. Sheng, T. Walz, Structure and different conformational states of native AMPA receptor complexes. *Nature* **433**, 545–549 (2005). doi: 10.1038/nature03328; pmid: 15690046

Downloaded from http://science.sciencemag.org/ on April 28, 2016

24. C. R. Midgett, D. R. Madden, The quaternary structure of a calcium-permeable AMPA receptor: Conservation of shape and symmetry across functionally distinct subunit assemblies. *J. Mol. Biol.* **382**, 578–584 (2008). doi: 10.1016/j.jmb.2008.07.021; pmid: 18656486
25. Y. Sun *et al*., Mechanism of glutamate receptor desensitization. *Nature* **417**, 245–253 (2002). doi: 10.1038/417245a; pmid: 12015593
26. I. Bahar, T. R. Lezon, L. W. Yang, E. Eyal, Global dynamics of proteins: Bridging between structure and function. *Annu Rev Biophys* **39**, 23–42 (2010). doi: 10.1146/annurev.biophys.093008.131258; pmid: 20192781
27. A. Dutta *et al*., Cooperative dynamics of intact AMPA and NMDA glutamate receptors: Similarities and subfamily-specific differences. *Structure* **23**, 1692–1704 (2015). doi: 10.1016/j.str.2015.07.002; pmid: 26256538
28. X. C. Bai, G. McMullan, S. H. Scheres, How cryo-EM is revolutionizing structural biology. *Trends Biochem. Sci.* **40**, 49–57 (2015). doi: 10.1016/j.tibs.2014.10.005; pmid: 25544475
29. M. Liao, E. Cao, D. Julius, Y. Cheng, Single particle electron cryo-microscopy of a mammalian ion channel. *Curr. Opin. Struct. Biol.* **27**, 1–7 (2014). doi: 10.1016/j.sbi.2014.02.005; pmid: 24681231
30. S. H. Scheres, RELION: Implementation of a Bayesian approach to cryo-EM structure determination. *J. Struct. Biol.* **180**, 519–530 (2012). doi: 10.1016/j.jsb.2012.09.006; pmid: 23000701
31. L. Chen, K. L. Dürr, E. Gouaux, X-ray structures of AMPA receptor-cone snail toxin complexes illuminate activation mechanism. *Science* **345**, 1021–1026 (2014). doi: 10.1126/science.1258409; pmid: 25103405
32. A. Robert, J. R. Howe, How AMPA receptor desensitization depends on receptor occupancy. *J. Neurosci.* **23**, 847–858 (2003). pmid: 12574413
33. C. Rosenmund, Y. Stern-Bach, C. F. Stevens, The tetrameric structure of a glutamate receptor channel. *Science* **280**, 1596–1599 (1998). doi: 10.1126/science.280.5369.1596; pmid: 9616121
34. D. M. Schauder *et al*., Glutamate receptor desensitization is mediated by changes in quaternary structure of the ligand binding domain. *Proc. Natl. Acad. Sci. U.S.A.* **110**, 5921–5926 (2013). doi: 10.1073/pnas.1217549110; pmid: 23530186
35. A. J. Plested, M. L. Mayer, AMPA receptor ligand binding domain mobility revealed by functional cross linking. *J. Neurosci.* **29**, 11912–11923 (2009). doi: 10.1523/JNEUROSCI.2971-09.2009; pmid: 19776277
36. J. Gonzalez, M. Du, K. Parameshwaran, V. Suppiramaniam, V. Jayaraman, Role of dimer interface in activation and desensitization in AMPA receptors. *Proc. Natl. Acad. Sci. U.S.A.* **107**, 9891–9896 (2010). doi: 10.1073/pnas.0911854107; pmid: 20457909
37. O. Cais *et al*., Mapping the interaction sites between AMPA receptors and TARPs reveals a role for the receptor N-terminal domain in channel gating. *Cell Reports* **9**, 728–740 (2014). doi: 10.1016/j.celrep.2014.09.029; pmid: 25373908
38. P. J. Reeves, J. M. Kim, H. G. Khorana, Structure and function in rhodopsin: A tetracycline-inducible system in stable mammalian cell lines for high-level expression of opsin mutants. *Proc. Natl. Acad. Sci. U.S.A.* **99**, 13413–13418 (2002). doi: 10.1073/pnas.212519199; pmid: 12370422
39. P. A. Longo, J. M. Kavran, M. S. Kim, D. J. Leahy, Transient mammalian cell transfection with polyethylenimine (PEI). *Methods Enzymol.* **529**, 227–240 (2013). doi: 10.1016/B978-0-12-418687-3.00018-5; pmid: 24011049
40. E. Seiradake, Y. Zhao, W. Lu, A. R. Aricescu, E. Y. Jones, Production of cell surface and secreted glycoproteins in mammalian cells. *Methods Mol. Biol.* **1261**, 115–127 (2014). doi: 10.1007/978-1-4939-2230-7_6; pmid: 25502196
41. G. Winter, C. M. Lobley, S. M. Prince, Decision making in xia2. *Acta Crystallogr. D Biol. Crystallogr.* **69**, 1260–1273 (2013). doi: 10.1107/S0907444913015308; pmid: 23793152
42. T. G. Battye, L. Kontogiannis, O. Johnson, H. R. Powell, A. G. Leslie, iMOSFLM: A new graphical interface for diffraction-image processing with MOSFLM. *Acta Crystallogr. D Biol. Crystallogr.* **67**, 271–281 (2011). doi: 10.1107/S0907444910048675; pmid: 21460445
43. P. R. Evans, G. N. Murshudov, How good are my data and what is the resolution? *Acta Crystallogr. D Biol. Crystallogr.* **69**, 1204–1214 (2013). doi: 10.1107/S0907444913000061; pmid: 23793146
44. A. Vagin, A. Teplyakov, Molecular replacement with MOLREP. *Acta Crystallogr. D Biol. Crystallogr.* **66**, 22–25 (2010). doi: 10.1107/S0907444909042589; pmid: 20057045
45. A. Dutta, I. H. Shrivastava, M. Sukumaran, I. H. Greger, I. Bahar, Comparative dynamics of NMDA- and AMPA-glutamate receptor N-terminal domains. *Structure* **20**, 1838–1849 (2012). doi: 10.1016/j.str.2012.08.012; pmid: 22959625
46. A. J. McCoy *et al*., Phaser crystallographic software. *J. Appl. Crystallogr.* **40**, 658–674 (2007). doi: 10.1107/S0021889807021206; pmid: 19461840
47. G. N. Murshudov *et al*., REFMAC5 for the refinement of macromolecular crystal structures. *Acta Crystallogr. D Biol. Crystallogr.* **67**, 355–367 (2011). doi: 10.1107/S0907444911001314; pmid: 21460454
48. M. D. Winn *et al*., Overview of the CCP4 suite and current developments. *Acta Crystallogr. D Biol. Crystallogr.* **67**, 235–242 (2011). doi: 10.1107/S0907444910045749; pmid: 21460441
49. P. Emsley, B. Lohkamp, W. G. Scott, K. Cowtan, Features and development of Coot. *Acta Crystallogr. D Biol. Crystallogr.* **66**, 486–501 (2010). doi: 10.1107/S0907444910007493; pmid: 20383002
50. G. Tang *et al*., EMAN2: An extensible image processing suite for electron microscopy. *J. Struct. Biol.* **157**, 38–46 (2007). doi: 10.1016/j.jsb.2006.05.009; pmid: 16859925
51. X. Li *et al*., Electron counting and beam-induced motion correction enable near-atomic-resolution single-particle cryo-EM. *Nat. Methods* (2013). doi: 10.1038/nmeth.2472; pmid: 23644547
52. K. Zhang, Gctf: Real-time CTF determination and correction. *J. Struct. Biol.* **193**, 1–12 (2016). pmid: 26592709
53. S. H. Scheres, S. Chen, Prevention of overfitting in cryo-EM structure determination. *Nat. Methods* **9**, 853–854 (2012). doi: 10.1038/nmeth.2115; pmid: 22842542
54. S. Chen *et al*., High-resolution noise substitution to measure overfitting and validate resolution in 3D structure determination by single particle electron cryomicroscopy. *Ultramicroscopy* **135**, 24–35 (2013). doi: 10.1016/j.ultramic.2013.06.004; pmid: 23872039
55. S. H. Scheres, R. Núñez-Ramírez, C. O. Sorzano, J. M. Carazo, R. Marabini, Image processing for electron microscopy single-particle analysis using XMIPP. *Nat. Protoc.* **3**, 977–990 (2008). doi: 10.1038/nprot.2008.62; pmid: 18536645
56. A. Kucukelbir, F. J. Sigworth, H. D. Tagare, Quantifying the local resolution of cryo-EM density maps. *Nat. Methods* **11**, 63–65 (2014). doi: 10.1038/nmeth.2727; pmid: 24213166
57. E. F. Pettersen *et al*., UCSF Chimera—a visualization system for exploratory research and analysis. *J. Comput. Chem.* **25**, 1605–1612 (2004). doi: 10.1002/jcc.20084; pmid: 15264254
58. K. Suhre, J. Navaza, Y. H. Sanejouand, NORMA: A tool for flexible fitting of high-resolution protein structures into low-resolution electron-microscopy-derived density maps. *Acta Crystallogr. D Biol. Crystallogr.* **62**, 1098–1100 (2006). doi: 10.1107/S090744490602244X; pmid: 16929111
59. N. Armstrong, E. Gouaux, Mechanisms for activation and antagonism of an AMPA-sensitive glutamate receptor: Crystal structures of the GluR2 ligand binding core. *Neuron* **28**, 165–181 (2000). doi: 10.1016/S0896-6273(00)00094-5; pmid: 11086992
60. D. Orain *et al*., 6-Amino quinazolinedione sulfonamides as orally active competitive AMPA receptor antagonists. *Bioorg. Med. Chem. Lett.* **22**, 996–999 (2012). doi: 10.1016/j.bmcl.2011.12.009; pmid: 22197388
61. W. L. DeLano, *The PyMOL Molecular Graphics System* (DeLano Scientific, 2002).
62. N. Armstrong, J. Jasti, M. Beich-Frandsen, E. Gouaux, Measurement of conformational changes accompanying desensitization in an ionotropic glutamate receptor. *Cell* **127**, 85–97 (2006). doi: 10.1016/j.cell.2006.08.037; pmid: 17018279
63. A. Robert, N. Armstrong, J. E. Gouaux, J. R. Howe, AMPA receptor binding cleft mutations that alter affinity, efficacy, and recovery from desensitization. *J. Neurosci.* **25**, 3752–3762 (2005). doi: 10.1523/JNEUROSCI.0188-05.2005; pmid: 15829627
64. A. R. Atilgan *et al*., Anisotropy of fluctuation dynamics of proteins with an elastic network model. *Biophys. J.* **80**, 505–515 (2001). doi: 10.1016/S0006-3495(01)76033-X; pmid: 11159421
65. C. Xu, D. Tobi, I. Bahar, Allosteric changes in protein structure computed by a simple mechanical model: Hemoglobin T↔R2 transition. *J. Mol. Biol.* **333**, 153–168 (2003). doi: 10.1016/j.jmb.2003.08.027; pmid: 14516750
66. E. Eyal, G. Lum, I. Bahar, The anisotropic network model web server at 2015 (ANM 2.0). *Bioinformatics* **31**, 1487–1489 (2015). doi: 10.1093/bioinformatics/btu847; pmid: 25568280
67. A. Bakan, L. M. Meireles, I. Bahar, ProDy: Protein dynamics inferred from theory and experiments. *Bioinformatics* **27**, 1575–1577 (2011). doi: 10.1093/bioinformatics/btr168; pmid: 21471012
68. W. Humphrey, A. Dalke, K. Schulten, VMD: Visual molecular dynamics. *J. Mol. Graph.* **14**, 33–38, 27–28 (1996). doi: 10.1016/0263-7855(96)00018-5; pmid: 8744570

ACKNOWLEDGMENTS

We thank O. Paulsen, A. Penn, and M. Farrant for comments on the manuscript. We also acknowledge P. da Fonseca and S. Scheres for helpful comments regarding cryo-EM, N. Unwin for carbon-coated grids, and C. Savva for help with the EM. We thank the staff at the Diamond Light Source (beamline I04-1) for the provision of synchrotron facilities. B.H., J.G.-N., O.C., R.F.-L., J.K., H.H., and I.H.G. were supported by the Medical Research Council (MC_U105174197). Coordinates and structure factors for the NTD have been deposited in the PDB under IDs 5FWX (GluA2/4) and 5FWY (GluA2/3). The cryo-EM density maps representing GluA2/3 model I and GluA2/3 model II have been deposited in Electron Microscopy Data Bank with accession numbers EMD 8090 and EMD 8091, respectively, and the corresponding models have been deposited in the PDB under IDs 5IDE and 5IDF.

SUPPLEMENTARY MATERIALS

www.sciencemag.org/content/352/6285/aad3873/suppl/DC1
Figs. S1 to S12
Tables S1 and S2
Movies S1 and S2

5 September 2015; accepted 24 February 2016
Published online 10 March 2016
10.1126/science.aad3873

Downloaded from http://science.sciencemag.org/ on April 28, 2016

RESEARCH ARTICLES

SLEEP RESEARCH

Changes in the composition of brain interstitial ions control the sleep-wake cycle

Fengfei Ding,[1,2]* John O'Donnell,[1]* Qiwu Xu,[1] Ning Kang,[1] Nanna Goldman,[1] Maiken Nedergaard[1,3]†

Wakefulness is driven by the widespread release of neuromodulators by the ascending arousal system. Yet, it is unclear how these substances orchestrate state-dependent, global changes in neuronal activity. Here, we show that neuromodulators induce increases in the extracellular K^+ concentration ($[K^+]_e$) in cortical slices electrically silenced by tetrodotoxin. In vivo, arousal was linked to AMPA receptor–independent elevations of $[K^+]_e$ concomitant with decreases in $[Ca^{2+}]_e$, $[Mg^{2+}]_e$, $[H^+]_e$, and the extracellular volume. Opposite, natural sleep and anesthesia reduced $[K^+]_e$ while increasing $[Ca^{2+}]_e$, $[Mg^{2+}]_e$, and $[H^+]_e$ as well as the extracellular volume. Local cortical activity of sleeping mice could be readily converted to the stereotypical electroencephalography pattern of wakefulness by simply imposing a change in the extracellular ion composition. Thus, extracellular ions control the state-dependent patterns of neural activity.

Wakefulness and sleep represent two fundamentally different behavioral states (*1*). While awake, we are responsive to our surroundings, integrate sensory input, recall memories, and make decisions, whereas contact with the outside world is limited during sleep. These two states of brain activity show characteristic patterns of cortical electroencephalography (EEG), gene expression, and metabolic signature (*2*, *3*). The concerted release of neuromodulators—including norepinephrine, acetylcholine, histamine, dopamine, and orexin—mediates arousal (*4*). All of these neuromodulators individually alter the membrane properties, spiking activity, and intracellular signaling pathways of subpopulations of neurons and glia (*5*), but how they implement the striking stereotypic patterns of EEG activity characterizing wakefulness versus sleep is not understood (*6*).

Neuronal excitability can be modulated by changes in the composition of extracellular ions. For example, moderate elevations of $[K^+]$ in the bath solution (1 to 2 mM) increase spontaneous and evoked excitatory activity in hippocampal slices, and more robust elevations (2 to 5 mM) trigger seizure-like activity (*7*). Lowering extracellular Ca^{2+} ($[Ca^{2+}]_e$) and extracellular Mg^{2+} ($[Mg^{2+}]_e$) also potently alters excitability (*7*).

[1]Center for Translational Neuromedicine, University of Rochester Medical Center, Rochester, NY 14642, USA. [2]Department of Neurology, Tongji Hospital, Tongji Medical College, Huazhong University of Science and Technology, Wuhan 430030, China. [3]Center for Basic and Translational Neuroscience, Faculty of Health and Medical Sciences, University of Copenhagen, Copenhagen 2200, Denmark. *These authors contributed equally to this work. †Corresponding author: Email: nedergaard@urmc.rochester.edu

Neuromodulators increase extracellular K^+ independently of synaptic activity

It is not known whether the changes in extracellular ion concentrations that occur during the natural sleep-wake cycle (*8*) are primary or secondary to alterations in electrical activity. In fact, the changes in extracellular ions that accompany behavioral states would be considered by most to be a consequence of different patterns of neuronal activity. However, ion transport is regulated by catecholamines outside the central nervous system (CNS) (*5*). We asked whether neuromodulators also regulate ion transport in the CNS and thereby the concentration of extracellular ions. We first recorded extracellular K^+ concentration ($[K^+]_e$) in cortical slices prepared from adult mice using K^+-sensitive microelectrodes (K^+-ISMs). Superfusion of a cocktail of neuromodulators at a concentration comparable with previous slice studies containing norepinephrine, acetylcholine, dopamine, orexin, and histamine triggered a rapid increase in $[K^+]_e$, averaging 0.43 ± 0.07 mM. Surprisingly, blocking neuronal activity by addition of tetrodotoxin (TTX) (1 μM) neither altered basal $[K^+]_e$ nor significantly suppressed the neuromodulator cocktail–induced $[K^+]_e$ increase, despite completely blocking spontaneous and evoked activity (Fig. 1). As a positive control, we inhibited energy metabolism by short-lasting exposure to the glycolytic inhibitor iodoacetate (10 min, 3.5 mM), triggering an abrupt increase in $[K^+]_e$, which partly recovered during washout (Fig. 1F). As expected, TTX suppressed the increase in $[K^+]_e$ induced by inhibition of glycolysis (*9*). The insensitivity of neuromodulator-induced $[K^+]_e$ elevations to TTX raises the question as to whether the concerted release of neuromodulators during arousal and wakefulness also drives an increase in $[K^+]_e$ in vivo, and if so, whether this elevation is upstream of excitatory transmission or merely secondary to changes in local neuronal activity.

Wakefulness triggers an increase in extracellular K^+ that is independent of AMPA receptors

We next measured state-dependent changes in extracellular ion concentrations in vivo (fig. S2A). All recordings were collected between zeitgeber times (ZT) 4 and 8 (ZT times are based on a 24-hour diurnal cycle standardized so that ZT0 is the beginning of the sleep period and ZT12 is the beginning of the awake period). Sleep was defined as periods with high electrocorticography (ECoG) delta activity and low electromyography (EMG) activity relative to periods when animals were awake. Starting from sleep, $[K^+]_e$ rose rapidly by 0.40 ± 0.05 mM (Fig. 2, A and B) as animals awoke, before returning to baseline as animals fell back asleep. These transitions occurred quickly, with increases peaking within 1.3 ± 0.02 s (range 0.1 to 8.6 s, n = 27 transitions), whereas the transition back to sleep was substantially slower and more variable, 13.9 ± 2.7 s [range 1.8 to 45.9 s, $t(55) = 3.22$, $P = 0.002$].

We next investigated the effect of isoflurane anesthesia on $[K^+]_e$ and collected recordings during the animals' natural wake period (ZT16 to ZT20). After obtaining a stable awake $[K^+]_e$ baseline, 2% isoflurane was administered, which consistently triggered a sharp decrease in $[K^+]_e$ of 0.37 ± 0.06 mM (Fig. 2C). This decrease in $[K^+]_e$ remained stable throughout isoflurane administration and recovered to pre-anesthesia awake levels over 148 ± 41 s after cessation of anesthesia (n = 9 animals). Both the shift into and recovery from anesthesia mirrored changes in ECoG and EMG activity (Fig. 2C).

To critically evaluate the stability of state-dependent ion shifts, microdialysis samples of the extracellular fluid were collected in freely behaving, unrestrained mice. We used the no-net flux paradigm to estimate $[K^+]_e$, with five samples collected over several hours in which the $[K^+]$ in artificial cerebrospinal fluid (ACSF) was stepwise altered (Fig. 2D). Estimates of $[K^+]_e$ were comparable with those recorded with K^+-ISMs in the cortex, 4.00 ± 0.17 mM versus 4.16 ± 0.09 mM in awake mice [$t(44) = 0.903$, $P = 0.371$, Student's t test]. Microdialysis also showed a significant reduction in $[K^+]_e$ during sleep and isoflurane periods, with values decreasing to 3.44 ± 0.11 mM in sleep and 3.26 ± 0.12 mM in isoflurane (Fig. 2D).

To test whether state-dependent $[K^+]_e$ shifts are the result of changes in excitatory activity in vivo, we applied the AMPA receptor antagonist 6-cyano-7-nitroquinoxaline-2,3-dione (CNQX) (200 μM). Although CNQX potently and rapidly

Downloaded from http://science.sciencemag.org/ on April 28, 2016

suppressed the ECoG power of awake mice, only a transient and short-lasting (<10 min) decrease in $[K^+]_e$ was observed, with $[K^+]_e$ returning to pre-CNQX concentrations despite continued suppression of synaptic activity (fig. S2, B, C, and F). Subsequent administration of isoflurane in the presence of CNQX decreased $[K^+]_e$ by 0.26 ± 0.02 mM (fig. S2C). Thus, regulation of $[K^+]_e$ is dependent on state-modulation and not a direct measure of local glutamatergic activity. State-dependent transitions in brain activity are also linked to changes in the extracellular space volume (*10*). Because the Na^+- and K^+-dependent adenosine triphosphatase (Na^+/K^+-ATPase) is the chief regulator of both $[K^+]_e$ and cell volume (*7*), we asked whether the decreased $[K^+]_e$ in response to isoflurane anesthesia is linked to expanded extracellular space. Despite markedly reducing ECoG power throughout recordings, CNQX neither changed awake extracellular space nor inhibited isoflurane-induced expansion (fig. S2E). This indicates that local synaptic transmission (ECoG power) is not the primary determinant of state-dependent changes of either $[K^+]_e$ or the extracellular space volume.

Together, cortical recordings of $[K^+]_e$ as well as sampling of the extracellular fluid by means of microdialysis showed consistent decreases in $[K^+]_e$ as animals transitioned from the awake state to sleep. Blocking local synaptic transmission with CNQX did not affect state-dependent changes in $[K^+]_e$ (Fig. 2E).

Extracellular Ca^{2+} decreases during wakefulness

Are cortical extracellular Ca^{2+} concentrations also regulated by the sleep-wake cycle? Opposite to the rise in $[K^+]_e$, $[Ca^{2+}]_e$ consistently decreased 0.13 ± 0.02 mM as mice transitioned from sleep to awake states and, conversely, increased by 0.11 ± 0.01 mM as the mice returned to sleep (Fig. 3, A and B). These state-dependent $[Ca^{2+}]_e$ shifts were slow compared with those of $[K^+]_e$, with sleep-to-awake transitions taking 51.5 ± 8.8 s [$[Ca^{2+}]_e$, 4.5 to 156.0 s, Student's *t* test; versus $[K^+]_e$, $t(20) = 5.379$, $P < 0.0001$] and awake-to-sleep occurring over 63.3 ± 8.9 s [$[Ca^{2+}]_e$, 19.3 to 116.1 s, Student's *t* test; versus $[K^+]_e$, $t(16) = 6.696$, $P < 0.0001$]. Isoflurane administered to awake mice drove a slow increase in $[Ca^{2+}]_e$ throughout the duration of anesthesia, with levels rising by 0.26 ± 0.02 mM (Fig. 3C). This rise in $[Ca^{2+}]_e$ continued throughout and past the cessation of anesthesia, peaking at 1.2 ± 1.6 min (−6.2 to 12.4 min, $n = 11$ animals) and taking 22.6 ± 4.8 min (4.3 to 49.2 min, $n = 10$ animals) to recover.

Microdialysis was used to assess the stability of state-dependent $[Ca^{2+}]_e$ shifts by using the no-net flux method. Because of the slow time-course of $[Ca^{2+}]_e$ transitions and short awakenings associated with sample collection, we pooled sleep and awake samples and compared them with isoflurane, finding that $[Ca^{2+}]_e$ increases by 0.25 ± 0.08 mM under isoflurane anesthesia (Fig. 3D), which is comparable with in vivo $[Ca^{2+}]_e$ isoflurane recordings (Fig. 3E).

CNQX suppressed ECoG power by >60% but did not alter awake $[Ca^{2+}]_e$ or isoflurane-induced $[Ca^{2+}]_e$ increases (Fig. 3E), indicating that local glutamatergic activity did not control the shifts in $[Ca^{2+}]_e$. Together, all shifts from awake to isoflurane-anesthetized states showed surprising consistency (Fig. 3E). However, state-dependent changes in $[Ca^{2+}]_e$ could be secondary to shifts in $[K^+]_e$. We therefore increased $[K^+]_e$ in the ACSF covering the cranial window from 2.8 to 4.5 mM, increasing $[K^+]_e$ 200 μm below the pial surface by 0.47 ± 0.07 mM [Student's *t* test, $t(7) = 6.861$, $P < 0.0001$]. However, imposing this increase in $[K^+]_e$ had no detectable effect on the local $[Ca^{2+}]_e$ concentration, suggesting that $[Ca^{2+}]_e$ changes are not secondary to state-dependent $[K^+]_e$ changes [paired *t* test, $t(2) = 0.855$, $P = 0.483$].

Extracellular Mg^{2+} is low during wakefulness and increases during sleep and anesthesia

In sleep and awake states, minor but consistent shifts in free $[Mg^{2+}]_e$ were identified, with $[Mg^{2+}]_e$ decreasing by 0.11 ± 0.01 mM (Fig. 4A) as mice transitioned from sleep to awake and increasing again by 0.13 ± 0.02 mM (Fig. 4B) as animals were observed to return to sleep. Transitions occurred slowly from both sleep to awake (68.9 ± 8.8 s; 5 to 342 s; $n = 55$ transitions) and awake to sleep (141.1 ± 14.8 s; 15.1 to 470 s; $n = 49$ transitions). Isoflurane anesthesia also increased $[Mg^{2+}]_e$ by 0.44 ± 0.07 mM in awake mice (Fig. 4C) before gradually returning to baseline over 26.7 ± 5.7 min (9.6 to 66.3 min, $n = 9$ animals) after the cessation of anesthesia.

Microdialysis samples were collected during the sleep (ZT2 to ZT8) and awake (ZT14 to ZT20) periods and were pooled and compared with isoflurane-induced shifts in $[Mg^{2+}]_e$, demonstrating an increase of 0.32 ± 0.13 mM $[Mg^{2+}]_e$ in isoflurane samples (Fig. 4D). CNQX neither altered basal $[Mg^{2+}]_e$ nor the previously observed isoflurane-induced increase in $[Mg^{2+}]_e$ (Fig. 4E). Thus, across all experiments $[Mg^{2+}]_e$ increased as mice went from awake to sleep or isoflurane (Fig. 4E).

Robust changes in pH were also noted with isoflurane anesthesia. Recordings with pH-sensitive

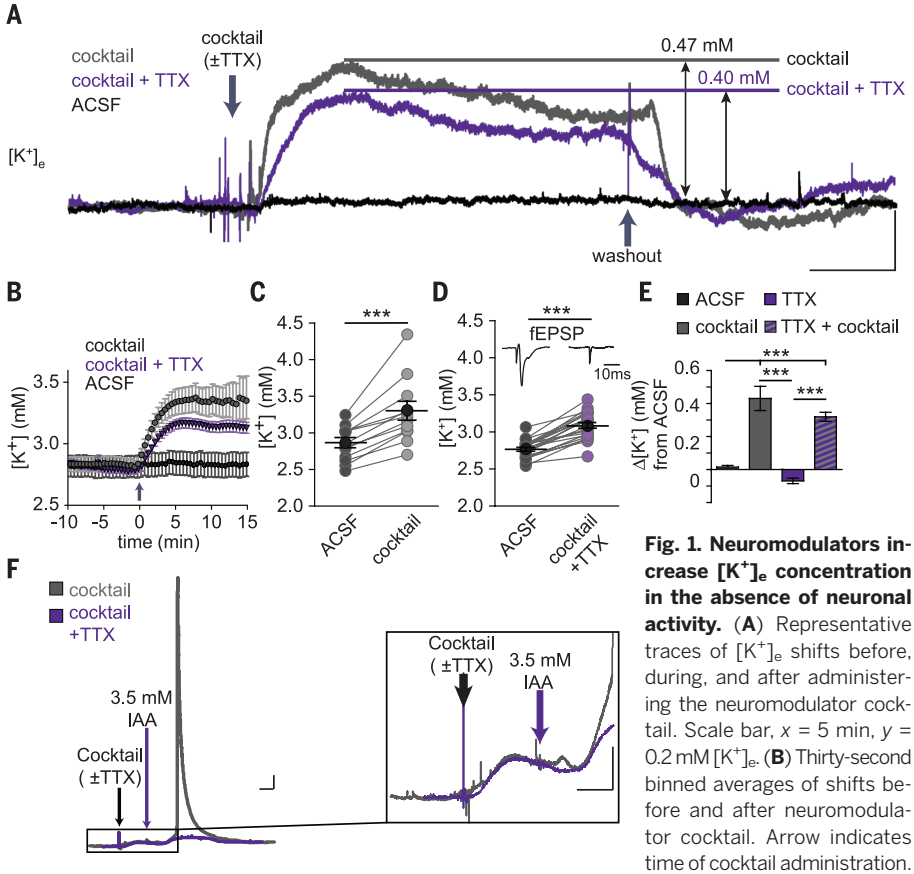

Fig. 1. Neuromodulators increase $[K^+]_e$ concentration in the absence of neuronal activity. (**A**) Representative traces of $[K^+]_e$ shifts before, during, and after administering the neuromodulator cocktail. Scale bar, *x* = 5 min, *y* = 0.2 mM $[K^+]_e$. (**B**) Thirty-second binned averages of shifts before and after neuromodulator cocktail. Arrow indicates time of cocktail administration. (**C** and **D**) Summary of $[K^+]_e$ increase after neuromodulator cocktail application in slices ± TTX [paired *t* test. (C) −TTX, $t(11) = 5.871$, $P = 0.0001$; (D) +TTX, $t(21) = 11.69$, $P < 0.0001$]. (Inset) Representative field excitatory postsynaptic potential (fEPSP) recordings before and after application of TTX. Scale bar, 10 ms. (**E**) Summarized shifts at 10 min after changing perfusion solution. $n = 6$ cocktail-free ACSF, 12 cocktail, 10 ACSF+TTX, and 22 cocktail+TTX slices. One-way analysis of variance (ANOVA), $F(3,46) = 25.94$, $P < 0.0001$. Post-hoc Tukey test, $^{**}P < 0.01$, $^{***}P < 0.001$. (**F**) Representative trace of large $[K^+]_e$ spike after metabolic stress by using iodoacetate (IA). Trace includes pre-cocktail baseline, ACSF + cocktail, ACSF + IA, and return to baseline ACSF. (Right) Magnified trace showing $[K^+]_e$ increases in slices treated with the neuromodulator cocktail (±TTX) followed by IA. Scale bars, *x* = 5 min, *y* = 0.2 mM $[K^+]_e$. Mean (black circle) ± SEM.

Downloaded from http://science.sciencemag.org/ on April 28, 2016

microelectrodes showed that pH decreased from an awake level of 7.39 ± 0.03 to a stable isoflurane-anesthetized level of 7.26 ± 0.02 (fig. S3).

Local manipulation of extracellular ions controls neuronal activity and extracellular space volume

Can interstitial ion composition be locally altered to mimic natural sleep or awake concentrations? Because ions in the ACSF covering the cranial window continuously exchange with those in the interstitial fluid, we formulated awake-inducing and sleep-inducing ACSFs (table S1) to drive local cortex to the ionic composition of the state opposite the overarching behavioral state (fig. S4). In sleeping mice (ZT4 to ZT8), the awake-inducing ACSF increased $[K^+]_e$ by 0.47 ± 0.07 mM (versus 0.37 ± 0.06 mM in awake-to-isoflurane transitions), decreased $[Ca^{2+}]_e$ by 0.31 ± 0.06 mM (versus 0.26 ± 0.02 mM), and decreased $[Mg^{2+}]_e$ by 0.35 ± 0.02 mM (versus 0.44 ± 0.07 mM). Sleep-inducing ACSF applied to cortex of awake mice (ZT16 to ZT20) resulted in similar shifts, although in the opposite direction. Thus, both solutions could elicit local changes in $[K^+]_e$, $[Ca^{2+}]_e$, and $[Mg^{2+}]_e$ comparable with those seen in transitions from awake to isoflurane anesthesia (fig. S4, B and D). It was not possible to produce pH shifts of the magnitude seen in awake-to-isoflurane transitions with moderate changes in ACSF pH (~1 pH), likely reflecting the efficacy by which CO_2/HCO_3^- system buffer pH (fig. S4, B and D) (*7*).

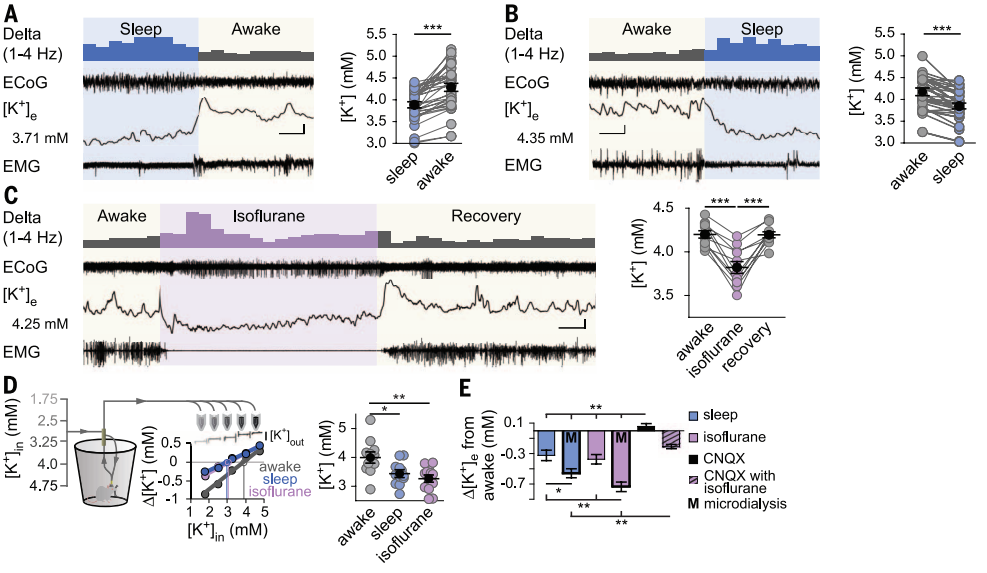

Fig. 2. Extracellular K^+ is higher during wakefulness. (**A** and **B**) Representative ECoG, $[K^+]_e$, and EMG recordings with a data summary of state transitions in (A) sleep-to-awake or (B) awake-to-sleep. Initial $[K^+]_e$ concentrations are shown to the left, and the 1- to 4-Hz power is displayed above so as to illustrate state-dependent shifts, binned at 10 s for clarity. n = 34 transitions; one-way, repeated measures ANOVA, $F(3,99) = 9.536$, $P < 0.0001$. Tukey post-hoc multiple comparisons test, ***$P < 0.001$. Scale bar, x = 20 s, y = 0.1 mM $[K^+]_e$; ECoG = 0.75 mV; EMG = 0.3 mV (A) and 1 mV (B). (**C**) Representative recording of awake-to-isoflurane transitions recorded during the natural awake period (ZT16 to ZT20); n = 11 animals. One-way repeated measures ANOVA, $F(2,20) = 35.61$, $P < 0.0001$. Post-hoc Tukey test, ***$P < 0.001$. Scale bar, x = 1.5 min, y = 0.15 mM $[K^+]_e$, 0.75 mV EMG and ECoG. (**D**) Microdialysis samples collected from freely moving mice during their awake (ZT14 to ZT20) or sleeping (ZT2 to ZT8) period, and under isoflurane anesthesia. (Left) Schematic illustrating setup and inflow $[K^+]$ gradient, with representative ISM trace and sample no-net flux method plot used for $[K^+]_e$ estimate. (Right) Summary of $[K^+]_e$ by state. n = 12 awake, 12 sleep, and 13 isoflurane animals. One-way ANOVA, $F(2,34) = 8.055$, $P = 0.0014$. Post-hoc Tukey test, *$P < 0.05$, **$P < 0.01$. (**E**) Comparison of all state-dependent transitions. One-way ANOVA comparing mean shifts by group, $F(5,161) = 16.61$, $P < 0.0001$. Post-hoc Tukey test, *$P < 0.05$, **$P < 0.01$. Mean (black circle) ± SEM.

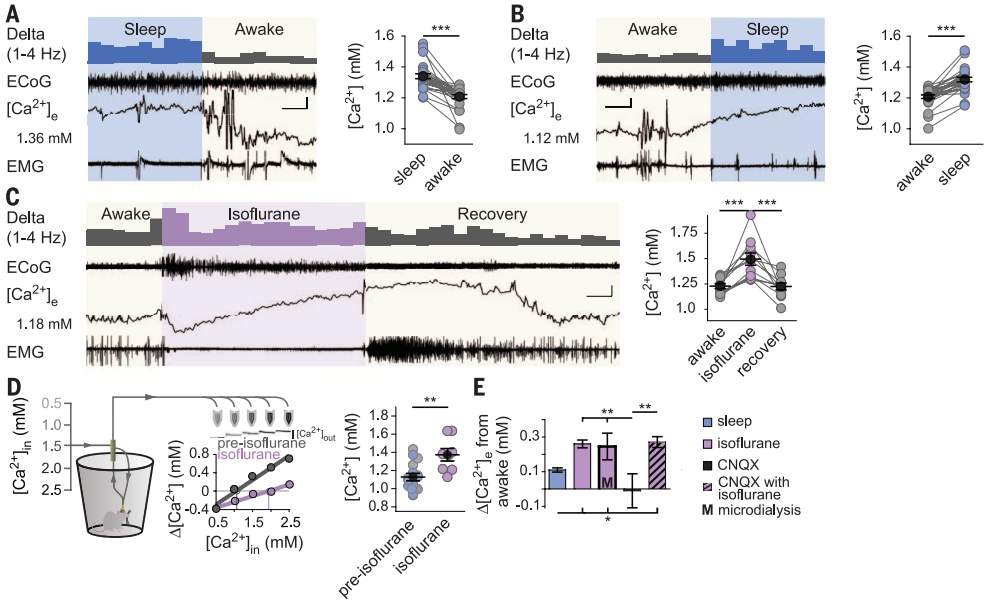

Fig. 3. Extracellular Ca^{2+} decreases during wakefulness. (**A** and **B**) Representative ECoG, EMG, and $[Ca^{2+}]_e$ recordings in (A) sleep-to-awake and (B) awake-to-sleep. Initial $[Ca^{2+}]_e$ is listed to the left with 1- to 4-Hz power presented above. n = 28 transitions. One-way, repeated measures ANOVA, $F(3,81) = 39.91$, $P < 0.0001$. Post-hoc Tukey test, ***$P < 0.001$. Scale bars, x = 20 s (A) and 40 s (B); y, $[Ca^{2+}]_e$ = 0.05 mM, 0.75 mV EMG/ECoG. (**C**) Representative recording of isoflurane induction and recovery (ZT16 to ZT20) and data summary. n = 11 animals. One-way repeated measures ANOVA, $F(2,20) = 18.52$, $P < 0.0001$. Post-hoc Tukey test, ***$P <$ 0.001. Scale bar, x = 6 min, y = $[Ca^{2+}]_e$ = 0.2 mM, 0.5 mV EMG/ECoG. (**D**) Schematic of microdialysis collection. Individual sleep (light blue) and awake (gray) data are pooled and compared with isoflurane. n = 8 awake, 8 sleep, and 8 isoflurane animals. Two-tailed t test of isoflurane versus non-isoflurane, $t(22) = 3.420$, $P = 0.003$, **$P < 0.01$. (**E**) Comparisons of $[Ca^{2+}]_e$ shifts from the awake-to-sleep, isoflurane, CNQX, and CNQX + isoflurane. n = 8 animals; CNQX and CNQX + isoflurane one-way ANOVA comparison of state-dependent shifts, $F(4,117) = 5.824$, $P = 0.0003$; Post-hoc Tukey test, *$P < 0.05$, **$P < 0.01$. Mean (black circle) ± SEM.

Downloaded from http://science.sciencemag.org/ on April 28, 2016

Can local manipulation of extracellular ions in itself drive sleep- or awake-like patterns of neuronal activity? We prepared mice with two separate cranial windows located over the left and right hemisphere and recorded ECoG symmetrically from each (Fig. 5A). Starting in sleeping mice (ZT4 to ZT8) with sleep ACSF (table S1) over each window, recordings were collected from each hemisphere. After this baseline period, the ACSF over the left window was removed and replaced with awake-inducing ACSF. When activity in the left hemisphere was normalized to the right in order to preclude changes from global state transitions, we observed a 34 ± 5% decrease in 1- to 4-Hz ECoG power after application of awake-inducing ACSF, with no change in activity in the contralateral hemisphere (Fig. 5B). In comparison, natural sleep-to-wake transitions decrease the 1- to 4-Hz power by 31.1 ± 3.1% (mean ± SEM of all data, n = 128 transitions). Conversely, could sleep-inducing ACSF increase local delta power in awake mice? Recording between ZT16 and ZT20, awake mice were prepared with awake ACSF covering each cranial window. After a baseline recording, the ACSF over the left hemisphere was replaced with sleep-inducing ACSF, resulting in a 43 ± 13% relative increase in 1- to 4-Hz delta power in the left hemisphere exposed to the sleep-inducing ACSF (Fig. 5C).

Because state-dependent changes in brain activity are also linked to marked changes in the extracellular space volume (*10*), we asked whether altering the local ion composition can drive extracellular space volume changes. Tetramethylammonium (TMA^+) recordings showed that in lightly anesthetized mice (1% isoflurane administered so as to avoid arousal episodes), changing ACSF from sleep ACSF to awake-inducing induced a 21.7 ± 1.2% decrease in the local extracellular space volume (Fig. 5D). Tortuosity (λ) was consistent with previous studies (*11*). Conversely, the extracellular space volume increased by 32.2 ± 2.9% from baseline recordings obtained with awake ACSF to those recorded by using sleep-inducing ACSF in awake mice, despite mice remaining awake and mobile, with tortuosity remaining unchanged (Fig. 5D).

Brain-wide manipulations of extracellular ions can override behavioral states

Would global manipulation of the extracellular ion composition be sufficient to change the behavioral state of mice? We implanted EEG and EMG electrodes, as well as a cannula in cisterna magna (*10*). In sleeping mice (ZT4), a baseline recording was acquired by infusing sleep ACSF followed by a switch to a modified awake-inducing ACSF (Fig. 5E). This switch triggered a robust change in EEG/EMG activity (Fig. 5E), with decreased EEG amplitude and delta prevalence and increased EMG activity, indicative of an awake-phenotype. Infusion rates were comparable with CSF production, and ion concentrations were chosen to account for total brain and CSF volume (supplementary materials, materials and methods). Typically, ACSF infusion itself did not alter EEG activity (fig. S5, A and B). Mice returned to sleep shortly after discontinuation of awake-inducing ACSF infusion (Fig. 5F). We next tested whether infusion of a modified sleep-inducing ACSF could alter the behavioral state of mice during their awake-period. Baseline EEG/EMG activity characteristic of awake mice was recorded while infusing awake ACSF followed by a modified sleep-inducing ACSF. Infusion induced a sharp reduction in EMG activity coupled to a marked increase in slow-wave EEG activity, indicating a shift toward sleep. EEG/EMG activity typical of wakefulness rapidly recovered upon stopping infusion of the modified sleep-inducing ACSF (Fig. 5G).

Discussion

Understanding what drives arousal is essential for deciphering key aspects of consciousness and the lack thereof during sleep and anesthesia. We found that the transition from wakefulness to sleep is accompanied by a marked and sustained change in the concentration of key extracellular ions and the volume of the extracellular space. Arousal triggers a rapid rise in $[K^+]_e$, combined with a decrease in $[Ca^{2+}]_e$, $[Mg^{2+}]_e$, and $[H^+]_e$ and a shrinkage of extracellular space. Natural sleep or anesthesia induces the inverse changes in extracellular ion concentrations and is accompanied by an expansion of extracellular space volume. State-dependent shifts in $[K^+]_e$ occurred within seconds, whereas the changes in $[Ca^{2+}]_e$ and $[Mg^{2+}]_e$ were slow, taking 51.5 ± 8.8 s and 68.9 ± 8.8 s, respectively, for sleep-to-awake transitions. Extracellular fluid samples from microdialysis confirmed and extended the in vivo recordings by documenting that state-dependent differences in extracellular $[K^+]_e$, $[Ca^{2+}]_e$, and $[Mg^{2+}]_e$ concentrations persisted over prolonged period of hours in freely behaving animals (Figs. 2 to 4). Microdialysis experiments suggested that state-dependent changes in extracellular ions included

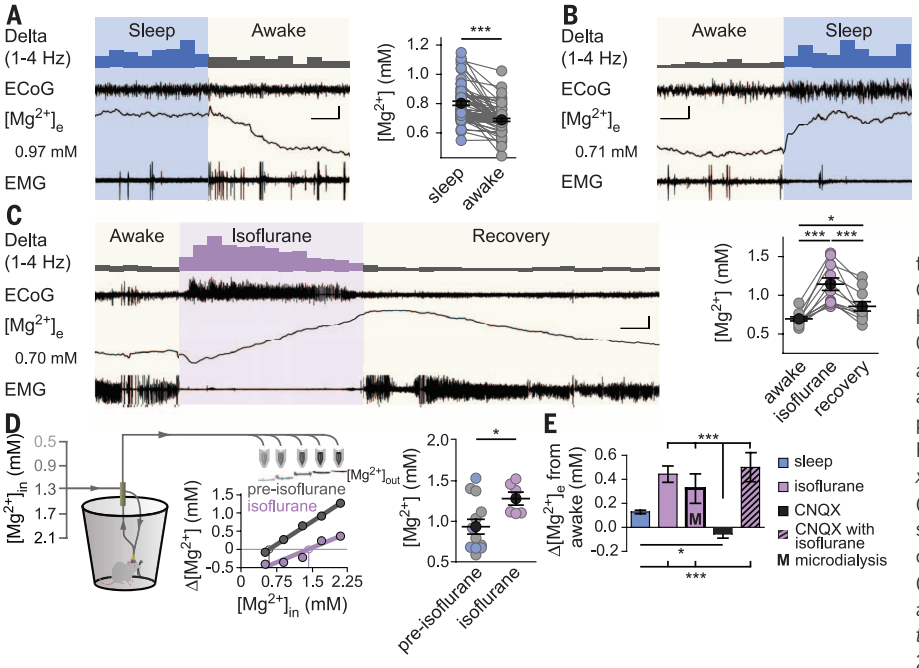

Fig. 4. Extracellular Mg^{2+} decreases during wakefulness. (**A** and **B**) Representative state transitions between sleep and awake ECoG, EMG, and Mg^{2+}-sensitive microelectrodes, with data summary. Initial $[Mg^{2+}]_e$ is given to the left of the ISM trace. n = 73 sleep-to-awake transitions (A) and 58 awake-to-sleep transitions (B). One-way ANOVA, $F(3, 258) = 28.13$, $P < 0.0001$. Post-hoc Tukey test, ***$P < 0.001$. Scale bars, x = 20 s, y = 0.05 mM $[Mg^{2+}]_e$, 0.33 mV EMG/ECoG. (**C**) Representative awake-to-isoflurane recording (ZT16 to ZT20) and summary of changes. n = 11 animals. One-way repeated measures ANOVA, $F(2,20) = 28.13$, $P < 0.0001$. Post-hoc Tukey test, *$P < 0.05$, ***$P < 0.001$. Scale bar, x = 5 min, y = 0.25 mM $[Mg^{2+}]_e$, 0.6 mV EMG/ECoG. (**D**) Schematic of microdialysis collection with data summary. Representative Mg^{2+}-ISM and no-net flux calculation are shown. Sleep (light blue) and awake (gray) are pooled and compared with isoflurane. n = 8 awake, 8 sleep, and 8 isoflurane animals. Two-tailed t test of isoflurane versus pre-isoflurane, $t(16) = 2.427$, $P = 0.0274$ (*$P < 0.05$). (**E**) Comparison of state-dependent $[Mg^{2+}]_e$ shifts from awake-to-sleep, isoflurane, CNQX, and awake + CNQX to isoflurane + CNQX. n = 6 awake-to-CNQX animals and 6 awake + CNQX-to-isoflurane + CNQX animals. One-way ANOVA of relative state-dependent shifts, $F(4,167) = 27.31$, $P < 0.0001$. Post-hoc Tukey test, **$P < 0.01$, ***$P < 0.001$. Mean (black circle) ± SEM.

Downloaded from http://science.sciencemag.org/ on April 28, 2016

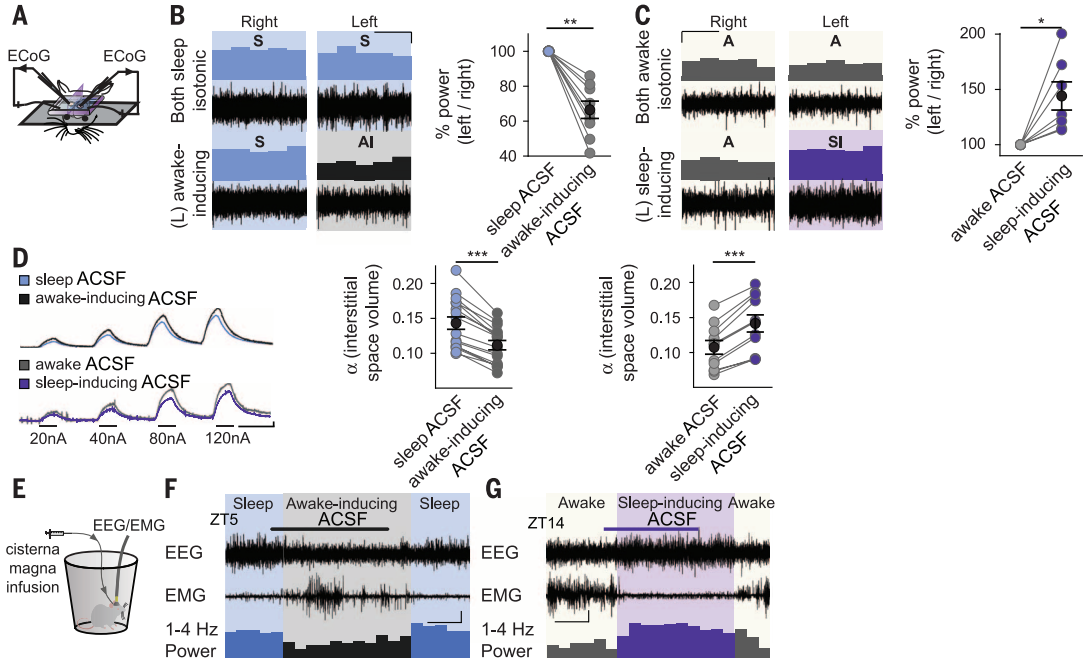

Fig. 5. Imposing changes in extracellular ion concentrations alter local activity, extracellular space, and behavioral state. (**A**) Schematic of double-cranial window recording setup. Symmetrically positioned, separate cranial windows over opposing somatosensory cortices were prepared with ECoGs simultaneously recorded in both hemispheres. (**B** and **C**) Representative ECoG recordings in (B) sleeping (ZT4 to ZT8), and (C) awake (ZT16 to ZT20) mice. (Top) Representative recordings in ACSF mimicking natural state-dependent interstitial ion composition. (Bottom) Recordings after change of left-hemisphere ACSF to (B) awake-inducing or (C) sleep-inducing ACSF. (Right) Summary of 1- to 4-Hz ECoG power shift in the left hemisphere, normalized to the right, after change to (B) awake-inducing or (C) sleep-inducing ACSF. Paired *t* test of 1- to 4-Hz power shifts, (A) $t(8) = 3.530$, $P = 0.008$; (B) $t(6) = 3.091$, $P = 0.0214$. $^{*}P < 0.05$, $^{**}P < 0.01$. Scale bar, $x = 4$ min, $y = 10\%$. (**D**) TMA^{+} traces of shifts in extracellular space volume (α) after switch from sleep to awake-inducing ACSF (top trace) or awake to sleep-inducing ACSF (bottom trace). Higher amplitude equals decreased dilution of TMA^{+} and smaller extracellular space. Data are summarized to the right. Paired *t* test, awake-inducing, $n = 16$ animals; $t(15) = 11.04$, $P < 0.0001$; sleep-inducing, $n = 11$ animals; $t(10) = 8.95$, $P < 0.0001$, $^{**}P < 0.01$. Scale bars, $x = 2$ min, $y = 2$ mV. (**E**) Schematic of cisterna-magna infusion and wire EEG/EMG recording setup. (**F** and **G**) Representative traces showing EEG and EMG activity before, during, and after a 0.3- to 0.5-μl min^{-1} infusion of modified (F) awake-inducing or (G) sleep-inducing ACSF into the cisterna magna. The 1- to 4-Hz relative power (percentage of 1 to 32 Hz) is presented in averaged 10-min bins below. Infusion was run between (F) ZT5.5 and ZT7 (gray bar) and (G) ZT15 and ZT16.5 (purple bar) during sleep and awake periods, respectively. Scale bar, $x = 30$ min, $y = 0.5$ mV (F) and 1mV (G).

widespread cortical areas because the samples were collected by 2-mm-long probes.

All ions exhibited far more consistent, rapid transitions during arousal relative to falling asleep. This is consistent with the need to quickly shift from sleep to awake states when presented with novel, threatening, or unexpected stimuli, and with the overarching ability of brainstem neuromodulatory centers to drive near-immediate responses to behaviorally relevant events (*12*). Relative to $[K^{+}]_e$, the fivefold slower transition of $[Ca^{2+}]_e$ and $[Mg^{2+}]_e$ may reflect differences in the transport or buffering of these ions and suggests that beyond the immediate capacity of neuromodulators to drive quick arousal, it takes longer for composition of interstitial ions to fully stabilize. $[Ca^{2+}]_e$ and $[Mg^{2+}]_e$ exhibited very slow recoveries after anesthesia, often lasting 10 to 30 min. Ions appeared to exhibit larger shifts in the immediate post-induction and recovery period. This biphasic activity may suggest a complex shift in neuromodulatory activity during these anesthetic transitions and, with $[Ca^{2+}]_e$ and $[Mg^{2+}]_e$ taking much longer than $[K^{+}]_e$ to return to a stable awake concentration, may relate to the confusion and postoperative delirium that follows general anesthesia. In fact, high levels of serum $[Ca^{2+}]_e$ and $[Mg^{2+}]_e$ can manifest as subacute delirium (*7*).

Previous studies have shown that $[Mg^{2+}]_e$ in the CNS is in the range of ~0.8 to 1.2 mM or slightly lower than in plasma (*13*, *14*), but $[Mg^{2+}]_e$ homeostasis has received little attention (*15*). In electrophysiological studies, manipulation of $[Mg^{2+}]_e$ is commonly used because low $[Mg^{2+}]_e$ relieves the depolarization block of the *N*-methyl-D-aspartate (NMDA) receptors and facilitates induction of long-term potentiation (LTP) and, in more extreme cases, seizure (*7*, *16*). Wakefulness and sleep deprivation are linked to up-regulation of pathways downstream of NMDA receptor activation, including CamKII, extracellular signal–regulated kinase (ERK), and pCreb (*1*, *17*). The decline in $[Mg^{2+}]_e$ during wakefulness may thereby, in combination with membrane depolarization induced by the elevation of $[K^{+}]_e$, contribute to the gene expression pattern characteristic of wakefulness. The finding that $[Mg^{2+}]_e$ increases during sleep is consistent with the observation that changes in dietary magnesium can have a profound impact on learning and memory, possibly by improving both the amount and quality of sleep (*18*, *19*).

Arousal is triggered by the concerted activity of neurons located in the brainstem, hypothalamus, and basal forebrain (*1*, *4*). Projections from these clusters of neurons release norepinephrine, acetylcholine, orexin, serotonin, dopamine, and histamine over widespread areas of the CNS (*12*). Considerable redundancy exists in the system; acute antagonism, ablation, or activation has documented the importance of the individual components in regulating arousal, but such perturbations rarely produce long-term effects (*12*). An unanswered question is how these neuromodulators drive global changes in EEG activity. Conventional thinking is that the neuromodulators alter the membrane properties and spiking activity of select subtypes of neurons (*5*). Our findings show that a parallel path exists: A cocktail of neuromodulators consistently increased $[K^{+}]_e$ in cortical slices, and TTX did not significantly suppress the $[K^{+}]_e$ increase, suggesting that this shift is not merely a consequence of local synaptic activity. In vivo, inhibition of AMPA receptors only transiently reduced $[K^{+}]_e$, with levels returning to baseline in <10 min despite continued suppression of ECoG activity by >60% (Fig. 2E and fig. S2). This response to an external challenge suggests that ionic homeostasis is tightly regulated in a state-dependent, neuronal activity–independent manner. On the basis of this, we propose that the neuromodulators—in addition to their well-documented, direct effect on neuronal activity—maintain sleep and awake states by creating a state-dependent set-point for interstitial ion concentrations that stabilize over seconds to minutes, minimizing changes that result from transient burst firing or suppression of these brainstem nuclei. In sleep and anesthesia, lower concentrations of $[K^{+}]_e$ will tend to hyperpolarize neurons, with high $[Ca^{2+}]_e$ and $[Mg^{2+}]_e$ enhancing this effect through

Downloaded from http://science.sciencemag.org/ on April 28, 2016

surface-charge screening and inactivation of the NALCN channel–dependent Na^+-leak current (*20*). High $[Mg^{2+}]_e$ in combination with hyperpolarization will reduce the likelihood of NMDA receptor activation during sleep, reducing the brain's ability to undergo activity-dependent changes in excitatory transmission (LTP). Manipulation of $[K^+]_e$, $[Ca^{2+}]_e$, and $[Mg^{2+}]_e$ in the CSF bathing the brain drove behavioral shifts between sleep and awake states (Fig. 5). Astrocytic Ca^{2+} signaling is also enhanced by lowering of $[Ca^{2+}]_e$ and $[Mg^{2+}]_e$ (*21*–*23*) and is strongly inhibited by anesthesia (*24*).These observations suggest that regulation of extracellular ion homeostasis is sufficient to alter behavioral state both locally and globally, providing a path for neuromodulators to exert consistent, stable shifts in neuronal and astrocytic activity across the brain.

A myriad of electrophysiological slice studies have in the past taken advantage of minor modifications in the ion composition of the bath solution to induce stable and highly reproducible changes in neural excitability. The observations presented here suggest that the CNS itself uses the same trick to control state-dependent changes in neuronal activity. One advantage of this "ionostatic control" of neural activity is to provide a backdrop for coordinating shifts in behavioral state through the widespread regulation of excitability without relying on complex receptor activation in diverse subclasses of neurons. The characteristic state-dependent pattern of EEG activity can, at least in part, be explained by differences in extracellular ion composition in sleep versus wakefulness. Our observations add new and critical insight into understanding what drives arousal, as well as the loss of consciousness during sleep and anesthesia. Future studies should define whether changes in extracellular ion concentrations are involved in disorders such as stupor and coma.

REFERENCES AND NOTES

1. G. Tononi, C. Cirelli, *Neuron* **81**, 12–34 (2014).
2. J. H. Benington, H. C. Heller, *Prog. Neurobiol.* **45**, 347–360 (1995).
3. V. Hinard *et al.*, *J. Neurosci.* **32**, 12506–12517 (2012).
4. C. B. Saper, T. E. Scammell, J. Lu, *Nature* **437**, 1257–1263 (2005).
5. J. O'Donnell, D. Zeppenfeld, E. McConnell, S. Pena, M. Nedergaard, *Neurochem. Res.* **37**, 2496–2512 (2012).
6. M. Steriade, D. A. McCormick, T. J. Sejnowski, *Science* **262**, 679–685 (1993).
7. G. G. Somjen, *Ions in the Brain: Normal Function, Seizures, and Stroke* (Oxford Univ. Press, 2004).
8. J. Seigneur, D. Kroeger, D. A. Nita, F. Amzica, *Cereb. Cortex* **16**, 655–668 (2006).
9. S. M. Rothman, *Science* **220**, 536–537 (1983).
10. L. Xie *et al.*, *Science* **342**, 373–377 (2013).
11. M. Anděrová *et al.*, *Glia* **35**, 189–203 (2001).
12. C. B. Saper, P. M. Fuller, N. P. Pedersen, J. Lu, T. E. Scammell, *Neuron* **68**, 1023–1042 (2010).
13. A. J. Hansen, *Physiol. Rev.* **65**, 101–148 (1985).
14. L. Sun *et al.*, *Magnes. Res.* **22**, 266–272 (2009).
15. A. M. Romani, *Arch. Biochem. Biophys.* **512**, 1–23 (2011).
16. W. W. Anderson, D. V. Lewis, H. S. Swartzwelder, W. A. Wilson, *Brain Res.* **398**, 215–219 (1986).
17. G. F. Gilestro, G. Tononi, C. Cirelli, *Science* **324**, 109–112 (2009).
18. B. Abbasi *et al.*, *J. Res. Med. Sci.* **17**, 1161–1169 (2012).
19. I. Slutsky *et al.*, *Neuron* **65**, 165–177 (2010).
20. B. Lu *et al.*, *Neuron* **68**, 488–499 (2010).
21. J. Schummers, H. Yu, M. Sur, *Science* **320**, 1638–1643 (2008).
22. H. Sontheimer, *Glia* **11**, 156–172 (1994).
23. A. Torres *et al.*, *Sci. Signal.* **5**, ra8 (2012).
24. A. S. Thrane *et al.*, *Proc. Natl. Acad. Sci. U.S.A.* **109**, 18974–18979 (2012).

ACKNOWLEDGMENTS

This study was supported by NIH (NS078167 and NS078304) and the Office of Naval Research/Department of the Navy. We thank W. Song, R. Rasmussen, E. Nicholas, and W. Peng for expert technical assistance and C. Cirelli, G. Tononi, W. Wang, and C. Nicholson for comments on the manuscript. All authors contributed to data collection, technical design, and writing.

SUPPLEMENTARY MATERIALS

www.sciencemag.org/content/352/6285/550/suppl/DC1
Materials and Methods
Figs. S1 to S5
Table S1
References (*25*–*45*)

18 September 2015; accepted 24 March 2016
10.1126/science.aad4821

REPRODUCTIVE BIOLOGY

Unconventional endocannabinoid signaling governs sperm activation via the sex hormone progesterone

Melissa R. Miller,[1] Nadja Mannowetz,[1] Anthony T. Iavarone,[2] Rojin Safavi,[1] Elena O. Gracheva,[3] James F. Smith,[4] Rose Z. Hill,[1] Diana M. Bautista,[1] Yuriy Kirichok,[5] Polina V. Lishko[1]*

Steroids regulate cell proliferation, tissue development, and cell signaling via two pathways: a nuclear receptor mechanism and genome-independent signaling. Sperm activation, egg maturation, and steroid-induced anesthesia are executed via the latter pathway, the key components of which remain unknown. Here, we present characterization of the human sperm progesterone receptor that is conveyed by the orphan enzyme α/β hydrolase domain–containing protein 2 (ABHD2). We show that ABHD2 is highly expressed in spermatozoa, binds progesterone, and acts as a progesterone-dependent lipid hydrolase by depleting the endocannabinoid 2-arachidonoylglycerol (2AG) from plasma membrane. The 2AG inhibits the sperm calcium channel (CatSper), and its removal leads to calcium influx via CatSper and ensures sperm activation. This study reveals that progesterone-activated endocannabinoid depletion by ABHD2 is a general mechanism by which progesterone exerts its genome-independent action and primes sperm for fertilization.

According to the conventional model of steroid signaling, steroid hormones act through their corresponding genomic receptors to regulate gene expression in development, metabolism, and reproduction (*1*, *2*). The time scale of these signaling events ranges from hours to days (*2*). However, there is a much faster pathway that alters ion channel activity through steroid activation of membrane receptors. Nongenomic signaling of the steroid hormone progesterone (P4) occurs on a time scale of seconds and is required for distinct physiological events, such as oocyte maturation (*3*) and human sperm cell activation (*4*, *5*), and P4 likely triggers anesthesia in rodents (*6*). Many tissues have both nuclear and membrane progesterone receptors, which complicates identification of the latter. Because sperm are transcriptionally silent cells and, therefore, lack the nuclear progesterone receptor effect, we used human spermatozoa as a cellular model to identify the nongenomic progesterone receptor.

Progesterone is a major component of follicular fluid and is released by ovaries and cumulus cells that surround the oocyte. Nanomolar concentrations of P4 act through the nongenomic P4 receptor pathway and cause robust elevation of sperm cytoplasmic $[Ca^{2+}]$ (*7*–*9*) through the activation of the cation channel, CatSper (*10*–*14*). This rise in intracellular $[Ca^{2+}]$ leads to changes in sperm motility, known as hyperactivation, and primes sperm for acrosomal exocytosis (*4*, *5*, *15*). Here, we show that the orphan enzyme α/β hydrolase domain–containing protein 2 (ABHD2) serves as a sperm progesterone receptor. It functions as a lipid hydrolase by removing endogenous CatSper inhibitors upon association with P4. Thus,

[1]Department of Molecular and Cell Biology, University of California, Berkeley, CA 94720, USA. [2]QB3/Chemistry Mass Spectrometry Facility, University of California, Berkeley, CA 94720, USA. [3]Department of Cellular and Molecular Physiology; Department of Neuroscience, Program in Cellular Neuroscience, Neurodegeneration, and Repair (CNNR), Yale School of Medicine, Yale University, New Haven, CT 06536, USA. [4]Department of Urology, University of California, San Francisco, CA 94143, USA. [5]Department of Physiology, University of California, San Francisco, CA 94158, USA.
***Corresponding author. Email: lishko@berkeley.edu**

Downloaded from http://science.sciencemag.org/ on April 28, 2016

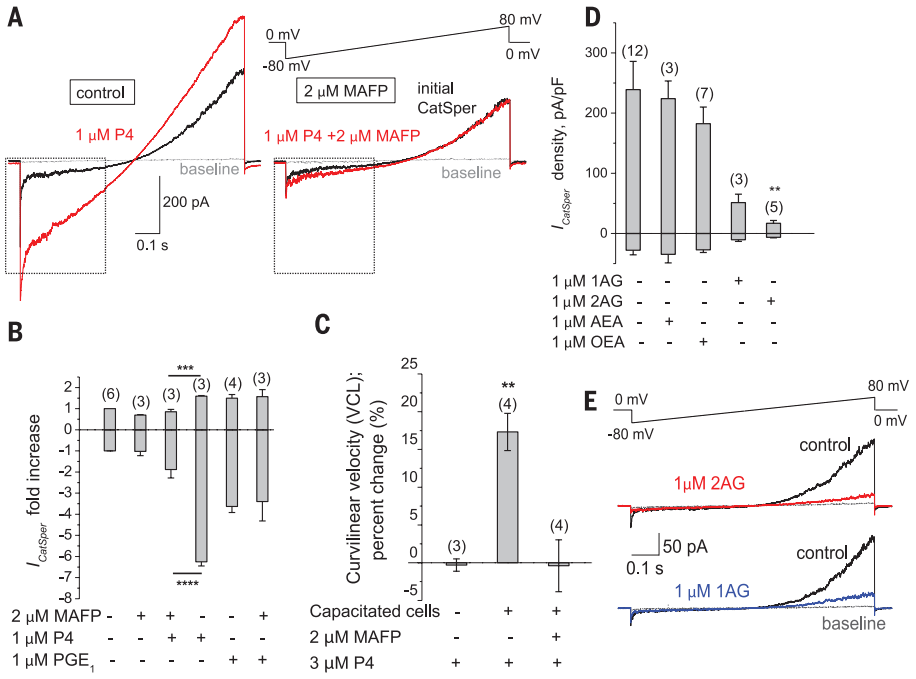

Fig. 1. Inhibition of sperm mSHs removes P4-dependent CatSper activation. (**A**) (Left) Representative $I_{CatSper}$ recorded from control human spermatozoa in the absence (black) and presence (red) of P4. (Right) $I_{CatSper}$ recorded from human spermatozoa pretreated with MAFP, an irreversible serine hydrolase inhibitor, for 30 min in the absence or presence of P4. (**B**) Fold increase of $I_{CatSper}$ in response to P4, PGE_1, and MAFP. (**C**) Human capacitated spermatozoa do not hyperactivate in response to P4 if pretreated with MAFP, as recorded with computer-aided sperm analyses (CASA). (**D**) Arachidonoylglycerols are inhibitors of $I_{CatSper}$. $I_{CatSper}$ densities are obtained at +80 mV (positive scale) or −80 mV (negative scale). (**E**) Representative $I_{CatSper}$ in the absence (black) or presence of the corresponding endocannabinoid. Data are represented as means ± SEM; numbers in parentheses indicate the number of experiments; and ****P < 0.0001, ***P < 0.001, **P < 0.005.

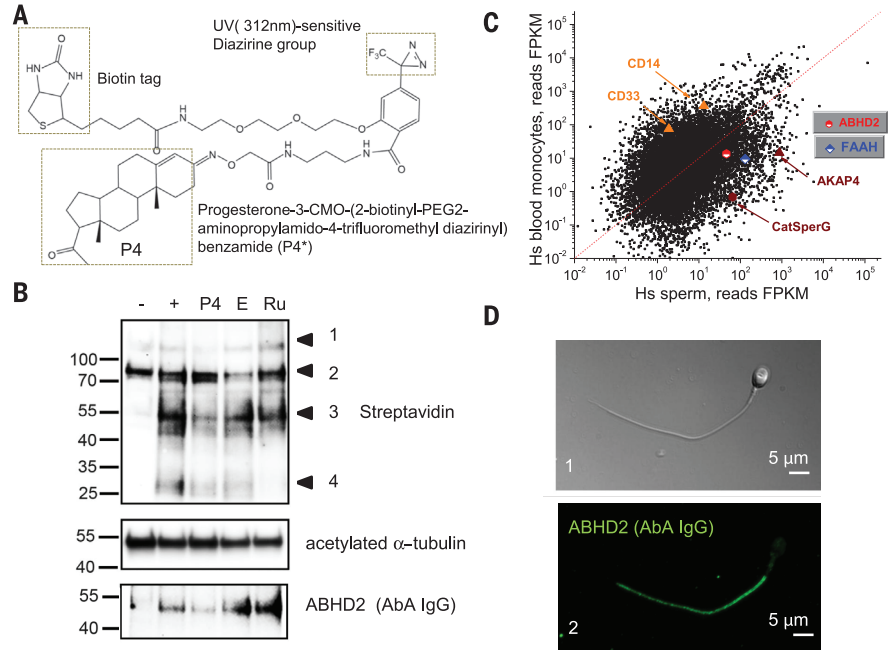

Fig. 2. Photoreactive progesterone analog P4* activates $I_{CatSper}$ and associates with P4 receptor. (**A**) P4* consists of an active group (progesterone), a diazirine–UV-sensitive moiety, and a biotin tag that allows for pull-down of bound proteins. CMO, (*O*-carboxymethyl)oxime; PEG, polyethylene glycol. (**B**) Western blot from P4* binding experiments resolves biotinylated (P4*-bound) proteins. Lanes are labeled –, mock-irradiated cells; +, UV-treated cells; P4, P4 (20 µM); E, estrogen (0.5 µM); and Ru, Ru486 (0.5 µM). Acetylated α-tubulin (middle) staining was used as the loading control. (Bottom) The blot was probed with AbA. One experiment out of six independent pull-downs is shown. (**C**) ABHD2 is present in the human sperm transcriptome. mRNA sequencing (mRNA-seq) reads from human blood monocytes and sperm cells. FPKM, fragments per kilobase of transcript per million mapped reads. Red line indicates expected number of sequencing reads for genes with similar expression levels in the two samples. *CatSperG* and *AKAP4* indicate sperm-specific transcripts; *CD14* and *CD33* indicate monocyte-specific transcripts. Transcripts for *FAAH* and *abhd2* are also shown. (**D**) Immunostaining of human spermatozoa with AbA and a corresponding differential interference contrast (DIC) image of the same cell.

this unconventional lipid-signaling event is responsible for sperm activation and is vital for sperm fertility.

Serine hydrolases are involved in CatSper activation by progesterone

The CatSper complex comprises seven subunits that together form the sperm-specific cation channel expressed exclusively within the flagellum (*11*–*14*, *16*, *17*). Functional expression of CatSper in heterologous systems has not been achieved; therefore, characterization of this channel is limited to sperm. Spermatozoa are transcriptionally silent and, therefore, lack conventional P4 genomic signaling. By applying the patch-clamp technique in whole-cell mode (*13*, *18*) and depleting sperm from all hydrophilic intracellular and extracellular second messengers, we have shown that CatSper is activated by P4 in a nongenomic manner (*7*). This activation could take place under two scenarios: Either P4 binds directly to CatSper or P4 binds to a separate target, which initiates lipid signaling within the sperm plasma membrane and ultimately leads to CatSper activation. To test the latter, we pharmacologically inhibited sperm metabolic serine hydrolases (mSHs), enzymes that participate in metabolism of phospholipids and endocannabinoids (*19*). Recording P4-induced channel activation in the absence or presence of the irreversible mSH inhibitor, methyl arachidonyl fluorophosphanate (MAFP), resulted in complete removal of P4-dependent activation of CatSper (Fig. 1, A and B) but showed no effect on basal CatSper activity (Fig. 1B and fig. S1, A and B). Moreover, MAFP treatment ablated P4-induced motility changes,

Downloaded from http://science.sciencemag.org/ on April 28, 2016

which further supports the idea that physiological P4 effects are a result of indirect activation of CatSper (Fig. 1C and fig. S1C). Note that MAFP had no appreciable influence on prostaglandin E1 (PGE_1)–stimulated CatSper activation, which indicates a potential direct effect of PGE_1 on CatSper (Fig. 1B and fig. S1D).

Regulation of CatSper by endocannabinoids

Lysophospholipids and endocannabinoids were previously found to be mSH substrates (*19*). We have therefore assessed these lipids for their involvement in CatSper regulation. Neither lysophosphatidylinositol nor lysophosphatidylethanolamine affected $I_{CatSper}$ (fig. S2); thus, their involvement in CatSper activation is unlikely. The family of endocannabinoids includes anandamide (AEA), oleamide (OEA), and monoacylglycerols: 2-arachidonoylglycerol (2AG) and 1-arachidonoylglycerol (1AG). Application of either AEA or OEA had no effect (Fig. 1D and fig. S2), whereas 1AG and 2AG (AGs) inhibited $I_{CatSper}$ (Fig. 1, D and E, and fig. S3A). The compounds differ, however, in their rate of CatSper inactivation: 2AG acts twice as fast as 1AG (fig. S3, B to D). When applied extracellularly, 2AG inhibits $I_{CatSper}$ with a median inhibitory concentration (IC_{50}) of 350 nM for outward currents and 670 nM for inward currents (fig. S3, E and F). Intracellular application of 2AG could not mimic this effect (fig. S4, A and B), which highlights the importance of an extracellular pool of this lipid in the mechanism of action. Extracellular glycerol did not ablate $I_{CatSper}$ or its regulation by P4, which indicated that hydrophobic tails of AGs are likely responsible for their effect on $I_{CatSper}$ (fig. S4, B and C).

To investigate whether AGs are endogenous CatSper regulators, we performed selective lipid extraction from sperm plasma membrane followed by unbiased identification of lipids by liquid chromatography–mass spectrometry (LC-MS). To selectively extract lipids, we developed a cyclodextrin-based protocol that allows removal of steroids and single-tailed lipids, such as AGs, while leaving multitailed lipids in the membrane. We determined that spermatozoa initially have relatively large amounts of AGs and that, after normalization to internal standards and taking into account the dimensions of human sperm flagellum (45 μm by 0.5 μm, with an average volume of 8.8 fl), the concentration of AGs in a spermatozoon could reach at least 0.7 μM. Upon P4 treatment, AG content decreases to that observed in cell-free controls (figs. S4D and S5). Our results show that AGs are detected in the sperm plasma membrane and that their content is drastically reduced upon P4 stimulation. Thus, P4 appears to act through mSHs to deplete AGs in plasma membrane, which leads to CatSper activation.

P4 receptor identification

On the basis of our previous work using cell-impermeable P4 to activate $I_{CatSper}$ (*7*), the P4 target is localized to the outer leaflet of the plasma membrane. This suggests that the P4 receptor is either a peripheral membrane protein or a transmembrane protein with mSH activity. The P4 receptor is not anchored by glycosylphosphatidylinositol (GPI), because removing GPI-anchored proteins from sperm by treating them with phosphoinositide phospholipase C does not remove $I_{CatSper}$ P4 sensitivity (fig. S6, A and B). In order to identify human spermatozoa's P4 binding partner, we designed a P4 analog (P4*) that is active toward CatSper, and upon activation with ultraviolet (UV) light, this analog covalently binds to its neighboring molecules (Fig. 2A; fig. S6, B and C; and fig. S7). The same compound contains a biotin tag that allows for pull-down. Next, we treated human spermatozoa with P4*, followed by UV exposure, streptavidin-assisted purification, and binding-protein identification using LC and tandem MS (LC-MS/MS) (Fig. 2B). To determine the specificity of P4* binding, mock-irradiated cells, as well as cells treated in the presence of excess unlabeled P4, were included as negative controls. To triage P4*-positive bands, we used estrogen and progestin Ru486, which do not interfere with P4 activation of CatSper (*7*). Pull-down experiments revealed four distinct biotin-positive bands (Fig. 2B, bands 1 to 4), although only a single ~50 kD band was present in positive controls and absent or reduced from all negative controls. MS analysis of this specific protein band resulted in 1233 unique peptides that correspond to 169 proteins (database S1). We did not identify any CatSper subunits from our six independent pull-down experiments, which suggests that the sperm P4 receptor is not a component of CatSper. Next, we searched for the candidate molecules that specifically bind P4*. We based this search on five criteria applicable to proteins identified by our pull-down: (i) the candidate should be present in all pull-down experiments except for negative controls; (ii) it should be either a transmembrane protein with an extracellular domain, or a protein tightly associated with the membrane, through a linkage distinct from GPI-anchor; and (iii) the P4 target should function independently from CatSper with mSH activity, as the P4 effect on CatSper is fully reversible in the absence of exogenous energy sources (*7*, *8*). The enzymatic changes imposed on mSH substrates can be removed in an energy-independent manner, unlike the effect of other serine protease or amidases. Also, (iv) the P4 target should be expressed in sperm on the level of mRNA and

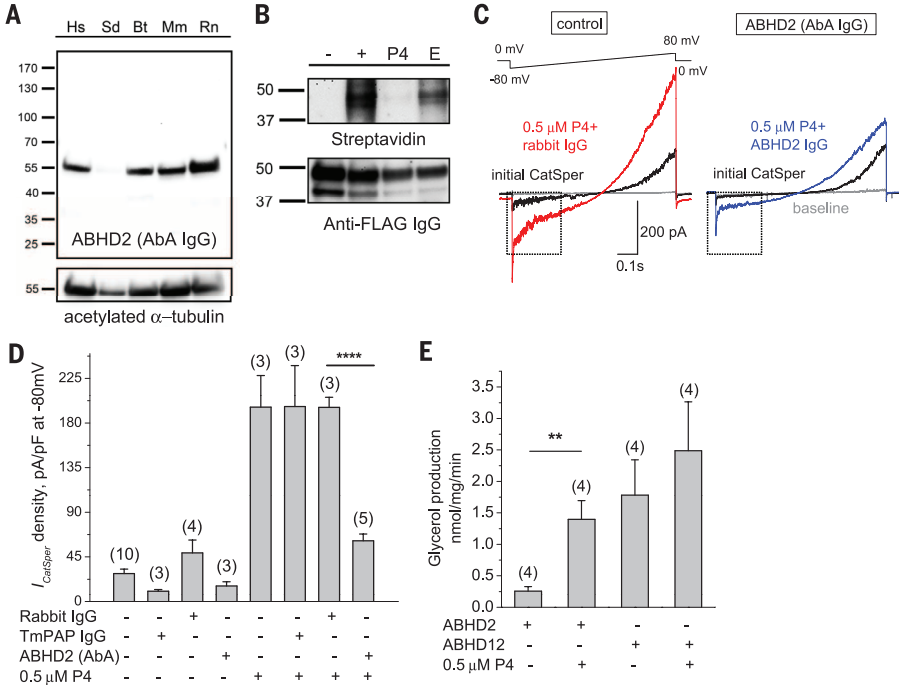

Fig. 3. ABHD2 is expressed in human spermatozoa and acts as a P4-dependent lipid hydrolase. (**A**) ABHD2 expression in sperm from various mammalian species: Hs, humans; Sd, boar; Bt, bovine; Mm, mouse; and Rn, rat. Acetylated α-tubulin was used as the loading control. (**B**) Western blot from P4*-binding experiments of recombinant ABHD2 expressed in human embryonic kidney 293 (HEK293) cells resolves biotinylated proteins. Lane labeling is as in Fig. 2B. FLAG staining was used as the loading control for recombinant ABHD2 expression. (**C**) AbA prevents P4 activation of human $I_{CatSper}$. Representative $I_{CatSper}$ treated with nonspecific IgG (left) or ABHD2 immunoglobulin G (IgG) (right). $I_{CatSper}$ values were recorded from control sperm or sperm treated with 1:100 dilutions of either nonspecific IgG or AbA for ~30 min. (**D**) $I_{CatSper}$ densities extracted from ramps shown in (C). (**E**) Monoacylglycerol hydrolysis by recombinant ABHD2 and ABHD12 in the presence or absence of 0.5 μM P4. Data are represented as means ± SEM; numbers in parentheses indicate number of experiments; and $^{****}P < 0.0001$, $^{***}P < 0.001$, $^{**}P < 0.005$.

Downloaded from http://science.sciencemag.org/ on April 28, 2016

protein to exclude epididymal-derived proteins, as testicular CatSper retains P4 sensitivity (*8*). Finally, (v) the P4 receptor should localize to the flagellum, because flagellar CatSper is P4 sensitive (*7*).

Selection of the candidates

Based on the three initial criteria, top candidates were identified: fatty-acid amide hydrolase 1 (FAAH), ABHD2, and prostatic acid phosphatase, which has a transmembrane domain containing splice isoform (TmPAP) (fig. S8). The first two candidates are members of a large family of mSHs, whereas the last candidate is an acid-activated phosphatase with hydrolase activity. We ruled out TmPAP involvement by exposing $I_{CatSper}$ to two extracellular pHs, 6.6 and 7.4 (fig. S2), and observed no activity differences between these recordings, which suggested that activation of TmPAP is not sufficient for CatSper stimulation. In addition, activity of recombinantly expressed TmPAP is not altered by P4 or by addition of TmPAP-specific antibodies (fig. S9). To test FAAH involvement, we recorded $I_{CatSper}$ from spermatozoa before and after treatment with PF750, an irreversible selective FAAH inhibitor. This treatment had no effect upon $I_{CatSper}$ (fig. S2). If FAAH is the P4 target, its native substrate, AEA, would mimic P4 action. However, AEA does not change $I_{CatSper}$ (Fig. 1D and fig. S2), which suggests that neither activation nor inhibition of FAAH affects CatSper and so rules out FAAH involvement in P4-dependent CatSper activation.

ABHD2 is present in sperm and acts as a P4-activated lipid hydrolase

Our last candidate, ABHD2, is a member of a superfamily of mSHs with unknown activity. In pull-down experiments, ABHD2 was specifically detected in all lanes, except for negative controls (Fig. 2B). We confirmed that ABHD2 meets our last two requirements: It is functionally expressed in sperm at the level of mRNA and protein and is confined to the same cellular compartment as the CatSper (Fig. 2, B to D, and figs. S10 and S11A). Antibodies (Abs) against ABHD2 (AbAs) detected the protein in spermatozoa of various mammalian species: humans, boar, bovine, mouse, and rat (Fig. 3A and fig. S11B). ABHD2 transcripts are abundant in sperm, as evidenced by unbiased RNA deep sequencing of human spermatozoa and reverse transcription polymerase chain reaction experiments (Fig. 2C, fig. S11A, and database S2). To confirm that ABHD2 binds P4, we have carried out a P4* binding assay using recombinantly expressed ABHD2 (figs. S10 and S11C). Indeed, positive streptavidin staining revealed that ABHD2 binds P4* specifically and in a UV-dependent manner, and this binding is competed off by excess unlabeled P4 (Fig. 3B). Additionally, when human spermatozoa were incubated with AbAs, the result was a significant decrease of the CatSper activation by P4, whereas sperm treated with nonspecific antibodies retained their P4 sensitivity (Fig. 3, C and D, and figs. S9C and S11D). These results indicate that human ABHD2 is expressed in the sperm flagellum and is actively involved in P4-dependent signaling. Next, we explored human ABHD2's enzymatic activity. Because our lipid MS data showed a P4-dependent decrease in sperm AGs, we examined whether recombinant ABHD2 could hydrolyze AGs. Such hydrolysis results in the formation of glycerol and arachidonic acid (AA) (*20*), so we monitored free glycerol production as an indicator of ABHD2 activity. As controls, we used mock-transfected cells or recombinant ABHD12 (fig. S11E), another mSH with known activity toward AGs (*20*). ABHD2 revealed modest hydrolase activity unless supplemented with 0.5 μM P4 (Fig. 3E). P4 significantly enhanced ABHD2 activity, whereas it had no significant effect on ABHD12 (Fig. 3E). We also tested whether ABHD2 is responsible for P4-induced calcium influx in sperm flagella. Indeed, inactivation of ABHD2 with protein-specific antibodies or sperm exposure to MAFP both abolished P4-activated calcium influx into sperm flagella (Fig. 4, A and B, and movies S1 to S6).

ABHD2 is present in rodent acrosome

ABHD2 expression was also detected in mouse epididymal sperm cells (Fig. 4C). Our report (*7*) showed that murine CatSper is insensitive to P4 and, therefore, may lack ABHD2-dependent regulation. Murine and human ABHD2 proteins share a high degree of sequence similarity; however, their subcellular localizations in sperm are different. Unlike that in humans, murine ABHD2 is restricted to the acrosomal region and is absent from the flagellum (Fig. 4C). This may explain the absence of CatSper P4 sensitivity in these species, whereas P4-induced acrosome reaction (AR) is retained (*15*). On the basis of the ABHD2 localization in acrosome, it is possible that P4 activation of ABHD2 and consequent AA release could be required for AR. Indeed, both P4 and AA stimulate mouse AR to similar levels, whereas MAFP blocks the P4 effect (Fig. 4D and fig. S12). This suggests that mouse AR is dependent on mSH action and that ABHD2 may play a role in this process. Note that 2AG also inhibits mouse $I_{CatSper}$ but with less efficacy than it inhibits human $I_{CatSper}$ (fig. S13). Murine sperm gradually lose 2AG content as they travel through the epididymis (*21*), and high activity of monoacylglycerol AG hydrolase, the lipase MAGL, contributes to low resting AG levels (*22*). Thus, murine CatSper is no longer inhibited by endogenous AGs and, therefore, does not require P4 stimulation. In contrast, human spermatozoa retain substantial amounts of AGs, which keep CatSper shut and, thus, require ABHD2 to eliminate AGs upon P4 exposure. As ABHD2 degrades AGs and activates CatSper, the human sperm

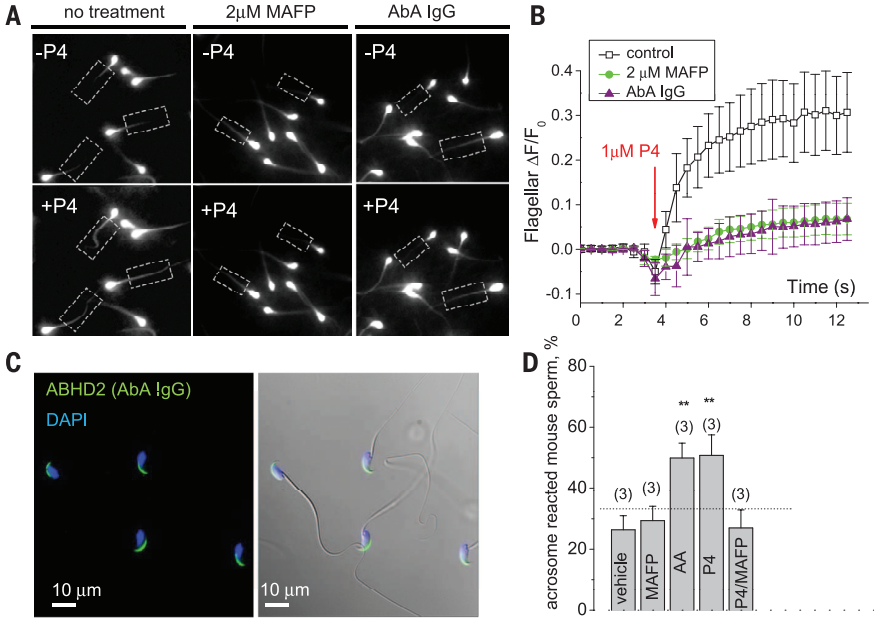

Fig. 4. ABHD2 regulates Ca^{2+} influx in human flagellum and is involved in mouse acrosome reaction. (**A**) Representative images from calcium imaging experiments before and after P4 treatment with regions of interest (ROIs) indicated. (**B**) Preincubation with either MAFP or AbA impeded P4-induced calcium influx. ΔF/F, the change in intensity from the original intensity before stimulation. Between 40 and 60 sperm flagella were assessed per condition. (**C**) Immunostaining of mouse cauda epididymal spermatozoa with AbA shows acrosomal localization. (Right) An overlay with DIC images. Nuclei were stained by 4′,6-diamidino-2-phenylindole (DAPI). (**D**) Percentage of AR murine spermatozoa in response to indicated treatments. Live, capacitated mouse spermatozoa were incubated with 3 μM P4, 3 μM AA, 2 μM MAFP, or vehicle (ethanol), after which they were imaged for the presence of intact acrosome. Data are represented as means ± SEM; numbers in parentheses indicate number of experiments; and $^{**}P < 0.005$.

Downloaded from http://science.sciencemag.org/ on April 28, 2016

membrane must also have a feedback mechanism for CatSper inactivation. Indeed, the sperm plasma membrane constantly produces AGs in order to keep CatSper closed. P4 application produced prolonged CatSper activation that slowly returns to basal levels when P4 is removed from the external solution (fig. S14). The rate of this "washout" matches precisely the rate of 2AG inhibition (fig. S3D), which supports the idea that human sperm cells constantly make AGs and that slow "washout" of P4 activation reflects the time-dependent replenishment of 2AG (figs. S3D and S14).

Human ABHD2 is a 425–amino acid molecule with a predicted N-terminal transmembrane domain, followed by an extracellularly facing domain. ABHD2 was identified as a candidate protein from our pull-down experiments. This fulfills two of our five requirements for the sperm nongenomic P4 receptor. ABHD2 participates in bioactive lipid signaling by hydrolyzing AGs in a P4-dependent manner, so they act as true mSHs. ABHD2 is functionally expressed in sperm and is confined to the flagellum alongside the CatSper channel. Taking into account that (i) ABHD2 is the only candidate molecule that meets all five search requirements and (ii) modulation of its function by pharmacological perturbation disrupts P4 signaling in sperm and impairs sperm activation, we conclude that the serine hydrolase ABHD2 is the nongenomic progesterone receptor of sperm.

Discussion

Metabolic serine hydrolases acting as monoacylglycerol lipases convert AGs into glycerol and AA. By hydrolyzing AGs in a P4-dependent manner, ABHD2 releases CatSper from AG inhibition, which liberates AA (fig. S15). During sperm transit through the epididymis, the plasma membrane undergoes lipid remodeling, which results in reduced levels of AA (*23*) and altered sperm motility (*24*), perhaps by means of modification of the ion channels' function. Indeed, we found that application of AA briefly activates CatSper, whereas prolonged incubation in 3 μM AA results in CatSper inactivation and loss of P4 sensitivity (fig. S16, A and B). In accordance with our model, an overabundance of AA should negatively regulate ABHD2 activity; therefore, continuous P4 application will result in a considerable accumulation of AA in the outer leaflet of the sperm plasma membrane, which would ultimately lead to CatSper desensitization. However, prolonged P4 exposure does not cause CatSper desensitization (*7*). It is possible then, that during exposure to P4, liberated AA diffuses into the inner membrane leaflet or is released into the extracellular medium. Indeed, under our experimental conditions, any compound released from the plasma membrane will be removed by continuous perfusion. It is possible that AA removal from the outer leaflet in vivo could be achieved by either fatty acid transporters or chelation by albumin, which is abundant in the female reproductive tract.

Both murine and human CatSper are upregulated by intracellular alkalinization (*7*, *13*); however, P4 exposure is also required for full human CatSper activation. This is explained by the fact that ejaculated human spermatozoa retain a substantial amount of 2AG; therefore, P4 activation of ABHD2 is needed for 2AG clearance. That MAFP-treated cells still respond to PGE_1 points to an intriguing possibility that PGE_1 may stimulate CatSper by allosteric activation of CatSper or may compete with 2AG directly for the binding site. Prostaglandins are derivatives of AA and are structurally similar to the 2AG tail; however, such a hypothesis requires additional experimental confirmation.

Regulation of male and female fertility by endocannabinoids has been explored previously, with particular focus on anandamide (*25*), whereas the role of 2AG in reproductive tissues is not well investigated. This study fills the gap by showing an important role of 2AG in sperm activation. It is possible that the P4-ABHD2-endocannabinoid axis could also regulate female reproduction by a similar mechanism. In fact, the expression of endocannabinoid system components was previously linked with genomic steroid activity (*26*, *27*). However, our results indicate that progesterone can affect the level of endocannabinoids by binding ABHD2 and directly activating its hydrolase activity. The P4 binding site for this protein seems to be unique and does not resemble the classical steroid-binding pocket (*28*) on the basis of sequence similarity. Furthermore, competitive ligands of classical P4 signaling have no effect on the nongenomic action (Fig. 2B) (*7*).

In conclusion, we have characterized a novel function of ABHD2, which metabolizes endocannabinoids 1AG and 2AG only in the presence of progesterone. Moreover, we show that AGs act as endogenous inhibitors of CatSper. Upon P4 stimulation, ABHD2 hydrolyzes these endocannabinoids and that, together with intracellular alkalinization, leads to CatSper opening and triggers sperm hyperactivation, which makes spermatozoa fertile. Characterization of P4-dependent endocannabinoid hydrolysis reveals the missing link in nongenomic steroid signaling that regulates sperm activation. In addition, our model suggests that AGs are continuously produced to block CatSper, unless progesterone stimulates their hydrolysis by ABHD2 contradicting the "on-demand synthesis model" of endocannabinoid activity, whereby these lipids act only upon stimulus-dependent release from their precursors. Identification of ABHD2 as the nongenomic progesterone receptor of sperm provides a new target for developing novel contraceptives. Given the widespread expression of ABHD2 (*29*), the progesterone-ABHD2 axis is likely a critical component of the nongenomic action of this steroid in other tissues.

REFERENCES AND NOTES

1. R. M. Evans, *Science* **240**, 889–895 (1988).
2. R. Lösel, M. Wehling, *Nat. Rev. Mol. Cell Biol.* **4**, 46–55 (2003).
3. A. Revelli, M. Massobrio, J. Tesarik, *Endocr. Rev.* **19**, 3–17 (1998).
4. P. F. Blackmore, S. J. Beebe, D. R. Danforth, N. Alexander, *J. Biol. Chem.* **265**, 1376–1380 (1990).
5. E. Baldi *et al.*, *J. Androl.* **12**, 323–330 (1991).
6. P. Poisbeau *et al.*, *Front. Cell. Neurosci.* **8**, 174 (2014).
7. P. V. Lishko, I. L. Botchkina, Y. Kirichok, *Nature* **471**, 387–391 (2011).
8. J. F. Smith *et al.*, *Proc. Natl. Acad. Sci. U.S.A.* **110**, 6823–6828 (2013).
9. T. Strünker *et al.*, *Nature* **471**, 382–386 (2011).
10. T. A. Quill, D. Ren, D. E. Clapham, D. L. Garbers, *Proc. Natl. Acad. Sci. U.S.A.* **98**, 12527–12531 (2001).
11. D. Ren *et al.*, *Nature* **413**, 603–609 (2001).
12. A. E. Carlson *et al.*, *Proc. Natl. Acad. Sci. U.S.A.* **100**, 14864–14868 (2003).
13. Y. Kirichok, B. Navarro, D. E. Clapham, *Nature* **439**, 737–740 (2006).
14. P. V. Lishko *et al.*, *Annu. Rev. Physiol.* **74**, 453–475 (2012).
15. R. A. Osman, M. L. Andria, A. D. Jones, S. Meizel, *Biochem. Biophys. Res. Commun.* **160**, 828–833 (1989).
16. J. J. Chung *et al.*, *Cell* **157**, 808–822 (2014).
17. H. Qi *et al.*, *Proc. Natl. Acad. Sci. U.S.A.* **104**, 1219–1223 (2007).
18. P. Lishko, D. E. Clapham, B. Navarro, Y. Kirichok, *Methods Enzymol.* **525**, 59–83 (2013).
19. J. Z. Long, B. F. Cravatt, *Chem. Rev.* **111**, 6022–6063 (2011).
20. J. L. Blankman, G. M. Simon, B. F. Cravatt, *Chem. Biol.* **14**, 1347–1356 (2007).
21. G. Cobellis *et al.*, *Biol. Reprod.* **82**, 451–458 (2010).
22. G. Catanzaro *et al.*, *Mol. Cell. Endocrinol.* **343**, 88–92 (2011).
23. H. Rejraji *et al.*, *Biol. Reprod.* **74**, 1104–1113 (2006).
24. A. Lenzi *et al.*, *Mol. Hum. Reprod.* **6**, 226–231 (2000).
25. V. Di Marzo, M. Bifulco, L. De Petrocellis, *Nat. Rev. Drug Discov.* **3**, 771–784 (2004).
26. P. Grimaldi *et al.*, *Cell. Mol. Life Sci.* **69**, 4177–4190 (2012).
27. M. Maccarrone, M. Bari, M. Di Rienzo, A. Finazzi-Agrò, A. Rossi, *J. Biol. Chem.* **278**, 32726–32732 (2003).
28. S. P. Williams, P. B. Sigler, *Nature* **393**, 392–396 (1998).
29. K. Miyata *et al.*, *Biochem. Biophys. Res. Commun.* **329**, 296–304 (2005).

ACKNOWLEDGMENTS

The authors thank L. Kohlstaedt for protein mass spectrometry and peptide identification. This work was supported by NIH R01GM111802 to P.V.L. and J.F.S; R21HD081403, Pew Scholars, and Alfred P. Sloan Awards to P.V.L.; NIH R01HD068914 to Y.K.; and NIH R01AR059385 to D.M.B. The Vincent J. Proteomics and Mass Spectrometry Laboratory at University of California (UC) Berkeley, is supported by NIH S10 Instrumentation grant S10RR025622. The combined QB3/Chemistry Mass Spectrometry Facility at UC Berkeley is supported by NIH S10 grant 1S10OD020062-01. The authors thank R. Heald (UC Berkeley) for critical reading of the manuscript, D. Julius (UC San Francisco) for help with next-generation sequencing, and M. Okabe (Osaka University, Japan) and J.-J. Chung (Yale University) for transgenic mice used in this study. P.V.L., M.R.M., and Y.K. are inventors on a patent application filed by UC Berkeley related to usage and application of ABHD2. B6D2-Tg(CAG/Su9-DsRed2,Acr3-EGFP) RBGS002Osb transgenic mice were transferred to UC Berkeley under material transfer agreement 13-176 with Osaka University. M.R.M. and P.V.L. conceived the project, designed the experiments, and wrote the manuscript. M.R.M. performed most of the experiments. P.V.L. led the study, helped with pilot experiments, generated transcriptomes, and provided financial support for the project. A.T.I. performed lipid mass spectrometry, and lipid analysis and identification. N.M. helped with pilot experiments. R.S. helped with recombinant protein binding experiments. Y.K. provided support for the transcriptome construction and P4* synthesis. E.O.G. generated libraries for the transcriptomes. J.F.S. helped with computer-aided sperm analysis experiments. R.Z.H. and D.M.B. helped with calcium imaging. All authors discussed the results and commented on the manuscript.

SUPPLEMENTARY MATERIALS

www.sciencemag.org/content/352/6285/555/suppl/DC1
Materials and Methods
Supplementary Text
Figs. S1 to S16
Movies S1 to S6
References (*30*–*35*)
Databases S1 and S2

22 October 2015; accepted 8 March 2016
Published online 17 March 2016
10.1126/science.aad6887

Downloaded from http://science.sciencemag.org/ on April 28, 2016

MICROBIOME

Population-level analysis of gut microbiome variation

Gwen Falony,[1,2]* Marie Joossens,[1,2,3]* Sara Vieira-Silva,[1,2]* Jun Wang,[1,2]* Youssef Darzi,[1,2,3] Karoline Faust,[1,2,3] Alexander Kurilshikov,[4,5] Marc Jan Bonder,[6] Mireia Valles-Colomer,[1,2] Doris Vandeputte,[1,2,3] Raul Y. Tito,[1,2,3] Samuel Chaffron,[1,2,3] Leen Rymenans,[1,2,3] Chloë Verspecht,[1,2] Lise De Sutter,[1,2,3] Gipsi Lima-Mendez,[1,2] Kevin D'hoe,[1,2,3] Karl Jonckheere,[2,3] Daniel Homola,[2,3]† Roberto Garcia,[2,3] Ettje F. Tigchelaar,[6,7] Linda Eeckhaudt,[2,3] Jingyuan Fu,[6,8] Liesbet Henckaerts,[1,9] Alexandra Zhernakova,[6,7] Cisca Wijmenga,[6] Jeroen Raes[1,2,3]‡

Fecal microbiome variation in the average, healthy population has remained underinvestigated. Here, we analyzed two independent, extensively phenotyped cohorts: the Belgian Flemish Gut Flora Project (FGFP; discovery cohort; *N* = 1106) and the Dutch LifeLines-DEEP study (LLDeep; replication; *N* = 1135). Integration with global data sets (*N* combined = 3948) revealed a 14-genera core microbiota, but the 664 identified genera still underexplore total gut diversity. Sixty-nine clinical and questionnaire-based covariates were found associated to microbiota compositional variation with a 92% replication rate. Stool consistency showed the largest effect size, whereas medication explained largest total variance and interacted with other covariate-microbiota associations. Early-life events such as birth mode were not reflected in adult microbiota composition. Finally, we found that proposed disease marker genera associated to host covariates, urging inclusion of the latter in study design.

Sequencing-based assessment of microbial communities in human fecal material has linked alterations in gut microbiota composition to disease, as well as chronically suboptimal health and well-being (*1*–*3*). The discovery of these associations has stimulated the search for specific microbiome-based biomarkers for a wide range of pathologies (*4*–*9*). However, major challenges still hamper the once assumed imminent translation of microbiome monitoring into diagnostic and clinical practice. One such hurdle is the lack of knowledge about the impact of host and environmental factors on microbiota variation within an average, healthy population. Such information is essential for robust disease marker identification in clinical metagenomics (*10*). To identify and characterize major microbiome-associated variables, the Flemish Gut Flora Project (FGFP) initiated a large-scale cross-sectional fecal sampling effort in a confined geographic region (Flanders, Belgium). FGFP collection protocols combined rigorous sampling logistics, including frozen sample collection and cold chain monitoring, with exhaustive phenotyping through online questionnaires, standardized anamnesis and health assessment by general medical practitioners (GPs), and extended clinical blood profiling (fig. S1). Encompassing an equilibrated range of age, gender, health, and lifestyle, the FGFP cohort is expected to be representative for the average gut microbiota composition in a Western European population (table S1). From this cohort, fecal samples of 1106 individuals (98.5% of Western or Eastern European ethnicity; 96.8% born in Belgium) with time-matched blood and questionnaire data were analyzed. Microbiome phylogenetic profiling was performed using 16*S* ribosomal RNA (rRNA) gene amplicon sequencing. In addition, a Dutch cohort (*N* = 1135, LifeLines-DEEP, LLDeep;

[1]KU Leuven–University of Leuven, Department of Microbiology and Immunology, Leuven, Belgium. [2]VIB, Center for the Biology of Disease, Leuven, Belgium. [3]Vrije Universiteit Brussel, Faculty of Sciences and Bioengineering Sciences, Microbiology Unit, Brussels, Belgium. [4]Institute of Chemical Biology and Fundamental Medicine SB RAS, Novosibirsk, Russia. [5]Novosibirsk State University, Novosibirsk, Russia. [6]University of Groningen, University Medical Center Groningen, Department of Genetics, 9700 RB Groningen, Netherlands. [7]Top Institute Food and Nutrition, Wageningen, Netherlands. [8]University of Groningen, University Medical Center Groningen, Department of Pediatrics, 9700 RB Groningen, Netherlands. [9]KU Leuven–University Hospitals Leuven, Department of General Internal Medicine, Leuven, Belgium.
*These authors contributed equally to this work. †Present address: Computation and Systems Medicine Section, Department of Surgery and Cancer, Imperial College London, London, UK.
‡Corresponding author. Email: jeroen.raes@kuleuven.be

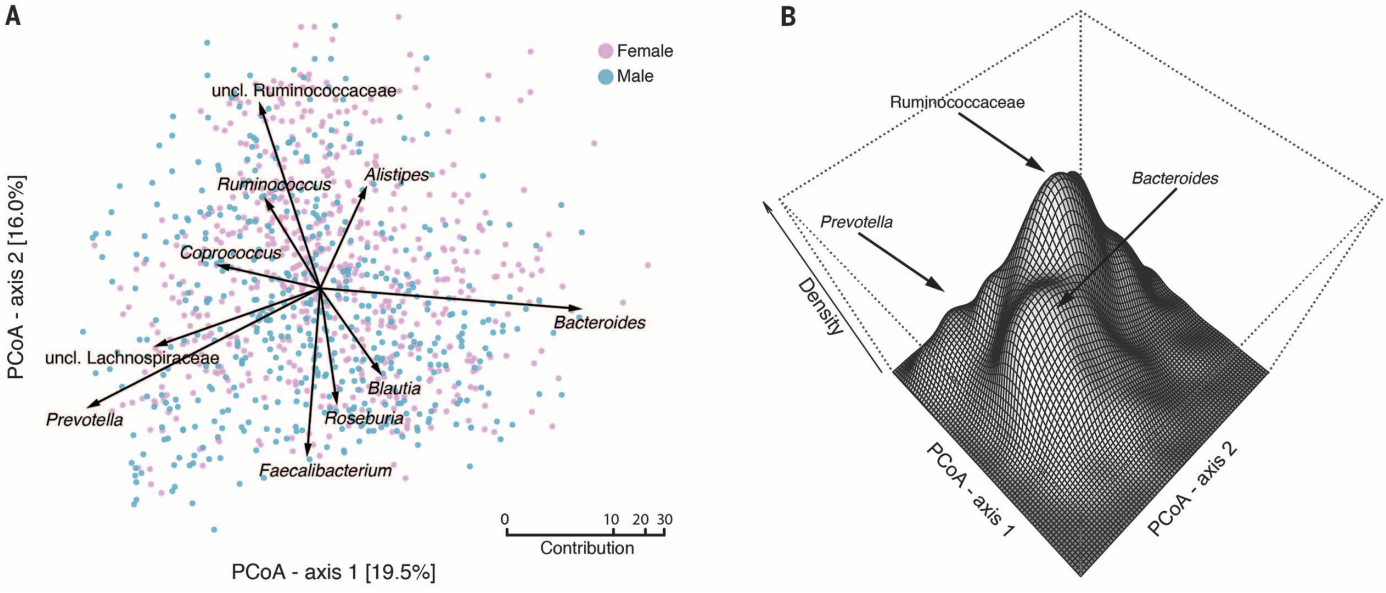

Fig. 1. Microbial community variation in the FGFP cohort, represented by principal coordinates analysis (PCoA, genus-level Bray-Curtis dissimilarity). (**A**) Top 10 contributors to community variation as determined by canonical correspondence analysis on unscaled genera abundances, plotted on the two first PCoA dimensions (arrows scaled to contribution). (**B**) FGFP sample density on the PCoA plot; arrows indicate density peaks enriched in the three previously proposed enterotype drivers: *Prevotella*, *Bacteroides*, and Ruminococcaceae genera.

Downloaded from http://science.sciencemag.org/ on April 28, 2016

the Netherlands) was profiled and analyzed (*11*) for validation purposes.

Characterizing the core microbiota

First, we identified a human core microbiota by combining the FGFP and LLDeep data with other U.K. and U.S. studies (*12*–*14*), yielding nearly 4000 well-profiled individuals. Combined, these data sets comprised a total richness of 664 genera (fig. S2A). Extrapolation estimated total western genus richness at 784 ± 40 (fig. S2B), suggesting that total western richness is still undersampled. Observing total richness would require sampling an estimated additional 40,739 individuals. The current data set yielded a core microbiota (i.e., the genera shared by 95% of samples) composed of 17 genera with a median core abundance (MA) of 72.20% (fig. S2, C and D, and table S2). Complementing this data set with 308 samples collected in Papua New Guinea (*15*), Peru (*16*), and Tanzania (*17*) reduced the size of the human core microbiota to 14 genera. Notably, *Alistipes*, *Clostridium IV*, *Parabacteroides*, and all Actinobacteria were excluded from the global core composition (fig. S3 and table S2). Within the FGFP data set specifically, 35 genera meet the core definition proposed (MA 90.40%), while a 99% cutoff reduced core composition to 20 genera (MA 80.67%; table S2). These 20 core genera also occurred among the top 33 most abundant taxa in the FGFP cohort (table S2). Independently of gender, genus richness correlated positively with age, whereas total core abundance decreased (fig. S4).

Based on unconstrained canonical correspondence analysis of genus-level community composition, we identified the main genera contributing to microbiome variation within the FGFP data set (table S3). Interindividual variation in microbiota composition mainly resulted from changes in relative abundance of core taxa (Fig. 1A). The taxa showing the largest variation in abundance were Ruminococcaceae, *Bacteroides*, and *Prevotella*; all previously proposed as enterotype identifiers (*18*). However, microbiota variation was not only defined by fluctuations in the core or dominant microbiota members, as less abundant genera, such as *Akkermansia* and *Methanobrevibacter*, were also discriminative (table S3). The density of individuals within the FGFP microbiome composition landscape resolved into three major peaks, coinciding with the three main contributors to variation identified above (Fig. 1B), as well as enterotypes [based on clustering (*18*) or Dirichlet multinomial mixtures (*19*, *20*); fig. S5].

Identifying microbiome covariates

Building upon the extensive FGFP phenotyping, we tested 503 metadata variables (table S1) to identify microbiome covariates. To achieve a balance between number of phenotypes of interest and rates of false discovery, a stepwise approach was applied. After removing collinear variables (table S4), 69 factors were shown to correlate significantly [false discovery rate (FDR) <10%] with overall microbiome community variation (Bray-Curtis dissimilarity; Fig. 2 and table S5). Of those covariates, 26 had an analog in the LLDeep record (*11*). Despite differences in study population and sample analysis (e.g., DNA extraction methods), 24 matching covariates were found to be significantly associated with microbiome composition in the LLDeep cohort, leading to an overall replication success rate of 92% (Fig. 2). All 69 covariates identified correlated with alpha-diversity measures and individual taxa abundances (table S6). However, the predictive power of the linear covariate-based models was limited, as they only explained 1.50 to 14.74% of genus abundance variation (table S7), suggesting additional contribution from unknown factors, stochastic effects, and/or biotic interactions (*21*). Moreover, correlations were affected by interactions between specific covariates, notably medication (see below; table S8).

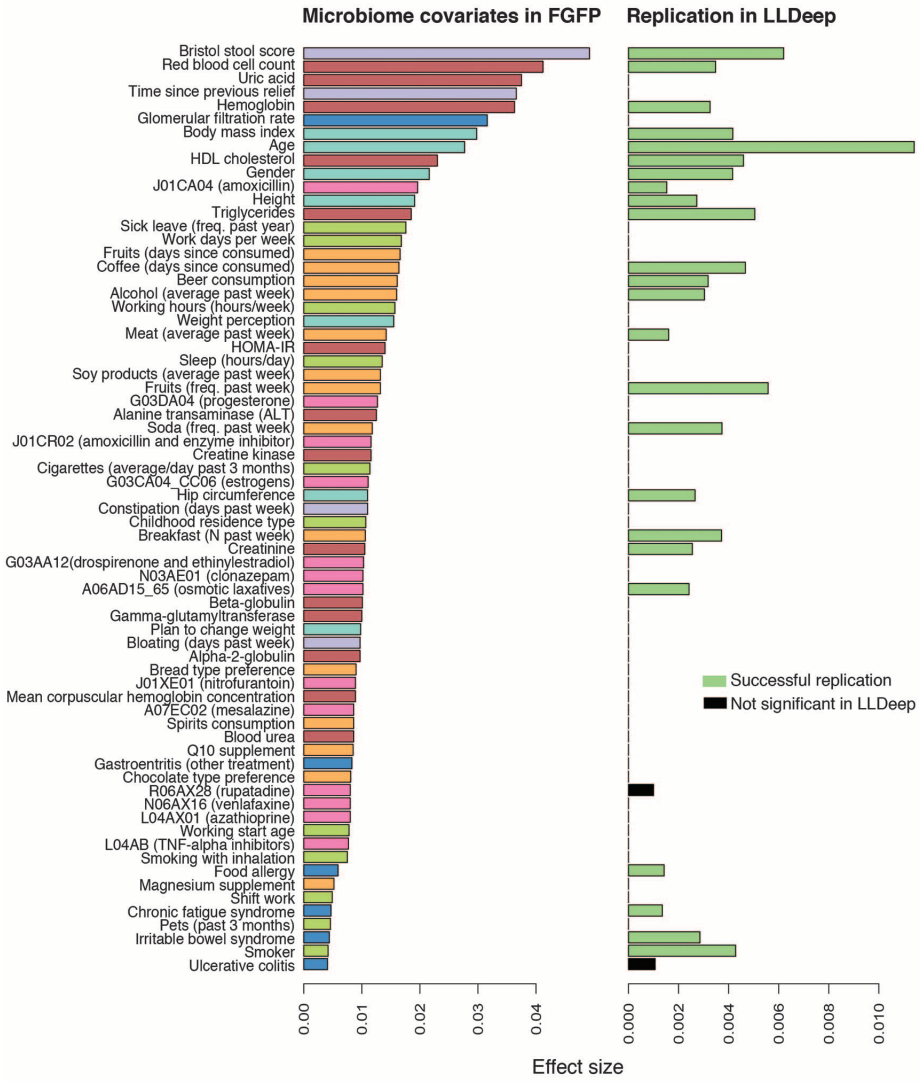

Fig. 2. Microbiome covariates identified in the FGFP cohort (left) and their replication in the LLDeep study (right). Factors are sorted according to their effect size in FGFP and colored based on metadata category (fig. S1), with "Medication" (pink) here split out of the "Health" category (dark blue). Covariates identified in the FGFP and successfully replicated in LLDeep ($P < 5\%$) are colored in green; nonreplicated covariates are in black.

Calculation of the covariates' combined effect size per phenotypical category revealed that medication had the largest explanatory power on microbiome composition, including 10.04% of community variation (Fig. 3A and table S9). Blood parameters, bowel habits, health status, anthropometric features, and lifestyle followed with decreasing combined correlation, raising the total additive effect size of all categories to 16.43%. To identify nonredundant covariates of microbiome variations from our shortlist of 69 correlating factors, we performed a forward stepwise redundancy analysis (RDA) that resulted in a set of 18 variables (Fig. 3B and table S10) with a cumulative (nonredundant) effect size on community variation of 7.63%. Here, we identified stool consistency as the top single, nonredundant microbiome covariate in the FGFP metadata (see below) (*22*, *23*). Among the other

Downloaded from http://science.sciencemag.org/ on April 28, 2016

nonredundant covariates were age (*12*) and gender (*24*), but also the intake of specific drugs and dietary information (including fiber uptake, bread preference, and fruit consumption; Fig. 3B). Regarding the ongoing debate on the association between microbiome composition and body mass index (BMI) (*25*, *26*), our analyses revealed that effect size is small but significant (table S10). Notably, previously unidentified factors such as red blood cell (RBC) count and hemoglobin concentration indicated covariation of microbiome composition with blood oxygen uptake capacity (*27*). Previous work in mice has shown an effect of oxygen diffusion on the microbiota (*28*). Moreover, correlations between RBC counts and *Faecalibacterium* abundances are in line with the known oxygen requirements of this genus (*29*). Of the 18 covariates with nonredundant contributions to microbiome variation, 10 were found to be significant by generalized linear model analysis (table S11). This approach confirmed the top covariate status of stool consistency (*22*, *23*) and revealed associations between genus abundances and hip circumference, uric acid concentrations, amoxicillin intake, and chocolate-type preference (namely, an increased abundance of unclassified Lachnospiraceae in participants with a preference for dark chocolate).

Out of a total of 503 parameters, stool consistency, as measured by self-assessed Bristol stool scale (BSS) score, emerged as the top feature covarying with fecal microbiome composition. BSS score has been put forward as an indicative measure of transit time (*30*), but also reflects water availability and potential niche differentiation within the colon ecosystem (*23*). We confirmed previously reported associations of stool consistency with microbiota richness, prevalence of *Prevotella*-enterotyped samples, and *Akkermansia* and *Methanobrevibacter* abundances (*22*, *23*) (Fig. 4, fig. S6, and table S12). In addition, we showed that 12 out of 20 of the FGFP 99% core genera covary with BSS scores, with overall core abundance increasing in looser stools. We assessed the confounding effect of stool consistency on the remaining 68 microbiome covariates using RDA. Among the features losing most explanatory power were time since previous relief (also indicative of passage rates), blood uric acid and hemoglobin levels, BMI, gender, and frequency of beer consumption (table S12).

Bacterial genera associated with disease

Years of disease-targeted microbiome research have generated an extensive inventory of bacterial genera with a reported association with one or more pathologies. We have assessed correlations between taxa that have been reported to be more abundant or depleted in individuals suffering from specific conditions (table S13) and the set of 18 nonredundant microbiome covariates identified. Our analyses confirmed previous work showing that *Akkermansia* abundance positively correlated with time since previous relief (*23*), but it was also negatively associated with insulin resistance risk factors such as BMI and

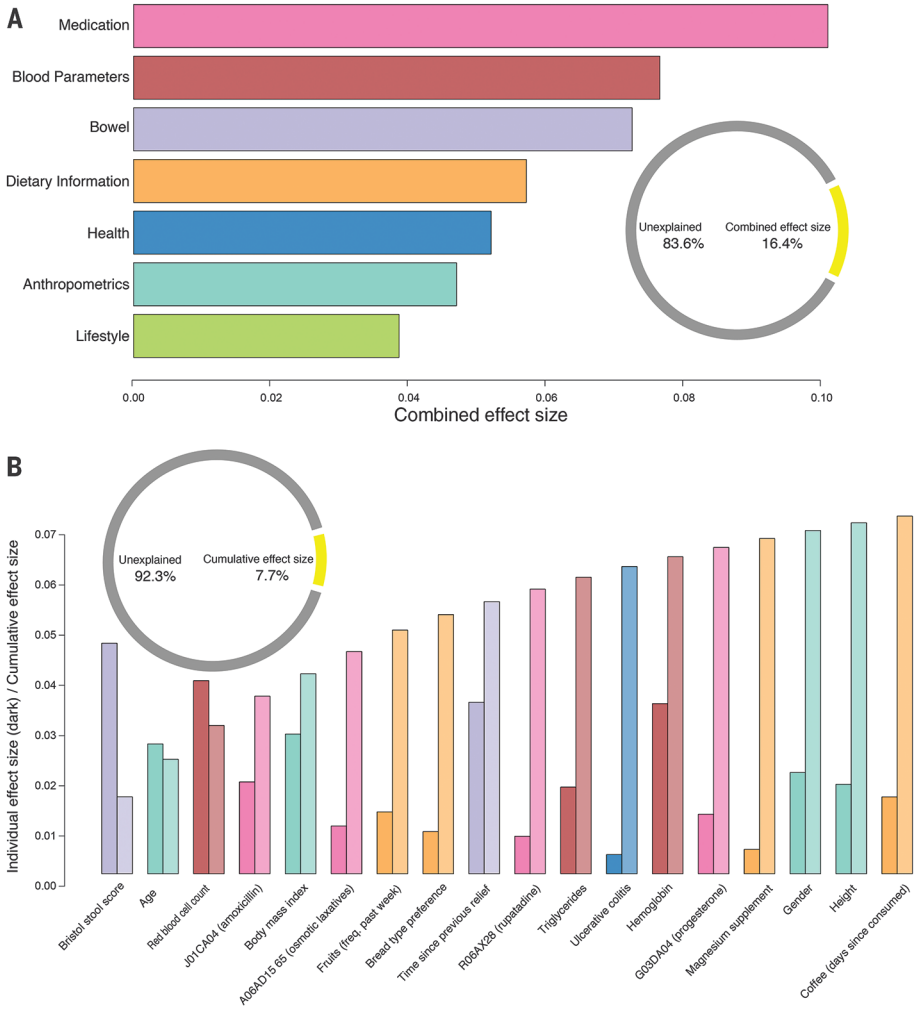

Fig. 3. Effect sizes of covariates of FGFP microbiome composition. (**A**) Combined effect size of FGFP covariates pooled in predefined categories (Fig. 2 color codes) with covariate distance-based selection. (**B**) Cumulative effect size of nonredundant covariates selected by stepwise RDA analysis (right bars) as compared to individual effect sizes assuming independence (left bars). Rings in each panel show the fraction of microbial variation explained with the approach.

blood triglyceride concentrations (*31*). *Faecalibacterium* numbers were, as discussed, dependent on RBC counts, but our analysis did find a decreased abundance in ulcerative colitis patients (*32*). The presence of *Fusobacterium* could not be linked to any of the nonredundant covariates identified in this study, which could indicate the specificity of its association with colorectal cancer (*8*). Given these associations, inclusion of the identified covariates in future clinical study design seems appropriate.

Next, we identified sample subsets with specific taxonomic signatures using a biclustering approach (*33*). Two stable biclusters were detected, spanning 410 and 374 samples, respectively, with an intersection of 92 (table S14). The first bicluster comprised 15 genera, including several Clostridia, as well as hydrogenotrophic genera, such as *Methanobrevibacter* and *Desulfovibrio*. The cluster was predominantly composed of women, individuals with a lower weight, and participants with a longer transit time, as reflected both by stool consistency and time since previous relief. Both microbiota richness and evenness were elevated in this cluster. In contrast, the second bicluster, consisting of seven genera, including *Bacteroides* and *Parabacteroides*, comprised individuals with reduced microbiome diversity. Characterization of these individuals revealed a preference for white, low-fiber bread [bread being the major source of carbohydrates in an average Belgian diet (*34*)] and higher prevalence of recent amoxicillin treatment. Thus, this biclustering analysis hinted at microbiome configurations that at least partially overlap with previously described enterotypes. Indeed, while the *Ruminococcus* enterotype was overrepresented in the first bicluster, the second was enriched in *Bacteroides*-type individuals. This, together with the results from Fig. 1B, suggested that although not discrete, enterotypes do indeed represent "densely populated areas in a

Downloaded from http://science.sciencemag.org/ on April 28, 2016

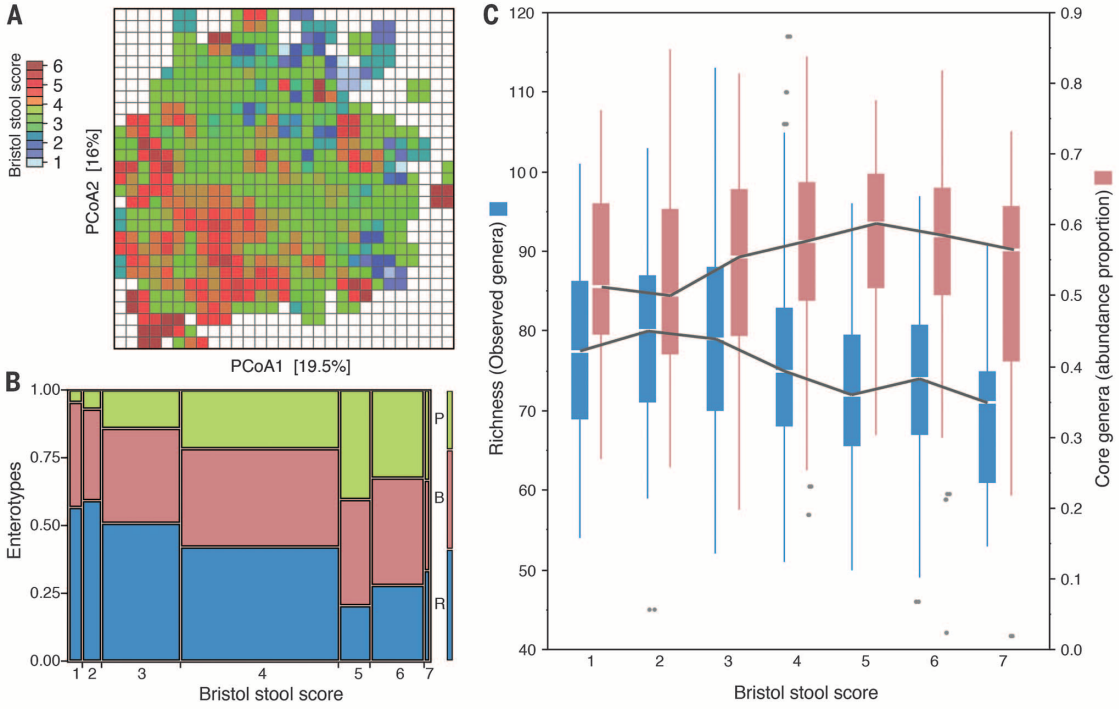

Fig. 4. BSS score association to microbiota variation. (**A**) BSS score variation across the FGFP cohort, as represented on the genus-level PCoA ordination (Bray-Curtis dissimilarity). Each cell is colored according to median BSS score of individual samples allocated to the cell coordinates. (**B**) Enterotype distribution over BSS scores [JSD enterotyping (*18*)] showing an increase in *Prevotella* individuals with looser stool consistency. (**C**) Median differences in abundance of the core microbiota (FGFP genus-level core at 99%) and in observed genus richness across BSS score.

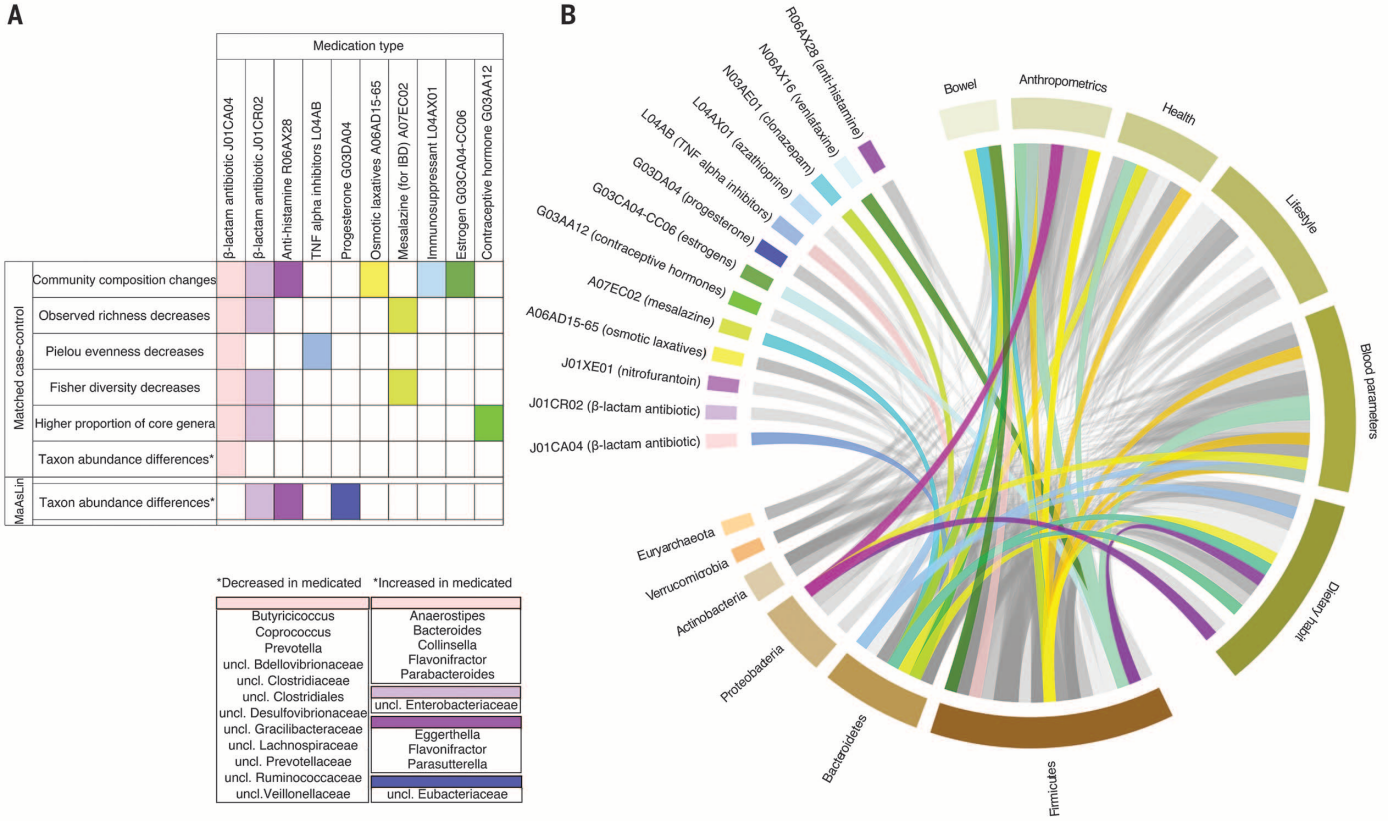

Fig. 5. Drug interactions in the FGFP. (**A**) Overview of the association between different types of medication and microbiome composition. Colored boxes (color coding according to medication) represent a significant result in the matched case-control (FDR<5%) or boosted additive general linear modeling (FDR<10%, table S11) analyses. The effect (decrease/increase) of medication on genera abundances is specified. (**B**) Circos plot showing correlations between covariates and genus abundances (FDR<10%) interacting with drugs. Genera are grouped at phylum level; ribbons represent genus-phenotype associations and are colored according to the confounding medication (gray indicates nonconfounded).

Downloaded from http://science.sciencemag.org/ on April 28, 2016

multidimensional space of community composition," as stated in the original publication (*18*).

The effect of medical interventions

When combining FGFP covariates in predefined categories (fig. S1 and table S15), the use of medication showed the largest explanatory value for microbiome variation in our study. The use of medication in the FGFP cohort was widespread [with 1950 records of over-the-counter plus prescription drug intake during the past 12 (antibiotics) or 6 months (all others) prior to sampling]. On the shortlist of 69 FGFP microbiome covariates figured 13 drugs, including antibiotics, osmotic laxatives, inflammatory bowel disease (IBD) medication, female hormones, benzodiazepines, antidepressants, and antihistamine. Independently of other covariates, intake of several of these substances was associated with community composition variation (Fig. 5A and table S15). The only drugs significantly associated with the abundance of specific genera in phenotype-matched case-control analyses were β-lactam antibiotics (FDR <5%). As medication was shown to affect the outcome of microbiome association studies (*35*), we performed an interaction analysis of covariate-microbiome correlations in the FGFP data set (table S8). Of the covariate interactions detected, 63% was driven by medication (Fig. 5B). This result highlights the versatility of drug-microbiome associations and stresses their importance as potentially confounding factors in clinical studies.

Some early-life events that are generally thought to affect adult microbiota composition were not associated with microbiota composition variation in our study, including mode of birth [cesarean section (N = 36) or vaginal delivery (N = 1036)], place of birth [home (N = 207) or hospital (N = 899); increased diversity in home-born individuals, FDR>5% when controlling for age], and infant nutrition [breastfed (N = 537) or not breastfed (N = 359)] (fig. S7). Residence type [ranging from countryside (N = 77) over rural village (N = 500), small town (N = 272), suburb (N = 137), to city (N = 102)] during early childhood (up to 5 years old), one of the 69 FGFP microbiome covariates, was linked to adult microbial community composition, with a positive correlation between evenness and residence in more industrialized areas, though not statistically significant (FDR >5%) when correcting for age, gender, and BMI. Although the lack of signal in the data was unexpected, these results by no means imply that early-life events do not affect microbiota assembly during infancy, nor do they question previous associations with disease or allergy (*36*, *37*); our analyses only indicated that such events were not significantly associated with microbiome composition at adult age in the FGFP cohort.

Power analysis and conclusions

Finally, the sample size and phenotypic breadth of the FGFP data set provided a unique opportunity to perform an informed power analysis for clinical microbiome studies. In a first approach, we calculated the number of samples needed to assess a difference in dominant microbiota members in a case-control setting where the type of microbiota shift is unknown (e.g., for a discovery project in an unstudied disease). We could detect a 9% difference between taxon proportions with 400 samples per group at a power above 95% and a 5% difference with 500 samples per group at a power of 80% (table S16). In a second approach, we estimated the sample size needed to identify a microbiome shift specific to a known association in a background of other factors (e.g., for intervention studies). Focusing on the prevalent concern of BMI increase and suboptimal health, we assessed the sample size needed to evaluate microbiota compositional changes associated to obesity. To do so, we calculated the independent effect sizes of obesity status, gender, age, and BSS on microbiota variation (table S16). This allowed us to estimate that 865 lean (BMI <25) and 865 obese (BMI ≥30) volunteers would be necessary to study microbiota compositional shifts with $P < 5\%$ significance level and a power of 80%. When taking into account gender, age, and BSS score as covariates, the estimated sample size was reduced to 535 (table S16).

Overall, this study identified a global human core microbiota, while also highlighting that total gut diversity is not yet covered, even combining microbiome data from almost 4000 individuals. Building upon rich metadata and a two-cohort design, we identified a set of microbiota covariates with a replication rate of over 92% and a cumulative, nonredundant effect size of 7.63%. This suggests the influence of additional, currently unknown covariates as well as intrinsic microbial ecological processes such as founder effects, species interactions, and dynamics. We showed that some of the medical conditions targeted by fecal microbiota research have much smaller microbiome effect sizes than commonly assumed. However, some of the covariates that we identified (such as BSS and medication) are currently largely ignored and should be taken into account in future clinical studies. Our power analyses showed that large-scale study design is indispensable for characterizing microbiome shifts, even in a controlled setting, confirming that scale indeed matters, but knowledge of confounders can help to ease power issues. The results from this study form a solid basis for the development of microbiome research as a clinical and diagnostic field.

REFERENCES AND NOTES

1. M. Rajilić-Stojanović *et al.*, *Am. J. Gastroenterol.* **110**, 278–287 (2015).
2. J. C. Clemente, L. K. Ursell, L. W. Parfrey, R. Knight, *Cell* **148**, 1258–1270 (2012).
3. J. F. Cryan, T. G. Dinan, *Nat. Rev. Neurosci.* **13**, 701–712 (2012).
4. E. Le Chatelier *et al.*, *Nature* **500**, 541–546 (2013).
5. J. Qin *et al.*, *Nature* **490**, 55–60 (2012).
6. F. H. Karlsson *et al.*, *Nature* **498**, 99–103 (2013).
7. J. Stock, *Atherosclerosis* **229**, 440–442 (2013).
8. M. R. Rubinstein *et al.*, *Cell Host Microbe* **14**, 195–206 (2013).
9. E. A. Eloe-Fadrosh, D. A. Rasko, *Annu. Rev. Med.* **64**, 145–163 (2013).
10. F. Bäckhed *et al.*, *Cell Host Microbe* **12**, 611–622 (2012).
11. A. Zhernakova *et al.*, *Science* **352**, 565–569 (2016).
12. T. Yatsunenko *et al.*, *Nature* **486**, 222–227 (2012).
13. J. K. Goodrich *et al.*, *Cell* **159**, 789–799 (2014).
14. P. J. Turnbaugh *et al.*, *Nature* **449**, 804–810 (2007).
15. I. Martínez *et al.*, *Cell Rep.* **11**, 527–538 (2015).
16. A. J. Obregon-Tito *et al.*, *Nat. Commun.* **6**, 6505 (2015).
17. S. L. Schnorr *et al.*, *Nat. Commun.* **5**, 3654 (2014).
18. M. Arumugam *et al.*, *Nature* **473**, 174–180 (2011).
19. M. J. Claesson *et al.*, *Nature* **488**, 178–184 (2012).
20. I. Holmes, K. Harris, C. Quince, *PLOS ONE* **7**, e30126 (2012).
21. K. Faust, J. Raes, *Nat. Rev. Microbiol.* **10**, 538–550 (2012).
22. E. F. Tigchelaar *et al.*, **65**, 540–542 (2016).
23. D. Vandeputte *et al.*, *Gut* **65**, 57–62 (2016).
24. C. Huttenhower *et al.*, *Nature* **486**, 207–214 (2012).
25. W. A. Walters, Z. Xu, R. Knight, *FEBS Lett.* **588**, 4223–4233 (2014).
26. M. M. Finucane, T. J. Sharpton, T. J. Laurent, K. S. Pollard, *PLOS ONE* **9**, e84689 (2014).
27. H. Mairbäurl, *Front. Physiol.* **4**, 332 (2013).
28. L. Albenberg *et al.*, *Gastroenterology* **147**, 1055–63.e8 (2014).
29. M. T. Khan *et al.*, *ISME J.* **6**, 1578–1585 (2012).
30. S. J. Lewis, K. W. Heaton, *Scand. J. Gastroenterol.* **32**, 920–924 (1997).
31. A. Tirosh *et al.*, *Diabetes Care* **31**, 2032–2037 (2008).
32. H. Sokol *et al.*, *Inflamm. Bowel Dis.* **15**, 1183–1189 (2009).
33. S. Hochreiter *et al.*, *Bioinformatics* **26**, 1520–1527 (2010).
34. S. Devriese, I. Huybrechts, M. Moreau, H. Van Oyen, The Belgian food consumption survey 1-2004 (IPH/EPI Reports N° 2006 - 016, Epidemiology Unit, Scientific Institute of Public Health, Brussels, 2006; www.wiv-isp.be/epidemio/epinl/foodnl/table04.htm.
35. K. Forslund *et al.*, *Nature* **528**, 262–266 (2015).
36. M. G. Dominguez-Bello *et al.*, *Proc. Natl. Acad. Sci. U.S.A.* **107**, 11971–11975 (2010).
37. C. J. Lodge *et al.*, *Acta Paediatr.* **104** (suppl. S467), 38–53 (2015).

ACKNOWLEDGMENTS

FGFP procedures were approved by the medical ethics committee of the University of Brussels–Brussels University Hospital (approval 143201215505, 5/12/2012). A declaration concerning the FGFP privacy policy was submitted to the Belgian Commission for the Protection of Privacy. Written informed consent was obtained from all participants. The FGFP was funded with support of the Flemish government (IWT130359), the Research Fund–Flanders (FWO) Odysseus program (G.0924.09), the King Baudouin Foundation (2012-J80000-004), FP7 METACARDIS HEALTH-F4-2012-305312, VIB, the Rega institute for Medical Research, and KU Leuven. D.V. is funded by the Agency for Innovation by Science and Technology (IWT). S.V.S. is supported by Marie Curie Actions FP7 People COFUND–Proposal 267139 (acronym OMICS@VIB). M.J., S.V.S., G.L.M, S.C., K.F., J.W., and M.V., K.D. are supported by postdoctoral (six) and predoctoral (two) fellowships, respectively, from the FWO. The LifeLines-DEEP study was funded by the Top Institute Food and Nutrition (TiFN GH001), CardioVasculair Onderzoek Nederland (CVON 2012-03), the Netherlands Organization for Scientific Research (NWO-VIDI 864.13.013), and an FP7 ERC Advanced Grant to C.W. (Agreement no. 2012-322698). We thank P. Cornelis and all members of the Raes lab for lively discussions and feedback. We acknowledge the contribution of Flemish GPs and pharmacists to data and sample collection. Finally, we thank all FGFP volunteers for participating in the project. Data are available at the European Genotyping Agency (https://www.ebi.ac.uk/ega/)–study no. EGAS00001001689.

SUPPLEMENTARY MATERIALS

www.sciencemag.org/content/352/6285/560/suppl/DC1
Materials and Methods
Figs. S1 to S9
Additional Data tables S1 to S17
References (*38*–*57*)

1 September 2015; accepted 11 March 2016
10.1126/science.aad3503

Downloaded from http://science.sciencemag.org/ on April 28, 2016

REPORTS

MICROBIOME

Population-based metagenomics analysis reveals markers for gut microbiome composition and diversity

Alexandra Zhernakova,[1,2]* Alexander Kurilshikov,[3,4]† Marc Jan Bonder,[1]† Ettje F. Tigchelaar,[1,2]† Melanie Schirmer,[5,6] Tommi Vatanen,[5,7] Zlatan Mujagic,[2,8] Arnau Vich Vila,[9] Gwen Falony,[10,11] Sara Vieira-Silva,[10,11] Jun Wang,[10,11] Floris Imhann,[9] Eelke Brandsma,[12] Soesma A. Jankipersadsing,[1] Marie Joossens,[10,11,13] Maria Carmen Cenit,[1,14,15] Patrick Deelen,[1,16] Morris A. Swertz,[1,16] LifeLines cohort study, Rinse K. Weersma,[9] Edith J. M. Feskens,[2,17] Mihai G. Netea,[18] Dirk Gevers,[5]‡ Daisy Jonkers,[8] Lude Franke,[1] Yurii S. Aulchenko,[4,19,20,21] Curtis Huttenhower,[5,6] Jeroen Raes,[10,11,13] Marten H. Hofker,[12] Ramnik J. Xavier,[5,22,23,24] Cisca Wijmenga,[1]*§ Jingyuan Fu[1,12]*§

Deep sequencing of the gut microbiomes of 1135 participants from a Dutch population-based cohort shows relations between the microbiome and 126 exogenous and intrinsic host factors, including 31 intrinsic factors, 12 diseases, 19 drug groups, 4 smoking categories, and 60 dietary factors. These factors collectively explain 18.7% of the variation seen in the interindividual distance of microbial composition. We could associate 110 factors to 125 species and observed that fecal chromogranin A (CgA), a protein secreted by enteroendocrine cells, was exclusively associated with 61 microbial species whose abundance collectively accounted for 53% of microbial composition. Low CgA concentrations were seen in individuals with a more diverse microbiome. These results are an important step toward a better understanding of environment-diet-microbe-host interactions.

The human gut microbiome plays a major role in the production of vitamins, enzymes, and other compounds that digest and metabolize food and regulate our immune system (*1*). It can be considered as an extra organ, with remarkable dynamics and a major impact on our physiology. The composition of the gut microbiome can be considered as a complex trait, with the quantitative variation in the microbiome affected by a large number of host and environmental factors, each of which may have only a small additive effect, making it difficult to identify the association for each separate item. In this study, we present a systematic metagenomic association analysis of 207 intrinsic and exogenous factors from the LifeLines-DEEP cohort, a Dutch population–based study (*2*, *3*). Our study reveals covariates in the microbiome and, more importantly, provides a list of factors that correlate with shifts in the microbiome composition and functionality.

This study includes stool samples from 1179 LifeLines-DEEP participants from the general population of the northern part of the Netherlands (*2*). The cohort comprised predominantly Dutch participants; 93.7% had both parents born in the Netherlands. The gut microbiome was analyzed with paired-end metagenomic shotgun sequencing (MGS) on a HiSeq 2000, generating an average of 3.0 Gb of data (about 32.3 million reads) per sample (*4*). After excluding 44 samples with low read counts, 1135 participants (474 males and 661 females) remained for further analysis. We tested 207 factors with respect to the microbiomes of these participants: 41 intrinsic factors of various physiological and biomedical measures, 39 self-reported diseases, 44 categories of drugs, 5 categories of smoking status, and 78 dietary factors (fig. S1 and table S1). These factors cover dietary habits, lifestyle, medication use, and health parameters. Most of the factors showed a low or modest intercorrelation (table S2, A to C, and fig. S2, A to D); many are highly variable, including, as expected in the Dutch population, the high consumption of milk products and low use of antibiotics. Antibiotic use in the Netherlands is the lowest in Europe, at a level half that of the UK and one-third that of Belgium. To cover health-domain factors relevant to the host immune system and gut health, we collected cell counts for eight different blood cell types, measured blood cytokine concentrations, assessed stool frequency and stool type by Bristol stool score, and measured fecal levels of several secreted proteins, including calprotectin as a marker for the immune system activation, human β-defensin-2 (HBD-2) as a marker for defense against invading microbes, and chromogranin A (CgA) as a marker for neuroendocrine system activation.

After quality control and removal of sequence reads mapping to the human genome, the microbiome sequence reads were mapped to ~1 million microbial-taxonomy–specific marker genes with MetaPhlAn 2.0 (*5*) to predict the abundance of microorganisms (fig. S3A). For each participant, we predicted the abundances for 1649 microbial taxonomic clades ranging from four different domains to 632 species (Fig. 1A). Most of the reads (97.6%) came from *Bacteria*; 2.2% were from *Archaea*, 0.2% from *Viruses*, and <0.01% from *Eukaryotes*. Comparison to previous taxonomic profiles of the same subjects by 16*S* ribosomal RNA (rRNA) gene sequencing (Fig. 1B) showed that MGS predicted more microbial species but fewer families and genera. At the phylum level, the abundances of dominant bacterial phyla *Firmicutes* (63.7%) and *Bacteroidetes* (8.1%) were similar to estimates based on 16*S* rRNA gene sequencing, but the abundance of *Actinobacteria* was higher in MGS (22.3%) than 16*S* (12.3%) (fig. S4). The microbiome quality control project has recently suggested that microbial composition estimates may not be comparable between studies if sample preparation and data analysis are not done in the same way (*6*). For instance, compared to the composition reported in other studies of a similar size that used different methods (*7*, *8*), our study

[1]University of Groningen, University Medical Center Groningen, Department of Genetics, Groningen, Netherlands. [2]Top Institute Food and Nutrition, Wageningen, Netherlands. [3]Institute of Chemical Biology and Fundamental Medicine SB RAS, Novosibirsk, Russia. [4]Novosibirsk State University, Novosibirsk, Russia. [5]The Broad Institute of MIT and Harvard, Cambridge, MA, USA. [6]Department of Biostatistics, Harvard T. H. Chan School of Public Health, Boston, MA, USA. [7]Department of Computer Science, Aalto University School of Science, Espoo, Finland. [8]Division of Gastroenterology-Hepatology, Department of Internal Medicine, NUTRIM School of Nutrition and Translational Research in Metabolism, Maastricht University Medical Center, Maastricht, Netherlands. [9]University of Groningen, University Medical Center Groningen, Department of Gastroenterology and Hepatology, Groningen, Netherlands. [10]KU Leuven–University of Leuven, Department of Microbiology and Immunology, Rega Institute for Medical Research, Laboratory of Molecular Bacteriology, Leuven, Belgium. [11]VIB, Center for the Biology of Disease, Leuven, Belgium. [12]University of Groningen, University Medical Center Groningen, Department of Pediatrics, Groningen, Netherlands. [13]Vrije Universiteit Brussel, Faculty of Sciences and Bioengineering Sciences, Microbiology Unit, Brussels, Belgium. [14]Microbial Ecology, Nutrition and Health Research Group, Institute of Agrochemistry and Food Technology, National Research Council (IATA-CSIC), Valencia, Spain. [15]Department of Pediatrics, Dr. Peset University Hospital, Valencia, Spain. [16]University of Groningen, University Medical Center Groningen, Genomics Coordination Center, Groningen, Netherlands. [17]Division of Human Nutrition, Wageningen University, Wageningen, Netherlands. [18]Department of Internal Medicine and Radboud Center for Infectious Diseases, Radboud University Medical Center, Nijmegen, Netherlands. [19]Centre for Global Health Research, Usher Institute of Population Health Sciences and Informatics, University of Edinburgh, Teviot Place, Edinburgh EH8 9AG, UK. [20]PolyOmica, Groningen, Netherlands. [21]Institute of Cytology and Genetics SB RAS, Novosibirsk, Russia. [22]Center for Computational and Integrative Biology, Massachusetts General Hospital, Boston, MA, USA. [23]Gastrointestinal Unit and Center for the Study of Inflammatory Bowel Disease, Massachusetts General Hospital, Boston, MA, USA. [24]Center for Microbiome Informatics and Therapeutics, Massachusetts Institute of Technology, Cambridge, MA, USA.
***Corresponding author. Email: a.zhernakova@umcg.nl (A.Z.); c.wijmenga@umcg.nl (C.W.); j.fu@umcg.nl (J.F.)** †These authors contributed equally to this work. ‡Present address: Janssen Human Microbiome Institute, Janssen Research and Development, Cambridge, MA, USA. §These authors contributed equally to this work.

Downloaded from http://science.sciencemag.org/ on April 28, 2016

detected a higher abundance of *Actinobacteria* but a lower abundance of *Bacteroidetes*. Notably, all samples in our study were isolated and processed with the same pipeline, ensuring low technical variation and high analysis power to access the association of multiple factors with the microbiome.

The high interindividual variation reflects the community composition (fig. S5) and is clearly driven by the abundance of the dominant phyla (Fig. 2A). Our further analysis of microbial composition was confined to the 632 unique species (table S3). For the functional profiling, the abundances of 568,874 UniRef gene families were grouped into clusters of orthologous groups (COG) on the basis of the EggNOG database and MetaCyc pathways (fig. S3A). Although the distribution of diversity, genes, and COG richness showed high intervariability (Fig. 2 , B to D), functional profiles based on 23 nonredundant, Gene Ontology molecular function categories remained stable (fig. S6) within our cohort, similar to previous reports (*9*).

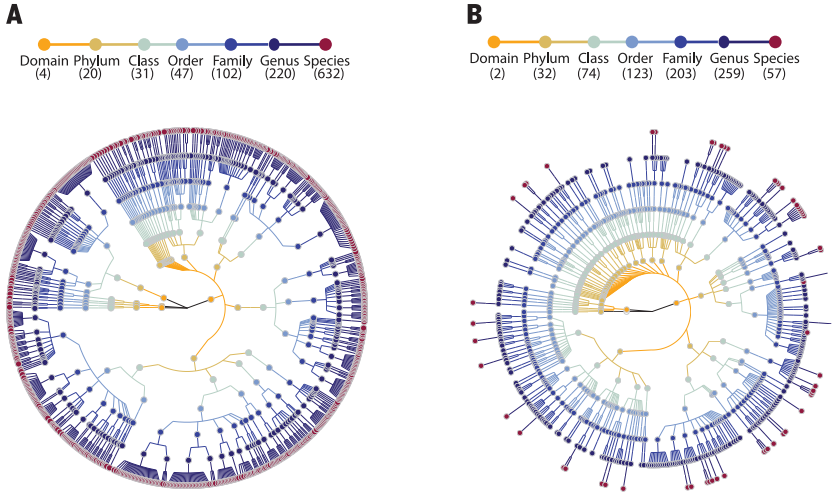

Fig. 1. The taxonomic tree of microbial taxonomies predicted by MGS and 16S rRNA gene sequencing. (**A**) Taxonomic tree based on MGS shotgun sequencing data. (**B**) Taxonomic tree based on 16S rRNA gene sequencing data. Each dot represents a taxonomic entity. From the inner to outer circles, the taxonomic levels range from domains to species. Different colors of dots indicate different taxonomy levels according to the color key shown. Numbers in parentheses indicate the total number of unique taxonomies detected at each level.

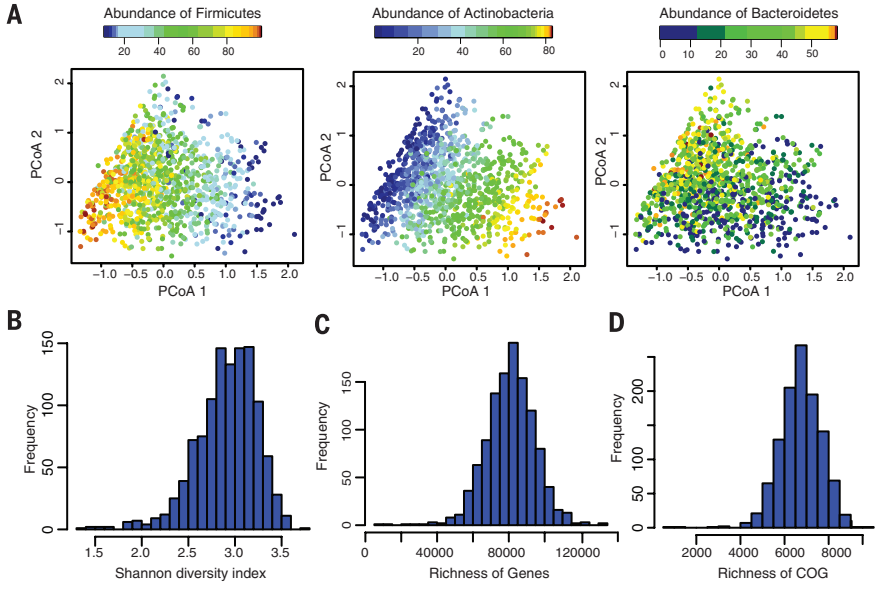

Fig. 2. The interindividual variation of microbial composition and function profile. (**A**) Principal coordinates analysis (PCoA) plots of Bray-Curtis distance of microbial composition. The composition was driven by the most dominant phyla: *Firmicutes*, *Actinobacteria*, and *Bacteroidetes*. Each dot represents one individual. Color indicates the relative abundance of each phylum. (**B**) Distribution of Shannon's diversity index. (**C**) Distribution of the gene richness. (**D**) Distribution of the clusters of orthologous groups (COG) richness.

We correlated 207 factors to the interindividual variation in microbial composition, diversity, richness of genes, and COGs (fig. S3B). At a false discovery rate (FDR) of <0.1, 126 factors were associated with interindividual distance of microbial composition (Bray-Curtis distance) (Fig. 3 and table S4), of which 90% could be replicated in 16*S* rRNA data from the same subjects (table S5 and fig. S7), together explaining 18.7% of the variation in composition distance (fig. S8A). A total of 35 factors were associated with Shannon's diversity index of microbial composition (together explaining 13.7% variation; table S6 and fig. S8A), of which 80% were replicated in 16S rRNA data from the same subjects (table S7); 31 factors were associated with gene richness (together explaining 16.7% of variation; table S8) and 34 factors with COG richness (explaining 18.8% of variation) (table S9 and fig. S8A; for replication rates, see table S10). We saw a large overlap between different diversity and richness analyses, and most of them were also associated with composition distance (fig. S8B).

We performed multivariate association analyses between each factor with 170 abundant species (>0.01% of total microbial composition and present in at least 10 individuals) and 215 MetaCyc pathways (fig. S3C). When corrected for age, gender, and sequence depth, we found 485 associations at FDR<0.1 between 110 factors and 125 species (table S11) and 524 associations between 71 factors and 176 MetaCyc pathways (table S12). By correcting the correlation structures among all 207 factors, the number of associations was reduced to 128 independent associations with species (table S13) and 215 associations with pathways (table S14).

Our data confirmed some previous findings and also yielded novel associations. In our study, age and gender were correlated not only with microbial composition distance and diversity but also with functional richness. Women showed higher COG richness than men (adjusted $P = 0.03$), and COG richness increased with age (adjusted $P = 0.002$) (fig. S9). Multiple intrinsic parameters, such as blood cell counts and lipid concentrations, were associated to composition and function levels as well. For example, a higher amount of hemoglobin was consistently associated with lower diversity and functional richness (Fig. 3 and tables S6 to S9). The strongest associations that we found were for the fecal levels of several secreted proteins, including human β-defensin-2 (HBD-2), calprotectin (*10*, *11*), and chromogranin A (CgA), with microbial composition, diversity, and functional richness (Figs. 3 and 4A), as well as with specific species (table S11) and pathways (table S12). Among these associations, CgA showed the strongest association with composition distance (adonis $R^2 = 0.03$, adjusted $P = 0.0006$), microbial diversity (Spearman $r = -0.22$, adjusted $P = 1.49 \times 10^{-12}$), gene richness (Spearman $r = -0.23$, adjusted $P = 9.4 \times 10^{-13}$), and COG richness (Spearman

Downloaded from http://science.sciencemag.org/ on April 28, 2016

r = −0.285, adjusted $P = 2.53 \times 10^{-20}$) (tables S4 to S9). The association of CgA with composition distance was then validated in an independent cohort of 19 individuals for whom 16*S* rRNA gene sequencing data were available ($P = 0.0065$) (fig. S10). A lower amount of CgA was associated with higher diversity, with functional richness, with high concentrations of high-density lipoprotein (HDL), and with intake of fruits and vegetables. In contrast, elevated fecal CgA was associated with high fecal levels of calprotectin, high blood concentrations of triglycerides, high stool frequency, soft stool type, and self-reported irritable bowel syndrome (IBS) (Fig. 4B). After correcting for the confounding effect of all other factors, our analysis revealed 61 species exclusively associated with CgA (Fig. 4, C and D, and table S13) whose abundances collectively accounted for 53% of the total abundance of the microbiome on average, and with 40 MetaCyc pathways (table S14) that accounted for 34.6% of the pathway profiles. The strongest association to CgA was observed for the *Archaea* species *Methanobrevibacter smithii* (fig. S11A), which plays an important role in the digestion of polysaccharides by consuming the end products of bacterial fermentation and methanogenesis (*12*) (fig. S11B). A negative association with CgA abundance was observed for 24 out of 36 species from phylum *Bacteroidetes* (Fig. 4, C and D).

CgA is a member of the granine peptides, which are secreted in nervous, endocrine, and immune cells under stress (*13*) and during active periods of gut-related diseases such as IBS and inflammatory bowel disease, although some findings are contradictory (*14*–*16*). Many different functions have been proposed for CgA and other granine peptides, including roles in neurological pathways, pain regulation, and antimicrobial activity against bacteria, fungi, and yeasts (*17*, *18*). However, their mechanism of action and physiological importance need further detailed investigation. To test whether genetic variants that influence *CHGA* gene expression (encoding CgA) can affect fecal CgA level and the gut microbiome, we tested the effect of six single-nucleotide polymorphisms known to regulate gene expression of CHGA on fecal CgA and abundances of species (table S15). No significant association was observed, suggesting that genetic variation in *CHGA* expression does not explain the variation observed in the fecal CgA levels and microbiome composition (tables S16 and S17). Our observation that CgA strongly correlates with microbiome composition, especially with a large number of species from *Bacteroidetes* phylum, and with diversity will hopefully encourage studies to unravel the role of CgA in gut health.

We also observed associations (FDR<0.1) between 63 dietary factors and interindividual distances in microbiota composition, including energy (kilocalories); intake of carbohydrates, proteins, and fats; and intake of specific food items such as bread and soft drinks (Fig. 3 and table S4). Drinking buttermilk (sour milk with a low fat content) was associated with high diversity, whereas drinking high-fat (whole) milk (3.5% fat content) was associated with lower diversity (table S6). Two of the species most strongly associated with drinking buttermilk are *Leuconostoc mesenteroides* ($q = 9.1 \times 10^{-46}$) and *Lactococcus lactis* ($q = 2.5 \times 10^{-8}$), both used as a starter culture for industrial fermentation (table S11). The abundance of dairy-fermentation–related bacteria increased with increasing dairy consumption, indicating potential for the use of probiotic drinks to augment and alter the gut microbiome composition. Consumption of alcohol-containing products, coffee, tea, and sugar-sweetened drinks was also correlated with microbial composition. Consumption of sugar-sweetened soda had a negative effect on microbial diversity (adjusted $P = 5 \times 10^{-4}$), whereas consumption of coffee, tea, and red wine, which all have a high polyphenol content, was associated with increased diversity (*19*–*21*). Red wine consumption correlated with *Faecalibacterium prausnitzii* abundance, which has anti-inflammatory properties, correlates negatively with inflammatory bowel disease (*22*), and shows higher abundance in high-richness microbiota (*23*). Apart from the negative associations between sugar-sweetened soda and bacterial diversity, other features of a Western-style diet, such as higher intake of total energy, snacking, and high-fat (whole) milk, were also associated with lower microbiota diversity (Fig. 3). A higher amount of

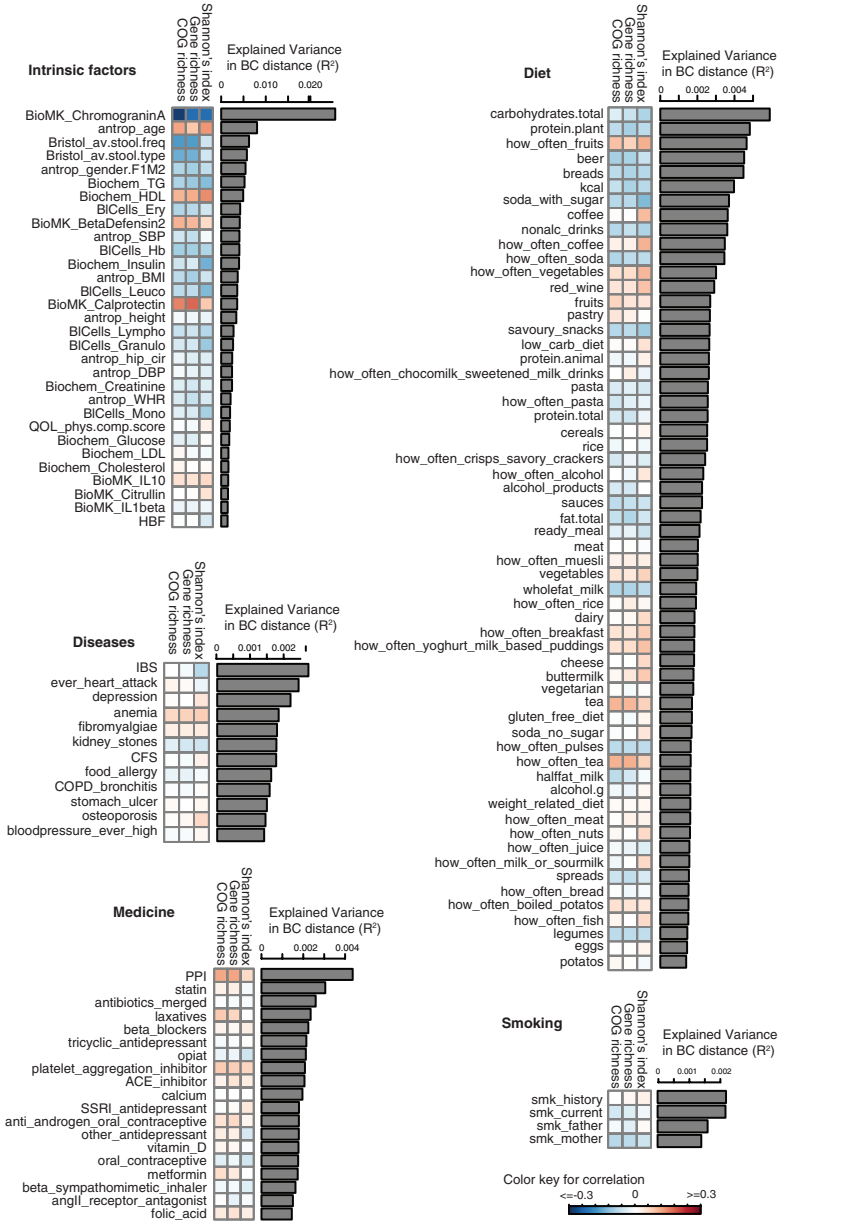

Fig. 3. Factors associated with interindividual variation of gut microbiome. A total of 126 factors (FDR<0.1) were associated with interindividual variation of the gut microbiome. The bar plot indicates the explained variation of each factor in the interindividual variation of microbial composition [Bray-Curtis (BC) distance]. The heatmap next to the bar plot shows the correlation coefficients of each factor with Shannon's index of diversity, gene richness, and COG richness, respectively. Color key for correlation is shown.

Downloaded from http://science.sciencemag.org/ on April 28, 2016

carbohydrates in the diet was associated with lower microbiome diversity. Total carbohydrate intake was positively associated with Bifidobacteria but negatively associated with *Lactobacillus*, *Streptococcus*, and *Roseburia* species. A low-carbohydrate diet consistently showed opposite directions of association for these species. We did not observe an association of carbohydrate intake to *prevotella* species, as has been described previously (*24*).

As expected, the use of antibiotics was significantly associated with microbiome composition, in particular with strong and significant decreases in two species from the genus *Bifidobacterium* (*Actinobacteria* phylum) (table S11), in line with previous studies (*25*). Several other drug categories, such as proton-pump inhibitors (PPIs) (95 users), metformin (15 users), statins (56 users), and laxatives (21 users), also had a strong effect on the gut microbiome. PPI users were found to have profound changes in 33 bacterial pathways (table S12). The most significant positive correlation of PPIs was observed with the pathway of 2,3-butanediol biosynthesis ($q = 5.3 \times 10^{-14}$). We also observed overlap between species and pathways associated to PPI and with calprotectin levels, particularly for bacteria typical of the oral microbiome (table S2, A to C; table S11; and fig. S12). This is in line with the correlations of PPIs with calprotectin levels reported in the literature (*26*). Even after excluding the 95 PPI users from our analysis, the positive correlation of calprotectin to most oral bacteria remained significant, indicating that this association is not due to the confounding effect of PPIs (fig. S12). Furthermore, the amounts of calprotectin were positively correlated with age and metabolic phenotypes [body mass index (BMI), diabetes, use of statins and metformin, glycated hemoglobin (HbA1c), and systolic blood pressure], but negatively correlated with the consumption of vegetables, plant proteins, chocolate, and breads. Multivariate analysis correcting for all factors revealed 14 species (table S13) and 114 bacterial metabolic pathways (table S14) exclusively associated with calprotectin, suggesting that calprotectin is robustly associated with the gut microbiome.

Metformin is commonly used to control blood sugar concentrations for treating type 2 diabetes, but can cause gastrointestinal intolerance (*27*). In 15 metformin users, we observed an increased abundance of *Escherichia coli* and a positive correlation with specific pathways, including the degradation and utilization of D-glucarate and D-galactarate and pyruvate fermentation pathways. Previous studies in *Caenorhabditis elegans* indicated the specific drug-bacteria interaction of metformin and *E. coli* (*28*). Our results are in line with recent observations in humans (*29*) that suggest that metformin can affect the microbiome through short-chain fatty acid (SCFA) production. To confirm this observation, we profiled acetate, propionate, and butyrate in 24 type 2 diabetes patients in our cohort—9 nonmetformin users and 15 users (*4*)—and found that SCFA concentrations were consistently higher in metformin users, especially for propionate (Wilcoxon test, $P = 0.035$) (fig. S13).

We assessed the effect of current smoking status, smoking history, parental smoking, and maternal smoking during pregnancy on the gut microbiome. These parameters were associated with Bray-Curtis distance, albeit with very modest effect. We did not detect significant associations for individual species or at pathways. In this study, we included 39 self-reported diseases, for which participants had reported at least five cases. IBS was reported by 9.9% of participants ($n = 112$, table S1) and was associated with changes in the gut microbiome and a lower microbial diversity (adjusted $P = 0.05$) (table S6). Species from the *Eggerthella* and *Coprobacillus* genera were positively associated with medication and food allergies, respectively. Individuals who had suffered a heart attack ($n = 10$) in the past had a significantly lower abundance of *Eubacterium eligens* bacterium, even after correcting for all other factors ($q = 4.6 \times 10^{-4}$).

Linking the deep-sequenced MGS data to various intrinsic and exogenous factors from the same individual not only allowed us to detect associations at species level, but also provided new insights into the interaction between the host, microbiota, and environmental factors, including diet. For instance, we have replicated and expanded our association of BMI and blood lipid concentrations with the gut microbiota based on 16*S* rRNA gene sequencing data (*30*) by showing associations with four specific species of the family Rikenellaceae. We previously associated this family with BMI and triglycerides in 16*S* rRNA data. In this study, we observed that a higher BMI was associated with

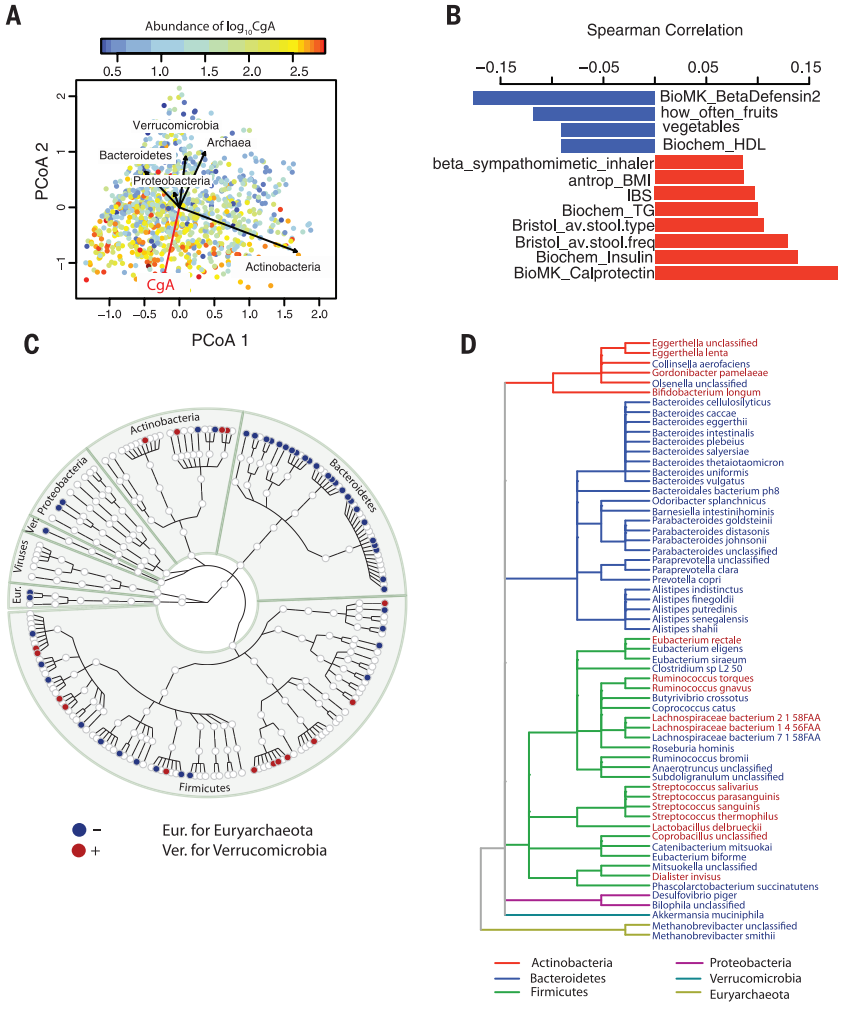

Fig. 4. The association of fecal level of chromogranin A. (**A**) Principal coordinate plots of Bray-Curtis distance of microbial composition. Each dot represents one individual, and its color is based on the abundance level of CgA: Warm colors indicate high abundance and cool colors, low abundance. The red arrow indicates the association direction of CgA, while the directions of the CgA-associated phyla are shown as black arrows. (**B**) Correlation between CgA and other factors at FDR<0.1. (**C**) Taxonomic tree of 170 species, of which 61 species were exclusively associated with CgA level. Each dot represents a taxonomic entity. Red dots indicate positively associated species. Blue dots indicate negatively associated species. (**D**) Taxonomic tree of the 61 species exclusively associated with CgA level. The branches are colored to show phylum levels as shown in the color key. Species in red show increased abundance associated with higher CgA levels. Species in blue show lower abundance associated with higher CgA levels.

Downloaded from http://science.sciencemag.org/ on April 28, 2016

a lower abundance of two species from the family Rikenellaceae, *Alistipes finegoldii*, and *Alistipes senegalensis*, whereas blood lipids were associated with two other species, *Alistipes shahii* and *Alistipes putredinis* (table S11). Notably, these species were also associated to certain dietary factors and drugs. For instance, a high level of *A. shahii*, which was associated to low triglyceride (TG) levels, was linked to higher fruit intake (q = 0.00027). Individuals with a higher abundance of *A. shahii* had a higher number of different species in the gut (species richness) (Spearman r = 0.2, adjusted $P = 3.96\text{x}10^{-11}$), suggesting a beneficial effect on the microbial ecosystem (table S18). Correlations with the number of different species were also found for other bacteria, including *Roseburia hominis*, *Coprococcus catus*, and *Barnesiella intestinihominis* and unclassified species from genus *Anaerotruncus* that also showed correlation both with fruit, vegetable, and nut consumption and with intrinsic phenotypes like HDL, triglycerides, and quality of life. On the basis of these data, it would be interesting to explore the potential to modulate disease-associated species through medication or diet, although we still need to address the causality and underlying mechanism.

Our study revealed significant associations between the gut microbiome and various intrinsic, environmental, dietary and medication parameters, and disease phenotypes, with a high replication rate between MGS and 16*S* rRNA gene sequencing data from the same individuals. Moreover, our study provides many new intrinsic and exogenous factors that correlate with shifts in the microbiome composition and functionality that potentially can be manipulated to improve microbiome-related health, and we hope our results will inspire further experiments to explore the biological relevance of associated factors. Although most of the factors that we assessed exerted a very modest effect, fecal levels of CgA showed a high potential as a biomarker for gut health.

REFERENCES AND NOTES

1. J. C. Clemente, L. K. Ursell, L. W. Parfrey, R. Knight, *Cell* **148**, 1258–1270 (2012).
2. E. F. Tigchelaar *et al.*, *BMJ Open* **5**, e006772 (2015).
3. S. Scholtens *et al.*, *Int. J. Epidemiol.* **44**, 1172–1180 (2015).
4. Information on materials and methods is available at *Science* Online.
5. N. Segata *et al.*, *Nat. Methods* **9**, 811–814 (2012).
6. R. Sinha, C. C. Abnet, O. White, R. Knight, C. Huttenhower, *Genome Biol.* **16**, 276 (2015).
7. J. K. Goodrich *et al.*, *Cell* **159**, 789–799 (2014).
8. G. Falony *et al.*, *Science* **352**, 560–564 (2016).
9. C. Huttenhower *et al.*, *Nature* **486**, 207–214 (2012).
10. F. Hildebrand *et al.*, *Genome Biol.* **14**, R4 (2013).
11. C. Hedin *et al.*, *Gut* 10.1136/gutjnl-2014-308896 (2015).
12. T. L. Miller, M. J. Wolin, E. Conway de Macario, A. J. Macario, *Appl. Environ. Microbiol.* **43**, 227–232 (1982).
13. T. Lee *et al.*, *Acta Paediatr.* **95**, 935–939 (2006).
14. L. Öhman, M. Stridsberg, S. Isaksson, P. Jerlstad, M. Simrén, *Am. J. Gastroenterol.* **107**, 440–447 (2012).
15. V. Sciola *et al.*, *Inflamm. Bowel Dis.* **15**, 867–871 (2009).
16. M. Wagner *et al.*, *Inflammation* **36**, 855–861 (2013).
17. R. Aslam *et al.*, *Curr. Med. Chem.* **19**, 4115–4123 (2012).
18. A. Bartolomucci *et al.*, *Endocr. Rev.* **32**, 755–797 (2011).
19. M. I. Queipo-Ortuño *et al.*, *Am. J. Clin. Nutr.* **95**, 1323–1334 (2012).
20. A. Duda-Chodak, T. Tarko, P. Satora, P. Sroka, *Eur. J. Nutr.* **54**, 325–341 (2015).
21. C. E. Mills *et al.*, *Br. J. Nutr.* **113**, 1220–1227 (2015).
22. H. Sokol *et al.*, *Proc. Natl. Acad. Sci. U.S.A.* **105**, 16731–16736 (2008).
23. E. Le Chatelier *et al.*, *Nature* **500**, 541–546 (2013).
24. G. D. Wu *et al.*, *Science* **334**, 105–108 (2011).
25. K. Korpela *et al.*, *Nat. Commun.* **7**, 10410 (2016).
26. A. Poullis, R. Foster, M. A. Mendall, D. Shreeve, K. Wiener, *Eur. J. Gastroenterol. Hepatol.* **15**, 573–574 (2003).
27. J. H. Burton *et al.*, *J. Diabetes Sci. Technol.* **9**, 808–814 (2015).
28. F. Cabreiro *et al.*, *Cell* **153**, 228–239 (2013).
29. K. Forslund *et al.*, *Nature* **528**, 262–266 (2015).
30. J. Fu *et al.*, *Circ. Res.* **117**, 817–824 (2015).

ACKNOWLEDGMENTS

We thank the LifeLines-DEEP participants and the Groningen LifeLines staff for their collaboration. We thank J. Dekens, M. Platteel, and A. Maatman for management and technical support. We thank J. Senior and K. McIntyre for editing the manuscript. This project was funded by grants from the Top Institute Food and Nutrition, Wageningen, to C.W. (TiFN GH001); the Netherlands Organization for Scientific Research to J.F. (NWO-VIDI 864.13.013), L.F. (ZonMW-VIDI 917.14.374), and R.K.W. (ZonMW-VIDI 016.136.308); and CardioVasculair Onderzoek Nederland to M.H.H. and A.Z. (CVON 2012-03). A.Z. holds a Rosalind Franklin Fellowship (University of Groningen), and M.C.C. holds a postdoctoral fellowship from the Fundación Alfonso Martín Escudero. This research received funding from the European Research Council (ERC) under the European Union's Seventh Framework Program: C.W. is supported by FP7/2007-2013)/ERC advanced Grant Agreement no. 2012-322698. M.G.N. is supported by an ERC Consolidator Grant (no. 310372). L.F. is supported by FP7/2007–2013, grant agreement 259867, and by an ERC Starting Grant, grant agreement 637640 (ImmRisk). J.R. and G.F. are supported by FP7 METACARDIS HEALTH-F4-2012-305312, VIB, FWO, IWT (Agency for Innovation by Science and Technology), the Rega institute for Medical Research, and KU Leuven. S.V.-S. and M.J. are supported by postdoctoral fellowships from FWO. T.V., M.S., and R.J.X. are supported by NIH, JDRF, and CCFA. A.Z., C.W., and J.F. designed the study. A.Z., E.F.T., L.F., and C.W. initiated the cohort and collected cohort data. A.Z., E.F.T., Z.M., S.A.J., M.C.C., and D.G. generated data. A.Z., A.K., M.J.B., E.F.T., M.S., T.V., A.V.V., G.F., S.V.-S., J.W., F.I., P.D., M.A.S., C.H., R.J.X., and J.F. analyzed data. G.F, S.V.-S., J.W., E.B., M.J., R.K.W., E.J.M.F., M.G.N., D.G., D.J., L.F., Y.S.A., C.H., J.R., R.J.X., and M.H.H. participated in integral discussions. A.Z., A.K., M.J.B., R.J.X., C.W., and J.F. wrote the manuscript. The authors have no conflicts of interest to report. The raw sequence data for both MGS and 16*S* rRNA gene sequencing data sets, and age and gender information per sample are available from the European genome-phenome archive (https://www.ebi.ac.uk/ega/) at accession number EGAS00001001704. Other phenotypic data can be requested from the LifeLines cohort study (https://lifelines.nl/lifelines-research/access-to-lifelines) following the standard protocol for data access. The study was approved by the institutional review board of UMCG, ref.M12. 113965. D.J. has additional funding from EU FP7/ no. 305564 and EU FP7/ no. 305479. C.H. is on the Scientific Advisory Board for Seres Therapeutics. Y.S.A. is a director and co-owner of PolyOmica, which provides services in statistical (gen)omics.

SUPPLEMENTARY MATERIALS

www.sciencemag.org/content/352/6285/565/suppl/DC1
Materials and Methods
Figs. S1 to S13
Tables S1 to S19
References (*31*–*54*)

1 September 2015; accepted 11 March 2016
10.1126/science.aad3369

ORGANIC CHEMISTRY

Kinetically controlled *E*-selective catalytic olefin metathesis

Thach T. Nguyen,[1] Ming Joo Koh,[1] Xiao Shen,[1] Filippo Romiti,[1] Richard R. Schrock,[2] Amir H. Hoveyda[1]*

A major shortcoming in olefin metathesis, a chemical process that is central to research in several branches of chemistry, is the lack of efficient methods that kinetically favor *E* isomers in the product distribution. Here we show that kinetically *E*-selective cross-metathesis reactions may be designed to generate thermodynamically disfavored alkenyl chlorides and fluorides in high yield and with exceptional stereoselectivity. With 1.0 to 5.0 mole % of a molybdenum-based catalyst, which may be delivered in the form of air- and moisture-stable paraffin pellets, reactions typically proceed to completion within 4 hours at ambient temperature. Many isomerically pure *E*-alkenyl chlorides, applicable to catalytic cross-coupling transformations and found in biologically active entities, thus become easily and directly accessible. Similarly, *E*-alkenyl fluorides can be synthesized from simpler compounds or more complex molecules.

Olefin metathesis is an enormously enabling chemical process for which well-defined catalysts were discovered nearly three decades ago (*1*, *2*). Kinetically controlled *Z*-selective reactions were introduced in 2009 (*3*), but there are no corresponding transformations that are broadly applicable and through which *E* isomers can be synthesized in high yield. Although *E*-selective cross-metathesis (CM) reactions involving Ru catechothiolate complexes (*4*) were reported very recently in 2016, only the thermodynamically preferred *E* isomers of simple (unfunctionalized) 1,2-disubstituted aliphatic alkenes could be obtained in 3 to 31% yield (*5*). *E* alkenes are often lower in energy and thus generated preferentially; nonetheless, olefin metathesis strategies that furnish them are needed for several reasons: The energy gap between the geometric forms is often too small to ensure high selectivity; *E* olefin isomers are not always thermodynamically preferred; and, in many cases,

[1]Department of Chemistry, Merkert Chemistry Center, Boston College, Chestnut Hill, MA 02467, USA. [2]Department of Chemistry, Massachusetts Institute of Technology, Cambridge, MA 02139, USA.
***Corresponding author. Email: amir.hoveyda@bc.edu**

Downloaded from http://science.sciencemag.org/ on April 28, 2016

E and *Z* alkene isomers cannot be easily separated. Perhaps the most notable instance relates to acyclic alkenyl halides, where hyperconjugative donation of electron density from a filled σ_{C-H} into a low-lying vacant $\sigma^*_{C-halogen}$ orbital causes stabilization of the *Z* isomers (*6*). Herein, we disclose the design of efficient and kinetically *E*-selective CM reactions through which *E*-alkenyl chlorides and fluorides can be obtained in good yield and with exceptional stereoselectivity.

E-1,2-Disubstituted chloroalkenes can be used in catalytic cross-coupling, one of the most influential transformations in modern chemistry (*7*). These isomers are found in biologically active molecules as well (*8*); two examples are pitinoic acid B, a potent anti-inflammatory agent (*9*), and kimbeamide A, a natural product with notable antitumor activity (*10*) (Fig. 1A). *E*-Alkenyl fluorides are of interest because of the substantial value of organofluorines in medicine (*11*) and agrochemicals (*12*). A biologically active fluoroalkenyl entity that inhibits *Bacillus subtilis S*-ribosyl-homocysteinase (LuxS) (*13*) is presented in Fig. 1A; only an *E*/*Z* mixture of this compound has been evaluated, due to the difficulties associated with accessing a stereoisomerically pure alkenyl fluoride. Functionalization of a stereochemically defined fluoro-substituted olefin would facilitate preparation of other desirable F-containing molecules (*14*).

Equally important, by conversion of an alkene to an *E*-alkenyl fluoride through catalytic and stereoselective CM, a hydrogen may be substituted with a fluorine atom within a complex molecule, such as the methyl ester of the potassium channel activator isopimaric acid (Fig. 1A) (*15*). Such modification can result in the alteration and/or enhancement of the molecule's biological activity (*16*, *17*).

E-1,2-Disubstituted alkenyl chlorides can be prepared in a number of ways (see the supplementary materials for comprehensive bibliography). Terminal alkynes may be transformed to nucleophilic *E*-alkenylmetal intermediates that are then treated with an electrophilic halogen source (*18*–*20*). *E*-Alkenyl boronic acids, prepared from a terminal alkyne by a two-step procedure (such as hydroboration followed by hydrolysis), can be converted by a third step to the corresponding chlorides (*21*), which may alternatively be synthesized by treatment of an aldehyde with excess chromium chloride and chloroform (*22*). A small number of procedures furnish *E*-alkenyl fluorides from aldehydes (*23*) or alkynes (*24*, *25*), but none are catalytic and several require stoichiometric amounts of strongly basic [e.g., *tert*-butyllithium (*t*-BuLi)] and/or toxic reagents (e.g., hexamethylphosphoramide). In another case, a stereochemically defined fluorine-substituted alkenyl tosylate must first be secured by the use of *n*-BuLi and $LiAlH_4$ before it is subjected to a cross-coupling reaction (*26*). Efficient and *E*-selective catalytic CM strategies that deliver alkenyl chlorides and fluorides (Fig. 1B)—involving robust, abundant, and less costly alkenes (versus aldehydes or alkynes)—would complement the aforementioned methods, offering a more direct and economical approach on most occasions.

We recently demonstrated that molybdenum-based monoaryloxide pyrrolide (MAP) complexes possess the distinctive ability to promote efficient *Z*-selective CM reactions that afford alkenyl halides (*27*). These transformations probably proceed

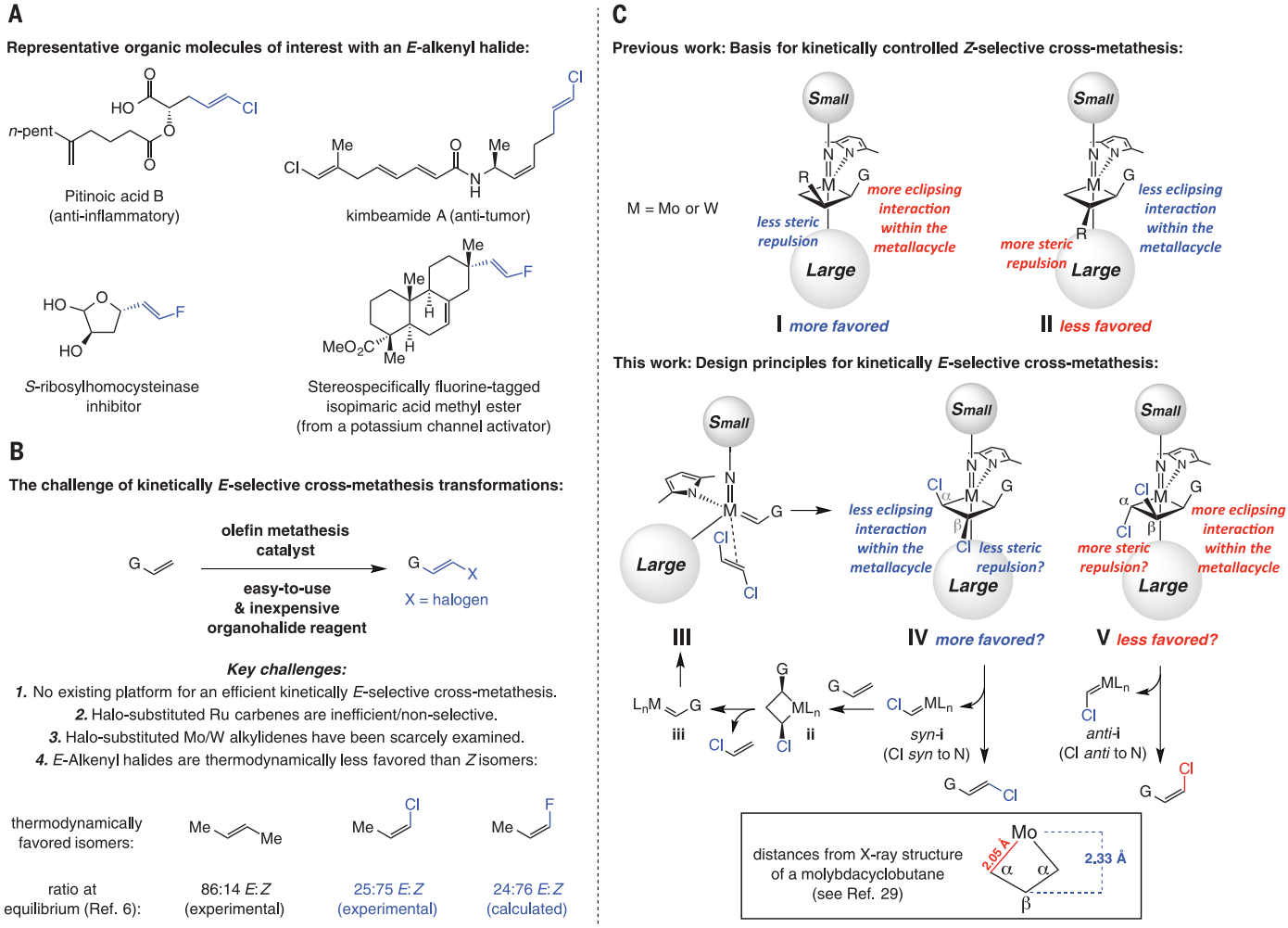

Fig. 1. Kinetically *E*-selective CM: potential effect and challenges. (**A**) Examples of biologically active organic molecules that contain an *E* alkenyl chloride or fluoride. (**B**) Challenges in designing a kinetically *E*-selective CM route to prepare alkenyl halides. (**C**) Analysis of stereochemical models that suggest a strategy for the design of kinetically *E*-selective olefin metathesis processes. pent, pentane; Me, methyl; Ln, ligand. G and R denote functional groups.

Downloaded from http://science.sciencemag.org/ on April 28, 2016

via olefin-derived alkylidenes that then react with a halo-olefin reagent. Reactions with widely used complexes (e.g., dichloro-Ru carbenes) are either inefficient and/or nonstereoselective (*27*). Designing a kinetically *E*-selective variant, however, poses several distinct challenges. Not only was there no blueprint for high-yielding and kinetically controlled *E*-selective olefin metathesis when these studies were initiated, but the desired products would also be thermodynamically less favored: The *Z*-haloalkenes are the more preferred isomers, as indicated by the relative energies shown in Fig. 1B (*6*).

In contemplating a strategy for achieving kinetic *E* selectivity, we evaluated the stereochemical model proposed for the corresponding *Z*-selective CM reactions (*28*), realizing an implicit principle. Reaction via metallacyclobutane **I** is preferred versus reaction via **II** (Fig. 1C) because the eclipsing interaction between the C–R and C–G bonds in **I** is less destabilizing than the steric repulsion between the C–R unit and the larger catalyst ligand in **II**. The question then became: If an alkylidene complex were to react with *E*-1,2-dichloroethene via **III**, would metallacycle **IV** or its corresponding diastereomer **V** be favored? In **IV**, the eclipsing interactions between C_α–G or C_α–Cl and C_β–H bonds in a structurally flat (*29*) molybdacyclobutane (nonpuckered due to the longer C–Mo bonds) would be less severe compared with those involving the C_α–G and C_β–Cl bonds of **V** (the C_α–C_α distance is ~2.75 Å). Whereas in **IV**, which would release an *E*-alkene, the C_β–Cl bond is oriented toward the more sizeable ligand, in **V** it would be a C_α–Cl unit that is so disposed. Moreover, collapse of **IV** would yield a presumably lower-energy *syn*-alkylidene (Cl pointing toward the imido ligand) (*30*). The resulting highly active (*27*) chloro-substituted *syn*-alkylidene (*syn*-**i**) would then react with the olefin substrate via the lower-energy α,α′-disubstituted metallacyclobutane **ii** (minimal eclipsing interaction or steric repulsion with the aryloxide ligand, with G and Cl oriented toward the smaller imido unit) to generate complex **iii**, which could be converted to **III**. It was unclear which of the latter pathways would be dominant and how high the stereoselectivity would be.

In search of more clues, we examined the crystal structure of an unsubstituted molybdacyclobutane derived from a MAP complex (*29*), noting that the molybdenum–C_β distance is longer than the metal–C_α bond length (2.33 versus 2.05 Å) (Fig. 1C). This observation suggested that there might be less steric repulsion between the halogen and the larger aryloxide ligand in **IV** (versus in **V**), which could translate to an *E*-selective process. However, the above analysis pointed to another possible complication: The vinyl chloride by-product might cause a diminution in selectivity by reaction via metallacyclobutane **I**, affording the thermodynamically favored *Z*-alkenyl halide. The use of vacuum (*28*) would not be an option: Although the volatility of *E*-1,2-dichloroethene allows it to be easily handled and readily removed (boiling point: 48°C), a substantial amount (if not all) would be lost under even mildly reduced pressure.

The above reasoning implied that an entirely distinct catalyst construct would not be needed for achieving high kinetic *E* selectivity and could be validated experimentally: CM of alkene **1** and

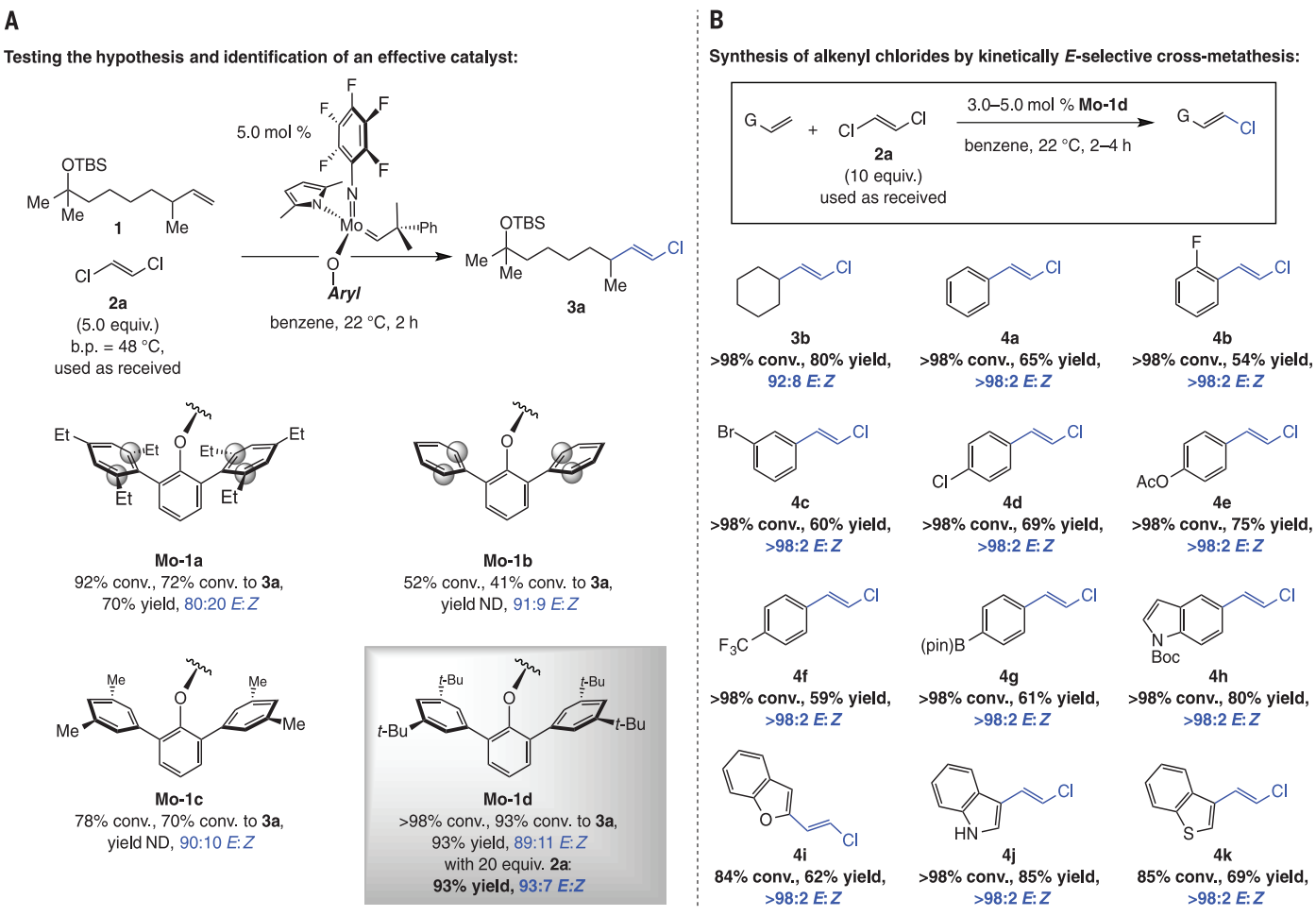

Fig. 2. Kinetically controlled *E*-selective CM reactions that generate alkenyl chlorides. (**A**) Model studies involving commercially available and easy-to-handle *E*-dichloroethene (**2a**) indicated that structural adjustment of the catalyst's aryloxide ligand is needed for maximal efficiency and stereoselectivity. b.p., boiling point; ND, not determined. (**B**) A range of alkyl-, aryl-, and heteroaryl-substituted *E*-alkenyl chlorides can be obtained in up to >98/2 *E*/*Z* selectivity. Yields are for purified products. TBS, *tert*-butyldimethylsilyl; Et, ethyl; G, functional group; Ac, acetyl; pin, pinacolato; Boc, *tert*-butoxycarbonyl. See the supplementary materials for details.

Downloaded from http://science.sciencemag.org/ on April 28, 2016

E-1,2-dichloroethene **2a** with 5.0 mol % **Mo-1a** (Fig. 2A) affords *E*-alkenyl chloride **3a** with an 80/20 *E*/*Z* ratio. Equally encouraging was that the products were obtained in 70% yield after purification, without resorting to long reaction times or elevated temperatures (2 hours, 22°C).

We envisioned that removing the ortho aryl substituents within the aryloxide ligand (highlighted in **Mo-1a** and **Mo-1b**, Fig. 2A) might alleviate steric repulsion with the C_β chlorine atom, favoring reaction via **IV**. We therefore prepared and examined the selectivity of the CM reaction with **Mo-1b**, which led to substantially improved stereoselectivity (91/9 *E*/*Z*) but lower efficiency (41% versus 72% conversion with **Mo-1a**), probably due to competitive bimolecular alkylidene decomposition (*30*). To retain high selectivity without efficiency loss, we evaluated the performance of **Mo-1c** and **Mo-1d** and established that either complex can produce **3a** with appreciable efficiency in ~90% *E* selectivity (Fig. 2A). With **Mo-1d** and 20 equivalents (equiv.) of **2a**, selectivity improved to 93% *E*, probably due to diminished competitiveness of nonselective CM involving the vinyl chloride by-product (via **I**, Fig. 1C). Excess **2a** was easily removed in vacuo.

An array of *E*-alkenyl chlorides was accessed by reaction between a terminal olefin and commercially available **2a**, which was used as received (no purification). Transformations may be performed with sterically congested alkenes: cyclohexyl-substituted **3b** was obtained in 80% yield and 92/8 *E*/*Z* selectivity. CM with various aryl (**4a** to **4g**) and heteroaryl α-olefins (**4h** to **4k**) generated the products in 54 to 85% yield after 4 hours at room temperature. The difference between the conversion and yield is largely due to the formation of homocoupling products. We did not detect the *Z* isomer in any reaction [by analysis of 400-MHz ^{1}H nuclear magnetic resonance (NMR) spectra of the unpurified product mixtures]. Product **4a** was obtained from the reaction with *E*-β-methyl styrene. Aryl halides **4c** and **4d** and arylboronate **4g** are noteworthy because their synthesis through cross-coupling could pose chemoselectivity issues (*31*, *32*).

Preparation of *E*-1,2-disubstituted alkenyl chlorides with unhindered aliphatic alkenes (versus

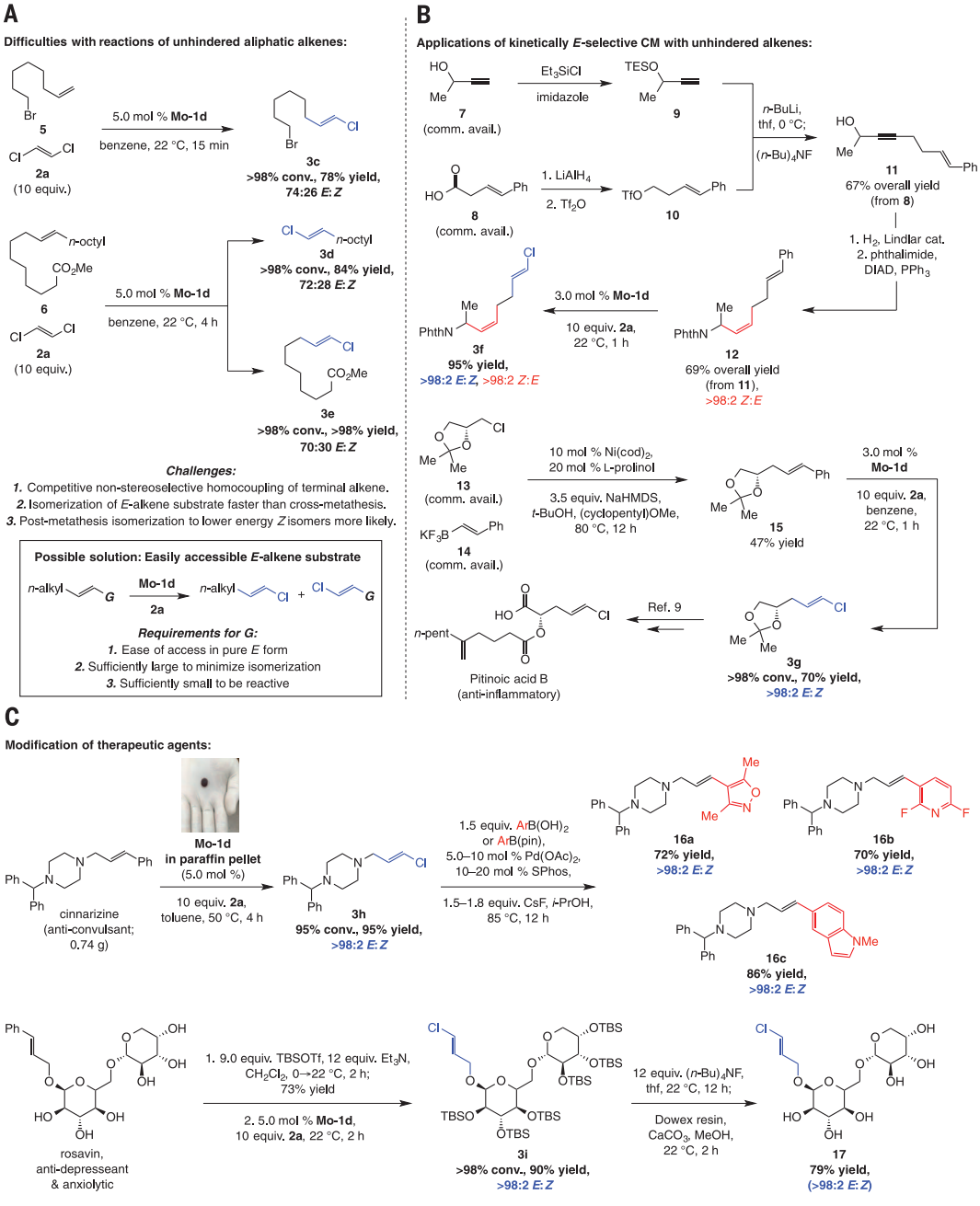

Fig. 3. Synthesis of unhindered *E*-alkenyl chlorides by catalytic and stereoselective substituent swapping. (**A**) With unhindered aliphatic α-olefins, catalytic CM with **2a** is efficient but moderately *E*-selective. This may be attributed to the rapid formation of an *E*/*Z* mixture of 1,2-disubstituted alkenes, formed by homocoupling, that reacts with **2a**. Thus, readily available *E*-1,2-disubstituted alkenes may be used instead (**G** = Ph). (**B**) Through the use of easily accessible β-alkyl styrenes, a number of biologically active compounds can be readily prepared. (**C**) The catalytic method, in combination with catalytic cross-coupling, may be used to access a variety of potentially valuable derivatives. An air- and moisture-resistant paraffin tablet containing a Mo MAP complex can easily be used. Yields are for purified products. TES, triethylsilyl; thf, tetrahydrofuran; Tf, trifluoromethanesulfonyl; DIAD, di(*iso*-propyl)azodicarboxylate; Phth, phthalyl; Ph, phenyl; cod, cyclooctadiene; HMDS, hexamethyldisilazide; *i*-Pr, *iso*-propyl; SPhos, 2-dicyclohexylphosphino-2′,6′-dimethoxybiphenyl. See the supplementary materials for details.

Downloaded from http://science.sciencemag.org/ on April 28, 2016

those with an allylic substituent as in **3a** and **3b**) presented another complication (Fig. 3A). CM was efficient with olefin **5**, affording chloroalkene **3c** in 78% yield, but selectivity was moderate (74% *E* isomer). Other than the possibility of a more facile post-metathesis isomerization of the relatively uncongested olefin, this discrepancy might originate from a more competitive and moderately selective generation of homocoupling products, which can then react with **2a** to afford isomeric mixtures. Further, the finding that CM with *E*-1,2-disubstituted olefin **6** produced **3d** and **3e** with similar selectivity (~70/30 *E*/*Z*) implies that 1,2-dialkyl olefins might undergo rapid nonstereoselective isomerization by self-metathesis before reaction with **2a**.

The above data show that alkylidenes derived from **Mo-1d** can catalyze CM between 1,2-disubstituted alkenes with *E*-dichloroethene **2a**: Within 4 hours at room temperature, **3d** was obtained in 84% yield despite its volatility, and **3e** was isolated in >98% yield. Such high activity indicated the need for a strategy for accessing alkenyl chlorides with better stereocontrol. We surmised that with an appropriate *E*-1,2-disubstituted olefin, chloro-olefins might become accessible with kinetic *E* selectivity by what amounts to an efficient catalytic and stereospecific group exchange. The ideal substituent would be easily and efficiently accessible and would be sufficiently large to discourage self-metathesis and adventitious *E*-to-*Z* isomerization, but not so large as to inhibit CM with **2a**. We selected *E*-β-substituted styrenes because these comparatively robust compounds can be prepared by various methods, as showcased by the findings in Fig. 3, B and C.

The first example (Fig. 3B) is a concise synthesis of the amine segment of kimbeamide A (compare with Fig. 1A). The substrate (**12**) was synthesized from commercially available (racemic or as either enantiomeric form) propargyl alcohol

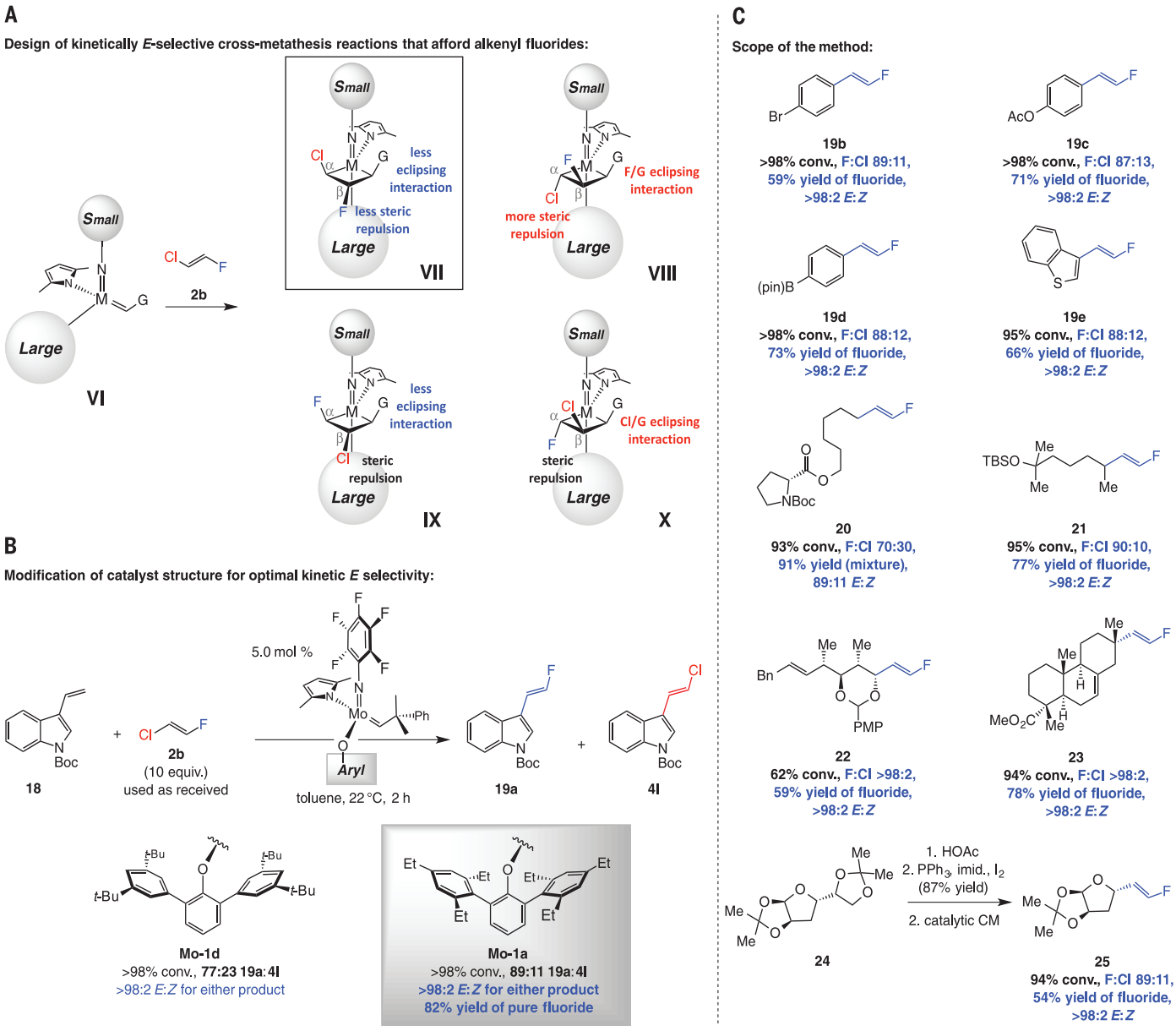

Fig. 4. Preparation of *E*-alkenyl fluorides by catalytic CM. (**A**) Mechanistic analysis that serves as the basis for the development of the catalytic processes. (**B**) Examination of a model process and identification of an effective complex. (**C**) With **Mo-1a** and commercially available *E*-1-chloro-2-fluoroethene **2b**, an assortment of *E*-1,2-alkenyl fluorides can be synthesized efficiently and with *E*/*Z* ratios that are typically >98/2. Yields are for purified products. G, functional group; Bn, benzyl; PMP, *para*-methoxyphenyl; imid., imido. See the supplementary materials for details.

Downloaded from http://science.sciencemag.org/ on April 28, 2016

(**7**) and carboxylic acid (**8**). Partial hydrogenation of enyne **11**, followed by a Mitsunobu reaction, afforded diene **12** (>98% *E*-β-alkylstyrene, >98% *Z* allylic amine; 69% overall yield). Subsequent treatment with 3.0 mol % **Mo-1d** and **2a** generated **3f** in 95% yield and >98/2 *E*/*Z* selectivity after 1 hour at room temperature. The *Z*-alkene was left untouched in the course of CM (>98% *Z* at the allylic amine site), highlighting exceptional chemoselectivity. Another case corresponds to pitinoic acid B (Fig. 3B); here, catalytic cross-coupling of commercially available and enantiomerically pure alkyl chloride **13** and trifluoroborate **14** afforded **15** (*33*) directly in 47% yield. *E*-β-Substituted styrene **15** was then converted to *E*-alkenyl chloride **3g**, which has been formerly transformed to the anti-inflammatory agent (*9*).

Other than facilitating synthesis of biologically active compounds, the approach offers a convenient route for their modification—two cases are shown in Fig. 3C. We were able to convert 0.74 g of cinnarizine, a potent anticonvulsant agent, to *E*-alkenyl chloride **3h** in 94% yield and with >98% *E* selectivity (5.0 mol % **Mo-1d**, 10 equiv. **2a**, toluene, 22°C, 4 hours). Importantly, the Mo MAP complexes can be delivered in the form of air- and moisture-resistant paraffin pellets. For example, with a pellet containing **Mo-1d** (Fig. 3C) (~5 mg in ~95 mg of paraffin wax; 5.0 mol % loading), reaction of cinnarizine with **2a** cleanly afforded **3h** in 95% yield (>98% *E* isomer). To ensure complete release of the MAP species, the transformation was performed at 50°C in toluene under nitrogen atmosphere (Fig. 3C). After 4 hours, the resulting mixture was purified by routine silica gel chromatography (see the supplementary materials for further details). The entire procedure was carried out in a fume hood.

Compounds such as **3h** are a convenient entry to analogs that cannot be accessed efficiently or with high *E* selectivity by alternative methods, including direct CM; the three examples shown in Fig. 3C (**16a** to **16c**), obtained by catalytic cross-coupling with commercially available boronic acids or pinacol esters (*34*), are illustrative. In another case, a persilylated derivative of the antidepressant rosavin was converted to *E*-alkenyl chloride **3i** in 90% yield and >98% *E* selectivity. As with cinnarizine-derived **3h**, analogs may be easily synthesized via **3i** or its deprotected form **17**. The applications to pitinoic acid B, cinnarizine, and rosavin underscore the advantages of the CM approach to synthesis of *E* alkenyl chlorides versus the existing methods involving terminal alkynes or aldehydes (see above).

Reactions with 1,2-dibromoethene, which can be purchased only as an isomeric mixture (64/36 *E*/*Z*), were inefficient and nonselective. For example, CM of alkene **1** and 1,2-dibromoethene (8.0 equiv.) with 5.0 mol % **Mo-1d** proceeded to 16% conversion after 4 hours, with 61/39 *E*/*Z* selectivity.

Kinetically *E*-selective reactions that might furnish fluoro-substituted olefins present the additional issue of cost and practicality: *E*-1,2-difluoroethene is too expensive and volatile (boiling point: −42°C). One option would be to use *E*-1-chloro-2-fluoroethene (**2b**), which is commercially available, economically far more viable, and easier to use (boiling point: −4°C). The issue was whether with **2b** the transformations would be appreciably product-selective (alkenyl fluoride versus chloride), as CM can proceed via four distinct metallacyclobutane isomers (**VII** to **X**, Fig. 4A), only one of which would produce the desired *E*-fluoroalkene (**VII**). We posited that CM might be preferentially channeled via **VII** for several reasons: (i) Overall, there should be less steric strain in **VII** and **IX** versus **VIII** and **X**, respectively. There are no severe eclipsing interactions in **VII** and **IX**, and steric repulsion between a halogen atom and the larger aryloxide ligand would be more costly at the C_α position (as compared with **VIII** and **X**, respectively). (ii) Matching polarity of the Mo=C and C=C bonds of the dihaloethene, as indicated by the distinct chemical shifts in the ^{1}H NMR spectrum of the latter [δ 6.90 and 6.15 parts per million for CH(F) and CH(Cl), respectively, in $CDCl_3$], as well as the smaller size of a fluorine atom (0.42 Å atomic radius versus 0.79 Å for Cl), should favor **VII** over **IX**. In the event (Fig. 4B), CM between aryl alkene **18** and **2b** (solution in toluene) with 5.0 mol % **Mo-1d** favored the formation of alkenyl fluoride **19a** over the chloro-substituted alkene **4l** (77/23). Both products were generated with >98% *E* selectivity.

While contemplating how we could improve the ratio of fluoroalkenes to chloroalkenes, we noted that because **19a** and **4l** are formed with >98% *E* selectivity, reaction via **IX** is probably the major competing pathway. If so, reverting to the original MAP complex **Mo-1a**, containing 2,6-disubstituted aryl moieties [versus 3,5-(*t*-Bu)$_2$ in **Mo-1d**], could prove beneficial. We hoped that this alteration would further exacerbate steric repulsion between the substituent at C_β and the aryloxide in **IX** (C_β–Cl), as compared with **VII** (C_β–F), because of the smaller size of a fluorine atom and the shorter C–F bond length (1.35 Å versus 1.80 Å for C–Cl). Indeed, with **Mo-1a**, under otherwise identical conditions, CM of **18** and **2b** proceeded to >98% conversion in 2 hours at ambient temperature (Fig. 4B), generating **19a** with improved selectivity (89% versus 77% **19a** with **Mo-1d**). Pure *E*-fluoroalkene **19a** could be isolated in 82% yield (silica gel chromatography). The use of bulkier aryloxides (e.g., *iso*-propyl versus -ethyl substituents) led to lower conversion.

A variety of *E*-alkenyl fluorides may be directly accessed (Fig. 4C); **2b** was used without purification, and reactions generated up to >98/2 fluoroalkene/chloroalkene selectivity. As with **19a**, pure alkenyl fluorides could easily be obtained in most cases (54 to 78% yield). In only one instance (**20**) did we detect any of the *Z*-alkene. Different styrenes, including those with versatile functional groups (e.g., **19b** and **19d**), were effective cross partners. Several examples involving transformations with alkyl-substituted α-olefins are presented in Fig. 4C. Similar to the cases in Fig. 3, reactions with the less congested alkyl-substituted olefins were less *E*-selective (compare **20** versus **21**). Unlike when symmetrical **2a** was used, CM between *E*-β-alkyl styrenes and **2b** led to substantial amounts of β-fluorostyrene and aliphatic chloroalkene products. Formation of **22** (>98% fluoro product, 59% yield, >98% *E*) shows that acid-sensitive moieties, such as a *para*-methoxyphenyl acetal, are tolerated. The transformation leading to fluorine-tagged isopimaric acid methyl ester (**23**) involves a particularly congested alkene. A precursor to the aforementioned LuxS inhibitor, alkenyl-fluoride **25**, was prepared in three steps from **24** in 51% overall yield with >98% *E* selectivity. The present approach affords the *E*-fluoroalkene in its stereoisomerically pure form and is substantially more efficient than the previously reported route (7% overall yield from **24**) (*13*).

Thus, we have devised strategies that allow for olefin metathesis processes to proceed with high efficiency and kinetic *E* selectivity, delivering a valuable set of organic halides where *Z* isomers are thermodynamically favored. The possibility of using easy-to-handle paraffin tablets, soon to be commercially available, further enhances the potential effect of this approach (*35*). The strategies delineated above are expected to lead to the development of other efficient, practical, and kinetically *E*-selective olefin metathesis transformations; this is especially relevant to cases where there is minimal energy difference between the two stereoisomeric forms and/or the *Z*-alkene is preferentially generated with the more commonly used catalysts (e.g., alkenyl sulfides, alkenyl nitriles, or enynes) (*36*).

REFERENCES AND NOTES

1. A. H. Hoveyda, A. R. Zhugralin, *Nature* **450**, 243–251 (2007).
2. R. H. Grubbs, A. G. Wenzel, D. J. O'Leary, E. Khosravi, Eds., *Handbook of Metathesis* (Wiley, 2014).
3. I. Ibrahem, M. Yu, R. R. Schrock, A. H. Hoveyda, *J. Am. Chem. Soc.* **131**, 3844–3845 (2009).
4. M. J. Koh *et al.*, *Nature* **517**, 181–186 (2015).
5. A. M. Johns, T. S. Ahmed, B. W. Jackson, R. H. Grubbs, R. L. Pederson, *Org. Lett.* **18**, 772–775 (2016).
6. K. B. Wiberg, Y. G. Wang, G. A. Petersson, W. F. Bailey, *J. Chem. Theory Comput.* **5**, 1033–1037 (2009).
7. C. C. C. Johansson Seechurn, M. O. Kitching, T. J. Colacot, V. Snieckus, *Angew. Chem. Int. Ed.* **51**, 5062–5085 (2012).
8. W.- Chung, C. D. Vanderwal, *Angew. Chem. Int. Ed.* **55**, 4396–4434 (2016).
9. R. Montaser, V. J. Paul, H. Luesch, *Org. Lett.* **15**, 4050–4053 (2013).
10. J. K. Nunnery *et al.*, *J. Org. Chem.* **77**, 4198–4208 (2012).
11. K. Müller, C. Faeh, F. Diederich, *Science* **317**, 1881–1886 (2007).
12. T. Fujiwara, D. O'Hagan, *J. Fluor. Chem.* **167**, 16–29 (2014).
13. S. F. Wnuk *et al.*, *Bioorg. Med. Chem.* **16**, 5090–5102 (2008).
14. S. Fustero, A. Simón-Fuentes, P. Barrio, G. Haufe, *Chem. Rev.* **115**, 871–930 (2015).
15. Y. Imaizumi *et al.*, *Mol. Pharmacol.* **62**, 836–846 (2002).
16. E. P. Gillis, K. J. Eastman, M. D. Hill, D. J. Donnelly, N. A. Meanwell, *J. Med. Chem.* **58**, 8315–8359 (2015).
17. M. G. Campbell, T. Ritter, *Org. Process Res. Dev.* **18**, 474–480 (2014).
18. R. B. Miller, G. McGarvey, *J. Org. Chem.* **43**, 4424–4431 (1978).
19. G. A. Molander, L. N. Cavalcanti, *J. Org. Chem.* **76**, 7195–7203 (2011).
20. F. Gao, A. H. Hoveyda, *J. Am. Chem. Soc.* **132**, 10961–10963 (2010).
21. N. A. Petasis, I. A. Zavialov, *Tetrahedron Lett.* **37**, 567–570 (1996).

Downloaded from http://science.sciencemag.org/ on April 28, 2016

22. K. Takai, K. Nitta, K. Utimoto, *J. Am. Chem. Soc.* **108**, 7408–7410 (1986).
23. L. Zhu, C. Ni, Y. Zhao, J. Hu, *Tetrahedron* **66**, 5089–5100 (2010).
24. S. H. Lee, J. Schwartz, *J. Am. Chem. Soc.* **108**, 2445–2447 (1986).
25. T. Furuya, T. Ritter, *Org. Lett.* **11**, 2860–2863 (2009).
26. H. Zhang, C.-B. Zhou, Q.-Y. Chen, J.-C. Xiao, R. Hong, *Org. Lett.* **13**, 560–563 (2011).
27. M. J. Koh, T. T. Nguyen, H. Zhang, R. R. Schrock, A. H. Hoveyda, *Nature* **531**, 459–465 (2016).
28. S. J. Meek, R. V. O'Brien, J. Llaveria, R. R. Schrock, A. H. Hoveyda, *Nature* **471**, 461–466 (2011).
29. S. C. Marinescu, R. R. Schrock, P. Müller, A. H. Hoveyda, *J. Am. Chem. Soc.* **131**, 10840–10841 (2009).
30. R. R. Schrock, A. H. Hoveyda, *Angew. Chem. Int. Ed.* **42**, 4592–4633 (2003).
31. K. L. Billingsley, S. L. Buchwald, *J. Org. Chem.* **73**, 5589–5591 (2008).
32. J. Barluenga, P. Moriel, P. Aznar, C. Valdés, *Adv. Synth. Catal.* **348**, 347–353 (2006).
33. G. A. Molander, O. A. Argintaru, *Org. Lett.* **16**, 1904–1907 (2014).
34. A. Thakur, K. Zhang, J. Louie, *Chem. Commun.* **48**, 203–205 (2012).
35. A. C. Sather, H. G. Lee, J. R. Colombe, A. Zhang, S. L. Buchwald, *Nature* **524**, 208–211 (2015).
36. S. Torker, M. J. Koh, R. K. M. Khan, A. H. Hoveyda, *Organometallics* **35**, 543–562 (2016).

ACKNOWLEDGMENTS

This research was financially supported by the NIH (grant GM-59426). We thank S. Torker for helpful discussions and L. Ondi, J. B. Czirok, and G. M. Nagy for support and helpful advice. We are grateful to XiMo AG for gifts of paraffin tablets.

SUPPLEMENTARY MATERIALS

www.sciencemag.org/content/352/6285/569/suppl/DC1
Materials and Methods
References (*37*–*58*)
NMR Spectra

11 February 2016; accepted 30 March 2016
10.1126/science.aaf4622

CHEMISTRY

Conformational photoswitching of a synthetic peptide foldamer bound within a phospholipid bilayer

Matteo De Poli,[1] Wojciech Zawodny,[1] Ophélie Quinonero,[1] Mark Lorch,[2] Simon J. Webb,[1,3] Jonathan Clayden[4]*

The dynamic properties of foldamers, synthetic molecules that mimic folded biomolecules, have mainly been explored in free solution. We report on the design, synthesis, and conformational behavior of photoresponsive foldamers bound in a phospholipid bilayer akin to a biological membrane phase. These molecules contain a chromophore, which can be switched between two configurations by different wavelengths of light, attached to a helical synthetic peptide that both promotes membrane insertion and communicates conformational change along its length. Light-induced structural changes in the chromophore are translated into global conformational changes, which are detected by monitoring the solid-state ^{19}F nuclear magnetic resonance signals of a remote fluorine-containing residue located 1 to 2 nanometers away. The behavior of the foldamers in the membrane phase is similar to that of analogous compounds in organic solvents.

In the field of synthetic biology, substantial progress has been made in the use of light to control biological function by customization of membrane-bound proteins with artificial chromophores (*1*). In parallel, synthetic molecular photoswitches have been used to control chemical processes such as ligand binding and catalysis in isotropic solution (*2*, *3*). Here, we report the design and synthesis of a fully synthetic photoresponsive helical molecule that can insert into a phospholipid bilayer. We show that light-induced switching between configurational isomers can be used to induce global conformational change that propagates over several nanometers in a synthetic molecule within a membrane environment. Membrane-bound artificial photoswitchable synthetic structures capable of translating photochemical information into extended conformational changes, in a manner reminiscent of the operation of natural photoswitchable proteins such as rhodopsin (*4*), could ultimately provide opportunities for controlling chemical processes within membrane-defined compartments.

A detailed understanding of how the phospholipid bilayer affects long-range conformational changes in membrane-bound molecules is impeded by the difficulty of directly observing conformational changes in the membrane phase and by a lack of examples of biomolecules that adopt well-defined structures both in the membrane phase and in solution (*5*–*7*). A simplified yet functional synthetic analog of the membrane-spanning domains of natural proteins, containing in-built spectroscopic handles that are diagnostic of conformation, would be a powerful tool. Dynamic conformational changes in a membrane-bound molecule could then be explored, free of the complexities of protein structure, and compared with analogous changes in isotropic solution.

Given the requirement for a synthetic structure with a tendency to embed into membranes and with well-understood conformational dynamics, we chose to explore the membrane insertion of foldamers [synthetic polymeric molecules with well-defined conformations (*8*)] built from oligomers of the achiral amino acid Aib (2-aminoisobutyric acid; Fig. 1A, shown in black). These Aib foldamers show a strong preference for helical conformations (*9*) and therefore have two principal conformational states, in which the helix adopts a global left- or right-handed screw sense. Furthermore, helical Aib-rich peptides have a known tendency to insert into phospholipid bilayers because they occur naturally in the form of membrane-disrupting fungal antibiotics known as peptaibols (*10*).

A chiral amino acid residue was covalently linked to the N terminus of an $(Aib)_n$ foldamer and then N-acylated by an azobenzene motif (Fig. 1A, shown in red) to enable photochemical induction of conformational change (*11*). This motif manifests well-understood photochemical interconversion between *E* and *Z* configurations and thus offers a reversible light-driven means of initiating conformational reorganization from the terminus of the oligomer. The influence of azobenzene geometry on the relative population of conformational states of the $(Aib)_n$ helix was first explored in solution using foldamers **1** (Fig. 1A) that carry a C-terminal glycinamide as a solution-state ^{1}H nuclear magnetic resonance (NMR)–compatible reporter of helical conformation (*12*). An unequal conformational population can result when the first turn of a helical Aib-containing foldamer incorporates a single chiral tertiary amino acid residue, and the magnitude of this bias depends on the detailed structure of the first (N-terminal) β-turn of the helix (*12*).

^{1}H NMR spectra of valine-containing foldamers **1a** to **1d** were acquired in deuterated methanol (CD_3OD) solution as their thermally equilibrated mixtures of *E* (major) and *Z* (minor) geometrical isomers (analogous behavior in phenylalanine-containing foldamers is reported in table S1). Methanol has a polarity similar to that of the interfacial region of the phospholipid bilayer and prevents aggregation of the foldamers in solution (*13*, *14*). Because the left- and right-handed conformational states of an $(Aib)_n$ helix interconvert on a submillisecond time scale at ambient temperature, the ^{1}H NMR spectrum that is observed results from a weighted average of both conformational states, reflecting their relative population. The diagnostic feature in the averaged spectra of foldamers **1** is the signal or signals due to the methylene protons of the C-terminal glycinamide residue. A single signal indicates equal populations of the two states; a pair of signals indicates unequally populated

[1]School of Chemistry, University of Manchester, Manchester M13 9PL, UK. [2]Department of Chemistry, University of Hull, Hull HU6 7RX, UK. [3]Manchester Institute of Biotechnology, University of Manchester, Manchester M1 7DN, UK. [4]School of Chemistry, University of Bristol, Bristol BS8 1TS, UK.
***Corresponding author. E-mail: j.clayden@bristol.ac.uk**

Downloaded from http://science.sciencemag.org/ on April 28, 2016

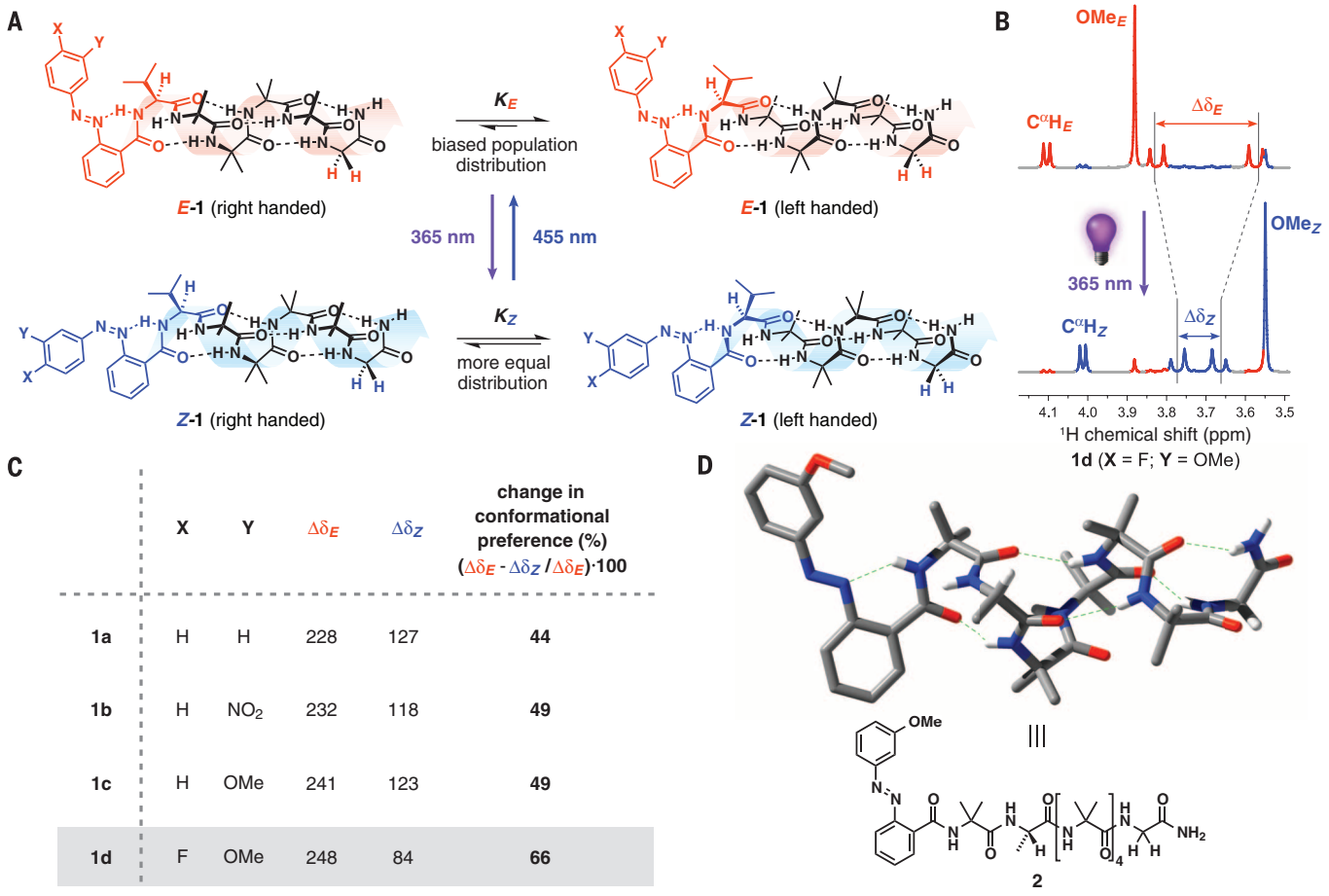

	X	Y	$\Delta\delta_E$	$\Delta\delta_Z$	change in conformational preference (%) $(\Delta\delta_E - \Delta\delta_Z / \Delta\delta_E)\cdot 100$
1a	H	H	228	127	**44**
1b	H	NO_2	232	118	**49**
1c	H	OMe	241	123	**49**
1d	F	OMe	248	84	**66**

Fig. 1. Validation of the photoswitchable foldamer architecture 1 in solution. (**A**) Switching the terminal azobenzene chromophore between *E* and *Z* configurations changes the population distribution between right- and left-handed conformations of foldamers **1a** to **1d** with general structure Azo-Val-Aib_4-$GlyNH_2$. (**B**) Portions of ^{1}H NMR spectra showing the change in chemical shift separation Δδ between the signals arising from the glycinamide methylene protons of foldamer **1d** in CD_3OD upon irradiation with light of 365 nm. (**C**) Percentage change in population distribution for foldamers **1a** to **1d**, calculated from Δδ values. (**D**) The intramolecular hydrogen bonding network (shown in green) in the x-ray crystal structure of Azo-Aib-Ala-Aib_4-$GlyNH_2$ **2**.

states. Furthermore, the magnitude of the chemical shift difference Δδ between these signals is proportional to the excess population of one screw-sense conformation over the other. A change in Δδ therefore indicates a change in population distribution across these two conformational states (*12*).

A comparison of the chemical shift differences Δδ in the glycinamide residue of the *E* and *Z* geometrical isomers of **1a** to **1d** (Fig. 1B) showed that the *E* isomers consistently exhibit greater Δδ values than the *Z* isomers. This indicates that the *E* isomer of the azobenzene induces a more powerful conformational preference K_E than that of the *Z* isomer K_Z, and induces a more unequal distribution of screw-sense populations (Fig. 1, A to C). The sensitivity of the conformational preference of **1** to the geometry of the azobenzene was tuned by varying the substituent in the *meta* position of the terminal ring (*15*, *16*). Methoxy-substituted **1c** and **1d** showed the greatest differences in conformational populations between their *E* and *Z* isomers (Fig. 1C) and were cleanly photoswitched from *E* to *Z* upon irradiation at 365 nm and from *Z* to *E* upon irradiation at 455 nm (fig. S2). Both **1c** and **1d** exhibited particularly slow thermal relaxation from *Z* to *E* [$t_{1/2}$ of 64 hours for **1d** (fig. S6)], and the *para*-fluoro substituent of **1d** additionally provided a local ^{19}F NMR reporter of azobenzene geometry.

We assume that the conformational switching of **1** is driven by a difference in electronic properties between the *E* and *Z* azobenzene-2-carboxamides. The population distribution between screw-sense conformations across a series of related $(Aib)_n$ foldamers is sensitive to the basicity of the carbonyl group linked to the N-terminal residue that initiates the first β-turn of the helix (*12*). The x-ray crystal structure of an azobenzene-2-carboxamide capped foldamer **2** (Fig. 1D) reveals that the proximal azo nitrogen atom forms an intramolecular hydrogen bond in the solid state with the NH of this N-terminal residue. Given the persistence of the intramolecular hydrogen bond network of Aib foldamers even in polar, hydrogen-bonding solvents (*17*), we assume that this hydrogen bond is retained in solution. Upon photoisomerization from *E* to *Z*, the azobenzene loses planarity and the diazo group becomes more basic (*18*), likely strengthening this hydrogen bond and in turn altering the geometry of the hydrogen bonding—and hence the conformational preference—within the β-turn. This change in conformational preference is propagated through the helical chain, leading to a detectable shift in the relative populations of left- and right-handed helical conformations, reported by the ^{1}H NMR signals of the C-terminal glycinamide reporter.

Having established that the conformational populations of the foldamers in solution could be perturbed by photochemical switching and detected by solution-state ^{1}H NMR, we needed to devise a means of detecting conformational changes in related foldamers when embedded in a membrane. Solid-state NMR [ss-NMR (*19*)] is a powerful analytical technique that can determine structures in nondissolved systems with quasi-atomic resolution. It can be used to characterize membrane-bound structures (*20*, *21*) and can yield detailed information on the conformation and dynamics of membrane-bound proteins and peptides (*22*–*24*) and their artificial mimics (*25*). It has recently been used to investigate the structure and dynamics of the photoswitchable

Downloaded from http://science.sciencemag.org/ on April 28, 2016

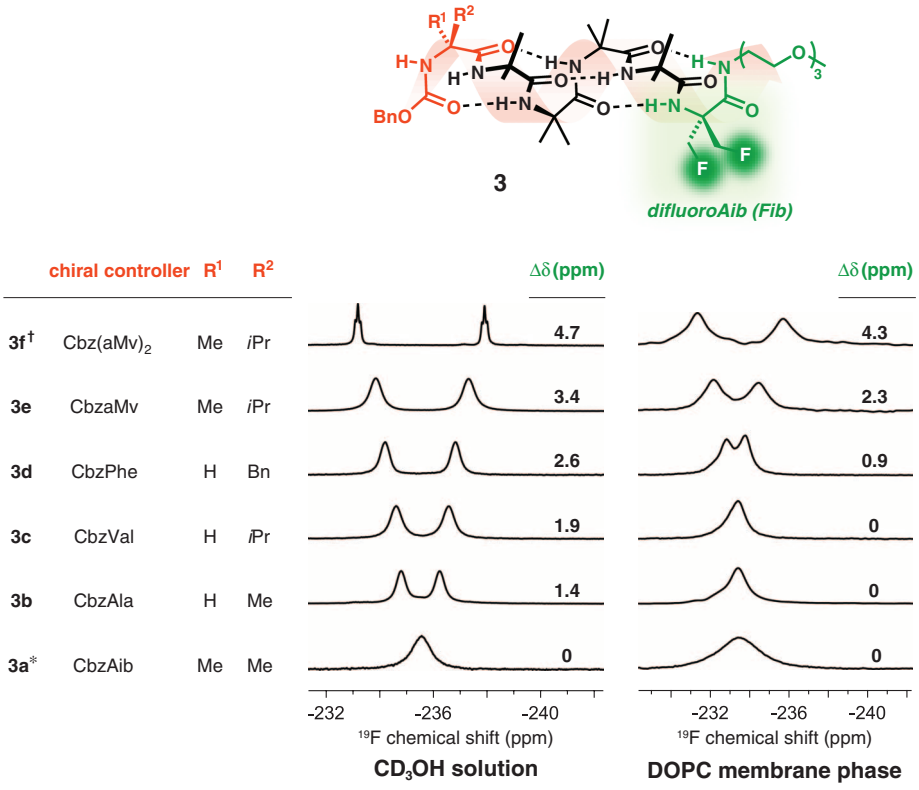

Fig. 2. Solution-phase and membrane-phase ^{19}F NMR signals of fluorinated foldamers 3a to 3f along with their corresponding chemical shift separations Δδ. aMv = L-α-methylvaline. *Achiral residue; †two consecutive aMv residues.

vision protein rhodopsin (*26*) and provides evidence that the solution-phase conformational preference of the Aib-rich peptaibol alamethicin is preserved when embedded in phospholipid bilayers (*27*). Magic angle spinning (MAS) is the most commonly used ss-NMR method (*28*), and in a lipid bilayer, MAS spin rates of ~10 kHz generate well-resolved ^{1}H ss-NMR signals within an experimental time scale of 1 hour (*29*). In the H-, C-, and P-rich membrane environment, details of orientation, conformation, folding, and association can be obtained through incorporation of fluorine substituents into natural (*30*) and artificial molecules (*31*). Temperature-, drug-, and solvation-dependent conformational changes of labeled membrane-bound proteins have been detected by ss-NMR (*32*), but the method has rarely been used to quantify conformational ratios or to observe dynamic conformational changes in membrane-bound artificial molecules (*33*).

To identify the foldamer in the phospholipid bilayer, we incorporated into its structure a 2,2-difluoroAib [Fib (*34*)] residue (Fig. 2, shown in green). Located at the foldamer's C terminus, several nanometers remote from the chromophore, Fib allows the use of ^{19}F ss-NMR (*29*, *35*) to detect changes in the conformational population distributions, because chemical shift differences (Δδ) between the ^{19}F NMR signals of the two fluorine atoms of Fib report on the conformational preferences of helical foldamers in solution, in a similar way to the glycinamide probe of **1** (*33*). Initially, a series of foldamers **3a** to **3f** (Fig. 2) lacking the azobenzene chromophore was synthesized to validate the use of Fib as a conformational reporter in the membrane phase. To enhance membrane solubility, we ligated a triethylene glycol (TEG) tail to the C terminus of the foldamers, adjacent to the Fib residue. The spatial separation between the FibTEG reporter and the N-terminal chiral residue ensures that the chemical shift difference Δδ between the ^{19}F NMR signals is insensitive to configurational changes in the chromophore, and thus reports only on induced conformational changes in the helical part of the foldamer. The ^{19}F NMR spectra of foldamers **3a** to **3f** in trideuterated methanol (CD_3OH) at 23°C showed pairs of signals with chemical shift differences Δδ that are proportional to the screw-sense population distributions reported for related compounds (*12*). The Δδ value provides a measure of population distribution between conformations only when exchange between screw senses is fast on the NMR time scale, so variable-temperature ^{19}F NMR (fig. S7) was used to confirm that the conformations of **3a** interconvert rapidly (i.e., at a rate of >6000 s^{-1}) in both CD_3OH (coalescence temperature T_c of **3a** = 0°C) and deuteriochloroform ($CDCl_3$, T_c of **3a** = +7°C), a low–dielectric constant solvent that simulates the low polarity at the center of a phospholipid bilayer (*36*).

We then used ss-NMR to study the dynamic conformational behavior of the helical foldamers **3** in a membrane environment. Multilamellar vesicles [MLVs (*37*)] were prepared by codissolving **3** and the phospholipid 1,2-dioleoyl-*sn*-glycero-3-phosphocholine (DOPC) [peptide/DOPC weight ratio (w/w) of 1:19 to 1:9] in chloroform (*38*). After removal of solvent under reduced pressure, the residue was rehydrated, freeze-dried, and resuspended in phosphate buffer solution (pH 7.2). Centrifugation and removal of the aqueous supernatant layer afforded a viscous lipid phase, which was loaded into a MAS zirconia rotor (fig. S6). The ^{31}P static NMR spectrum showed an anisotropic signal, whereas the ^{1}H MAS ss-NMR spectrum showed resolved, sharp peaks from both the lipids and foldamer (fig. S7) indicative of a lipidic fluid lamellar phase into which the oligomer is embedded but remains freely mobile (*39*–*41*).

^{19}F MAS ss-NMR spectra of **3a** to **3f** embedded in DOPC membranes were acquired with a spinning rate of 10 kHz and were compared with solution-phase ^{19}F NMR spectra of the same compounds **3a** to **3f** in CD_3OH (Fig. 2). In every case, either one or two ^{19}F signals centered around δ −234 ppm were observed in the ss-NMR spectrum, further confirming that the fluorinated foldamers **3a** to **3f** had partitioned into the lipid bilayer. The single ^{19}F NMR signal of the achiral foldamer **3a** in both solution-phase NMR and ss-NMR suggested that the rapid screw-sense inversion observed in solution persists in the membrane phase, allowing use of chemical shift differences Δδ in the ^{19}F ss-NMR spectrum to measure the population distribution of helical conformations in the membrane. The increasing separation of the ^{19}F NMR signals of the FibTEG probe in the series **3b** to **3f** in both solution and solid state confirms the increasingly strong chiral influence at the remote N terminus in both environments. Strongly helicogenic, C_α-tetrasubstituted residues (α-methylvaline, aMv), and in particular two consecutive aMv residues, induced the greatest bias in the conformational population in both environments. Although some subtle differences are evident, probably due to a weakening of conformational induction in a membrane environment, the similar conformational behavior of **3a** to **3f** both in isotropic solution and in the liquid crystal (*42*) environment of the DOPC bilayer suggests that the population of foldamer conformations in the membrane phase may be predicted by studying their population distribution in solution. ^{19}F ss-NMR spectra were concentration-independent: There was no change in Δδ upon varying the loading of foldamer **3d** from 3 to 15% w/w (fig. S12), nor upon adding a nonfluorinated chiral foldamer to a lipid bilayer already containing **3d** (fig. S13), indicating that screw-sense preferences detected by ^{19}F ss-NMR are not the result of intermolecular communication between helices. The single ^{19}F ss-NMR signal of **3a** confirms that the chirality of DOPC has no discernible influence on screw-sense preference.

Having shown that the constituent parts function successfully in isolation, we brought them together in the synthesis of a foldamer designed

Downloaded from http://science.sciencemag.org/ on April 28, 2016

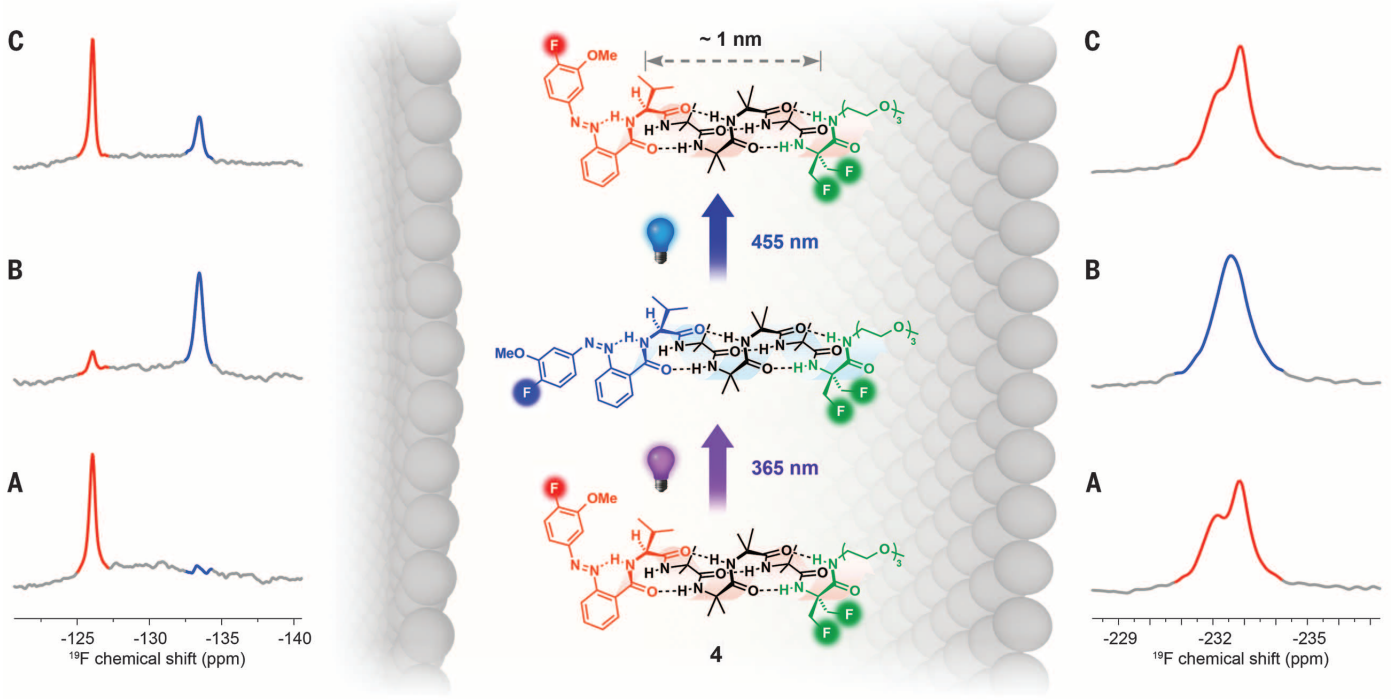

Fig. 3. Conformational switching of 4 by irradiation in a DOPC phospholipid bilayer (5% w/w). Molecular dimensions, but not necessarily orientation, of **4** are shown in proportion to the thickness of the bilayer, with the bilayer boundary indicated by gray spheres representing the phosphate head groups. Portions of the ^{19}F ss-NMR spectra corresponding to the N-terminal fluoroarene substituent (δ –125 to –140 ppm, left) and the C-terminal FibTEG reporter (δ –230 to –235 ppm, right) are shown as well. (**A**) Dark-equilibrated sample (>99:1 *E/Z* azobenzene ratio). (**B** and **C**) The same sample after irradiation at 365 nm (14:86 *E/Z* ratio) (B) and after subsequent irradiation at 455 nm (69:31 *E/Z* ratio) (C).

for photoswitching in the membrane phase. The most effective azobenzene motif **1d** (Fig. 1) was ligated to the N terminus of an Aib-containing foldamer carrying the C-terminal FibTEG ss-NMR conformational reporter. The resulting oligomer **4** (Fig. 3) carries ^{19}F labels at both the N and C termini, allowing parallel monitoring by ^{19}F ss-NMR of both configurational *E/Z* photoswitching in the azobenzene unit and consequent global conformational population switching of the foldamer. (The similar behavior of a Phe-containing analog is described in fig. S17.)

Foldamer **4** was equilibrated in the dark to a >99:1 *E/Z* ratio and embedded into the DOPC membrane phase using the procedure described earlier, but minimizing exposure to light. The ^{19}F ss-NMR spectrum (Fig. 3A) of the membrane-embedded foldamer showed a fluoroarene signal at δ –126 ppm, accompanied by two equally populated but unequally broadened signals (due to chemical shift anisotropy differences) in the region of δ –234 ppm. The single signal at δ –126 ppm confirmed that the azobenzene was still a single geometrical isomer after incorporation into the lipid bilayer. The appearance of two signals at δ –234 ppm, separated by ~1 ppm (Fig. 3A), indicates that the foldamer is in its "on" state, with one of the equilibrating screw-sense conformers of the helical structure preferentially populated. By analogy to the behavior of related Aib foldamers in solution, we infer that the preferred conformational state is left-handed and accounts for approximately 60 to 65% of the equilibrium population (*43*).

The suspension of MLVs containing foldamer (*E*)-**4** was then transferred to a quartz cuvette and illuminated using an LED of wavelength 365 nm (fig. S11). After 5 min, the phospholipid mixture was spun out from the cuvette and directly loaded into the MAS rotor. The ^{19}F ss-NMR spectrum (Fig. 3B) now revealed relative intensities of 14:86 for the signals corresponding to the *E* and *Z* azobenzenes, indicating substantial switching of the azobenzene geometry from *E* to *Z* within the phospholipid bilayer. Simultaneously, the pair of signals arising from the FibTEG reporter had collapsed into a broad singlet (Fig. 3B). This indicates that the photoinduced change in geometry at the N-terminal azobenzene had induced a global conformational switch into an "off" state, in which an approximately equal population of left- and right-handed screw-sense conformers is detected by the C-terminal reporter.

This *Z*-rich sample of **4** was transferred back into a quartz cuvette and illuminated a second time, with light of wavelength 455 nm, and again a ss-NMR sample was prepared using this now twice-illuminated, membrane-bound oligomer. This longer-wavelength illumination changed back the *E/Z* isomer population to a 69:31 ratio and restored the initial peak separation of the FibTEG reporter (Fig. 3C). This second irradiation at longer wavelength thus switched the foldamer back into its "on" state, reinstating its original conformational preference for a preferred screw sense and demonstrating the reversibility of the photoswitching process (see also fig. S16 for multiple, reversible photoswitching cycles).

No changes were evident in the FibTEG region of the ^{19}F ss-NMR spectrum when a similar illumination procedure was applied to an azobenzene-free foldamer, nor when using an azobenzene-capped but achiral foldamer after irradiation at 365, 405, or 455 nm (figs. S14 and S15). The slow *Z* to *E* thermal relaxation exhibited by the fluorinated azobenzene-valine moiety in CD_3OD solution ($t_{1/2}$ = 64 hours for **1d**; fig. S6) became only slightly faster in the phospholipid bilayer ($t_{1/2}$ ≈ 44 hours for both **4** and **5**; figs. S19 and S20). This proved particularly helpful for the purposes of this study, given the acquisition time required (0.5 to 1 hour) for each ss-NMR spectrum.

With the aim of transmitting conformational information over multi-nanometer distances comparable to the reach of the photoinduced conformational changes in rhodopsin that underpin the biochemistry of vision (*44*), we also studied foldamers with a much more extended helical structure. Foldamer **5** was synthesized, in which the azobenzene chromophore was separated from the FibTEG reporter by eight Aib residues, or about three turns of a 3_{10} helix, corresponding to a distance of 2 nm (*45*), a distance commensurate the hydrophobic thickness of a DOPC bilayer (Fig. 4A) (*40*). (A related phenylalanine-containing

Downloaded from http://science.sciencemag.org/ on April 28, 2016

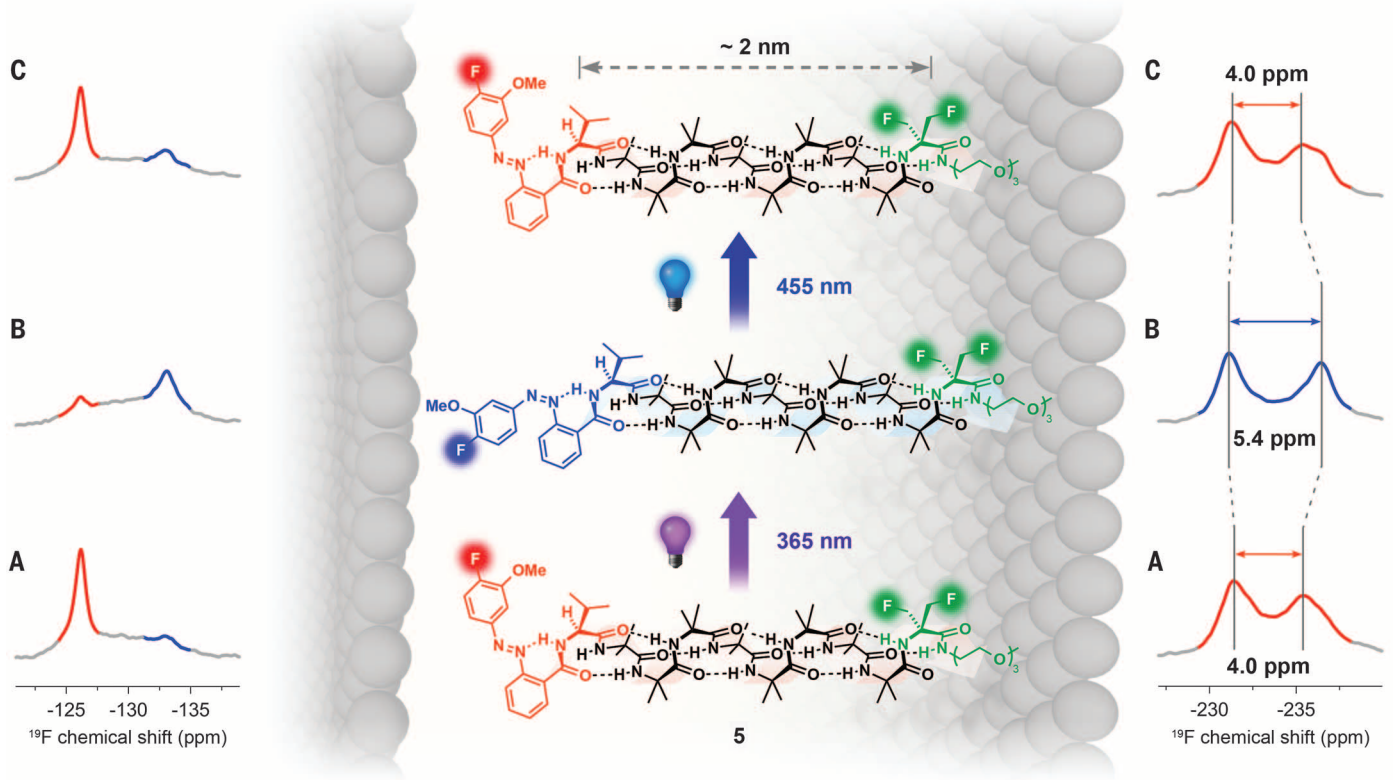

Fig. 4. Conformational switching of 5 by irradiation in a DOPC phospholipid bilayer (5% w/w). Molecular dimensions, but not necessarily orientation, of **5** are shown in proportion to the thickness of the bilayer, with the bilayer boundary indicated by gray spheres representing the phosphate head groups. Portions of the ^{19}F ss-NMR spectra corresponding to the N-terminal fluoroarene substituent (δ −125 to −135 ppm, left) and the C-terminal FibTEG reporter (δ −230 to −240 ppm, right) are shown as well. (**A**) Dark-equilibrated sample (92:8 *E/Z* azobenzene ratio). (**B** and **C**) The same sample after irradiation at 365 nm (18:82 *E/Z* ratio) (B) and after subsequent irradiation at 455 nm (71:29 *E/Z* ratio) (C).

foldamer is shown in fig. S18.) Preliminary ^{19}F NMR studies in $CDCl_3$ (fig. S8) indicated that the rate of exchange between conformational states is slower in these longer homologs [$T_c \approx +35$°C, indicating a rate of <6000 s^{-1} at room temperature (*46*)]. After insertion into the DOPC bilayer but before irradiation, integration of the ^{19}F ss-NMR signals at ~ δ −130 ppm indicated that **5** exists as a 92:8 mixture of *E* and *Z* geometrical isomers. Foldamer **5** showed two FibTEG NMR signals in the region of δ −234 ppm separated by 4.0 ppm (Fig. 4A). The membrane-embedded foldamers were irradiated for 7 min with light of wavelength 365 nm, which switched the azobenzene chromophore to an 18:82 *E/Z* geometrical ratio and simultaneously caused a marked change in the FibTEG reporter signal, increasing the separation of the peaks to 5.4 ppm (Fig. 4B). A second period of illumination at 455 nm switched back the population of azobenzene geometrical isomers to a 71:29 *E/Z* ratio and returned the chemical shift separation to its initial value (Fig. 4C). As in $CDCl_3$ solution, the spectroscopic responses of **5** in the membrane phase are characteristic of slower exchange between screw-sense conformations (they are in intermediate exchange on the NMR time scale), which at this stage in the work prevents us from quantifying the relative populations of the conformational states. These findings demonstrate that light-induced configurational switching at one location in extended membrane-bound synthetic molecules induces local changes in structure that propagate through the oligomers to induce global changes in conformation, causing a change in conformational populations that is detected by spatially remote reporters.

Our results show that the dynamic control over the conformational behavior of foldamers in solution may be replicated in a phospholipid bilayer. We envisage that replacement of the spectroscopic reporter with a catalytic or binding site in related switchable oligomers should allow photoswitchable changes in conformation leading to the stimulated release of a chemical messenger, or to catalytic formation of a secondary messenger to be up- or down-regulated (*47*). Incorporation of such switchable functional molecules into membranes would allow localized, photoinduced chemical changes to be translated into chemical responses in the lumen of artificial vesicles, or even the controlled release or uptake of a chemical signal in the cytosol of individual live cells. The work demonstrates that simplified synthetic molecules may be designed to display the essential functions of much more complex, evolved biomolecules.

REFERENCES AND NOTES

1. J. Broichhagen, D. Trauner, *Curr. Opin. Chem. Biol.* **21**, 121–127 (2014).
2. R. Göstl, A. Senf, S. Hecht, *Chem. Soc. Rev.* **43**, 1982–1996 (2014).
3. B. L. Feringa, W. E. Browne, Eds., *Molecular Switches* (Wiley-VCH, ed. 2, 2011).
4. W. J. De Grip, K. J. Rothschild, in *Molecular Mechanisms of Visual Transduction*, D. G. Stavenga, W. J. De Grip, E. N. Pugh Jr., Eds. (Elsevier, 2000), pp. 1–54.
5. R. Nygaard *et al.*, *Cell* **152**, 532–542 (2013).
6. K. Henzler-Wildman, D. Kern, *Nature* **450**, 964–972 (2007).
7. F. Hu, W. Luo, M. Hong, *Science* **330**, 505–508 (2010).
8. S. H. Gellman, *Acc. Chem. Res.* **31**, 173–180 (1998).
9. C. Toniolo, E. Benedetti, *Trends Biochem. Sci.* **16**, 350–353 (1991).
10. C. Toniolo, H. Brückner, Eds., *Peptaibiotics* (Wiley-VCH, 2009).
11. H. M. D. Bandara, S. C. Burdette, *Chem. Soc. Rev.* **41**, 1809–1825 (2012).
12. M. De Poli *et al.*, *J. Org. Chem.* **79**, 4659–4675 (2014).
13. G. Shanmugam, P. L. Polavarapu, *Biophys. J.* **87**, 622–630 (2004).
14. S. J. Pike, V. Diemer, J. Raftery, S. J. Webb, J. Clayden, *Chemistry* **20**, 15981–15990 (2014).
15. Electron-donating groups *para* to the azo linkage were avoided, as they are known to promote fast thermal relaxation to the *E* isomer [see (*16*)].
16. N. Nishimura *et al.*, *Bull. Chem. Soc. Jpn.* **49**, 1381–1387 (1976).
17. B. A. F. Le Bailly *et al.*, *Chem. Sci.* **6**, 2313–2322 (2015).
18. F. Gerson, E. Heilbronner, A. van Veen, B. M. Wepster, *Helv. Chim. Acta* **43**, 1889–1898 (1960).
19. M. J. Duer, *Introduction to Solid-State NMR Spectroscopy* (Blackwell, 2004).
20. D. Huster, *Biochim. Biophys. Acta Mol. Cell Biol. Lipids* **1841**, 1146–1160 (2014).
21. E. Strandberg, A. S. Ulrich, *Concepts Magn. Reson. A* **23**, 89–120 (2004).

Downloaded from http://science.sciencemag.org/ on April 28, 2016

22. M. Hong, Y. Zhang, F. Hu, *Annu. Rev. Phys. Chem.* **63**, 1–24 (2012).
23. E. D. Watt, C. M. Rienstra, *Anal. Chem.* **86**, 58–64 (2014).
24. L. A. Baker, M. Baldus, *Curr. Opin. Struct. Biol.* **27**, 48–55 (2014).
25. C. Aisenbrey, N. Pendem, G. Guichard, B. Bechinger, *Org. Biomol. Chem.* **10**, 1440–1447 (2012).
26. A. V. Struts, U. Chawla, S. M. Perera, M. F. Brown, *Methods Mol. Biol.* **1271**, 133–158 (2015).
27. T. Nagao *et al.*, *Biochim. Biophys. Acta* **1848**, 2789–2798 (2015).
28. T. Polenova, R. Gupta, A. Goldbourt, *Anal. Chem.* **87**, 5458–5469 (2015).
29. A. Ramamoorthy, J. Xu, *J. Phys. Chem. B* **117**, 6693–6700 (2013).
30. K. Koch, S. Afonin, M. Ieronimo, M. Berditsch, A. S. Ulrich, *Top. Curr. Chem.* **306**, 89–118 (2012).
31. Y. Su, W. F. DeGrado, M. Hong, *J. Am. Chem. Soc.* **132**, 9197–9205 (2010).
32. J. K. Williams *et al.*, *J. Am. Chem. Soc.* **135**, 9885–9897 (2013).
33. N. H. Joh *et al.*, *Science* **346**, 1520–1524 (2014).
34. S. J. Pike *et al.*, *Org. Biomol. Chem.* **11**, 3168–3176 (2013).
35. P. Wadhwani, E. Strandberg, in *Fluorine in Medicinal Chemistry and Chemical Biology*, I. Ojima, Ed. (Wiley, 2009), pp. 463–494.
36. S. Mazères, V. Schram, J.-F. Tocanne, A. Lopez, *Biophys. J.* **71**, 327–335 (1996).
37. F. Szoka Jr., D. Papahadjopoulos, *Annu. Rev. Biophys. Bioeng.* **9**, 467–508 (1980).
38. D. E. Warschawski *et al.*, *Biochim. Biophys. Acta Biomembr.* **1808**, 1957–1974 (2011).
39. J. H. Davis, M. Auger, R. S. Hodges, *Biophys. J.* **69**, 1917–1932 (1995).
40. M. Bouchard, J. H. Davis, M. Auger, *Biophys. J.* **69**, 1933–1938 (1995).
41. A. V. Filippov, A. M. Khakimov, B. V. Munavirov, *Annu. Rep. NMR Spectr.* **85**, 27–92 (2015).
42. N. Kučerka *et al.*, *Biophys. J.* **95**, 2356–2367 (2008).
43. R. A. Brown, T. Marcelli, M. De Poli, J. Solà, J. Clayden, *Angew. Chem. Int. Ed.* **51**, 1395–1399 (2012).
44. H.-W. Choe *et al.*, *Nature* **471**, 651–655 (2011).
45. R. Gessmann, H. Brückner, K. Petratos, *J. Pept. Sci.* **9**, 753–762 (2003).
46. R.-P. Hummel, C. Toniolo, G. Jung, *Angew. Chem. Int. Ed. Engl.* **26**, 1150–1152 (1987).
47. B. A. F. Le Bailly, L. Byrne, J. Clayden, *Angew. Chem. Int. Ed.* **55**, 2132–2136 (2016).

ACKNOWLEDGMENTS

Supported by the European Research Council (Advanced Investigator Grant ROCOCO) and UK Engineering and Physical Sciences Research Council grants EP/K039547/1 and EP/N009134/1. We thank B. Gore for assistance with ss-NMR experiments, R. Adams and G. Morris for helpful discussions on solution and solid-state NMR data, and S. Koehler and L. Natrajan for valuable suggestions for preliminary irradiation studies. Detailed experimental procedures and all data supporting this publication are presented in the supplementary materials. Metrical parameters for the structure of **2** are available free of charge from the Cambridge Crystallographic Data Centre under accession number CCDC 1415763. Author contributions: M.D.P., S.J.W., and J.C. conceived the project and designed the experiments; M.D.P. synthesized the compounds with assistance from W.Z. and O.Q.; M.D.P. and M.L. devised and carried out the ss-NMR experiments; M.D.P., S.J.W., and J.C. analyzed the data and wrote the paper.

SUPPLEMENTARY MATERIALS

www.sciencemag.org/content/352/6285/575/suppl/DC1
Materials and Methods
Supplementary Text
Figs. S1 to S21
Tables S1 to S9
References (*48*–*59*)

11 November 2015; accepted 24 February 2016
Published online 31 March 2016
10.1126/science.aad8352

GEOCHEMISTRY

Pressure-dependent isotopic composition of iron alloys

A. Shahar,[1]* E. A. Schauble,[2] R. Caracas,[3] A. E. Gleason,[4] M. M. Reagan,[5] Y. Xiao,[6] J. Shu,[1] W. Mao[5]

Our current understanding of Earth's core formation is limited by the fact that this profound event is far removed from us physically and temporally. The composition of the iron metal in the core was a result of the conditions of its formation, which has important implications for our planet's geochemical evolution and physical history. We present experimental and theoretical evidence for the effect of pressure on iron isotopic composition, which we found to vary according to the alloy tested (FeO, FeH_x, or Fe_3C versus pure Fe). These results suggest that hydrogen or carbon is not the major light-element component in the core. The pressure dependence of iron isotopic composition provides an independent constraint on Earth's core composition.

The separation of iron metal from silicate to form Earth's core represents a fundamental physical and chemical differentiation process in our planet's history. Differentiation of planets and asteroids in general is based on temperature, pressure (or size of body), oxygen fugacity, and impact history. On Earth, core formation left behind many clues in the form of siderophile element patterns, seismic observations, and radiogenic isotope ratios that enable studies on how and when differentiation occurred. Seismic data show a density difference between pure iron and the inferred density from the velocities of the seismic waves within Earth's interior. This discrepancy implies that there are "light" elements other than iron within the core of Earth. However, because direct sampling of the core is impossible, its composition remains a hotly debated topic [e.g., (*1*)]. During the differentiation process, the molten iron metal will alloy with other elements on its route to the center of the planetary body. The elements it bonds with will be a function of the conditions attending core formation. To understand the history of our planet (or of any planetary body that experienced core formation), we must constrain this light element in the core.

The principle of using stable isotopes to probe the bulk chemical composition of planets is rooted in understanding isotope fractionation during the sequestration of elements in unseen reservoirs such as the core. Isotope fractionation will exist between phases with distinct bonding environments (e.g., Earth's core and mantle), and separation of elements between reservoirs manifests this fractionation. Many variables influence the fractionation, including temperature, oxygen fugacity, and composition. For example, isotopic partitioning between metal and silicate was shown to increase when increasing amounts of sulfur were added to iron metal (*2*). However, those experiments were performed at low-pressure conditions (1 GPa) relative to the putative conditions of core formation (~60 GPa), and pressure was not considered a critical variable in affecting isotope fractionation. Joy and Libby (*3*) calculated the effect of pressure on isotope fractionation and suggested that oxygen isotope fractionation might be pressure-dependent at low temperatures. However, the following year, a study (*4*) examined the effect of pressure experimentally and observed no pressure effect on oxygen isotope partitioning between water and bicarbonate. Later, Clayton and co-workers (*5*–*7*) found no pressure effect on mineral-water fractionation over a range of pressures (up to 2 GPa) and temperatures (up to 1000 K). As a result of these initial studies, the effect of pressure on isotope fractionation has been assumed to be negligible for all elements. A pressure effect on isotope fractionation was suggested in other theoretical work (*8*) and confirmed experimentally for hydrogen (*9*) but not for heavier elements and higher pressures (*10*). However, better instrumentation may eventually be able to resolve very small fractionation effects, and higher pressures may illuminate the predicted fractionation (*11*, *12*).

To test whether the light element bonded with iron alters iron isotope fractionation between metal and silicate, we conducted nuclear resonant inelastic x-ray scattering (NRIXS) experiments on FeO, FeH_x, Fe_3C, and Fe from 2 to 40 GPa. Polyakov and co-workers (*11*, *13*, *14*) pioneered the use of synchrotron NRIXS data to obtain vibrational properties of minerals for calculating isotopic fractionation factors. We can use NRIXS data to derive reduced partition function ratios (β factors), from which we can determine equilibrium isotopic fractionation factors: $\delta_A - \delta_B = 1000 \times (\ln \beta_A - \ln \beta_B)$, where A and B are two

[1]Geophysical Laboratory, Carnegie Institution for Science, Washington, DC 20015, USA. [2]Department of Earth, Planetary and Space Sciences, University of California, Los Angeles, CA 90095, USA. [3]CNRS, Ecole Normale Supérieure de Lyon, Université Claude Bernard Lyon 1, Laboratoire de Géologie de Lyon, UMR 5276, 69364 Lyon Cedex 07, France. [4]Los Alamos National Laboratory, Los Alamos, NM 87545, USA. [5]Department of Geological Sciences, Stanford University, Stanford, CA, USA. [6]High Pressure Collaborative Access Team (HPCAT), Carnegie Institution for Science, Argonne, IL, USA.
*Corresponding author. Email: ashahar@carnegiescience.edu

Downloaded from http://science.sciencemag.org/ on April 28, 2016

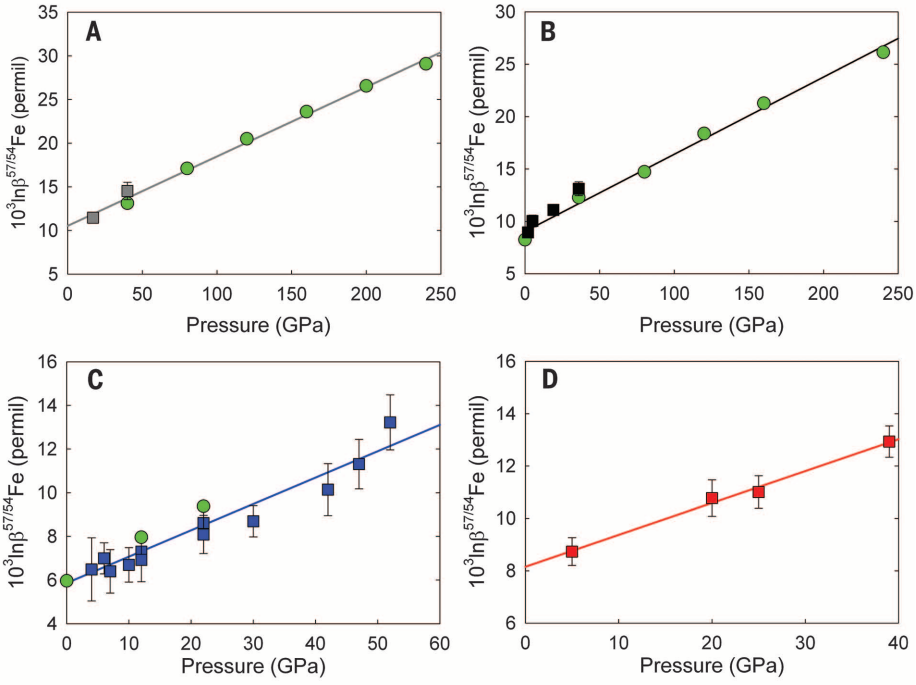

Fig. 1. Pressure dependence of the $^{57/54}$Fe β factor for the different iron phases investigated. A clear pressure dependence on the β factor can be seen for all the phases analyzed. (**A**) The β factor as a function of pressure for pure Fe. Gray squares are experimental data; green circles are theoretical calculations. (**B**) The β factor as a function of pressure for Fe_3C. Black squares are experimental data; green circles are theoretical calculations. (**C**) The β factor as a function of pressure for FeH_x. Blue squares are experimental data; green circles are theoretical calculations. (**D**) The β factor as a function of pressure for FeO. Red squares are experimental data. Each pressure point was measured at least 19 times and as many as 40 times. The errors on the experimental data are ±2 SD.

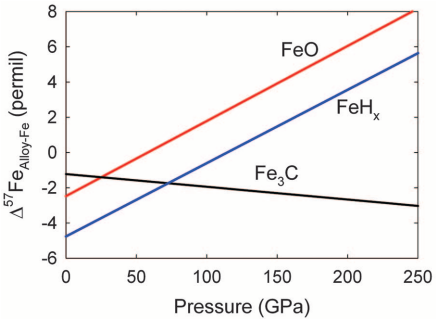

Fig. 2. Difference in the iron isotope ratios of the alloy with respect to pure Fe as a function of pressure. The red line is the isotope ratio difference of FeO – Fe, the blue line is FeH_x – Fe, and the black line is Fe_3C – Fe. Where the lines cross 0 on the *y* axis represents the pressure where there is no isotope fractionation between the phases and pure Fe. The iron isotope fractionation can be seen to change with pressure. $\Delta^{57}Fe_{alloy\ -\ Fe} = \delta^{57}Fe_{alloy} - \delta^{57}Fe_{Fe} = 10^3 \times (\ln \beta_{alloy}{}^{57/54}Fe - \ln \beta_{Fe}{}^{57/54}Fe)$.

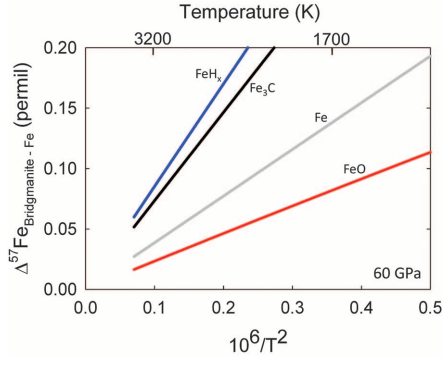

Fig. 3. Iron isotope fractionation between bridgmanite and iron phases as a function of temperature. The red line is the isotope ratio difference of bridgmanite – FeO, the gray line is bridgmanite – Fe, the black line is bridgmanite – Fe_3C, and the blue line is bridgmanite – FeH_x. At the conditions of core formation, a small but resolvable fractionation can be seen in all alloys, with that for Fe_3C and FeH_x much greater than for Fe and FeO. $\Delta^{57}Fe_{bridgmanite\ -\ Fe} = \delta^{57}Fe_{bridgmanite} - \delta^{57}Fe_{Fe}$.

different phases of interest. Dauphas *et al.* (*15*) provided an excellent introduction to this technique and its applicability to isotope geochemistry. A major benefit of NRIXS experiments is that we can probe the vibrational properties of one phase at a time. More traditional methods used for measuring isotope fractionation require having two phases at equilibrium that then need to be separated and analyzed for their isotope ratios.

We conducted high-pressure NRIXS experiments at sector 16-ID-D (HPCAT) of the Advanced Photon Source at Argonne National Laboratory. We obtained energy spectra from –120 meV to +150 meV in steps of 0.5 meV with an energy resolution of 2 meV. The counting time varied between 6 and 7 s per point, with each NRIXS scan lasting about 1 hour and with 19 to 50 scans per pressure point. One hundred percent isotopically enriched ^{57}FeO, $^{57}Fe_3C$, or ^{57}Fe powder was loaded into a sample chamber drilled into a beryllium gasket in a panoramic diamond anvil cell. For the hydride, the chamber was loaded with pure ^{57}Fe and fluid H_2, which reacted to form FeH_x. Pressure was calibrated using the ruby scale at HPCAT (*16*). We also calculated the theoretical β factors from the vibrational levels of different isotope-bearing structures. We computed these using density functional perturbation theory (*17*) in the ABINIT and Quantum Espresso implementation (*18*, *19*) with plane waves and pseudopotentials, from which we obtained the theoretical phonon density of states (*20*).

We found linear relationships with pressure for Fe, Fe_3C, FeH_x, and FeO that showed excellent agreement with our theoretical calculations of β factors (Fig. 1). Each phase shows an increase in the β factor with pressure; moreover, the slopes of each line are different. The isotopic fractionation between each phase and pure Fe metal shows different slopes and intercepts indicative of varying pressure dependences (Fig. 2). We can explain this by the expected differences in bonding between iron and its different alloying elements.

At equilibrium, isotope fractionation is a quantum mechanical effect caused by differences in the free energy of structures populated by different isotopes. Isotopic pressure dependences can be the result of isotopic effects on molar volume or can be caused by force constant stiffening as structures contract. The molar volume isotope effect has been discussed extensively [e.g., (*8*, *11*, *21*, *22*)] and occurs when heavy isotopes make slightly shorter bonds and therefore pack more tightly than light ones. Theoretical and experimental studies of isotope effects on the molar volumes of elements with atomic numbers spanning iron (e.g., carbon and germanium) indicate that isotope effects on volume are very small at standard temperature and pressure (less than one part in 10^{-3} for ^{13}C versus ^{12}C in diamond, ~10^{-5} for ^{74}Ge versus natural germanium). Furthermore, molar volume effects fade as temperature increases beyond the Debye temperature (*21*, *22*) and also as pressure increases (*22*). We therefore expect this effect to be negligible for iron isotope fractionation at pressures and temperatures relevant to core segregation. The same conclusion was reached in a previous theoretical study of high-pressure iron isotope fractionation (*11*). Our theoretical calculations target the increase in force constants and corresponding vibrational frequencies due to bond stiffening under compression.

Downloaded from http://science.sciencemag.org/ on April 28, 2016

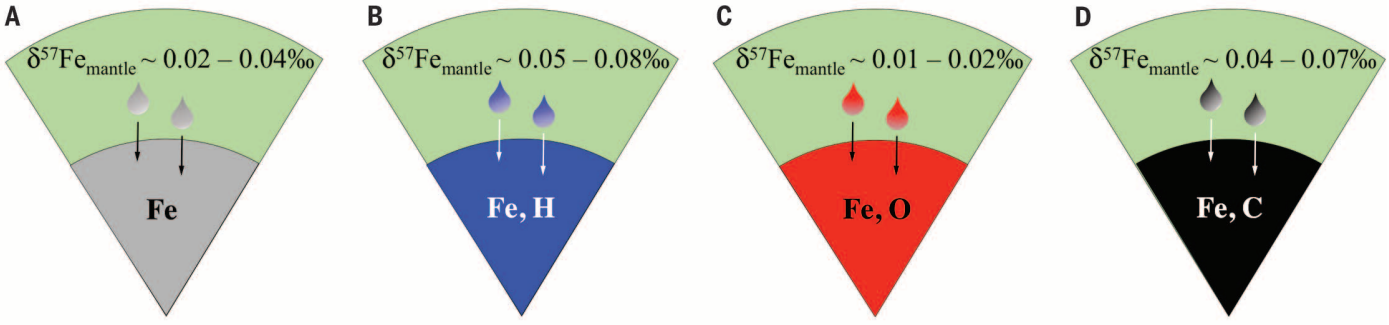

Fig. 4. A schematic of the implications of this study with regard to the iron isotope ratios of the current mantle. (**A**) Cross section of Earth showing the iron isotope ratio of the mantle after core formation if Fe were the only element in the core. (**B** to **D**) Same as (A) if hydrogen (B), oxygen (C), or carbon (D) were present. The $^{57}Fe_{mantle}$ values in (A) and (C) are not resolvable with current technological capabilities, but the values in (B) and (D) are very resolvable.

We find that pressure has a clear effect on isotope fractionation between solid phases, and that this effect is different for the different alloys (Figs. 1 and 2). In particular, we find that the iron alloys we studied do not concentrate the iron isotopes to the same degree. As carbon, hydrogen, and oxygen are all cosmochemically abundant and have been proposed as possible candidates for the main light element in planetary cores, iron isotope fractionation may be a tracer of light-element compositions in planetary cores. The iron-hydrogen alloy and the iron-carbon alloy have the largest fractionation relative to pure iron in a typical magma ocean setting at ~60 GPa (*23*). The hydrogen content in the core is poorly constrained, with estimates ranging from negligible up to the equivalent of 100 hydrospheres (*24*). Estimates for the carbon content of the core are less than ~1 weight percent (*25*, *26*). Because our data were collected at room temperature, we calculated the temperature effect on the fractionation of bridgmanite (*27*) relative to the iron phases (Fig. 3) (*18*). At 3500 K, the fractionation for pure Fe is ~0.03 per mil (‰) and that for FeH_x is ~0.07‰.

Initial iron isotope work on natural samples determined that "Earth" (i.e., mantle-derived rocks) was ~0.1‰ heavier in $\delta^{57/54}$ than rocks from Mars and Vesta (*28*). Predictions (*11*) concluded that core-mantle differentiation would leave an imprint on the iron isotope signature of Earth because of the valence state difference of Fe between lower-mantle Fe^{2+}-bearing minerals and Fe^0 metal at the core-mantle boundary. That study suggested that the enrichment of terrestrial and lunar basalts in heavy iron isotopes relative to those from Mars or Vesta is due to equilibrium iron isotope fractionation during Earth's core formation. Subsequent explanations, however, argued that the bulk silicate Earth is chondritic and that it is the terrestrial basalts that are anomalous (*29*). The model suggests that the iron isotopic composition of the basalts was different from that of the source rock from which they came; that is, fractionation of iron isotopes occurs during partial melting. Therefore, if the bulk silicate Earth is chondritic in its iron isotope ratios, it should have a $\delta^{57/54}$ of 0‰. If that is the case, then any light element that causes a large enough fractionation at high pressure and temperature to deviate from that value cannot be a major constituent of the core. A caveat is that if the bulk silicate Earth were found to be nonchondritic, then the light element that causes a fractionation large enough to be seen—such as hydrogen—would be the most likely candidate for the light element in the core.

Our results suggest that core formation could leave an isotopic imprint on the silicate portion of Earth even at the highest pressures and temperatures. Moreover, the addition of different light element(s) will modulate this imprint. In particular, our results indicate that if hydrogen or carbon were used to explain the density deficit in Earth's core, we would expect an isotopic signature imprinted in mantle rocks, which is not seen in the rock record. The lack of evidence for this signature suggests that hydrogen and carbon should be excluded as the main light element in Earth's core (Fig. 4). There has been substantial disagreement in the literature concerning whether carbon and/or hydrogen are likely major constituents of the core, on the basis of other evidence [e.g., (*30*–*32*)], so this study provides an independent constraint. In contrast, we found that oxygen does not leave an imprint on the silicate mantle, implying that at least for the phases we have analyzed, oxygen is a possible light element in the core (*1*). It is intriguing that the light element changes the isotope ratios with these end-member compositions. The effects of other light elements (such as silicon and sulfur) on the iron isotope ratios need to be investigated, as well as the effects of nickel and pressure-induced structure, electronic, and magnetic transitions. However, it is now clear that pressure cannot be ignored when discussing equilibrium stable isotope fractionation in the deep Earth.

REFERENCES AND NOTES

1. J. Badro, A. S. Côté, J. P. Brodholt, *Proc. Natl. Acad. Sci. U.S.A.* **111**, 7542–7545 (2014).
2. A. Shahar *et al.*, *Geochim. Cosmochim. Acta* **150**, 253–264 (2015).
3. H. W. Joy, W. F. Libby, *J. Chem. Phys.* **33**, 1276 (1960).
4. T. C. Hoering, *Carnegie Inst. Wash. Yearb.* **60**, 201–204 (1961).
5. R. N. Clayton, J. R. Goldsmith, K. J. Karel, T. K. Mayeda, R. C. Newton, *Geochim. Cosmochim. Acta* **39**, 1197–1201 (1975).
6. Y. Matsuhisa, J. R. Goldsmith, R. N. Clayton, *Geochim. Cosmochim. Acta* **43**, 1131–1140 (1979).
7. A. Matthews, J. R. Goldsmith, R. N. Clayton, *Geochim. Cosmochim. Acta* **47**, 631–644 (1983).
8. V. Polyakov, *Geochim. Cosmochim. Acta* **62**, 3077–3085 (1998).
9. J. Horita, T. Driesner, D. R. Cole, *Science* **286**, 1545–1547 (1999).
10. F. Poitrasson, M. Roskosz, A. Corgne, *Earth Planet. Sci. Lett.* **278**, 376–385 (2009).
11. V. B. Polyakov, *Science* **323**, 912–914 (2009).
12. J. R. Rustad, Q.-Z. Yin, *Nat. Geosci.* **2**, 514–518 (2009).
13. V. Polyakov, S. D. Mineev, R. Clayton, G. Hu, K. S. Mineev, *Geochim. Cosmochim. Acta* **69**, 5531–5536 (2005).
14. V. Polyakov, R. Clayton, J. Horita, S. Mineev, *Geochim. Cosmochim. Acta* **71**, 3833–3846 (2007).
15. N. Dauphas *et al.*, *Geochim. Cosmochim. Acta* **94**, 254–275 (2012).
16. H. K. Mao, J. Xu, P. M. Bell, *J. Geophys. Res.* **91**, 4673–4676 (1986).
17. S. Baroni, S. de Gironcoli, A. Dal Corso, P. Giannozzi, *Rev. Mod. Phys.* **73**, 515–562 (2001).
18. X. Gonze *et al.*, *Comput. Phys. Commun.* **180**, 2582–2615 (2009).
19. P. Giannozzi *et al.*, *J. Phys. Condens. Matter* **21**, 395502 (2009).
20. See supplementary materials on *Science* Online.
21. R. C. Buschert, A. E. Merlini, S. Pace, S. Rodriguez, M. H. Grimsditch, *Phys. Rev. B* **38**, 5219–5221 (1988).
22. C. P. Herrero, *J. Phys. Condens. Matter* **13**, 5127–5134 (2001).
23. J. Siebert, J. Badro, D. Antonangeli, F. J. Ryerson, *Science* **339**, 1194–1197 (2013).
24. Q. Williams, R. J. Hemley, *Annu. Rev. Earth Planet. Sci.* **29**, 365–418 (2001).
25. B. Wood, J. Li, A. Shahar, *Rev. Mineral. Geochem.* **75**, 231–250 (2013).
26. B. Chen *et al.*, *Proc. Natl. Acad. Sci. U.S.A.* **111**, 17755–17758 (2014).
27. O. Tschauner *et al.*, *Science* **346**, 1100–1102 (2014).
28. F. Poitrasson, A. N. Halliday, D. C. Lee, S. Levasseur, N. Teutsch, *Earth Planet. Sci. Lett.* **223**, 253–266 (2004).
29. P. R. Craddock, J. M. Warren, N. Dauphas, *Earth Planet. Sci. Lett.* **365**, 63–76 (2013).
30. R. Caracas, *Geophys. Res. Lett.* **42**, 3780–3785 (2015).
31. K. D. Litasov, Z. I. Popov, P. N. Gavryushkin, S. G. Ovchinnikov, A. S. Fedorov, *Russ. Geol. Geophys.* **56**, 164–171 (2015).
32. T. Sakamaki *et al.*, *Sci. Adv.* **2**, e1500802 (2016).

ACKNOWLEDGMENTS

Supported by a Stanford University Blaustein Fellowship, during which this project developed, and NSF grant EAR1321858 (A.S.); NSF grant EAR1464008 (A.S. and W.M.); NSF grant EAR1530306 (E.A.S.); and CNRS PICS grant Carmelts and eDARI/CINES grant x2015106368 for computational resources (R.C.). The complete data tables for this study can be found on www.gl.ciw.edu/static/users/ashahar/shahar_nrixs/. We thank four anonymous reviewers for providing very helpful comments and suggestions.

SUPPLEMENTARY MATERIALS

www.sciencemag.org/content/352/6285/580/suppl/DC1
Materials and Methods
Supplementary Text
Figs. S1 to S7
References (*33*–*43*)

3 December 2015; accepted 11 March 2016
10.1126/science.aad9945

Downloaded from http://science.sciencemag.org/ on April 28, 2016

STRUCTURAL BIOLOGY

Structure of a bd oxidase indicates similar mechanisms for membrane-integrated oxygen reductases

Schara Safarian,[1] Chitra Rajendran,[1]* Hannelore Müller,[1] Julia Preu,[1] Julian D. Langer,[1]† Sergey Ovchinnikov,[2] Taichiro Hirose,[3] Tomoichirou Kusumoto,[3] Junshi Sakamoto,[3] Hartmut Michel[1]‡

The cytochrome bd oxidases are terminal oxidases that are present in bacteria and archaea. They reduce molecular oxygen (dioxygen) to water, avoiding the production of reactive oxygen species. In addition to their contribution to the proton motive force, they mediate viability under oxygen-related stress conditions and confer tolerance to nitric oxide, thus contributing to the virulence of pathogenic bacteria. Here we present the atomic structure of the bd oxidase from *Geobacillus thermodenitrificans*, revealing a pseudosymmetrical subunit fold. The arrangement and order of the heme cofactors support the conclusions from spectroscopic measurements that the cleavage of the dioxygen bond may be mechanistically similar to that in the heme-copper–containing oxidases, even though the structures are completely different.

Living in a reducing atmosphere more than 3 billion years ago, the ancestors of the cyanobacteria found a way to extract electrons from water via oxygenic photosynthesis. The released oxygen can form reactive oxygen species, and partly reduced oxygen is highly toxic. To cope with this threat, microorganisms had to survive in anaerobic niches and remove oxygen by reducing it to water. Several enzymatic machineries are employed for the reduction of oxygen to water. Oxygen-tolerant methanogenic archaea use a soluble di-iron flavoprotein (*1*), whereas most other organisms use membrane-integrated enzymes, primarily members of the heme-copper–containing oxidase (HCO) superfamily. Different HCOs use cytochromes or quinols as electron donors providing the electrons from the extracellular side, whereas the protons required for water formation are delivered from the intracellular side. This vectorial delivery of oppositely charged substrates also generates the electrochemical proton gradient used for energy-requiring processes such as adenosine triphosphate (ATP) synthesis.

The cytochrome bd oxidases form the other known family of membrane-spanning oxygen reductases of bacteria and archaea, unrelated to HCOs or the membrane-attached cyanide-resistant alternative oxidases (AOXs). The bd oxidases use quinols as electron donors from the extracellular side and protons from the intracellular side like HCOs, but do not pump protons (*2*). They possess a high oxygen affinity and thus play a role in protection against oxidative stress (*3*, *4*) and the colonization of O_2-poor environments by pathogenic bacteria (*5*, *6*). The bd oxidases also rapidly dissociate gaseous inhibitory nitrogen ligands and confer tolerance under nitric oxide stress conditions (*7*). This ability is crucial for the viability of pathogenic bacteria upon host infection (*5*, *8*). The hypersensitivity of a bd oxidase deletion strain of *Mycobacterium tuberculosis* to bedaquiline, a tuberculosis drug that inhibits the F_1F_o-ATP synthase (*9*, *10*), highlights the potential of bd oxidases as drug targets.

Crystal structures of representative members of all three HCO families (A, B, and C) are known, yet the structure of bd oxidases has remained elusive. The bd oxidases contain two individual protein subunits of ~45 kDa (CydA) and ~35 kDa (CydB) (*11*–*13*); those of the proteobacteria contain a third subunit consisting of a single transmembrane helix of ~4 kDa, which plays a crucial role in the activity of the enzyme (*14*, *15*). The bd oxidases contain a low-spin hexacoordinated heme B (b_{558}) and a high-spin pentacoordinated heme B (b_{595}) and a chlorin-type heme D (*2*, *16*, *17*) as electron-transferring prosthetic groups. The quinol to be reduced is initially bound via a conserved water-exposed loop (a Q loop) located in the hydrophilic extracellular space connecting transmembrane helices 6 and 7 of CydA. Subsequently, the quinol is oxidized and heme b_{558} acts as a primary electron acceptor, whereas two protons are released to the extracellular side. The electrons are transferred to the b_{595}/d high-spin active site, where oxygen binding and the reduction of oxygen to water take place (*2*, *18*). No Cu cofactor is present in the active site of the bd oxidases.

Here we present the crystal structure of the bd oxidase from *G. thermodenitrificans K1041*, using crystals diffracting anisotropically to 3.1 to 4 Å resolutions (*19*). The prominent structural feature of the bd oxidase is the presence of 19 transmembrane helices in a nearly oval arrangement when viewed down to the membrane (Fig. 1A). CydA and CydB possess the same fold, sharing a nine-transmembrane helix topology, each composed of two four-helix bundles and an additional peripheral helix. CydA and CydB are related by an approximate twofold rotation axis perpendicular to the membrane. A structural alignment of both subunits yields a relatively low root mean square deviation value of 3.1 Å (Fig. 1B and fig. S2). Such a pseudosymmetrical structural arrangement is most likely the result of a gene duplication of a single ancestral gene that encoded a homodimeric protein and subsequent mutations. The situation resembles that of the photosynthetic reaction centers, where the core is constituted by two structurally similar protein subunits, only one of them being used for electron transfer (*20*, *21*). The heterodimer formation is mediated by interactions of hydrophobic residues at the interface between α3, α4, and α9 of CydA and the symmetry-related helices α3, α4, and α9 of CydB. The Q loop, a hydrophilic region between transmembrane helices 6 and 7 of CydA (segments 249 to 319) facing the extracellular space, possesses a largely irregular protein fold apart from a short helical stretch leading to an antiparallel β sheet (Fig. 1A). A potentially accessible pocket for the binding of the substrate quinol was identified near Glu^{257} and Lys^{252} (Glu^{257} and Lys^{252} in *Escherichia coli*) in the Q loop (Fig. 2C); both residues, which are found in the short helix (segments 249 to 258), have already been associated with the binding and oxidation of quinol by site-directed mutagenesis experiments (*22*). Lys^{252} is in reasonable distance to form a polar contact with the O1/2A propionate group of heme b_{558}.

The HCOs generally exhibit a more compact and globular packing within the membrane than the bd oxidase. The conserved catalytic core subunits (subunit 1 or CcoN) of the HCO-family enzymes generally contain 12 transmembrane helices with a threefold rotational symmetric arrangement, resulting in the generation of three pores that are formed by semicircular arrangements of four helices each (*23*). Neither the overall topology of CydA with its nine transmembrane helices nor the heme organization indicates any evolutionary relation of any functional motif. Comparison with other structures in the Protein Data Bank (PDB) (*24*) reveals the uniqueness of the overall protein structure and the redox active site organization. The four-helix bundle motif as an individual structural unit is found in a few other bioenergetically important membrane proteins, such as cytochrome b_{651} (PDB accession number 4O7G) and the transmembrane part of a polysulfide reductase (PsrC) (PDB accession number 2VPX).

[1]Department of Molecular Membrane Biology, Max Planck Institute of Biophysics, Max-von-Laue-Straße 3, D-60438 Frankfurt/Main, Germany. [2]Department of Biochemistry, University of Washington, Seattle, WA, USA. [3]Department of Bioscience and Bioinformatics, Kyushu Institute of Technology, Kawazu 680-4, Iizuka, Fukuoka-ken 820-8502, Japan.
*Present address: Faculty of Biology and Preclinical Medicine, University of Regensburg, Universitätsstrasse 31, D-93051 Regensburg, Germany. †Present address: Department of Molecular Membrane Biology, Max Planck Institute for Brain Research, Max-von-Laue-Straße 4, D-60438 Frankfurt/Main, Germany. ‡Corresponding author. Email: hartmut.michel@biophys.mpg.de

Downloaded from http://science.sciencemag.org/ on April 28, 2016

A third subunit, which we designate CydS, consisting of only one single transmembrane helix, was identified in the electron density map. CydS, a short peptide of 33 amino acid residues, could be purified and sequenced by matrix-assisted laser desorption/ionization mass spectrometry (MALDI-MS) (fig. S3). We located its gene immediately downstream of the *cbdB* gene in the *Geobacillus* genome. Positioned at the peripheral interface of α5-6 of CydA, CydS may stabilize the heme b_{558} harboring a four-helix bundle (α5-8 of CydA) during potential structural rearrangements of the Q loop upon binding and oxidation of quinol (Fig. 1A). Although conserved in the order of Bacillales (fig. S5), there is no sequence similarity between CydS and the proteobacterial single transmembrane helix subunits. However, because a recent de novo blind structure prediction for the *E. coli* bd oxidase proposes an almost identical location of CydX, CydS and CydX might play analogous roles (*25*).

The three hemes are found in a triangular arrangement (Fig. 2A) and not in the form of a linear chain in the order b_{558}, b_{595}, and then d as expected (*2*). The low-spin heme b_{558} is located within the membrane core, with its plane tilted by ~110° to the membrane plane. The vertical distance from the heme iron to the extracellular surface is ~18 Å. It is in close proximity to the Q loop (Fig. 2, A and C). As inferred from mutagenesis experiments and electron paramagnetic resonance data (*16*, *26*), His^{186} and Met^{325} (His^{186} and Met^{393} in *E. coli*) are the axial ligands of heme b_{558} (Fig. 2C). The terminal electron acceptor heme d is located closer to the extracellular membrane surface, with its plane tilted by ~60° to the membrane plane. The vertical distance from the heme iron to the P side of the membrane is ~13.5 Å. Heme b_{595} is coordinated by the invariant axial ligand His^{21} (His^{19} in *E. coli*) on one side. On the opposite side, Glu^{101} (Glu^{99} in *E. coli*) appears to be ligated to the heme iron. Originally proposed to be ligated by Glu^{101} (*27*), heme d seems to possess another glutamate ligand, namely Glu^{378} (Glu^{445} in *E. coli*), which has been postulated to be a key residue taking up a charge-compensating proton, when the high-spin hemes become reduced (Fig. 2D) (*28*). Our MALDI-MS analyses indicate that heme d is present as a cis–heme d hydroxychlorin γ–spirolactone in the *Geobacillus* bd oxidase (fig. S4). This result is supported by the electron density map, which moreover implies a bent conformation of heme d.

Despite their close proximity, the arrangement of the two high-spin hemes does not support the existence of a binuclear active center (see the supplementary materials). The hemes are in van der Waals contacts, with edge-to-edge distances around 3.5 Å and a distance between the central Fe atoms of 11.6 Å. The highly conserved (>99%) Trp^{374} residue may be important for the electron transfer between heme b_{558} and heme d. Conserved Trp residues are often found between intermediate electron acceptors in biological electron transfer chains, such as in the active branch of the photosynthetic reaction centers from purple bacteria and of photosystem II between a (bacterio)phaeophytin and a quinone acceptor (*20*), or between the high-spin heme and the low-spin heme of the HCOs. In addition, Trp residues themselves can donate electrons and form Trp radicals. In particular, Trp^{374} could donate an electron to compound I (F^{+*} state)—a catalytic intermediate of heme d forming an oxoferryl-porphyrin radical during the splitting of the dioxygen bond by a single four-electron transfer reaction (*29*)—and then receive an electron from heme b_{558}.

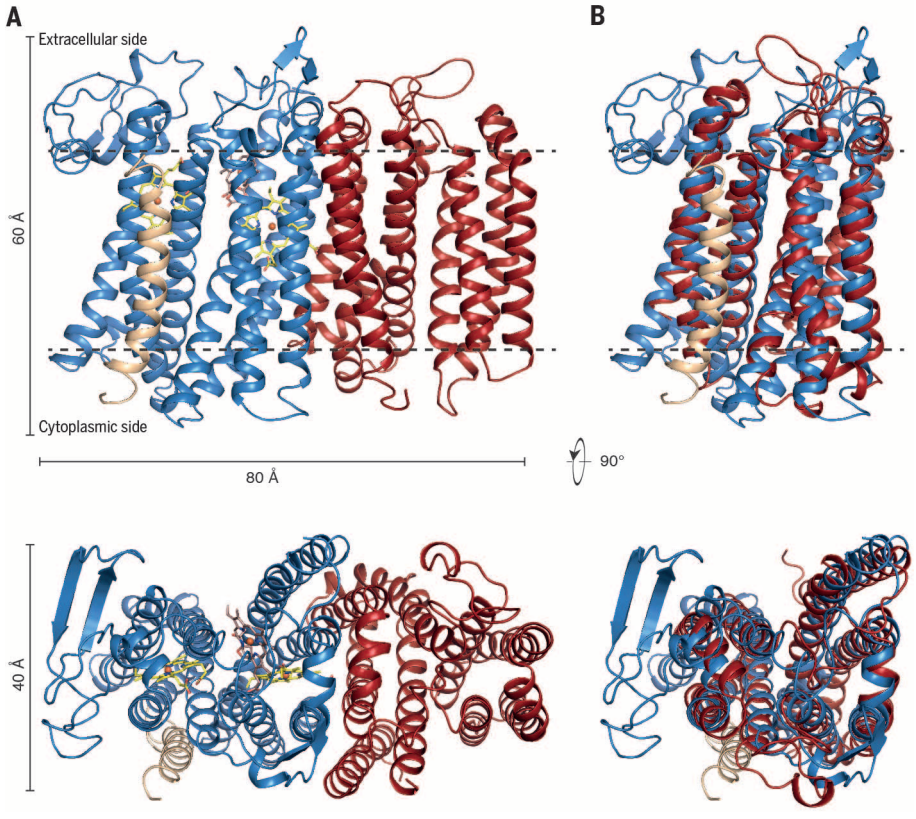

Fig. 1. Overall structure of the bd oxidase from *G. thermodenitrificans*. (**A**) Ribbon model of the bd oxidase consisting of the subunits CydA (blue), CydB (red), and CydS (beige). (**B**) Structural superposition of CydA and CydB. The dashed line indicates the border between the hydrophobic and hydrophilic layers of the membrane.

The triangular arrangement of the hemes and the distances between them suggest a direct electron transfer from heme b_{558} to heme d, because the edge-to-edge distance and the Fe-Fe distance between these hemes are significantly shorter (5.9 and 15.2 Å) than the respective distances between the two b hemes (8.5 and 19.4 Å). Finally, the electron would equilibrate between heme d and heme b_{595}. For the breakage of the dioxygen bond, four electrons are required. In the reduced enzyme, two of them could be supplied by the heme d iron by the formation of an oxoferryl state, the third one from heme b_{595}, and [according to (*29*)] the fourth one from the macrocycle of heme d. Therefore, the bd oxidases and the HCOs appear to use the same principle to avoid the formation of superoxide anions and of peroxides (*29*), namely a very rapid or simultaneous transfer of four electrons onto dioxygen, leading to breakage of the dioxygen bond. The main functional difference appears to be that one electron is provided by an amino acid side chain (tyrosine) in the case of the HCOs and by the heme d macrocycle in the case of the bd oxidases (*29*). The analogy goes further: The oxygen-binding heme (d or a_3 for the canonical heme aa_3 HCOs) is located between a low-spin heme (b_{558} versus a) and the donor of the third electron (heme b_{595} versus Cu_B). There is even a Trp residue between the low-spin heme and the dioxygen-binding high-spin heme in both the bd oxidases and the HCOs.

Although the bd oxidase doesn't pump protons across the membrane, the existence of proton transfer pathways from the cytoplasm is crucial for the access of protons to the oxygen-binding site and potentially also for protons involved in compensating for the negative charge of the electrons used for heme reduction. We identified two potential pathways through which protons could pass from the cytoplasm to the high-spin heme site. One pathway is formed inside of the four-helix bundle α1-4 of CydA and the second one in the symmetry-related α1-4 four-helix bundle of CydB. Therefore, we call these potential routes for proton transfer CydA and CydB pathways (Fig. 3 and fig. S7). The location of Glu^{108} (Glu^{107} in *E. coli*) in our structure,

Downloaded from http://science.sciencemag.org/ on April 28, 2016

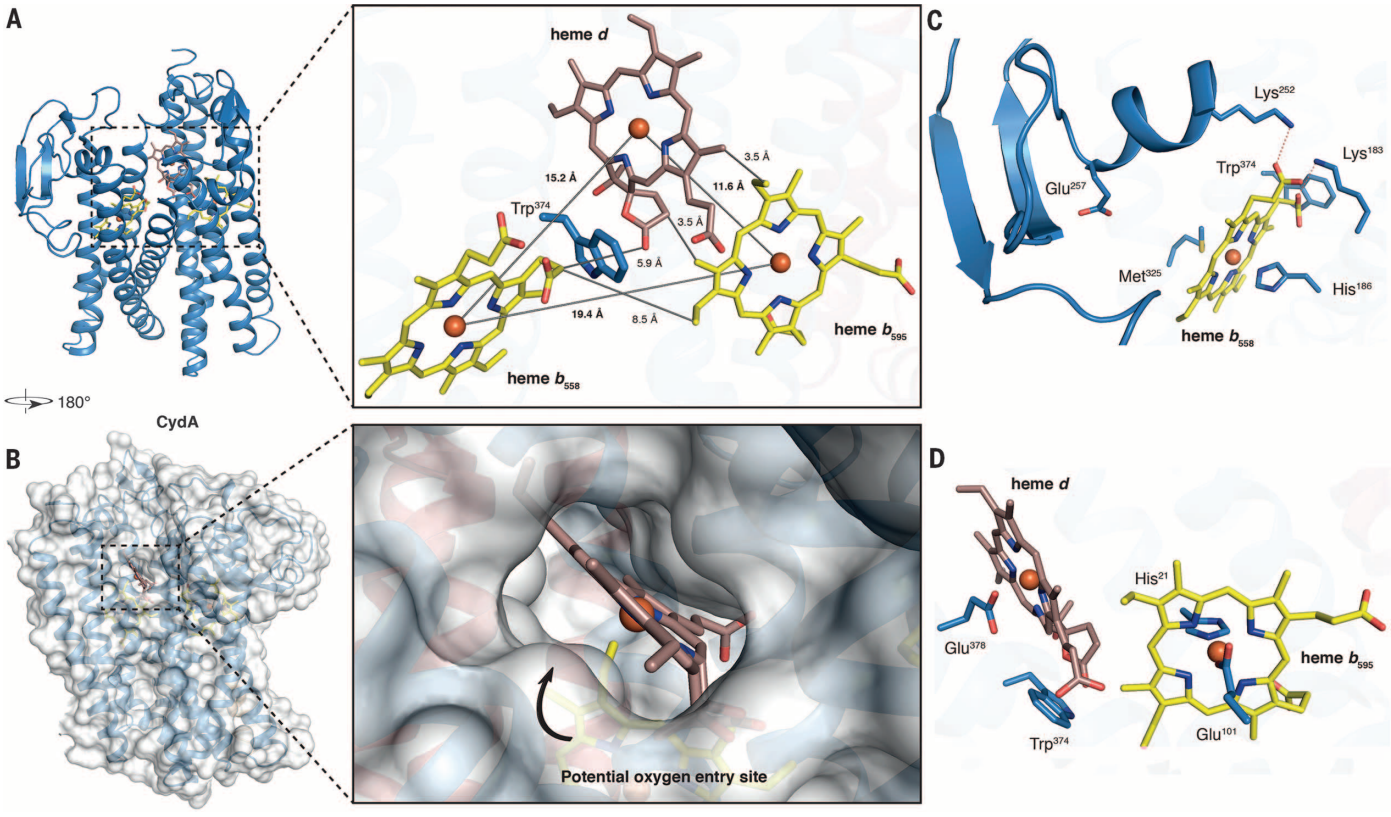

Fig. 2. The prosthetic groups in the bd oxidase. (**A**) Picture of the heme groups represented by stick models bound to CydA (blue). Heme b_{558} and b_{595} are depicted in yellow and heme d in brown. (**B**) Surface representation of CydA showing a pocket formed between α1 and α8 that could enable dioxygen to directly access heme d. (**C**) The initial electron acceptor heme b_{558} in proximity to the Q loop. (**D**) The high-spin heme site composed of hemes b_{595} and d.

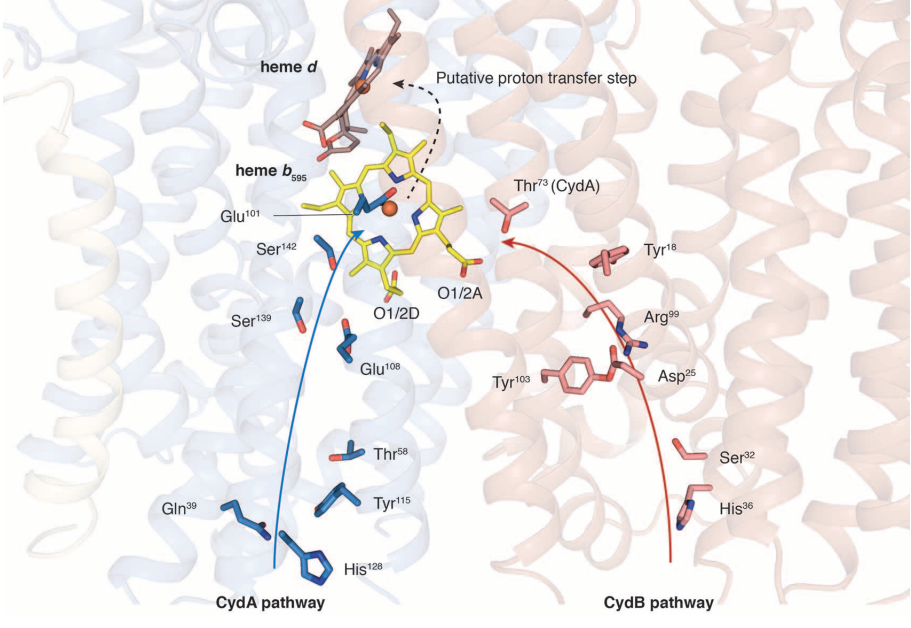

Fig. 3. The potential proton transfer pathways in the bd oxidase.

together with previous mutagenesis experiments and Fourier transform infrared spectroscopy data, supports the proposal that this glutamate residue is a redox state–dependent mediator of proton transfer to a charge compensation site (*30*). With the CydA pathway leading to Glu^{101}, this residue might be the hypothetical protonatable group used for charge compensation upon heme b_{595} reduction (*28*). It remains to be investigated whether protons entering the CydA pathway can be transferred from Glu^{101} to Glu^{378} for compensating the negative charge of a second electron used to reduce the two high-spin hemes. Protonation of Glu^{378} could alternatively also be accomplished by a proton accessing from the extracellular side. Currently it remains unclear whether the CydA pathway is solely providing protons for charge compensation or whether Glu^{108} can be a branching point that is able to pass protons via the heme b_{595} propionates to the oxygen-binding site. With both channels leading to heme b_{595}, there must be an additional proton transfer step from heme b_{595} to heme d in order to deliver protons to the oxygen reduction site (Fig. 3). Based on the current structure, we can exclude the possibility of direct proton transfer between the two high-spin hemes. It seems more plausible that the final proton transfer from heme b_{595} to heme d is facilitated by connecting unresolved water molecules. The heme propionates of heme b_{595} are in a hydrophobic environment without any charge compensation. They are thus most likely protonated and could supply protons for water formation. These protons would be replenished via the proton pathways (Fig. 3 and fig. S7).

HCOs contain oxygen channels lined by hydrophobic residues leading from the membrane interior to their binuclear heme-Cu active site

Downloaded from http://science.sciencemag.org/ on April 28, 2016

(*31*). Our bd oxidase structure does not indicate the presence of such voluminous pathways; instead, molecular oxygen may access heme d laterally from the alkyl chain interface with the membrane over a short distance (Fig. 2B). Hence, oxygen dissolved in the membrane could rapidly bind to heme d without traveling through any tunnel-like protein cavity.

REFERENCES AND NOTES

1. H. Seedorf *et al.*, *FEBS J.* **274**, 1588–1599 (2007).
2. V. B. Borisov, R. B. Gennis, J. Hemp, M. I. Verkhovsky, *BBA Bioenergetics* **1807**, 1398–1413 (2011).
3. S. E. Edwards *et al.*, *FEMS Microbiol. Lett.* **185**, 71–77 (2000).
4. R. K. Poole, S. Hill, *Biosci. Rep.* **17**, 303–317 (1997).
5. L. Shi *et al.*, *Proc. Natl. Acad. Sci. U.S.A.* **102**, 15629–15634 (2005).
6. A. D. Baughn, M. H. Malamy, *Nature* **427**, 441–444 (2004).
7. M. G. Mason *et al.*, *Nat. Chem. Biol.* **5**, 94–96 (2009).
8. A. Giuffrè, V. B. Borisov, M. Arese, P. Sarti, E. Forte, *BBA Bioenergetics* **1837**, 1178–1187 (2014).
9. M. Berney, T. E. Hartman, W. R. Jacobs Jr., *mBio* **5**, e01275–14 (2014).
10. P. Lu *et al.*, *Scientific Rep.* **5**, 10333 (2015).
11. M. J. Miller, R. B. Gennis, *J. Biol. Chem.* **258**, 9159–9165 (1983).
12. K. Kita, K. Konishi, Y. Anraku, *J. Biol. Chem.* **259**, 3375–3381 (1984).
13. J. Sakamoto, A. Matsumoto, K. Oobuchi, N. Sone, *FEMS Microbiol. Lett.* **143**, 151–158 (1996).
14. R. J. Allen *et al.*, *BMC Genomics* **15**, 946 (2014).
15. J. Hoeser, S. Hong, G. Gehmann, R. B. Gennis, T. Friedrich, *FEBS Lett.* **588**, 1537–1541 (2014).
16. F. Spinner *et al.*, *Biochem. J.* **308**, 641–644 (1995).
17. J. Sun *et al.*, *Biochemistry* **35**, 2403–2412 (1996).
18. F. G. M. Wiertz *et al.*, *FEBS Lett.* **575**, 127–130 (2004).
19. Materials and methods are available as supplementary materials on *Science* Online.
20. J. Deisenhofer, O. Epp, K. Miki, R. Huber, H. Michel, *Nature* **318**, 618–624 (1985).
21. J. P. Allen, J. C. Williams, *FEBS Lett.* **438**, 5–9 (1998).
22. T. Mogi *et al.*, *Biochemistry* **45**, 7924–7930 (2006).
23. S. Iwata, C. Ostermeier, B. Ludwig, H. Michel, *Nature* **376**, 660–669 (1995).
24. H. M. Berman *et al.*, *Nucleic Acids Res.* **28**, 235–242 (2000).
25. S. Ovchinnikov, L. Kinch, H. Park, Y. Liao, J. Pei, D. E. Kim, H. Kamisetty, N. V. Grishin, D. Baker, *eLife Sci.* **4**, e09248 (2015).
26. H. Fang, R. J. Lin, R. B. Gennis, *J. Biol. Chem.* **264**, 8026–8032 (1989).
27. T. Mogi, S. Endou, S. Akimoto, M. Morimoto-Tadokoro, H. Miyoshi, *Biochemistry* **45**, 15785–15792 (2006).
28. I. Belevich *et al.*, *Proc. Natl. Acad. Sci. U.S.A.* **102**, 3657–3662 (2005).
29. A. Paulus, S. G. Rossius, M. Dijk, S. de Vries, *J. Biol. Chem.* **287**, 8830–8838 (2012).
30. K. Yang *et al.*, *Biochemistry* **46**, 3270–3278 (2007).
31. V. M. Luna, Y. Chen, J. A. Fee, C. D. Stout, *Biochemistry* **47**, 4657–4665 (2008).

ACKNOWLEDGMENTS

This work was supported by the Max Planck Society and the Deutsche Forschungsgemeinschaft (Cluster of Excellence Macromolecular Complexes Frankfurt), by a Grant-in-Aid for Scientific Research (C) (25440050 to J.S.) from the Japan Society for the Promotion of Science, and by the National Institutes of Health (grant R01GM092802). We thank the staff of beamline X10SA of the Swiss Light Source for assistance. Parts of the experiments were performed on beamlines ID29, ID23.1, and ID23.2 at the European Synchrotron Radiation Facility, Grenoble, France. We are grateful to beamline scientists for providing assistance; D. Baker for support during model building; and R. Gennis, U. Ermler, R. Murali, and A. Resemann for scientific discussion and expertise. Coordinates and structure factors have been deposited under PDB accession codes 5DOQ and 5IR6.

SUPPLEMENTARY MATERIALS

www.sciencemag.org/content/352/6285/583/suppl/DC1
Materials and Methods
Supplementary Text
Figs. S1 to S7
Table S1
References (*32*–*59*)

13 January 2016; accepted 28 March 2016
10.1126/science.aaf2477

MICROBIOME

Durable coexistence of donor and recipient strains after fecal microbiota transplantation

Simone S. Li,[1,2] Ana Zhu,[1] Vladimir Benes,[3] Paul I. Costea,[1] Rajna Hercog,[3] Falk Hildebrand,[1] Jaime Huerta-Cepas,[1] Max Nieuwdorp,[4,5,6] Jarkko Salojärvi,[7,8] Anita Y. Voigt,[1,9,10] Georg Zeller,[1] Shinichi Sunagawa,[1]* Willem M. de Vos,[7,11,12]* Peer Bork[1,10,13,14]*

Fecal microbiota transplantation (FMT) has shown efficacy in treating recurrent *Clostridium difficile* infection and is increasingly being applied to other gastrointestinal disorders, yet the fate of native and introduced microbial strains remains largely unknown. To quantify the extent of donor microbiota colonization, we monitored strain populations in fecal samples from a recent FMT study on metabolic syndrome patients using single-nucleotide variants in metagenomes. We found extensive coexistence of donor and recipient strains, persisting 3 months after treatment. Colonization success was greater for conspecific strains than for new species, the latter falling within fluctuation levels observed in healthy individuals over a similar time frame. Furthermore, same-donor recipients displayed varying degrees of microbiota transfer, indicating individual patterns of microbiome resistance and donor-recipient compatibilities.

Fecal microbiota transplantation (FMT), which entails the transfer of a microbial community from a healthy donor to a patient (often after bowel lavage), has emerged as a promising treatment option for a range of chronic disorders (*1*–*3*). However, despite having a success rate of over 90% for recurrent *Clostridium difficile* infection (R-CDI) (*1*), there are indications that the therapy as currently performed is not as effective in treating other diseases (*4*). This, in addition to inherent risks (*5*), has created a need to characterize and understand the full effects of FMT on the microbiome of the recipient, across different diseases.

Recent studies have indicated that establishment of donor-specific species is possible alongside resident microbiota of the recipient (*6*–*9*) and that they can still be detected 70 days after FMT (*7*). However, the definitive origin of these newly observed species—whether they are indeed from the donor or from other sources (for example, diet or environment) or had simply been below detection levels in the recipient—is uncertain. Moreover, in the majority of these studies, the FMT procedure was preceded by a course of antibiotics, which is known to alter the gut flora (*10*, *11*) and may or may not facilitate implantation of exogenous microorganisms.

The full extent to which donor microbiota colonize in a recipient host has not yet been measured, as studies to date have been restricted to genus- and species-level comparisons and have not distinguished or elucidated the fate of donor and recipient strains of the same species (*6*–*9*, *12*). Genetic variants of bacterial species are known to coexist in the gut (*13*), and strain-level differences have recently been shown to have functional and clinically relevant consequences (*13*–*15*). However, other studies in humans and model systems have found that newly introduced nonpathogenic strains are unable to persist in an established gut ecosystem—especially if the species was already present—be they probiotics (*16*), xenomicrobiota (*17*), or even modified strains isolated from the same healthy individual (*18*).

Here, we quantify and describe the extent of changes to the population structure of the gut microbiome after FMT, at both species and strain level, using shotgun metagenomic data. Donor strains established extensively in the recipient and persisted over the 3-month observational period, either replacing or, more strikingly, existing alongside indigenous strains. Outcomes varied across donor-recipient pairs, indicating that microbiome compatibility (the likelihood that donor strain populations are able to coexist or even replace microbial strains in the recipient) is a factor that could provide a rationale for more targeted microbiota-based therapies.

[1]Structural and Computational Biology Unit, European Molecular Biology Laboratory, 69117 Heidelberg, Germany. [2]School of Biotechnology and Biomolecular Sciences, University of New South Wales, 2052 Sydney, Australia. [3]Genomics Core Facility, European Molecular Biology Laboratory, 69117 Heidelberg, Germany. [4]Department of Vascular Medicine, Academic Medical Center, 1105 AZ Amsterdam, Netherlands. [5]Diabetes Center, Vrije University Medical Center, 1018 HV Amsterdam, Netherlands. [6]Wallenberg Laboratory, University of Gothenburg, 41345 Gothenburg, Sweden. [7]Department of Veterinary Biosciences, University of Helsinki, 00014 Helsinki, Finland. [8]Department of Biosciences, University of Helsinki, 00014 Helsinki, Finland. [9]Department of Applied Tumor Biology, Institute of Pathology, University Hospital Heidelberg, 69120 Heidelberg, Germany. [10]Molecular Medicine Partnership Unit, University of Heidelberg and European Molecular Biology Laboratory, 69120 Heidelberg, Germany. [11]Laboratory of Microbiology, Wageningen University, 6703 HB Wageningen, Netherlands. [12]Immunobiology Research Program, Department of Bacteriology and Immunology, University of Helsinki, 00014 Helsinki, Finland. [13]Max Delbrück Centre for Molecular Medicine, 13125 Berlin, Germany. [14]Department of Bioinformatics, Biocenter, University of Würzburg, 97074 Würzburg, Germany.
***Corresponding author. Email: bork@embl.de (P.B.); willem.devos@wur.nl (W.M.dV.); sunagawa@embl.de (S.S.)**

Downloaded from http://science.sciencemag.org/ on April 28, 2016

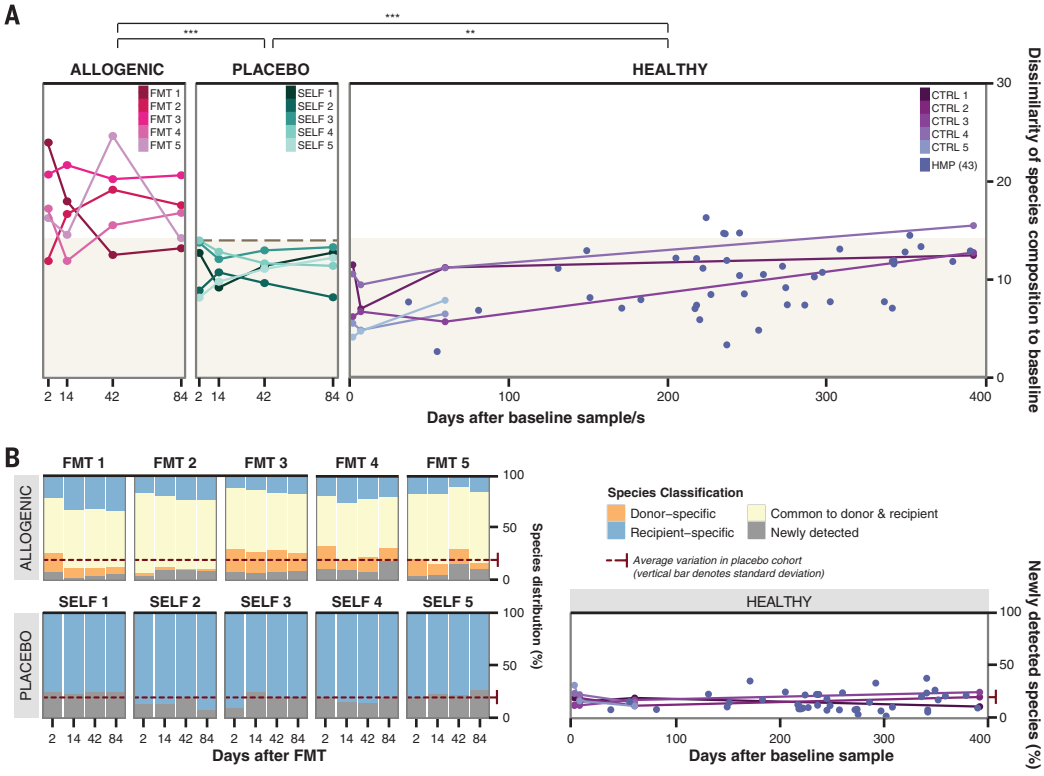

Fig. 1. Microbial communities undergo larger compositional changes after allogenic FMT compared with placebo-treated and healthy individuals but contain similar proportions of newly acquired species. (**A**) Post-allogenic FMT microbiomes display species composition changes above the range of temporal variation observed in placebo (beige) and healthy controls, persisting over 84 days (Wilcoxon rank-sum test; ***$P < 0.0002$; **$P < 0.004$; Euclidean distance) (*22*). Lines connect time point samples from the same individual. (**B**) Proportion of acquired donor species in allogenic FMT subjects is within, or close to, the level of variation observed in placebo (20.1 ± 5.0%) (dotted line) and healthy individuals for up to 400 days after initial sampling. These species thus may not necessarily have originated from the donor but may have been acquired from other sources or had previously been undetected. A majority of species is common to both donor and recipient (yellow). Same-donor FMT recipients are grouped by a black bar below the subject identifier.

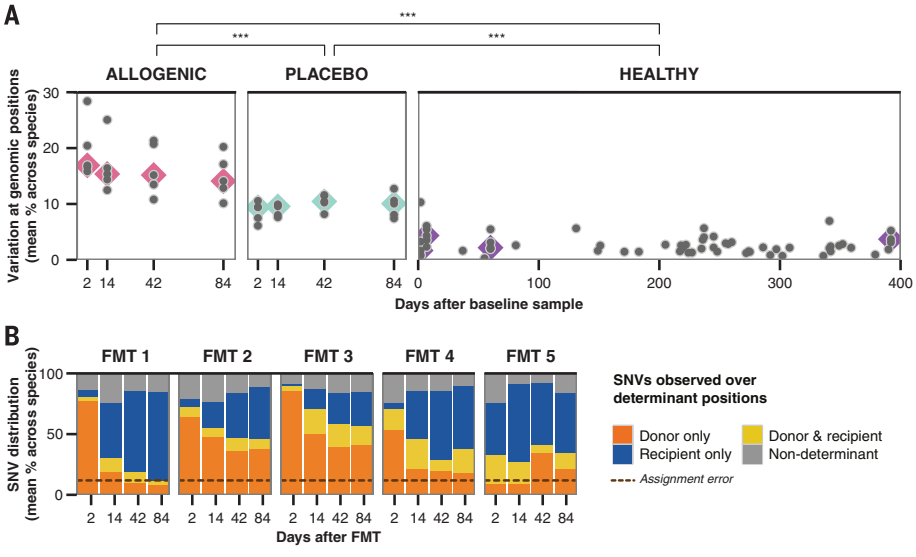

Fig. 2. Allogenic FMT instigates more variation at the strain level compared with placebo-treated and healthy individuals, most likely due to donor microbiota transfer. (**A**) Fraction of single-site allelic variation (compared to pre-FMT samples), averaged across species, is significantly higher in the allogenic FMT group than placebo-treated and healthy individuals (Wilcoxon rank-sum test; ***$P <$ 0.0001). Median values across individuals are highlighted by the diamond shape. (**B**) Average fraction of donor- and recipient-specific SNVs detected across 42 prevalent species in allogenic FMT recipients. Genomic positions containing both donor- and recipient-specific SNVs are shown in yellow; non-determinant positions (SNVs observed in none or both donor and recipient before FMT) are in gray. Presence of donor- and recipient-specific SNVs indicate durable coexistence of donor and recipient strains; decline of donor strains between 42 and 84 days after FMT is negligible. Retention of donor-specific SNVs is notably higher than the assignment error rate of 11.9% (dotted line) (*22*).

Using shotgun metagenomics, we sequenced 55 fecal samples from a recent FMT study of metabolic syndrome patients (*2*). In contrast to previous investigations, subjects in this study had not used antibiotics or other medication for at least 3 months before treatment, nor did they do so during treatment, thus minimizing associated confounding effects (*10*, *11*, *19*). The cohort of 10 subjects—half of whom received a single allogenic FMT (from one of three lean donors unrelated to the recipients) and the other half, an autologous FMT (i.e., a placebo equivalent)—had samples collected at consistent time points (once before treatment and four times after treatment). To contextualize our findings, we compared the cohort to 109 metagenomes of 48 healthy, FMT-naïve individuals from published longitudinal studies including the Human Microbiome Project (*20*–*22*). Changes after FMT were monitored over multiple time points, using pre-FMT samples of each donor-recipient pair as a baseline for allogenic FMT and placebo-treated recipients and initial time point (day 0) samples for healthy control subjects (fig. S1).

Using a taxonomic marker gene-based approach that accounts for both known and putative species (*22*, *23*), we observed compositional shifts in both allogenic and placebo-treated FMT recipients. These were above the range of natural temporal variation in healthy individuals (Wilcoxon rank-sum test, $P = 2.20 \times 10^{-6}$ and 3.86×10^{-3}) (Fig. 1A and fig. S2), suggestive of an additive effect of bowel lavage and microbiota transfer on the gut microbiome.

Downloaded from http://science.sciencemag.org/ on April 28, 2016

Compared with the other two groups, allogenic FMT microbiomes underwent considerably larger changes ($P = 7.49 \times 10^{-8}$) regardless of clinical outcome (table S1), which can thus be attributed to the introduction of donor microbiota and reflects previous reporting of increased microbial diversity in these subjects (*2*). These changes persisted for at least 3 months after treatment, even though recipient microbiomes gradually lost similarity to their respective donors (fig. S3), in contrast to findings in R-CDI patients (*7*, *12*).

Species putatively assigned as donor-specific varied across recipients and were observed throughout the 3 months of the study (Fig. 1B and fig. S4A). Retention of these new species positively correlated to the number of donor-specific species identified in pre-FMT samples ($R^2 = 0.83$) (fig. S4B). However, in four of five cases, the proportion of donor-specific species was either below or not significantly different from the fluctuations of new species detected over time in the placebo-treated group (20.8 ± 5.5%) and healthy group (17.7 ± 10.9%) (Fig. 1B and table S2), which was also observed using 16S ribosomal RNA gene-based profiling (fig. S5). We therefore propose that the detection of presumably donor-specific species in recipients after FMT is by itself not sufficient proof of colonization and in future studies should be contextualized by background variation.

A large fraction of species in allogenic FMT recipients was also present in their donor (64.5 ± 6.0%) (Fig. 1B). Determining the fate of these bacteria—that is, whether donor microbes are able to colonize and whether they replace or coexist with recipient microbiota—requires analytical resolution at the strain level. To this end, we used metagenomic single-nucleotide variant (SNV) analysis (*24*) to distinguish and trace donor- and recipient-specific strain populations, because the full genomic reconstruction of uncharacterized strains from a complex community is not yet available (*25*).

We extended the approach by Schloissnig *et al.* (*24*) to account for rare and less abundant strains and applied it to the 164 fecal metagenomes from the three study groups (*22*). This provided a starting set of 11.8 million variant positions across the genomes of 1105 detected prokaryotic species (table S3).

To compare the extent of strain-level changes among the study groups, SNVs identified in baseline samples were monitored over multiple time points (Fig. 2A and fig. S1). We observed a higher level of single-site allelic variation in allogenic FMT recipients than in the placebo and healthy groups

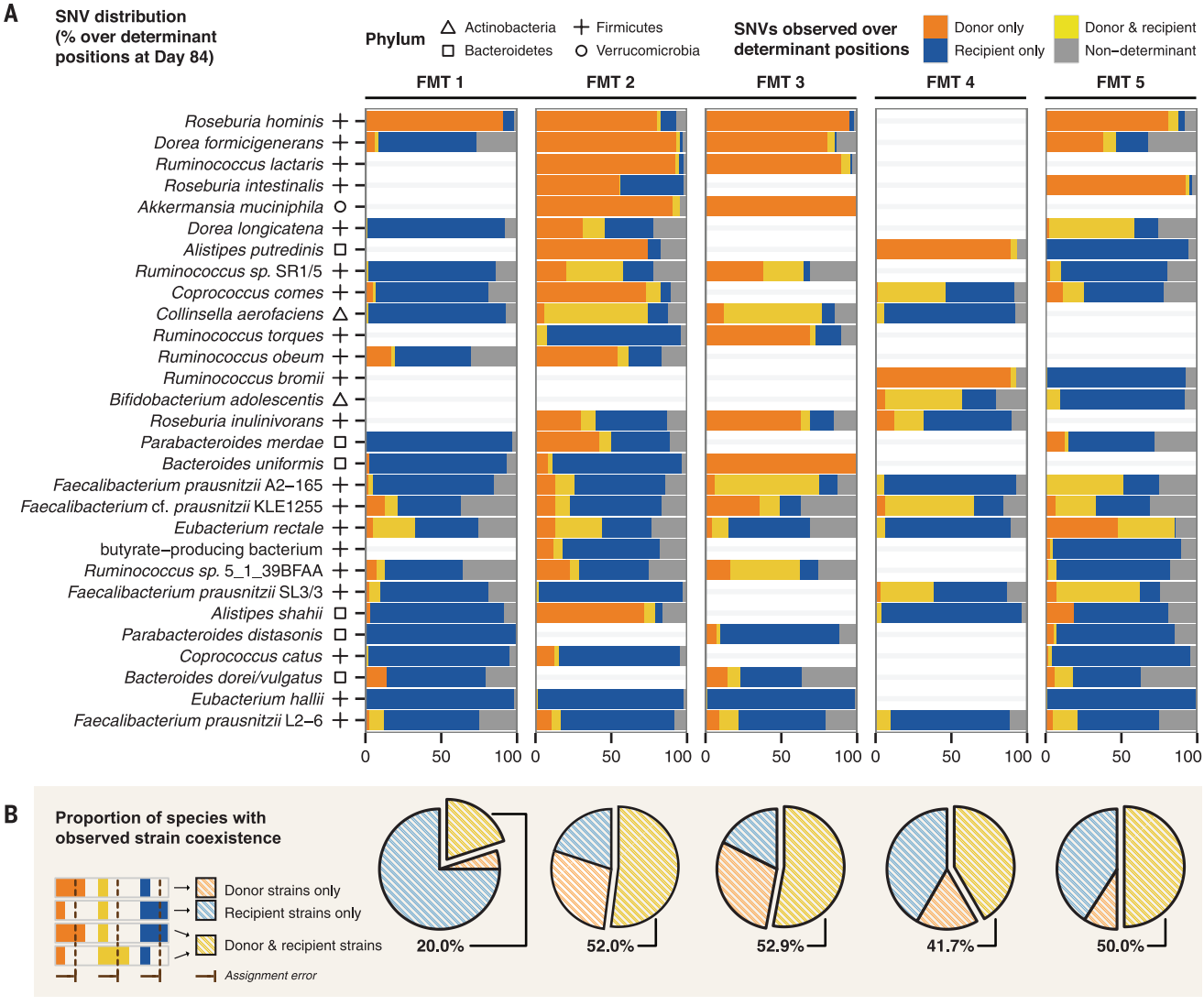

Fig. 3. Coexistence of donor and recipient strains across species, 84 days after FMT. (**A**) Distribution of donor- and recipient-specific SNVs for species detected in more than one recipient at day 84. Species are ranked by the likelihood of observing consistent donor (top) to recipient (bottom) strain dominance patterns (fig. S9). For clarity, full strain names are used in cases where species names were ambiguous (table S4). Blanks signify species that were not detected at day 84 or before FMT in donor and/or recipient. Coexistence of donor- and recipient-specific strains can be observed across species and recipients. The colonization success of donor strains does not appear to be associated with taxonomic affiliation of the species. (**B**) Extent of strain coexistence (yellow) in each recipient, summarized for detected species. Species with observed dominance of donor (orange) or recipient (blue) strains comprised a smaller proportion.

Downloaded from http://science.sciencemag.org/ on April 28, 2016

($P = 1.35 \times 10^{-5}$ and 1.50×10^{-6}, respectively), which indicated the presence of additional strains (*22*).

To investigate whether the increased variation was due to the transfer and establishment of donor microbiota, we defined a set of determinant genomic positions (containing both donor- and recipient-specific SNVs), which we monitored over time (fig. S1 and table S3) (*22*). For confident SNV detection and tracking, we focused on species that were consistently detected with sufficient abundance in at least one donor-recipient pair, resulting in 42 species across five phyla (table S4). Determinant positions for these species, which are prevalent in the general population (*24*), ranged from 66 to 161,800 (median 15,550) and were located throughout their respective genomes (fig. S6).

Across recipients, we observed transfer of donor strains (Fig. 2B and fig. S7). Donor-specific SNVs were most highly retained 2 days after FMT (69.3 ± 21.8% of determinant positions across recipients) and were still present 3 months later (37.6 ± 16.6%) (Fig. 2B and fig. S7). This contrasts with much lower rates of variation observed at equivalent time points in placebo-treated (day 84) and healthy (days 60 to 84) individuals (9.5 ± 1.8% and 2.9 ± 1.3%, respectively) (Fig. 2A) and shows that our findings result from donor-strain transfer and not only temporal variability or abundance variation beyond detection thresholds. Furthermore, it indicates that donor strains can colonize in the human gut after bowel lavage [which causes a short-term decrease in microbial diversity (*20*)] and without prior antibiotic treatment.

Marked differences in colonization success were observed between allogenic recipients who shared a donor (subjects FMT1, 2, and 3). Three months after treatment, FMT2 and 3 retained a higher amount of donor-specific SNVs compared with FMT1 (46.1%, 56.6%, and 12.0%, respectively) (Fig. 2B). The perceived resistance to incoming strains in FMT1 was also reflected in the overall microbiome composition of this subject, which reverted to the pre-FMT state, whereas FMT2 and 3 displayed more persistent compositional changes (Fig. 1A). Responses to FMT treatment may thus be idiosyncratic and depend on the compatibility of the donor and recipient microbiomes and/or the disease state involved. A "one-stool-fits-all" model currently supported by standardized donor stool banks may not be clinically appropriate (*26*).

Apart from the one case of microbiome resistance, we observed extensive coexistence of donor and recipient strains (in 50.7 ± 10.1% of shared species) in all other recipients, which persisted for at least 3 months (Fig. 2B). This suggests that novel strains can colonize in the gut without replacing the indigenous strain population of the recipient. It appears that introduced strains are more likely to establish in a new environment if the species is already present. The decline of donor-strain populations detected between 1.5 and 3 months after FMT was negligible, implying that potentially long-term strain coexistence might occur.

We sought to determine the extent of donor and recipient strain coexistence across species. Focusing on the 29 species that could be detected in more than one recipient at the end of the study, a pattern of donor strains establishing alongside indigenous strains of the recipient was seen (Fig. 3A). Whereas 39 ± 23% of species showed resistance to introduced strains, coexistence of donor and recipient strains was observed in 44 ± 14% of species detected in recipients (Fig. 3B). Durability of donor strains varied widely for most species, ranging from complete replacement of recipient strains to extinction (for example, *Alistipes putredinis* and *Ruminococcus bromii* fall at the extremes in FMT4 and 5). Most strikingly, however, donor strains of *Roseburia hominis*, *Ruminococcus lactaris*, and *Akkermansia muciniphila* appeared to dominate recipient strains, with almost complete substitution, even in the case of FMT1, who rejected most donor strains and species over time (Figs. 1B and 3A and fig. S8). By contrast, recipient strains of *Eubacterium hallii* and *Parabacteroides distasonis* showed resistance to donor strains by day 84 (fig. S8) (*22*). Based on these observations, we used a random permutation approach to rank species that showed consistent patterns of donor or recipient strain dominance (fig. S9) (*22*). Overall, colonization success and subsequent dominance or rejection of donor strains did not seem to depend on taxonomic affiliation of the species nor on differences in relative abundance between donor and recipient species (Fig. 3A and fig. S10), in contrast to previous findings in R-CDI patients (*6*, *9*). It was also not restricted to particular strains, genome size, phenotypic features (such as Gram stain), known functional capacities of a species, or clinical parameters (tables S1 and S5). Given these results, we propose that aspects such as strain and species fitness (*27*) and colonization resistance (*28*) should be studied in the context of microbiome resilience and immune responses of the recipient. Differences in the colonization success of donor strains across recipients also highlight the need for resolution beyond species level to understand the mechanisms (for example, how nonindigenous strains can elude host immune defense responses) and ecological effects underlying microbiota-based therapies.

Taken together, we have used intraspecies genetic variation to monitor strain populations within gut microbial communities. Applied to FMT, we observed an extensive and durable coexistence of donor and recipient strains of the same species, with a considerable amount of strain replacement (compared with a negligible uptake of donor species) that was not associated with clinical outcome. This suggests that introduced bacterial strains can be readily accepted and persist in an established gut microbial community, even when the species is already present. This contrasts with previous findings on isolated strains in non-FMT settings (*16*–*18*) and potentially extends to a wider context, such as the infant gut during development (*13*). The complete replacement of indigenous strains also introduces the possibility for the use of a consortia of characterized and/or customized strains to modulate the microbiome by, for example, outcompeting undesirable strains (*29*), hence encouraging the development of more defined microbiota-based precision treatments.

REFERENCES AND NOTES

1. E. van Nood *et al*., *N. Engl. J. Med.* **368**, 407–415 (2013).
2. A. Vrieze *et al*., *Gastroenterology* **143**, 913–916.e7 (2012).
3. L. P. Smits, K. E. C. Bouter, W. M. de Vos, T. J. Borody, M. Nieuwdorp, *Gastroenterology* **145**, 946–953 (2013).
4. N. G. Rossen *et al*., *Gastroenterology* **149**, 110–118.e4 (2015).
5. N. Alang, C. R. Kelly, *Open Forum Infect. Dis.* **2**, ofv004 (2015).
6. S. Angelberger *et al*., *Am. J. Gastroenterol.* **108**, 1620–1630 (2013).
7. S. Fuentes *et al*., *ISME J.* **8**, 1621–1633 (2014).
8. A. M. Seekatz *et al*., *MBio* **5**, e00893-14 (2014).
9. Y. Song *et al*., *PLOS One* **8**, e81330 (2013).
10. L. Dethlefsen, D. A. Relman, *Proc. Natl. Acad. Sci. U.S.A.* **108** (suppl. 1), 4554–4561 (2011).
11. C. F. Maurice, H. J. Haiser, P. J. Turnbaugh, *Cell* **152**, 39–50 (2013).
12. A. Weingarden *et al*., *Microbiome* **3**, 10 (2015).
13. I. Sharon *et al*., *Genome Res.* **23**, 111–120 (2013).
14. S. Greenblum, R. Carr, E. Borenstein, *Cell* **160**, 583–594 (2015).
15. A. Zhu, S. Sunagawa, D. R. Mende, P. Bork, *Genome Biol.* **16**, 82 (2015).
16. R. M. Robins-Browne, M. M. Levine, *Am. J. Clin. Nutr.* **34**, 514–519 (1981).
17. H. Seedorf *et al*., *Cell* **159**, 253–266 (2014).
18. J. D. Anderson, W. A. Gillespie, M. H. Richmond, *J. Med. Microbiol.* **6**, 461–473 (1973).
19. K. Forslund *et al*., *Nature* **528**, 262–266 (2015).
20. A. Y. Voigt *et al*., *Genome Biol.* **16**, 73 (2015).
21. B. A. Methé *et al*., *Nature* **486**, 215–221 (2012).
22. Materials and methods are available as supplementary materials on *Science* Online.
23. S. Sunagawa *et al*., *Nat. Methods* **10**, 1196–1199 (2013).
24. S. Schloissnig *et al*., *Nature* **493**, 45–50 (2013).
25. C. Luo *et al*., *Nat. Biotechnol.* **33**, 1045–1052 (2015).
26. M. B. Smith, C. Kelly, E. J. Alm, *Nature* **506**, 290–291 (2014).
27. C. Portal-Celhay, M. J. Blaser, *Infect. Immun.* **80**, 1288–1299 (2012).
28. C. G. Buffie *et al*., *Nature* **517**, 205–208 (2015).
29. W. M. de Vos, *Microb. Biotechnol.* **6**, 316–325 (2013).

ACKNOWLEDGMENTS

We thank M. R. Wilkins, A. Typas, and members of the Bork group, as well as B. Klaus from the Centre for Statistical Data Analysis at the European Molecular Biology Laboratory (EMBL) for helpful discussions. We acknowledge the EMBL Genomics Core Facility for sequencing support and Y. P. Yuan and the EMBL Information Technology Core Facility for support with high-performance computing. S.S.L. is the recipient of an Australian Postgraduate Award and EMBL Australia International Ph.D. Fellowship. F.H. received funding through the European Union's Horizon 2020 research and innovation program under the Marie Skłodowska-Curie grant agreement no. 600375. M.N. is supported by a VIDI 2013 grant (016.146.327) as well as a CVON 2012 grant (IN-CONTROL). This work has received funding through the CancerBiome and MicrobesInside projects (European Research Council project references 268985 and 250172), the Academy of Finland (grants 141140 and 271832), the Netherlands Organization for Scientific Research (Spinoza Prize and SIAM Gravity grant 024.002.002), the Metagenomics in Cardiometabolic Diseases project (FP7-HEALTH-2012-INNOVATION-I-305312) and the International Human Microbiome Standards project (HEALTH-F4-2010-261376). M.N. and W.M.dV. are founders and scientific advisory board members of Caelus Health. M.N. and W.M.dV. are inventors on the patent application entitled "Method for preventing and/or treating insulin resistance" (WO 2013032328, also published as CA2851602A1, CN104244733A, EP2753187A1, US20140294774), filed 30 August 2012 by Academic Medical Centre Amsterdam and Wageningen University. M.N. is a scientific advisory board member of Seres Therapeutics Inc., and has received funds for speaking from AstraZeneca plc, Danone, and Eli Lilly and Company. Study sequence data reported in this paper are deposited in the European Nucleotide Archive under accession number PRJEB12357. Author contributions: P.B., S.S., and S.S.L. conceived and managed the project. S.S.L. and P.B. wrote the manuscript with input from all other authors. W.M.dV., M.N., and A.Y.V. designed study protocol, recruited subjects, and obtained samples. R.H. and V.B. performed metagenomic shotgun sequencing. S.S.L., S.S., A.Z., P.I.C., J.S., G.Z., F.H., and J.H-C. designed and performed data analysis.

SUPPLEMENTARY MATERIALS

www.sciencemag.org/content/352/6285/586/suppl/DC1
Materials and Methods
Figs. S1 to S14
Tables S1 to S7
References (*30*–*46*)

17 November 2015; accepted 29 March 2016
10.1126/science.aad8852

Downloaded from http://science.sciencemag.org/ on April 28, 2016

REPTILE SLEEP

Slow waves, sharp waves, ripples, and REM in sleeping dragons

Mark Shein-Idelson,* Janie M. Ondracek,* Hua-Peng Liaw,† Sam Reiter,† Gilles Laurent‡

Sleep has been described in animals ranging from worms to humans. Yet the electrophysiological characteristics of brain sleep, such as slow-wave (SW) and rapid eye movement (REM) activities, are thought to be restricted to mammals and birds. Recording from the brain of a lizard, the Australian dragon *Pogona vitticeps*, we identified SW and REM sleep patterns, thus pushing back the probable evolution of these dynamics at least to the emergence of amniotes. The SW and REM sleep patterns that we observed in lizards oscillated continuously for 6 to 10 hours with a period of ~80 seconds. The networks controlling SW-REM antagonism in amniotes may thus originate from a common, ancient oscillator circuit. Lizard SW dynamics closely resemble those observed in rodent hippocampal CA1, yet they originate from a brain area, the dorsal ventricular ridge, that has no obvious hodological similarity with the mammalian hippocampus.

It is now generally agreed that animals ranging from invertebrates to humans sleep. The principal attributes of sleep are shared by all animals and define what is often described as "behavioral sleep," which has been identified in many invertebrates and vertebrates (*1*–*8*). The first electrophysiological studies of sleep were conducted in humans and revealed clear electroencephalographic (EEG) correlates of brain states during sleep (*9*–*11*). Researchers now divide mammalian sleep EEG patterns into two main types: (i) slow-wave sleep (SWS) and (ii) non-SWS or REM sleep (REMS), which is accompanied by conspicuous rapid eye movement (REM) and an otherwise atone axial and limb musculature (*12*). So far, these electrophysiological attributes of sleep have been demonstrated only in mammals and birds (*7*, *13*–*17*).

Mammals and birds belong to different branches of an early bifurcation of the amniotes, which occurred over 300 million years ago (Fig. 1A). Because mammals and birds are the only homeotherms among living vertebrates, and because it has been thought that only they manifest REMS and SWS, it has been suggested that REMS and SWS are the expression of convergent evolution driven by common constraints and selective pressures correlated with homeothermia (*18*, *19*). REMS and SWS, however, could be ancestral to mammals and birds; if so, their electrical signatures should also exist in nonavian reptiles. Evidence for such signatures from sleeping reptiles has thus far been inconclusive (*1*, *14*, *15*, *17*, *18*, *20*–*22*). We reexamined this issue by recording from the brain of a lizard, the Australian dragon *Pogona vitticeps*. Because lizards belong to the lepidosaurs, the earliest subclass to branch out from the sauropsid trunk and thus the one that is most distant from avians (*23*), *Pogona* is ideal for examining the evolution of sleep among amniotes.

We confirmed the existence of behavioral sleep in adult *Pogona* dragons (Fig. 1, B and C, and fig. S1) (*24*). Behavioral sleep features were highly consistent across individual lizards and nights (Fig. 1C), and the transition between awake and behavioral-sleep states usually anticipated the programmed transition from light to dark. We implanted five lizards with either tetrode arrays (*25*) or linear silicon probes inserted in the dorsal forebrain (in the cortex and the dorsal ventricular ridge, or DVR). After recovery from surgery and slow electrode advance, we recorded extracellular electrical activity [local field potential (LFP), multi- and single-unit activity] continuously over 18 to 20 hours centered on the middle of the night, usually combining behavioral monitoring with electrophysiology. Recordings from individual animals were repeated over days to weeks.

LFP recordings from the DVR in the middle of the animals' behavioral sleep revealed a slow oscillation (red, Fig. 2A) and negative deflections of varying amplitude. Nocturnal LFPs could be segmented into two principal spectral clusters (Fig. 2B): (i) segments of low-frequency activity (<4 Hz, δ band; Fig. 2Ac; blue in Fig. 2C and fig. S2A) and (ii) segments of broadband activity (Fig. 2Ad; red in Fig. 2C), which were more similar to activity in the awake state (fig. S2, B to D). The frequency at which the curves of these two components intersected ($F_{trans.}$; Fig. 2C) was around 4 Hz and stable across animals and nights (Fig. 2D). We observed neither 10 to 15–Hz spindles nor clear activity in the 5 to 10–Hz (θ) band. By analogy with metrics that have been used with rodents (but to account for the absence of dominant θ-band activity in sleep), we chose the 10 to 30–Hz (β) band to quantify the broadband activity cluster and computed the ratio of δ to β power (rather than δ to θ power, as with rats) (*26*, *27*) over a sliding window. For a duration of 6 to 10 hours, starting shortly after the onset of imposed darkness and ending 1 to a few hours before the lights were turned on, the δ/β ratio oscillated regularly and continuously (Fig. 2E and figs. S3 and S4) with a period of about 80 s (Fig. 2F and fig. S4). We call this epoch "electrophysiological sleep" (e-sleep). E-sleep started shortly after the onset of behavioral sleep and ended 0.5 to several hours before the end of behavioral sleep (Fig. 2E). In all cases, e-sleep represented a dominant and continuous fraction of behavioral sleep (Fig. 2E and fig. S4).

The period of the δ/β oscillation was temperature-dependent. After initial recordings in animal 1 (temperature, ~25°C; period, >100 s; Fig. 2G), we raised and stabilized room temperature to 27°C. The mean oscillation period decreased to around 80 s. In one further experiment, we raised the temperature to 32°C, and the oscillation period further decreased to ~60 s [asterisk (animal 5), Fig. 2G]. Over a single night at constant temperature, the oscillation period typically increased slowly (by ~2 s/hour on average) from evening to morning (figs. S4 and S5). The envelope amplitude of the δ/β oscillation varied to a much greater extent, typically ramping up at the beginning and down at the end of the night, but with wide instantaneous variations (fig. S4). Similar results were obtained by analyzing the δ and β bands separately (rather than their ratio) (fig. S6).

δ power during SWS primarily reflected the repeated occurrence of large negative deflections of LFP (halfwidth, 100 to 400 ms at 27°C) at a rate of less than one per second (Fig. 2, A to Ac). Because their shape was relatively stereotyped, an averaged template could be obtained (Fig. 2Ae, red) and used to detect most events automatically from a night's recording. High-pass (HP) filtering of these selected LFP segments revealed that they nearly always contained short bursts of >70-Hz multi-unit activity, which were locked to the deflection's descending phase (Fig. 2Ae, bottom trace). The reliability of this association of HP and LFP features is illustrated by 1000 consecutive events (Fig. 2Af). By analogy with classical observations in rodent hippocampal CA1 (*26*–*30*), we will call the LFP events "sharp waves" and the corresponding HP events "ripples." They are each slower than their rat counterparts, possibly as a result of temperature differences (27°C in this study versus the 37° to 38°C body temperature of rats). The reliability of this sharp wave–ripple (SWR) association is illustrated in Fig. 2H (five animals, 18 nights).

In mammals, non-SWS is usually accompanied by eye movements (*10*–*12*, *31*). We thus tested whether this is the case in sleeping lizards. We monitored the eye contralateral to the LFP-recording site with infrared cameras and quantified eye movement by computerized video analysis (Fig. 3A, movie S1, and materials and methods). The eyes twitched during the night in discrete epochs interposed with immobility or slow drift. When matched against a simultaneously recorded contralateral LFP, REM occurred preferentially when δ/β was low—i.e., in

Max Planck Institute for Brain Research, Frankfurt am Main, Germany.
*These authors contributed equally to this work. †These authors contributed equally to this work. ‡Corresponding author. Email: gilles.laurent@brain.mpg.de

Downloaded from http://science.sciencemag.org/ on April 28, 2016

alternation with SWS (Fig. 3B and movie S1). Because δ/β was periodic, we measured the phase of eye movements relative to that of δ/β (red dots in Fig. 3, B and C). These measurements confirmed that REMS alternates with SWS and showed that eye movements occur preferentially in the quarter cycle before δ/β power reaches its minimum (Fig. 3, C to E). Hence, the lizard's two e-sleep states (high and low δ/β) fit phenotypically those classically described in mammals (SWS and REMS, respectively). These two states alternate in a clock-like fashion, defining up to 350 consecutive cycles per night, with SWS occupying just under 50% of each cycle on average (fig. S7). We next examined spiking activity during the two sleep states.

Instantaneous DVR firing frequencies during sharp waves were high (~100 Hz; Fig. 4A). These peaks, however, arose on top of an average SWS firing rate that was close to zero (Fig. 4A). In contrast, spiking activity during REMS was high, reaching values similar to those recorded in the awake state (stippled lines in Fig. 4B). The DVR ripples are thus short high-frequency bursts that correspond to sharp waves during SWS, intermittently interrupting a "silent" background (e.g., black trace at the top of Fig. 4A). Mean firing rates, however, slowly oscillate over the sleep cycle between near silence (SWS) and awake-like rates (REMS).

Given the apparent similarity between these SWRs and those described in rat hippocampal CA1 (*26*–*29*), we had initially expected our recordings to be centered in the lizard's putative hippocampal regions (cortex). Using micro-computed tomography (μ-CT) scans (fig. S8) and small electrolytic lesions followed by histology, we found unexpectedly that all SWS and REMS activity described above originated from the anterior DVR (Fig. 4C and fig. S9) and not from the cortex. Activities in the anterior DVR and cortex were correlated, however (fig. S10A). Immediately before the onset of a sharp wave (trough at time t = 0; Fig. 4D), firing probability decreased in cortical and DVR neurons. The spikes in Fig. 4, D and F, originated from 5000 sharp waves recorded during one night; single-neuron firing probabilities during SWS are thus extremely low, especially in the DVR, which is consistent with population data. Hence, phasic inhibition could be detected in single cells only if activity was examined over many individual sharp waves (Fig. 4, D and F), or when derived from population averages (Fig. 4G). About 100 ms before the trough of the sharp wave and coincident with its rapid onset (Fig. 4, D and G), DVR neuron activity increased sharply, and individual neurons fired only a few action potentials, if any (Fig. 4D), as observed in rat CA1 (*26*, *32*, *33*). As the sharp wave ended, the probability of DVR neuron firing declined sharply back to zero (Fig. 4, F and G).

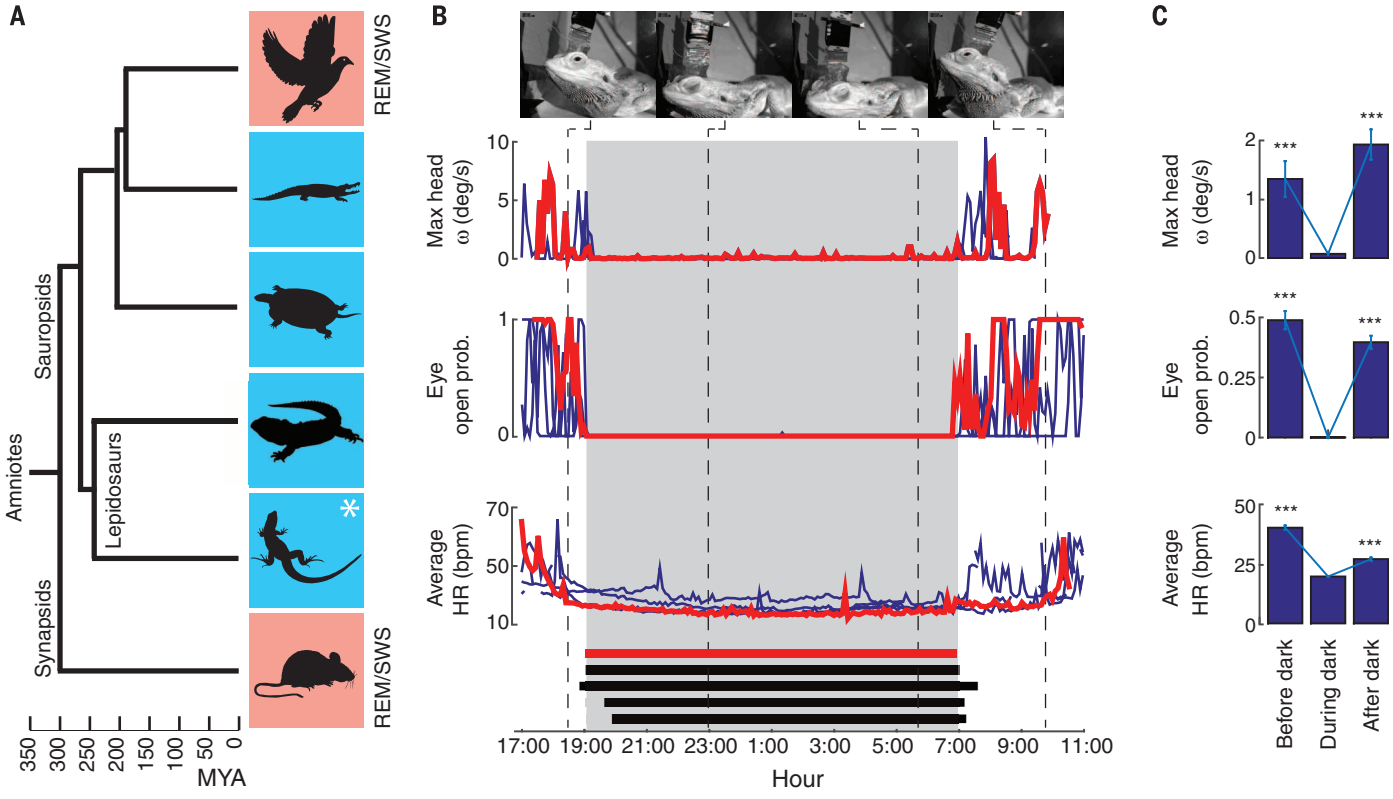

Fig. 1. Behavioral sleep in a reptile, the Australian dragon *Pogona vitticeps*. (**A**) Cladogram of vertebrate evolution, indicating those classes (avians and mammals; pink boxes) in which the electrophysiological signatures of vertebrate sleep (SWS and REMS) have been established. These classes are also characterized by homeothermia. Blue boxes denote the nonavian reptiles [from top to bottom: crocodilians; chelonians; tuatara (*Sphenodon*); and squamates (marked with an asterisk), including lizards and snakes], all of which are poikilotherms. *Pogona* is an agamid lizard. MYA, million years ago. The time scale follows (*23*). (**B**) Behavioral and physiological parameters used to assess the behavioral-sleep state in *Pogona* (red traces are from the animal pictured; blue traces are from other nights and animals). The top row includes representative photographs illustrating the awake (far left and far right) and sleep (middle) states. The second row shows maximum head angular velocity (ω, degrees per second) during and around nighttime (n = 3 recordings). Stationarity tends to precede the onset of darkness (gray shaded area). Plotted are peak values in successive 5-min periods. The third row shows the probability of the eye contralateral to LFP recording being open (n = 4 recordings). This probability was calculated over all movie images in successive 5-min segments. The fourth row shows heart rate (HR) in beats per minute, plotted as successive 5-min averages (n = 5 recordings from three animals). Curve interruptions (in awake segments) are due to animal movements, preventing reliable HR measurement. The bars in the fifth row indicate the periods defined as behavioral sleep, determined as the intersection of rest periods, as assessed from the above physiological and behavioral parameters (see the materials and methods section in the supplementary materials) (n = 5 recordings from three animals). Behavioral sleep is tightly aligned with the light-dark cycle, but the transition to behavioral sleep often anticipates the onset of darkness, as evident in head angular velocity, eye-open probability, and HR measurements (fig. S1 shows data from unoperated animal). (**C**) Means and SEM of the variables in (B), calculated over successive 5-min segments before, during, and after dark. ***P < 0.001; two-tailed t test with Bonferroni correction.

Downloaded from http://science.sciencemag.org/ on April 28, 2016

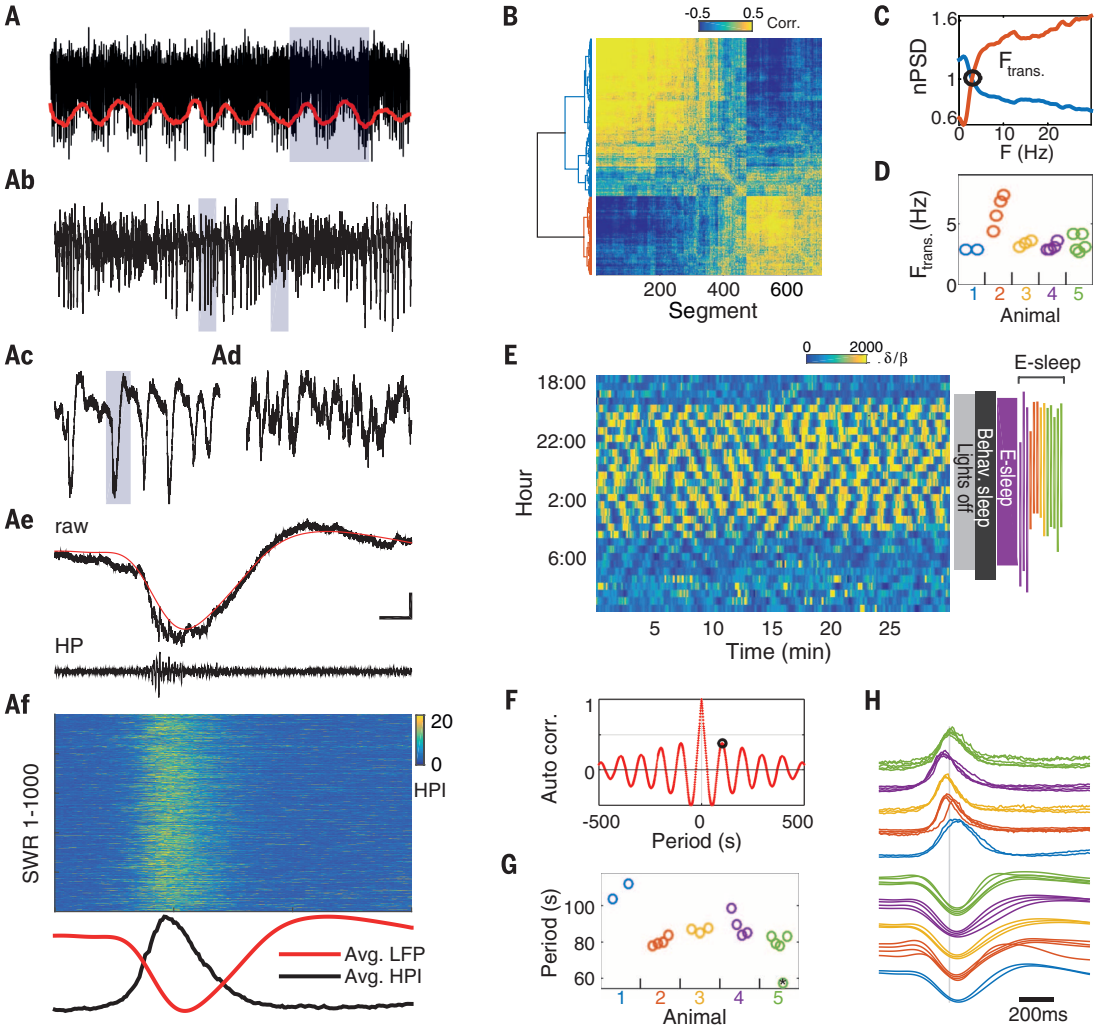

Fig. 2. Behavioral sleep includes a long uninterrupted epoch of regularly alternating SWS and non-SWS, defining e-sleep. Salient features of unfiltered LFP recorded in the DVR during sleep are shown in A to Af; all of these data are from the same animal and night. (**A**) Slow time base. The LFP envelope oscillates slowly, as evident in the order-filtered trace (red). The shaded area is expanded in (Ab). (**Ab**) Two alternating epochs are apparent, with and without large negative LFP spikes, with intermediate-sized deflections in between. The shaded areas are expanded in (Ac) and (Ad). (**Ac**) Stereotypical negative LFP spikes with positive rebound occur regularly every 1 to 3 s. The shaded area is expanded in (Ae). (**Ad**) The epoch alternating with that in (Ac) lacks stereotypical LFP spikes. (**Ae**) Close-up view of the shaded LFP spike in (Ac) (top, black) and the averaged template (red, average of 1000 LFP spikes aligned on the troughs). The same single trace is shown below after high-pass filtering (60 to 900 Hz). This combination resembles the mammalian SWR complex. (**Af**) One thousand successive ripples (HPI, HP signal intensity) aligned, for each trace, on the peak cross-correlation between the corresponding LFP waveform and the template [red trace in (Ae)]. Averages of all 1000 matching HPI (black) and LFP (red) traces are shown below. The horizontal scale bar is 90 s for (A), 20 s for (Ab), 2 s for (Ac) and (Ad), and 139 ms for (Ae). The vertical scale bar is 300 μV for (A) and (Ab), 200 μV for (Ac) and (Ad), and 180 μV for (Ae). (**B**) Night LFPs define two main spectral clusters. Shown is an ordered correlation matrix of spectral characteristics, calculated from 10-s data segments from one LFP channel over one night. Two dominant clusters are evident. The dendrogram (left) is based on a Euclidian metric that uses Ward linkage. The original data are the same as in (A) to (Af). (**C**) Normalized power spectral density (nPSD) of the nighttime LFP for the two clusters in (B). $F_{trans.}$ is the frequency at which curves intersect (~4 Hz). One cluster dominates with higher-than-average power at low frequencies (δ), defining SWS and corresponding to LFP segments containing SWRs [as in (Ac)]. The other cluster (β) dominates with higher power at $F > F_{trans.}$ (see also fig. S2). (**D**) $F_{trans.}$ measured across animals and nights (each circle is a night). The variance is low (except for animal 2, in which the signal-to-noise ratio was lowest). (**E**) Epochs of high and low δ power oscillate regularly throughout the night, forming a continuous period of e-sleep. The evolution of the δ/β power ratio (measured piecewise over 10-s moving windows shifted in 1-s steps) around nighttime is plotted on the left for one animal. Each horizontal row represents a 30-min segment (running left to right); successive 30-min segments run continuously from top to bottom. This slow alternation (high versus low δ) starts shortly after the lights are turned off and continues uninterrupted until less than an hour before the end of behavioral sleep (though with smaller-amplitude modulation in the last 2 hours). Epochs of behavioral sleep and e-sleep (defined by δ-power alternation) for this animal are shown on the right. The thin vertical bars are epochs of e-sleep for this (purple) and three other animals over several nights each, showing the consistency of the pattern. E-sleep occupies a major fraction of behavioral sleep and usually occurs toward the beginning of it (figs. S3 and S4). (**F**) Autocorrelation function of the e-sleep δ/β data in (E). The average period (circled) is around 80 s (27°C) (see also fig. S5). (**G**) Period of the autocorrelation function [measured as in (F)] across five animals and 18 nights, showing relative consistency for each animal. Both nights for animal 1 were at 25°C. All nights for animals 2 to 4 were at 27°C. Animal 5 spent four nights at 27°C and one night (*) at 32°C. (**H**) Averaged SWR components (top five sets, HPI; bottom five sets, LFP) for the animals in (G). The alignment is as in (Af).

Downloaded from http://science.sciencemag.org/ on April 28, 2016

Activity in the cortex also changed around individual sharp waves. Cortical neuron firing rates decreased shortly before a sharp wave and then increased, less abruptly than in DVR neurons, to peak some 400 ms after the DVR population (Fig. 4, D, F, and G). This relationship between DVR and cortical firing during a sharp wave was observed in all cortical and DVR units along a recording probe (Fig. 4F) and aligned precisely with a correlation analysis of signal amplitude as a function of recording depth (Fig. 4E): Units with cortical activity were physically clustered and separated from the DVR-unit cluster by a region that lacked a high-frequency signal (the ventricle) (Fig. 4, E and F). These results were consistent across animals in single- and multi-unit data (Fig. 4, D, F, and G).

Last, we compared the modulation of firing rates of cortical and DVR neurons over sleep cycles. Both populations oscillated with the ~80-s period (fig. S10A) and were phase-locked with one another (Fig. 4H). Hence, SWR-related firing activities in the DVR and cortex occur near the nadir of their respective sleep-cycle modulation, and mean firing rates are always higher in the cortex than in the DVR (fig. S10, A to C).

Sleep-related brain dynamics similar to mammalian SWS (including SWRs) and REMS exist in *Pogona*, a nonavian reptile. This decreases the probability that SWS and REMS result from convergent evolution among homeotherms. Rather, it suggests that the circuits underlying the electrophysiological signatures of sleep evolved in a common ancestor early in amniote evolution, before the synapsid-sauropsid bifurcation over 300 million years ago, if not earlier (Fig. 1A). Sleep-related brain states should probably be reexamined in amphibians and fish as well.

Although similar to mammalian sleep, lizard SWS and REMS resemble a stripped-down (two-state) version of the richer mammalian repertoire (especially in comparison to sleep in large mammals). In *Pogona*, SWS and REMS alternate regularly throughout the night with a short period (~80 s), generating up to 350 SWS-REMS cycles (compared with four to five 90-min cycles in humans, in which the fraction constituted by REMS changes throughout the night) (*19*, *31*). Given the ancient origin of the brain areas associated with sleep in mammals (the thalamus, hypothalamus, and brainstem) (*34*–*39*), reptilian brain sleep may point to an ancestral control system for sleep-related brain dynamics. Reptiles could thus provide a useful experimental testbed for mechanistic models of SWS-REMS alternation.

The SWRs in lizards resemble those identified in rodent hippocampal CA1 (*26*, *28*). That they arise in the DVR is unexpected, because the region of the reptilian brain that is assumed to be equivalent to the mammalian hippocampus is the medial cortex, not the DVR (*23*, *40*). The cortex was inhibited just before the occurrence of DVR ripples and was excited immediately during and after them, in a pattern reminiscent of the correlation between hippocampal ripples and cortical spindles in rats (*26*). Does this then suggest hippocampus-like functions for the DVR? So far, no functional, hodological, or architectonic arguments exist to support this possibility. Oscillatory rhythms associated with SWS are not an exclusive property of the mammalian hippocampus; they are seen also in the neocortex

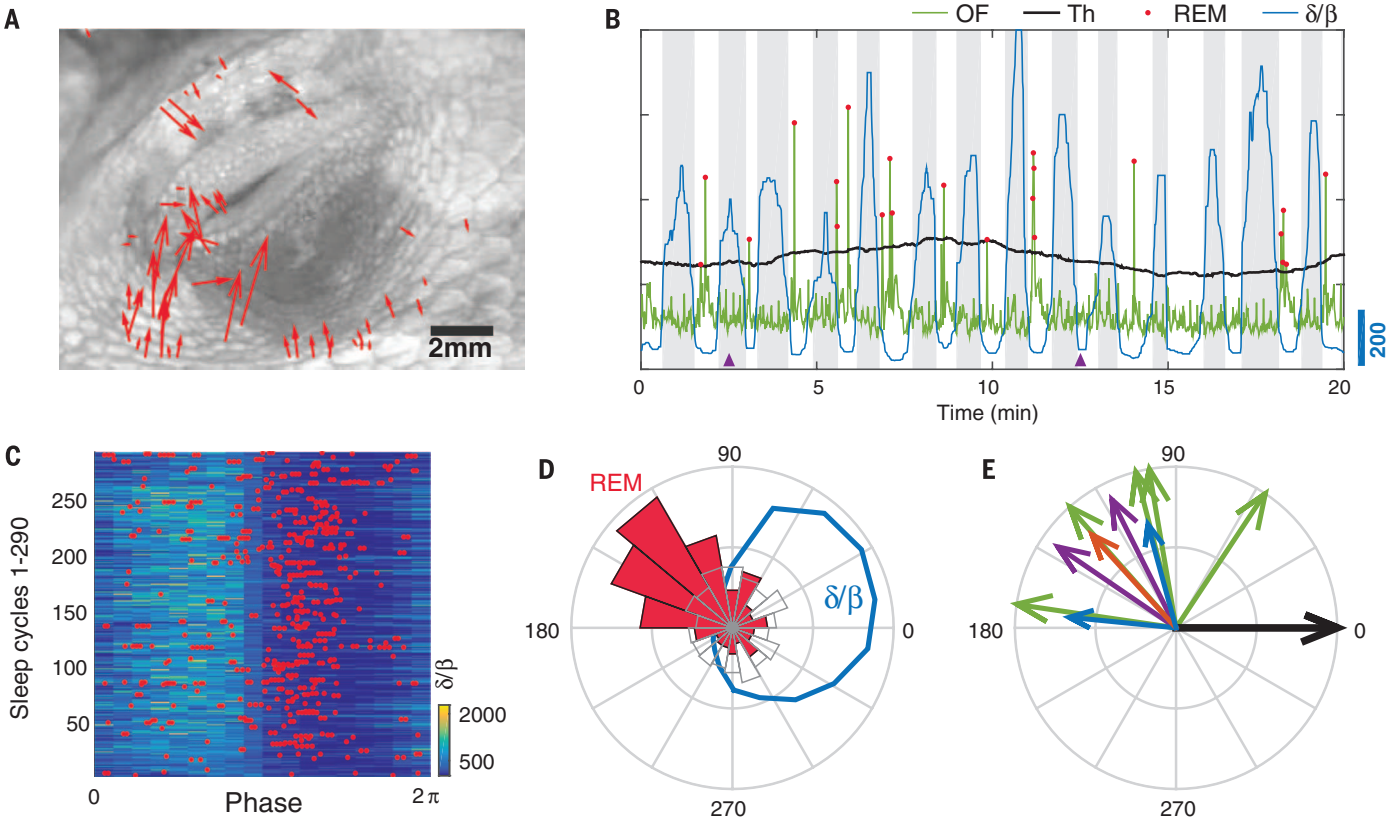

Fig. 3. Rapid eye movements alternate with SWS. (**A**) Quantitative analysis of videos of closed eyes reveals regular epochs of REM, detected as local flow fields of eyelid and orbital skin features (arrows) (movie S1). (**B**) The summed magnitude of these optical flow-field vectors (OF, green), plotted here as a function of time, peaks periodically and nearly always in periods of low δ/β LFP power (white bands). Using a floating threshold crossing (Th, black) for the detection of the fastest-motion events, the timing of peak eye movements was recorded (red dots). The epoch between the two purple arrowheads is shown in movie S1. (**C**) Because δ/β power is a near-periodic function of time during e-sleep (period, ~80 s), cycles can be normalized linearly, and the timing of eye movements [red dots, as in (B)] can be plotted relative to the phase of the cycle for a full night. Most eye movements cluster in the same phase (first half of the low-δ phase; dark blue). (**D**) Rose diagram of phases of eye movement (red) and SWS (high δ/β, blue) from the data in (C), confirming the phase shift between REMS and SWS. Shuffle control of the REM phase bias is shown in gray. (**E**) Polar plot of the mean phase angle of REMS relative to SWS (set at 0) for four animals (colors are as in Fig. 2) and 10 nights. The phase shift is consistent: 9 of 10 vectors are contained in the quarter cycle corresponding to the beginning of non-SWS. (Vector norms in the diagram are meaningless, except in indicating individual animals.)

Downloaded from http://science.sciencemag.org/ on April 28, 2016

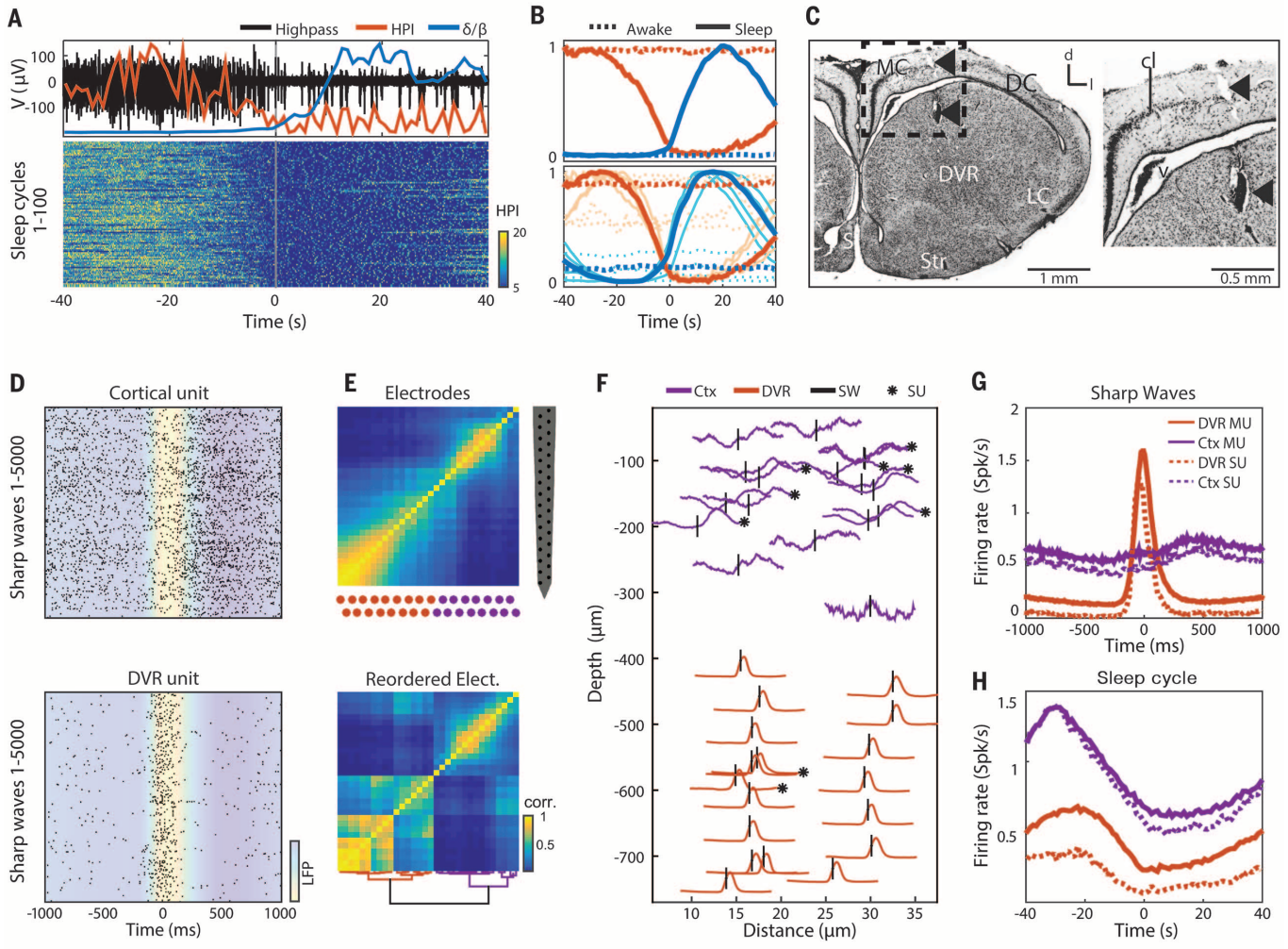

Fig. 4. Firing rates vary in antiphase with δ activity, SWRs originate in the DVR area, and DVR activity during sharp waves is correlated with activity in the cortex. (**A**) Firing activity (band pass, 0.1 to 2 kHz; black, top panel) is anticorrelated with δ/β (blue, top panel) around the sleep cycle (*V*, voltage). HPI (50-ms bins; materials and methods) was measured for each sleep cycle (red, top panel) and plotted for 100 successive sleep cycles (bottom panel). High-frequency bursts occur during the high-δ/β phase, as seen in the single trace (black) in the top panel, corresponding to individual sharp waves. (**B**) The relationship between firing and δ/β(*t*) is consistent and systematic across animals. The top panel shows means over all sleep cycles for a single animal [same lizard as in (A)]. Stippled lines (red, firing rates; blue, δ/β) indicate values measured during the awake state over consecutive 80-s segments. Peak firing rates during REMS (non-SWS) match those in the awake state. Maximum and minimum values measured during sleep (continuous lines) are normalized to range from 0 to 1, and values in the awake state are plotted in same normalized range. The bottom panel shows data from this and three other animals for all nights. The stippled curves (average values in the awake state) differ, due to variations across animals in the fraction of rest within the awake state. (**C**) Coronal section through a lizard's forebrain, showing the electrode track (along the two arrowheads) and main anatomical features. The area framed at left is magnified in the right panel (cl, cell layer; d, dorsal; l, lateral; DC, dorsal cortex; LC, lateral cortex; MC, medial cortex; S, septum; Str, striatum; v, ventricle) (figs. S8 and S9). (**D**) Simultaneous recording from one isolated cortical unit (top) and one DVR unit (bottom) around 5000 successive sharp waves. The alignment is on the trough of the sharp-wave LFP (color-coded) at $t = 0$. Each dot represents an action potential. (**E**) Physical clustering of HP intensities along the length of a multisite recording electrode (top right). Shown on the top left is a correlation matrix, ordered by physical position along the recording probe, of the HP intensities measured from each one of the 32 sites during REMS. Two principal clusters, separated by an intermediate zone, are apparent. The bottom panel shows the same correlation matrix reordered to cut two clusters (a dendrogram is shown at the bottom, based on a Spearman metric using the unweighted pair group method with arithmetic mean). The purple cluster of the dendrogram contains a smaller subcluster that indicates nonzero correlation between signals from the most superficial electrodes and those located in between the two cell clusters. This subcluster corresponds to electrodes located in cerebrospinal fluid (above the pia for the superficial electrode and in the ventricle for the intermediate electrodes). The distribution of activity clusters matches that determined from unit identification in (F). (**F**) Distribution of units recorded from electrodes in (E) along probe depth (*y* axis) and width (*x* axis) (same recording and same night). Cortical (Ctx) units, purple; DVR units, red. Each unit's position in space is determined by triangulation across the electrodes and is indicated by a vertical dash. The region between 300 and 400 μm has reduced unit density. Each waveform represents the firing rate around a sharp wave (±1000 ms from the trough of the LFP sharp wave; peak-to-peak amplitudes are normalized). Single-unit firing rate distributions were uniform within each cell population, with cortical units locked and delayed relative to DVR units. Asterisks indicate well-isolated single units (materials and methods). (**G**) Firing rate distributions (in spikes per second) locked to the sharp-wave LFP trough ($t = 0$) for nine DVR single units (SU, stippled red), 230 DVR multi-units (MU, solid red), 21 cortical SUs (stippled purple), and 66 cortical MUs (solid purple) during SWS. (**H**) Firing rate distributions of the units in (G), but around the transition between low and high δ/β (i.e., over all sleep cycles). Firing rates covary and are higher in the cortex at all times (fig. S10).

Downloaded from http://science.sciencemag.org/ on April 28, 2016

of cats (*41*) and in the amygdaloid complex of rats, which expresses both slow and fast rhythms (but no ripple-like events during SWS) (*42*). Conversely, rat hippocampal firing patterns during cortical slow waves (*43*) resemble the cortical firing in *Pogona* around DVR sharp waves. Further work is thus needed to clarify the relationship between DVR, a dominant part of the reptilian forebrain, and its potential mammalian equivalent (*44*).

Recent work on mammalian hippocampal ripples focuses on their potential importance for memory transfer and consolidation through accelerated replay of awake-state activity and activation of synaptic plasticity rules in cortical targets (*32*, *33*). In rats, correlations between CA1 ripples and cortical spindles have been demonstrated (*26*). Our results in a reptile suggest that there is also a functional relationship between the DVR and cortex. The projections between the DVR and cortex are extensive, direct, and reciprocal. This offers an opportunity to test the potential generality of the principle whereby sleep ripples participate in memory transfer and consolidation. More generally, the existence of sleep-related dynamics in the brains of reptiles may shed new light on general principles of information processing during sleep.

REFERENCES AND NOTES

1. A. P. Vorster, J. Born, *Neurosci. Biobehav. Rev.* **50**, 103–119 (2015).
2. R. Allada, J. M. Siegel, *Curr. Biol.* **18**, R670–R679 (2008).
3. R. V. Rial *et al*., *Neurosci. Biobehav. Rev.* **34**, 1144–1160 (2010).
4. C. Smith, *Neurosci. Biobehav. Rev.* **9**, 157–168 (1985).
5. J. E. Zimmerman, N. Naidoo, D. M. Raizen, A. I. Pack, *Trends Neurosci.* **31**, 371–376 (2008).
6. D. Bushey, G. Tononi, C. Cirelli, *Science* **332**, 1576–1581 (2011).
7. P. S. Low, S. S. Shank, T. J. Sejnowski, D. Margoliash, *Proc. Natl. Acad. Sci. U.S.A.* **105**, 9081–9086 (2008).
8. R. J. Greenspan, G. Tononi, C. Cirelli, P. J. Shaw, *Trends Neurosci.* **24**, 142–145 (2001).
9. A. L. Loomis, E. N. Harvey, G. A. Hobart III, *J. Exp. Psychol.* **21**, 127–144 (1937).
10. E. Aserinsky, N. Kleitman, *Science* **118**, 273–274 (1953).
11. M. Jouvet, *Prog. Brain Res.* **18**, 20–62 (1965).
12. R. E. Brown, R. Basheer, J. T. McKenna, R. E. Strecker, R. W. McCarley, *Physiol. Rev.* **92**, 1087–1187 (2012).
13. M. Monnier, *Experientia* **36**, 16–19 (1980).
14. N. C. Rattenborg, *Brain Res. Bull.* **69**, 20–29 (2006).
15. N. C. Rattenborg, D. Martinez-Gonzalez, J. A. Lesku, *Neurosci. Biobehav. Rev.* **33**, 253–270 (2009).
16. J. M. Siegel, *Trends Neurosci.* **31**, 208–213 (2008).
17. R. V. Rial *et al*., *Brain Res. Bull.* **72**, 183–186 (2007).
18. P. A. Libourel, A. Herrel, *Biol. Rev. Camb. Philos. Soc.* (2015).
19. J. A. Hobson, *Nature* **437**, 1254–1256 (2005).
20. W. F. Flanigan Jr., *Brain Behav. Evol.* **8**, 401–416 (1973).
21. K. Hartse, in *Principles and Practice of Sleep Medicine*, M.H. Kryger, T. Roth, D.W. Dement, Eds. (Elsevier Saunders, ed. 2, 1994), pp. 95–104.
22. F. Ayala-Guerrero, G. Mexicano, *Comp. Biochem. Physiol. A* **151**, 305–312 (2008).
23. G. F. Striedter, *J. Comp. Neurol.* **524**, 496–517 (2016).
24. The animals, which were raised in controlled feeding, light, and temperature conditions (see the materials and methods section in the supplementary materials), were observed continuously by means of video and physiological monitoring over epochs of 18 to 20 hours in a familiar experimental arena. Light-dark cycles were identical and synchronized to those in their home terrarium. About 1 to 2 hours before normal nighttime (daylight off), the lizards spontaneously became drowsy, settled in one location, and started closing their eyes intermittently (Fig. 1B). During this pre-sleep phase, axial and limb postural tone decreased until the animals assumed a fully relaxed, horizontal sleeping posture with their heads resting on the floor. Their cardiac rhythms decreased over 1 to 2 hours from 40 to 60 beats per minute (bpm) in the awake state to 20 to 30 bpm, by which time their eyes were closed. A low heart rate was maintained throughout the night, except for occasional peaks correlated with brief body repositioning. Toward the end of the night, the lizards' postural tone increased, and they slowly lifted their heads; they opened their eyes, intermittently at first, then reliably at or shortly after the onset of light (Fig. 1B).
25. J. Voigts, J. H. Siegle, D. L. Pritchett, C. I. Moore, *Front. Syst. Neurosci.* **7**, 8 (2013).
26. A. G. Siapas, M. A. Wilson, *Neuron* **21**, 1123–1128 (1998).
27. J. O'Keefe, *Exp. Neurol.* **51**, 78–109 (1976).
28. G. Buzsáki, Z. Horváth, R. Urioste, J. Hetke, K. Wise, *Science* **256**, 1025–1027 (1992).
29. G. Buzsáki, *Hippocampus* **25**, 1073–1188 (2015).
30. A. Draguhn, R. D. Traub, D. Schmitz, J. G. Jefferys, *Nature* **394**, 189–192 (1998).
31. J. M. Siegel, in *Principles and Practice of Sleep Medicine*, M. H. Kryger, T. Roth, W. C. Dement, Eds. (Elsevier Saunders, ed. 4, 2005), pp. 120–135.
32. D. J. Foster, M. A. Wilson, *Nature* **440**, 680–683 (2006).
33. M. A. Wilson, B. L. McNaughton, *Science* **265**, 676–679 (1994).
34. J. Lu, D. Sherman, M. Devor, C. B. Saper, *Nature* **441**, 589–594 (2006).
35. F. Weber *et al*., *Nature* **526**, 435–438 (2015).
36. J. A. Hobson, R. W. McCarley, P. W. Wyzinski, *Science* **189**, 55–58 (1975).
37. Y. Hayashi *et al*., *Science* **350**, 957–961 (2015).
38. C. B. Saper, T. C. Chou, T. E. Scammell, *Trends Neurosci.* **24**, 726–731 (2001).
39. C. B. Saper, T. E. Scammell, J. Lu, *Nature* **437**, 1257–1263 (2005).
40. R. G. Northcutt, *Annu. Rev. Neurosci.* **4**, 301–350 (1981).
41. F. Grenier, I. Timofeev, M. Steriade, *J. Neurophysiol.* **86**, 1884–1898 (2001).
42. D. Paré, D. R. Collins, J. G. Pelletier, *Trends Cogn. Sci.* **6**, 306–314 (2002).
43. A. Sirota, J. Csicsvari, D. Buhl, G. Buzsáki, *Proc. Natl. Acad. Sci. U.S.A.* **100**, 2065–2069 (2003).
44. H. J. Karten, *Brain Behav. Evol.* **38**, 264–272 (1991).

ACKNOWLEDGMENTS

This research was funded by the Max Planck Society and the European Research Council (G.L.) and by fellowships from the Minerva Foundation (M.S.-I.) and the Swiss National Science Foundation (J.M.O.). The code for analysis and partial data are available at www.brain.mpg.de/sheinidelsonetal2016, and the full primary data are available from G.L. on request. The authors are grateful to G. Wexel for help in surgery and postoperative care; M. Klinkmann, A. Arends, Á. M. Pardo, T. Manthey, and C. Thum for technical assistance; F. Baier, T. Maurer, G. Schmalbach, and A. Umminger for help with mechanical design and fabrication; N. Heller for help with electronics; K. Schröder and C. Schürmann (Goethe University Medical School, Institute for Cardiovascular Physiology) for help with μ-CT scanning of lizards; the animal caretaker crew for lizard care; and T. Tchumatchenko, H. Ito, M. Kaschube, E. Schuman, A. Siapas, and the Laurent laboratory for their suggestions during the course of this work or on the manuscript.

SUPPLEMENTARY MATERIALS

www.sciencemag.org/content/352/6285/590/suppl/DC1
Materials and Methods
Figs. S1 to S10
References (*45*–*53*)
Movie S1

29 January 2016; accepted 1 April 2016
10.1126/science.aaf3621

SIGNAL TRANSDUCTION

Phase separation of signaling molecules promotes T cell receptor signal transduction

Xiaolei Su,[1,2]* Jonathon A. Ditlev,[1,3]* Enfu Hui,[1,2] Wenmin Xing,[1,3] Sudeep Banjade,[1,3] Julia Okrut,[1,2] David S. King,[4] Jack Taunton,[1,2] Michael K. Rosen,[1,3]† Ronald D. Vale[1,2]†

Activation of various cell surface receptors triggers the reorganization of downstream signaling molecules into micrometer- or submicrometer-sized clusters. However, the functional consequences of such clustering have been unclear. We biochemically reconstituted a 12-component signaling pathway on model membranes, beginning with T cell receptor (TCR) activation and ending with actin assembly. When TCR phosphorylation was triggered, downstream signaling proteins spontaneously separated into liquid-like clusters that promoted signaling outputs both in vitro and in human Jurkat T cells. Reconstituted clusters were enriched in kinases but excluded phosphatases and enhanced actin filament assembly by recruiting and organizing actin regulators. These results demonstrate that protein phase separation can create a distinct physical and biochemical compartment that facilitates signaling.

Many cell surface receptors and downstream signaling molecules coalesce into micrometer- or submicrometer-sized clusters upon initiation of signaling (*1*, *2*). However, the effect of this clustering on signal transduction is poorly understood. T cell receptor (TCR) signaling is a well-studied example of this general phenomenon (*3*). TCR signaling proceeds through a series of biochemical reactions that can be viewed as connected modules. In the upstream module, the TCR is phosphorylated by Lck, a membrane-bound protein kinase of the Src family. TCR phosphorylation is opposed by a transmembrane phosphatase, CD45 (*3*). The phosphorylated cytoplasmic domains of the TCR complex recruit and activate the cytosolic tyrosine kinase ZAP70 (*4*). In the intermediate module, ZAP70 phosphorylates the transmembrane protein LAT (linker for activation of T cells) on multiple tyrosine residues. These phosphotyrosines

Downloaded from http://science.sciencemag.org/ on April 28, 2016

are binding sites for adapter proteins Grb2 and Gads, which further interact with Sos1 [a guanine nucleotide exchange factor (GEF) for the small guanosine triphosphatase Ras] or SLP-76 (another adaptor in TCR signaling). Components of the LAT complex activate several downstream modules that mediate calcium mobilization, mitogen-activated protein kinase (MAPK) activation, and actin polymerization (*5*, *6*).

LAT and its binding partners coalesce into micrometer- or submicrometer-sized clusters at the plasma membrane upon TCR activation (*7*–*10*). Elimination of these microclusters by deletion of key components (for example, LAT or Grb2) impairs downstream signaling and transcriptional responses (*5*, *11*). However, effects due to loss of clusters have not been distinguished from those due to loss of component molecules. Nor do we understand the changes in biochemistry and consequent signaling that emerge specifically when signaling molecules are organized from an unclustered to a clustered state (*12*).

To explore the mechanism of formation and functional consequences of T cell microclusters, we reconstituted a TCR signaling pathway from purified components. To substitute for the plasma membrane, we used supported bilayers composed of a defined, simple lipid composition. We initially reconstituted the intermediate module of the TCR signaling cascade, composed of phosphorylated LAT (pLAT), Grb2, and Sos1. Multivalent interactions between these proteins (Fig. 1A) are thought to drive the formation of signaling microclusters on the T cell membrane (*8*, *13*), although direct experimental evidence for the sufficiency of this mechanism has been lacking. We prepared fluorescently labeled pLAT, containing the four C-terminal phosphotyrosine residues that are sufficient for TCR signaling (*14*); this pLAT also contains an N-terminal His_8 tag that allowed its attachment to Ni^{2+}-containing supported lipid bilayers (*15*). pLAT was uniformly distributed (Fig. 1B) and freely diffused on the lipid bilayer (movie S1). Upon addition of Grb2 and Sos1, submicrometer-sized clusters formed within 1 min and gradually grew in size. Cluster formation required tyrosine phosphorylation of LAT (fig. S1D).

[1]Howard Hughes Medical Institute (HHMI) Summer Institute, Marine Biological Laboratory, Woods Hole, MA 02543, USA. [2]Department of Cellular and Molecular Pharmacology and Howard Hughes Medical Institute, University of California, San Francisco, CA 94158, USA. [3]Department of Biophysics and Howard Hughes Medical Institute, University of Texas Southwestern Medical Center, Dallas, TX 75390, USA. [4]HHMI Mass Spectrometry Laboratory and Department of Molecular and Cellular Biology, University of California, Berkeley, CA 94720, USA.
*These authors contributed equally to this work. **†Corresponding author. Email: ron.vale@ucsf.edu (R.D.V.); michael.rosen@utsouthwestern.edu (M.K.R.)**

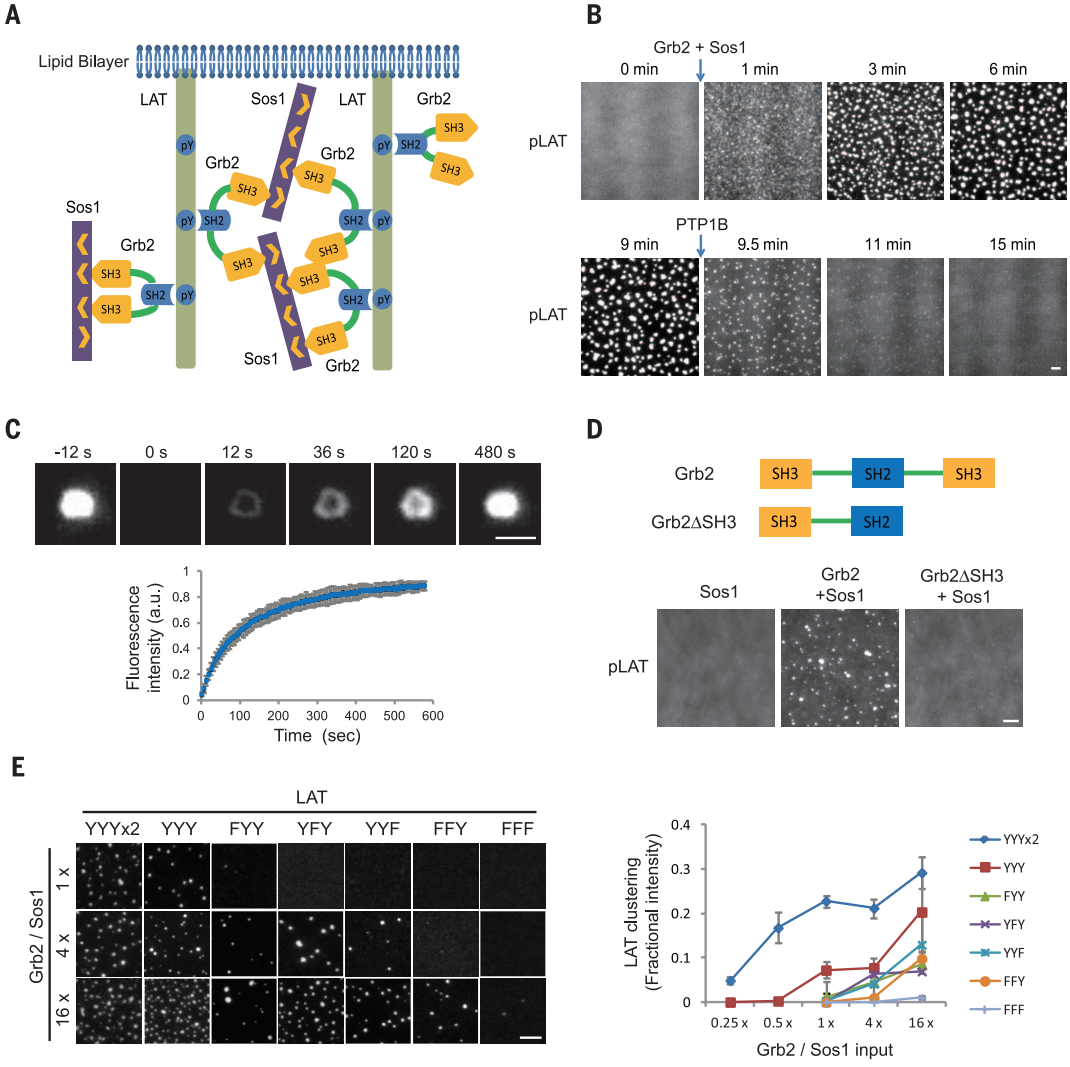

Fig. 1. Multivalent interactions drive LAT cluster formation. (**A**) Schematic of the proteins and interactions in the clustering assay. (**B**) Total internal reflection fluorescence microscopy (TIRF) imaging of LAT clustering and declustering. Clusters formed after adding Grb2 (0.5 μM) and Sos1 (the proline-rich motifs) (0.25 μM) to membrane-bound pLAT-Alexa488 (1000 molecules/μm^2) at 0 min and dissolved after adding the protein tyrosine phosphatase PTP1B (2 μM) at 9 min. Scale bar, 2 μm. See movie S2. (**C**) FRAP of clustered pLAT on planar lipid bilayers; time 0 indicates the time of the photobleaching pulse. The bottom plot shows the time course of the recovery of pLAT clusters formed with 1 μM Grb2 and 2 μM Sos1. Shown are the mean ± SD. $N = 7$ pLAT clusters. Scale bar, 2 μm. (**D**) TIRF imaging of pLAT-Alexa488 (300 molecules/μm^2) with Sos1 (0.5 μM) alone or additionally with wild-type Grb2 (0.5 μM) or Grb2ΔSH3 (1 μM) (concentrations were set to maintain identical total SH3 concentrations in the experiments containing Grb2 and Grb2ΔSH3). Scale bar, 2 μm. (**E**) Valency-dependent clustering of pLAT. (Left) pLAT wild-type with three Grb2 phosphorylation sites (YYY) or mutants that contain six (2xYYY), two (FYY, YFY, and YYF), one (FFY), or zero (FFF) phosphotyrosines were incubated with increasing concentrations of Grb2 and Sos1. 1x indicates 125 nM Grb2 and 62 nM Sos1. pLAT valency mutants were plated at a density of ~300 molecules/μm^2. Clusters were imaged by TIRF microscopy. Scale bar, 5 μm. (Right) Quantification of clustering of pLAT valency mutants. Clustering degree was quantified by fractional intensity. Phase diagrams of pLAT mutants using a larger range of Grb2 and Sos1 concentrations are shown in fig. S5. Values shown are the mean ± SD. $N = 3$ independent experiments.

Downloaded from http://science.sciencemag.org/ on April 28, 2016

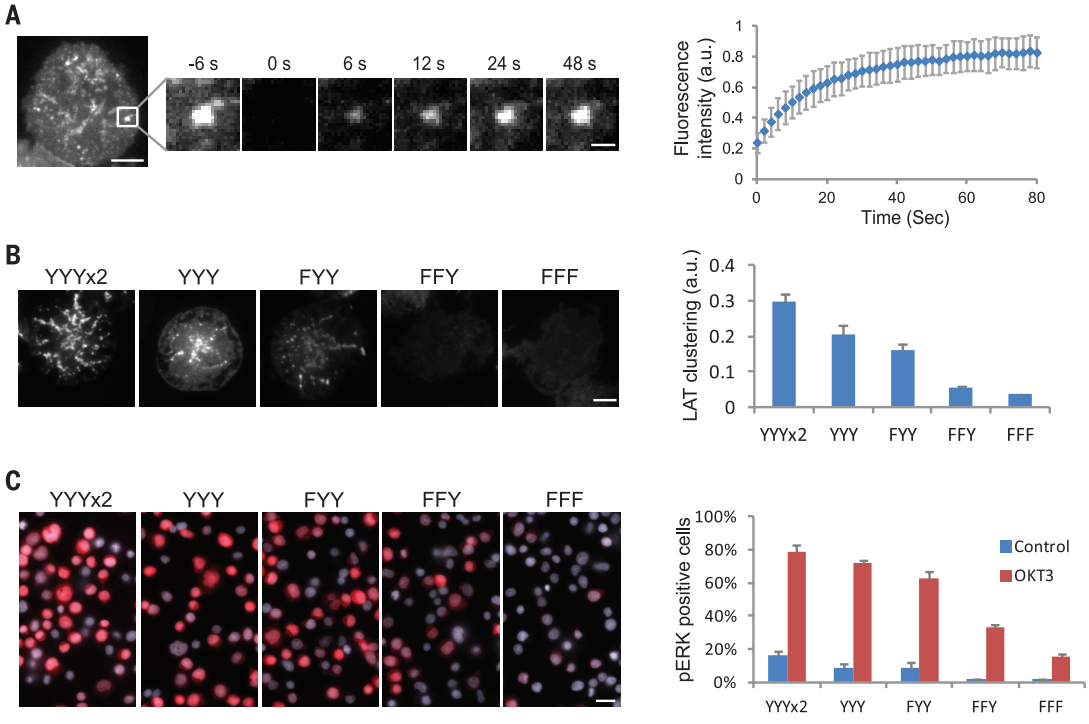

Fig. 2. LAT clustering promotes MAPK(ERK) signaling in T cells. (**A**) FRAP of LAT-mCitrine clusters on plasma membranes of Jurkat T cells activated by plate-presented antibody to CD3 (OKT3 at 5 μg/mL); time 0 indicates the time of the photobleaching pulse. Scale bar, 5 μm or 1 μm on the enlarged panel. Right plot shows the time course of the recovery (mean ± SD) of 15 cells. (**B**) TIRF microscopy revealed cluster formation of LAT variants in activated T cells. A LAT-deficient line (Jcam2.5) stably expressing LAT variants containing six (2x YYY), three (YYY), two (FYY), one (FFY), or zero (FFF) tyrosines for Grb2 binding was activated by plate-presented OKT3 at 5 μg/mL. See the supplementary materials for clustering quantification. Scale bar, 5 μm. Shown are mean ± SEM. $N = 16$ to 20 cells. (**C**) MAPK(ERK) activation in Jurkat T cells expressing LAT valency mutants. Cells were activated by OKT3 at 5 μg/mL, fixed at 10 min, and stained with an antibody to phosphorylated ERK (red) and a nucleus dye Hoechst (blue). Scale bar, 20 μm. Right plot shows the percentage of pERK positive cells. About 200 to 300 cells were scored for each data point. Shown are mean ± SEM. $N = 3$ independent experiments.

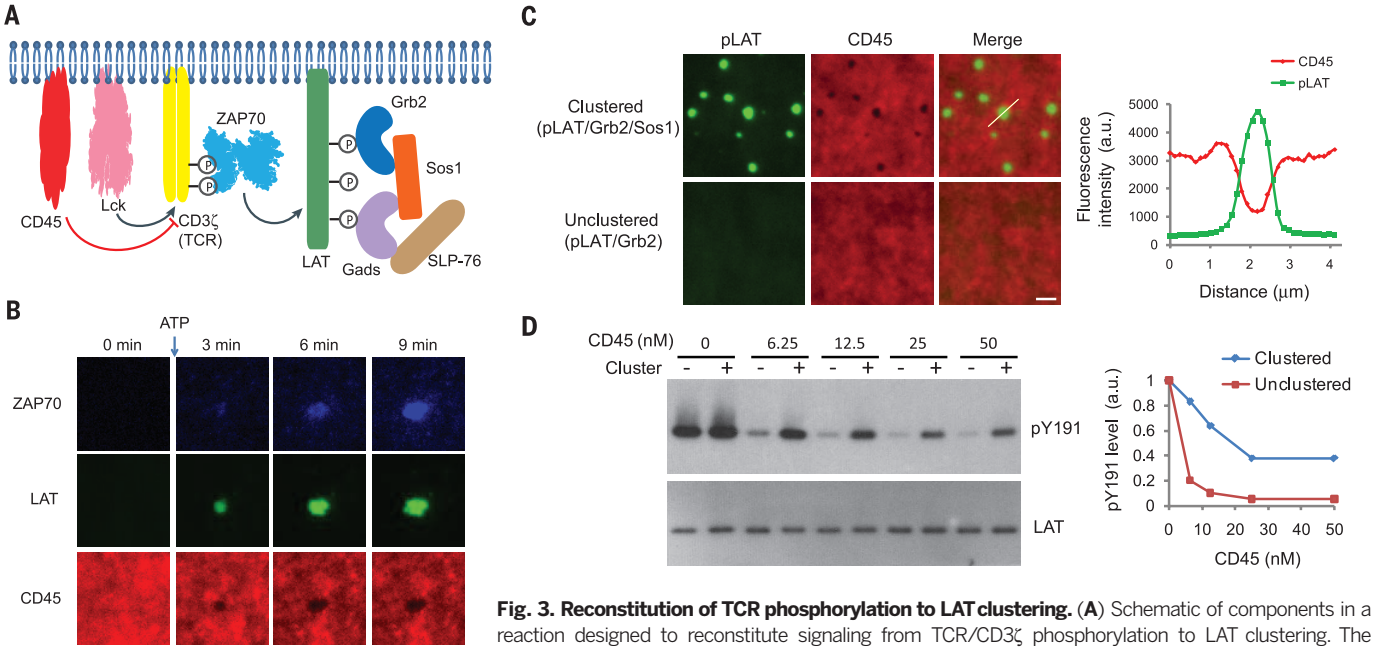

Fig. 3. Reconstitution of TCR phosphorylation to LAT clustering. (**A**) Schematic of components in a reaction designed to reconstitute signaling from TCR/CD3ζ phosphorylation to LAT clustering. The cytoplasmic domains of CD45, Lck, CD3ζ, and LAT were polyhistidine-tagged for membrane attachment and incubated with other components in solution. ATP was added to trigger the phosphorylation cascade. Input: CD45-SNAP-TMR, Lck, CD3ζ, and LAT-Alexa647 at 30, 250, 500, and 1000 molecules/μm^2, respectively; 10 nM ZAP70-505-Star; 250 nM Grb2; 125 nM Sos1; 250 nM Gads; 125 nM SLP-76; and 0.5 mM ATP-Mg. (**B**) TIRF microscopy revealed time courses of ZAP70 membrane recruitment, CD45 exclusion, and LAT clustering in the reconstituted pathway. A larger field view of LAT clusters is shown in fig. S6B. Scale bar, 2 μm. (**C**) (Left) pLAT-Alexa488 (300 molecules/μm^2) bound to planar lipid bilayers was incubated with Grb2 (1 μM) in the presence (top) or absence (bottom) of Sos1 (1 μM). Then the cytoplasmic domain of CD45-TMR (4 nM, with an N-terminal His_{10} tag) was added, and its localization was visualized by TIRF microscopy. Scale bar, 2 μm. (Right) Quantification of fluorescence intensity of pLAT and CD45 along the line scan indicated by a white line in the top merged image. (**D**) Western blot analysis of pLAT dephosphorylation by CD45. pLAT bound to membrane (300 molecules/μm^2) was incubated with 1 μM Grb2 (unclustered pLAT) or 1 μM Grb2 plus 1 μM Sos1 (clustered pLAT). His_{10}-CD45 was then added, and the reactions were stopped after 5 min by adding SDS–polyacrylamide gel electrophoresis loading buffer containing 2 mM vanadate. Quantification of pLAT phosphorylation normalized to the total LAT signal is shown in the right plot.

Downloaded from http://science.sciencemag.org/ on April 28, 2016

Furthermore, dephosphorylation of pLAT by high concentrations of the soluble protein tyrosine phosphatase 1B (PTP1B, 2 μM) caused the clusters to disassemble (Fig. 1B and movie S2). pLAT, Grb2, and Sos1 all colocalized within clusters, and clusters did not form if either Grb2 or Sos1 was omitted (fig. S1, E and F). pLAT also clustered with Gads and SLP-76, two other components of LAT clusters (*6*, *7*), but less efficiently than with Grb2 and Sos1 (fig. S2, A and B). Clustering efficiency, however, increased dramatically with the addition of Nck (fig. S2C), an adaptor protein known to link SLP-76 to actin regulators (*16*).

pLAT, Grb2, and Sos1 clusters exhibited dynamic liquid-like properties. The rounded edges of clusters fluctuated (extending and retracting) on a time scale of seconds, and clusters sometimes fused with one another (movie S2). pLAT molecules exchanged into and out of clusters, as revealed by fluorescence recovery after photobleaching (FRAP) (Fig. 1C). Single pLAT molecules diffused rapidly outside of clusters but slowly within them (fig. S3, A to C). We also observed capture and release of single molecules by clusters (movie S3). These results show that pLAT microclusters are liquid-like, phase-separated structures (*17*, *18*) on membranes.

Both SH3 domains of Grb2 were required for cluster formation, indicating a role of protein cross-bridging by this adaptor protein (Fig. 1D and fig. S4A). Clustering initially increased with increasing pLAT density but then decreased at higher pLAT densities on the membrane (fig. S4B), consistent with a theoretical multivalent interaction model (*19*). The valency of phosphotyrosines on LAT also affected clustering efficiency. Three of the four distal phosphotyrosines in LAT are recognized by the SH2 domain of Grb2 (*20*). Clustering in vitro progressively decreased by mutating one, two, or all three tyrosines and was enhanced by doubling the number of

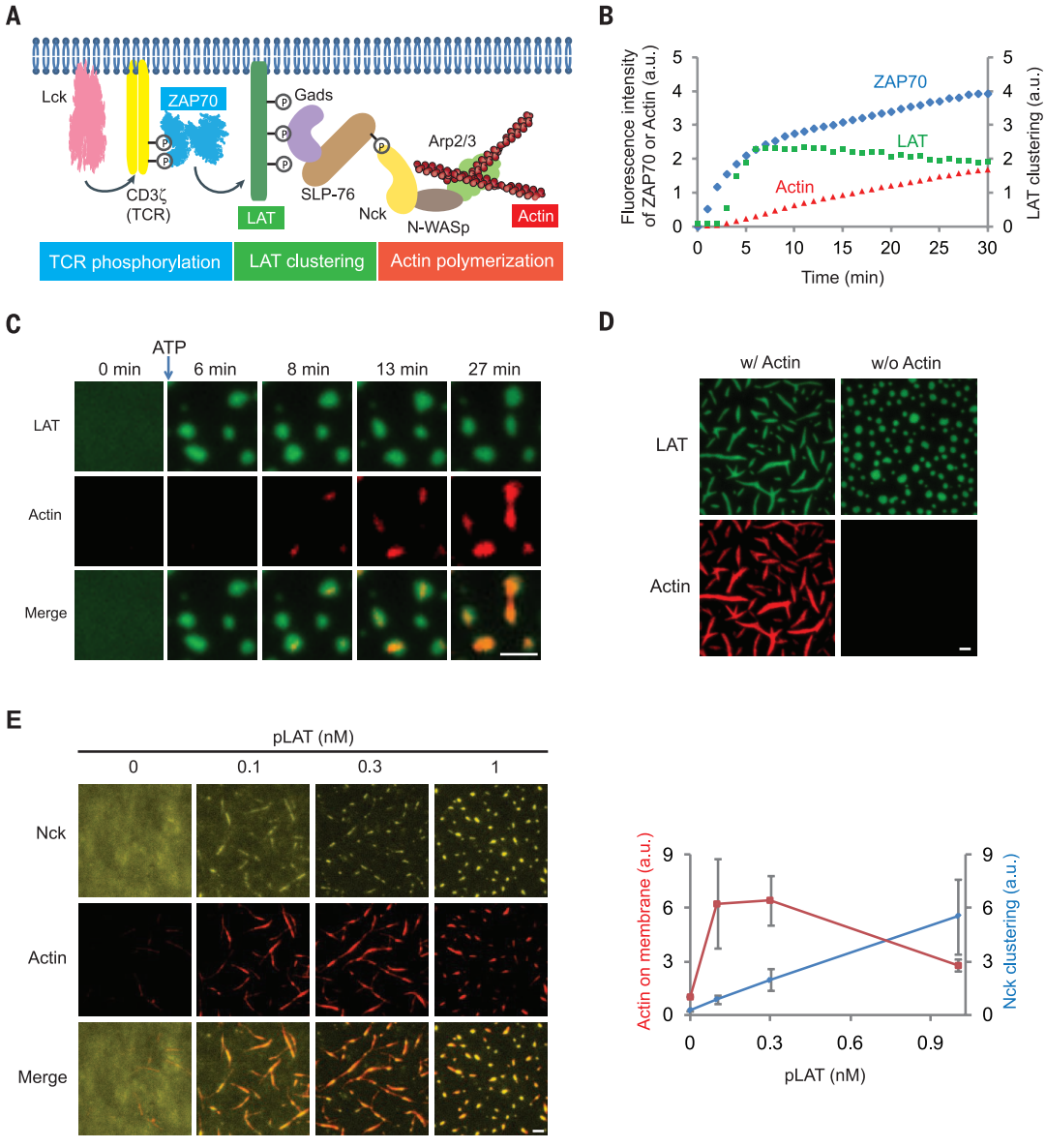

Fig. 4. LAT clustering promotes actin polymerization. (**A**) Schematic of the reconstituted signaling pathway from CD3ζ/TCR phosphorylation to actin polymerization. ZAP70-505-Star, LAT-Alexa647, and actin-rhodamine serve as reporters for TCR phosphorylation, LAT clustering, and actin assembly, respectively. Lck, CD3ζ, and LAT were membrane-attached through a polyhistidine tag and incubated with other components in solution. ATP was then added to trigger the signaling cascade. Input: same for Lck, CD3ζ, pLAT-Alexa647, and ZAP70-505-Star as described in Fig. 3A. The rest are 250 nM Gads, 125 nM SLP-76, 500 nM Nck, 250 nM N-WASP, 2.5 nM Arp2/3 complex, 500 nM actin (5% rhodamine labeled), and 0.5 mM ATP-Mg. (**B**) Time courses of ZAP70 membrane recruitment, LAT clustering, and actin polymerization in the reconstituted assay after addition of ATP at time 0. LAT clustering was quantified as variance of fluorescence intensities on membranes (see the supplementary materials). (**C**) TIRF imaging showing actin assembly on the LAT clusters. Scale bar, 2 μm. (**D**) TIRF imaging of pLAT-Alexa647 and actin-rhodamine 45 min after adding ATP to the reaction. Input: same as in Fig. 4A except with higher concentrations of components of actin and actin regulators [500 nM SLP-76, 1000 nM Nck, 500 nM N-WASP, 5 nM Arp2/3 complex, 1000 nM actin (5% rhodamine-labeled)]. Scale bar, 2 μm. (**E**) (Left) TIRF microscopy images of His_{10}-Nck-Pacific Blue and actin-rhodamine on the bilayer. Nck (150 molecules/μm^2) was attached to the bilayer, and N-WASP (5 nM), Arp2/3 complex (0.25 nM), actin (200 nM, 5% rhodamine labeled), and 0.5 mM ATP-Mg were in solution. Increasing concentrations of His-tagged pLAT were added as indicated, along with Gads and pSLP-76. At 0.1 nM pLAT, Gads and pSLP-76 concentrations were 8 nM and 4 nM, respectively. As pLAT concentration was increased, more Gads and pSLP-76 were added to maintain a constant ratio of the clustering components. Scale bar, 2 μm. (Right) Mean actin fluorescence (red) and Nck clustering level (blue), quantified as variance of His_{10}-Nck fluorescence intensity, are plotted for increasing concentrations of pLAT. Shown are mean ± SEM. $N = 3$ independent experiments.

Downloaded from http://science.sciencemag.org/ on April 28, 2016

tyrosines (Fig. 1E and fig. S5). Together, our data indicate that LAT cluster formation is driven by dynamically rearranging, multivalent protein-protein interactions.

We compared the properties of LAT clusters in cells with those of reconstituted clusters in vitro and tested their functional importance. As in vitro, LAT microclusters in T cells sometimes fused with one another (fig. S3D). FRAP revealed that molecules exchange into and out of clusters in cells faster than in vitro (halftime of the recovery of 12 s versus 76 s), possibly due to different cluster size (see the supplementary text) or membrane fluidity. To assess valency dependence in cells, we expressed LAT tyrosine mutants with zero, one, two, three, or six Grb2 binding sites in a LAT-deficient Jurkat T cell line. A minimum of two Grb2 binding sites was required for robust cluster formation, and the degree of clustering increased with increasing number of phosphotyrosine sites (Fig. 2B). The degree of clustering correlated with activation of MAPK(ERK) (extracellular signal–regulated kinase) (Fig. 2C), suggesting that clustering of LAT and its partners is important for TCR signaling.

We used our in vitro assay to gain insight into the biochemical reactions that underlie the TCR signaling pathway. To LAT and its binding partners, we introduced the upstream signaling module consisting of (i) the cytoplasmic domain of the TCR subunit CD3ζ [which is sufficient to induce signaling in T cells (*21*)]; (ii) Lck, which phosphorylates the TCR; (iii) the cytoplasmic domain of the tyrosine phosphatase CD45, which opposes this reaction (*22*); and (iv) the protein kinase ZAP70, which is recruited to the phosphorylated TCR and phosphorylates LAT (*4*, *5*) (Fig. 3A). Initially, unphosphorylated LAT was evenly distributed on the membrane. After adenosine triphosphate (ATP) was added to initiate Lck phosphorylation of CD3ζ, ZAP70 was recruited to the membrane and LAT clustered (Fig. 3B and fig. S6A). ZAP70 was enriched in the clusters, as observed in T cells (*7*), whereas CD45 was excluded (Fig. 3B). The exclusion of CD45 was recapitulated in a simpler system in which clusters were formed by pLAT, Grb2, and Sos1 (Fig. 3C). The cytoplasmic domain of CD45 has a negative charge (isoelectric point 6.4). Assays with a series of differentially charged proteins revealed that, in general, positive charge favors inclusion into and negative charge favors exclusion from LAT clusters (fig. S7 and supplementary text). Consistent with limited access of CD45 to pLAT in the cluster center, CD45-mediated dephosphorylation of pLAT was reduced compared with that in unclustered conditions (Fig. 3D). In summary, our data demonstrate that LAT clusters are depleted in the phosphatase CD45 but enriched in the kinase ZAP70, which would be expected to promote LAT phosphorylation and increase the strength of TCR signaling.

We sought to integrate a downstream module that controls an important signaling output, actin polymerization (*23*, *24*). We attached His-tagged Lck, CD3ζ, and unphosphorylated LAT-Alexa647 to the supported lipid bilayer and added soluble ZAP70-505-Star, Gads, SLP-76, Nck, N-WASP (neuronal Wiskott-Aldrich syndrome protein), Arp2/3 (actin-related protein 2 and 3) complex, and rhodamine-labeled monomeric actin to the solution (Fig. 4A). Previous data have shown that Nck recruits N-WASP, which in turn activates the Arp2/3 complex to nucleate actin filaments (*16*, *25*). When ATP was added to initiate TCR phosphorylation, ZAP70 was recruited to the membrane, followed by LAT clustering and then actin polymerization from the LAT clusters (Fig. 4, B and C, and fig. S8). Later, when actin bundles formed, LAT clusters became rodlike and aligned with actin bundles (Fig. 4D and movies S4 and S5). This shape change is reversible, because clusters became round after depolymerization of F-actin by latrunculin A (fig. S9C). In summary, we show that actin polymerization is initiated from and can reorganize LAT clusters.

We next investigated whether clustering of Nck affects the efficiency of actin polymerization. In principle, actin polymerization could be stimulated by (i) recruitment of Nck from solution to the membrane, (ii) concentration and organization of Nck within clusters, or (iii) both effects. To isolate spatial distribution as a variable, we attached His_{10}-Nck to Ni-modified lipids in the planar bilayer and added soluble N-WASP, Arp2/3 complex, and actin. Increasing the density of Nck on the membrane resulted in a dose-dependent increase in assembly of actin (fig. S10). Using a density of Nck (150 molecules/μm^2) at which little actin polymerized, we tested whether clustering of Nck by pLAT, Gads, and pSLP-76 affected actin assembly. Clustering of Nck enhanced total actin assembly on the membrane by a factor of 6 (Fig. 4E). These results reveal that the clustering of actin regulators by LAT promotes actin polymerization beyond what can be achieved by recruitment to the membrane.

In summary, we reconstituted biochemical reactions of TCR signaling in an in vitro system, in which the components and their concentrations in the reaction can be controlled, rates can be measured, and molecular behaviors can be observed in ways that are difficult to achieve using intact cells. We observed multivalent assembly and consequent phase separation of LAT and its binding partners into liquid-like, micrometer-sized clusters. By manipulating clustering using LAT phosphorylation mutants, we show that clustering occurs through analogous mechanisms in vitro and in cells and that clustering promotes MAPK(ERK) signaling. Thus, as in three-dimensional phase separation (*17*, *26*), our results demonstrate that phase separation on membranes can create an environment that promotes biochemical reactions. LAT clusters excluded CD45 and retained ZAP70 to create an environment that perpetuated the phosphorylated state of LAT. Clustering of LAT promoted downstream biochemical reactions in the signaling pathway, specifically the ability of Nck to promote N-WASP–Arp2/3–mediated actin polymerization (fig. S11), as suggested by Nck density-dependent actin polymerization in cells (*27*). Multivalent interactions have been proposed to drive the assembly of many other cellular structures, including PML (promyelocytic leukemia) bodies, stress granules, and focal adhesions (*17*, *26*); thus, the mechanisms of spatial organization of biochemical reactions revealed here may apply to other cellular processes as well.

REFERENCES AND NOTES

1. H. Wu, *Cell* **153**, 287–292 (2013).
2. M. Bienz, *Trends Biochem. Sci.* **39**, 487–495 (2014).
3. A. K. Chakraborty, A. Weiss, *Nat. Immunol.* **15**, 798–807 (2014).
4. A. C. Chan, M. Iwashima, C. W. Turck, A. Weiss, *Cell* **71**, 649–662 (1992).
5. W. Zhang, J. Sloan-Lancaster, J. Kitchen, R. P. Trible, L. E. Samelson, *Cell* **92**, 83–92 (1998).
6. R. T. Abraham, A. Weiss, *Nat. Rev. Immunol.* **4**, 301–308 (2004).
7. S. C. Bunnell *et al.*, *J. Cell Biol.* **158**, 1263–1275 (2002).
8. A. D. Douglass, R. D. Vale, *Cell* **121**, 937–950 (2005).
9. R. Varma, G. Campi, T. Yokosuka, T. Saito, M. L. Dustin, *Immunity* **25**, 117–127 (2006).
10. K. L. Singleton *et al.*, *Sci. Signal.* **2**, ra15 (2009).
11. M. Y. Bilal, J. C. Houtman, *Front. Immunol.* **6**, 141 (2015).
12. M. L. Dustin, J. T. Groves, *Annu. Rev. Biophys.* **41**, 543–556 (2012).
13. J. C. Houtman *et al.*, *Nat. Struct. Mol. Biol.* **13**, 798–805 (2006).
14. M. Zhu, E. Janssen, W. Zhang, *J. Immunol.* **170**, 325–333 (2003).
15. Materials and methods are available as supplementary materials on *Science* Online.
16. L. Wunderlich, A. Faragó, J. Downward, L. Buday, *Eur. J. Immunol.* **29**, 1068–1075 (1999).
17. P. Li *et al.*, *Nature* **483**, 336–340 (2012).
18. S. Banjade, M. K. Rosen, *eLife* **3**, e04123 (2014).
19. A. Nag, M. I. Monine, J. R. Faeder, B. Goldstein, *Biophys. J.* **96**, 2604–2623 (2009).
20. M. Tinti *et al.*, *Cell Reports* **3**, 1293–1305 (2013).
21. B. A. Irving, A. Weiss, *Cell* **64**, 891–901 (1991).
22. E. Hui, R. D. Vale, *Nat. Struct. Mol. Biol.* **21**, 133–142 (2014).
23. S. Kumari *et al.*, *eLife* **4**, 04953 (2015).
24. S. C. Bunnell, V. Kapoor, R. P. Trible, W. Zhang, L. E. Samelson, *Immunity* **14**, 315–329 (2001).
25. R. Rohatgi, P. Nollau, H. Y. Ho, M. W. Kirschner, B. J. Mayer, *J. Biol. Chem.* **276**, 26448–26452 (2001).
26. A. A. Hyman, C. A. Weber, F. Jülicher, *Annu. Rev. Cell Dev. Biol.* **30**, 39–58 (2014).
27. J. A. Ditlev *et al.*, *J. Cell Biol.* **197**, 643–658 (2012).

ACKNOWLEDGMENTS

We thank S. Ross and L. Chang at Nikon Instruments for their loan of TIRF-capable microscopes, N. Stuurman for help with microscopy, A. Weiss for providing JCam2.5 cells, D. Liu for providing charged green fluorescent protein (GFP) constructs, C. Pak for providing charged GFP, J. Muller for providing intercellular adhesion molecule–1 protein, and L. Rice, X. Zeng, and members from the Vale Laboratory for comments on this manuscript. This work was supported by the HHMI's Collaborative Innovation Awards, NIH (R01-GM56322 to M.K.R.), and the Welch Foundation (I–1544 to M.K.R.). X.S. was supported by a Cancer Research Institute Irvington postdoctoral fellowship. J.A.D. was supported by National Research Service Award F32 (5-F32-DK101188). E.H. was supported as a fellow of the Leukemia and Lymphoma Society. J.O. was supported by funds from the Tobacco-Related Disease Research Program of the University of California (19FT-0090).

SUPPLEMENTARY MATERIALS

www.sciencemag.org/content/352/6285/595/suppl/DC1
Materials and Methods
Supplementary Text
Figs. S1 to S11
Tables S1 and S2
Movies S1 to S5
References (*28*–*32*)

3 December 2015; accepted 23 March 2016
Published online 7 April 2016
10.1126/science.aad9964

Downloaded from http://science.sciencemag.org/ on April 28, 2016

HUMAN GENETICS

RNA splicing is a primary link between genetic variation and disease

Yang I. Li,[1] Bryce van de Geijn,[2] Anil Raj,[1] David A. Knowles,[3,4] Allegra A. Petti,[5] David Golan,[1] Yoav Gilad,[2]* Jonathan K. Pritchard[1,6,7]*

Noncoding variants play a central role in the genetics of complex traits, but we still lack a full understanding of the molecular pathways through which they act. We quantified the contribution of cis-acting genetic effects at all major stages of gene regulation from chromatin to proteins, in Yoruba lymphoblastoid cell lines (LCLs). About ~65% of expression quantitative trait loci (eQTLs) have primary effects on chromatin, whereas the remaining eQTLs are enriched in transcribed regions. Using a novel method, we also detected 2893 splicing QTLs, most of which have little or no effect on gene-level expression. These splicing QTLs are major contributors to complex traits, roughly on a par with variants that affect gene expression levels. Our study provides a comprehensive view of the mechanisms linking genetic variation to variation in human gene regulation.

Expression quantitative trait loci (eQTLs) are highly enriched among the risk loci for complex diseases (*1*, *2*), suggesting that risk variants often act by affecting aspects of gene regulation. Previous attempts to elucidate the mechanisms underlying eQTLs revealed that a large fraction of eQTLs are due to single-nucleotide polymorphisms (SNPs) that affect transcription factor binding or other aspects of chromatin function at enhancers or promoters (*3*–*9*). Moreover, SNPs that lie within active chromatin regions in relevant cell types are highly enriched among the signals obtained through genome-wide association studies (GWASs) (*10*, *11*). In a few cases, specific links were identified between genetic variation, variation in chromatin, gene expression differences, and disease risk (*12*). Genetic variation might also affect gene regulation and function through pre-mRNA splicing by affecting either the expression levels or amino acid sequences of the resulting proteins (*13*). There are reports of splicing variants contributing to complex traits (*14*); however, a recent comprehensive study of splicing found no enrichment of predicted splicing variants among signals identified in GWASs (*15*).

We aimed to compile a detailed accounting of the effects of genetic variants on gene regulation from chromatin to proteins. To do this, we analyzed molecular data for eight regulatory traits measured in lymphoblastoid cell lines (LCLs) derived from Yoruba individuals (Fig. 1A), for which genome sequence data are available (*16*). Altogether, data are available for all eight molecular phenotypes in 32 individuals and at least six phenotypes in 68 individuals (table S8).

Seven of the eight main molecular measurements analyzed in this study were characterized previously (*4*–*6*, *17*–*19*). We additionally measured transcription rates in 65 individuals, using 4sU-labeled RNA sequencing (4sU-seq). The 4sU assay uses a pulse of modified uridine to label the accumulation of new transcripts during a fixed time interval, in order to measure the rate of RNA synthesis (*16*). To confirm that the 4sU-seq data do indeed measure transcription rates, we examined them in the context of mRNA decay measurements for the same LCLs (Fig. 1B). Steady-state mRNA levels should reflect a balance between transcription and decay. We found that the ratio of new transcript levels (based on 4sU data) to steady-state RNA levels is negatively correlated with RNA decay estimates ($P = 10^{-167}$, χ^2 goodness of fit).

We also computed correlations between read counts across five molecular measurements (Fig. 1C). As expected, 4sU and RNA-seq data are highly correlated [Spearman correlation (rho) > 0.90]. Histone H3 lysine 27 acetylation (H3K27ac) read counts at transcription start sites (TSSs) are more strongly correlated with 4sU-seq than with RNA-seq data ($P = 4 \times 10^{-7}$, permutation). This is consistent with the expectation that the effect of

[1]Department of Genetics, Stanford University, Stanford, CA, USA. [2]Department of Human Genetics, University of Chicago, Chicago, IL, USA. [3]Department of Computer Science, Stanford University, Stanford, CA, USA. [4]Department of Radiology, Stanford University, Stanford, CA, USA. [5]Genome Institute, Washington University in St. Louis, St. Louis, MO, USA. [6]Department of Biology, Stanford University, Stanford, CA, USA. [7]Howard Hughes Medical Institute, Stanford University, Stanford, CA, USA.
***Corresponding author. Email: gilad@uchicago.edu (Y.G.); pritch@stanford.edu (J.K.P.)**

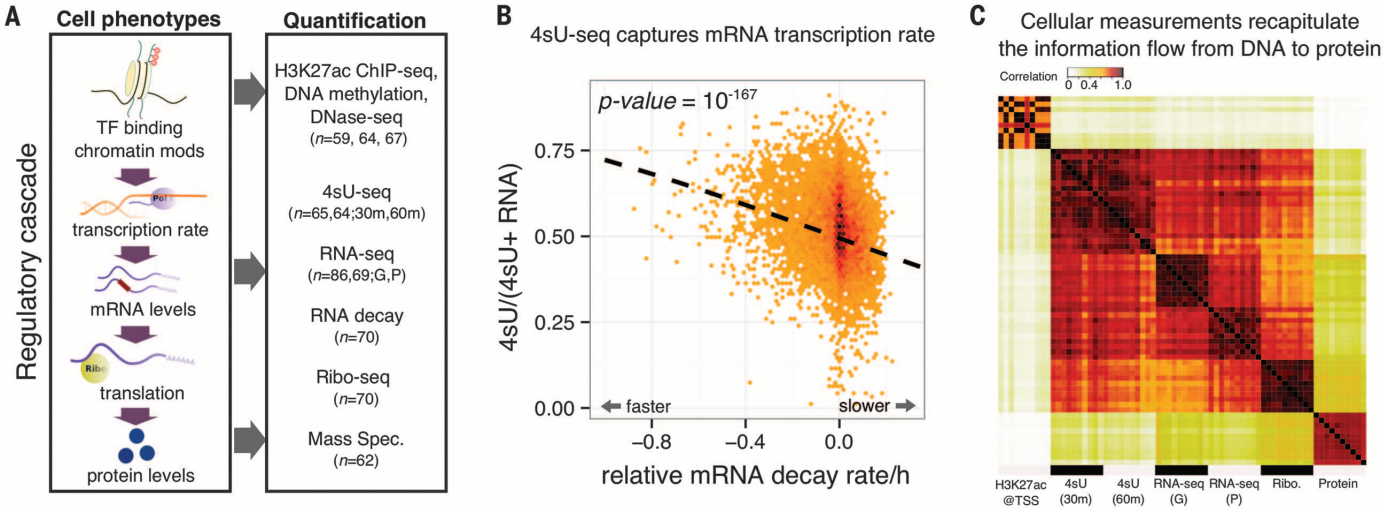

Fig. 1. Systematic mapping of genetic variation that affects the gene-regulatory cascade. (**A**) QTLs mapped for eight cellular phenotypes in LCLs. For 4sU, 30 m and 60 m refer to different measurement time points. For RNA-seq, G and P refer to data from two studies (*6*, *17*). TF, transcription factor. (**B**) Steady-state RNA levels reflect a balance between transcription and decay. Normalized mRNA decay rates (*x* axis) are plotted against the ratio of new mRNA to steady-state mRNA (*y* axis). Each data point is a gene. (**C**) A correlation matrix of seven data sets reflects the expected order of steps in gene regulation. Each entry in the matrix shows the correlation across genes between measurements of a pair of samples and/or data types. The plot shows 10 different random samples for each data type.

Downloaded from http://science.sciencemag.org/ on April 28, 2016

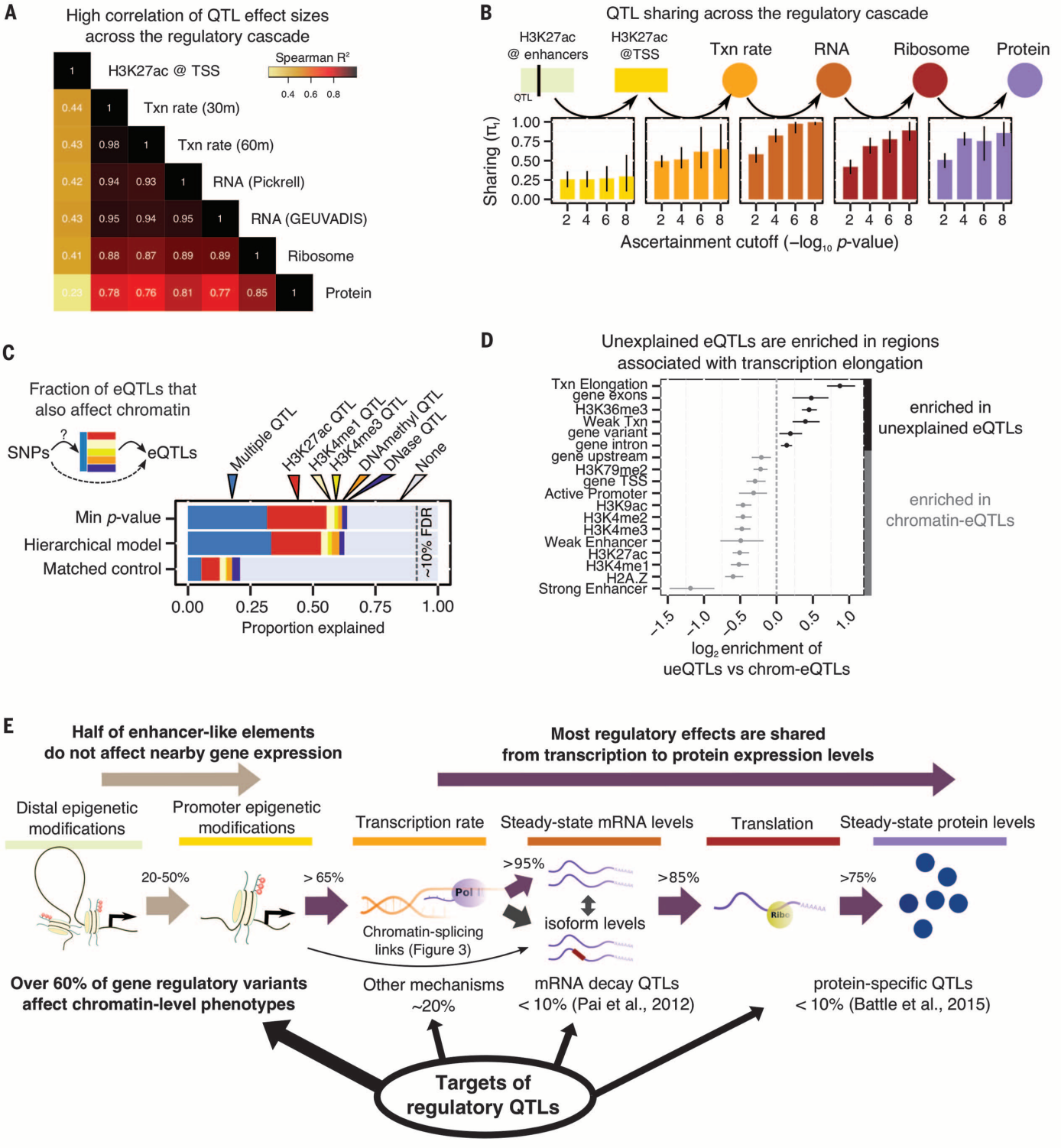

Fig. 2. Percolation of genetic effects through the gene regulatory cascade. (**A**) Correlation of effect sizes across different measurements from eQTLs identified in the GEUVADIS YRI sample (*6*). Txn rate, transcription rate. (**B**) QTL sharing across the regulatory cascade. Each panel shows the estimated fraction of QTLs identified at one stage that are preserved at the next stage of regulation. The four bars in each panel correspond to the *P*-value threshold for ascertaining QTLs in each assay, using the linear regression *t* statistics. Bars represent 80% confidence intervals on π_1, the fraction of true positives (*16*). The enhancer→TSS panel considers the effect of H3K27ac QTLs on the nearest TSS. (**C**) The fraction of expression QTLs that also affect chromatin-level phenotypes, as estimated by two models, and for matched control SNPs. About 35% of gene eQTLs do not appear to affect chromatin traits. QTLs for H3K4me1 and H3K4me3 are from (*8*). (**D**) Functional context of eQTL SNPs that are not associated with chromatin changes ("unexplained") versus those eQTLs that are also chromatin QTLs. 5′ untranslated regions were excluded from the "gene exons" annotation. Five annotations with bootstrap $P > 0.05$ are not shown. (**E**) Summary of the effects of regulatory QTLs and of their sharing through the regulatory cascade.

Downloaded from http://science.sciencemag.org/ on April 28, 2016

promoter function on transcription rate is more direct than on steady-state mRNA levels. Overall, the correlation structure reflects the fact that promoter activity, transcription rates, mRNA expression levels, translation levels, and protein expression levels are regulated in a sequential ordered cascade.

We next performed mapping of QTLs across the eight molecular phenotypes, using a uniform QTL mapping pipeline [Fig. 2 and table S1 (*16*)]. We found that effect sizes are correlated across all phenotypes, with a minimum correlation of 0.23 between H3K27ac marks and protein levels (Fig. 2A). Effect sizes for the RNA-related phenotypes are all highly correlated (minimum r^2 = 0.87). Effect sizes at the protein level are smaller on average than for translation (P = 0.002, Mann-Whitney U test), which is consistent with a previous report of potential protein expression buffering (fig. S4) (*19*).

The high correlations of QTL effect sizes across regulatory stages suggest high proportions of shared QTLs. To quantify this, we considered the set of significant QTLs at each phenotype and estimated the sharing of QTLs at downstream stages of regulation (*16*) (Fig. 2C and fig. S2). Starting with enhancers, we observed that ~25% of H3K27ac QTLs [histone acetylation QTLs (haQTLs)] affect the expression levels of their nearest genes and ~50% affect the expression of any gene within 500 kb (fig. S2). In contrast, the majority of promoter haQTLs also affect expression (>65%) (Fig. 2B).

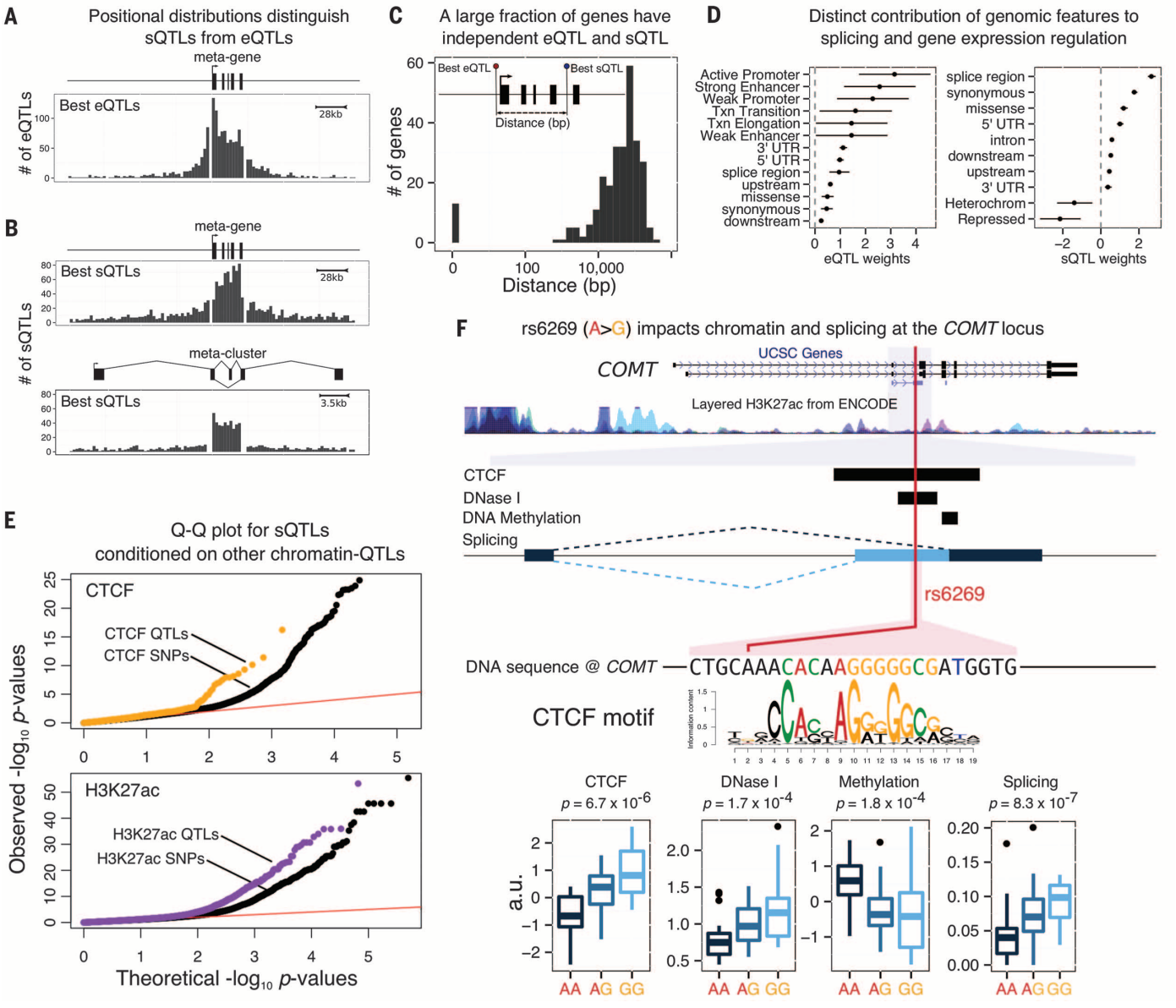

Fig. 3. Properties of sQTLs. Most sQTLs act independently from eQTLs: Positional distributions of (**A**) eQTLs and (**B**) sQTLs at 5% FDR are consistent with our mechanistic understanding of gene transcription and splicing. (**C**) The distance between the best eQTL and best sQTL for genes with both types of QTL is typically large, suggesting distinct causal variants. (**D**) A hierarchical model reveals distinct genomic features that are most relevant for eQTLs and sQTLs, respectively. (**E**) QTLs for CTCF binding, and H3K27ac levels are more likely to be sQTLs than matched SNPs within CTCF and H3K27ac ChIP-seq peaks, respectively. (**F**) Example of an sQTL (rs6269) that is also a QTL for CTCF, DNaseI sensitivity, and DNA methylation. The allele that is associated with increased CTCF occupancy is also associated with increased use of an alternative upstream splice site for an exon of the catechol-*O*-methyltransferase gene, *COMT*, which is consistent with the model that PolII pausing at CTCF binding sites can promote upstream exon inclusion (*21*). *COMT*, which regulates dopamine, has possible roles in neuropsychiatric conditions (*25*). In Europeans, the sQTL is in nearly complete linkage disequilibrium with a missense variant, rs4680, which has been the main focus of attention to date.

Downloaded from http://science.sciencemag.org/ on April 28, 2016

When we used the same approach starting at transcription, we found that over 85% of QTLs were shared from one regulatory stage to the next, from 4sU to protein (Fig. 2B and fig. S2E). Using a Bayesian model to quantify QTL sharing among traits, we estimated that 73% of QTLs that affect transcription rates also affect protein expression (*16*) (fig. S3). These observations are consistent with a general percolation of genetic effects from transcription through the regulatory cascade; however, it remains possible that some QTLs might affect multiple aspects of posttranscriptional regulation independently.

We next examined how often eQTLs can be explained by inter-individual variation in chromatin properties (Fig. 2C), by estimating the fraction of eQTLs that are also QTLs for a chromatin-level trait, such as DNaseI-sensitive sites, DNA methylation, H3K27ac, and H3K4me1 and H3K4me3 QTLs as determined in (*8*). We confirmed that the majority of eQTLs are also nearby chromatin QTLs (65 versus 20% for matched control SNPs), which is consistent with previous reports (*4*).

Thus ~35% of eQTLs are not associated with known chromatin QTLs. To investigate whether these represent a distinct functional class, we asked whether the unexplained eQTLs are biased toward particular genomic regions or functional annotations (Fig. 2D). Indeed, compared to eQTLs that also affect chromatin, the chromatin-independent eQTLs were enriched within gene bodies (exons: $P = 5.4 \times 10^{-8}$; and introns: $P = 0.006$; Mann-Whitney U test). Further, there is particular enrichment in regions associated with transcriptional elongation marks ($P = 3.0 \times 10^{-21}$; Mann-Whitney U test). Hence, many of the unexplained eQTLs may affect transcriptional or posttranscriptional processes, alongside the more widely studied effects on chromatin function. Together, these analyses help us provide an overview of the genetic effects on diverse aspects of gene regulation (Fig. 2E).

We next turned to the effects of genetic variation on pre-mRNA splicing (Fig. 3). Most studies of splicing QTLs (sQTLs) have measured either expression levels of individual exons or of transcript isoforms (*6, 14, 17,*). Because both of these are difficult to estimate accurately from short-read data, we developed a new method to detect splicing variation, LeafCutter (*20*), which focuses on reads that span splice junctions (*16*). Using this approach, we identified 2893 sQTLs in 2313 genes at 10% false discovery rate (FDR) (*16*).

We verified that sQTLs and eQTLs tend to be independent. Unlike eQTLs, which are enriched near TSSs, the sQTLs are enriched within gene bodies and in particular within the introns they regulate (Fig. 3, A and B). Moreover, most of the sQTLs are not associated with gene expression levels (74% have P values $>10^{-2}$, t test; fig. S9).

We examined 275 genes associated with both an sQTL and an eQTL at 10% FDR. The lead eQTL and sQTL SNP is the same for only 14 of these genes. In most cases, the lead SNPs are more than 10 kb apart, suggesting that the majority of these effects are independent (Fig. 3C and fig. S12). Although most sQTLs do not affect overall expression, the majority (89%) affect the predicted coding sequences, thereby potentially affecting protein function (fig. S10).

We used a hierarchical model to identify which genomic annotations are most relevant to splicing versus gene expression (*16*). As expected, genetic variants located in active promoters, strong enhancers, and weak promoters were most likely to affect gene expression. In contrast, splicing was most strongly affected by variants near splice sites and by synonymous and missense variants (Fig. 3D).

Although active chromatin does not seem to be the primary driver of sQTLs, DNA-binding proteins such as the CTCF transcription factor may affect transcription speed and thereby affect splicing, which occurs cotranscriptionally (*21*). sQTL SNPs show a modest enrichment for association with chromatin QTLs (17.5%) compared to matched control SNPs (13.3%). Overall, we identified 171 sQTLs associated with two or more chromatin-level phenotypes (table S7; example in Fig. 3F). Specifically considering QTLs for CTCF (*16*) and for H3K27ac, we found that chromatin QTLs are more likely to affect splicing than matched control SNPs ($P = 2 \times 10^{-5}$ and $P = 1 \times 10^{-34}$, respectively, likelihood-ratio test; Fig. 3E). Variations in CTCF binding and H3K27ac levels have been shown to correlate with differences in splicing (*21, 22*). Our findings, however, provide direct evidence that genetic variation can affect splicing by altering chromatin-level traits.

Our results indicate that splicing is a primary target of common genetic variation, which, in most cases, has direct effects on protein sequences.

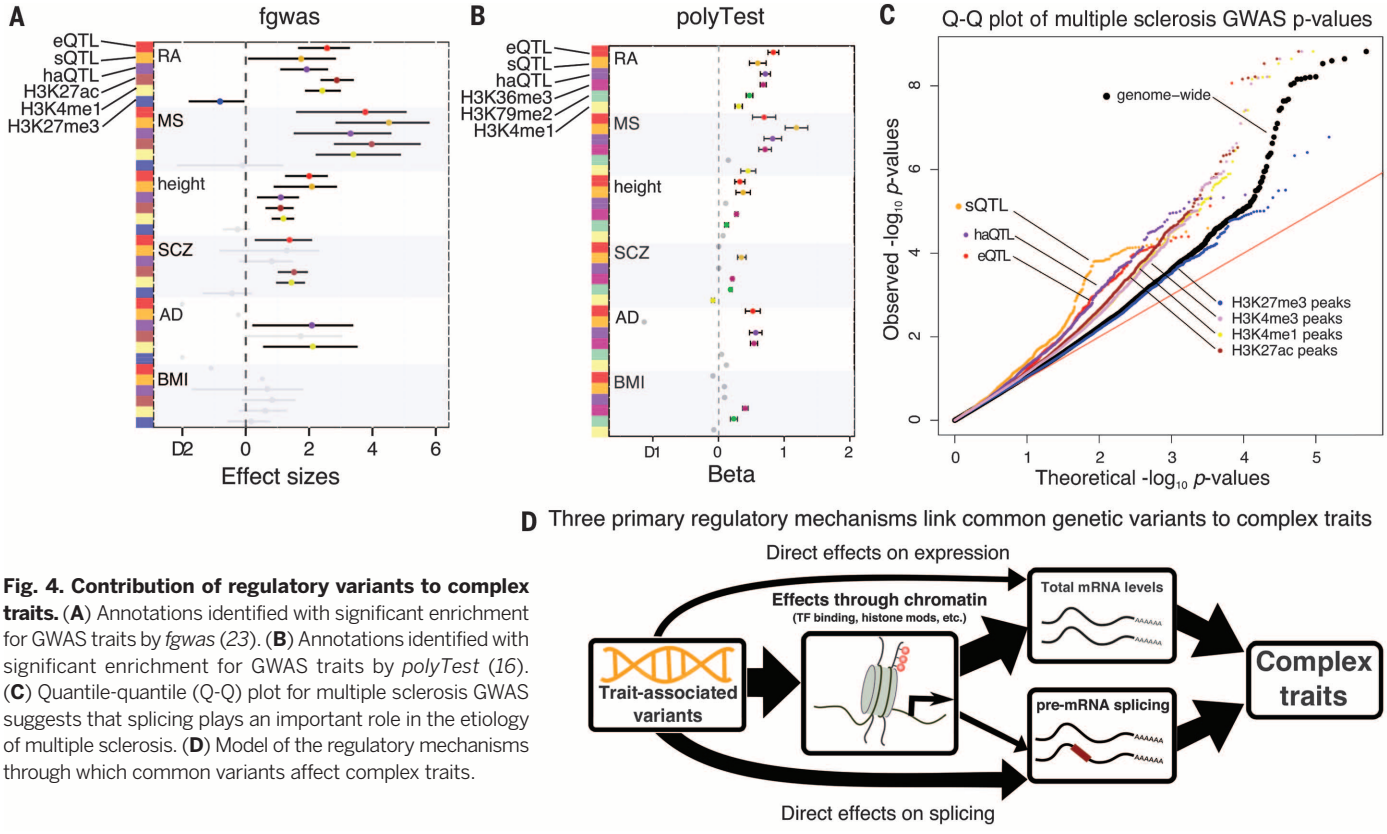

Fig. 4. Contribution of regulatory variants to complex traits. (**A**) Annotations identified with significant enrichment for GWAS traits by *fgwas* (*23*). (**B**) Annotations identified with significant enrichment for GWAS traits by *polyTest* (*16*). (**C**) Quantile-quantile (Q-Q) plot for multiple sclerosis GWAS suggests that splicing plays an important role in the etiology of multiple sclerosis. (**D**) Model of the regulatory mechanisms through which common variants affect complex traits.

Downloaded from http://science.sciencemag.org/ on April 28, 2016

Although studies have implicated variants in active chromatin regions and eQTLs as contributing significantly to complex traits (*2, 8, 10, 23*), the importance of splicing remains unclear. We therefore wondered what role common sQTLs might play in complex diseases.

Owing to the extensive sharing of QTLs across cell types (*2, 24*), we reasoned that QTLs identified in LCLs should be informative about the relative contribution of different regulatory mechanisms to complex traits, in particular to immune-related diseases (*8*). We thus compiled genome-wide summary statistics for rheumatoid arthritis, multiple sclerosis, Alzheimer's disease, schizophrenia, height, and body mass index (*16*). Using two tests with different underlying statistical models, we searched for functional annotations that are associated with GWAS signals (*16, 23*).

As expected, eQTLs and haQTLs are predicted to contribute to rheumatoid arthritis, multiple sclerosis, and height according to one or both methods (Fig. 4). Consistent with the notion that disease SNPs in histone modification peaks are mediated through the SNPs' effect on chromatin, haQTLs are more enriched in risk loci than are variants that lie within H3K27ac peaks overall (Fig. 4C and fig. S14).

sQTLs appear to have effects of similar or even larger magnitude than eQTLs. For instance, there is an enrichment of sQTLs with low *P* values in the multiple sclerosis GWASs, even when compared to eQTLs (Fig. 4C and fig. S15). These enrichments are robust to the eQTL and sQTL detection cutoffs, suggesting that they are not simply due to the power of detection (fig. S16). We also found similar patterns when we compared the effect of sQTLs on multiple sclerosis to the effects of eQTLs identified in three purified immune cell types (fig. S17).

In conclusion, three main pathways mediate the impact of genetic variation on gene regulation with phenotypic and pathogenic consequences. Of these, our work uncovers an unexpectedly important role of RNA splicing in modulating phenotypic traits (Fig. 4D). These findings indicate that RNA splicing should be a focal point in future work on connecting genetic variation to complex disease.

REFERENCES AND NOTES

1. D. L. Nicolae *et al.*, *PLOS Genet.* **6**, e1000888 (2010).
2. The GTEx Consortium, *Science* **348**, 648–660 (2015).
3. M. Kasowski *et al.*, *Science* **328**, 232–235 (2010).
4. J. F. Degner *et al.*, *Nature* **482**, 390–394 (2012).
5. G. McVicker *et al.*, *Science* **342**, 747–749 (2013).
6. T. Lappalainen *et al.*, *Nature* **501**, 506–511 (2013).
7. R. C. del Rosario *et al.*, *Nat. Methods* **12**, 458–464 (2015).
8. F. Grubert *et al.*, *Cell* **162**, 1051–1065 (2015).
9. S. M. Waszak *et al.*, *Cell* **162**, 1039–1050 (2015).
10. H. K. Finucane *et al.*, *Nat. Genet.* **47**, 1228–1235 (2015).
11. A. Kundaje *et al.*, *Nature* **518**, 317–330 (2015).
12. M. Claussnitzer *et al.*, *N. Engl. J. Med.* **373**, 895–907 (2015).
13. M. A. Garcia-Blanco, A. P. Baraniak, E. L. Lasda, *Nat. Biotechnol.* **22**, 535–546 (2004).
14. H. B. Fraser, X. Xie, *Genome Res.* **19**, 567–575 (2009).
15. H. Y. Xiong *et al.*, *Science* **347**, 1254806 (2015).
16. See the supplementary materials and methods on *Science* Online.
17. J. K. Pickrell *et al.*, *Nature* **464**, 768–772 (2010).
18. N. E. Banovich *et al.*, *PLOS Genet.* **10**, e1004663 (2014).
19. A. Battle *et al.*, *Science* **347**, 664–667 (2015).
20. Y. I. Li, D. A. Knowles, J. K. Pritchard, http://biorxiv.org/content/early/2016/03/16/044107 (2016).
21. S. Shukla *et al.*, *Nature* **479**, 74–79 (2011).
22. M. Gutierrez-Arcelus *et al.*, *PLOS Genet.* **11**, e1004958 (2015).
23. J. K. Pickrell, *Am. J. Hum. Genet.* **94**, 559–573 (2014).
24. T. Flutre, X. Wen, J. Pritchard, M. Stephens, *PLOS Genet.* **9**, e1003486 (2013).
25. E. Ira, M. Zanoni, M. Ruggeri, P. Dazzan, S. Tosato, *J. Psychiatry Neurosci.* **38**, 366–380 (2013).

ACKNOWLEDGMENTS

We thank S. Prabhakar for early access to the H3K27ac data; J. Blischak for technical assistance with the 4sU experiments; the anonymous reviewers for helpful comments; and A. Battle, A. Pai, N. Banovich, A. Fu, X. Lan, A. Harpak, and other members of the Pritchard/Gilad Labs for helpful discussions. This work was supported by NIH grants R01MH084703, R01MH101825, U01HG007036, and U54CA149145; by a Center for Computational, Evolutionary and Human Genomics Fellowship; and by the Howard Hughes Medical Institute. The 4sU-seq data have been deposited in the Gene Expression Omnibus (www.ncbi.nlm.nih.gov/geo/) under accession no. GSE75220; other accession numbers can be found in table S8.

SUPPLEMENTARY MATERIALS

www.sciencemag.org/content/352/6285/600/suppl/DC1
Materials and Methods
Figs. S1 to S18
Tables S1 to S8
References (*26–53*)
Data Table S1

24 November 2015; accepted 25 March 2016
10.1126/science.aad9417

BIOPHYSICS

Broken detailed balance at mesoscopic scales in active biological systems

Christopher Battle,[1,2]* Chase P. Broedersz,[2,3,4]* Nikta Fakhri,[1,2,5]* Veikko F. Geyer,[6] Jonathon Howard,[6] Christoph F. Schmidt,[1,2]† Fred C. MacKintosh[2,7]†

Systems in thermodynamic equilibrium are not only characterized by time-independent macroscopic properties, but also satisfy the principle of detailed balance in the transitions between microscopic configurations. Living systems function out of equilibrium and are characterized by directed fluxes through chemical states, which violate detailed balance at the molecular scale. Here we introduce a method to probe for broken detailed balance and demonstrate how such nonequilibrium dynamics are manifest at the mesosopic scale. The periodic beating of an isolated flagellum from *Chlamydomonas reinhardtii* exhibits probability flux in the phase space of shapes. With a model, we show how the breaking of detailed balance can also be quantified in stationary, nonequilibrium stochastic systems in the absence of periodic motion. We further demonstrate such broken detailed balance in the nonperiodic fluctuations of primary cilia of epithelial cells. Our analysis provides a general tool to identify nonequilibrium dynamics in cells and tissues.

When a system reaches thermodynamic equilibrium, its properties become stationary in time, which requires a net balance between rates of transitions into and out of any particular microstate of the system. Systems in thermodynamic equilibrium, however, are known to be balanced in an even stronger way. They obey detailed balance, in which transition rates between any two microstates are pairwise balanced (Fig. 1A). This means there can be no net flux of transitions anywhere in the phase space of system states. This principle was identified and used by Ludwig Boltzmann in his pioneering development of statistical mechanics, the microscopic basis for thermodynamics (*1*). In contrast, living systems operate far from equilibrium, and molecular-scale violations of detailed balance lie at the heart of their dynamics. For instance, metabolic and enzymatic processes drive closed-loop fluxes through the system's chemical states (Fig. 1B) (*2*).

Nonequilibrium driving can boost intracellular transport (*3–5*), the fidelity of transcription (*6*), chemotaxis (*7, 8*), and the accuracy of sensory perception (*9, 10*). To understand cell

[1]Drittes Physikalisches Institut, Georg-August-Universität, 37077 Göttingen, Germany. [2]The Kavli Institute for Theoretical Physics, University of California, Santa Barbara, CA 93106, USA. [3]Arnold-Sommerfeld-Center for Theoretical Physics and Center for NanoScience, Ludwig-Maximilians-Universität München, Theresienstrasse 37, D-80333 München, Germany. [4]Lewis–Sigler Institute for Integrative Genomics and Joseph Henry Laboratories of Physics, Princeton University, Princeton, NJ 08544, USA. [5]Department of Physics, Massachusetts Institute of Technology, Cambridge, MA 02139, USA. [6]Department of Molecular Biophysics and Biochemistry, Yale University, New Haven, CT, USA. [7]Department of Physics and Astronomy, Vrije Universiteit, Amsterdam, Netherlands.
*These authors contributed equally to this work. **†Corresponding author. Email: fcmack@gmail.com (F.C.M.); christoph.schmidt@phys.uni-goettingen.de (C.F.S.)**

Downloaded from http://science.sciencemag.org/ on April 28, 2016

function, it is thus important to determine whether particular cellular processes result from nonequilibrium activity, but this can be challenging. For instance, the stochastic nonequilibrium motion of tracer particles or fluorescently labeled proteins in cells is often deceptively similar to that of thermally agitated Brownian particles (*3*–*5*, *11*). It is unclear, however, to what extent the dynamics at such mesoscopic scales violate detailed balance, even if the system is out of equilibrium. Theoretically, detailed balance can reemerge at large scales for nonequilibrium systems, which break detailed balance at small scales (*12*). To test for detailed balance and diagnose nonequilibrium dynamics at mesoscopic scales, we introduce a noninvasive approach based on quantifying flux loops (*13*) in configurational phase spaces of

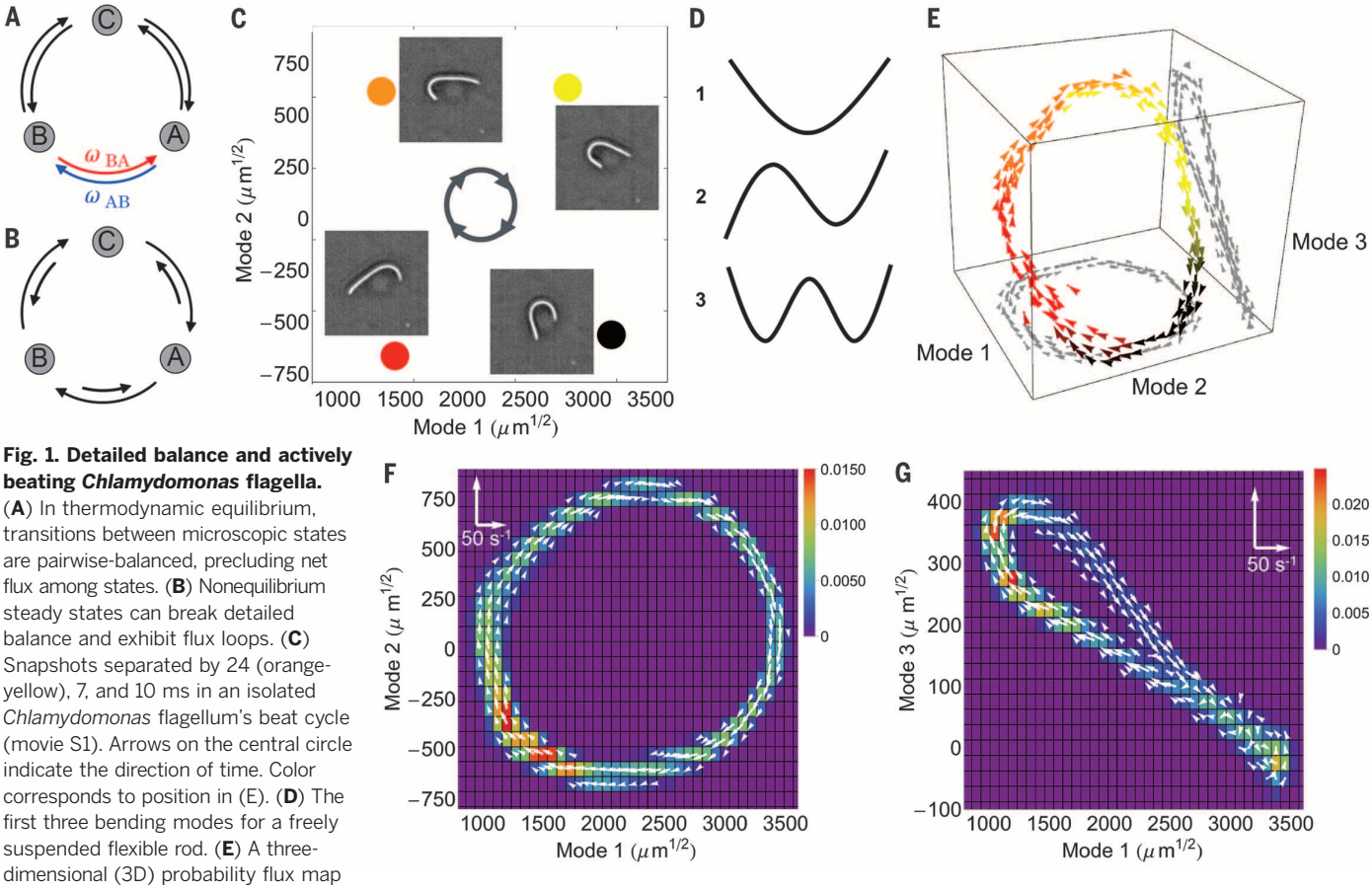

Fig. 1. Detailed balance and actively beating *Chlamydomonas* flagella. (**A**) In thermodynamic equilibrium, transitions between microscopic states are pairwise-balanced, precluding net flux among states. (**B**) Nonequilibrium steady states can break detailed balance and exhibit flux loops. (**C**) Snapshots separated by 24 (orange-yellow), 7, and 10 ms in an isolated *Chlamydomonas* flagellum's beat cycle (movie S1). Arrows on the central circle indicate the direction of time. Color corresponds to position in (E). (**D**) The first three bending modes for a freely suspended flexible rod. (**E**) A three-dimensional (3D) probability flux map of flagellar dynamics in the CGPS spanned by the first three modes. (**F** and **G**) Probability distribution (color) and flux map (white arrows) of flagellar dynamics in CGPS spanned by first and second modes (F), and first and third modes (G). The white legend indicates the flux scale.

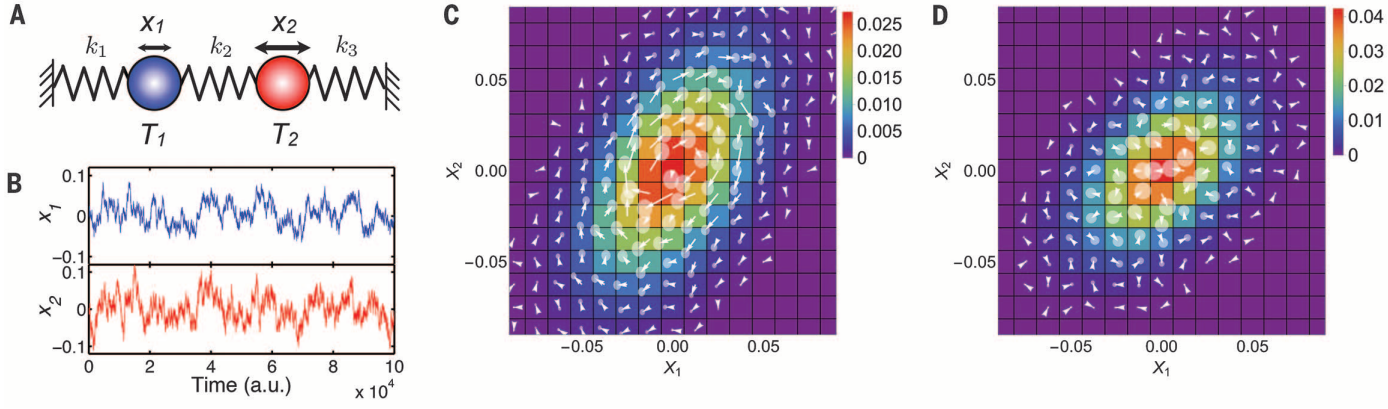

Fig. 2. Brownian-dynamics simulation of 1D bead-spring model. (**A**) Model schematic. (**B**) Time series of the bead positions for $T_2 = 1.5T_1$ and equal spring constants. See figs. S4 and S5 for the general case (*18*). (**C** and **D**) Probability distribution (color) and flux map (white arrows) in CGPS spanned by x_1 and x_2 for the simulation in panel B (C) and for a simulation with $T_2 = T_1$ (D). Translucent disks represent a 2σ confidence interval for fluxes.

Downloaded from http://science.sciencemag.org/ on April 28, 2016

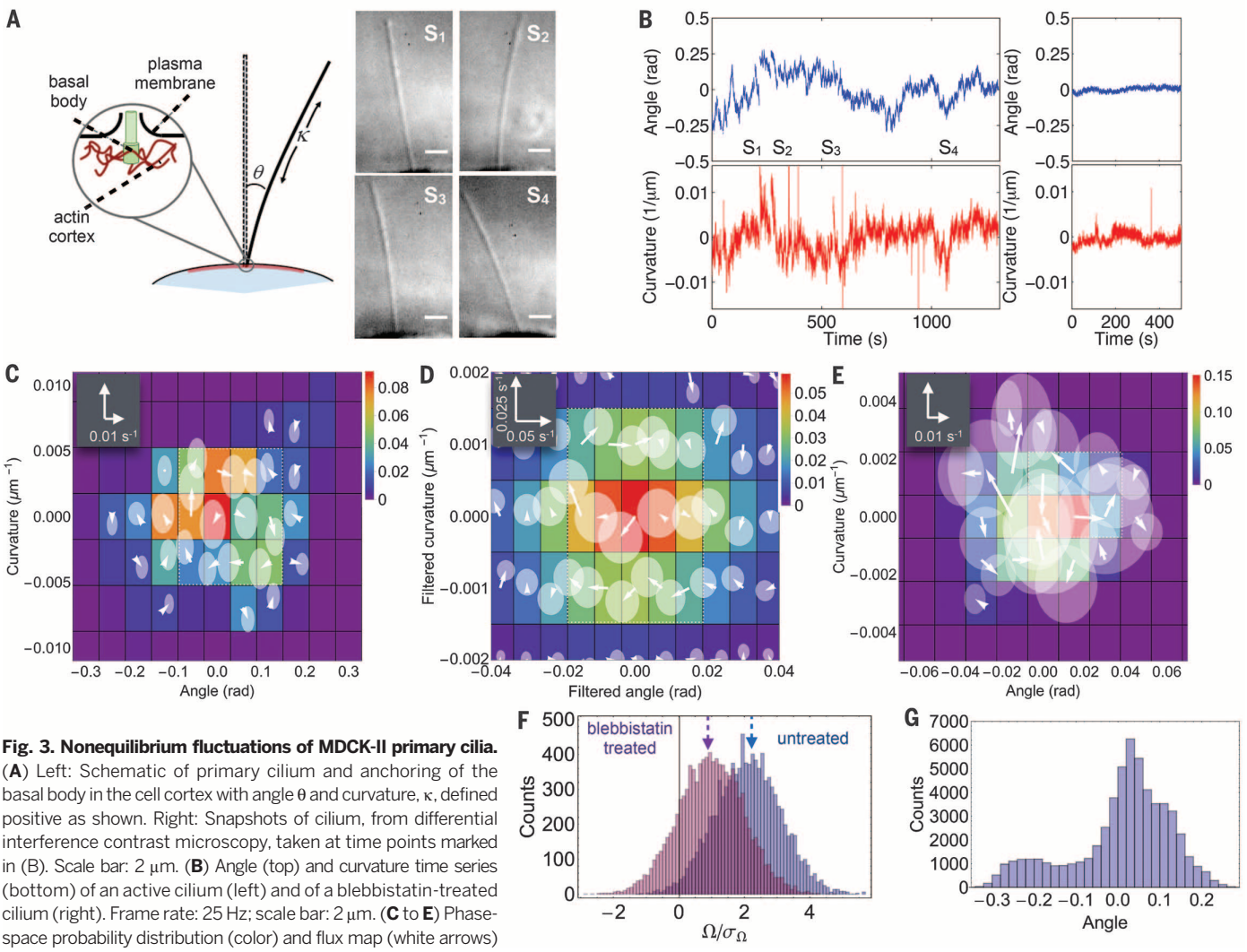

Fig. 3. Nonequilibrium fluctuations of MDCK-II primary cilia. (**A**) Left: Schematic of primary cilium and anchoring of the basal body in the cell cortex with angle θ and curvature, κ, defined positive as shown. Right: Snapshots of cilium, from differential interference contrast microscopy, taken at time points marked in (B). Scale bar: 2 μm. (**B**) Angle (top) and curvature time series (bottom) of an active cilium (left) and of a blebbistatin-treated cilium (right). Frame rate: 25 Hz; scale bar: 2 μm. (**C** to **E**) Phase-space probability distribution (color) and flux map (white arrows) of ciliary fluctuations in CGPS spanned by θ and κ for (C): the untreated time series from (B); (D) a high-pass filtered time series of an untreated cilium (window size = 200 s); (E) the fluctuations of the blebbistatin-treated cilium from (B). The translucent disks represent a 2σ confidence interval for fluxes. (**F**) Distributions of flux contour integrals for untreated (purple) and blebbistatin-treated (pink) cilia. (**G**) Angle distribution for the high-pass filtered cilium data in (D).

strongly fluctuating stochastic steady-state systems. This should be contrasted with the deterministic dynamics of active swimmers, for which broken detailed balance is evident in the nonreciprocal nature of their motion (*14*). Moreover, our method is not limited to measuring conformational degrees of freedom, but can also include chemical variables, such as pH or ion concentrations.

We first illustrate this approach on a system displaying unmistakable nonequilibrium motion: a beating flagellum of *Chlamydomonas reinhardtii*. The main mechanical component of eukaryotic flagella is a conserved microtubule structure, the axoneme. Dynein motors drive relative axial sliding of the microtubules composing the axoneme, resulting in periodic beating (*15*, *16*). We isolated and demembranated flagella from *C. reinhardtii* (*17*, *18*) and reactivated the axonemes by addition of adenosine triphosphate (ATP). Figure 1C shows snapshots of the beat cycle acquired by high-speed phase contrast microscopy (movie S1). We decomposed the axoneme shapes into the dynamic normal modes of a finite elastic filament freely suspended in a liquid (*19*), obtaining amplitudes $a_1(t)$, $a_2(t)$, $a_3(t)$ for the first three modes (Fig. 1D). From the time series of these amplitudes, we constructed a trajectory in the phase space spanned by the three modes. We discretized this space into a coarse-grained phase space (CGPS) (fig. S1) and determined the probabilities p_α to be in box α by temporal averaging (*18*). The steady-state dynamics are described by net transition rates $w_{\alpha,\beta} = (N_{\alpha,\beta} - N_{\beta,\alpha})/t_{\text{total}}$ determined by counting the number of transitions between adjacent states α and β in the time window t_{total}. These rates $w_{\alpha,\beta}$ determine the vector components of the flux $\vec{j}$ from α to β (Fig. 1, F and G). In thermodynamic equilibrium, all these fluxes must vanish. By contrast, flux in closed loops is possible in a nonequilibrium steady state. The results of such a probability flux analysis (PFA) for the beating cilium are shown in Fig. 1E, with vector fields indicating the fluxes for the first three modes. Figure 1, F and G, shows the $a_1 \times a_2$ and $a_1 \times a_3$ projections of CGPS probability and flux map. The clearly visible flux loops in phase space reflect the nonequilibrium, steady-state dynamics of the beating flagellum, and these fluxes are absent in the equilibrium dynamics of a microtubule (figs. S17 and S18).

The beating flagellum is an obvious nonequilibrium system, driven through its configurations at a defined frequency with relatively little stochasticity (*20*), resulting in a narrow band of populated states in phase space through which the trajectory cycles unidirectionally. To test our approach on a purely stochastic system, we numerically studied two overdamped, tethered beads at positions $x_1(t)$ and $x_2(t)$ coupled by a spring (Fig. 2A). This model system can be driven out of equilibrium by connecting the two beads to different heat baths at temperatures T_1 and T_2,

Downloaded from http://science.sciencemag.org/ on April 28, 2016

respectively, leading to heat flux from hot to cold. This minimal model is similar to a class of thermal ratchet models that have been studied, perhaps most famously by Feynman (*21*, *22*). With $T_2 = 1.5T_1$ (Fig. 2B), the two simulated time series of random displacements were individually still indistinguishable from equilibrium dynamics. In particular, displacements maintained a Gaussian distribution, even in this nonequilibrium situation (fig. S6) (*18*). When we applied PFA, however, we found significant probability fluxes in the $x_1 \times x_2$ plane of CGPS (Fig. 2C). These flux loops demonstrate broken detailed balance, revealing the nonequilibrium nature of the system's dynamics. At equilibrium ($T_2 = T_1$), flux loops vanished (Fig. 2D).

The finite length of time trajectories creates a noise floor in the measured transition rates. To assess the statistical significance of the fluxes determined by PFA, we used trajectory bootstrapping (*18*, *23*). Error estimates are shown as disks centered on flux arrowheads (fig. S2). The comparison with noise demonstrates the statistical significance of fluxes for the nonequilibrium system ($T_2 = 1.5T_1$, Fig. 2C), and their statistical insignificance in equilibrium ($T_2 = T_1$, Fig. 2D). The simulations thus demonstrate that even a purely stochastically driven system can be probed for nonequilibrium behavior by detecting broken detailed balance (figs. S4 and S5).

We next turned to a biological system that exhibits a stochastic steady state (*18*) (figs. S7 to S13). We imaged primary cilia of Madin-Darby canine kidney II (MDCK-II) epithelial cells grown in culture to a confluent layer (Fig. 3A). Primary cilia are hairlike organelles that project from many eukaryotic cells and can transduce mechanical and chemical stimuli into intracellular signals (*24*). Using invasive biochemical treatments, prior work (*25*) provided indirect evidence for nonequilibrium dynamics of these cilia. Flagella and primary cilia are structurally related, but the latter often lack the dynein machinery necessary for flagellar beating (*26*). Indeed, in marked contrast to the flagellum, we found that primary cilia of MDCK cells fluctuate in a way that appears random (Fig. 3B, movie S2, and figs. S14 and S15).

To analyze cilia dynamics, we characterized their state by the average deflection angle $\theta(t)$ from the normal and the average curvature $\kappa(t)$ (Fig. 3A) and calculated the probability flux map in the $\theta \times \kappa$ phase space (Fig. 3, C to E). From the time series $\theta(t)$ and $\kappa(t)$ in Fig. 3B (left), we found a clockwise circulation pattern (white box, Fig. 3C), indicative of broken detailed balance. To quantify the statistical robustness of this pattern, we calculated the contour integral along the flux loop (fig. S3) enclosed by the white box (Fig. 3C), $\Omega = \oint \vec{j} \cdot d\vec{\ell}$. We found $\mu_\Omega/\sigma_\Omega = 2.1$, where μ_Ω and σ_Ω are the bootstrapped mean and standard deviation of Ω (Fig. 3F) (*18*), indicating a statistically significant flux loop ($P = 0.018$, z-test). Long trajectories sometimes exhibited multimodal behavior in the angle distribution originating from a slow drift in the steady-state angle (Fig. 3G). In such cases, high-pass filtering resulted in a statistically significant clockwise circulation pattern (Fig. 3D) (*18*). Actin-myosin dynamics underlie many types of cellular dynamics (*4*, *5*, *27*, *28*), and the cilium basal body is embedded in the actin cortex (Fig. 3A, inset), providing a mechanism for the nonequilibrium motion of the cilium (*25*, *29*, *30*). To test whether detailed balance was restored when the main driving force was turned off, we treated MDCK-II cells with blebbistatin, a drug that inhibits nonmuscle myosin II (Fig. 3E). This treatment suppressed the amplitude of angle and curvature fluctuations (Fig. 3B, right), as seen previously (*25*). The analysis of phase-space trajectories revealed that blebbistatin treatment (Fig. 3E) decreased phase space flux and rendered the residual fluxes statistically insignificant (P = 0.16) (Fig. 3F). As a further control, we observed that ATP depletion also suppressed, albeit not completely, cilia fluctuations and strongly decreased the flux pattern in phase space (P = 0.16) (fig. S16) (*18*). Finally, we verified the steady-state nature of cilia dynamics by the vanishing divergence of the fluxes in phase space (fig. S13). Taken together, these results demonstrate that the stochastic dynamics of the cilium can be clearly identified to be of nonequilibrium origin.

Steady-state fluctuations are common in living systems. It has, however, proved challenging to determine whether such stochastic dynamics result from nonequilibrium activity in given cases (*3*, *11*). The PFA approach described here uses commonly observable conformational degrees of freedom to identify nonequilibrium dynamics in steady-state systems. This approach is broadly applicable to active biological systems, ranging from bacteria and the cell nucleus (*11*), all the way to tissues. Our method is intrinsically noninvasive, being based on imaging alone without requiring biochemical or mechanical manipulation. This is in contrast to other methods, where nonequilibrium fluctuations can be identified by the fluctuation-dissipation theorem or its nonequilibrium generalizations (*27*, *31*). Furthermore, our method does not focus on rare events (*32*) or transitions between equilibrium states (*33*–*35*), nor does it rely on Markovian dynamics (*33*). It is interesting to consider possible extensions of our method to quantify energy dissipation or entropy production (*36*).

REFERENCES AND NOTES

1. L. Boltzmann, *Sitzungsberichte Akad. Wiss., Vienna, part II* **66**, 275–370 (1872).
2. B. Alberts *et al.*, *Molecular Biology of the Cell* (Garland Science, New York, ed. 5 2007).
3. C. P. Brangwynne, G. H. Koenderink, F. C. MacKintosh, D. A. Weitz, *J. Cell Biol.* **183**, 583–587 (2008).
4. N. Fakhri *et al.*, *Science* **344**, 1031–1035 (2014).
5. M. Guo *et al.*, *Cell* **158**, 822–832 (2014).
6. J. J. Hopfield, *Proc. Natl. Acad. Sci. U.S.A.* **71**, 4135–4139 (1974).
7. H. C. Berg, E. M. Purcell, *Biophys. J.* **20**, 193–219 (1977).
8. M. E. Cates, *Rep. Prog. Phys.* **75**, 042601 (2012).
9. G. Lan, P. Sartori, S. Neumann, V. Sourjik, Y. Tu, *Nat. Phys.* **8**, 422–428 (2012).
10. B. Nadrowski, P. Martin, F. Jülicher, *Proc. Natl. Acad. Sci. U.S.A.* **101**, 12195–12200 (2004).
11. S. C. Weber, A. J. Spakowitz, J. A. Theriot, *Proc. Natl. Acad. Sci. U.S.A.* **109**, 7338–7343 (2012).
12. D. A. Egolf, *Science* **287**, 101–104 (2000).
13. R. Zia, B. Schmittmann, *J. Stat. Mech.* **2007**, P07012 (2007).
14. E. M. Purcell, *Am. J. Phys.* **45**, 3–11 (1977).
15. I. H. Riedel-Kruse, A. Hilfinger, J. Howard, F. Jülicher, *HFSP J.* **1**, 192–208 (2007).
16. K. Y. Wan, R. E. Goldstein, *Phys. Rev. Lett.* **113**, 238103 (2014).
17. J. Alper, V. Geyer, V. Mukundan, J. Howard, *Methods Enzymol.* **524**, 343–369 (2013).
18. Materials and methods are available as supplementary materials on *Science* Online.
19. S. R. Aragon, R. Pecora, *Macromolecules* **18**, 1868–1875 (1985).
20. R. Ma, G. S. Klindt, I. H. Riedel-Kruse, F. Jülicher, B. M. Friedrich, *Phys. Rev. Lett.* **113**, 048101 (2014).
21. R. P. Feynman, R. B. Leighton, M. Sands, *The Feynman Lectures on Physics, Vol. 1* (Addison-Wesley, Reading, MA, 1966).
22. K. Sekimoto, *J. Phys. Soc. Jpn.* **66**, 1234–1237 (1997).
23. C. E. Shannon, W. Weaver, *The Mathematical Theory of Communication* (Univ. of Illinois Press, Urbana, 1949).
24. V. Singla, J. F. Reiter, *Science* **313**, 629–633 (2006).
25. C. Battle, C. M. Ott, D. T. Burnette, J. Lippincott-Schwartz, C. F. Schmidt, *Proc. Natl. Acad. Sci. U.S.A.* **112**, 1410–1415 (2015).
26. B. G. Barnes, *J. Ultrastruct. Res.* **5**, 453–467 (1961).
27. D. Mizuno, C. Tardin, C. F. Schmidt, F. C. Mackintosh, *Science* **315**, 370–373 (2007).
28. C. P. Brangwynne, G. H. Koenderink, F. C. Mackintosh, D. A. Weitz, *Phys. Rev. Lett.* **100**, 118104 (2008).
29. I. Antoniades, P. Stylianou, P. A. Skourides, *Dev. Cell* **28**, 70–80 (2014).
30. W. F. Marshall, *Curr. Top. Dev. Biol.* **85**, 1–22 (2008).
31. J. Prost, J. F. Joanny, J. M. Parrondo, *Phys. Rev. Lett.* **103**, 090601 (2009).
32. C. Bustamante, J. Liphardt, F. Ritort, *Phys. Today* **58**, 43–48 (2005).
33. G. E. Crooks, *Phys. Rev. E Stat. Phys. Plasmas Fluids Relat. Interdiscip. Topics* **60**, 2721–2726 (1999).
34. C. Jarzynski, *Phys. Rev. Lett.* **78**, 2690–2693 (1997).
35. J. Liphardt, S. Dumont, S. B. Smith, I. Tinoco Jr., C. Bustamante, *Science* **296**, 1832–1835 (2002).
36. U. Seifert, *Phys. Rev. Lett.* **95**, 040602 (2005).

ACKNOWLEDGMENTS

We thank J. Lippincott-Schwartz, U. Seifert, G. Berman, A. El-Hady, B. Machta, and J. Gore for discussions. This research was supported by a Lewis-Sigler fellowship (C.P.B.), the German Excellence Initiative via the program "NanoSystems Initiative Munich" (C.P.B.), and the Cluster of Excellence and Deutsche Forschungsgemeinschaft (DFG) Research Center Nanoscale Microscopy and Molecular Physiology of the Brain (CNMPB) (C.F.S.), a Human Frontier Science Program Fellowship (N.F.), the European Research Council Advanced Grant PF7 ERC-2013-AdG, Project 340528 (C.F.S), the DFG Collaborative Research Center SFB 937 (Project A2), and a research program of the Foundation for Fundamental Research on Matter (FOM), which is part of the Netherlands Organization for Scientific Research (NWO). This work was initiated at the Aspen Center for Physics, which is supported by NSF grant PHY-1066293, and was further supported in part by the NSF under grant NSF PHY11-25915. Experiments with *Chlamydomonas* flagella were performed during the 2011 Physiology Course at the Marine Biological Laboratory, Woods Hole, MA, supported in part by NIH grants R13GM085967 and P50GM068763.

SUPPLEMENTARY MATERIALS

www.sciencemag.org/content/352/6285/604/suppl/DC1
Materials and Methods
Figs. S1 to S17
References (*37*–*54*)
Movies S1 and S2

18 June 2015; accepted 26 January 2016
10.1126/science.aac8167

Downloaded from http://science.sciencemag.org/ on April 28, 2016

MICROBIOTA

Helminth infection promotes colonization resistance via type 2 immunity

Deepshika Ramanan,[1,2]* Rowann Bowcutt,[3]* Soo Ching Lee,[4] Mei San Tang,[3] Zachary D. Kurtz,[2,3] Yi Ding,[5] Kenya Honda,[6,7] William C. Gause,[8] Martin J. Blaser,[3] Richard A. Bonneau,[9,10,11] Yvonne A.L. Lim,[4]† P'ng Loke,[3]†‡ Ken Cadwell[1,3]†‡

Increasing incidence of inflammatory bowel diseases, such as Crohn's disease, in developed nations is associated with changes to the microbial environment, such as decreased prevalence of helminth colonization and alterations to the gut microbiota. We find that helminth infection protects mice deficient in the Crohn's disease susceptibility gene *Nod2* from intestinal abnormalities by inhibiting colonization by an inflammatory *Bacteroides* species. Resistance to *Bacteroides* colonization was dependent on type 2 immunity, which promoted the establishment of a protective microbiota enriched in Clostridiales. Additionally, we show that individuals from helminth-endemic regions harbor a similar protective microbiota and that deworming treatment reduced levels of Clostridiales and increased Bacteroidales. These results support a model of the hygiene hypothesis in which certain individuals are genetically susceptible to the consequences of a changing microbial environment.

Dramatic increases in the incidence of inflammatory bowel disease (IBD) in the developed world point toward alterations in the microbial environment, including changes to the gut microbiota (*1*) and decreased exposure to intestinal parasites such as helminths (*2*). Evidence supporting a central role of the microbiota in the pathogenesis of IBD has led to a growing interest in defining the symbiotic relationship between the host and specific microbial species (*3*). In insects, symbiotic relationships can develop to defend against environmental hazards (defensive symbiosis) (*4*); this concept may be applicable to host-microbiota interactions. For example, specific bacterial taxa found within the human gut microbiota probably mediate resistance to antibiotic-associated diarrhea caused by *Clostridium difficile* (*5*). The loss of beneficial members of the microbiota potentially contributes to chronic inflammatory diseases. Additionally, helminths and the gut microbiota have coevolved with their mammalian

[1]Kimmel Center for Biology and Medicine at the Skirball Institute, New York University School of Medicine, New York, NY 10016, USA. [2]Sackler Institute of Graduate Biomedical Sciences, New York University School of Medicine, New York, NY 10016, USA. [3]Departments of Microbiology and Medicine, New York University School of Medicine, New York, NY 10016, USA. [4]Department of Parasitology, Faculty of Medicine, University of Malaya, Kuala Lumpur, Malaysia. [5]Department of Pathology, New York University Langone Medical Center, New York, NY 10016, USA. [6]RIKEN Center for Integrative Medical Sciences (IMS), Yokohama, Kanagawa 230-0045, Japan. [7]Japan Agency for Medical Research and Development (AMED)–Core Research for Evolutional Science and Technology (CREST), Tokyo 100-0004, Japan. [8]Center for Immunity and Inflammation, New Jersey Medical School, Rutgers, The State University of New Jersey, Newark, NJ 07101, USA. [9]Department of Biology, Center for Genomics and Systems Biology, New York University, New York, NY 10003, USA. [10]Courant Institute of Mathematical Sciences, New York University, New York, NY 10012, USA. [11]Simons Center for Data Analysis, Simons Foundation, New York, NY 10011, USA.
*These authors contributed equally to this work. **†Corresponding author. Email: ken.cadwell@med.nyu.edu (K.C.); png.loke@nyumc.org (P.L.); limailian@um.edu.my (Y.A.L.L.)**
‡These authors contributed equally equally to this work.

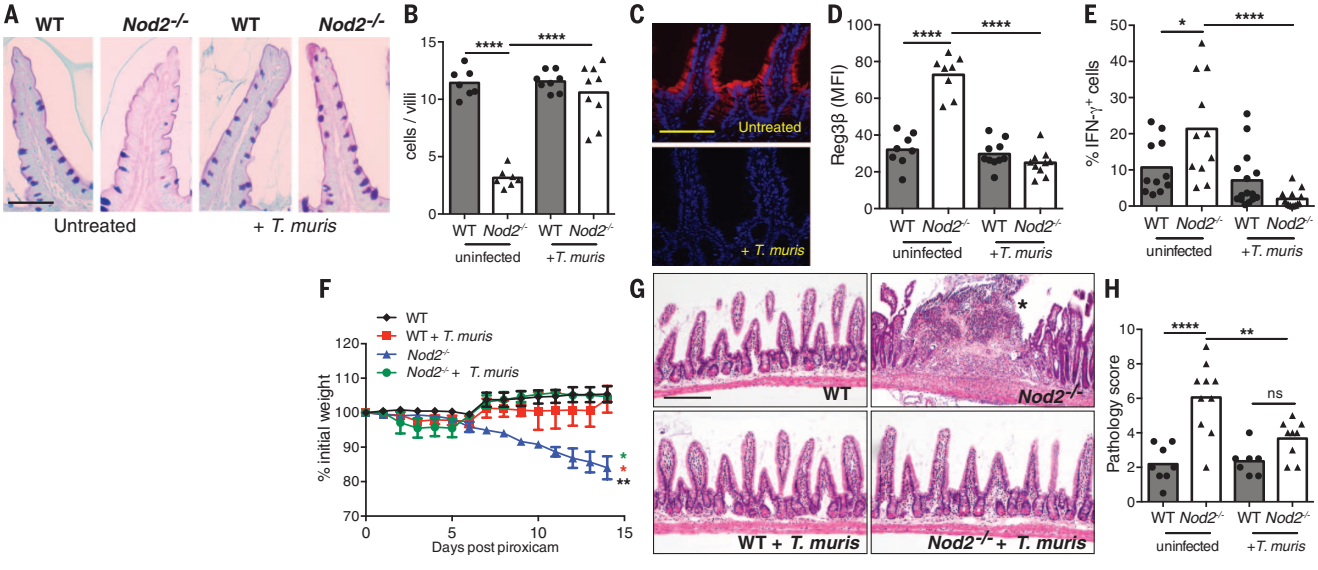

Fig. 1. *Trichuris muris* infection reverses intestinal abnormalities in *Nod2*$^{-/-}$ mice. (**A** and **B**) SI sections stained with PAS (periodic acid–Schiff)–Alcian blue (A) and quantification of the number of goblet cells displaying normal morphology per villi (B) from uninfected and *T. muris*–infected WT and *Nod2*$^{-/-}$ mice ($n \geq 7$ per genotype). (**C** and **D**) Immunofluorescence (IF) analysis of Reg3β in the small intestine (C) and quantification of the mean fluorescence intensity (D) of the aforementioned mice ($n \geq 8$ per genotype). (**E**) Quantification of the proportion of CD8$^+$ IELs expressing IFN-γ by flow cytometry ($n \geq 11$ per genotype). (**F** to **H**) Quantification of weight loss (F), SI sections stained with hematoxylin and eosin (G), and quantification of pathology (*19*) (H) after piroxicam treatment of uninfected and *T. muris*–infected WT and *Nod2*$^{-/-}$ mice. The asterisk in (G) denotes an abscess ($n \geq 7$ per genotype). *P < 0.05; **P < 0.01; ****P < 0.0001 by analysis of variance (ANOVA), with Holm-Sidak multiple comparisons test for (B), (D) to (F), and (H). ns, not significant. Scale bars represent 50 μm in (A) and 100 μm in (C) and (G). Data are represented in (F) as mean ± SEM (error bars) from at least two independent experiments. In (B), (D), (E), and (H), each data point represents an individual mouse, and each horizontal bar denotes a mean value (at least two independent experiments).

Downloaded from http://science.sciencemag.org/ on April 28, 2016

hosts, but the mechanisms of these interactions and the consequence of decreased exposure to intestinal helminths remain unclear. We find that helminths can reduce intestinal inflammatory responses by promoting expansion of protective bacterial communities that inhibit proinflammatory bacterial taxa.

We previously reported that mice deficient in *Nod2* develop several small intestinal (SI) abnormalities, in a manner dependent on a ubiquitous member of the gut microbiota, *Bacteroides vulgatus* (*6*). Consistent with the specific association between human *NOD2* variants and ileal Crohn's disease (*7*), an IBD that affects the small intestine, the most notable abnormality was a SI goblet cell defect that resulted in a compromised mucus layer, allowing sustained colonization by *B. vulgatus*. We found that chronic infection of *Nod2*$^{-/-}$ mice with the parasitic worm *Trichuris muris* restored SI goblet cell numbers and morphology (Fig. 1, A and B, and fig. S1, A and B). These changes were not detected in the colon, and wild-type (WT) mice infected with *T. muris* did not display nonspecific goblet cell hyperplasia (fig. S1C). Elevated epithelial levels of the antimicrobial lectin Reg3β and interferon-γ$^+$ (IFN-γ$^+$) CD8$^+$ intraepithelial lymphocytes (IELs), inflammatory markers associated with goblet cell defects in *Nod2*$^{-/-}$ mice (*6*), were also reduced upon *T. muris* infection (Fig. 1, C to E; and figs. S1, D and E, and S2). *Nod2*$^{-/-}$ mice develop severe intestinal pathologies after SI injury induced by the nonsteroidal anti-inflammatory drug piroxicam. Infection with *T. muris* prevented the intestinal bleeding and perforation, exaggerated weight loss, mucus depletion, splenomegaly, and bacterial translocation observed in uninfected *Nod2*$^{-/-}$ mice treated with piroxicam (Fig. 1F and figs. S3, A to C, and S4). Blind histology analysis confirmed reductions in specific pathologies such as abscesses, epithelial hyperplasia, villus blunting, and immune infiltrates (Fig. 1, G and H, and fig. S3, D to J). These results indicate that *T. muris* infection ameliorates spontaneous and inducible intestinal defects in *Nod2*$^{-/-}$ mice.

Consistent with the dependence of these inflammatory pathologies on *B. vulgatus* (*6*), infection with *T. muris* reduced the bacterial burden to the limit of detection in the stool and SI tissue of *Nod2*$^{-/-}$ mice (Fig. 2, A and F). *B. vulgatus* inhibition was dependent on lymphocytes (fig. S5, A to C), potentially reflecting goblet cell activation by type 2 cytokines [interleukin-4 (IL-4) and IL-13] produced by T helper (T_H) cells during helminth infections. We found increased phosphorylation of the type 2 transcription factor Stat6 in the SI epithelium of *T. muris*–infected *Nod2*$^{-/-}$ mice (Fig. 2B and fig. S5D). Additionally, *T. muris* infection inhibited *B. vulgatus* only transiently and did not restore goblet cells in *Stat6*$^{-/-}$ mice reconstituted with *Nod2*$^{-/-}$ bone marrow (Fig. 2C and fig. S5E). *Nod2*$^{-/-}$ mice infected with *T. muris* displayed a dominant T_H2 response characterized by a >10-fold increase in IL-13$^+$ CD4$^+$ T cells in the lamina propria (Fig. 2, D and E, and fig. S5, F and G). We confirmed these results with a second helminth, *Heligmosomoides polygyrus*, which induced an even greater T_H2 response compared with *T. muris*, perhaps reflecting the distinct anatomical niches of these parasites (Fig. 2, H and D, and figs. S6, C and D, and S7B). *H. polygyrus* completely abolished tissue-associated *B. vulgatus*, restored goblet cells, and reduced IFN-γ$^+$ IELs in *Nod2*$^{-/-}$ mice (Fig. 2, F and G, and figs. S6, A and B, and S7A). Blockade of IL-13 inhibited the effect of *H. polygyrus* on *B. vulgatus* and goblet cells, and administration of recombinant IL-13 (rIL-13) or rIL-4 to *Nod2*$^{-/-}$ mice was sufficient to reproduce the effect of helminth infection (Fig. 2, I to L, and

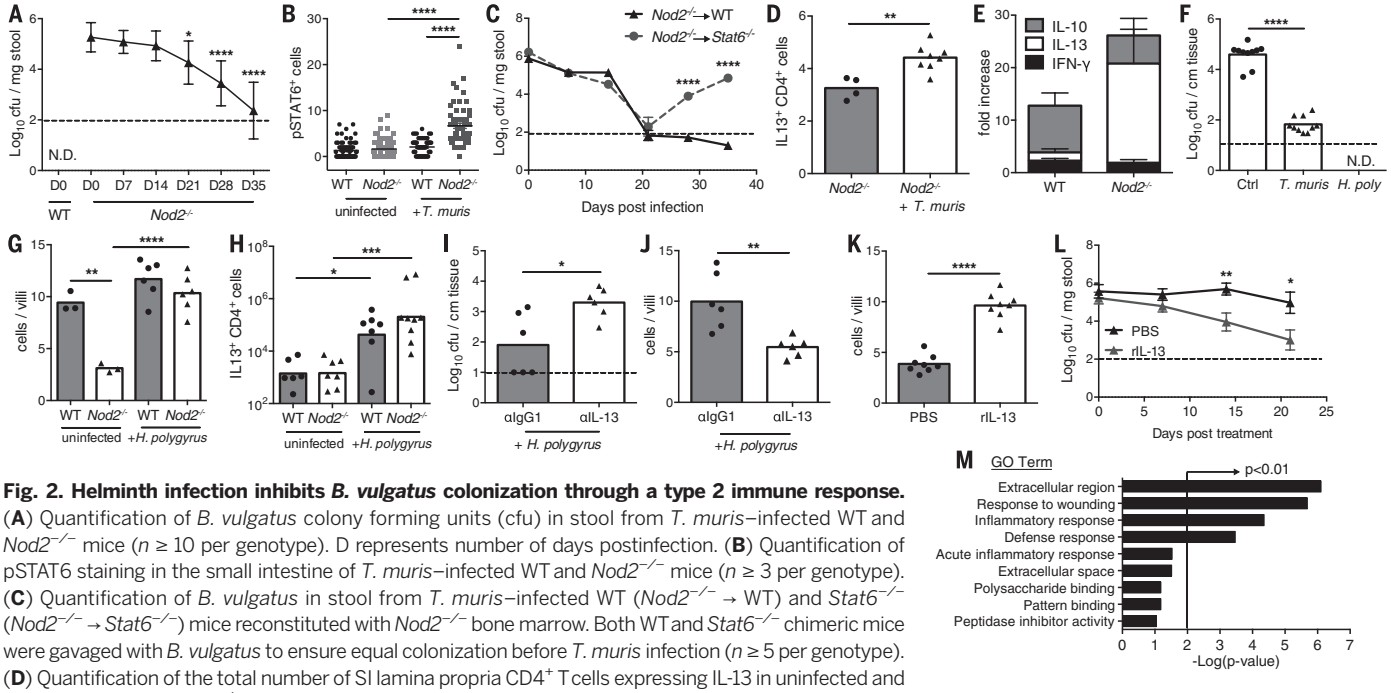

Fig. 2. Helminth infection inhibits *B. vulgatus* colonization through a type 2 immune response. (**A**) Quantification of *B. vulgatus* colony forming units (cfu) in stool from *T. muris*–infected WT and *Nod2*$^{-/-}$ mice ($n \geq 10$ per genotype). D represents number of days postinfection. (**B**) Quantification of pSTAT6 staining in the small intestine of *T. muris*–infected WT and *Nod2*$^{-/-}$ mice ($n \geq 3$ per genotype). (**C**) Quantification of *B. vulgatus* in stool from *T. muris*–infected WT (*Nod2*$^{-/-}$ → WT) and *Stat6*$^{-/-}$ (*Nod2*$^{-/-}$ → *Stat6*$^{-/-}$) mice reconstituted with *Nod2*$^{-/-}$ bone marrow. Both WT and *Stat6*$^{-/-}$ chimeric mice were gavaged with *B. vulgatus* to ensure equal colonization before *T. muris* infection ($n \geq 5$ per genotype). (**D**) Quantification of the total number of SI lamina propria CD4$^+$ T cells expressing IL-13 in uninfected and *T. muris*–infected *Nod2*$^{-/-}$ mice ($n \geq 4$ per genotype). (**E**) Fold increase in the number of CD4$^+$ T cells producing IFN-γ, IL-13, or IL-10 in the SI lamina propria of *T. muris*–infected WT and *Nod2*$^{-/-}$ mice, normalized to uninfected mice ($n \geq 4$ per genotype). (**F**) Quantification of *B. vulgatus* associated with SI tissue of uninfected, *T. muris*–infected, and *H. polygyrus*–infected *Nod2*$^{-/-}$ mice ($n \geq 10$ per genotype). (**G** and **H**) Quantification of goblet cells displaying normal morphology per villi (G) and total number of SI lamina propria CD4$^+$ T cells expressing IL-13 (H) in uninfected and *H. polygyrus*–infected WT and *Nod2*$^{-/-}$ mice ($n \geq 3$ per genotype). (**I** and **J**) Quantification of *B. vulgatus* in SI tissue (I), and goblet cells displaying normal morphology (J) in *H. polygyrus*–infected *Nod2*$^{-/-}$ mice treated with antibody to IL-13 or isotype control ($n = 6$ per genotype). (**K** and **L**) Quantification of goblet cells displaying normal morphology (K) and *B. vulgatus* in stool (L) in *Nod2*$^{-/-}$ mice treated with recombinant IL-13 or phosphate-buffered saline (PBS) ($n = 8$ per genotype). (**M**) Pathway analysis based on Gene Ontology (GO) terms of genes up-regulated in *Nod2*$^{-/-}$ mice treated with recombinant IL-13 compared with PBS controls. *$P < 0.05$; **$P < 0.01$; ***$P < 0.001$; ****$P < 0.0001$ by ANOVA, with Holm-Sidak multiple comparisons test for (A), (B), (G) and (H) and unpaired *t* test for (C), (D), (F), and (I) to (L). N.D., not detected. Data in (A), (B), (C), (E), and (L) are represented as mean ± SEM (error bars) from at least two independent experiments. In (D) and (F) to (K), each data point represents an individual mouse, and each bar denotes a mean value [at least two independent experiments, excluding the generation of bone marrow chimeras in (C)].

Downloaded from http://science.sciencemag.org/ on April 28, 2016

fig. S6E). RNA sequencing (RNA-seq) analysis of intestinal tissues from rIL-13–treated *Nod2*$^{-/-}$ mice revealed a wound-healing response characterized by expression of M2 macrophage genes (Fig. 2M, fig. S6F, and table S1). These results are consistent with the anti-inflammatory role of M2 macrophages in the gut (*8*, *9*) and help to explain how helminth infection ameliorates the exacerbated intestinal injury response in *Nod2*$^{-/-}$ mice. These results do not contradict the regulatory response induced by *H. polygyrus* in the colon (*9*, *10*), because type 2 immunity and regulatory T cells can function concurrently to reduce inflammation (*11*).

The reduction of *B. vulgatus* in the presence of helminths could be mediated indirectly through alterations to the gut microbiota downstream of the type 2 response. Cohousing mice allows for coprophagic transmission of microbial populations without transfer of parasites, because the worms are not sexually mature until ~35 days postinfection and eggs require several weeks for germination (*12*). We found that uninfected *Nod2*$^{-/-}$ mice cohoused with *T. muris*–infected *Nod2*$^{-/-}$ mice showed a similar decrease in *B. vulgatus* colonization (Fig. 3A and fig. S8A). This reduction in *B. vulgatus* levels was not observed in uninfected *Nod2*$^{-/-}$ mice when they were instead cohoused with *T. muris*–infected WT mice (fig. S8, B and C). 16*S* ribosomal DNA sequencing analysis of stool samples indicated that the alterations to microbial community compositions are different for *T. muris*–infected WT and *Nod2*$^{-/-}$ mice (Fig. 3B), which may reflect different intestinal responses between WT and *Nod2*$^{-/-}$ mice (Fig. 2E). Whereas infected WT mice have reduced alpha diversity, as previously reported (*13*, *14*), *Nod2*$^{-/-}$ mice increased their alpha diversity at day 21 postinfection (fig. S8D). The most significantly reduced bacterial taxa in infected *Nod2*$^{-/-}$ mice were the *Prevotella* and *Bacteroides* genera (belonging to the order Bacteroidales), and the Lachnospiraceae family of the order Clostridiales was the most significantly increased (Fig. 3C). The increase in Clostridiales was less evident in WT mice (Fig. 3B), which potentially explains why cohousing *Nod2*$^{-/-}$ mice with *T. muris*–infected WT mice was not effective in reducing the *B. vulgatus* burden. The expansion of Clostridiales was also observed in the stool of uninfected *Nod2*$^{-/-}$ mice treated with rIL-13 or rIL-4 (Fig. 3D and fig. S8E). The expansion of Clostridiales was even more pronounced among tissue-associated bacteria in the small intestine after infection with *T. muris* or *H. polygyrus* (fig. S8, F and G). Thus, helminth infection and type 2 cytokines inhibit *B. vulgatus* and expand Clostridiales strains.

To determine whether Clostridia can directly inhibit *B. vulgatus*, we inoculated *Nod2*$^{-/-}$ mice with a mixture of *Clostridium* clusters IV, XIVa, and XVIII and Erysipelotrichales strains isolated from human feces (*15*). Repetitive gavaging of *Nod2*$^{-/-}$ mice with this mixture, but not sterile broth or an equivalent number of *Lactobacillus johnsonii* [a host-interactive commensal bacterium (*16*)], led to a decrease in *B. vulgatus* colonization over time (Fig. 3E). The addition of mucin to anaerobic cultures accelerates the growth of all three representative Clostridia strains tested, but not *B. vulgatus* (Fig. 3, F and G, and fig. S8, H and I), which suggests that increased mucus production by goblet cells may alter the intestinal environment to favor Clostridiales. Hence, our results indicate that in *Nod2*$^{-/-}$ mice, the mucus response associated with type 2 immunity during helminth infection expands Clostridia strains that can inhibit colonization of *B. vulgatus*.

Inflammatory bowel disease is less prevalent in regions where helminth colonization is endemic. We previously found that helminth-colonized individuals among indigenous populations in Malaysia, known as the Orang Asli, have higher microbial diversity than helminth-negative individuals (*17*). We compared individuals living in urbanized Kuala Lumpur with rural Orang Asli of the Temuan subtribe from a village 40 km away (5.3% versus 96% of individuals colonized by intestinal helminths, respectively) (table S2). People living in Kuala Lumpur predominantly cluster in a group driven by the abundance of a single *Bacteroides* operational taxonomic unit (OTU) (TaxID 3600504), which is less widespread in the Orang Asli (Fig. 4, A and B). In contrast, the helminth-positive Orang Asli people fall into

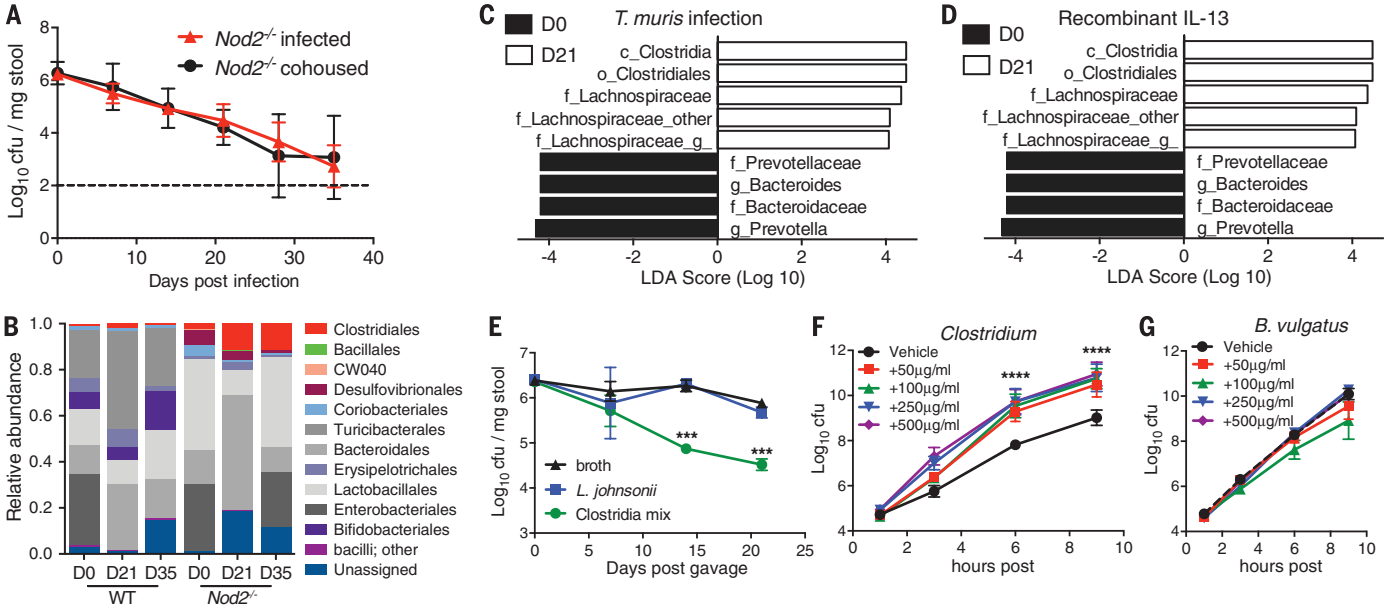

Fig. 3. Inhibition of *B. vulgatus* is associated with expansion of Clostridiales after helminth infection. (**A**) Quantification of *B. vulgatus* in stool harvested from uninfected and *T. muris*–infected *Nod2*$^{-/-}$ mice cohoused for the duration of the experiment ($n \geq 4$). (**B**) Relative abundance of taxonomic groups in response to *T. muris* infection in the stool of WT and *Nod2*$^{-/-}$ mice, as determined by 16*S* sequencing ($n \geq 5$ per genotype). (**C**) Supervised analysis of 16*S* sequencing data with LDA effect size (LEfSe), comparing *Nod2*$^{-/-}$ mice at D0 and D21 postinfection with *T. muris* using an LDA threshold score of 4 ($n \geq 5$). (**D**) LEfSE analysis to determine alterations to the stool microbiota after recombinant IL-13 treatment of *Nod2*$^{-/-}$ mice using an LDA threshold score of 4 ($n \geq 5$). (**E**) Quantification of *B. vulgatus* in stool harvested from *Nod2*$^{-/-}$ mice gavaged with sterile broth, *L. johnsonii*, or a mix of 17 Clostridiales and Erysipelotrichales strains ($n \geq 3$). (**F** and **G**) Quantification of *Clostridium* species (Clostridiales 28) (F) or *B. vulgatus* (G) in the presence of varying concentrations of pig intestinal mucin or vehicle in the culture media. ***$P <$ 0.001; ****$P < 0.0001$ by ANOVA, with Holm-Sidak multiple comparisons test for (E) and (F). Data are represented as mean ± SEM (error bars) from at least two independent experiments.

Downloaded from http://science.sciencemag.org/ on April 28, 2016

a second group characterized by *Faecalibacterium* and *Prevotella* (Fig. 4A). This division between the microbiota dominance of urban and rural populations is also observed in other Asian countries (*18*).

To control for factors other than helminth colonization (e.g., diet), we analyzed stool samples collected from the Orang Asli before and after deworming treatment with albendazole (fig. S9, A and B, and table S3). Alpha diversity of microbial communities was significantly reduced after treatment (Fig. 4F and fig. S9, C and D). We used the linear discriminant analysis (LDA) effect size (LEfSe) algorithm to show that Clostridiales was the most significantly reduced order, whereas Bacteroidales (*Prevotella*) was significantly expanded after treatment (Fig. 4, C to E, and fig. S9E). Using the egg-burden data, we combined centered log-ratio transformation with partial least squares regression to examine within-subject changes, incorporating a repeated measures design (*19*). The resulting model showed that posttreatment intraindividual changes in *Trichuris trichiura* egg burden are strongly associated with a small set of bacterial taxa, independent of age and gender (Fig. 4G; fig. S10, A to C; and table S4). Specifically, *Dialister* and *Coprococcus* are two members of the order Clostridiales that are positively associated with changes in egg burden, whereas the Bacteroidales species *Prevotella* and another OTU are negatively associated (Fig. 4H and fig. S10D). Individuals without reduced egg burden did not show these microbiome changes, indicating that these findings are unlikely to be due to nonspecific effects of albendazole treatment (fig. S10, E to G). Overall, these data support our hypothesis that helminth infection promotes the expansion of Clostridiales communities that outcompete Bacteroidales communities, although we did not examine the T_H2 response. Finally, we applied a method [sparse inverse covariance estimation for ecological association inference (SPIEC-EASI)] for inference of microbial ecological networks (*20*) to publicly available human microbiome data sets consisting of healthy U.S. residents (Human Microbiome Project and American Gut Project) and pediatric IBD patients (RISK cohort) (*21*–*23*) and found that the antagonistic relationship between Clostridiales and Bacteroidales is the most consistently observed negative relationship (Fig. 4, I and J, and fig. S11).

In this study, Clostridiales are an example of defensive symbionts that display an antagonistic interaction with another common commensal bacteria (Bacteroidales), which we consistently observed in all human gut microbiome data sets. Bacteroidales are pathogenic only in susceptible *Nod2*-deficient hosts, and this competition reverses disease pathologies. Many Crohn's disease patients do not carry *NOD2* variants and, hence, may not respond to helminths, which have failed in clinical trials. Helminths may be beneficial

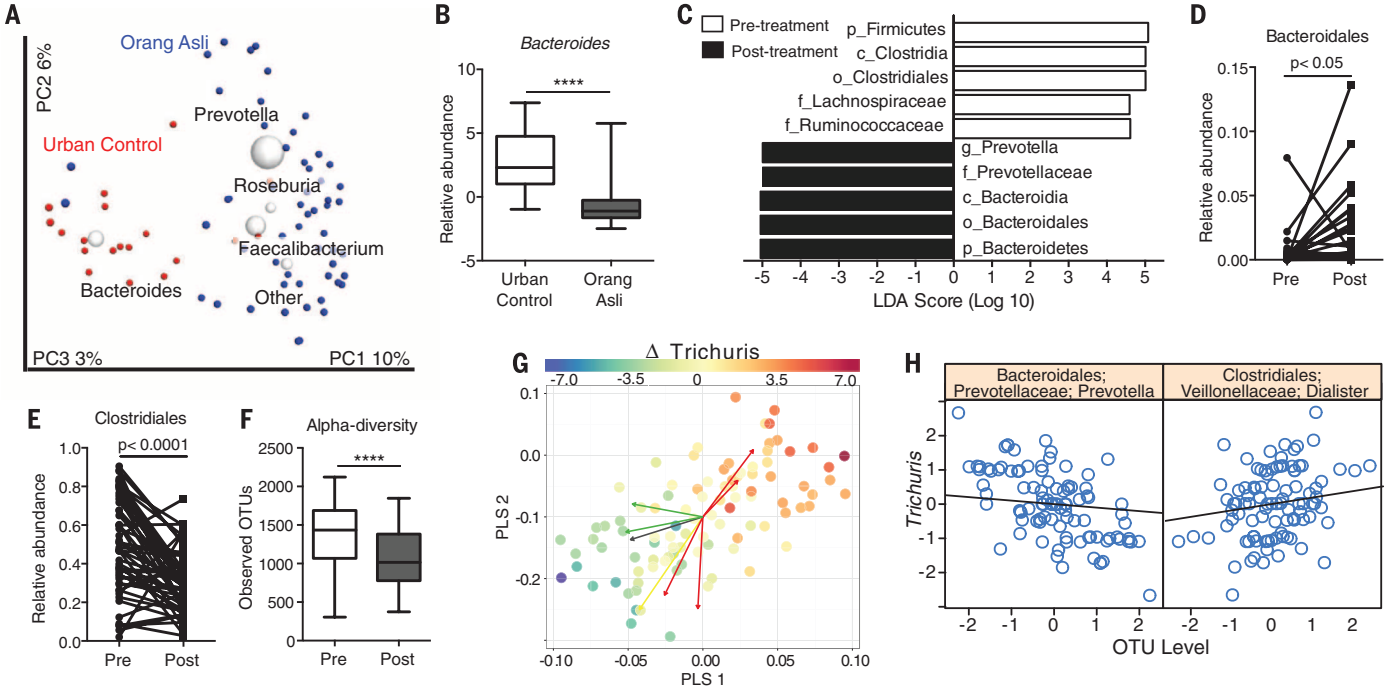

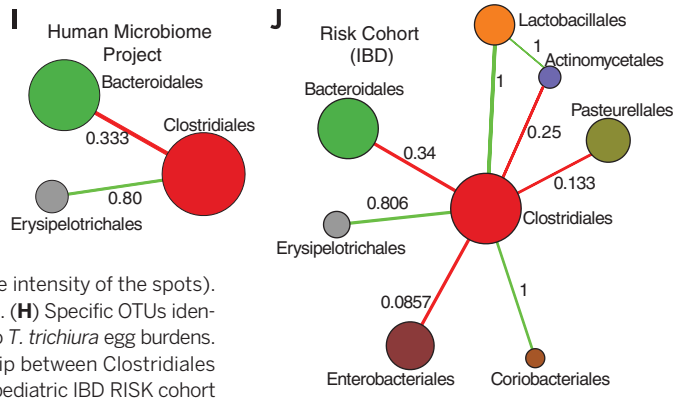

Fig. 4. Helminth colonization in humans is associated with a decrease in Bacteroidales and an increase in Clostridiales levels. (**A**) Beta diversity plots of gut microbiota from urban controls in Kuala Lumpur (red dots) and the Orang Asli (blue dots). (**B**) Relative abundance of a dominant *Bacteroides* OTU in the Orang Asli and urban controls. (**C** to **F**) Supervised LEfSE analysis (C), relative abundance of Bacteroidales (D) and Clostridiales (E), and alpha diversity as observed OTUs (F) of the Orang Asli stool microbiota before and after treatment with albendazole (n = 19 for urban controls and 55 Orang Asli; n = 53 for deworming experiments). (**G**) Partial least squares regression biplots examining within-subject variances with repeated measures design to identify bacterial taxa associated with *T. trichiura* worm burden (illustrated by the intensity of the spots). Red arrows represent Clostridiales taxa; green arrows denote Bacteroidales taxa. (**H**) Specific OTUs identified to be positively (*Dialister*) or negatively (*Prevotella*) associated with changes to *T. trichiura* egg burdens. (**I** and **J**) Microbial network inference demonstrating an antagonistic relationship between Clostridiales and Bacteroidales communities from the Human Microbiome Project (I) and the pediatric IBD RISK cohort (J). The node diameter is proportional to the geometric mean of the OTU's relative abundance. Numerical values on the edges represent the fraction of edges that are either majority-positive (green) or majority-negative (red). Also see fig. S10. ****P < 0.0001 by unpaired t test in (B) and paired t test in (D) to (F).

Downloaded from http://science.sciencemag.org/ on April 28, 2016

only in patients with *NOD2* variants or proinflammatory *Bacteroidales* species. We propose that certain individuals may be more susceptible to deleterious consequences of a changing microbial environment, and an understanding of the contribution of genetic and environmental factors toward the development of inflammatory diseases is essential to devise therapeutic strategies that consider the heterogeneity of etiologies.

REFERENCES AND NOTES

1. Y. Belkaid, T. W. Hand, *Cell* **157**, 121–141 (2014).
2. J. V. Weinstock, D. E. Elliott, *Inflamm. Bowel Dis.* **15**, 128–133 (2009).
3. N. Kamada, G. Núñez, *Gastroenterology* **146**, 1477–1488 (2014).
4. J. Jaenike, R. Unckless, S. N. Cockburn, L. M. Boelio, S. J. Perlman, *Science* **329**, 212–215 (2010).
5. C. G. Buffie *et al*., *Nature* **517**, 205–208 (2015).
6. D. Ramanan, M. S. Tang, R. Bowcutt, P. Loke, K. Cadwell, *Immunity* **41**, 311–324 (2014).
7. I. Cleynen *et al*., *Lancet* **387**, 156–167 (2016).
8. M. M. Hunter *et al*., *Gastroenterology* **138**, 1395–1405 (2010).
9. T. Ziegler *et al*., *J. Immunol.* **194**, 1555–1564 (2015).
10. L. Hang *et al*., *J. Immunol.* **191**, 1927–1934 (2013).
11. M. M. Zaiss *et al*., *Immunity* **43**, 998–1010 (2015).
12. J. E. Klementowicz, M. A. Travis, R. K. Grencis, *Semin. Immunopathol.* **34**, 815–828 (2012).
13. J. B. Holm *et al*., *PLOS ONE* **10**, e0125495 (2015).
14. A. Houlden *et al*., *PLOS ONE* **10**, e0125945 (2015).
15. K. Atarashi *et al*., *Nature* **500**, 232–236 (2013).
16. R. D. Pridmore *et al*., *Proc. Natl. Acad. Sci. U.S.A.* **101**, 2512–2517 (2004).
17. S. C. Lee *et al*., *PLOS Negl. Trop. Dis.* **8**, e2880 (2014).
18. J. Nakayama *et al*., *Sci. Rep.* **5**, 8397 (2015).
19. Materials and methods are available as supplementary materials on *Science* Online.
20. Z. D. Kurtz *et al*., *PLOS Comput. Biol.* **11**, e1004226 (2015).
21. D. Gevers *et al*., *Cell Host Microbe* **15**, 382–392 (2014).
22. D. Gevers *et al*., *PLOS Biol.* **10**, e1001377 (2012).
23. "Preliminary characterization of the american Gut population" (Technical Report, American Gut Project, 2014); www.microbio.me/AmericanGut/static/img/mod1_main.pdf.

ACKNOWLEDGMENTS

We thank D. Artis for seed stock of *T. muris*, H. Silva for assistance with flow cytometry panels, B. Zeck and L. Chiriboga for assistance with immunohistochemistry, and New York University School of Medicine Flow Cytometry and Cell Sorting Center, Genomics Core, and Immunohistochemistry Core (supported in part by NIH grants P30CA016087 and UL1 TR00038). The data presented in this manuscript are tabulated in the main paper and in the supplementary materials. RNA-seq data have been made publicly available and can be accessed using the Gene Expression Omnibus accession number GSE76504. Fastq files and corresponding mapping files for 16S sequencing data are available on request. Clostridia strains derived from human microbiota are available from K.H. under a material transfer agreement with RIKEN. K.H. is an inventor on patent applications (U.S. 14/362,097, PCT/JP2012/007687) filed by the University of Tokyo, related to the human-derived Clostridia, and is a scientific adviser to Vedanta Biosciences. P.L., K.C., D.R., and R.B. are inventors on a patent application filed by New York University, related to the studies reported here. This work was supported by NIH grants DK103788 (K.C. and P.L.), DK093668 (K.C.), HL123340 (K.C.), AI093811 (P.L.), AI007180 (Z.D.K. and M.J.B.), DK090989 (Z.D.K. and M.J.B.), and AI107588 (W.C.G.); the Broad Medical Research Program (P.L.); the Kevin and Marsha Keating Family Foundation (P.L.); The MCJ Amelior Foundation (W.C.G.); NIH National Center for Advancing Translational Sciences grant UL1 TR000038 (K.C. and P.L.); a philanthropic contribution from B. Levine (K.C. and P.L.); and University of Malaya–Ministry of Education HIR grant UM.C/625/HIR/MOE/MED/23 (Y.A.L.L. and P.L.). K.C. is a Burroughs Wellcome Fund Investigator in the Pathogenesis of Infectious Diseases.

SUPPLEMENTARY MATERIALS

www.sciencemag.org/content/352/6285/608/suppl/DC1
Materials and Methods
Figs. S1 to S11
Table S1 to S4
References (*24*–*48*)

25 August 2015; accepted 21 March 2016
Published online 14 April 2016
10.1126/science.aaf3229

Downloaded from http://science.sciencemag.org/ on April 28, 2016

Too young to win a prize
in Stockholm this December?

We don't think so.

Science & SciLifeLab
PRIZE
FOR YOUNG SCIENTISTS

Get published in *Science* and win $30,000 USD. Enter today: www.sciencemag.org/scilifelabprize

Cell and Molecular Biology | Ecology and Environment | Genomics and Proteomics | Translational Medicine

Science
AAAS

Knut och Alice Wallenbergs Stiftelse

SciLifeLab

There's only one Stericup® filter.

Don't be fooled.

CAUTION:

- Sterile filters are posing as high-quality Stericup® filters, but are rather thinly disguised.
- These filters may exhibit clogging, loss of volume and unwanted binding of serum proteins and other additives.
- Victims report anxiety due to potential damage to cell health.

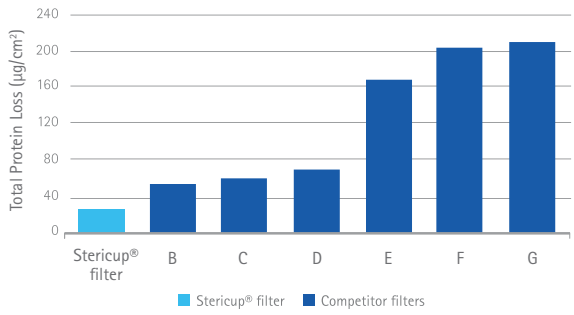

Protein Binding Performance

Don't be fooled – EMD Millipore's history of membrane technology and filter device engineering is unmatched.

View more data and place an order for the one and only true **Stericup® filter** at www.emdmillipore.com/oneStericup

EMD Millipore is a division of Merck KGaA, Darmstadt, Germany

EMD Millipore, the M logo and Stericup are registered trademarks of Merck KGaA, Darmstadt, Germany.
© 2015 EMD Millipore Corporation, Billerica, MA, USA. All rights reserved. BS GEN-15-11097 03/2015

ADVERTISEMENT

2016 Cottrell Scholars

Through its Cottrell Scholar program, Research Corporation for Science Advancement nurtures outstanding teacher-scholars recognized for innovative, high-quality research as well as academic leadership skills. In addition to the 24 new scholars awarded $100,000 each this year, two accomplished Cottrell Scholars have received RCSA's TREE Award (Transformational Research and Excellence in Education). The TREE Award celebrates integration of outstanding research and science education at America's universities and colleges.

2016 Cottrell Scholar Awardees

NANDINI ANANTH
Assistant Professor of Chemistry, Cornell University
Quantum Dynamic Investigations of Photo-induced Electron Transfer Catalyzed by Transition Metal Complexes

JOHN M. ANTOS
Assistant Professor of Chemistry, Western Washington University
Structural Characterization of Substrate Promiscuity in Bacterial Sortases

TAMARA BOGDANOVIC
Assistant Professor of Physics, Georgia Institute of Technology
Shedding Light on Supermassive Black Holes

EVA-MARIA SCHOETZ COLLINS
Assistant Professor of Physics, University of California, San Diego
Unraveling the Role of Mechanics for Tissue Self-organization In Vivo

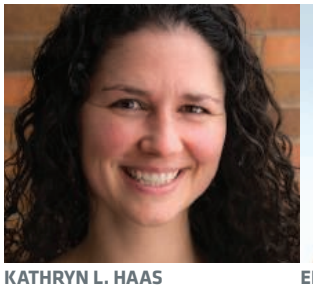

KATHRYN L. HAAS
Assistant Professor of Chemistry, Saint Mary's College, Indiana
Transporting Cu(I) as Cargo and Using Cu(III) as a Killer Cofactor

ELIZA KEMPTON
Assistant Professor of Physics, Grinnell College
Atmospheric Structure and Emission Spectrum Calculations for Extrasolar Super-Earths: Looking Toward JWST and Beyond

DUŠAN KEREŠ
Assistant Professor of Physics, University of California, San Diego
Using Cosmological Hydrodynamic Simulations to Constrain Evolution of Galaxies and Their Gaseous Halos

DMYTRO KOSENKOV
Assistant Professor of Chemistry, Monmouth University
Exciton Energy Transfer in Light Harvesting Proteins with Covalently Bound Pigments: The Role of Molecular Vibrations

WILLIAM C. K. POMERANTZ
Assistant Professor of Chemistry, University of Minnesota, Twin Cities
Fluorinated Peptides and Proteins for ^{19}F MRI and Integrated Research Experiences in an Organic Chemistry Lab Course

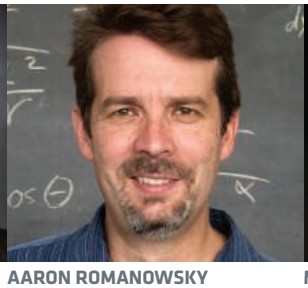

AARON ROMANOWSKY
Assistant Professor of Physics, San Jose State University
The Nature and Nurture of Galaxies: Dynamics, Dark Matter, and Data Mining

MICHAEL J. ROSE
Assistant Professor of Chemistry, University of Texas at Austin
Imparting Precious Metal Properties to First-Row Metals with Heavy Atom Ligands

SCOTT K. SHAW
Assistant Professor of Chemistry, University of Iowa
Characterization and Control of Molecular Architectures within Thin Fluid Films

2016 TREE Awardees

RIGOBERTO HERNANDEZ
Chemistry, Georgia Institute of Technology, Cottrell Scholar 1999

VINCENT ROTELLO
Chemistry, University of Massachusetts, Amherst, Cottrell Scholar 1996

"RCSA believes the right combination of high-caliber research integrated with modern, interactive educational tools creates the perfect environment for scientific breakthroughs and outstanding learning outcomes for the next generation of U.S. scientists."

Robert Shelton, President, Research Corporation for Science Advancement

JAHAN DAWLATY
Assistant Professor of Chemistry,
University of Southern California
A New Handle in Solar-to-Fuel Light Harvesting: Creating Protons Where They are Most Needed

RAFAEL M. FERNANDES
Assistant Professor of Physics,
University of Minnesota, Twin Cities
A Tale of Two States: Interplay between Magnetism and Superconductivity in Quantum Materials

SERGEY FROLOV
Assistant Professor of Physics,
University of Pittsburgh
Experimental Investigation of One-Dimensional Topological Phases

SHARON GERBODE
Assistant Professor of Physics,
Harvey Mudd College
Interactions between Impurities and Dislocations in Small Colloidal Crystals

AARON LECONTE
Assistant Professor of Chemistry,
The Claremont Colleges
Biochemical Characterization and Engineering of Luciferases through Statistical Coupling Analysis

THOMAS MAIMONE
Assistant Professor of Chemistry,
University of California, Berkeley
Redesigning Natural Products for the Treatment of Human Disease

BRENT C. MELOT
Assistant Professor of Chemistry,
University of Southern California
Design of Safe and Sustainable Materials to Enable Large-Scale Energy Storage

MAIKEN H. MIKKELSEN
Assistant Professor of Physics,
Duke University
Exploring the Interplay between Nanoscale Design and Optical Properties of Materials: A Research and Educational Approach

LEVI STANLEY
Assistant Professor of Chemistry,
Iowa State University
Catalyst Design and Development to Unlock the Synthetic Potential of Olefin Hydroacylation Reactions

LAUREN WATERS
Assistant Professor of Chemistry,
University of Wisconsin, Oshkosh
Manganese Homeostasis in Bacteria: Characterization of a Mn-Regulated Small Protein and Identification of Novel Mn Exporters

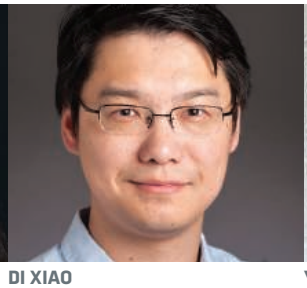

DI XIAO
Assistant Professor of Physics,
Carnegie Mellon University
Topological Excitonics in Gapped Dirac Materials

YAN YU
Assistant Professor of Chemistry,
Indiana University at Bloomington
Exploiting Nanomaterials to Unravel Trafficking Inside Cells

For additional information visit
www.rescorp.org or call 520.571.1111.

RESEARCH CORPORATION
for SCIENCE ADVANCEMENT
A foundation dedicated to science since 1912.

eppendorf & Science

PRIZE FOR NEURO BIOLOGY

2015 Winner
Shigeki Watanabe, Ph.D.
Johns Hopkins University
For research on synaptic vesicle endocytosis

Application Deadline
June 15, 2016

Call for Entries

Eppendorf & Science Prize for Neurobiology
The annual Eppendorf & Science Prize for Neurobiology is an international award which honors young scientists for their outstanding contributions to neurobiological research based on methods of molecular and cell biology. The winner and finalists are selected by a committee of independent scientists, chaired by Science's Senior Editor, Dr. Peter Stern. Researchers who are not older than 35 years are invited to apply.

You could be next to win this prize and to receive
> Prize money of US$25,000
> Publication of your work in Science
> Full support to attend the Prize Ceremony held in conjunction with the Annual Meeting of the Society for Neuroscience in the USA
> An invitation to visit Eppendorf in Hamburg, Germany

It's easy to apply!
Learn more about the Prize and its past winners at:

www.eppendorf.com/prize

eppendorf Science AAAS

AAAS® and Science® are registered trademarks of the American Association for the Advancement of Science, USA. Eppendorf® and the Eppendorf logo are registered trademarks of Eppendorf AG, Germany. U.S. Design Patents are listed on www.eppendorf.com/ip. All rights reserved, including graphics and images. Copyright © 2016 by Eppendorf AG. Kurstin Roe Photography.

BOYALIFE

Science & Science Translational Medicine Award in Stem Cells and Regenerative Medicine

The first global award for stem cells and regenerative medicine

Stem cells and regenerative medicine is the new frontier in life sciences. *Boyalife, Science, and Science Translational Medicine* jointly establish a global award to recognize and reward scientists in the fields of stem cells and/or regenerative medicine with a focus on developing cell-based treatments for cancer, degenerative disorders, immunotherapy and stem cells transplantation.

The 2016 award ceremony will be held in San Francisco, on 23rd June, 2016.

The winners will receive:

☆A Grand Prize of $25,000 and a Runner-Up Prize of $5,000 will be awarded.

☆The Grand Prize Winning Essay will be published in Science; a brief abstract of the Runner-Up Essay will be published in Science.

Learn more about the Prize,
visit : *www.sciencemag.org/prize/boyalife/rules*

BOYALIFE Stem Cell

Science AAAS

Science Translational Medicine AAAS

myIDP:
A career plan customized for you, by you.

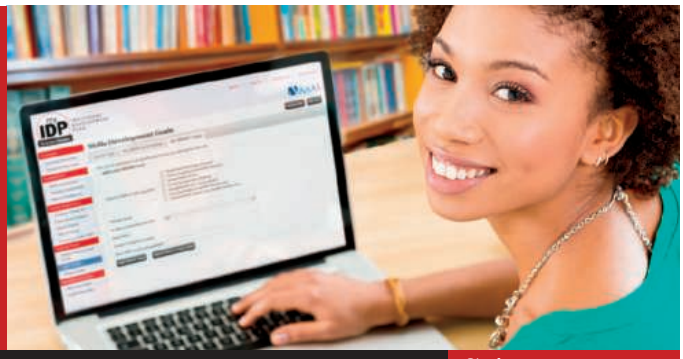

For your career in science, there's only one Science

my IDP
Science Careers

Recommended by leading professional societies and the NIH

Features in myIDP include:

- Exercises to help you examine your skills, interests, and values
- A list of 20 scientific career paths with a prediction of which ones best fit your skills and interests
- A tool for setting strategic goals for the coming year, with optional reminders to keep you on track
- Articles and resources to guide you through the process
- Options to save materials online and print them for further review and discussion
- Ability to select which portion of your IDP you wish to share with advisors, mentors, or others
- A certificate of completion for users that finish myIDP.

Visit the website and start planning today!
myIDP.sciencecareers.org

Science Careers In partnership with:

FASEB · UCSF University of California San Francisco · Medical College of Wisconsin · Burroughs Wellcome Fund

AAAS Travels

Kashmir & Ladakh
September 11-23, 2016

Kashmir has long been legendary as a destination of travelers from India and beyond. Ladakh is a trans-Himalayan kingdom that retains a strong Tibetan Buddhist identity with alpine desert valleys, watered by glacial melt where surrounding peaks display an astonishing geology. Join Dr. Chris Carpenter for an amazing and intriguing adventure! $5,295 pp + air.

For a detailed brochure, call (800) 252-4910
All prices are per person twin share + air

Betchart Expeditions Inc.
17050 Montebello Rd, Cupertino, CA 95014
Email: AAASInfo@betchartexpeditions.com
www.betchartexpeditions.com

LIFE SCIENCE TECHNOLOGIES
GENERAL LAB EQUIPMENT

Adding efficiency to general lab equipment

Sometimes the latest equipment in a laboratory, say a next-generation sequencer, grabs lots of attention, but it's the workhorses—centrifuges, hoods, freezers, incubators, and more—that keep experiments and workflows moving. These general lab tools often determine how smoothly and cost effectively a lab runs.

See the full story on page 614.

Upcoming Features
Microscopy—May 13
Exosomes/Microvesicles—June 10
Proteomics—July 15

Produced by the *Science*/AAAS Custom Publishing Office

Don't miss the debut of *Science Immunology*.

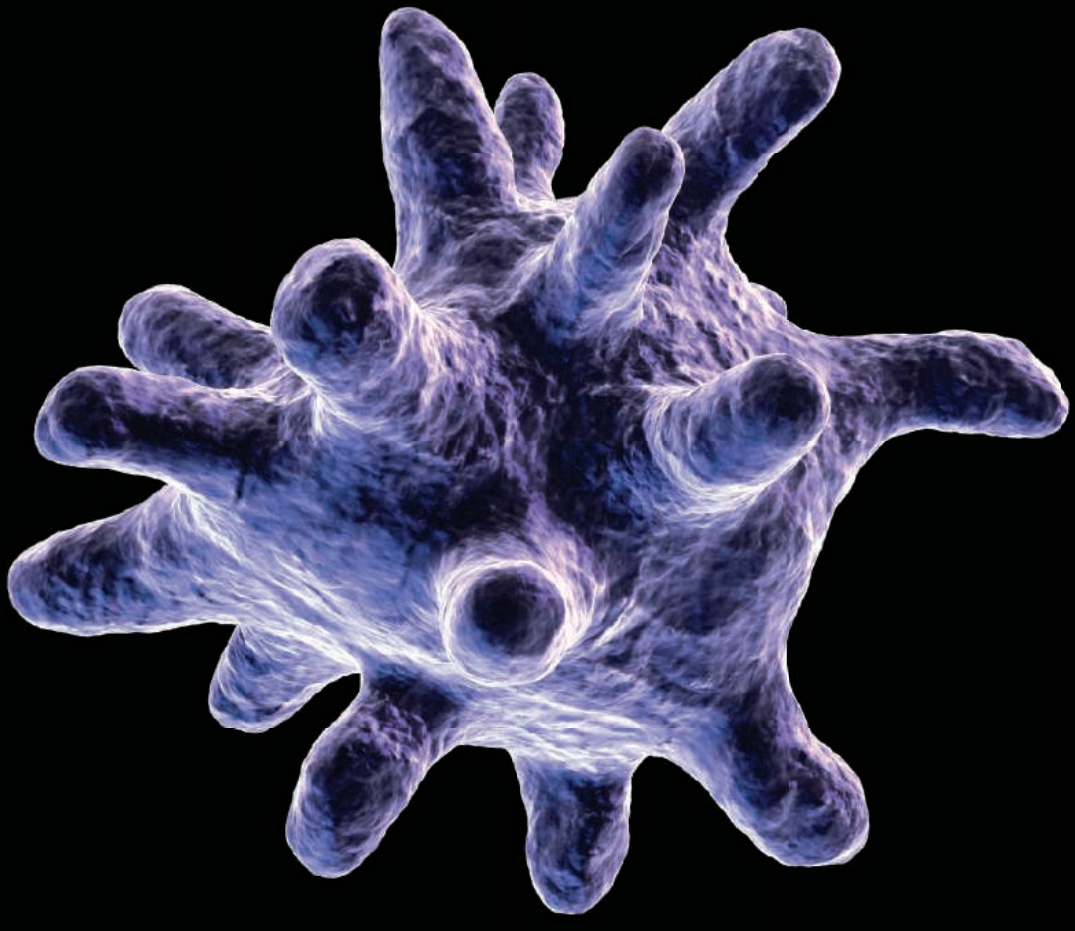

Image: Eraxion / iStockPhoto

NOW ACCEPTING PAPERS

Science is expanding its reach into immunology—now offering the newest online-only, weekly journal in the *Science* family of publications. *Science Immunology* will provide original, peer-reviewed research articles that report critical advances in all areas of immunological research, including studies that provide insight into the human immune response in health and disease.

Be a part of the *Science Immunology* debut issue publishing Summer 2016!

Submit your manuscript today at **ScienceImmunology.org.**

Science Immunology

AAAS

Adding efficiency to general lab equipment

Sometimes the latest equipment in a laboratory, say a next-generation sequencer, grabs lots of attention, but it's the workhorses—centrifuges, hoods, freezers, incubators, and more—that keep experiments and workflows moving. These general lab tools often determine how smoothly and cost effectively a lab runs. In large part, the results can be measured in one word—efficiency. In this case, efficiency means saving energy and time. **By Mike May**

General equipment makes up a lab's foundation. Without these crucial tools, few experiments could be performed, because nearly every research project depends on one or more of such technologies. As fundamental elements of research, general lab equipment must also be efficient. "Energy efficiency in laboratory equipment is extremely important," says John Dilliott, energy manager at the **University of California, San Diego.** "It's a major, yet virtually untapped area." He mentions that **My Green Lab,** a California-based nonprofit, published a 2015 report estimating that there are more than 1.2 billion square feet of laboratory space in the United States. "These spaces are three to five times more energy intensive than office areas due to energy-intensive equipment, around-the-clock operations, 100 percent outside-air requirements, and high airflow rates," Dilliott says. "Not only does laboratory equipment consume a substantial amount of energy, but anyone who has ever been in a lab knows that the heat generated by lab equipment can lead to overcompensation by heating, ventilation, and air-conditioning systems, resulting in an additional increase in energy consumption."

By saving energy, it takes less capital to run a piece of equipment, and some of the most basic equipment consumes a lot of electricity. According to the website of the **International Institute for Sustainable Laboratories** (I^2SL) in Arlington, Virginia: "The energy used by [plug-in] equipment (e.g., freezers, autoclaves, centrifuges) constitutes from 10 to as much as 50 percent of the total energy use in a laboratory (not including associated cooling energy use)." I^2SL's web page adds, "Many scientists, laboratory managers, and laboratory design consultants are beginning to use energy efficiency as a selection criterion for laboratory equipment, and some manufacturers are starting to advertise the 'green features' of their products." In an effort to start a central database of energy-efficiency information, I^2SL created the Energy-Efficient Laboratory Equipment Wiki (http://scim.ag/EELEWiki).

When considering any technology upgrade for energy efficiency, scientists wonder about the payback: How long will it take to recoup the price of the new equipment through energy savings? "Payback is a difficult question to answer as it's dependent on the initial purchase price, the cost of energy, how the equipment is used, and the type of equipment that is being replaced," says Allison Paradise, executive director of My Green Lab. "In addition, so few studies have been done on energy consumption of laboratory equipment that it's often difficult to know, without metering, what the baseline energy consumption is of the existing equipment and what the energy consumption is of the new equipment." She adds, "Our nonprofit cofounded the Center for Energy Efficient Laboratories (CEEL) to address this specific need"—gathering real-world data on the energy used by general lab equipment. Only with those data in hand can scientists choose the most efficient devices.

Go with less flow

Of all of a lab's general equipment, fume hoods probably carry the most energy-inefficient reputation, and with good reason—at least for older equipment. "Market Assessment of Energy Efficiency Opportunities in Laboratories," prepared by Paradise, indicates that fume hoods consume far more energy than other standard pieces of equipment, more than twice as much as a –80°C freezer (when considering the highest end of the energy-consumption range for both hood and freezer), which is the second-highest energy consumer among a lab's general equipment. Other sources agree on the energy intensity of fume hoods. As noted by **Harvard University's Green Labs Program:** "Fume hoods are one of the most energy-intensive types of equipment in a laboratory environment, but significant savings can be achieved by keeping them closed when not in use." That advice works for a fume hood of any age.

Making a fume hood more energy efficient depends largely on how air flows through it. One solution is provided by **Labconco** in Kansas City, Missouri, whose three-speed blower on its fume hoods offers flow-rate options. "This came from market demand—people wanted to turn down the blower at night, like a night setback mode," says

PHOTO: © YENYU SHIH/SHUTTERSTOCK.COM

Upcoming Features

Microscopy—May 13 ■ *Exosomes/Microvesicles—June 10* ■ *Proteomics—July 15*

Beth Mankameyer, sales engineer at Labconco and certified as a Leadership in Energy and Environmental Design (LEED) Green Associate by the U.S. Green Building Council. "They wanted their hood to exhaust less volume while it was unoccupied at night."

The motor in a fume hood blower also matters. For example, Labconco's three-speed blower uses an electronically commutated motor, which is more energy efficient than a traditional alternating current (AC) motor.

The electronics that control a fume hood also play a part in its energy efficiency. At **TSI** in Shoreview, Minnesota, saving energy in a fume hood comes from a sophisticated controller. According to the company website, its fume-hood controller adjusts the flow velocity for containment and safety, but it also "reduces laboratory airflow usage, optimizing energy savings."

When it comes to a return on investment, a fume hood might make the best bet. "The three-speed blower can pay for itself in a very short amount of time," says Mankameyer, "not only because of reduced energy costs at the hood but because less air needs to be conditioned for the lab." The actual time of the payback depends on many factors, including the lab's heating, ventilation, and air conditioning system, and how much a fume hood gets used, among others. But no matter what, a more energy-efficient fume-hood system will save on operational costs.

Air movement also matters in incubators, where the air's composition comes into play. To keep an incubator effectively doing its job, the technology must include an easy way to decontaminate the device. In some incubators, that requires half a day of high heat. Instead, using a vapor hydrogen-peroxide method takes only four hours, says Kara Held, science director at **The Baker Company** in Sanford, Maine. That saves energy and time. So, as incubators reveal, the energy savings is not only about ordinary running, but also relates to the overall energy use for all operations of the technology.

For both hoods and incubators, modern versions provide forms of efficiency beyond saving energy. The three-speed fan can be set to automatically slow down during off hours, and some controls can do the same. That way, the lab manager can be sure of getting the best efficiency—in saving money and time. In addition, modern incubators, says Held, do a better job of controlling the conditions for cells. "You can find the optimal conditions, and they will stay there and not be affected by the external environment or room where the incubator is located." That's because of improved sensors that control more features, such as temperature, humidity, oxygen, and carbon dioxide. To ensure your cells experience the optimal conditions as much as possible, explains Held, be sure to check how long it takes an incubator to reestablish the internal conditions after opening the doors. If it takes 20 to 30 minutes, be aware that other incubators can do it faster—often in half that time.

Keep it cool

Many items in a lab, from reagents to cell lines, need to be kept cool, even frozen—sometimes deeply frozen. All freezers are big consumers of energy, some more than others. "Generally speaking, ultra-low temperature freezers, –80°C, are some of the largest consumers of energy in life science research labs," Dilliott says. "Individually, each freezer can consume as much energy as a single-family home, 20 to 25 kilowatt hours per day." As a general rule of thumb, Dilliott says, "It is worth noting that any piece of equipment that requires an operating set temperature or pressure and is kept on 24/7 is likely to consume a lot of energy."

"Fume hoods are one of the most energy-intensive types of equipment in a laboratory environment, but significant savings can be achieved by keeping them closed when not in use."

For lab-freezer shoppers, a new one can be much more efficient, but that's not always the case. "It depends on the freezer," Dilliott says. "Several models have been designed with energy efficiency in mind . . . often consuming 60 percent less energy than freezers using older technology." He adds, "These numbers are supported by the long-term metering data collected at the University of California, San Diego and at other organizations across the country."

Depending on the lab in question, upgrading a freezer could be even more efficient than expected. For example, Dilliott says, "The savings realized by UC San Diego's replacement of old freezers with more energy-efficient ones resulted not only in an operational cost reduction for the university, but also in additional rebates from the utility company."

Some vendors do focus on overall energy efficiency in freezers. Santanu Das from technical product support at **VWR International** in Radnor, Pennsylvania, says, "VWR General-Purpose Upright Freezers, which maintain –20 or –30°C, are available with manual or automatic defrost and are designed to provide dependable, energy-efficient performance." He adds that they are manufactured with chlorofluorocarbon (CFC)-free high-density urethane cont.>

PHOTO: © POLAKPHOTO/SHUTTERSTOCK.COM

Featured Participants

Harvard University's Green Labs Program
green.harvard.edu/programs/green-labs

IKA Works
www.ika.com

International Institute for Sustainable Laboratories
www.i2sl.org

Labconco
www.labconco.com

My Green Lab
www.mygreenlab.org

The Baker Company
www.bakerco.com

Thermo Fisher Scientific
www.thermofisher.com

TSI
www.tsi.com

University of California, San Diego
ucsd.edu

VWR International
us.vwr.com

Additional Resources

Energy-Efficient Laboratory Equipment Wiki
labs21.lbl.gov/wiki/equipment

foam cabinet and door insulation to maintain temperature stability. Those features help to reduce the energy required by any freezer.

In Cambridge, Massachusetts, Harvard's Green Labs Program goes beyond the freezer technology and reveals energy-saving tips in using freezers. For example, this program recommends keeping your freezer organized so that you know where to look when you open the door and will thus open it less and for less time. As the program's website states: "By limiting door openings you will save energy and increase the life of your freezer."

VWR freezers can also be easier to organize and access. In describing VWR's ultra-low temperature freezers, Das says, "Four gasketed inner doors are standard, creating four compartments that can be subdivided with adjustable interior shelves." That design allows for better organization and easier location of items, which should lead to less time with the door open.

To help vendors design better freezers in the future, the CEEL is collecting energy-use data on existing –80°C freezers. Scientists can help by taking part in a 10-minute survey (https://www.surveymonkey.com/r/CEEL_ULTfreezers). "All responses will remain completely confidential," Paradise says. "You will not be contacted by any vendors as a result of your participation."

Other changes can make your existing freezer use less energy. With a –80°C freezer, Paradise says, "Changing the set point to –70°C can save 20 to 30 percent, depending on the age of the freezer and its baseline energy consumption, according to the U.S. Department of Energy." She adds, "My Green Lab has a saying that '–70 is the new –80,' and we like to encourage people to chill up their freezers."

Simpler spinning

For some general laboratory equipment, the main improvement in efficiency comes from ease of use. That is the case with centrifuges.

"A centrifuge is a fundamental piece of separation equipment," says Hugh Tansey, worldwide product director at **Thermo Fisher Scientific,** headquartered in Waltham, Massachusetts, "and scientists want it to be easy to use and be more productive." Today's centrifuges allow scientists to easily change the rotor to spin down mixtures in microtubes, microplates, cell-culture containers, and so on.

In some cases, efficiency comes from being sure that a centrifuge does what you need it to do. For example, Daniela Dockweiler, senior application specialist at **IKA Works** in Staufen, Germany, says, "Today's centrifuges provide constant speed while the rotor is attached on the drive shaft, even if there is a higher density of a liquid." She adds that this consistency provides "reproducible results for all samples in one experiment."

Some advances in centrifuges, like carbon-fiber rotors, also improve energy efficiency. "These are lightweight, corrosion-resistant, and durable, and enable much higher performance," says Tansey. "This rotor can spin up and down faster, so the centrifuge uses less energy."

Keep it organized

In almost any lab, the list of general equipment gets pretty long. That makes it complicated to figure out the best way to keep a lab efficient. Held once worked as the lab manager for a facility with 24 incubators. To keep everything organized, she recommends, "Build little zones into the lab, so that the equipment for one task is in the same area." Also, she suggests building a spreadsheet that includes all of the lab's equipment. That lets you keep track of what you have in the lab, as well as when it was purchased and serviced.

Staying organized also helps a lab manager decide when something should be replaced. When asked about how to make that decision for a piece of general lab equipment, Held says, "It depends on the lab's funding and what the equipment is being used for." She adds, "For very general equipment, you usually wait until it breaks and the cost of fixing it is close to the cost of buying a new one."

To keep a lab working as efficiently as possible, though, it's worth thinking about replacing general equipment earlier in some cases. For example, a new hood might soon save a lab more than it costs. Likewise, a new freezer might be easier to keep organized that an old one. In the end, the most efficient lab—in terms of energy and time—gets the most done.

Mike May is a publishing consultant for science and technology.

DOI: 10.1126/science.opms.p1600104

Blue LED Transilluminator

Over the last few years, the use of blue light illumination for the excitation of some dyes (including ethidium bromide) has increased. The most significant reasons for this are that blue light around 470 nm is "safe" and does not have the hazards associated with the use of ultraviolet (UV) illumination, and also that blue light does not damage the DNA sample. Herolab's four new models cover filter sizes from 11 cm × 14 cm up to a large 22 cm × 28 cm version, and use special filter glass for optimum blue light excitation. The illumination is provided by premium-quality blue light-emitting diodes (LEDs) that render a homogenous area of light because of the high-quality diffuser screen. This homogeneity is essential for ensuring evenly illuminated gels with good image quality and accuracy when undertaking analysis. Furthermore, the enhanced filter and lighting configuration ensures a reduced background signal, aiding the capture of high-contrast images that are ideal for publication purposes and for working in preparative modes.

Herolab
For info: +49-(0)-6222-5802-0
www.herolab.de

–70°C Walk-In Chamber

A revolutionary –70°C walk-in chamber, the Polar50 is a 50-m^3 chamber that offers customers from industry and academia a unique opportunity to store biological, pharmaceutical, and medical products at ultralow temperatures. This capability includes storage of cell lines/extracts, DNA/RNA, blood, tissue, and many other substances. The chamber provides –70°C storage capabilities with a +/–1% tolerance. This temperature is maintained by a purpose-designed, dual refrigeration system that provides 100% operating redundancy to ensure 24/7 compliance for a consistent and controlled environment. The Polar50 is available not only for outsourced storage, but is designed to allow easy installation into any existing stability suite, eliminating the need for multiple upright freezers and offering significant savings in power usage, floor space, and costs.

Source BioScience
For info: +44-(0)-115-973-9012
www.sourcebioscience.com

Thermal Mixer

The Heat Cool Thermal Mixer II has a large intuitive touchscreen, interchangeable auto-recognized blocks to fit most laboratory consumables, multiple modes for increased process performance, and a large and accurate temperature and mixing range. The Heat Cool Thermal Mixer II has up to five programmable timed steps to create unique temperature and mixing profiles. The parameters can be quickly changed for warming, cooling, or mixing of samples. Typical laboratory uses include extraction, expression, labeling, and purification and analysis of proteins, DNA, plasmids, RNA, from gels, magnetic beads, tissue, or biological samples. Cloning through vector ligation and insertion, host cell transformation, transfection, cell cultivation, and in vitro synthesis of proteins can be performed via this versatile instrument. General buffer and sample preparation, enzymatic reactions and digestion, nucleic acid purification, prep work for immune assays, and blots as well as time, temperature, mixing rate, and the operation mode can be tailored for the sample analysis process.

Boekel Scientific
For info: 800-336-6929
www.boekelsci.com

Filtered Chemical Workstations

Isola Series Filtered Chemical Workstations are the next advanced solution in ductless technology. These workstations are high-efficiency products that protect the end user and the environment from hazardous chemical fumes and vapors. Their key safety feature is the filtration matrix, which consists of three stages of filtration media that effectively adsorb and capture a wide range of contaminates. The Isola Filtered Chemical Workstation Series offers three models, providing customers a variety of options without compromising safety. The Isola VUE features a 360° clear viewing area, which makes it ideal for demonstration experiments. The Isola PRO is a polypropylene-filtered workstation, providing excellent chemical resistance for corrosive applications. The Isola EDGE offers a dual-wall, thermally fused solid polypropylene main chamber, allowing the installation of common laboratory fixtures and electrical outlets if needed.

Mystaire
For info: 877-328-3912
www.mystaire.com

Environmental Chambers

A new range of 230-V environmental chambers are designed to provide highly stable environmental conditions. There are two models available in the range: the wide temperature units with humidity control (available in 311 L and 821 L) and a heat-only model (available in 821 L) that is tailored for large-scale clinical applications and microbiology. For applications requiring close control of a CO_2 environment, there's an optional infrared CO_2 package available that can be added to the wide temperature model. The interior of the environmental chambers is designed for stability. The horizontal laminar airflow system enables ideal temperature uniformity and fast recovery rates, which provide an optimal growth and testing environment even with large product loads or heat-generating equipment. The environmental chambers feature a broad temperature range spanning from 0°C to 60°C, and the relative humidity is easily controlled to meet the needs of different applications.

Thermo Fisher Scientific
For info: 800-556-2323
www.thermoscientific.com

Electronically submit your new product description or product literature information! Go to www.sciencemag.org/about/new-products-section for more information.

Newly offered instrumentation, apparatus, and laboratory materials of interest to researchers in all disciplines in academic, industrial, and governmental organizations are featured in this space. Emphasis is given to purpose, chief characteristics, and availability of products and materials. Endorsement by *Science* or AAAS of any products or materials mentioned is not implied. Additional information may be obtained from the manufacturer or supplier.

want new technologies?

antibodies
apoptosis
biomarkers
cancer
cytometry
data
diseases
DNA
epigenetics
genomics
immunotherapies
medicine
microbiomics
microfluidics
microscopy
neuroscience
proteomics
sequencing
toxicology
transcriptomics

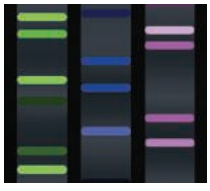

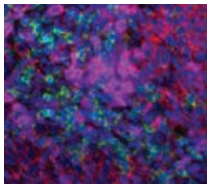

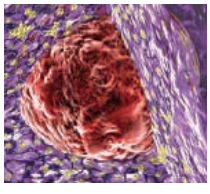

watch our webinars

Learn about the latest breakthroughs, new technologies, and ground-breaking research in a variety of fields. Our expert speakers explain their quality research to you and answer questions submitted by live viewers.

VIEW NOW!
webinar.sciencemag.org

Science
AAAS

Brought to you by the *Science*/AAAS Custom Publishing Office

@SciMagWebinars

NEW ENGLAND BioLabs® Inc.

Time for change.

Introducing Monarch™ Nucleic Acid Purification Kits

It's time to transform your DNA purification experience. NEB's Monarch Nucleic Acid Purification Kits are optimized for maximum performance and minimal environmental impact. With an innovative column design, buffer retention is prevented, eliminating risk of carryover contamination and enabling elution in smaller volumes. The result – highly pure DNA for your downstream applications.

Make the change and migrate to Monarch today.

Optimized design of Monarch Miniprep Columns

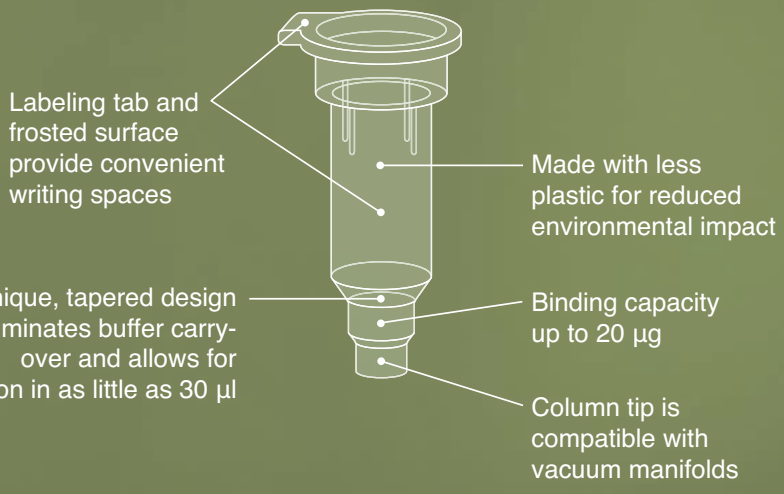

Request your free sample at **NEBMonarch.com**

NEW ENGLAND BIOLABS® and NEB® are registered trademarks of New England Biolabs, Inc.
MONARCH™ is a trademark of New England Biolabs, Inc.

Science Careers Advertising

For full advertising details, go to ScienceCareers.org and click For Employers, or call one of our representatives.

Tracy Holmes
Worldwide Associate Director
Science Careers
Phone: +44 (0) 1223 326525

THE AMERICAS

E-mail: advertise@sciencecareers.org
Fax: +1 (202) 289 6742

Tina Burks
Phone: +1 (202) 326 6577

Nancy Toema
Phone: +1 (202) 326 6578

Online Job Posting Questions
Phone: +1 (202) 312 6375

EUROPE / INDIA / AUSTRALIA / NEW ZEALAND / REST OF WORLD

E-mail: ads@science-int.co.uk
Fax: +44 (0) 1223 326532

Sarah Lelarge
Phone: +44 (0) 1223 326527

Kelly Grace
Phone: +44 (0) 1223 326528

Online Job Posting Questions
Phone: +44 (0) 1223 326528

JAPAN

Katsuyoshi Fukamizu (Tokyo)
E-mail: kfukamizu@aaas.org
Phone: +81 3 3219 5777

Hiroyuki Mashiki (Kyoto)
E-mail: hmashiki@aaas.org
Phone: +81 75 823 1109

CHINA / KOREA / SINGAPORE / TAIWAN / THAILAND

Ruolei Wu
E-mail: rwu@aaas.org
Phone: +86 186 0082 9345

All ads submitted for publication must comply with applicable U.S. and non-U.S. laws. *Science* reserves the right to refuse any advertisement at its sole discretion for any reason, including without limitation for offensive language or inappropriate content, and all advertising is subject to publisher approval. *Science* encourages our readers to alert us to any ads that they feel may be discriminatory or offensive.

ScienceCareers
FROM THE JOURNAL SCIENCE AAAS

ScienceCareers.org

hhmi | Howard Hughes Medical Institute

INTERNATIONAL RESEARCH SCHOLARS PROGRAM

Grants for Biomedical Research

The Howard Hughes Medical institute (HHMI) and philanthropic partners, the Bill & Melinda Gates Foundation, the Wellcome Trust, and the Calouste Gulbenkian Foundation, have created a new grant program to help develop scientific talent worldwide.

Application Deadline:
June 30, 2016, 3 p.m.
U.S. Eastern Time

Application information:
hhmi.org/IRS2017

hhmi | Howard Hughes Medical Institute

BILL & MELINDA GATES foundation

wellcome trust

CALOUSTE GULBENKIAN FOUNDATION

The International Research Scholars Program will select and support up to 50 outstanding early career scientists working in selected countries.

Grant Term and Award Amount
$250,000 in year 1; $100,000 each subsequent year

Application Deadline
June 30, 2016, **3 p.m.** U.S. Eastern Time

Application Information
hhmi.org/IRS2017

Successful applicants will have trained through the postdoctoral level in a vigorous basic research environment. Eligible candidates must have trained in the United States or United Kingdom at the doctoral, medical, or postdoctoral level. Applicants are expected to have outstanding scientific training records and exceptional potential for significant productivity and originality in their independent careers.

HHMI and its partners recognize that a supportive research environment is crucial to launching a successful research program, so awards will be made only to institutions that can clearly support the research activities of the grant recipient.

Eligibility Criteria
Applicants must:

- Hold a doctoral degree or medical degree and have completed postdoctoral research training
- Hold a full-time appointment as an independent scientist at a research-oriented university, medical school, or nonprofit institution in any eligible country
- Have received training at the doctoral, medical, or postdoctoral level in the US or UK for at least one year
- Have been the first or senior author on at least two peer-reviewed, English-language, original research publications
- Started their first independent research position on or after April 1, 2009
- Control their own research direction, laboratory space, and funding and devote most of their professional time to research, mentoring, and teaching; applicants must have no major administrative duties

Eligible Countries
This program is open to scientists working in all countries except G7 countries (Canada, France, Germany, Italy, Japan, United Kingdom and United States) and *countries identified by the US Department of Treasury, Office of Foreign Assets Control (OFAC) as being subject to comprehensive country or territory-wide sanctions or where current OFAC regulations prohibit U.S. persons or entities from engaging in the funding arrangements contemplated by this grant program. For this program, such sanctioned countries or territories currently include Iran, North Korea, Sudan, Syria, and the Crimea region of Ukraine*

Science Careers online @sciencecareers.org

Max Planck Institute for Terrestrial Microbiology

The Max Planck Institute for Terrestrial Microbiology (MPITerMic) announces the position of

Department Director

The MPITerMic is seeking an outstanding scientist to lead a department and establish a world-leading forward looking research programme in microbiology. We seek expressions of interest from or nominations of individuals with a high international reputation and a proven track record in research areas that complement, strengthen or expand the research agenda of the MPITerMic (for details, please see **http://www.mpi-marburg.mpg.de/**) and who are capable of inspiring the research of junior scientists including graduate students, postdoctoral fellows and group leaders. Excellent resources will be provided in terms of start-up funding, laboratory infrastructure, equipment and running costs. The appointed individual will also contribute to the scientific direction and management of the MPITerMic by working closely with the other three directors. The working language is English and qualified individuals of all nationalities will be considered.

Remuneration is internationally competitive and negotiable.

The Max Planck Society seeks to increase the number of women in those areas where they are underrepresented and therefore we explicitly encourage expressions of interest from and nominations of women. The Max Planck Society is committed to employing more disabled individuals and especially encourages them to express interest.

Both expressions of interest and nominations are welcome. Expressions of interest should contain a full CV including a complete list of publications, a brief summary of research accomplishments and a brief description of future goals. Further information can be obtained from the managing director Prof. Dr. Lotte Sogaard-Andersen. Expressions of interest and nominations should be sent by e-mail as a single pdf file to **director@mpi-marburg.mpg.de**

Zertifikat seit 2011 audit berufundfamilie

Expressions of interest and nominations should be received by **June 13th 2016**.

MAX-PLANCK-GESELLSCHAFT

Integrative Biology and Physiology

University of Minnesota Driven to Discover℠ Medical School

Tenure Track Associate/Full Professor Faculty Positions in Obesity, Metabolism and Diabetes

The Department of Integrative Biology and Physiology, University of Minnesota Medical School, seeks outstanding faculty candidates at the associate or full professor rank in the areas of metabolism, obesity and diabetes, with a strong emphasis on integrative physiology.

We offer a highly collaborative and diverse research environment, generous start-up, modern laboratory space and state-of-the-art core facilities. Successful candidates will have expertise that complements current faculty and be committed to excellence in education and have the opportunity to hire future faculty positions in their area of expertise. Further information can be found at http://physiology.med.umn.edu, and please contact **Cathy Kotz**, search committee chair, at **kotzx004@umn.edu** with additional questions.

Links to the Minnesota obesity, diabetes and metabolism community: http://www.mnoc.umn.edu, http://www.opc.umn.edu, http://www.opc.umn.edu/obesity-education/, http://www.health.umn.edu/research/research-topics/diabetes

To apply for this position, visit the University of Minnesota website at **http://www.umn.edu/ohr/employment/** and enter job number **#301596** under jobs posted "anytime."

The University of Minnesota is an Equal Opportunity Educator and Employer.

University of Minnesota Driven to Discover℠

Department of Medicine/Division of Diabetes and Endocrinology Physician-Scientist/Ph.D. (Associate Professor - Tenure Track)

The Division of Diabetes and Endocrinology at the University of Minnesota is seeking an outstanding scientist in the field of diabetes and obesity to participate in building a nationally recognized research division within a growing department. The ideal candidate will have a proven track record in extramural funding, a history of collaborative research, and experience in teaching and mentoring to allow appointment at the level of associate professor or higher. Physician scientists are urged to apply, but will have limited responsibilities in the clinical aspects of the division. Opportunities exist for joint appointments in basic science departments for candidates interested in graduate education.

Additional information about the Division can be found at http://www.dom.umn.edu/divisions/diabetes-endocrinology-and-metabolism.

Apply online at **http://www.umn.edu/ohr/employment/** and enter job number **#302569** under jobs posted "anytime." Contact Elizabeth Seaquist, Division Director, at **seaqu001@umn.edu** with additional questions.

The University of Minnesota is an Equal Opportunity Educator and Employer.

For recruitment in science, there's only one *Science*.

Special Job Focus:

Biotechnology

Issue date: May 27

Book ad by May 10 to guarantee space

Ads accepted until May 20 if space allows

Why choose this Biotechnology Focus for your advertisement?

- Relevant ads lead off the career section with special biotechnology banner
- Bonus distributions:
  - BIO, June 6–9, San Francisco, CA
  - BIO Career Fair, June 9, San Francisco, CA.

Produced by the *Science*/AAAS Custom Publishing Office.

SCIENCECAREERS.ORG

Science Careers AAAS

To book your ad: **advertise@sciencecareers.org**

The Americas
202 326 6582

Europe/RoW
+44 (0) 1223 326500

Japan
+81 3 3219 5777

China/Korea/Singapore/Taiwan
+86 186 0082 9345

MANCHESTER 1824
The University of Manchester

Faculty of Life Sciences

Research Associate in Macrophage Biology

£30,738 to £37,768 per annum (Ref: LSX-08078)

Two full time postdoctoral research positions are available to investigate type 2 mediate immunity in helminth infection and tissue repair. The programme of research funded by the Wellcome Trust will focus on the Chitinase like proteins (CLPs), which are some of the most abundant proteins during type 2 mediated pathology. Two research projects will address how CLPs regulate type 2 immunity and how they mediate tissue repair. The projects will primarily use a model of nematode migration through the lung. By studying the CLP family in the context of helminth infection, we hope not only to reveal why CLPs are so abundant in situations of ill health, in both humans and animals, but make fundamental discoveries about how the immune system strikes the balance between injury, repair, suppression of inflammation and parasite control.

We are looking for enthusiastic individuals who will enjoy working in a team of researchers headed by Prof Judi Allen. You will be expected to develop and drive your own research project related to the main aims of the programme. You must have a PhD related to immunology and a track record of success. We are looking for individuals with excellent organisational skills who show initiative and work independently but also interact well as part of a team. Laboratory skills required include flow cytometry, and most standard immunological assays, as well as relevant experience with in vivo models.

The positions are available immediately and will be for two years in the first instance.

Successful candidates will be subject to pre-employment screening carried out on our behalf by a third party. The offer of employment will be dependent on the successful candidate passing that screening. Whilst you will be required to provide express consent at a later stage, by continuing with your application now you acknowledge that you are aware that such screening will take place, and agree to take part in the process.

The Faculty of Life Sciences is committed to promoting equality and diversity, including the Athena SWAN charter for promoting women's careers in STEMM subjects (science, technology, engineering, mathematics and medicine) in higher education. The School received a Silver Award in 2009 for their commitment to the representation of women in the workplace and we particularly welcome applications from women for this post. Appointment will always be made on merit. For further information, please visit http://www.wils.ls.manchester.ac.uk/athenaswanawards/.

For further information and to apply for this vacancy please visit our website http://www.manchester.ac.uk/aboutus/jobs

If you are unable to apply online please request an application form by emailing HRServices@manchester.ac.uk quoting the reference number or by calling 0161 275 4499.

Closing date: 1 June 2016.

The University of Manchester values a diverse workforce and welcomes applications from all sections of the community.

www.manchester.ac.uk/jobs

Download the *Science* Careers jobs app from Science

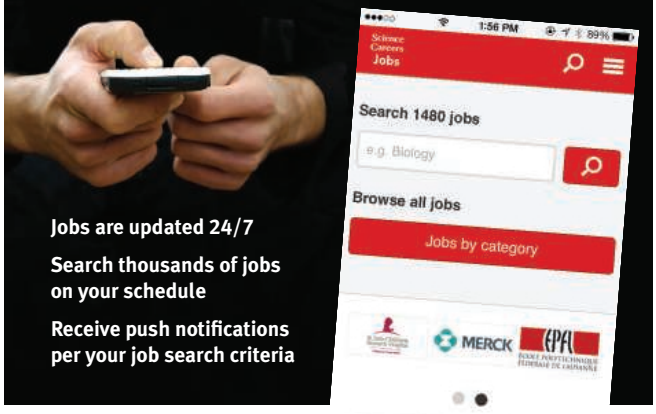

Jobs are updated 24/7

Search thousands of jobs on your schedule

Receive push notifications per your job search criteria

Get a job on the go.

Search worldwide for thousands of scientific jobs in academia, industry, and government. The application process is seamless, linking you directly to job postings from your customized push notifications.

Scan this code to download app or visit **apps.sciencemag.org** for information.

ScienceCareers FROM THE JOURNAL SCIENCE | AAAS

ScienceCareers.org

The National Academies of
SCIENCES · ENGINEERING · MEDICINE

ARL Distinguished Postdoctoral Fellowships

The Army Research Laboratory (ARL) is the nation's premier laboratory for land forces. The civilians working at ARL and its predecessors have had many successes in basic and applied research. Currently, ARL scientists and engineers are pioneering research in such areas as neuroscience, energetic materials and propulsion, electronics technologies, network sciences, virtual interfaces and synthetic environments and autonomous systems. They are leaders in modeling and simulation and have high performance computing resources on-site. They are expanding into frontier areas, including fields such as quantum information and quantum networks.

We invite outstanding young researchers to participate in this excitement as ARL Distinguished Postdoctoral Fellows. These Fellows will display extraordinary ability in scientific research and show clear promise of becoming outstanding future leaders. Candidates are expected to have already successfully tackled a major scientific or engineering problem or to have provided a new approach or insight evidenced by a recognized impact in their field. ARL offers these named Fellowships in honor of distinguished researchers and work that has been performed at Army labs.

The ARL Distinguished Postdoctoral Fellowships are three-year appointments. The annual stipend is $100,000, and the fellowship includes benefits and potential additional funding for selected proposals. Applicants must hold a Ph.D., awarded within the past three years, at the time of application. For complete application instructions and more information, visit: http://sites.nationalacademies.org/PGA/Fellowships/ARL.

Applications must be received by July 1, 2016.

ARL

By **Nathan Johnson**

The hidden perks of grad school

When I was in grad school, I couldn't wait to get out. The learning curve was distressingly steep, everyone seemed to know more than I did, and I was scraping by at just above the poverty line. That's why, after successfully convincing the university that I could graduate without being a total embarrassment, I was thrilled to take a job with a small nongovernmental organization that provides outdoor environmental education and habitat restoration activities to the local community. Just 1 year in the rat race, however, has given me a new perspective. I'm just far enough removed from graduate school to look back fondly on many of the experiences I had and to truly appreciate some of the lessons I learned.

Easy access to peer-reviewed literature is one of the biggest perks of grad school. Mining this resource was a crucial part of my first semester, when my adviser was on sabbatical and decided (wisely) that I should hold off on beginning my research until she returned. Instead, she gave me a reading list and told me to learn my way around the lab and help the other graduate students with their research so that we could hit the ground running when she got back.

This freedom to read and explore was particularly important for me because I was a business major in college and lacked much of the scientific background that the rest of my graduate school cohort had. I was determined to show that I belonged in my program, so I made a goal of reading three papers a day to catch up. By the time my adviser returned, I had read more than 100 papers and gained the knowledge and confidence I needed to design and carry out my master's research.

"I took for granted the fact that I could get my hands on just about any paper."

I took for granted the fact that I could get my hands on just about any paper I wanted. If you leave academia, there's a good chance that your access to the literature will be limited. If you have friends who are still in grad school, you can usually trade drinks for PDFs, but it's not as easy as logging on with an institutional subscription. So, if you're in school and you aren't already an avid reader, my advice is to start now.

A second privilege of being a graduate student is having the time to read in the first place. I left academia partly because I wanted to work on applying research findings to make a difference in the world. The thing I didn't acknowledge, though, is the basic principle of scarcity (I never said I was a *good* business major): The more time you spend implementing research, the less time you have to consume and digest new research in your field.

These days, I squeeze in most of my reading on evenings and weekends. It's difficult to find time during the workday to read primary literature when you're also responsible for advancing projects with lofty deliverables and tight deadlines, often on a tight budget. In academia, in contrast, many advisers value students who dedicate time to reading the literature. I wish I had more fully appreciated the culture of curiosity that academia fosters while I was part of it.

There are many perks to working outside academia, including, in my case, the incredibly rewarding and satisfying opportunity to work on projects that apply scientific knowledge to real-world problems. And there are things about grad school that I'm happy to have left behind: I despised grading papers and resented living in near poverty, and I still fundamentally disagree with the publish-or-perish mentality that drives most academics.

But there are also things unique to higher education that are pretty amazing. And although graduate school can seem endless at times, in hindsight, the time between your orientation and your thesis defense will feel like a blur. So, to those of you still in grad school, my advice is to appreciate what you have while you have it because, for better or worse, it won't last forever. ■

Nathan Johnson is an environmental program manager in Galveston, Texas. For more on life and careers, visit sciencecareers.org. Send your story to SciCareerEditor @aaas.org.

ILLUSTRATION: ROBERT NEUBECKER

Downloaded from http://science.sciencemag.org/ on April 28, 2016

Published by AAAS